UNIVERSITÉ DE LORRAINE
École Doctorale SIReNa

Centre de Recherches Pétrographiques et Géochimiques

THÈSE DE DOCTORAT DE L'UNIVERSITÉ DE LORRAINE
Spécialité : Géosciences

par

Sébastien TERNOIS

Reconstruction de la Dynamique Précoce d'un Orogène
Mise en évidence de la Transition Rifting-Collision dans le système est-pyrénéen (France) par la Géo-thermochronologie

Défendue et soutenue publiquement le 5 juillet 2019 devant le jury composé de :

Mme Eva ENKELMANN (Université de Calgary, Calgary)	Rapportrice
Mr Antonio TEIXELL (Universitat Autònoma de Barcelona, Barcelona)	Rapporteur
Mr Matthias BERNET (Université Grenoble Alpes, Grenoble)	Examinateur
Mme Charlotte FILLON (TOTAL SA, Pau)	Examinatrice
Mr Raphaël PIK (CRPG, Nancy)	Directeur
Mme Mary FORD (CRPG, Nancy)	Co-directrice
Mr Julien MERCADIER (Georessources, Nancy)	Invité
Mr Emmanuel MASINI (M&U SA, Saint-Egrêve)	Invité

CRPG-CNRS Université de Lorraine,
15, Rue Notre Dame des Pauvres 54500 VANDOEUVRE-LÈS-NANCY

UNIVERSITY OF LORRAINE
Doctoral School SIReNa

Centre de Recherches Pétrographiques et Géochimiques

PHD THESIS FROM THE UNIVERSITY OF LORRAINE
Major: Geosciences

by

Sébastien TERNOIS

Reconstruction of Early Orogen Dynamics
Geo-thermochronological Evidence of the Rift-to-Collision Transition in the Eastern Pyrenees (France)

Defended in public on July, 5th 2019 in front of the examining committee composed of:

Dr. Eva ENKELMANN (University of Calgary, Calgary)	Principal examiner
Pr. Antonio TEIXELL (Universitat Autònoma de Barcelona, Barcelona)	Principal examiner
Dr. Matthias BERNET (University of Grenoble Alpes, Grenoble)	Defense examiner
Dr. Charlotte FILLON (TOTAL SA, Pau)	Defense examiner
Dr. Raphaël PIK (CRPG, Nancy)	Supervisor
Pr. Mary FORD (CRPG, Nancy)	Co-Supervisor
Dr. Julien MERCADIER (Georessources, Nancy)	Invitee
Dr. Emmanuel MASINI (M&U SA, Saint-Egrêve)	Invitee

CRPG-CNRS Université de Lorraine,
15, Rue Notre Dame des Pauvres 54500 VANDOEUVRE-LÈS-NANCY

"Dans la vie, y'a pas de grands, y'a pas de petits. La bonne longueur pour les jambes, c'est quand les pieds touchent par terre."

Coluche

REMERCIEMENTS

À vous qui vous lancez dans la lecture de cette thèse, je vous avouerai que c'est ici que j'en termine son écriture. Je conclus donc ici, en quelques mots et quelques phrases, une aventure de trois ans (et demi) qui a filé bien plus vite que je ne l'aurais pensé.

Les premières personnes à qui je dédie mes remerciements les plus sincères et chaleureux sont mes directeurs de thèse, Raphaël Pik (directeur de thèse) et Mary Ford (co-directrice de thèse), ou "Papa" et "Maman" pour celles et ceux qui sont ouverts d'esprit. Merci à vous deux pour votre encadrement et votre pédagogie durant cette thèse. Merci à vous deux pour chacune de ces longues discussions que nous avons pu avoir, à tout moment, dans toute situation et sur n'importe quel sujet. Que ce soit à propos du nerf de la guere de cette thèse, le développement méthodologique gaz rare que je découvrais, ou au sujet de ce qui fait que l'on peut passer des heures dans un laboratoire à faire des calibrations, préparer des échantillons et les analyser, la géologie. Je ne me suis jamais senti seul et cela permet de rebondir quand il le faut. Raph, il y en aura eu des passages de ma tête à travers la porte de ton bureau pour te demander si tu avais cinq petites minutes dans ton planning de directeur de labo pour discuter de la ligne, des avancées dans les tests de calibration et dans les analyses, tout en sachant qu'on en discuterait pendant une petite voire une très grosse heure. Mary, il y en aura eu des petits états des lieux de la mise en place de la procédure analytique dans le couloir ou à la cafette du 3ème, tout en sachant qu'on finirait dans ton bureau par refaire la géologie des Pyrénées orientales. Vous avez toujours su être présents aux moments cruciaux tout en me laissant libre de collaborer avec d'autres chercheurs et d'explorer des pistes aux issues parfois plus qu'incertaines. De tout cela, j'ai vécu et je retiendrai de cette thèse une expérience scientifiquement et humainement très enrichissante.

Je tiens également à remercier sincèrement les membres du jury, Eva Enkelmann, Antonio Teixell, Matthias Bernet, Charlotte Fillon, Emmanuel Masini et Julien Mercadier, mais aussi les membres de mon comité de suivi, Cécile Gautheron et Hugh Sinclair, pour tous nos échanges scientifiques au cours de cette thèse et/ou de sa soutenance.

Je remercie toutes les personnes (encore non mentionnées) que j'ai rencontrées aux différentes réunions de projet OROGEN et S2S, en congrès ou sur le terrain. Merci à Thierry Baudin, Sylvain Calassou, Olivier Vidal, Isabelle Thinon, Frédéric Mouthereau, Laurent Jolivet, Eric Lasseur, Kerry Gallagher, Stéphanie Brichau et les bizantins Didier Marquer, Pierre Trap et Philippe Goncalves. Merci aux thésards-postdocs Constance, Nicolas, Maxime et Maxime, Juliette, Alexandre, Jessica, Riccardo et Margo (amazing collaboration!). Vous avez toujours montré de l'intérêt pour mes travaux et les discussions ont toujours été très constructives. Merci à Philippe Olivier, Bernard Laumonier et Michel de Saint Blanquat de m'avoir accompagné sur notre cher Agly et d'avoir très amicalement accepté de concilier l'ancien et le récent à de très nombreuses reprises en tout objectivité (Varisque et Crétacé, bien sûr !). Merci à Frédéric Christophoul pour les discussions et le ré-échantillonnage à distance (elles sont sacrément belles ces deux boites métalliques rouges !).

Je remercie Bouchaïb Tibari de la plateforme Gaz Rares au CRPG pour tout son jus de cerveau technique concernant la mise en place de la ligne d'extraction et de purification hélium. Merci à toi, Bouch, de m'avoir guidé au cours de mes premières analyses de datation hélium conventionnelle et d'avoir pris en main les différentes étapes de calibration et datation lorsque je n'en avais pas ou plus la possibilité. Notre duo était quand même plutôt pas mal, je trouve ! Merci également à Laurent Zimmermann pour son aide, ses conseils et sa formation à la mesure de volume (dilution et ablation). Je remercie Julien Mercadier (dit aussi "Le Merca") du laboratoire Géoressources pour son expertise technique de l'ICP-MS et sa personnalité. Merci à toi pour ta patience et ton aide certaine à obtenir des données robustes malgré les différentes embuches. Je remercie également Florimonde Lebel de l'Institut Jean Lamour pour sa collaboration dans l'estimation de mes petits volumes d'ablation par microscopie confocale. Merci pour ta confiance et ta sympathie. Enfin, merci à vous deux d'avoir toujours accepté de m'aménager des créneaux horaires particuliers pour que je puisse concilier toutes les étapes de mon protocole, à cheval sur trois laboratoires différents et avec des délais parfois incompressibles. Merci également à Chantal Peiffert et Guillaume Geandier pour votre aide.

Puis vient le CRPG dans son ensemble. Avant d'être un laboratoire gadget dans lequel on peut rentrer sur présentation de son empreinte digitale (en vrai, c'est génial !), c'est un laboratoire où il fait bon vivre pour travailler. Bon vivre d'un point de vue infrastructure et logistique : merci Bruno et Yannick. Bon vivre d'un point de vue gérance administrative quand bien même on aurait deux pieds tantôt gauches tantôt droits suivant la tâche à réaliser : merci Aurélie, Cati, Isabelle, Corinne et Joëlle, pour l'aiguillage du train qui déraille souvent dans les dédales de l'administration, pour votre savoir-faire et votre efficacité redoutable. Enfin, bon vivre d'un point de vue dépannage de matériel et entraide : merci Pierre, Nordine, Delphine, Manu, Abdallah.

Puis revient le CRPG, de manière plus spécifique. Merci à l'équipe des géologues perdus parmi tous ces géochimistes parfois cosmo. Merci Julien (CRPG et en dehors: TDs Géologie Structurale et encadrement terrain des étudiants avec Yann), Jérôme (j'utilise toujours ton expression "tir de chevrotine"), Gianluca et Armin (mes deux postdocs OROGEN). Merci à mes prédécesseurs Paul (alias "mon Paulo", tu le sais déjà !) et Arjan pour vos conseils et votre transmission d'expérience. Merci à mon homonyme co-bureau/même promo doctorante Seb (alias "Small Seb" !) pour toutes ces discussions qui continueront car elles continuent déjà. Merci à mes successeurs pour toute leur aide, psychologique et professionnelle, Antoine (alias "mon Poulet") et Julien (alias "(mon) petit Juju", tu le sais déjà toi aussi !). Des mercis en vrac reviennent également aux doctorants-postdoctorants sans qui ce serait radicalement très différent (Lionel et Nina les co-bureaux, Cécile qui me donne ses restes pour ne pas gâcher, Marion le sourire, Delphine du chnord encore plus chnord, Valentin dit "Vincent", Julien dit "Jazote", Matthis, Matthieu, David, Guillaume le Spring Box, Imène et Appoline les patronnes, Ruben et Camille Cam-Cam ; et les ancien.ne.s Precilia, Léa, Romain, Yumi, Gaëlle, Rémi D., Jesse et Christine). Merci à Christophe et aux ami.e.s du SARM, ça fait du bien de faire

des pauses avec vous. Merci aussi à la quadruplette François (avec trois, c'est difficile donc je me dis qu'avec une en plus...), Gaston (l'esprit sage), Karine (la tâquinerie) et Pierre (alias "le Pierrot joyeux") pour leur sympathie, leur conseils, le café matinal ou la fin de journée. Et puis il y a le dernier merci en vrac, celui à ma fillotte qui me supporte depuis l'école d'ingé (en même temps, t'as choisi de faire une thèse aussi hein !), Marine. À vous tou.te.s, merci pour votre amitié au quotidien et merci de m'avoir supporté.

Je terminerai ici en remerciant mes proches. La famille pour le soutien dans tout et notamment dans chacun de mes choix (impression de ce manuscrit aux rapporteurs et soutenance incluses). Les amis extérieurs pour un peu tout et rien (Florian H., Claire B. dite "Boss", Julien R. dit "Poussin", Marianne T., Sophie A., Charles, Nico, Fabrice, Tim et Coco). Et puis toi, qui malgré tout et notamment la distance, me supporte et m'attend depuis un certain Crozon. Merci du fond du coeur.

À mes soeurs

RÉSUMÉ

Les orogènes collisionnels sont classiquement décrits comme le résultat de l'accrétion continentale de marges proximales. Cette accrétion conduit à la surrection des reliefs et à l'export important de produits d'érosion dans les bassins d'avant-pays qui les jalonnent. Dans ce schéma géodynamique sont alors uniquement considérés les domaines pré-orogéniques les moins déformés. Pourtant, un nombre croissant d'évidences géologiques de terrain indiquent la conservation voire la réutilisation de structures héritées de la phase extensive précédant la convergence et la collision au coeur des orogènes. À partir de l'étude géo-thermochronométrique de la bordure orientale du domaine hyper-étiré nord-pyrénéen (massif de l'Agly, Zone Nord Pyrénéenne) et de son avant-pays précoce (synclinal de Rennes-les-Bains, Bassin Aquitain), cette thèse a pour objectifs de décrire l'évolution d'une marge distale au cours des premiers stades de convergence, de quantifier les processus source-réceptacle associés et d'apporter des contraintes temporelles et paléogéographiques quant à la création des tout premiers reliefs pyrénéens issus de son inversion. Grâce à l'utilisation des multi-thermochronomètres (U-Th)/He sur zircon et apatite, deux épisodes de refroidissement sont mis en évidence dans le prisme nord-pyrénéen (Campano-Maastrichtien et Eocène), chacun d'eux synchrone d'une phase de subsidence dans le bassin d'avant-pays. J'ai ainsi pu proposer un modèle équilibré d'évolution d'une marge distale hyper-amincie par inversion de structures héritées, chevauchements de socle et sous-placage continental se matérialisant par une signature thermochronologique claire de refroidissement sans érosion au début de la convergence. L'absence d'enregistrement de refroidissement au Paléocène par l'arrêt prématuré de l'inversion précoce dans le prisme nord-pyrénéen indique l'absence significative d'érosion et la position bordière de ce prisme par rapport à un édifice déjà construit plus à l'est à cette époque. Pour caractériser cet édifice aujourd'hui disparu du fait de l'ouverture du Golfe du Lion, j'ai utilisé une approche détritique de double datation *in situ* (U-Th)/He - U/Pb sur zircon et mis en évidence une histoire de dénudation rapide pendant le Campano-Maastrichtien, caractéristique de la création d'une topographie précoce. Ce travail montre pour la première fois clairement la migration progressive de la déformation d'est en ouest par l'inversion de structures héritées au début de la convergence pyrénéenne, ce qui suggère l'existence d'un domaine ouvert à l'est à la fin de l'épisode extensif précédant la convergence. Cette étude met en avant le rôle de l'architecture des systèmes hyper-amincis dans la formation des orogènes collisionnels et confirme les liens étroits existant entre un orogène et ses bassins d'avant-pays.

ABSTRACT

Collisional orogens are classically described as the result of continental accretion of proximal margins. This accretion leads to the creation of relief and to the important export of erosional products in the directly adjacent foreland basins. In this geodynamic scheme, only the least deformed pre-orogenic domains are considered. However, a growing number of geological field evidences indicate the preservation or even the reuse of structures inherited from the rifting phase preceding convergence and collision within orogens. By conducting a geo-thermochronometric study of the easternmost, inverted hyperextended Aptian-Cenomanian rift system (Agly massif, North Pyrenean Zone) and the adjacent early retroforeland (Rennes-les-Bains syncline, Aquitaine Basin), this thesis aims to describe the evolution of a distal rifted margin during the first stages of convergence, to quantify the associated source-to-sink processes and to provide temporal and paleogeographic constraints regarding the creation of the very first Pyrenean reliefs resulting from inversion of the margin. Using the zircon and apatite (U-Th)/He multi-thermochronometers, I show that the Pyrenean retro-wedge records two clear phases of orogenic cooling, Late Campanian-Maastrichtian and Ypresian-Bartonian, which I relate to early inversion of the distal rifted margin and main collision, respectively. I have thus been able to propose a crustal-scale sequentially restored model for the tectonic and thermal transition from extension to peak orogenesis in the eastern Pyrenees, which suggests that both thrusting and underplating processes contributed to early inversion of the Aptian-Cenomanian rift system. The absence of Paleocene cooling record indicates little to no erosion of the Pyrenean retro-wedge during the Paleocene, suggesting the existence of a more easterly source area supplying early retroforeland sediments at this time. To characterize this eastern edifice, which has since been destroyed by the Oligocene-Miocene opening of the Gulf of Lion, I used *in situ* (U-Th)/He - U/Pb double dating of detrital zircons and show rapid denudation rates during early convergence, characteristic of early topographic growth. This work shows for the first time clearly the progressive migration of deformation from east to west by inversion of inherited structures at the beginning of Pyrenean convergence. This suggests the existence of an open domain to the east at the end of the rifting phase preceding convergence. This study highlights the role of the architecture of hyper-thinned systems in the formation of collisional orogens and confirms the close links between an orogen and its associated foreland basins.

RÉSUMÉ ÉTENDU

Pourquoi la Terre est-elle si fabuleuse?

La planète Terre, dont le rayon moyen est estimé à 6378 km (hypothèse de sphéricité), n'est pas une énorme boule froide qui serait composée uniquement de roches solides figées dans le temps et dans l'espace sur lesquelles nous pouvons poser le pied et marcher. Le caractère rigide (cassant) des roches n'existe que dans les 10-15 premiers kilomètres sous la surface terrestre pour lesquels on parle alors de croûte supérieure. C'est la partie la plus superficielle de la Terre, telle la pellicule externe d'un oignon. En dessous, les roches ont un comportement plus ou moins ductile, à l'image de la pâte à modeler. On distingue deux types de croûte selon qu'il s'agit d'un océan ou d'un continent : la croûte océanique ou la croûte continentale. L'enveloppe externe de la Terre (environ 100 km d'épaisseur) est morcelée en un certain nombre d'ensembles rigides, les plaques tectoniques ou lithosphériques, qui s'emboitent les unes dans les autres à l'image des pièces d'un puzzle, et dont les continents ne représentent que la partie émergée. Ces plaques, de superficie variable, bougent les unes par rapport aux autres à cause de mouvements de convection dans le manteau sur lequel elles sont "posées". À des centaines de kilomètres sous nos pieds, les conditions de pression et température sont telles que les roches acquièrent un comportement visqueux à l'échelle des temps géologiques, un peu comme du miel ou de la colle à l'échelle des temps biologiques. Par contraste de densité (en lien avec la température et la pression), certaines masses de roches, moins denses, remontent vers la surface quand d'autres, plus denses, plongent vers les profondeurs, un peu à l'image de l'eau qui chauffe dans une casserole. Ce mécanisme convectif permet à la Terre de dissiper la chaleur interne produite dans le noyau vers la surface. La partie supérieure du manteau terrestre joue alors le rôle de tapis roulant sous les plaques : c'est la (théorie de la) tectonique des plaques.

Cette théorie, résumée ci-avant de manière simple (mais non simpliste) en un nombre de mots qui dépasse de loin le nombre d'années qui nous sépare de son acceptation par l'ensemble de la communauté scientifique (50 ans; *Colloque: 50 Years of Plate Tectonics: Then, Now, and Beyond* au Collège de France, juin 2018), explique la dynamique globale de la lithosphère terrestre. Il y transparaît par essence la notion d'évolution au cours du temps. En particulier, des objets tels que les continents, les océans et certains systèmes à leurs frontières telles que les chaînes de montagne et les rides médio-océaniques, se forment (augmentation surfacique et volumique) et disparaissent (réduction) depuis la mise en place de la machinerie interne terrestre précédemment décrite. C'est ainsi que les continents tels que nous les connaissons aujourd'hui auraient autrefois formé un supercontinent, la Pangée, *de facto* impliquant l'absence des océans actuels tel que l'Océan Atlantique. Un tel cycle de dislocation d'un supercontinent en masses continentales, ou *a contrario* rassemblement de masses continentales en supercontinent, se serait répété plusieurs fois au cours de l'histoire de

la Terre (le supercontinent Rodinia, avant la Pangée, par exemple), sans pour autant se produire à période constante ni même aboutir au même résultat.

À une échelle plus locale, la nature évolutive, et non fixiste, des processus terrestres précédemment évoqués peut être décrite par un modèle d'ouverture (rifting) et de fermeture d'un océan avec formation d'une croûte océanique et d'une croûte continentale : le cycle de Wilson (Figure 0.1). Il découle donc que toute modification d'un des états crustaux de ce cycle a une conséquence sur l'état suivant. De même, il apparait que tout processus qui a lieu au cours d'une étape modifie, de manière plus ou moins marquée, l'enregistrement de l'étape qui le précède. C'est ainsi que naissent les notions d' "héritage" et de "préservation" de cet héritage. Cet héritage peut être structural (épaisseurs, failles, etc), thermique (anomalie du flux de chaleur, magmatisme) et/ou compositionnel (densité par exemple).

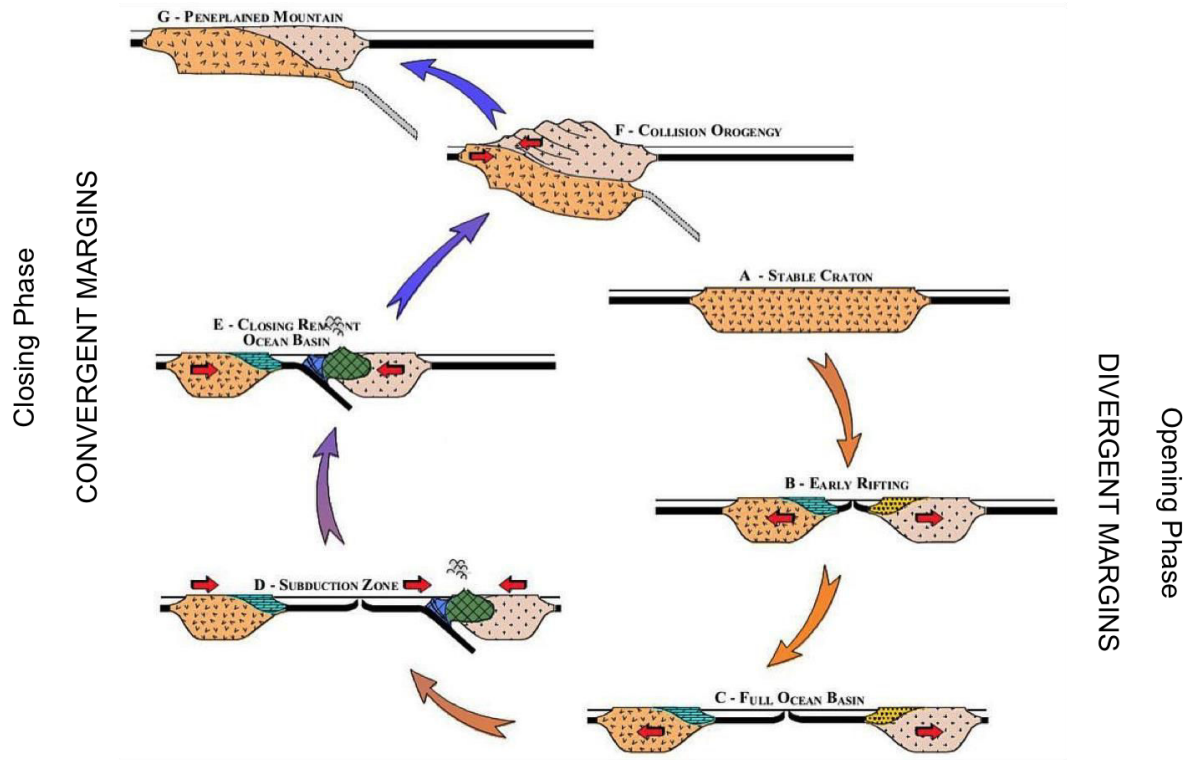

Figure 0.1: Le cycle de Wilson, ou le modèle de remaniement perpétuel et cyclique de la surface terrestre au cours des temps géologiques. Celui-ci postule l'ouverture puis la fermeture de bassins océaniques par subduction et collision continentale. Modifié d'après Fichter (2006) dans Whitmeyer et al. (2007).

Cadre de travail

Le présent travail de thèse s'inscrit dans le cadre du projet OROGEN, collaboration scientifique d'une durée de 5 ans (2016-2021) entre trois acteurs majeurs des géosciences que sont TOTAL S.A., le BRGM (Bureau de Recherches Géologiques et Minières) et l'INSU-CNRS (Institut National des Sciences de l'Univers, Centre National de la Recherche Scientifique). Ce projet tend à repousser les frontières des concepts géologiques dans des environnements de marges convergentes, chaînes de montagnes et

bassins d'avant pays. Cette thèse fut réalisée au sein du Centre de Recherches Pétrographiques et Géochimiques (CRPG), et bénéficia d'un accès instrumental à deux autres laboratoires, Georessources (collaboration avec Julien Mercadier) et l'Institut Jean Lamour (collaboration avec Florimonde Lebel). Elle fait suite à plusieurs travaux financés par l'ANR PYRAMID (responsable : Mary Ford) ayant eu pour objet d'étude le prisme nord-pyrénéen et le Bassin Aquitain.

Contexte scientifique

La mise en place d'un système orogénique (orogénèse; une chaîne de montagne et les bassins sédimentaires qui l'entourent) par rapprochement de deux plaques en contexte de subduction voire collision est une étape importante du cycle de Wilson (Wilson, 1966; Figure 0.1). Elle a d'ailleurs de tout temps intrigué, faisant naître de nombreuses hypothèses, spéculations et théories, souvent contradictoires. Avec l'avènement de la tectonique des plaques, la formation d'une chaine de montagne a fait l'objet d'un certain nombre d'études, à visée aussi bien fondamentale qu'industrielle. La compréhension actuelle de ce mécanisme, en tant que "mouvement vertical" que l'on peut observer à la surface, repose sur l'étude poussée des bassins qui entourent l'orogène, dits d' "avant-pays", et qui concentrent en leur sein les produits d'érosion de la chaine (Price, 1973 ; Beaumont, 1981 ; Jordan, 1981; Figure 0.2). Les chaines de montagne sont ainsi perçues comme des objets verticaux, qui s'élèvent et s'érodent, ce qui est somme toute assez paradoxal dès lors que l'on réalise qu'il faut mobiliser des roches sur des distances hozirontales allant de la dizaine à la centaine de kilomètres (raccourcissement) pour quelques 2 à 4 km de relief. Ces bassins se développent au front de l'orogène par flexure de la lithosphère, principallement due à la charge de matière accrétée par raccourcissement au sein de l'orogène. La flexure, en tant que réponse élastique d'un objet à une force qui lui est imposée (ici, la charge), dépend de la rigidité (modélisée comme une "épaisseur élastique") de cet objet, de la longueur d'onde des masses qui exercent la force (ici, orogène et bassins sédimentaires adjacents), et elle participe au soutien isostatique de l'orogène (Watts, 2001). On distingue le pro-système (prisme et bassin d'avant-pays) qui se développe sur la plaque inférieure (ou subduite) et le rétro-système qui se développe sur la plaque supérieure (ou chevauchante).

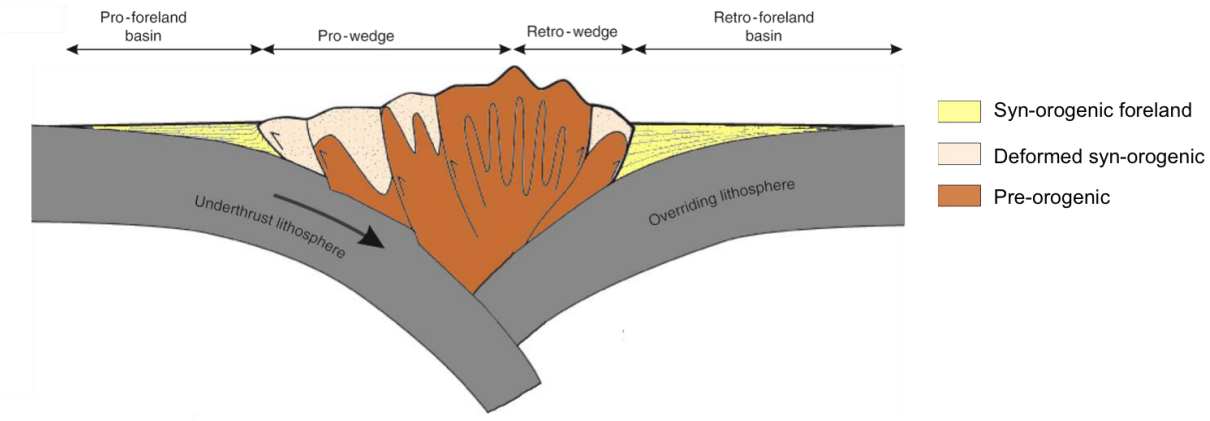

Figure 0.2: Le système orogénique typique pyrénéen. Modifié d'après Naylor et Sinclair (2008).

La formation d'un système orogénique par accrétion de matériel continental repose essentiellement sur le modèle du prisme critique de Coulomb. Ce modèle assimile le prisme d'accrétion à un tas de neige poussé par un bulldozer (Dahlen, 1990). Le bulldozer représente alors le bord rigide que joue la plaque supérieure dans l'accrétion de matériel de la plaque inférieure vers la plaque supérieure et la formation d'une chaine d'avant-pays de plissements et chevauchements. Bien que cette théorie physique se soit avérée fondamentale dans la description et la prédiction des géometries naturelles dans le pro-bassin (e.g. Taïwan, Canadian Rockies, Appalaches), elle ne permettait pas d'expliquer fidèlement l'assymétrie (la double vergence) de certains systèmes collisionnels tels que les Pyrénées (Figure 0.2). Certains auteurs adaptèrent cette théorie, analogiquement (Malavielle, 1984) puis numériquement (Willett et al., 1993), en considérant un bloc relativement rigide et fixe à la place du bord rigide convergent. De part et d'autre de ce bloc se trouvent un ensemble crustal fixe (future plaque supérieure, vitesse nulle) et un ensemble convergent (future plaque inférieure, vitesse positive). À un point de singularité caractérisé par une discontinuité dans le champ de vitesse (vitesse entre les deux ensembles, à la fois nulle et positive), l'ensemble convergent subducte sous l'ensemble fixe, générant une assymétrie du système qui dépend de l'orientation de l'ensemble plongeant. L'érosion est également invoquée comme facteur prépondérant sur les transferts de matière au sein du prisme doublement vergent, conduisant à l'exhumation des roches les plus déformées sur le versant où elle opère.

Ainsi, les orogènes collisionnels sont classiquement décrits comme le résultat de l'accrétion de marges continentales proximales, peu déformées. Cependant, parmi les régions immergées de la bordure d'un continent qui amenent aux fonds océaniques et seront impliquées dans la collision, on distingue les marges continentales proximales et les marges continentales distales. Alors que les premières constituent les zones les plus proches des continents, les moins amincies et les moins déformées, les dernières représentent les zones les plus amincies, en position intermédiaire avec la croûte océanique si celle-ci existe, et au-dessus desquelles la tranche d'eau est la plus importante. Grâce à l'acquisition continue de données et les avancées numériques permettant la modélisation et le quantification de processus complexes, de nombreux paradoxes ont récemment été mis en évidence et suggèrent que la compréhension des orogènes et des processus conduisant à leur formation nécessite de tenir compte de la géométrie complète du système au début de l'accrétion (épaisseurs, accidents tectoniques, structures). Par extension, elle nécessite de tenir compte de l'évolution de la rigidité des plaques au cours du temps. Au cours de chaque étape du cycle de Wilson, une plaque voit son épaisseur varier. S'agissant de la croûte continentale, l'épaisseur diminue durant l'ouverture conduisant à la formation d'un océan mais augmente durant la fermeture et l'accrétion de matériel. S'agissant de la croûte océanique, l'épaisseur varie au cours de sa production et est par nature faible (10 km) comparée à une croûte continentale normale (30 km). Une plaque lithosphérique voit également sa composition changer. La croûte océanique formée durant l'ouverture est plus dense que la croûte continentale. La croûte continentale peut avoir été affectée par le magmatisme au cours

d'un épisode subductif ou collisionnel ancien, voire du métamorphisme. Ainsi, tout modèle qui considère l'épaisseur élastique d'une plaque comme constante ne prend pas non plus en compte les propriétés thermo-mécaniques de cette plaque. Comment les marges évoluent-elles au cours de l'orogenèse ? En particulier, que deviennent les marges distales ? Quel est l'impact de l'héritage (structural, thermique, compositionnel) sur la formation d'un système orogénique (taux de raccourcissement, distribution du raccourcissement) ?

L'accrétion continentale conduit à la surrection des reliefs et à l'export de produits d'érosion dans les bassins d'avant-pays qui les jalonnent. Cependant, les modèles de développement des bassins d'avant-pays et de construction orogénique, bien qu'incluant les couplages tectonique-érosion-incorporation, ont été essentiellement basés sur l'observation des pro-systèmes. Ce n'est que récemment que l'assymétrie des prismes doublement vergent a conduit à réaliser que chacun des bassins flexuraux enregistre sa propre histoire flexurale (Naylor and Sinclair, 2008; Sinclair and Naylor, 2012). Du fait du plongement de la plaque inférieure sous la plaque supérieure, les structures et sédiments pré- et syn-orogéniques (les témoins des évènements antérieurs à et synchrones de l'orogenèse) dans le pro-système sont progressivement intégrés dans le prisme orogénique. *A contrario*, les vestiges de toute histoire passée sont mieux préservés dans le retro-système, relativement statique sur la plaque chevauchante. De par l'observation du pro-système, les modèles décrivant les relations entre érosion du prisme et sédimentation dans le bassin ont donc été essentiellement focalisés sur l'histoire tardive de l'orogène, en particulier lorsque celui-ci est déjà en place, lorsque la collision a déjà débuté et lorsque l'export sédimentaire est important. Qu'en est-il de la croissance orogénique précoce, au début de l'orogenèse ? Quels sont les processus qui conduisent à mettre en place les premiers reliefs d'une chaine de montagne ? Comment sont-ils distribués ? Quelle est la réponse sédimentaire à la mise en place d'une topographie orogénique précoce ?

Objectif et cas d'étude

Cette thèse a pour objectif principal de caractériser la transition rifting-collision en s'intéressant aux processus de croissance orogénique précoce et en mettant en évidence les liens existants entre héritage extensif et initiation de la topographie orogénique. Pour cela, il convient de trouver l'objet d'étude approprié : l'orogène pyrénéen.

Les Pyrénées sont une chaine de montagnes engendrée par la convergence des plaques européenne et ibérique de la fin du Santonien (84 Ma) jusqu'au Miocène moyen (âge débattu). On distingue le rétro-système d'avant-pays au Nord, la Zone Nord Pyrénéenne et le Bassin Aquitain (Sud-Ouest de la France), et le pro-système d'avant-pays au Sud, la Zone Sud Pyrénéenne et le Bassin de l'Ebre (Espagne). L'orogène collisionnel pyrénéen se met en place dans une région fortement impactée par les évènements antérieurs tels que l'orogenèse varisque (Carbonifère supérieur, ~300-330 Ma), le rifting triassique-jurassique et le rifting majeur qui débute à l'Aptien tardif et se termine au Cenomanien (114-97 Ma). Durant ce dernier épisode extensif, avorté avant la

production de croûte océanique (Figure 0.3), la croûte continentale fut fortement amincie, résultant en l'exhumation du manteau sous-continental et un métamorphisme régional de haute température-basse pression. La convergence commença donc environ 10 Ma après la fin du rifting, impliquant mécaniquement une lithosphère qui n'a pas atteint son état d'équilibre thermique.

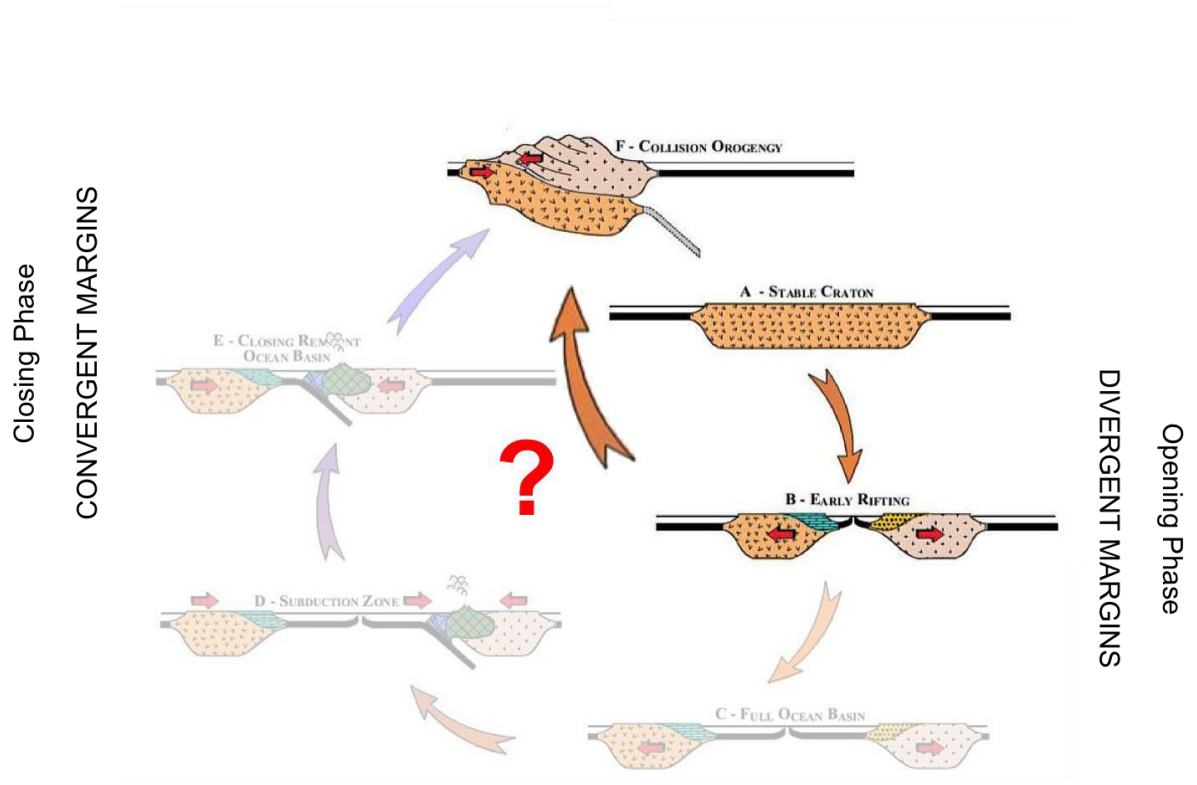

Figure 0.3: Problématique de la thèse, ou qu'advient-il d'un système qui n'a pas atteint le ré-équilibrage thermique lorsque celui-ci est inversé précocément (fermeture précoce d'un bassin (océanique ?) au regard du cycle de Wilson complet). Modifié d'après Fichter (2006) dans Whitmeyer et al. (2007).

Les Pyrénées présentent l'avantage d'un orogène collisionnel sans subduction océanique ni processus magmatique et métamorphique associés à la collision. Du fait d'une quantité de raccourcissement relativement faible pour un orogène collisionnel, l'enregistrement sédimentaire pré- et syn-orogénique est exceptionnelement bien conservé. En particulier, la Zone Nord Pyrénéenne préserve le domaine de rift aptien-cenomanien, bien qu'inversé durant la compression. Le rétro-système d'avant-pays nord-pyrénéen représente donc un excellent laboratoire naturel pour étudier la transition rifting-collision dans un orogène.

Les grandes questions abordées au cours de cette thèse sont :

- L'orogenèse précoce a-t-elle une signature thermique distinguable de l'anomalie thermique engendrée par l'épisode extensif antérieur ?
- Comment une marge distale (hyper-) amincie est-elle incorporée dans le prisme d'accrétion continentale au début de la convergence ?

- L'héritage thermique et structural joue-t-il un rôle dans la structuration d'un orogène collisionnel ?
- Quelles sont la réponse sédimentaire et la contribution de la topographie dynamique sur les couloirs sédimentaires ?

Plus spécifiquement à la région d'étude pyrénéenne :

- Quand l'orogène précoce pyrénéen se met-il en place et comment évolue-t-il ?
- Quand et où la topographie se met-elle en place ? Y a-t-il un diachronisme temporel et spatial de mise en place ?
- Où se situe la source sédimentaire au début de l'orogénèse pyrénéenne ? Est-elle unique ou multiple ? Est-ce l'édifice orogènique précoce ?

Pour répondre à ces questions qui mettent en jeu des mouvements tectoniques et le régime thermique de la croûte, il convient d'utiliser un outil d'investigation sensible à ces processus : la géo-thermochronologie. La thermochronologie basse température (U-Th)/He sur zircon peut être appliquée sur des roches en place tout comme dans les sédiments pour retracer l'histoire thermique des zircons qui les composent. Dans le dernier cas, néanmoins, ceci nécessite l'acquisition d'une importante quantité de données en vue de représenter statistiquement la ou les source(s) de ces sédiments. Il en est de même pour la géochronologie U/Pb sur zircon qui s'avère être un outil indispensable pour le traçage de source. Conduites sur les mêmes grains, ces deux méthodes de datation permettent alors de reconstruire précisément l'histoire des sources sédimentaires. Cependant, les protocoles analytiques couramment utilisés en thermochronologie (U-Th)/He sur zircon avec dissolution des grains (datation conventionnelle) sont longs et fastidieux à mettre en oeuvre, ce qui contraint fortement la quantité de données pouvant être produite en un temps de recherche raisonnable. Compte tenue de l'inadéquation entre ces protocoles et l'étude de processus orogéniques nécessitant une documentation extensive, une méthodologie de double datation géo-thermochronologique par ablation laser *in situ* au coeur des grains a été mise en place et développée au sein de la plateforme de recherche Gaz Rares du CRPG. Cette méthodologie a déjà été proposée dans la littérature (Tripathy-Lang et al., 2013; Horne et al., 2016) mais n'a, à ce jour, que peu été appliquée sur des objets géologiques en raison de l'information particulière qu'elle fournit. Essentiellement, dater en thermochronologie basse température un grain au coeur revient en effet à ne dater que l'épisode de refroidissement majeur, parfois ancien, qui a affecté ce grain. En appliquant cette méthodologie dans les Pyrénées, où deux évènements majeurs se succèdent en moins de 30 Ma (rifting et convergence), l'enjeu est alors double. D'une part, il s'agit de voir si le thermochronomètre (U-Th)/He sur zircon enregistre distinctement ces deux évènements tectoniques et thermiques. D'autre part, il s'agit de voir si le caractère partiel de l'information obtenue par ablation laser ne va pas à l'encontre d'une meilleure représentation et identification des souces sédimentaires.

Organisation du mémoire

Ce manuscrit est divisé en 7 chapitres et un corpus d'annexes, entièrement écrits en anglais.

Le premier chapitre (Chapter 1) est un chapitre d'introduction générale, présentant les grandes questions traitées dans ces travaux de thèse.

Le deuxième chapitre (Chapter 2) présente une synthèse des concepts et travaux relatifs aux systèmes flexuraux d'avant-pays, incluant les modèles de développement d'un prisme d'accrétion et des bassins d'avant-pays.

Le troisième chapitre (Chapter 3) comprend une présentation du système pyrénéen dans sa globalité, allant de la description des principales zones tectono-sédimentaires à la synthèse des données de thermochronologie basse température, tout en évoquant les modèles géodynamiques grande échelle proposés.

Le quatrième chapitre (Chapter 4) représente le socle de ce manuscrit : le chapitre analytique et méthodologique. Il est consacré à la présentation exhaustive (i) des méthodes d'analyses mises en place au laboratoire et utilisées durant cette thèse, et (ii) des méthodes de traitement statistique utilisées durant cette thèse. Il cristallise les concepts, justifie les avantages et utilisations, et présente les limitations de ces méthodes.

Le cinquième chapitre (Chapter 5) présente le premier chantier mené au cours de cette thèse : la reconstruction de l'histoire tectono-thermique d'une marge considérée comme la marge la plus distale aujourd'hui préservée du système orogénique pyrénéen (la marge nord-pyrénéenne, Agly-Salvezines), au moyen de la thermochronologie basse température (U-Th)/He sur zircon et apatite. Ce travail propose une réponse aux questions 1, 2, 3, 5 et 6, évoquées précédemment. Il a fait l'objet d'une publication dans la revue Tectonics.

Le sixième chapitre (Chapter 6) présente le deuxième chantier mené au cours de cette thèse : l'étude de l'enregistrement sédimentaire du rétro-bassin d'avant-pays quant à la mise en place des tout premiers reliefs pyrénéens, au moyen de la technique de double datation *in situ* (U-Th)/He et U/Pb sur zircon détritique. Ce travail propose une réponse aux questions 3, 4, 5, 6, et 7, évoquées précédemment. Il représente un article en préparation.

Le septième chapitre (Chapter 7) est consacré aux conclusions et perspectives de cette thèse.

Apports scientifiques

Une meilleure compréhension d'un système, quel qu'il soit, nécessite une étude des intéractions temporelles et spatiales qu'il possède avec d'autres. Dans le cas d'un système orogénique collisionnel, l'intervalle considéré dans cette thèse est la transition rifting-collision. En particulier, cette thèse vise à étudier les processus gouvernant la mise en place d'un orogène depuis l’extension jusqu’à la collision, afin d'apporter des

réponses aux questions suivantes : (1) L'orogenèse précoce a-t-elle une signature thermique distinguable de l'anomalie thermique engendrée par l'épisode extensif antérieur ? (2) Comment une marge distale (hyper-) amincie est-elle incorporée dans le prisme d'accrétion continentale au début de la convergence ? (3) L'héritage thermique et structural joue-t-il un rôle dans la structuration d'un orogène collisionnel ? (4) Quelles sont la réponse sédimentaire et la contribution de la topographie dynamique sur les couloirs sédimentaires ?

En vue de répondre à ces problématiques, une attention particulière fut portée au rétro-système d'avant-pays nord-pyrénéen. Un tel système s'est développé sur la plaque européenne de la fin du Santonian (84 Ma) au Miocène moyen. Le rétro-prisme orogénique (Zone Nord Pyrénéenne) s'est formé en lieu et place d'un ancien système de rift d'âge Aptien-Cenomanien (114-97 Ma) où la croûte continentale fut fortement amincie et le manteau sous-continental exhumé. Seuls 10 Ma séparent la fin du rifting et le début de la convergence, si bien que la lithosphère impliquée dans la convergence n'a pas atteint son état d'équilibre thermique. Dans un premier temps, il convient donc de caractériser l'évolution thermique d'une marge distale hyper-amincie de sa formation jusqu'à son inversion dans le système collisionnel (Chapter 5). Dans un second temps, il s'agit d'étudier le couplage tectonique-érosion existant entre le prisme orogénique et les bassins d'avant-pays précoces (Chapter 6).

La première étude de cette thèse (Chapter 5, questions 1, 2 et 3) a porté sur la reconstruction de l'histoire thermique et structurale du massif nord-pyrénéen de l'Agly-Salvezines en utilisant une approche combinée de thermochronologie basse température (U-Th)/He sur deux phases minérales que sont le zircon et l'apatite. La gamme de sensibilité thermique de ces deux thermochronomètres permet d'investiguer des mouvements verticaux dans une portion de croûte comprise entre 45 et 250 °C. Le massif de l'Agly-Salvezines appartient à la Zone Nord Pyrénéenne et se situe entre deux domaines sédimentaires affectés par le métamorphisme haute température-basse pression (250-600 °C) qui s'est développé lors de la phase de rifting aptien-cenomanien. Ainsi, ce massif est classiquement représenté comme la marge continentale distale européenne du système de rift aptien-cénomanien qui a été inversée lors de la convergence. Les datations obtenues par la méthode conventionnelle de dissolution des grains sur 17 échantillons de socle, et les modélisations numériques inverse et forward, révèlent deux périodes de refroidissement rapide du massif, chacune mise en évidence par l'un des deux thermochronomètres utilisés. La première, mise en évidence par le thermochronomètre (U-Th)/He sur zircon, se déroule entre le Campanien et le Maastrichtien (*ca.* 80-66 Ma) et caractérise l'orogenèse précoce. La seconde, mise en évidence par le thermochronomètre (U-Th)/He sur apatite, a lieu entre l'Yprésien et le Bartonien (*ca.* 55-45 Ma) et correspond à la collision pyrénéenne. Aucune évidence de refroidissement n'est enregistrée entre ces deux périodes, ce qui traduit des conditions thermiques globalement stables rappellant la quiscence tectonique enregistrée ailleurs dans le bassin d'avant-pays. Par ailleurs, un signal thermochronologique basse température d'âge Crétacé inférieur a également été décelé par le thermochronomètre

(U-Th)/He sur zircon. Bien que les modélisations numériques entreprises dans cette étude ne permettent pas de conclure quant à la signification de ce signal (complexité des processus de diffusion et d'endommagement dans le zircon), une récente étude de thermochronologie moyenne température a mis en évidence son lien avec le rifting et/ou post-rift. Sur la base de ces datations, d'observations et de données géologiques de terrain, mais aussi de la littérature, un modèle équilibré d'évolution de la marge distale européenne a été proposé. Celui-ci montre l'inversion vers le Nord de la marge distale dès les premiers stades de la convergence (Campanien-Maastrichtien). En absence d'érosion à cette époque, la relaxation thermique ne peut se faire que par chevauchement du domaine distal sur le domaine proximal, moins aminci et plus froid. Le raccourcissement diminue fortement durant le Paléocène et les roches datées restent à une profondeur de *ca.* 2 km. Au début de l'Eocène, la convergence a repris et la marge distale est de nouveau raccourcie avant que la déformation ne se propage plus au Nord dans l'avant-pays. Cette reconstruction thermo-tectonique de la marge distale européenne montre ainsi une inversion en deux temps de la marge et l'absence des roches profondes de socle à l'érosion à la fin de l'orogenèse précoce dans les Pyrénées Orientales actuelles. Les reliefs formés dans cette région ne furent pas importants au début de la convergence.

La seconde étude de cette thèse (Chapter 6, questions 1, 3 et 4) a porté sur la reconstruction de l'histoire thermique et structurale de l'édifice orogénique encore plus précoce que celui identifié précédemment. En vue d'étudier un édifice maintenant probablement disparu du fait de l'ouverture du Golfe du Lion pendant l'Oligo-Miocène, une approche de thermochronologie basse température détritique sur zircon a été utilisée et un échantillonage des dépôts pré- et syn-orogéniques a été mené dans le rétro-bassin d'avant-pays (région de Rennes-les-Bains/Couiza, Bassin Aquitain). De manière à identifier précisément la signature de l'édifice orogénique précoce (thermique et spatiale), l'approche de thermochronologie basse température détritique a été combinée à une approche de géochronologie U/Pb détritique sur zircon, sur les mêmes grains (concept de double datation). Compte tenue de l'inadéquation entre les méthodes couramment utilisées en thermochronologie (U-Th)/He sur zircon et les objectifs de cette étude, une méthode de double datation géo-thermochronologique par ablation laser *in situ* a été mise en place et développée au sein de la plateforme de recherche Gaz Rares du CRPG, en collaboration avec deux autres laboratoires que sont Georessources et l'Institut Jean Lamour. Les instruments, le protocole analytique et les conditions d'analyses ont été testés, calibrés et optimisés pour une utilisation en routine dans cette étude. Les doubles datations obtenues par la méthode nouvellement installée au CRPG sur 5 échantillons détritiques pré- à syn-orogéniques (Turonien au Campanien basal) révèlent l'existence d'un haut topographique au début de la convergence, néanmoins hérité d'une phase antérieure à la convergence. La signature géo-thermochronologique de ce haut topographique est similaire à celle de la Sardaigne à l'actuel, et semble pointer cette région comme une source probable des sédiments déposés entre le Turonien et le Campanien inférieur sur la marge proximale européenne. Les doubles datations obtenues sur 5 autres échantillons détritiques syn-

orogéniques (Maastrichtien moyen à Yprésien inférieur) mettent en évidence la dualité thermochronologique existant entre les signaux de refroidissement liés au rifting aptien-cenomanien et à l'orogenèse précoce campano-maastrichtienne : à partir du Maastrichtien inférieur, les deux signaux sont transfèrés dans le bassin et en grande partie portés par des grains typiques des granites varisques pyrénéens. D'une part, ceci traduit l'exhumation de roches crustales profondes (connues entre 5 et 10 km de profondeur) ayant enregistré à la fois un évènement thermique majeur de rifting aptien-cenomanien et un évènement thermique majeur lié à l'orogenèse précoce (faible et fort eU, 140-160 °C). D'autre part, ceci indique un transfert de matériel érodé très rapide de la source vers le bassin (10 Ma) au cours de l'orogenèse précoce, suggérant des taux d'exhumation moyens proches de 500 m/Ma au début de l'orogenèse. Plusieurs fluctuations dans le signal géochronologique sont enregistrées, et favorisent un scénario de migration de l'exhumation vers l'ouest au cours de l'orogenèse précoce et au début de la collision. Ce type de migration est cohérent avec les résultats obtenus par d'autres équipes sur le versant sud des Pyrénées. Là aussi, de nombreuses études de double datation détritique ont été menées de manière extensive, avant et pendant ce travail de thèse (par exemple Odlum et al., 2019; Thomson et al., 2019). En revanche, elles ont toujours utilisé la méthode conventionnelle de dissolution des grains pour l'(U-Th)/He sur zircon, limitant ainsi l'information géologique sur une vingtaine de grains. Ces études révèlent un changement majeur de source au début de la collision (Yprésien), l'apport sédimentaire passant alors d'une source type Massif de l'Ebro-Sardaigne-Corse au sud et à l'est vers une source type Pyrénées au nord. L'enregistrement de l'orogenèse précoce dans les sédiments maastrichtiens-paléocènes dans le pro-bassin d'avant-pays est présent mais fortement dilué par la signature des zones d'apport déjà présentes dans le paysage à cette époque. Les passages d'apports sédimentaires parallèles à transerves au nord et au sud semblent relativement synchrones

En mettant en évidence la dualité thermochronologique existant entre les signaux de refroidissement liés au rifting et à l'orogenèse précoce et en proposant une migration progressive de l'exhumation vers l'ouest au cours de l'orogenèse précoce et au début de la collision sur la base des double datations, cette thèse montre le rôle fondamental de l'héritage thermique et structural de la lithosphère dans la croissance orogénique au début de la convergence. Dans les Pyrénées, cet héritage extensif ancien, voire peut-être même pré-extensif (Varisque par exemple) influence l'épisode suivant en conditionnant et localisant préférentiellement la déformation compressive dans les zones de faiblesse rhéologique. Il apparait que l'édice orogénique précoce et le domaine de rift aptien-cenomanien continuaient à l'est, dans la région où se trouve maintenant le Golfe du Lion. Grâce à la géo-thermochronologie détritique et *in situ*, cette thèse apporte des contraintes temporelles, thermiques, structurales et spatiales quant au calendrier de l'inversion, à la distribution du raccourcissement précoce et à la localisation des zones en érosion au début de la convergence pyrénéenne.

Pour aller plus loin dans le futur et confirmer/préciser les conclusions de ces travaux de thèse :

- Appliquer d'autres outils de traçage de source sur les échantillons détritiques double datés en (U-Th)/He et U/Pb sur zircon : minéraux lourds et U/Pb sur rutile pour mieux contraindre la provenance des sédiments ;
- Documenter en (U-Th)/He sur zircon (et U/Pb sur rutile) les régions telles que la Corse, la Sardaigne, le Massif du Mouthoumet et le Massif Central, pour lesquelles aucune donnée de ce type n'existe, empêchant de mieux contraindre la provenance des sédiments ;
- Densifier l'échantillonnage dans les sédiments paléocenes pour préciser le calendrier de la quiscience tectonique enregistrée plus à l'est dans l'orogène précoce Lion-Pyrénées : y a-t-il un diachronisme E-W relatif à la reprise de la convergence et le début de la collision continentale dans les Pyrénées ?
- Comparer le système pyrénéen avec un système (hyper-) étendu non inversé pour mieux caractériser l'héritage thermique, structural et compositionnel d'une marge distale (hyper-) amincie.

D'un point de vue méthodologique, cette thèse montre le potentiel de la thermochronologie (U-Th)/He sur zircon, seule ou combinée avec d'autres approches de datation. Le caractère multi-thermochronomètrique de ce type de datation permet un enregistrement, certes complexe, mais continue de l'histoire de refroidissement d'une roche à travers diverses isothermes. Bien que les modèles de diffusion et d'endommagement disponibles pour le zircon ne permettent pas, à l'heure actuelle, d'utiliser ce thermochronomètre dans l'estimation précise de taux d'exhumation ou de vitesse de refroidissement, il s'avère capable de différencier des évènements thermiques majeurs sur des échelles de temps inaccessibles à d'autres méthodes telles que les traces de fission. Grâce à la technique de datation *in situ* par ablation laser, cet effet est même renforcé et bénéficie d'une relative facilitée d'échantillonnage et d'analyse.

Suite à ces résultats prometteurs, deux pistes principales sont envisagées :

- Continuer le développement de la multi-datation sur zircon en pratiquant d'abord la datation en traces de fission puis la double datation (U-Th)/He - U/Pb (ceci a été commencé durant la thèse mais abandonné en raison d'un manque de précision analytique évoqué dans le Chapter 4) ;
- Concevoir une approche statistique adaptée au système (U-Th)/He sur zircon (et à la multi-datation en général) dans l'interprétation de données détritiques.

Références

Beaumont, C. (1981). Foreland basins. Geophysical Journal International, 65(2), 291–329. https://doi.org/10.1111/j.1365-246X.1981.tb02715.x

Dahlen, F. A. (1990). Critical taper model of fold-and-thrust belts and accretionary wedges. Annual Review of Earth and Planetary Sciences, 18, 55.

Horne, A. M., van Soest, M. C., Hodges, K. V., Tripathy-Lang, A., & Hourigan, J. K. (2016). Integrated single crystal laser ablation U/Pb and (U–Th)/He dating of detrital accessory minerals – Proof-of-concept studies of titanites and zircons from the Fish Canyon tuff. Geochimica et Cosmochimica Acta, 178, 106–123. https://doi.org/10.1016/j.gca.2015.11.044

Jordan, T. E. (1981). Thrust loads and foreland basin evolution, Cretaceous, western United States. AAPG Bulletin, 65(12), 2506–2520.

Malavieille, J. (1984). Modélisation expérimentale des chevauchements imbriqués: application aux chaînes de montagnes. Retrieved from http://geoscienceworld.org/highwire/filestream/458370/ field_highwire_a_download_vars/0/ 129.full.pdf

Naylor, M., & Sinclair, H. D. (2008). Pro- vs. retro-foreland basins: Pro- vs. retro-foreland basins. Basin Research, 20(3), 285–303. https://doi.org/10.1111/j.1365-2117.2008.00366.x

Odlum, M. L., Stockli, D. F., Capaldi, T. N., Thomson, K. D., Clark, J., Puigdefàbregas, C., & Fildani, A. (2019). Tectonic and sediment provenance evolution of the South Eastern Pyrenean foreland basins during rift margin inversion and orogenic uplift. Tectonophysics, S0040195119301921. https://doi.org/10.1016/j.tecto.2019.05.008

Price, R. A. (1973). Large-scale gravitational flow of supracrustal rocks, southern Canadian Rockies. Gravity and Tectonics, 491–502.

Sinclair, H. D., & Naylor, M. (2012). Foreland basin subsidence driven by topographic growth versus plate subduction. Geological Society of America Bulletin, 124(3–4), 368–379.

Thomson, K. D., Stockli, D. F., Odlum, M. L., Tolentino, P., Puigdefàbregas, C., Clark, J., & Fildani, A. (2019). Sediment provenance and routing evolution in the Late Cretaceous–Eocene Ager Basin, south-central Pyrenees, Spain. Basin Research, 0(0). https://doi.org/10.1111/bre.12376

Tripathy-Lang, A., Hodges, K. V., Monteleone, B. D., & van Soest, M. C. (2013). Laser (U-Th)/He thermochronology of detrital zircons as a tool for studying surface processes in modern catchments: Detrital zircon thermochronology. Journal of Geophysical Research: Earth Surface, 118(3), 1333–1341. https://doi.org/10.1002/jgrf.20091

Watts, A. B. (2001). Isostasy and Flexure of the Lithosphere. Cambridge University Press.

Willett, S., Beaumont, C., & Fullsack, P. (1993). Mechanical model for the tectonics of doubly vergent compressional orogens. Geology, 21(4), 371–374.

Wilson, J. T. (1966). Did the Atlantic Close and then Re-Open? Nature, 211(5050), 676–681. https://doi.org/10.1038/211676a0

Whitmeyer, S. J., Fichter, L. S., & Pyle, E. J. (2007). New directions in Wilson Cycle concepts: Supercontinent and tectonic rock cycles. Geosphere, 3(6), 511–526

GENERAL TABLE OF CONTENTS

First Part

Introduction and Background

Chapter 1
I. General Introduction

I.1 Framework

The present thesis is part of the OROGEN project, a 5-year scientific collaboration (2016-2021) between three major geoscience players such as TOTAL S.A., the BRGM (Bureau of Geological and Mining Research) and the INSU-CNRS (National Institute of Sciences of the Universe, National Center for Scientific Research). This project tends to push the boundaries of geological concepts in environments of convergent margins, mountain ranges and foreland basins. This thesis was carried out at the Center for Petrographical and Geochemical Research (CRPG), and benefited from instrumental access to two other laboratories, Georessources (collaboration with Julien Mercadier) and the Jean Lamour Institute (collaboration with Florimonde Lebel). It follows several works funded by the ANR PYRAMID (responsible: Mary Ford) that studied the North Pyrenean retro-wedge and the Aquitaine retro-foreland basin.

I.2 Scientific context

In the classic Wilson plate-tectonic cycle, plate convergence and orogenesis follow plate divergence. With the advent of plate tectonics, the formation of a mountain range has been the subject of a number of studies, both fundamental and industrial. Our current understanding of this mechanism, as a "vertical movement" that can be observed on the surface of the Earth, is based on the extensive study of the basins surrounding the orogen, known as "foreland basins" (Price, 1973, Beaumont, 1981, Jordan, 1981). Mountain ranges are thus perceived as vertical objects that uplift and erode, which is quite paradoxical when we realize that we need to move rocks over distances ranging from tens to hundreds kilometers (shortening) for some 2 to 4 km of relief. These basins develop at the front of the orogen by flexure of the lithosphere, mainly due to the charge of the forming orogen. We distinguish the pro- and retro-system (wedge and foreland basin) that develop on the lower and upper plate, respectively.

The formation of an orogenic system by accretion of continental material is essentially based on the model of Coulomb's critical prism. This model likens the accretionary wedge to a pile of snow pushed by a bulldozer (Dahlen, 1990). The bulldozer then represents the rigid edge played by the upper plate while accreting material from the lower plate and forming fold-and-thrust belts. Although this physical theory proved to be fundamental in the description and prediction of natural geometries in the pro-foreland basin (eg, Taiwan, Canadian Rockies, Appalachians), it did not allow to accurately explain asymmetry (double vergence) in some collisional systems such as the Pyrenees. Some authors adapted this theory, analogically (Malavielle, 1984) then numerically (Willett et al., 1993), considering a relatively rigid and fixed block instead of the convergent rigid edge. On either side of this block are a fixed crustal section (future upper plate, zero velocity) and a convergent crustal section (future lower plate, positive velocity). At a point of singularity characterized by a discontinuity in the velocity field (speed between the two sections, both null and positive), the convergent section subducts under the fixed section, leading to some sort of asymmetry that depends on the

orientation of the subducting section. Erosion is also invoked as a preponderant factor in the transfer of material within the doubly-emerging prism, leading to the exhumation of the most deformed rocks on the slope where it operates.

Thus, collisional orogens are classically described as the result of the accretion of proximal continental margins, which are little deformed. However, among the submerged regions of the edge of a continent that lead to ocean bottoms and will be involved in the collision, one can distinguish proximal continental margins and distal continental margins. While the former are the closest areas to the continents, little thinned and deformed, the latter are the most thinned areas, in the intermediate position with the oceanic crust if it exists, and above which the water column is the most important. Thanks to continuous data acquisition and numerical advances allowing modeling and quantification of complex processes, many paradoxes have recently been highlighted. These suggest that our understanding of orogens and of processes leading to their formation need to take into account the complete geometry of the system at the beginning of accretion (e.g. thicknesses, structures). By extension, it requires taking into account the evolution of the rigidity of the two plates over time. During each stage of Wilson's cycle, plate thickness varies. For the continental crust, its thickness decreases during the opening leading to the formation of an ocean but increases during closure and accretion of material. Regarding the oceanic crust, its thickness varies during its production and is by nature small (10 km) compared to a normal continental crust (30 km). A lithospheric plate also sees its composition change. The oceanic crust formed during the opening is denser than the continental crust. The continental crust may have been affected by magmatism during an earlier subduction or collisional episode, or even metamorphism. Thus, any model that considers the elastic thickness of a plate as a constant parameter does not take into account the thermomechanical properties of this plate. How do margins evolve during orogenesis? In particular, what happens to distal margins? How are these margins incorporated into the accretionary wedge? What is the impact of inheritance (structural, thermal, compositional) on the formation of an orogenic system (rate of shortening, distribution of shortening)?

Continental accretion leads to the surface uplift and the export of erosion products to the adjacent foreland basins. However, the models of foreland basin development and orogenic building, although including tectonic-erosion couplings, were mainly based on the observation of pro-systems. Only recently has the asymmetry of double-wedged prisms led to the realization that each of the flexural basins records its own flexural history (Naylor and Sinclair, 2008, Sinclair and Naylor, 2012). Due to the subduction of the lower plate under the upper plate, the pre- and syn-orogenic structures and sediments (the witnesses of the events previous to and synchronous with the orogenesis) in the pro-system are progressively integrated into the orogen. On the other hand, the remains of any past history are better preserved in the relatively static retro-system. From the observation of the pro-system, the models describing the relationships between erosion of the orogenic wedge and sedimentation into its associated foreland basins have therefore been mainly focused on the late history of the orogen, especially

when it is already in place, when the collision has already started and when the export toward the flexural basins is important (large subsidence recorded in these basins). What about orogenic growth during early convergence? What are the processes that lead to topographic growth? How are reliefs distributed during early convergence? What is the sedimentary response to the establishment of an early orogenic topography?

I.3 Objectives and case study

The main goal of this thesis is to characterize the rift-to-collision transition by focusing on early orogenic growth processes and highlighting the links between extensive inheritance and initiation of orogenic topography. For this, it is necessary to find the appropriate case study: the Pyrenean orogen.

The Pyrenean orogen was generated from late Santonian-early Campanian to middle Miocene by N-S convergence of the Iberian and European plates. Tectonic inversion of an Aptian-Cenomanian rift system, where mantle rocks were exhumed, resulted in the asymmetric doubly vergent collisional Pyrenean orogen. This orogen has a pro-foreland system to the south on the lower Iberian plate (South Pyrenean fold-and-thrust belt, Ebro Basin) and a retro-foreland system to the north on the upper European plate (North Pyrenean Zone, Aquitaine Basin). Convergence then began about 10 Ma after the end of rifting, so that the major thermal pulse generated by Early Cretaceous rifting was not reequilibrated before the onset of convergence.

The Pyrenean case study has the advantage of low-convergence orogens, allowing better preservation of early phases than in high-convergence orogens. There is also no thermal signature of subduction preceding collision, as is the case in many orogens, because no true oceanic crust was formed before the onset of convergence. The northern Pyrenees preserves one of the best geological records of a rift-to-collision transition. The north Pyrenean foreland retro-system is therefore an excellent natural laboratory for studying such a transition in an orogen.

The major questions addressed during this thesis are:

- Does early orogenesis have a thermal signature distinguishable from other thermal events such as those associated with preceding rifting or later collision?
- How is a (hyper-) thinned distal margin incorporated into the continental accretionary prism at the beginning of convergence?
- Does the thermal and structural inheritance play a role in early orogenesis?
- What is the sediment response and the contribution of dynamic topography to sedimentary passways?

More specifically to the Pyrenean study area:

- When did the early Pyrenean orogen grow and how did it evolve?
- When and where did topography initiate? Is there a temporal and spatial diachronism of topographic growth?

- Where is the sedimentary source during early orogenesis? Is the source unique or are there multiple sources?

To answer these questions that involve tectonic movements and the thermal regime of the crust, it is necessary to use a tool sensitive to these processes: geo-thermochronology. Low-temperature thermochronology (U-Th)/He on zircon can be applied to bedrock exposures as well as sediments to reconstruct the thermal history of a grain. In the latter case, however, it requires the acquisition of a large amount of data to statistically represent the source(s) of these sediments. A similar requirement goes for U/Pb zircon geochronology that proves to be a key tool for source tracing. Conducted on the same grains, these two dating methods allow to reconstruct precisely the history of sedimentary sources. However, the methodologies commonly used for (U-Th)/He dating involve grain dissolution, which is time-consuming, tedious to implement and strongly constrains the amount of data that can be produced. Given the inadequacy between these methodologies and the study of orogenic processes that requires extensive documentation, a geo-thermochronological double-dating method using *in situ* laser ablation at the core of the grains was implemented and developed at the CRPG. This technique has already been proposed in the literature (Tripathy-Lang et al., 2013; Horne et al., 2016) but has so far not been applied to geological objects because of the particular information it provides. Essentially, dating the core of a grain with low temperature thermochronology techniques involves dating the latest major cooling event, sometimes old, experienced by the grain. By applying the *in situ* laser ablation technique in the Pyrenees, where two major events followed each other in less than 30 Ma (rifting and convergence), the aim is two-fold. On the one hand, it is necessary to see if the zircon (U-Th)/He thermochronometer makes it possible to distinguish these two events. On the other hand, it is interesting and important to see if the fact that information obtained by laser ablation is partial does not go against a better representation and identification of the sedimentary sources when more data are acquired.

I.4 Organisation of the thesis

This thesis is divided into 7 chapters plus an appendices section, entirely written in English.

The first chapter (Chapter 1) is this general introductory chapter.

The second chapter (Chapter 2) presents a synthesis of the concepts and works related to foreland flexural systems, including the models of development an of accretionary prism and foreland basins.

The third chapter (Chapter 3) includes an overview of the Pyrenean system, ranging from the description of the main tectono-sedimentary zones to the synthesis of low temperature thermochronology data, while evoking the proposed geodynamic models.

The fourth chapter (Chapter 4) represents the core of this thesis: the analytical and methodological chapter. It is devoted to the exhaustive presentation of (i) the analytical methods implemented in the laboratory and used during this thesis, and (ii) the statistical treatment methods used during this thesis. It crystallizes the concepts, justifies the advantages and uses, and presents the limitations of these methods.

The fifth chapter (Chapter 5) presents the first project carried out during this thesis: the reconstruction of the tectono-thermal history of the most distal north-Pyrenean margin (Agly-Salvezines), using zircon and apatite (U-Th)/He thermochronometers. This work proposes an answer to questions 1, 2, 3, 5 and 6, mentioned previously. It has been published in the journal Tectonics.

The sixth chapter (Chapter 6) presents the second project carried out during this thesis: the study of the sedimentary record of topographic growth within the early retroforeland basin, using *in situ* laser ablation (U-Th)/He - U/Pb double dating on detrital zircon. This work proposes an answer to questions 3, 4, 5, 6, and 7, mentioned previously. This represents an article in preparation.

The seventh chapter (Chapter 7) is devoted to the conclusions and perspectives of this thesis.

REFERENCES

Beaumont, C. (1981). Foreland basins. Geophysical Journal International, 65(2), 291–329. https://doi.org/10.1111/j.1365-246X.1981.tb02715.x

Dahlen, F. A. (1990). Critical taper model of fold-and-thrust belts and accretionary wedges. Annual Review of Earth and Planetary Sciences, 18, 55.

Horne, A. M., van Soest, M. C., Hodges, K. V., Tripathy-Lang, A., & Hourigan, J. K. (2016). Integrated single crystal laser ablation U/Pb and (U–Th)/He dating of detrital accessory minerals – Proof-of-concept studies of titanites and zircons from the Fish Canyon tuff. Geochimica et Cosmochimica Acta, 178, 106–123. https://doi.org/10.1016/j.gca.2015.11.044

Jordan, T. E. (1981). Thrust loads and foreland basin evolution, Cretaceous, western United States. AAPG Bulletin, 65(12), 2506–2520.

Malavieille, J. (1984). Modélisation expérimentale des chevauchements imbriqués: application aux chaînes de montagnes. Retrieved from http://geoscienceworld.org/highwire/filestream/458370/field_highwire_a_download_vars/0/129.full.pdf

Naylor, M., & Sinclair, H. D. (2008). Pro- vs. retro-foreland basins: Pro- vs. retro-foreland basins. Basin Research, 20(3), 285–303. https://doi.org/10.1111/j.1365-2117.2008.00366.x

Price, R. A. (1973). Large-scale gravitational flow of supracrustal rocks, southern Canadian Rockies. Gravity and Tectonics, 491–502.

Sinclair, H. D., & Naylor, M. (2012). Foreland basin subsidence driven by topographic growth versus plate subduction. Geological Society of America Bulletin, 124(3–4), 368–379.

Tripathy-Lang, A., Hodges, K. V., Monteleone, B. D., & van Soest, M. C. (2013). Laser (U-Th)/He thermochronology of detrital zircons as a tool for studying surface processes in modern catchments: Detrital zircon thermochronology. Journal of Geophysical Research: Earth Surface, 118(3), 1333–1341. https://doi.org/10.1002/jgrf.20091

Watts, A. B. (2001). Isostasy and Flexure of the Lithosphere. Cambridge University Press.

Willett, S., Beaumont, C., & Fullsack, P. (1993). Mechanical model for the tectonics of doubly vergent compressional orogens. Geology, 21(4), 371–374.

Wilson, J. T. (1966). Did the Atlantic Close and then Re-Open? Nature, 211(5050), 676–681. https://doi.org/10.1038/211676a0

Chapter 2
II. Foreland Basin Systems

TABLE OF CONTENTS

LIST OF FIGURES

II.1 Systems due to flexure

Understanding how mountains form and explaining how topography is created has been a long-lived source of debate with the establishment of many hypotheses, speculations and theories. Although the first observation of rapid variations in stratal inclination is not attributed to James Hutton, the fact remains that he was the first one to interpret these as the result of sedimentary and tectonic processes (Hutton, 1788, 1795). His colleague James Hall continued his work and later highlighted the role of horizontal forces (shortening) in the formation of geometries as those observed on the Berwickshire Coast, northern UK (Hall, 1815): "*For this purpose it will be necessary to shew, first, that this peculiar conformation may be given to a set of horizontal beds by mechanical force of sufficient strength and secondly, that there are rational grounds for beleiving that such a force has been actually exerted in this case. [...] I have tried to establish the first point by experiment [...] and the second by a train of geological reasoning [...]*".

Not until the 1960's did the causes of such horizontal components be understood and scientific people agree with each other. In mid-50s, Birot (1958, and references therein) spots the two main theories on "orogenic building" (read folding): (1) orogens are predominantly formed as a result of horizontal movements, and (2) orogens are predominantly formed by vertical movements.

The first thinking school was based on the idea that invoking horizontal displacements (thermal contraction theory; e.g. Wegener, 1929; Kober, 1951, quoted in Bemmelen, 1954; Figure II.1) and/or movements (convection cells beneath the upper crust; e.g. Holmes, 1928a, 1928b; Figure II.2.a) is well suited to explain folding and thickening of orogenic series (Griggs, 1939; Figure II.2.b).

The so-called Wegener's "Continental Drift" hypothesis/scientific theory (1912-1929) (Figure II.1) is two-fold as it provides an explanation for how continents form and mountains build (orogenesis). This theory was taken from Ortelius (1596) who noticed the striking puzzle-piece fit between the continents. This, together with the paleontological observation that the same fossilized plants and animals from the same time period were found on both sides of the vast oceans that currently exist (Figure II.1.b), made him suggest that the continents would have been once gathered into a single enormous proto-continent or landmass, *Pangaea*, and would have "drifted" apart into their current locations over time (Figure II.1.a). Unlike Wegener's "drift" therory - that seemed more plausible though -, existence of past land bridges between Africa and South America, Europe and North America, as well as Madagascar and India, was also proposed as an attempt to explain the well-known paleontological observation (Schwarz, 1906). But scraping patterns of glaciers over the land surface (Figure II.1.d) was another observation that favored "continental drift", indicating that continents had been close together at the time of an ancient ice age - the continental glaciation in the Pensylvanian period -. Nonetheless, Wegener's hypothesis lacked a geological mechanism to explain how the continents could have "drifted" across the earth surface.

To support his theory, Wegener suggested several mechanisms to explain the formation of the Sierra Nevada mountains on the Pacific coast of North America and the Andes on the coast of South America ranging from (1) the "Contraction theory" (Figure II.1.c) that consists in considering that the earth was once a molten ball whose surface cracked and folded up on itself in the process of cooling, then forming mountains near the leading edges of the "drifting" continents; passing through (2) the rotation of the earth that created a centrifugal force causing the proto-continent originated near the south pole to break apart and the resultant continents to "drift" towards the equator; and also (3) the gravitational forces of the sun and the moon that caused the westward "drift" of America - see Taylor (1910): "*For a change in the degree of oblateness, either in oceanic oscillations or in deformations of the lithosphere, one is inclined to reject all internal causes and to look to some form of tidal force as the only possible agency.*" -. But, the first explanation suffers the fact that all mountain ranges should be approximately the same age, and this was known not to be true. Moreover, the prevailing belief that the earth was solid and immovable resulted in the scientific dismissal of his theories after 1960s (i.e. when plate tectonic theory came into existence; see four paragraphs below).

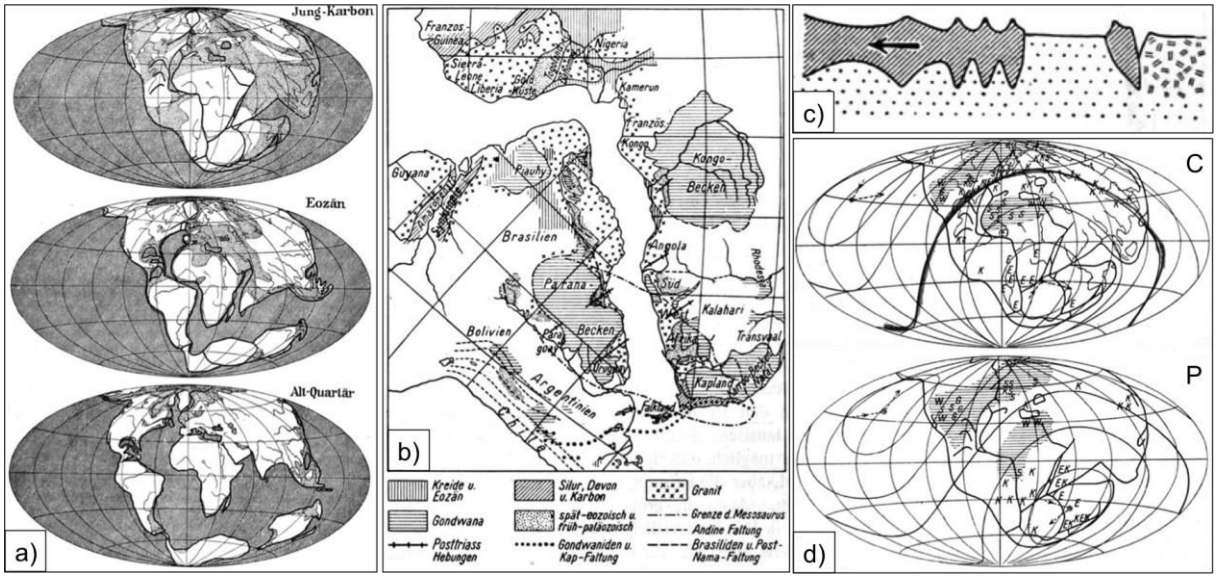

Figure II.1: Wegener's "Continental Drift" hypothesis (1912-1929). From Wegener (1929). (a) A mega, proto-continent Pangaea splitted up in Carboniferous times to form the Atlantic and Indian oceans. The Pacific Ocean is the primitive ocean. The periods displayed are from top to bottom: Early Carboniferous, Eocene, Quaternary; (b) One of the Wegener's reconstitutions based on the paleontological observation that the same fossilized plants and animals from the same time period were found onto Africa and South America; (c) Schematic diagram depicting the "Contraction theory"; (d) Scraping patterns of glaciers over the land surface in C = Carboniferous and P = Permian times.

Nonetheless, Argand (1924) includes Wegener's therory in his work and produces lithospheric cross-sections across continent-continent collisional zones (e.g. the Alps, the Himalayas and the Appenines; Figure II.3) that involve subduction-like motion of one of the two continents beneath the other one. This causes a zone of localized deformation bordered by major tectonic discontinuities where topography is created.

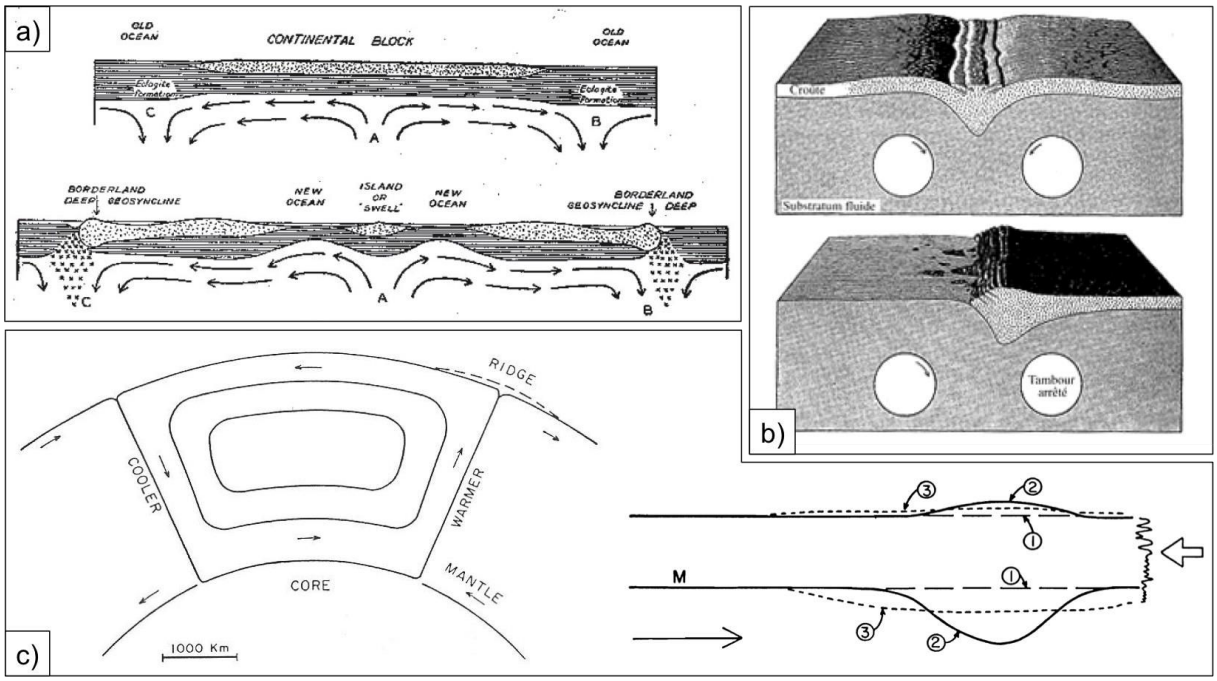

Figure II.2: Conceptual views about convection cell beneath the upper crust and resulting orogenesis. (a) Holmes' (1928a, 1928b) convection scheme. First-order convection results from the cooling of the earth. Due to difference in radiaoactive content in continents and oceans, second-order convection cells develop. Ascending currents occur beneath continents, resulting in stretching and fracturing of these continents and formation of a new ocean in-between. From Holmes (1928a). (b) Griggs' (1939) experiment. Folding of the crust (geosyncline development) results from action of two conjugate convection cells that leads to stability of the crust above them (top). When one cell stops working, part of the crust just above it acts as a stopper for the crust above the working cell that bumps into it (bottom). Material is then accreted on the edge of the motionless crust that is thickened and forms the orogen. From Griggs (1939). (c) Geometry of a mantle convection cell (left), and continantal thickening mechanism (right): "A continent will ride on convecting mantle until it reaches the downward-plunging limb of the cell. Because of its much lower density it cannot be forced down, so that its leading edge is strongly deformed and thickened when this occurs. It might override the downward-flowing mantle current for a short distance, but thickening would be the result as before." Numbers represent the different thickening steps from normal-thickness continental crust (1) to the formation of a mountain system and its crustal root (2) that eventually spread laterally with time and isostatic adjustment (3). Solid and dashed lines represent the surface and Moho. From Hess (1962).

Holmes (1928a, 1928b) suggested on the basis of physics- as a substance is heated its density decreases and rises to the surface until it is cooled and sinks again- that repeated heating and cooling of rocks could result in a current (the idea that the mantle undergoes thermal convection) which may be enough to cause continents to move. Thermal convection would be like a conveyor belt and the upwelling pressure could break apart a continent and then force the broken continent in opposite directions carried by the convection currents (Figure II.2.a). Once again, although somewhat different from Wegener's explanations, this implies to put the solid and immovable state of the earth into question. This idea received very little attention at the time.

The second thinking school was mainly based on magmatic differenciation processes at base or within the crust (e.g. Rich, 1951; Figure II.4) that would lead to variations in density, subsequent isostasic compensation and development of the so-

called geosynclines in which folding and faulting affecting sedimentary successions at the orogen front would be the result of isostasic re-equilibrium by viscous flow at base of the crust and at the surface.

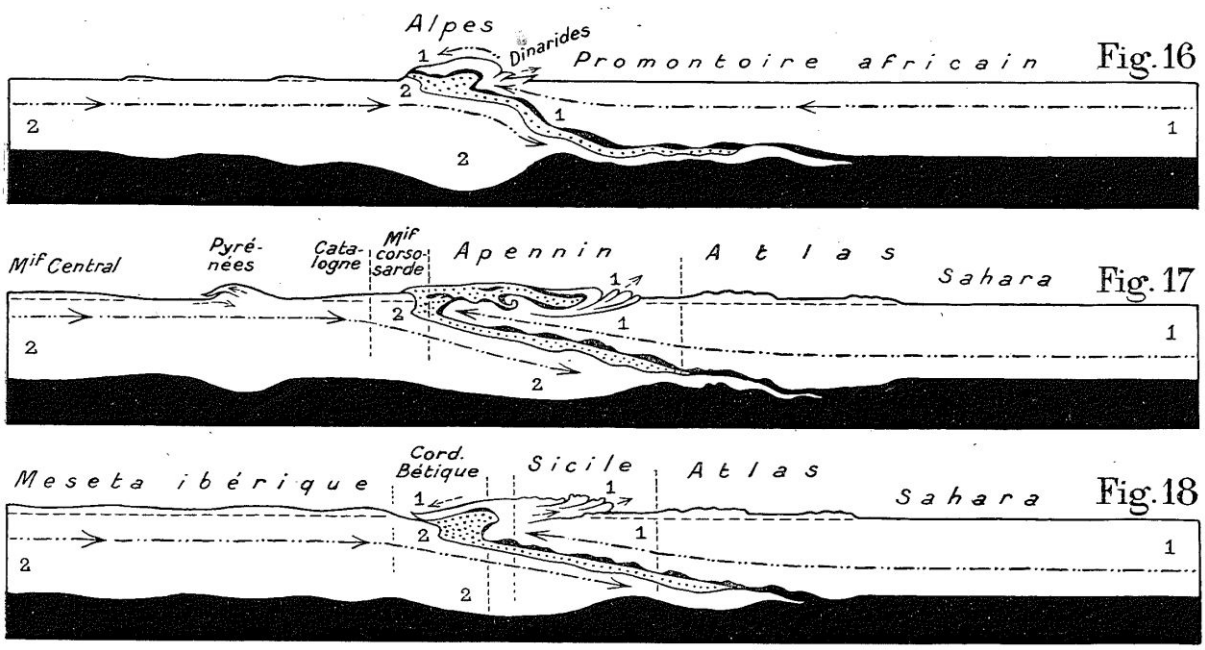

Figure II.3: First lithospheric-scale cross-sections based on the Wegener's "Continental Drift" theory. From Argand (1924). Gondwana and Eurasia are represented as the over-ridding (1) and the subducting (2) continents, respectively.

In the 1970s, geological, geophysical and geomagnetic evidences over the oceanic realm for mantle convection currents (e.g. Hess, 1962; Figure II.2.c), now known as seafloor spreading, allowed concurring what Wegener (1912-1929) and Holmes (1928) invoked 30 years earlier. Dewey and Bird (1970) cristallize these theories in a unified theory that links internal dynamics and its surfacial expression: the plate tectonics theory. Petrological, structural and geophysical data were then re-interpreted in this way.

II.1.1 The concept of flexural isostasy

Foreland basins develop on continental lithosphere around the margins of collisional and subduction orogenic belts during convergence as a result of the loading of the lithosphere (Dickinson, 1974; Figure II.5; Kingston et al., 1983). The formation of these flexural basins can be seen as the expression of regional isostatic compensation of the neighbouring growing topography during mountain building (Price, 1973). Basin subsidence is caused by lithospheric down-flexure due to the presence of the orogenic load. Foreland basins are therefore linked flexurally through the lithosphere to their adjacent overthrust belts (Watts, 2001; Sinclair, 2011).

The lithosphere appears to respond to loading in a similar manner to an elastic beam overlying a fluid substratum (Turcotte and Schubert, 1982), being able to bend when forces or loads are applied to it (flexure). It behaves (1) elastically on short time scales (stress proportional to the strain) or (2) visco-elastically over 100,000 years as

observed in Lake Algonquin, Canada, with rebound due to removal of ice-cap loading as the lithosphere relaxes (Allen and Allen, 2013).

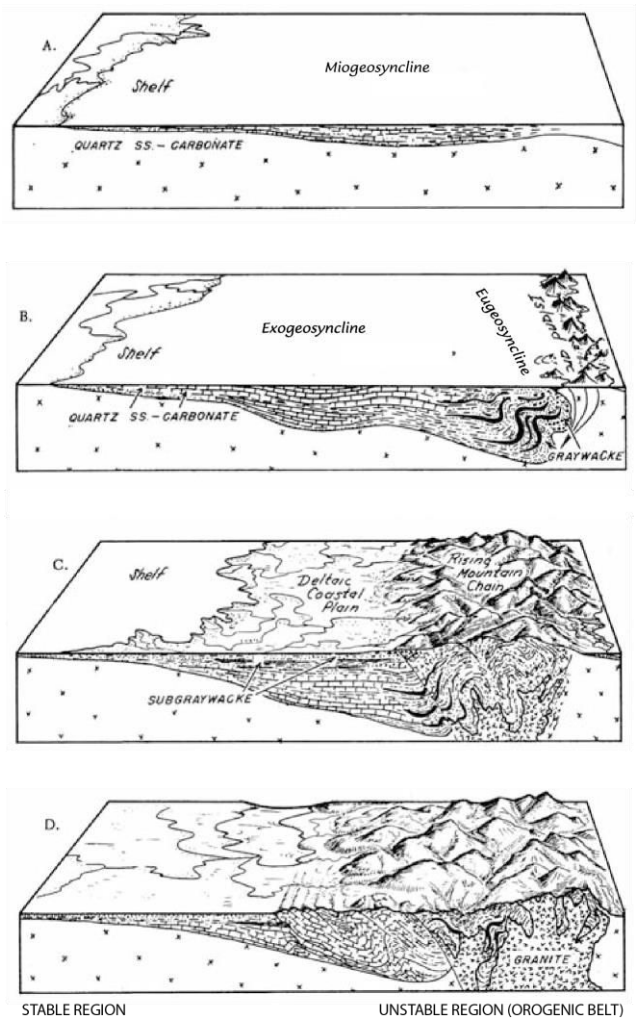

Figure II.4: Model of orogenesis and geosyncline development based on magmatic differenciation processes at the base of or within the crust. (A) Pre-orogenic miogeosyncline characterized by sediments acting as a thermal blanket. It is unclear to what the geosyncline transitions on the right hand side, but this is in this region that (B) a volcanic arc rises up. The miogeosyncline trasnforms into an exogeosyncline, filled with large quantity of sediments eroded from the volcanic arc/eugeosyncline lying beside it. A magma source for the volcanic arc is probable, as suggested by (C) granite intrusions into the eugeosyncline. This leads to widespread metamorphism, generates buldging and topography, accompanied by folding, faulting and migration of the geosynclinal depocentre. Once geosynclinal mountain building has ended (D), the moutains are eroded down. From Whitmeyer et al. (2007). See also Birot (1958) and Rich (1951).

Most workers now accept the elastic model and consider that lithosphere behaviour can be modelled using either elastic behaviour or viscoelastic behaviour during long-term loading (105 years). Lithospheric flexure is controlled by: (1) the strength of the lithosphere, (2) the types of loads imposed onto the lithosphere, (3) sediment supply, (4) intraplate stress (Cloetingh, 1988; Peper et al., 1992) and (5) the pre-existing stratigraphic template (Stockmal et al., 1986). What is the role of lithospheric inheritance in continent-continent collision? How will the rheological

structure of the subducting plate affect modelling of flexural deformation at the onset of orogenic contraction? What will be its impact on shortening rates and distribution and their subsequent influence on orogenic wedge growth? What if collision is superimposed on a thinned lithosphere of a distal rift/margin (often not in thermal equilibrium) where lithosphere weakening is at its most?

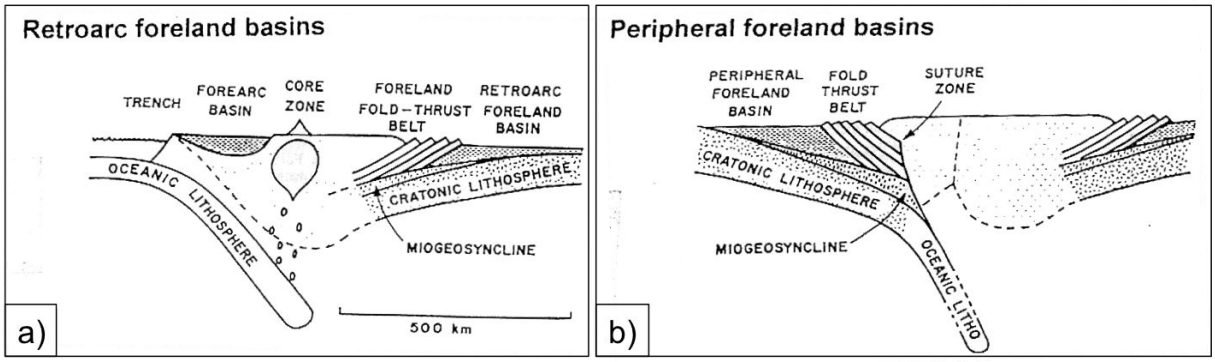

Figure II.5: The two principal types of foreland basins based on their position with respect to the subducting plate. From Dickinson (1974). (a) Retroarc foreland basins lie on the overriding plate and develop during subduction of oceanic lithosphere behind the magmatic arc or continent-continent collision. (b) Peripheral foreland basins lie on the subducting plate and develop on the outer arc of collisional orogens.

Flexure and orogenic loading are the two major parameters controlling the development of the stratigraphy of foreland basins. Early conceptual flexural models suggest that unconformities found in foreland basins formed by thrust/fold load-induced stress relaxation of the lithosphere (Beaumont, 1978). Another interpretation was to suggest that unconformities formed by changes in the rate of thrust wedge migration on an elastic plate (e.g. the North Alpine Foreland Basin, eastern Switzerland: Sinclair et al., 1991; the Sevier thrust belt, Western USA: Flemings and Jordan, 1990; Figure II.6). However, conclusions differ regarding the geodynamic significance of onlaps, offlaps and unconformities at distal basin margins: while Sinclair et al. (1991) conclude on the fact that progradation (renewed onlap over eroded forebulge) is a result of increase in thrust front advance rates, i.e. a pulse of the orogenic wedge growth, Flemings and Jordan (1991) intepret progradation results from decrease in erosion rate and subsidence rate, i.e. tectonic quiescence.

II.1.2 Flexural rigidity of the lithosphere

The rigidity or strength of the lithosphere can be quantified by calculating its elastic thickness or effective elastic thickness (*Te*), i.e. the thickness of the lithosphere that would behave perfectly elastically (Figure II.7). As this is not the depth to a specific boundary but simply an expression of the strength of the lithosphere, i.e. it does not represent the 'depth' of a real physical discontinuity in the lithosphere, another variable, the flexural rigidity, has been defined as proportional to the cube of the elastic thickness of the lithosphere. Probably the flexural rigidity is a better expression for this property. *Te* has been defined as an isotherm. Karner et al. (1983) have defined it as the 450 °C

isotherm for an oceanic lithosphere, but Willett et al. (1985) argue that this isotherm can vary between 300 °C and 900 °C.

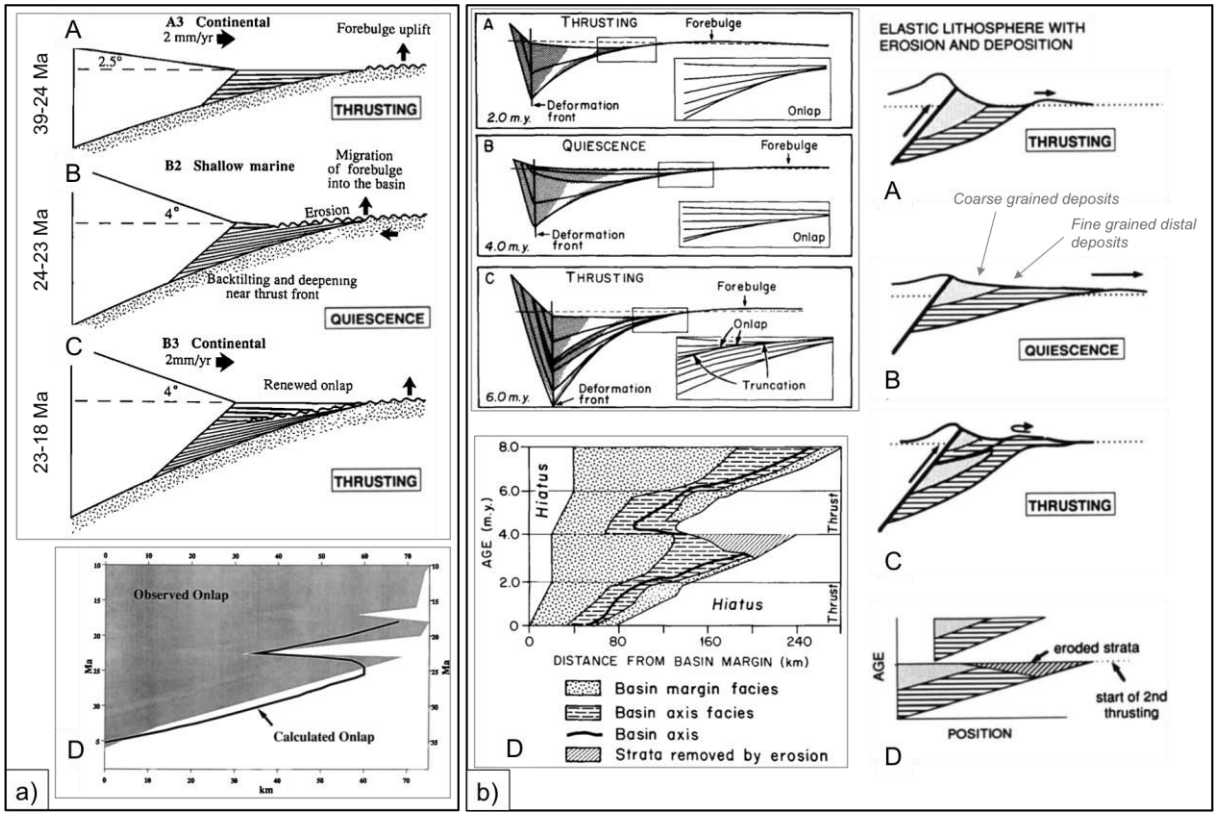

Figure II.6: Schematic diagrams (A, B and C) and chronostratigraphic plot of foreland basin (Wheeler diagram, D) showing two opposite views about mechanisms controlling the stratigraphic evolution of forland basins. In Wheeler diagrams horizontal position is measured from initial edge of basin at start of deformation. See differences in horizontal arrows. (a) Progradation of sediments is due to thrusting in the North Alpine Foreland Basin, eastern Switzerland. Modified from Sinclair et al. (1991); (b) Progradation of sediments is the result of tectonic quiescence in the Sevier thrust belt, Western USA. Rightmost cartoons depict the stratigraphic response for elastic lithosphere (no relaxation considered here). Modified from Flemings and Jordan (1991).

Beaumont (1978) uses the viscoelastic rheology model for the Canadian Rocky Mountain foredeep. The author assumes that the flexural rigidity decreases with time after the lithosphere is loaded, i.e. the plate becomes weaker (*Te* is lower). In contrast, Sinclair (1996) and Stewart and Watts (1997) propose that *Te* increases through time (lithospheric strengthening). In fact, Sinclair (1996) argues that the lithosphere in the Western Alps shows strengthening through time and space. Nonetheless, Burkhard and Sommaruga (1998) contradict this observation by finding no change as recorded by the foreland basin of the Western Swiss Alps (the North Alpine Foreland Basin, eastern Switzerland; Figure II.7).

The issue in Beaumont's concept (1978) lies in the fact that his model predicts that the flexural stresses will vanish to zero over geological time. Another question that remains is whether *Te* increases (lithosphere strengthening) or decreases through time (lithospheric weakening). How could lithospheric inheritance impact this parameter?

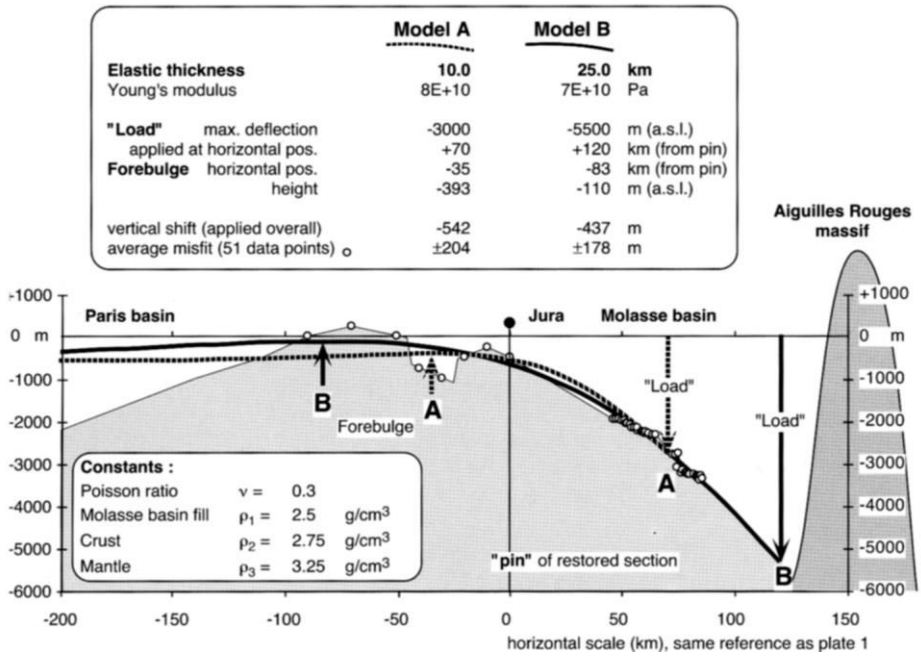

Figure II.7: Flexural model profiles along a NW-SE transect of the western Swiss Alps by applying the point load model. Black dots represent evidence of top of basement from boreholes, seismic lines and field data (basin profile) while black lines represent model profiles. Modelling parameters are depicted in the inset. From Burkhard and Sommaruga (1998).

To quantify the flexural rigidity of a plate, *Te* is first estimated by using either profile analysis (fitting) to match the shape of the observed bending of top basement with theoretical shapes generated for different values of *Te* (e.g. Turcotte and Schubert, 1982; Burkhard and Sommaruga, 1998; Figure II.7) or admittance analysis to analyze the relationship between topography/bathymetry and gravity anomalies in the spectral domain (e.g. McKenzie and Fairhead, 1997). While this works rather well for oceanic lithosphere- Watts (2001) and McKenzie et al. (2005) shows *Te* increases with the age in oceanic lithosphere at the time of loading (Figure II.8.a)-, estimating the elastic thickness of the continents has been shown to be more difficult as there is no clear relationship between thermal age and flexural rigidity of continental lithosphere, even if old cratons are strong (Watts, 2001; Figure II.8.b).

This gives rise to the idea that although the elastic model has been widely accepted, the continental lithosphere does indeed undergo some form of load-induced stress relaxation, as it relaxes from its short-term to its long-term elastic thickness (Watts, 2001). In other words, oceanic lithosphere is rightly known to behave elastically at geological time-scale while continental lithosphere appears to behave elastically without showing clear evidence regarding the reasons for such behaviour. This also highlights that loads cannot always be approximated by simple point/line loads (Figure II.7), and the density structure and thickness of the continental lithosphere is often poorly known. It might be reasonable to argue that weakening under high bending stresses (high curvatures), radiogenic heat, decoupling of layered lithosphere, plastic yielding, plate segmentation or inherited heterogeneities, all common in continental

realm, might be other parameters to consider and take into account when playing with values of *Te*.

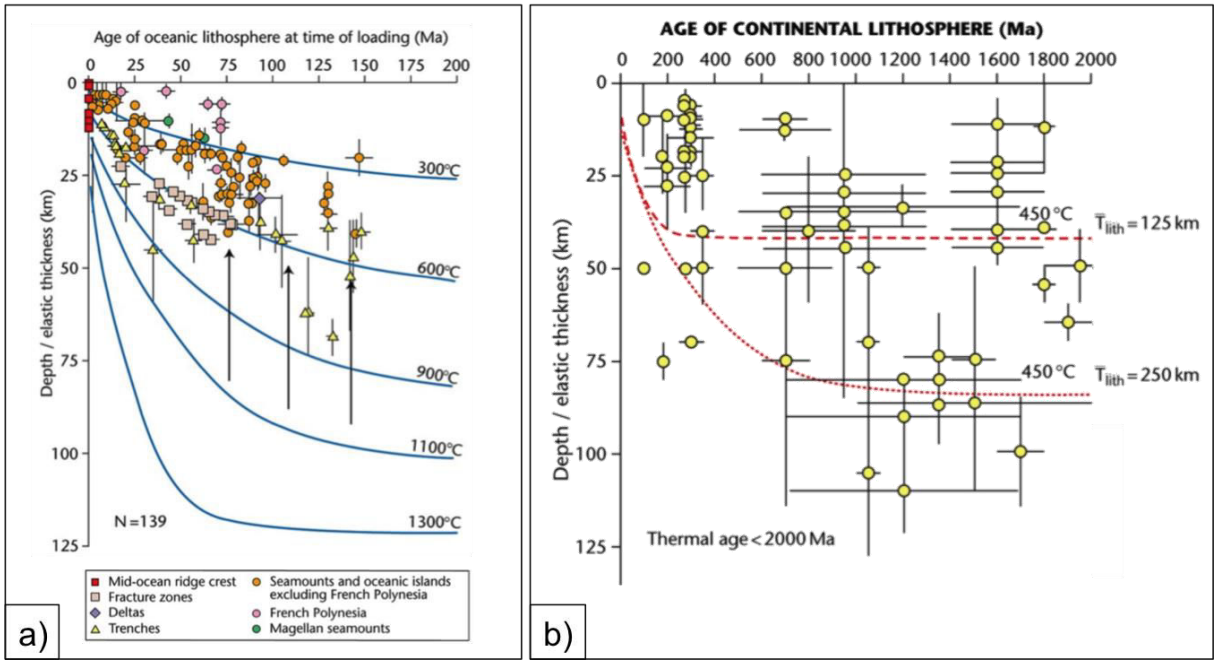

Figure II.8: Flexural rigidity and age of a) oceanic and b) continental lithospheres. From Watts (2001). (a) Most data (earthquake data) fall within 300-600 °C isotherms from cooling plate model, which suggests that the elastic portion of the oceanic lithosphere that is able to store stresses that eventually cause earthquakes, depends simply on temperature, which in turn depends on age. (b) Data from 66 foreland basins and 6 late glacial rebound sites (data from Watts, 2001). No correlation is seen between *Te* and age of the continental lithosphere.

II.1.3 Models of flexure

Models of flexure are diverse, and depend on regional settings and main loading type (Lyon-Caen and Molnar, 1985; Allen and Allen, 2013). The sources of loads are numerous but one can argue that loads are of two main types: (1) surface, topographic, orogenic type, and (2) buried type.

In a subduction zone trench, a vertical end load on a broken, semi-infinite plate is generally preferred to a vertical load on a continuous, infinite plate as assumed in the case of an oceanic seamount. In mountain belts, the applied load may be represented as a vertical point/line load (e.g. in the Appalachian foredeep; Turcotte and Schubert, 1982), in the western Swiss Alps (Burkhard and Sommaruga, 1998; Figure II.7) or by a distributed, topographic load (e.g. Watts, 2001). Horizontal (in-plane) loads and applied torques are also possible (e.g. in-plane stress and lithosphere buckling; Allen and Allen, 2013).

Surface loads comprise the excess topography created by shortening in fold-and-thrust belt. The excess topography is directly proportional to the thickened lithosphere below mountain belt. Bouguer anomalies such as those observed over the Ganges Basin and external Himalayas (Lyon-Caen and Molnar, 1985) agree with this statement and are indeed large-amplitude negative Bouguer anomalies that one can expect over

orogenic belts, getting more and more negative toward the orogen front (the Himalaya front).

However, some orogenic belts such as the Western Alps and the Appalachians show a different story. There, there is a striking contrast between the foreland basins that are characterized by negative Bouguer gravity anomalies, and the orogenic belts that are characterized by large-amplitude positive, rather than negative, Bouguer gravity anomalies (Karner et al., 1983; Lyon-Caen and Molnar, 1985). The observed topographic load is insufficient to cause the observed flexure of the plate and must be associated with a sub-surface load which is responsible for the large positive anomaly.

Loading may be generated as a consequence of a bathymetric low (inherited mass deficit as top of crust was below sea level at time of loading), "hidden" dense bodies (e.g.Alps), obduction (Oman), intra-crustal thrusting, subducting slabs (e.g. slab pull; Apennines), heterogeneities in the mantle lithosphere or thermal or mechanical heterogeneities in the deep mantle (aesthenosphere).

Controls on basin dimension are similar to those on lithosphere flexure and questions to address are linked. The dimensions of a basin depend on (e.g. Ford et al., 1999): (1) strength of the lithosphere: the higher *Te*, i.e. the greater the lithosphere's rigidity, the broader and shallower the resulting flexural basins; inversely, the lower *Te*, the narrower and deeper the basins (Figure II.9.a); (2) width and wavelength of the load (or amount of shortening,): with increasing displacement the depocentre migrates and increases in depth until displacements are so large that the depocentre migrates but does not increase in depth (Ford et al., 1999; Figure II.9.b) and (3) type of loading (continuous vs broken plate models; line load versus distributed load).

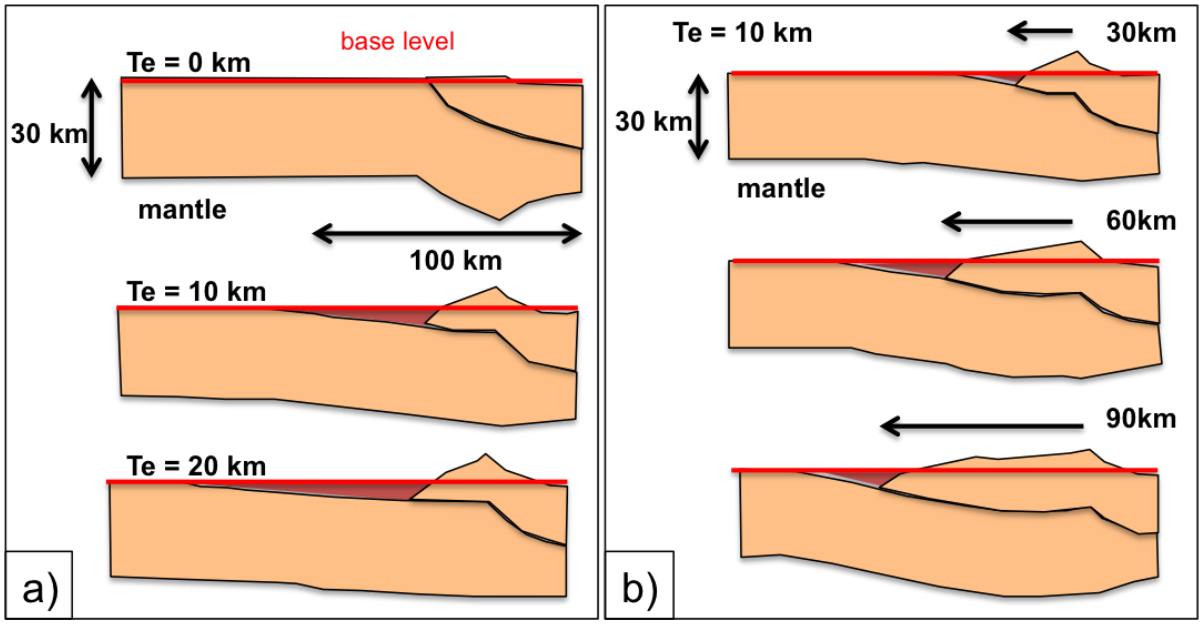

Figure II.9: Diagram illustrating controls on basin dimensions. Adapted from Ford et al. (1999). (a) Effect of lithospheric strength *Te* with constant shortening. (b) Effect of thrust displacement, i.e. the width of the load or amount of shortening, with constant *Te*. Horizontal black arrows indicate shortening values.

Questions to address therefore include the followings: how will the rheological structure of the subducting plate affect flexural deformation and so doing basin geometry? What if collision is superimposed on a thinned lithosphere of a distal rift/margin (often not in thermal equilibrium) where lithosphere weakening is at its most? How to model the flexural response to loading when rift inheritance exists and how can these models be calibrated?

II.2 Modelling the orogenic wedge as the load for a foreland basin

While the plate tectonics theory was on its way, thinking attempting to explain geometries and structures observed within orogenic wedges as well as their evolution started developping with an increasing number of data collection campaigns using direct sampling or well drilling, onshore and offshore structural analysis, etc, to understand the mechanical behaviour of orogenic wedges by characterizing rheologies and end-member conditions. Several rheologies and driving forces were invoked, giving rise to the establishment of two main models in chronological order of appearance: (1) gravity models, and (2) viscuous models.

Fold-and-thrust belts were first thought to be the result of giant gravity gliding processes (Bucher, 1956, 1963). Displacements are accommodated by the means of folding and thrusting and result from giant mass gliding on a decollement level(s) verging toward the foreland. These gliding surfaces crosscut the topographic level in an upstream position, as listric faults would do. However, this concept is shown by Price and Mountjoy (1970) and Price (1971, 1973) not to be applicable in the Canadian Rocky Mountains since those decollement levels are verging toward the range, which is in perfect contradiction with previous explanations. These authors therefore suggest that gravity spreading would be a better-suited process to explain fold-and-thrust belt development. In this model, the development of structures is driven by topographic variations between reliefs within the range and the non-deformed, peripheral craton (Elliott, 1976). As gravity forces overpass contractional forces (exept at the range front), the range is characterized by normal listric faults rooted in a weak decollement while the range front is dominated by shortening. In this model, Elliott (1976) invokes the existence of a rapidly ascending igneous body to generate important initial surface slope.

Nonetheless, as highlighted by Chapple (1978), these gravity-related models are questionnable: (1) Price (1971) rarely observes either the amount of shortening to be maximum at the front of the wedge or the amount of extension within the range to be as much as the discussed amount of shortening, (2) it is difficult to prove whether such magmatism-related mechanisms are always involved in initial surface slope creation, and (3) if the topographic slope drives shortening at front of the wedge as it is argued to do, this must imply that the amount of shortening must be equivalent in any orogenic system presenting similar topographic slope (e.g. the Zagros and Rockies)- yet, this is not the case.

This lack of consistency led to the establishment of viscous models. In these models, a viscuous rheology is considered to describe the formation and deformation style of accretionary prisms (e.g. Cowan and Silling, 1978; Cloos, 1984; Marshak et al., 1992). These authors use the Laws of Dynamics and take into consideration the viscuous parameters. By doing so, they manage to (1) reproduce the parabolic geometries observed for wedges in nature (Emerman and Turcotte, 1983), and (2) explain exhumation of metamorphic rocks within the range (Cowan and Silling, 1978).

Nonetheless, the issue in viscuous models lies in the fact that these predict geometries without taking into account any anisotropy caused by structures present within the upper crust under the form of clearly distinct tectonic units separated by shear zones.

II.2.1 Critical taper model as critical wedge model for foreland systems

This is in this scientific context and in an attempt to tackle these observational problems that Chapple (1978) goes back to geophysical data of the main wedges such as those acquired by Bally et al. (1966) and observes similarities between them. Very often is observable: (1) a basal detachment or décollement level (floor thrust) that detaches the deformation from the underlying succession and is rangeward-verging, (2) an important amount of shortening is accommodated in the overlying sucession, and (3) a wedge with the typical look of a prism that tapers toward the foreland.

Modelling an orogenic load consists of applying the critical taper model, which "*resembles the bulldozer principle*" and assumes that the developing orogenic belt behaves mechanically as "*a pile of snow or earth pushed in front of a bulldozer [...] with a critical taper in front of the indenter*" (Chapple, 1978; Davis et al., 1983; Dahlen et al., 1984; Dahlen, 1990; Figure II.10).

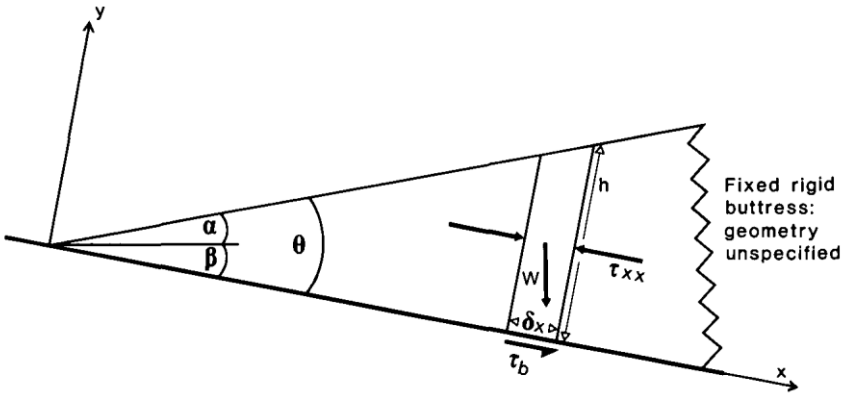

Figure II.10: An example of cartoon depicting the self-similar growth of a bulldozer wedge. This is the simplified model of an accretionary wedge or critically tapered orogenic wedge. α = the surface slope relative to the horizontal; β = the basal slope relative to the horizontal; θ = the taper angle (α+β); h = segment height; δx = segment length; W = body force; τb.δx = basal traction; τxx = longitudinal deviatoric normal stress producing push forces. From Platt (1986).

Critically tapered orogenic wedges (or fold-and-thrust belts) have been modelled as Coulomb material (Davis et al., 1983; Dahlen et al., 1984; Dahlen, 1990), in which case

longitudinal force applied at the rear of the wedge (push due to collision) is resisted by resistance to sliding at base (friction).The wedge attempts to maintain mechanical equilibrium (criticality): (1) when the taper angle is lower than criticality, the wedge attempts to thicken by internal thickening; (2) when the taper angle is higher than criticality, the wedge attempts to thin by extension and thus reduce the upper slope.

II.2.2 Evolution for accretionary wedge to emergent orogen

Based on concepts developed by Elliott (1976) and Chapple (1978), Davis et al. (1983) add pore-fluid pressure within the wedge and along the basal decollement. Platt (1986) summarizes the evolution of an accretionary wedge to form an emergent orogeny (Figure II.11). Davis and Engelder (1985) and Jaumé and Lillie (1988) study non-cohesive Coulomb wedges developed above a curved basement surface. These authors show that depositional wedge tops develop above low friction detachments, usually salt.

II.2.3 Coupled basin and range evolution

As a consequence of their proximity to the strongly eroding mountain belt, foreland basins can be filled with a large thickness of syn-orogenic deposits recording the temporal and spatial emplacement of tectonic loads and variations in lithosphere rheology during flexure (Beaumont, 1978; Jordan, 1981). Then, the early thermal and dynamic evolution of a mountain range is intimately coupled with that of its associated foreland basins.

Erosion of the wedge has been quickly incorporated into the critical taper model in order to analyse its effect on accretionary wedge dynamics (e.g. Dahlen, 1990; Figure II.12) as the stratigraphic record of the various stages of orogenic growth history indicates the existence of feedbacks between erosion of the wedge and the mass in the wedge generated by convergence. This, together with sedimentation into foreland basins, led to consider orogens and their foreland basins as part of a single dynamic system evolving from an early, out-of-equilibrium, growth stage to a late, mature, steady-state stage (Willett et al., 1993; Willett and Brandon, 2002).

External orogenic zones generally comprise an external orogenic wedge and a flexural foreland basin (Figure II.13) Two main types of interaction between these two systems are distinguished, regardless of the complexity of the depositional system (Lucchi, 1986; DeCelles and Giles, 1996; Ford, 2004).

In the ‘classic’ external orogenic zone, sediments are deposited in the flexural basin ahead of the migrating wedge front (deformation front) and are only incorporated into the thrust belt after deposition. Therefore, there is no overlap between the migrating wedge front and the area of active sedimentation (e.g. the eastern Swiss molasse basin).

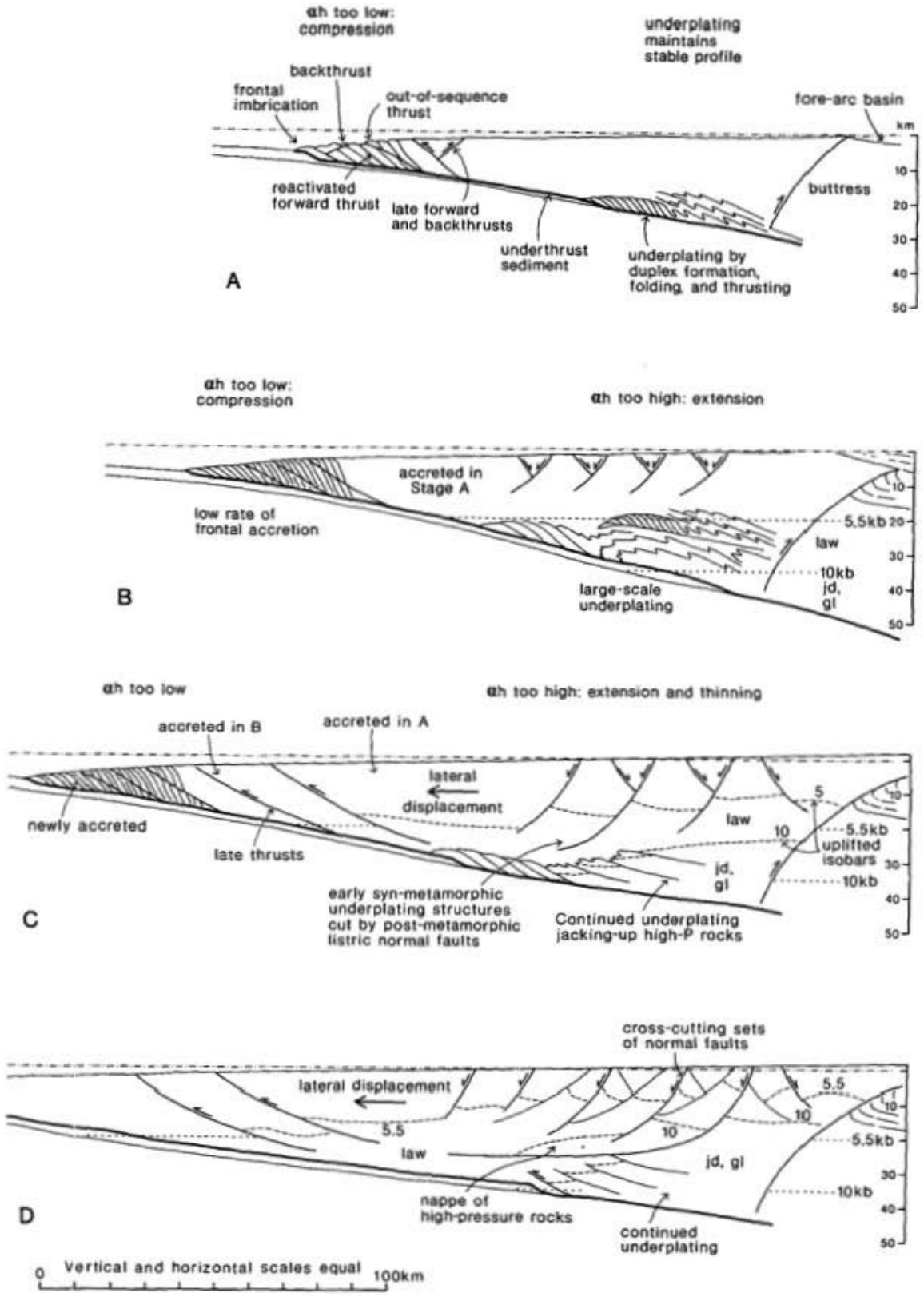

Figure II.11: Cartoon depicting the evolution of an accretionary wedge to form an emergent orogeny. As a result of frontal accretion, underplating, erosion or changes in basal shear stress that force the wedge out of dynamic equilibrium, it responds by shortening and thickening or by extending at the rear. High-pressure rocks are therefore pushed to surface and can be eroded (law = lawsonite + albite parageneses; jd = jadeite + quartz; gl = glaucophane). From Platt (1986).

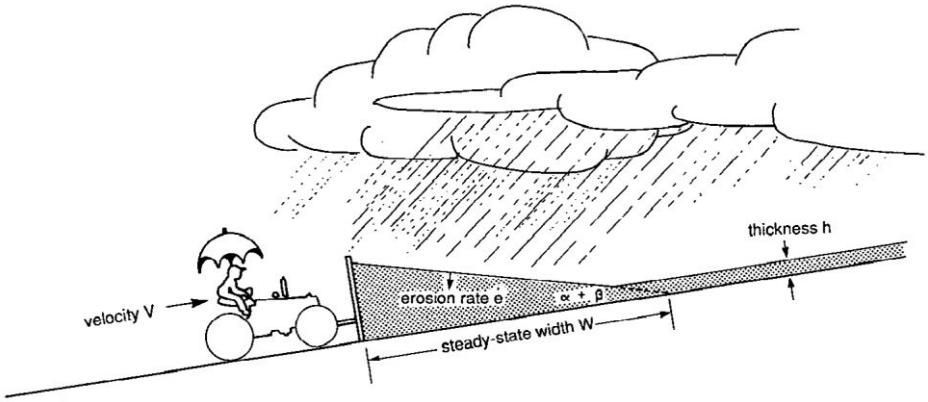

Figure II.12: Critical wedge model including effect of erosion for an eroding wedge in the late steady-state stage. α+β = the taper angle of the wedge; V = velocity; e = erosion rate; h = thickness; W = steady-state width of the wedge. From Dahlen (1990).

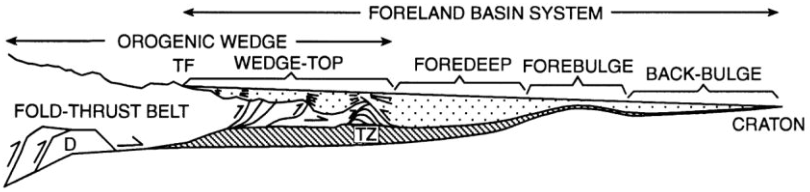

Figure II.13: Schematic cross-section revising the foreland basin system concept, showing the four main depositional zones of foreland basin systems. (1) Wedge-top depositional zone: partially preserved within orogenic belt, deformed, dominated by deep-water stratigraphy ('flysch'). (2) Foredeep depositional zone: extensive preservation, little-deformed, dominated by shallow water and continental stratigraphy. (3) Forebulge depositional zone: very low preservation potential, condensed if present, dominated by karst, unconformities, residual deposits. (4) Backbulge depositional zone: low preservation potential, condensed, shallow-water to terrestrial stratigraphy with many hiatus surfaces). TF = topographic front of the thrust belt; D = duplex in the hinterland part of the orogenic wedge; TZ = triangle zone at the front of the wedge-top depozone. From DeCelles and Giles (1996).

In the second type of external orogenic system the migrating wedge front penetrates below the subsiding flexural basin. Thus, sediments are deposited above and around actively growing structures in the wedge-top depositional zone (Figure II.13). There is therefore significant overlap between the zone of active sedimentation and the migrating wedge front (eg. the Ferrara-Romagna thust belt, northern Apennines). Further to DeCelles and Giles (1996) who only mention a wedge-top depositional zone within the orogen wedge, Ford (2004) adds another subdivision of a foreland basin system: the wedge-top erosional zone (Figure II.14).

In collisional orogens foreland basins occur on both sides of the orogenic belt, leading to the definition of peripheral and retroarc foreland basins proposed by Dickinson (1974). In the case of doubly-wedged orogenic belts, two foreland systems (a wedge and its associated foreland basin) develop in front of migrating internal zones: (1) the retro-wedge and (2) the pro-wedge foreland systems. The former develops on the upper, overriding plate while the latter develops on the lower, subducting plate. They can be distinguished from each other by their basinal and deformational characteristics (Naylor and Sinclair, 2008).

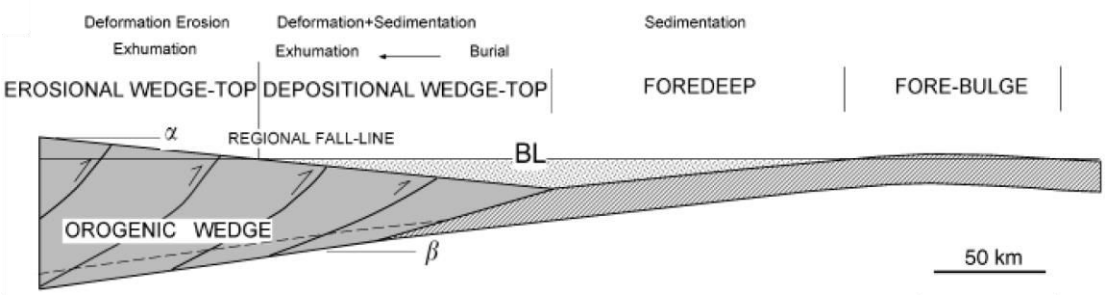

Figure II.14: Subdivisions of a foreland basin system added to the description by DeCelles and Gilles (1996): the erosional wedge-top and depositional wedge-top. BL = base line; α+β = the taper angle of the wedge. From Ford (2004).

Willet et al. (1993) extends the critical taper concept to bivergent wedges (e.g. Pyrenees) by developing numerical coupled tectonic-erosion dynamic models with subduction of mantle lithosphere beneath a crust with Coulomb plastic rheology and no bulldozer backstop required (Figure II.15). It is interesting to notice that such a bivergent structure has been obtained experimentally by Malavieille (1984) whose end-members conditions were used by Willet et al. (1993) and Beaumont et al. (2000) in their studies of orogenic wedges based on numerical models.

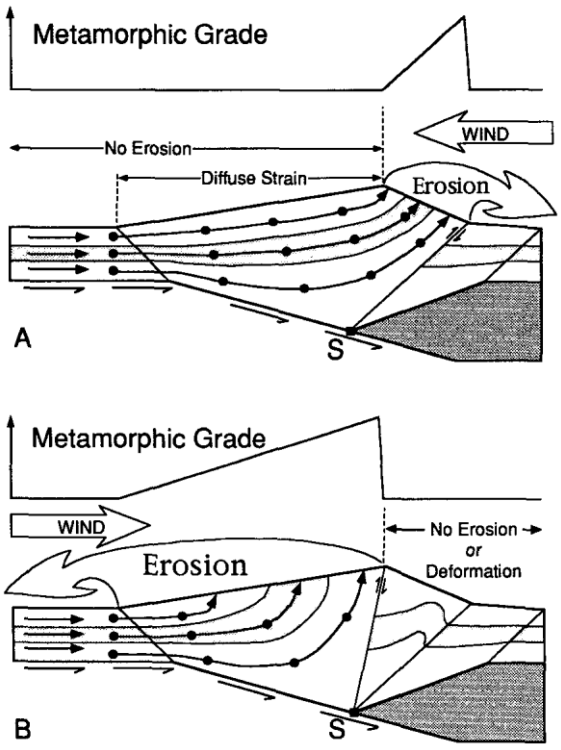

Figure II.15: Critical wedge model including effect of erosion in bivergent orogens. From Willett et al. (1993). (A) Rain is on retro-wedge. (B) Rain is on pro-wedge. High rates of erosion promote high tectonic fluxes into the wedge to replace material lost by erosion (black arrows), resulting in exhumation of high-grade metamorphic rocks (like "sucking up" rocks from depth). S = point of singularity characterized by a discontinuity in the velocity field (speed between the two crustal sections, both null and positive). The convergent section (positive velocity, left side) subducts under the fixed section (null velocity, right side), leading to some sort of asymmetry that depends on the orientation of the subducting section.

Modelling critically tapered orogenic wedges as Coulomb material with erosion processes and pore-fluid pressure within the wedge and along the basal decollement allows: (1) predicting sensible geometries and mechanical parameters for accretionary prisms by reproducing quite closely topographic slopes of accretionary prisms, either continental (Taiwan, the Himalayas) or marine (Japan, Java, Sunda, Peru, Makran, Aleutians, Barbados, Oregon; Davis et al., 1983), and predicting pore-fluid pressure values in agreement with those found within wells (e.g. Davis et al., 1983; Dahlen, 1990), and (2) providing us with a quite simply but rigourous mechanical framework to unravel accretionary prism dynamics using numerical or analogical modelling, and decipher controlling parametres and their impact.

Nonetheless, the wedge model suffers from the fact that thrust belt details are not explicitly represented in the "wedge" while these are important for understanding the development of foreland basins. Firstly, topography depends on continental rock deformation that, in turn, depends on fault development and evolution. Although they allow predicting displacements (e.g. exhumation) and speed rates similar to those observed in mountain ranges, plastic deformation models and viscuous deformation models do not produce major discontinuities with large displacement such as faults (concept of minimum work; Hardy et al., 1998; Masek and Duncan, 1998). The system is assumed to be at any point in space close to the failure criterion for shear failure (Navier-Coulomb criterion of shear failure), which does not allow localizing the deformation along a shear zone, i.e. a fault. Secondly, this model has been established for 10s-to-100s-km-wide and 10-15-km-thick geological objects. Thus, it only deals with brittle deformation in the upper crust and does not integrate neither change in mechanical behaviour with depth, nor elasticity. So, in case of collisional orogens resulting from the inversion of former hyperextended margins (e.g. the Pyrenees), what is the role of rift-inheritance (thermal, structural and compositional) during reactivation? What is the role of transfer zones and segmentation on the lithosphere-scale architecture of the mountain range? How can and how far does the rift inherited architecture and structures control mountain building processes and orogen architecture? Thirdly, it is considered a tendency for a wedge affected by erosion to maintain its equilibrium by frontal accretion of new units and shortening accommodation over its whole width (e.g. Dahlen and Barr, 1989). Yet in Taiwan, Simoès and Avouac (2006) show shortening is largely accommodated by the most frontal structures while Konstantinovskaia and Malavieille (2005) suggest other deformation mechanisms within a mountain range can compensate erosional fluxes (e.g. underplating).

II.3 Foreland basin development models

II.3.1 Transition from rifted margin to foreland basin

Stockmal et al. (1986) develop the concept of "transition from rifted margin to foreland basin". Pro-foreland basin systems are commonly superimposed on passive

margin megasequences, due to ocean closure and collision, whereas retro-foreland basin systems will often overlie back-arc or cratonic sequences.

The inception of foreland basins is complex and difficult to constrain as early-stage deposits of pro-foreland basins are commonly preserved only in highly deformed positions within the external orogenic wedge. Early deposits of 'Flysch' are commonly followed by late deposits of 'Molasse'. During the early convergent stage, foreland basins are marine or lacustrine and underfilled, showing inheritance of passive margin structures and well-developed flexural forebulge (e.g. Allen and Allen, 2013, and references therein). During the later convergent stage, the basin is filled with shallow marine to terrestrial material as it becomes overfilled, commonmy showing a forebulge buried by sediment.

This transition from underfilled (Flysch) conditions to overfilled (molasse) basins has been interpreted as the result of either migration of the orogenic load over the passive margin hingeline (Stockmal et al., 1986) or as a consequence of slab breakoff (Sinclair, 1997). But, would not there be a link between the two-phase evolution of orogens and the two-stage evolution of foreland basins? During the orogenic growth phase, the orogenic wedge is marine, sediment supply is low and often axial, so would this result in (and if positive, always result in) an early underfilled foreland basin? Inversely, as the orogen reaches the steady-state phase, the orogenic wedge becomes exhumed, sediment supply becomes higher and transverse, so would this result in (and if positive, always result in) a late overfilled foreland basin?

II.3.2 Coupled orogenic wedge growth and source-to-sink processes

Most studies on early convergence-stage deposits have been done in pro-foreland basins. The classic example of early fill of a pro-foreland basin is that of the North Alpine Foreland Basin (e.g. Allen et al., 1991; Sinclair et al., 1991; Sinclair, 1997; Burkhard and Sommaruga, 1998).

The stratigraphic record includes in ascending stratigraphic order and laterally ahead of the orogenic load (e.g. Allen et al., 1991; Sinclair et al., 1991; Sinclair, 1997): (1) a flexural, basal forebulge unconformity (a megasequence boundary marked by erosion, karst, paleosols), created by uplifting of the forebulge region, (2) shallow water limestones from distal foredeep (Nummulitic Limestone), (3) hemipelagic marls and shales from the foredeep (Globigerina Marls), and (4) turbidites derived from the orogenic wedge (Taveyannaz Sandstone).

Authors have noted a diachroneity in stratigraphy, i.e. the age of the basal unconformity and the age of the overlying stratigraphy are strongly diachronous, which is very distinctive of pro-foreland basin systems. It is commonly overlain by a deepening-up succession ('underfilled trinity') in internal positions, and by Molasse of the overfilled stage in external positions.

As stated by Naylor and Sinclair (2008), there was at that time (ndlr., 2008) a lack of consideration for retro-foreland system development in terms of stratigraphic

architecture and its impact on the stratigraphic development of the pro-foreland basin. The retro-foreland system preserves a much fuller history of the mountain building. As the orogen passes from the growth to steady-state phase, numerical models predict changes in wedge behaviour on each side of the mountain range, as follows (Willett et al., 2003; Hoth et al., 2008; Naylor and Sinclair, 2008; Sinclair, 2011; Sinclair and Naylor, 2012; Erdös, 2014; Erdös et al., 2014a, 2014b, 2015; Grool et al., 2018): (1) the retro-wedge system is static and relatively stable with no migration of the retro-foreland basin and its infill toward the subduction, while the pro-foreland basin migrates rapidly outward; (2) the retro-wedge is weakly deformed, it experiences predominantly thick-skinned deformation, mainly during the early stage of orogenic wedge growth; in contrast the pro-wedge is strongly deformed and accommodates relatively important shortening during the late orogenic steady-state stage; (3) the retro-foreland basin is characterised by a constant tectonic subsidence rate during the earlier wedge growth phase and near zero (significantly slowed down) tectonic subsidence during the later wedge steady-state phase as a result of balanced accretion-erosion processes, while the pro-foreland basin is characterized by accelerating subsidence at any point as it gets closer and closer to the mountain front; and (4) the entire orogenic growth phase is recorded by the retro basin stratigraphy while only little record of the orogenic steady-state phase is preserved in the pro basin; on the contrary, only the most recent orogenic history will be preserved in the pro-foreland basin as sediments are incorporated back into the range at the thrust front. Such predictions imply that a reduction in sediment accumulation rates associated with a decelerating subsidence should record the transition from growth to steady-state in the retrobasin.

Modelling of the foreland basin fill relies on parameters such as: (1) the kinematics (slope angle, advance rate) and dynamics (rheology, brittle-ductile transition, salt) of the orogenic wedge, (2) the erosion of the wedge, sediment transport, and deposition in foreland basin system depo-zones, (3) the response of the foreland plate (elastic thickness, brittle deformation, localization of deformation), and (4) the transport rate or flux of sediment and rate of erosion or sedimentation which are proportional to topographic gradient and to the curvature, respectively (diffusive case models).

Sinclair et al. (1991) apply sensitivity testing to a simple diffusion model of mountain belt erosion and foreland basin sedimentation, and show that (1) the basin widens over time with increasing *Te* (ageing plate) and transport coefficient, as seen by the onlap of stratigraphy onto the foreland plate; nonetheless, differences between the two sensitivity tests are subtle; (2) the lower the slope angle, the lower sediment discharges/yield, the thinner the chrons and the basin-fill; and (3) the higher the orogenic wedge advance rate, the narrower the basin. Sophisticated models looking at effects of surface processes relative to deformation have also been developed more recently (Simpson, 2006).

Sinclair (2011) model mass fluxes for a coupled thrust wedge and foreland basin system. This model accounts for (1) accretionary flux into the wedge as foreland basin

sediments are deformed and uplifted, and (2) erosional flux that transmits mass from the eroding mountain hinterlands into sediment routing systems (Figure II.16).

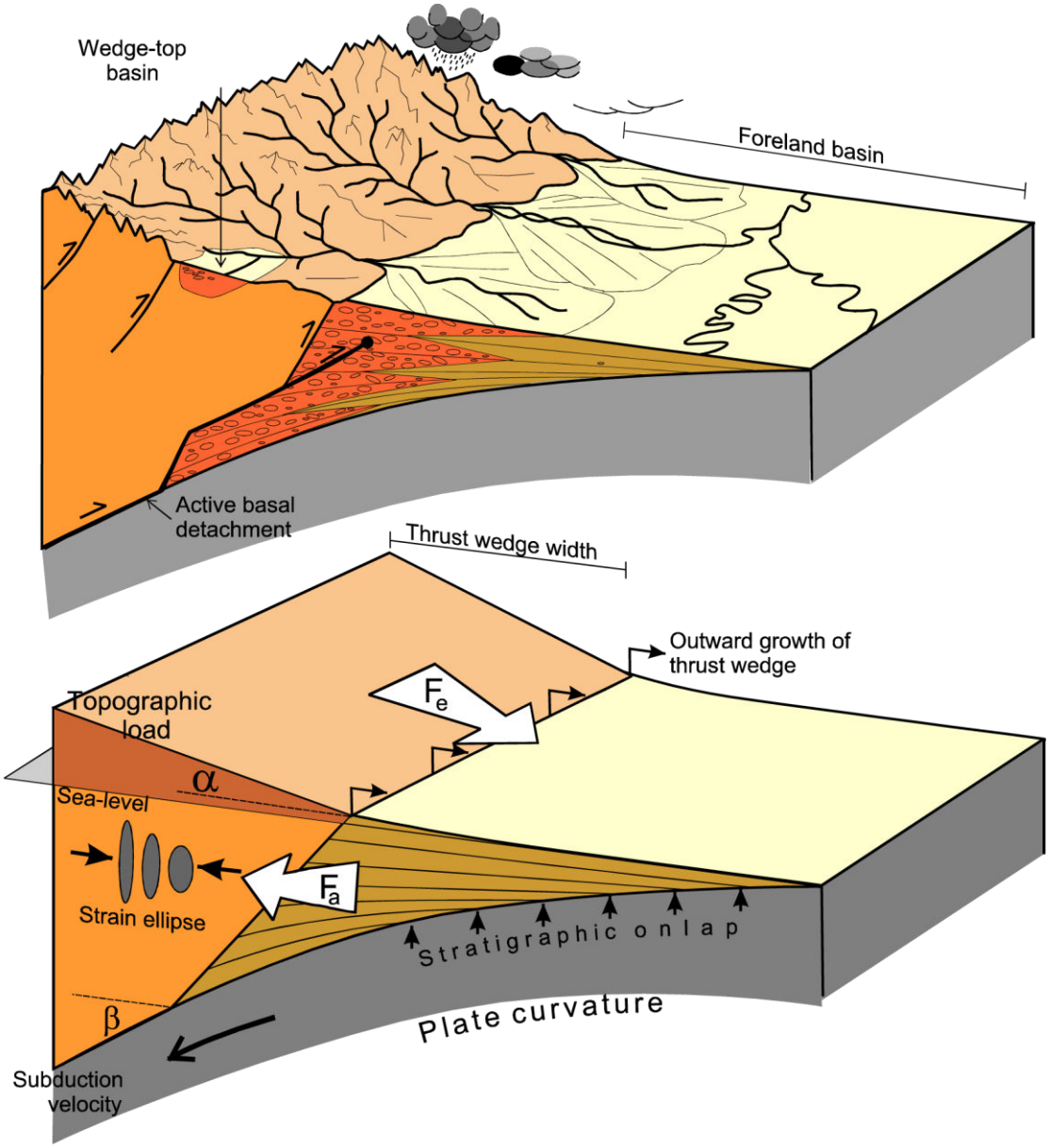

Figure II.16: Mass flux in foreland systems as a result of mountain range-basin coupling. Three main fluxes control foreland basin development: 1) Fe = erosional flux; 2) Fa = frontal accretion; and 3) Fad = advection into rear of wedge. α+β = the taper angle of the wedge. Modified from Sinclair (2011) and Sinclair and Naylor (2012).

This, together with the stratigraphic record, indicates that (1) marine underfilled basins (e.g. 'flysch'-type basin, in the Appenines) are favoured by low transport coefficients, low tapers and fast orogenic wedge advance rate, while (2) continental overfilled basins (e.g. 'molasse'-type basin, in the Ganges) are favoured by high transport coefficients, high tapers and low orogenic wedge advance rate.

SUMMARY

In the classic model of foreland basin evolution, flexure is controlled by the growth of the early orogenic wedge (submarine topographic load) that is approximated as a distributed load. The key assumption is that the lithosphere behaves as an elastic beam with a certain rigidity that will bend when subjected to loading. Thus, such a beam (with a finite strength) will deform by flexure, dependent on the magnitude and wavelength of the load and the flexural rigidity of the beam. In other words, loads of different wavelengths (i.e. sizes) are compensated to a greater or lesser degree depending upon the elastic properties of the lithospheric plate. It might therefore be wise to know: What is the role of lithospheric inheritance in continent-continent collision? How will the rheological structure of the subducting plate affect modelling of flexural deformation at the onset of orogenic contraction? What will be its impact on shortening rates and distribution and their subsequent influence on orogenic wedge growth? What if collision is superimposed on a thinned lithosphere of a distal rift/margin (often not in thermal equilibrium) where lithosphere weakening is at its most?

More and more studies are carried out on coupling orogenic wedge evolution and source-to-sink processes in order to quantify syn-orogenic exhumation/denudation, shortening and orogenic wedge growth, and link these to flexural basin infill. Over the last past 30 years, it has been admitted that the thermal and dynamic evolution of a mountain range is coupled with that of its associated foreland basins. However, most of our understanding of wedge/foreland dynamics comes from the pro-wedge, where mainly late orogenesis is well preserved. Studies have thus been largely focused on the latest, steady-state phase in the orogenic wedge evolution, assuming there is only a single phase with stable progress. Although observed, the earlier growth, submarine phase has therefore remained poorly studied. How to quantify the entire evolution of the orogenic wedge? What about the coupling of early submarine growth of an orogenic wedge with sediment supply? Where does the sediment come from during this early phase?

To address these general questions that all relate to the rift-to-collision transition, the present thesis aims at investigating more specific points:

- Does early orogenesis have a thermal signature distinguishable from other thermal events such as those associated with preceding rifting or later collision?
- How is a (hyper-) thinned distal margin incorporated into the continental accretionary prism at the beginning of convergence?
- Does the thermal and structural inheritance play a role in early orogenesis?
- What are the sediment response and the contribution of dynamic topography to sedimentary passways?

Contrary to the pro-foreland basin, the retro-foreland basin is believed to preserve the full orogen history due to lower shortening and translation values. This is the case in the NE Pyrenean retro-wedge, southwestern France, where recent studies suggest that

during early orogenesis the Pyrenees never reached a steady-state configuration. The Pyrenean orogen has the advantage of low-convergence orogens, allowing better preservation of early phases than in high-convergence orogens. In particular, the northern Pyrenees are recognised to preserve one of the best geological records of a rift-to-collision transition. There is also no thermal signature of subduction preceding collision in the Pyrenees, as is the case in many orogens, because no true oceanic crust was formed before the onset of convergence. The north Pyrenean foreland retro-system is therefore an excellent natural laboratory for deciphering early orogenic growth processes and highlighting the links between extensive inheritance and initiation of orogenic topography at the rift-to-collision transition. Chapter 3 provides background on the Pyrenean orogenic system.

Because such investigation involves quantifying tectonic movements and characterizing the thermal regime of the crust, it is necessary to use a tool sensitive to these processes. Chapter 4 is dedidated to a particularly well-suited tool in this regard, geo-thermochronology, which allows reconstructing the thermal history of rocks (Chapter 5 and Chapter 6) and tracing the source(s) of sediments (Chapter 6).

REFERENCES

Allen, P. A., & Allen, J. R. (2013). Basin Analysis: Principles and Application to Petroleum Play Assessment. John Wiley & Sons.

Allen, P. A., Crampton, S. L., & Sinclair, H. D. (1991). The inception and early evolution of the North Alpine Foreland Basin, Switzerland. Basin Research, 3(3), 143–163.

Argand, E. (1924). La tectonique de l'Asie. In Congrès géologique international (XIIIe session)-Belgique 1922 (pp. 171–372). Retrieved from https://hal.archives-ouvertes.fr/insu-00575289/

Bally, A. W., Gordy, P. L., & Stewart, G. A. (1966). Structure, Seismic Data, and Orogenic Evolution of Southern Canadian Rocky Mountains. Bulletin of Canadian Petroleum Geology, 14(3), 337–381.

Beaumont, C. (1978). The evolution of sedimentary basins on a viscoelastic lithosphere: theory and examples. Geophysical Journal International, 55(2), 471–497.

Beaumont, C., Muñoz, J. A., Hamilton, J., & Fullsack, P. (2000). Factors controlling the Alpine evolution of the central Pyrenees inferred from a comparison of observations and geodynamical models. Journal of Geophysical Research: Solid Earth, 105(B4), 8121–8145.

Bemmelen, R. W. van. (1954). Principles of Mountain Building. In Mountain Building (pp. 1–34). Springer Netherlands. https://doi.org/10.1007/978-94-017-6087-4_1

Birot, P. (1958). Morphologie structurale: Types d'évolution du relief. Théories orogéniques (Vol. 2). Presses universitaires de France.

Bucher, W. H. (1956). Role of gravity in orogenesis. Geological Society of America Bulletin, 67(10), 1295–1318.

Bucher, W. H. (1963). An experiment on the role of gravity in orogenic folding. Geologische Rundschau, 52(2), 804–810.

Burkhard, M., & Sommaruga, A. (1998). Evolution of the western Swiss Molasse basin: structural relations with the Alps and the Jura belt. Geological Society, London, Special Publications, 134(1), 279–298. https://doi.org/10.1144/GSL.SP.1998.134.01.13

Chapple, W. M. (1978). Mechanics of thin-skinned fold-and-thrust belts. Geological Society of America Bulletin, 89(8), 1189–1198. https://doi.org/10.1130/0016-7606(1978)89<1189:MOTFB>2.0.CO;2

Cloetingh, S. (1988). Intraplate Stresses: A New Element in Basin Analysis. In K. L. Kleinspehn & C. Paola (Eds.), New Perspectives in Basin Analysis (pp. 205–230). Springer New York. https://doi.org/10.1007/978-1-4612-3788-4_10

Cloos, M. (1984). Flow melanges and the structural evolution of accretionary wedges. Geological Society of America Special Papers, 198, 71–80.

Cowan, D. S., & Silling, R. M. (1978). A dynamic, scaled model of accretion at trenches and its implications for the tectonic evolution of subduction complexes. Journal of Geophysical Research: Solid Earth, 83(B11), 5389–5396.

Dahlen, F. A. (1990). Critical taper model of fold-and-thrust belts and accretionary wedges. Annual Review of Earth and Planetary Sciences, 18, 55.

Dahlen, F. A., & Barr, T. D. (1989). Brittle frictional mountain building: 1. Deformation and mechanical energy budget. Journal of Geophysical Research: Solid Earth, 94(B4), 3906–3922.

Dahlen, F. A., Suppe, J., & Davis, D. (1984). Mechanics of fold-and-thrust belts and accretionary wedges: Cohesive Coulomb Theory. Journal of Geophysical Research: Solid Earth, 89(B12), 10087–10101. https://doi.org/10.1029/JB089iB12p10087

Davis, D., Suppe, J., & Dahlen, F. A. (1983). Mechanics of fold-and-thrust belts and accretionary wedges. Journal of Geophysical Research: Solid Earth, 88(B2), 1153–1172. https://doi.org/10.1029/JB088iB02p01153

Davis, D. M., & Engelder, T. (1985). The role of salt in fold-and-thrust belts. Tectonophysics, 119(1), 67–88.

DeCelles, P. G., & Giles, K. A. (1996). Foreland basin systems. Basin Research, 8(2), 105–123.

Dewey, J. F., & Bird, J. M. (1970). Mountain belts and the new global tectonics. Journal of Geophysical Research, 75(14), 2625–2647.

Dickinson, W. R. (1974). Plate Tectonics and Sedimentation. Retrieved from http://archives.datapages.com/data/sepm_sp/SP22/Plate_Tectonics_and_Sedimentation.htm

Elliott, D. (1976). The motion of thrust sheets. Journal of Geophysical Research, 81(5), 949–963. https://doi.org/10.1029/JB081i005p00949

Emerman, S. H., & Turcotte, D. L. (1983). A fluid model for the shape of accretionary wedges. Earth and Planetary Science Letters, 63(3), 379–384.

Erdös, Z., Beek, P., & Huismans, R. S. (2014). Evaluating balanced section restoration with thermochronology data: A case study from the Central Pyrenees. Tectonics, 33(5), 617–634.

Erdös, Z., Huismans, R. S., Beek, P., & Thieulot, C. (2014). Extensional inheritance and surface processes as controlling factors of mountain belt structure. Journal of Geophysical Research: Solid Earth, 119(12), 9042–9061.

Erdös, Z., Huismans, R. S., & Beek, P. (2015). First-order control of syntectonic sedimentation on crustal-scale structure of mountain belts. Journal of Geophysical Research: Solid Earth, 120(7), 5362–5377.

Flemings, P. B., & Jordan, T. E. (1990). Stratigraphic modeling of foreland basins: Interpreting thrust deformation and lithosphere rheology. Geology, 18(5), 430–434.

Ford, M., Lickorish, W. H., & Kusznir, N. J. (1999). Tertiary foreland sedimentation in the Southern Subalpine Chains, SE France: a geodynamic appraisal. Basin Research, 11(4), 315–336.

Ford, Mary. (2004). Depositional wedge tops: interaction between low basal friction external orogenic wedges and flexural foreland basins. Basin Research, 16(3), 361–375. https://doi.org/10.1111/j.1365-2117.2004.00236.x

Griggs, D. T. (1939). A theory of mountain-building. American Journal of Science, 237(9), 611–650.

Grool, A. R., Ford, M., Vergés, J., Huismans, R. S., Christophoul, F., & Dielforder, A. (2018). Insights Into the Crustal‐Scale Dynamics of a Doubly Vergent Orogen From a Quantitative Analysis of Its Forelands: A Case Study of the Eastern Pyrenees. Tectonics, 37(2), 450–476. https://doi.org/10.1002/2017TC004731

Hall, J. (1815). II. On the Vertical Position and Convolutions of certain Strata, and their relation with Granite. Earth and Environmental Science Transactions of the Royal Society of Edinburgh, 7(01), 79–108. https://doi.org/10.1017/S0080456800019268

Hardy, S., Duncan, C., Masek, J., & Brown, D. (1998). Minimum work, fault activity and the growth of critical wedges in fold and thrust belts. Basin Research, 10(3), 365–373. https://doi.org/10.1046/j.1365-2117.1998.00073.x

Hess, H. H. (1962). History of ocean basins. Petrologic Studies, 4, 599–620.

Holmes, A. (1928a). Radioactivity and continental drift. Stephen Austin & Sons, Limited, printers.

Holmes, A. (1928b). Theory of continental drift: a symposium on the origin and movement of land masses, both inter-continental and intra-continental, as proposed by Alfred Wegener. Nature, 122, 431–433.

Hoth, S., Kukowski, N., & Oncken, O. (2008). Distant effects in bivergent orogenic belts—How retro-wedge erosion triggers resource formation in pro-foreland basins. Earth and Planetary Science Letters, 273(1), 28–37.

Hutton, J. (1788). X. Theory of the Earth; or an Investigation of the Laws observable in the Composition, Dissolution, and Restoration of Land upon the Globe. Earth and Environmental Science Transactions of the Royal Society of Edinburgh, 1(02), 209–304. https://doi.org/10.1017/S0080456800029227

Hutton, J. (1795). Theory of the earth: With proofs and illustrations (Vol. 1). Library of Alexandria. Retrieved from https://books.google.fr/books?hl=fr&lr=&id=kD1d1aubK3AC&oi=fnd&pg=PT6&dq=Theory+of+th

e+earth:+With+proofs+and+illustrations&ots=3d97yWZD1H&sig=J59VZk20UyVGYqOLJNTBsxsv0jU

Jaumé, S. C., & Lillie, R. J. (1988). Mechanics of the Salt Range-Potwar Plateau, Pakistan: A fold-and-thrust belt underlain by evaporites. Tectonics, 7(1), 57–71.

Jordan, T. E. (1981). Thrust loads and foreland basin evolution, Cretaceous, western United States. AAPG Bulletin, 65(12), 2506–2520.

Karner, G. D., Steckler, M. S., & Thorne, J. A. (1983). Long-term thermo-mechanical properties of continental lithosphere. Nature, 304, 1–4.

Kingston, D. R., Dishroon, C. P., & Williams, P. A. (1983). Hydrocarbon Plays and Global Basin Classification. AAPG Bulletin, 67(12), 2194–2198.

Kober, L. (1951). Atombau und Geologie. Verh. Geol. B. A., Sond. H. C, pp. 76–82.

Konstantinovskaia, E., & Malavieille, J. (2005). Erosion and exhumation in accretionary orogens: Experimental and geological approaches. Geochemistry, Geophysics, Geosystems, 6(2). https://doi.org/10.1029/2004GC000794

Lucchi, F. R. (1986). The Oligocene to Recent foreland basins of the northern Apennines. Foreland Basins, Special Publication of the International Association of Sedimentologists, 8, 105–139.

Lyon-Caen, H., & Molnar, P. (1985). Gravity anomalies, flexure of the Indian plate, and the structure, support and evolution of the Himalaya and Ganga Basin. Tectonics, 4(6), 513–538.

Malavieille, J. (1984). Modélisation expérimentale des chevauchements imbriqués: application aux chaînes de montagnes. Retrieved from http://geoscienceworld.org/highwire/filestream/458370/field_highwire_a_download_vars/0/129.full.pdf

Marshak, S., Wilkerson, M. S., & Hsui, A. T. (1992). Generation of curved fold-thrust belts: Insight from simple physical and analytical models. In Thrust tectonics (pp. 83–92). Springer. Retrieved from http://link.springer.com/chapter/10.1007/978-94-011-3066-0_7

Masek, J. G., & Duncan, C. C. (1998). Minimum-work mountain building. Journal of Geophysical Research: Solid Earth, 103(B1), 907–917. https://doi.org/10.1029/97JB03213

McKenzie, D., Jackson, J., & Priestley, K. (2005). Thermal structure of oceanic and continental lithosphere. Earth and Planetary Science Letters, 233(3), 337–349.

Naylor, M., & Sinclair, H. D. (2008). Pro- vs. retro-foreland basins: Pro- vs. retro-foreland basins. Basin Research, 20(3), 285–303. https://doi.org/10.1111/j.1365-2117.2008.00366.x

Peper, T., Beekman, F., & Cloetingh, S. (1992). Consequences of thrusting and intraplate stress fluctuations for vertical motions in foreland basins and peripheral areas. Geophysical Journal International, 111(1), 104–126.

Platt, J. P. (1986). Dynamics of orogenic wedges and the uplift of high-pressure metamorphic rocks. Geological Society of America Bulletin, 97(9), 1037–1053.

Price, R. A. (1973). Large-scale gravitational flow of supracrustal rocks, southern Canadian Rockies. Gravity and Tectonics, 491–502.

Price, R. A., & Mountjoy, E. W. (1970). Geologic structure of the Canadian Rocky Mountains between Bow and Athabasca Rivers: A progress report. Geological Association of Canada Special Paper, 6, 7–25.

Price, Raymond A. (1971). Gravitational sliding and the foreland thrust and fold belt of the North American Cordillera: Discussion. Geological Society of America Bulletin, 82(4), 1133–1138.

Rich, J. L. (1951). Origin of compressional mountains and associated phenomena. Geological Society of America Bulletin, 62(10), 1179–1222.

Schwarz, E. H. (1906). The Former Land Connection between Africa and South America. The Journal of Geology, 14(2), 81–90.

Simoes, M., & Avouac, J. P. (2006). Investigating the kinematics of mountain building in Taiwan from the spatiotemporal evolution of the foreland basin and western foothills. Journal of Geophysical Research: Solid Earth, 111(B10), B10401. https://doi.org/10.1029/2005JB004209

Simpson, G. D. (2006). Modelling interactions between fold–thrust belt deformation, foreland flexure and surface mass transport. Basin Research, 18(2), 125–143.

Sinclair, H. (2011). Thrust Wedge/Foreland Basin Systems. In C. Busby & A. Azor (Eds.), Tectonics of Sedimentary Basins (pp. 522–537). John Wiley & Sons, Ltd. Retrieved from http://onlinelibrary.wiley.com.biblioplanets.gate.inist.fr/doi/10.1002/9781444347166.ch26/summary

Sinclair, H. D. (1996). Plan-view curvature of foreland basins and its implications for the palaeostrength of the lithosphere underlying the western Alps. Basin Research, 8(2), 173–182.

Sinclair, H. D. (1997). Tectonostratigraphic model for underfilled peripheral foreland basins: An Alpine perspective. Geological Society of America Bulletin, 109(3), 324–346. https://doi.org/10.1130/0016-7606(1997)109<0324:TMFUPF>2.3.CO;2

Sinclair, H. D., & Naylor, M. (2012). Foreland basin subsidence driven by topographic growth versus plate subduction. Geological Society of America Bulletin, 124(3–4), 368–379.

Sinclair, H. D., Coakley, B. J., Allen, P. A., & Watts, A. B. (1991). Simulation of foreland basin stratigraphy using a diffusion model of mountain belt uplift and erosion: an example from the central Alps, Switzerland. Tectonics, 10(3), 599–620.

Stewart, J., & Watts, A. B. (1997). Gravity anomalies and spatial variations of flexural rigidity at mountain ranges. Journal of Geophysical Research: Solid Earth, 102(B3), 5327–5352. https://doi.org/10.1029/96JB03664

Stockmal, G. S., Beaumont, C., & Boutilier, R. (1986). Geodynamic models of convergent margin tectonics: transition from rifted margin to overthrust belt and consequences for foreland-basin development. AAPG Bulletin, 70(2), 181–190.

Taylor, F. B. (1910). Bearing of the tertiary mountain belt on the origin of the earth's plan. GSA Bulletin, 21(1), 179–226. https://doi.org/10.1130/GSAB-21-179

Turcotte, D. L., & Schubert, G. (1982). Geodynamics: Applications of continuum physics to geological problems, 450 pp. John Wiley, New York.

Watts, A. B. (2001). Isostasy and Flexure of the Lithosphere. Cambridge University Press.

Whitmeyer, S. J., Fichter, L. S., & Pyle, E. J. (2007). New directions in Wilson Cycle concepts: Supercontinent and tectonic rock cycles. Geosphere, 3(6), 511–526.

Willett, S., Beaumont, C., & Fullsack, P. (1993). Mechanical model for the tectonics of doubly vergent compressional orogens. Geology, 21(4), 371–374.

Willett, S. D., & Brandon, M. T. (2002). On steady states in mountain belts. Geology, 30(2), 175–178.

Willett, S. D., Chapman, D. S., & Neugebauer, H. J. (1985). A thermo-mechanical model of continental lithosphere. Nature, 314(6011), 520–523. https://doi.org/10.1038/314520a0

Willett, S. D., Fisher, D., Fuller, C., En-Chao, Y., & Chia-Yu, L. (2003). Erosion rates and orogenic-wedge kinematics in Taiwan inferred from fission-track thermochronometry. Geology, 31(11), 945–948.

Chapter 3
III. The Pyrenean Orogenic System

TABLE OF CONTENTS

LIST OF FIGURES

III.1 Pyrenean structure and stratigraphy

The Pyrenean mountain belt extends over 1500 km from the Cantabrian platform in northern Spain to the Mediterranean Sea in southwestern France. The whole orogen can be divided into five main tectono-stratigraphic zones from north to south (Canérot, 2008): (1) the Aquitaine Basin, (2) the North Pyrenean Zone, (3) the Axial Zone, (4) the South Pyrenean Zone, and (5) the Ebro Basin (Figure III.1).

These zones are delimited by three major faults from north to south: (1) the North Pyrenean Frontal Thrust, (2) the North Pyrenean Fault, and (3) the South Pyrenean Frontal Thrust, a south-vergent thrust between the South Pyrenean Zone and the Ebro Basin (Figure III.1.b).

III.1.1 The Aquitaine Basin

The stratigraphic scheme about to be used in this section is that of Ford et al. (2016) and Rougier et al. (2016), aiming at harmonizing the stratigraphic nomenclature along the central and the eastern proximal Aquitaine basin (Figure III.2).

The Aquitaine Basin is the Pyrenean retro-foreland basin system (Sinclair et al., 2005; Biteau et al., 2006; Naylor and Sinclair, 2008; Ford et al., 2016; Rougier et al., 2016), north of the North Pyrenean Frontal Thrust and south of the Celtaquitanian flexure (Brunet, 1986, 1991; Desegaulx and Brunet, 1990; Desegaulx et al., 1990; Bourrouilh et al., 1995; Serrano et al., 2001). Basin subsidence results from the superimposed tectonic, flexural subsidence related to Pyrenean orogenic thrust sheet loading from the North Pyrenean Zone and the Axial Zone (Santonian to Early Miocene) and thermal subsidence inherited from the pre-orogenic rifting phase (Aptian to Albian; Bourrouilh et al., 1995).

The Aquitaine Basin is divided along strike into two distinct domains by a N010°-trending fault, the Toulouse Fault, a reactivated Variscan structure (e.g. Chevrot et al., 2014; Figure III.1.b). To the west, the stratigraphic record comprises the entire Triassic to Miocene sedimentary succession (Upper Cretaceous to Miocene sediments are sitting on marine Mesozoic series). To the east only Upper Cretaceous to Miocene sediments were deposited above Paleozoic basement of the Carcassone High (e.g. Mouthoumet and Alaric massifs; Figure III.2).

Across strike the Aquitaine Basin consists of the Aquitaine Platform and the Aquitaine foredeep to the south (Figure III.2). The former is the least deformed zone of the foreland basin that extends towards the Variscan French Massif Central to the north.

The Aquitaine depocentre started developping during Triassic times with the deposition of the Bundsanstein/Red Sandstone Group (Ford et al., 2016; Rougier et al., 2016; Christophoul et al., in prep; Figure III.2). The syn-rift deposition continued until end Cenomanian (Black Flysch Group; e.g. Ford et al., 2016). The mid-Cenomanian to end Santonian time period saw wide deposition over an area extending from the Axial Zone to the Aquitaine platform, marking the end of the rifting phase in the North Pyrenean Zone and the beginning of thermal subsidence (post-rift deposition). The

Pyrenean contraction began end Santonian times, which led to the deposition of thick accumulations of deep-water siliciclastics (Petites Pyrénées Group) west of the Toulouse Fault (Bourrouilh et al., 1995), notably in sub-basins such as the Parentis, Arzacq, Tarbes, Mirandes and Comminges sub-basins (Biteau et al., 2006).

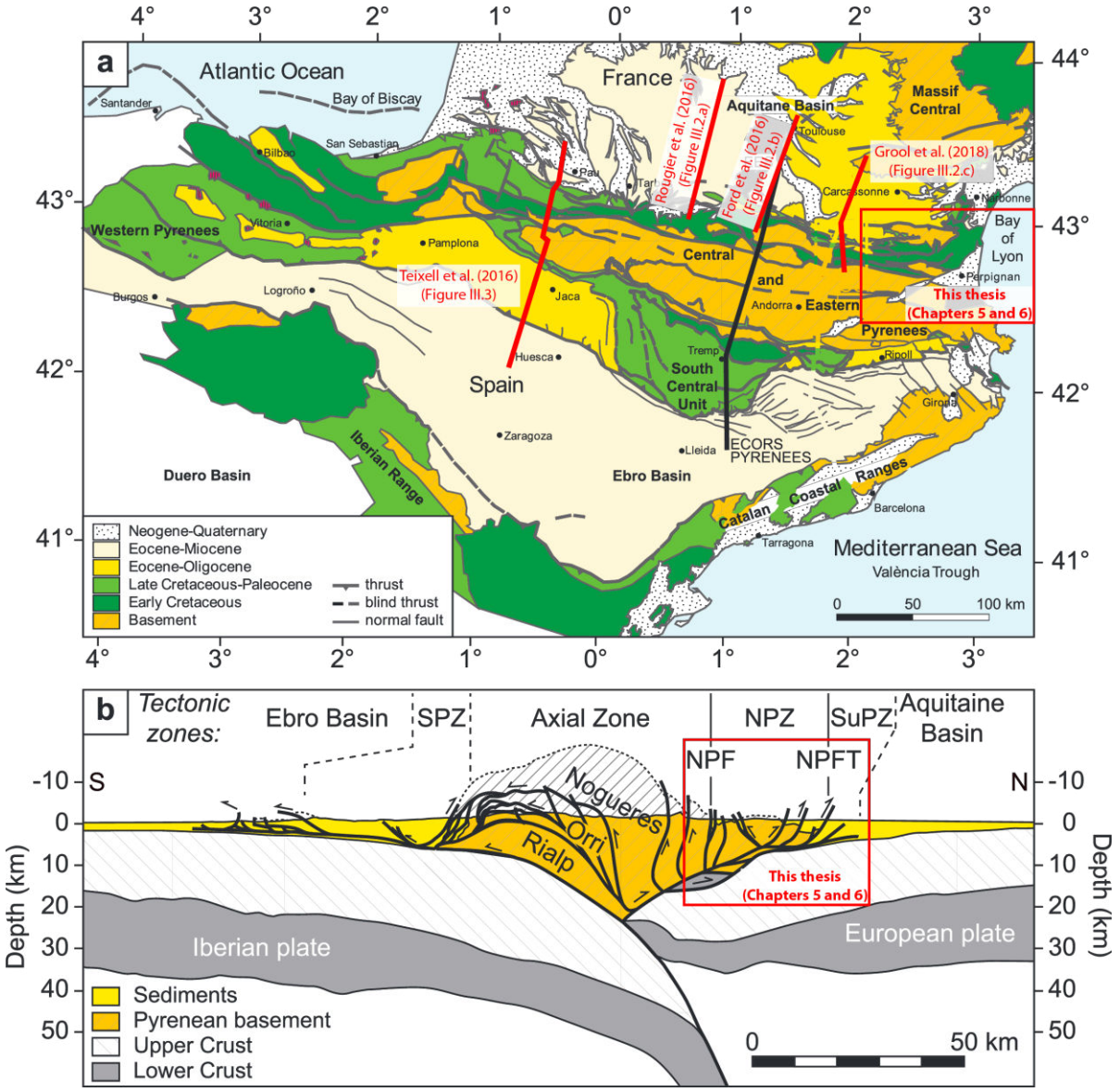

Figure III.1: Geological map and simplified crustal model for the Pyrenean orogen. Modified after Grool et al. (2018). (a) Simplified geologic map of the Pyrenees, showing the main tecto-stratigraphic units, the trace of the ECORS Pyrenees deep seismic profile (black line), the location of the cross-sections in Figure III.2 and Figure III.3 (red lines) and the approximate location of the study area in this thesis (red rectangle). (b) Simplified crustal model along the ECORS Pyrenees deep seismic profile, showing the main tectonic units in the Pyrenean orogen and the approximate location of the study area in this thesis (red rectangle). SuPZ = Subpyrenean Zone; NPFT = North Pyrenean Frontal Thrust; NPF = North Pyrenean Fault; NPZ, North Pyrenean Zone; SPZ = South Pyrenean Zone.

A Campanian-to-Late-Maastrichian, southward- and westward-thickening series is observed north of the North Pyrenean Frontal Thrust, passing from coarse-grained, fluvial to shallow marine delta-top facies (sand-dominated Plantaurel Group) in the east to fine-grained, deep water facies in the west (shale-dominated Petites Pyrénées Group)

into a partially preserved flysch trough, the Subpyrenean Trough also called Flysch Trough, located immediately to the north of the internal core of the Pyrenean mountain chain (Ricateau and Villemin, 1973; Dubois and Seguin, 1978; Bilotte et al., 2005; Bilotte, 2007; Monod et al., 2014; Ford et al., 2016). This trough was an E-W-trending, asymmetric, deep, narrow thrust-loaded foredeep basin. Deposition from Santonian onward occured only north of the North Pyrenean Frontal Thrust and resulted in a 4-to-6-km-thick succession (BRGM et al., 1974; Christophoul et al., 2003; Naylor and Sinclair, 2008; Ford et al., 2016; Rougier et al., 2016; Figure III.2 and Figure III.2).

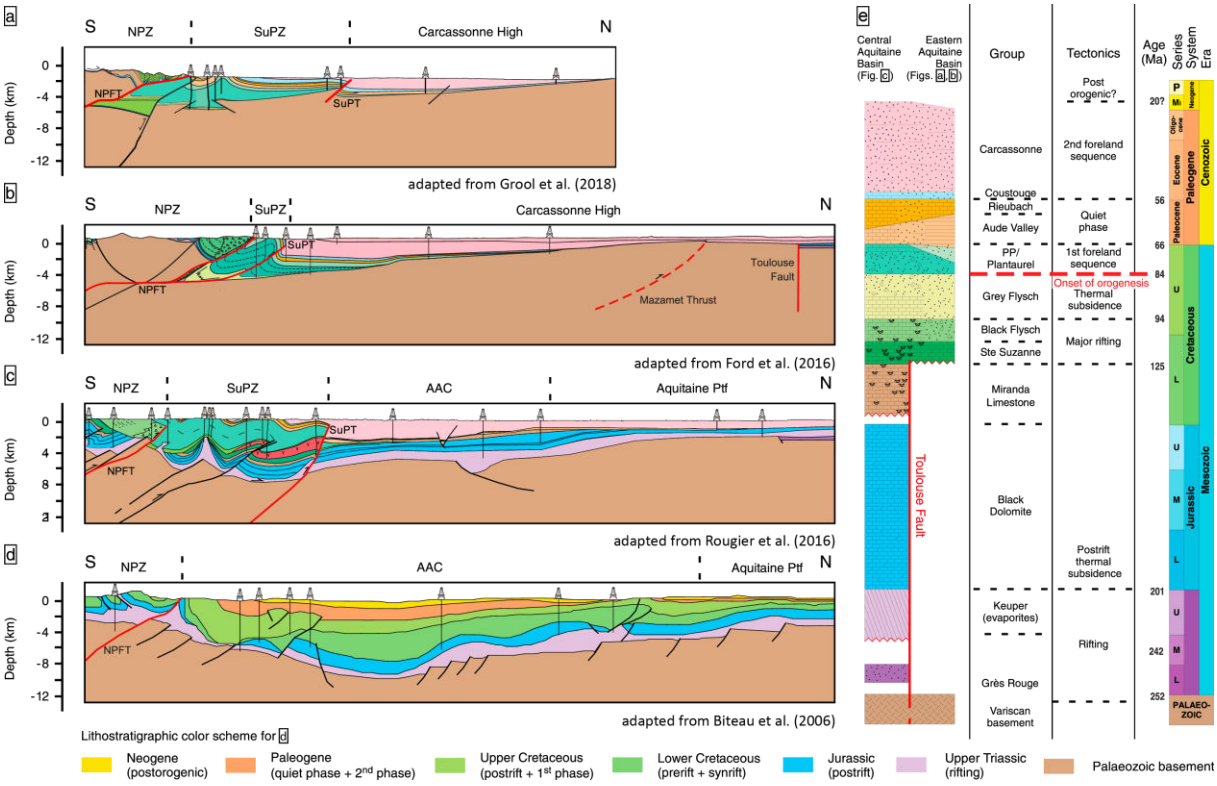

Figure III.2: Structural cross-sections, stratigraphy, and tectonic history summary for the central and eastern retro-wedge/foreland basin. Modified from Angrand et al. (2018). (a) Present-day cross-section through the central North Pyrenean Zone, Subpyrenean Zone and Aquitaine Basin. Modified from Rougier et al. (2016). (b) Present-day cross-section through the westernmost portion of the eastern North Pyrenean Zone, Subpyrenean Zone and Aquitaine Basin. Modified from Ford et al. (2016). (c) Present-day cross-section through the central portion of the eastern North Pyrenean Zone, Subpyrenean Zone and Aquitaine Basin. Modified from Grool et al. (2018). (d) Stratigraphic chart and major tectonic events, compiled from Ford et al. (2016) and Rougier et al. (2016) for the eastern and central Aquitaine Basin. The cross-sections are located in Figure III.1.a. The colors used in cross-sections are those in the stratigraphic chart in Figure III.2.d. SuPT = Subpyrenean Thrust; SuPZ = Subpyrenean Zone; NPFT = North Pyrenean Frontal Thrust; NPZ = North Pyrenean Zone; AAC = Adour-Arzacq-Comminges rift; Pft = platform; PP = Petites Pyrénées (Group); P = Pliocene; Mi = Miocene; U = Upper; M = Middle; L = Lower.

This system is completed in the latest Cretaceous (latest Maastrichian) to late Paleocene-early Eocene by thin, progressively northward-onlapping continental deposits (Aude Valley Group (equated to the Garumnian facies of the eastern Pyrenees) to lower levels of the Coustouge Group; Ford et al., 2016; Christophoul et al., in prep). In Early Ypresian, the early Ilerdian marine transgression coming from the west reached

the easternmost Aquitaine basin (Alaric Formation at base of the Coustouge Group). From mid-to-late Ilerdian to Cuisian, the sedimentary pile (Coustouge Group) records a major transgression-regression cycle, and the Eocene-Oligocene succession records a transition from marine (Alaric Formation) to continental, fluvial deposits (Carcassonne group) with periodic marine transgressions (BRGM et al., 1974; Ford et al., 2016; Christophoul et al., in prep) in the westernmost basin and alluvial fan systems close to the thrust front (Bourrouilh et al., 1995).

III.1.1.1 Foreland structures east of the Toulouse Fault

To the east of the Toulouse Fault, thick-skinned tectonics are observed across the foreland with local depocentres separated from each other by basement uplifts. These structures progressively disappear toward the Toulouse Fault.

On the S4 cross-section (Ford et al., 2016; Figure III.2), which is the central (Arize) ECORS deep seismic line, Upper Cretaceous deposits are preserved north of the North Pyrenean Frontal Thrust. Petites Pyrénées folds controlled Eocene deposition as recorded by progressive unconformities. Upper Cretaceous, Paleocene and Eocene series progressively onlap toward the north onto Variscan basement. Eocene deposits are eroded on the Montgiscard High, and directly overlain by Oligo-Miocene sediments. Subsidence analysis shows three phases: (1) a phase of accelerating subsidence in the Campano-Maastrichian, followed by (2) a period of relative tectonic quiescence marked by extremely slow subsidence from the Paleocene until (3) renewed acceleration of subsidence in the Eocene.

III.1.1.2 Foreland structures west of the Toulouse Fault

To the west of the Toulouse Fault (e.g. cross-section through the Chainons Béarnais; Teixell et al., 2016; Figure III.3), highly-deformed structures of the Subpyrenean Zone are not found, except just west of the Toulouse Fault (Rougier et al., 2016). In contrast to the central and eastern Aquitaine foreland basin that developped onto the Carcassone High (Paleozoic basement unaffected by Mezosoic extension; Baby, 1989; Ford et al., 2016; Grool et al., 2018; Figure III.2), the western foreland basin developed on a lithosphere thinned by Mesozoic extension, with crustal thinning increasing westward as indicated by the sedimentary succession that overlies a Jurassic to Cretaceous synrift series including Triassic Keuper evaporites. Salt tectonics is much more developped than that to the east of the Toulouse Fault (e.g. Teixell et al., 2016) with Keuper evaporites acting as a thin-skinned decollement layer and detached the deformation from underlying rift succession.

The basin infill also thickens westward with large depocentres developped in early Cretaceous times (e.g. Arzacq, Mirande or Tarbes basins; Biteau et al., 2006; Figure III.2). Upper Cretaceous, syn-orogenic sediments only lie in the Comminges basin, part of the Subpyrenean Zone developed eastward, south of the central and eastern Aquitaine foreland basin. As such, the whole syn-orogenic, Upper Cretaceous depocentre seems to be preserved exclusively in the Subpyrenean Zone, east of the Toulouse Fault. Ford et al.

(2016) argue that "*growth strata and progressive unconformities (Razin, 1989; Déramond et al., 1993; Serrano et al., 2006) record wedge-top conditions (DeCelles and Giles, 1996; Ford, 2004).*"

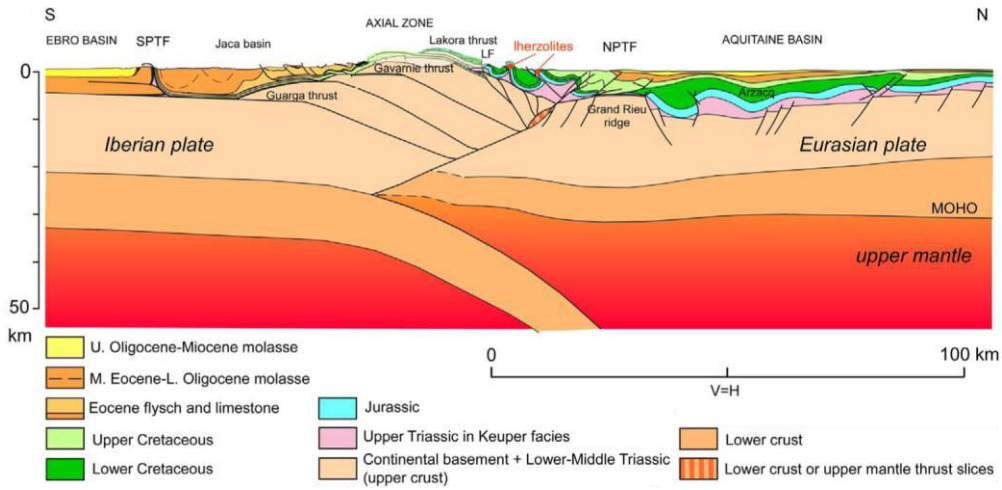

Figure III.3: Present-day crustal cross-section for the Western Pyrenees (Chainons Béarnais-Jaca). NPFT: North Pyrenean Frontal Thrust; LF: Licq fault; SPFT: South Pyrenean Frontal Thrust (External Sierras). From Teixell et al. (2018), modified after Teixell et al. (2016).

The Aquitaine retro-foreland basin is therefore the first Pyrenean foreland basin to develop, and more generally speaking, it integrates the earliest syn-orogenic depocentre (preserved in the Subpyrenean Zone) of the retro-foreland basin system.

III.1.2 The Subpyrenean Zone

The Subpyrenean Zone consists in kilometer-scale, north-verging folded structures of pre- and syn-orogenic sediments. The whole syn-orogenic, Upper Cretaceous depocentre seems to be preserved exclusively in this zone, and Late Cretaceous sediments seal the North Pyrenean Frontal Thrust to the south and abruptly thin then disappear to the north of the Petites Pyrénées Front. In the east the latter is bounded to the south by the narrow (30-10-km-wide), ENE-WSW-striking Subpyrenean Zone, also called Petites Pyrénées, that is bounded by the Subpyrenean Front to the north, also called the Petites Pyrénées Front, and the North Pyrenean Frontal Thrust to the south.

The Subpyrenean Front is a south-dipping blind thrust, primarily imaged on seismic in central Pyrenees, within the Saint-Marcet anticline; Paris and Cavaillé, 1974 Serrano et al., 2006). It was active during deposition of syn-orogenic Upper Cretaceous to Oligocene series and was sealed by Miocene post-orogenic deposits (upper levels of the Carcassonne Group; Ford et al., 2016; Figure III.2; Rougier et al., 2016; Figure III.2). This thrust displays a normal displacement component at the base and an inverse displacement component at the top. As such, it is interpreted as an extensional fault that formed the northern margin of a northern early Albian depocentre that was partially inverted in contractional setting (Rougier et al., 2016).

The Subpyrenean Zone presents deformation far more intense than in the Aquitaine basin, recording exclusively the Pyrenean post-Apto-Albian-extension and contraction and propagating northward through time.

III.1.3 The North Pyrenean Frontal Thrust

The North Pyrenean Frontal Thrust is a major thrust fault whose development and timing (Late Cretaceous or Eocene) have been debated for example in the eastern Pyrenees, in the Cucugnan region.

Some authors consider that this thrust formed after deposition of the Upper Cretaceous to Paleocene Garumnian facies because these strata would be involved within the fault deformation zone (Castéras et al., 1967; Freytet, 1970; Plaziat, 1984; Berger et al., 1997; Bilotte and Canerot, 2006).

In contrast, other authors (Mattauer and Proust, 1962; Charrière and Durand-Delga, 2004; Combes et al., 2004) argue that the North Pyrenean Frontal Thrust acted in Late Cretaceous as the Garumnian succession overlies and seals the North Pyrenean Zone and Subpyrenean Zone.

Recent work further west (Ford et al., 2016; Rougier et al., 2016) shows that the North Pyrenean Frontal Thrust would have become active in Santonian to Campanian times (Puigdefàbregas and Souquet, 1986; de Jong, 1990; Capote et al., 2002; Rosenbaum et al., 2002), based on well and borehole evidence. The authors (and references therein) also show that the fault cuts basement. This suggests thick-skinned deformation style in the Alpine deformation with involvement of the Variscan basement

It has been suggested that the North Pyrenean Frontal Thrust links southward to the main crustal fault that carried the high-density Saint Gaudens body (mantle or lower crust) to mid-cristal levels (strong positive Bouguer anomaly (Azambre and Pozzi, 1982) and high amplitude, south-dipping reflections on the ECORS line (Roure et al., 1989).

Stratigraphy shows that the North Pyrenean Frontal Thrust was the northern margin of the Early Cretaceous extensional domain (or the Bigorre Black Flysch basin; Debroas, 1990), i.e. a normal fault inherited from Early Cretaceous extension then inverted as a thrust during Pyrenean contraction. Although this feature is sometimes partly hidden by post-orogenic deposits, (e.g. in eastern Pyrenees; Berger et al., 1997), it has been shown generally to outcrop in eastern Pyrenees (S2, S3 and S4 cross-sections; Figure III.2), locally to be active until deposition of the upper levels of the Petites Pyrénées Group (Plagne Formation), i.e. some time in the Maastrichtian (Serrano et al., 2006; S5 cross-section (Rougier et al., 2016; Figure III.2) just west of the Toulouse Fault, even until deposition of Upper Oligocene-Miocene molasse in the Chainons Bearnais is western Pyrenees (Teixell et al., 2016; Figure III.3).

III.1.4 The North Pyrenean Zone

The North Pyrenean Zone is a fold-and-thrust belt developed on the upper European continental plate (retro-wedge). This is a 10-40-km-wide, WNW-ESE-trending thrust system advancing on and flanked by the Aquitaine Basin (Puigdefàbregas et al., 1986), involving both basement and sedimentary cover sequences (Morris et al., 1998; Jolivet et al., 2007; Metcalf et al., 2009). It is north-verging in central and eastern

Pyrenees but becomes southward-verging in the westernmost North Pyrenean Zone (Chainons Béarnais; Teixell et al., 2016; Figure III.3).

The North Pyrenean Zone represents a highly deformed zone of the Pyrenean system (e.g. in Paleogene deposits in western Pyrenees, Basque-Cantabrian region (Lacq, Donzacq regions); e.g. Kieken and Winnock, 1973), where deformation increases southward.

It comprises thick Mesozoic basins that are bordered by external crystalline Variscan basement massifs (e.g. Saint Barthémy; Baby et al., 1988; Deramond et al., 1993; Agly; Vielzeuf and Kornprobst, 1984; Vauchez et al., 2013). These depocentres represent zones of Early Cretaceous (Apto-Albian), hyper-extension/extreme lithospheric thinning and mantle exhumation (Lagabrielle and Bodinier, 2008; Jammes, 2009; Jammes et al., 2009, 2010a, 2010b; Lagabrielle et al., 2010; Clerc, 2012; Clerc et al., 2012, 2015). This is marked by the presence of fragments of sub-continental mantle rocks (peridotites; e.g. the Lherz lherzolithe massif; e.g. Monchoux, 1970; Hall and Bennett, 1979; Minnigh et al., 1980; Fabriès et al., 1991, 1998; Henry et al., 1998; Lagabrielle and Bodinier, 2008; Lagabrielle et al., 2010; Clerc et al., 2012, 2015) and lower continental crust rocks (granulites; e.g. the Agly basement massif; Vielzeuf and Kornprobst, 1984) near the North Pyrenean Fault in the Pyrenees (e.g. Mauléon; Masini et al., 2014; Chainons Béarnais; Corre et al., 2016; Teixell et al., 2016) and within the Nappe des Marbres in the Basque-Cantabrian basin (e.g. Lamare, 1936). These basins were inverted during Pyrenean convergence and subsequently thrust over the Subpyrenean Zone along the North Pyrenean Frontal Thrust.

The North Pyrenean Zone comprises in its southernmost part a quite narrow (up-to-10-km-wide), 300-km-long, E-W-trending zone of HT-LP metamorphism (e.g. Albarède and Michard-Vitrac, 1978; Choukroune and Mattauer, 1978; Peybernes and Souquet, 1984; Golberg et al., 1986a, 1986b; Golberg, 1987; Golberg and Maluski, 1988; Golberg and Leyreloup, 1990; Clerc, 2012; Clerc et al., 2012, 2015; Clerc and Lagabrielle, 2014; Corre et al., 2016) extending from the North Pyrenean Fault to the south to the Arize Massif to the north: the Metamorphic Internal Zone.

The westernmost and easternmost ends of the Metamorphic Internal Zone represent zones of low deformation where prior structures are quite nicely preserved (Ducoux et al., in prep). The central Metamorphic Internal Zone is highly deformed, resulting in vertical structures that hide the initial structural organization of the Metamorphic Internal Zone (Choukroune, 1974). HT-LP metamorphism there is concentrated in Mesozoic material, in particular Albian to Cenomanian terrains (Black Flysch Group; Peybernes and Souquet, 1984; Souquet et al., 1985; Golberg et al., 1986a, 1986b; Montigny et al., 1986; Golberg, 1987; Golberg and Maluski, 1988; Debroas, 1990; Golberg and Leyreloup, 1990; Souquet and Peybernes, 1991; Debroas et al., 2010). HT-LP metamorphism coincides temporally and spatially with alkaline magmatism (Azambre and Rossy, 1976; Albarède and Michard-Vitrac, 1978; Montigny et al., 1986; Golberg and Leyreloup, 1990; Clerc and Lagabrielle, 2014) and with large hydrothermal

fluid circulations that led to hydrothermal alteration such as the albitization of parts of the North Pyrenean Variscan massifs and the development of talc deposits in late Aptian to early Cenomanian times (Moine et al., 1989; Demange et al., 1999; Schärer et al., 1999; Boulvais et al., 2006, 2007; Poujol et al., 2010; Fallourd et al., 2014).

Montigny et al. (1986) was the first to notice an east-west asymmetry in mineralogical associations defining P-T conditions experienced by outcropping Mesozoic rocks, with higher temperature, higher pressure and de facto higher thermal gradients to the east. Most recently Clerc et al. (2012, 2015) offer a more complete review of metamorphism temperatures in the Metamorphic Internal Zone clearly confirming a first order temperature gradient increasing from west to east. Recent work (Chelalou et al., 2016; Ducoux et al., in prep) provides 173 additional Raman Spectroscopy on Carboneous Material temperature data on poorly-to-non-constrained locations indicating that temperatures may exceed 500 °C over the entire Metamorphic Internal Zone (including the Boucheville syncline).

III.1.5 The North Pyrenean Fault

The North Pyrenean Fault is a major fault along which the North Pyrenean Zone is overthrusted by the Axial Zone. It is interpreted as a major late-to-post Hercynian (Late Carboniferous-Early Permian), lithosphere-scale discontinuity associated with, and inherited from, dextral wrenching between Iberia and Europe during the Hercynian orogenic cycle whose late-to-post-Hercynian evolution is controversial (Arthaud and Matte, 1975, 1977; Burg et al., 1994; Matte, 2001). It was thought to define the plate boundary between the European and the Iberian plates (Mattauer, 1968; Choukroune and Mattauer, 1978; Choukroune, 1988, 1989; Roure et al., 1989).

The post-Hercynian story of this crustal discontinuity has been long debated, especially since interpretations related to its nature (strike-slip, dip-slip or transform/transfer fault), its lateral continuity and its role in accommodating the Bay of Biscay opening (Late Jurassic to Early Cretaceous) are still open to question (e.g. Mattauer and Séguret, 1971; Canérot et al., 2001, 2004, 2005; Canérot, 2008, and references therein).

The trace of the North Pyrenean Fault is fairly well-defined in the central and eastern Pyrenees with the presence of the Metamorphic Internal Zone (Figure III.1). It is marked by a zone of subvertical faulting and shearing separating the Axial Zone from the Metamorphic Internal Zone (e.g. Choukroune, 1972, 1974; Mattauer and Choukroune, 1974; Vielzeuf and Kornprobst, 1984). However, the fault zone is poorly defined in the western Pyrenees beneath the Mauléon Basin. To the west in the Basque-Cantabrian region, the Leiza Fault is controversially assumed to be its lateral equivalent (Choukroune, 1972; Boillot et al., 1973; Rat, 1988; Combes et al., 1998; Mathey et al., 1999) as fragments of mantle bodies and metamorphic Mesozoic rocks are encountered within the Nappe des Marbres (e.g. Lamare, 1936), similarly to what is observed to the east.

The North Pyrenean Fault is considered by many authors to have played a key role in both the Late Jurassic to Early Cretaceous rifting phase and the early phase of Pyrenean orogenesis (Choukroune, 1992; Muñoz, 1992; Vergés and Garcia-Senz, 2001; Lagabrielle et al., 2010). However, no field data is available to constrain the amount of shortening or the kinematics associated with the rifting episode.

Some authors argue that the North Pyrenean Fault was reactivated as a sinistral strike-slip or as an extensional dip-slip fault system between Iberia and Europe during the Aptian-Albian extension (e.g. Debroas, 1987a, 1987b, 1990; Bourrouilh et al., 1995; Le Vot et al., 1996; Vergés and Garcia-Senz, 2001; Canérot et al., 2005; Lagabrielle et al., 2010), with reactivation of pre-existing Variscan faults and subsequent development of a series of highly subsiding, rhomb-shaped, en-echelon pull-apart-like flysch basins (e.g. Le Pichon et al., 1970; Mattauer and Séguret, 1971; Choukroune and Mattauer, 1978; Boillot, 1986; Bourrouilh et al., 1995; Le Vot et al., 1996; Olivet, 1996; Larrasoaña, 2003a, 2003b; Roca et al., 2011). In other words, the North Pyrenean Fault would have accommodated the 200-300 km sinistral motion of the Iberial plate with respect to Europe (this is discussed in section III.2).

Some others consider that sinistral strike-slip motion between Iberia and Europe began during the opening of the North Atlantic in the Late Jurassic (e.g. Canérot and Delavaux, 1986; Canérot, 1987, 1989, 2008; Rat, 1988; Uchupi, 1988; Villien and Matheron, 1989; Le Vot et al., 1996; Schettino and Scotese, 2002; Jammes, 2009; Jammes et al., 2009, 2010b; Tugend et al., 2014). This would have resulted in a pre-Aptian transtensional setting along the European and Iberian plates, as stratigraphically evidenced in the Parentis and Cameros basins (e.g. Salas and Casas, 1993; Jammes, 2009; Jammes et al., 2009, 2010b). These authors conclude that there was no strike-slip after the late Aptian to early Albian. They therefore see the North Pyrenean Fault as a suture zone related to the inversion of the former hyperextended and exhumed mantle domains between Iberian and European plates (see section III.2).

Tugend (2013) and Tugend et al. (2014) propose that the North Pyrenean Fault and the North Pyrenean Frontal Thrust as the northern and southern inverted margins of the hyperextended domains between Iberian and European plates.

III.1.6 The Axial Zone

The Axial Zone is the main internal deformation zone of the Pyrenean range, flanked by the North Pyrenean Zone to the north (fold-and-thrust belt, retro-wedge) and the South Pyrenean Zone to the south (fold-and-thrust belt in the pro-wedge; Figure III.1.b).

The Axial Zone is essentially made up of Paleozoic metasediments (Cambrian to Carboniferous) that are locally intruded by Ordovician granitic material (Barbey et al., 2001; Cocherie et al., 2005; Denèle et al., 2009a, 2009b; Denèle et al., 2014). These were further deformed, metamorphosed and intruded from Late Carboniferous to Permian (Canérot, 2008; Denèle et al., 2012). Nonetheless, the metamorphic rocks are far less

metamorphosed (by up to 200 °C less at some locations) than Albian-Cenomanian deposits within the Metamorphic Internal Zone (Chelalou et al., 2016).

The Axial Zone consists of south-vergent upper crustal thrust sheets forming a complex antiformal duplex structure (Muñoz, 1992). This is the standard interpretation of the ECORS deep seismic reflection profiles (Mattauer, 1968; Choukroune and Mattauer, 1978; Choukroune, 1988, 1989; Roure et al., 1989; Vergés and Muñoz, 1990; Muñoz, 1992; Roure and Choukroune, 1998; Figure III.4). The model of Muñoz (1992) (Figure III.4.a) uses the sequential restoration technique, and contrasts with the model of Séguret (1972) (Figure III.4.a) who uses gravity gliding, and so doing, roots South Pyrenean thrust sheets in a different manner, as presented below. Séguret (1972) argues that the Pedraforca unit (south-eastern central Pyrenees) and most of the central South Pyrenean unit (the Boixols-Montsec-Sierras Marginales thrust sheet duplex in southern central Pyrenees) are allochtonous. Their initial location would have been on the southern Axial Zone for the whole Pedraforca unit and north of the central South Pyrenean unit only. Their present-day location would be due to the combination of (1) southward thrusting of the Nogueres (Gavarnie) thrust over the Rialp-Orri units by *ca.* 40 km, which led to uplift of the Axial Zone in Eocene times (displacement synchronous to sedimentary Eocene deposition to the south), and (2) subsequent gravity gliding of these units toward south. In this model, the floor thrust of both units roots into the floor thrust of the Nogueres thrust, i.e. within the Axial Zone: South Pyrenean thrust sheets are rooted into the basement thrusts of the Axial Zone.

In contrast, Muñoz (1992) considers that the central South Pyrenean unit (the only unit on the ECORS profile) was initially located to the south of the Axial Zone with the Montsec unit covering the Rialp basement unit (the Lower Cretaceous basin present in the Boixiols-Cotiella and Upper Pedraforca units being initially above the Orri unit but no longer present in the central South Pyrenean unit). He invokes the rooting of South Pyrenean thrust sheets beneath the Axial Zone (floor thrust beneath the Axial Zone) with an overall southward displacement of all units. By the means of (northward) backthrusting of the central South Pyrenean unit over the Hercynian basement, he restores the present day N-S succession (central South Pyrenean unit-Nogueres Zone-Orri thrust) and suggests that the Nogueres Zone and the Gavarnie thrust belong to the same unit (the so-called Nogueres thrust). In other words, the Nogueres Zone is the only unit to root into the Axial Zone. No gravity gliding is considered, only pure compressional tectonics. This implies that the Axial Zone basement has been highly shortened by the means of important Eocene thrusts, further steepened by doming. However, the model does not apply for neither the Boixols-Cotiella unit nor the Pedraforca unit (Vergés et al., 1995).

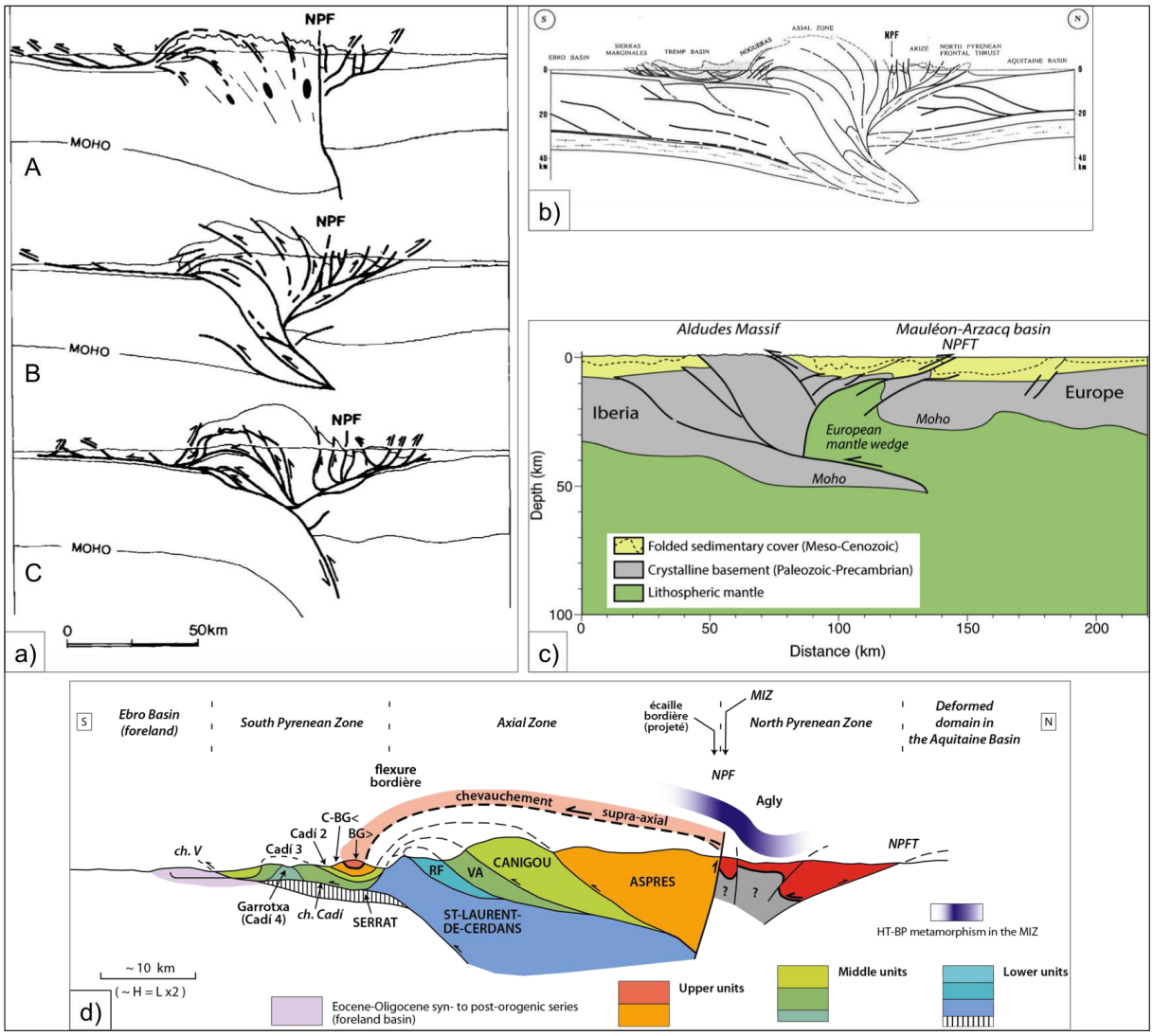

Figure III.4: Proposed models for the Pyrenean orogen, showing rooting of the South Pyrenean thrust sheets into (Séguret, 1972; Séguret and Daignieres, 1986), further north of (Laumonier et al., 2015) or beneath (Roure et al., 1989; Muñoz et al., 1992; Roure and Choukroune, 1998) the Axial Zone. (a) Synthesis by Muñoz (1992) of proposed models: A) from Séguret and Daignieres (1986), B) from Roure et al. (1989), and C) from Muñoz (1992). (b) Interpretation of Roure and Choukroune (1998). Note this is similar to that of Roure et al. (1989). (c) Geological interpretation of the tomographic model obtained along the western PYROPE seismic transect, similar to interpretation of Roure et al. (1989). From Wang et al. (2016). (d) Model of Laumonier et al. (2015). Colors indicate the different units and relationships between units in the Axial Zone and the South Pyrenean Zone, as interpreted by the author. See text for further information. NPFT = North Pyrenean Frontal Thrust; NPF = North Pyrenean Fault; MIZ = Metamorphic Internal Zone; VA = Vallespir unit; RF = Roc de France unit; BG> = Bac Grillera Superieure; C-BG< = Coustouge-Bac Grillera Inferieure; ch. Cadi = Cadi thrust; ch. V = Vallfogona thrust (South Pyrenean Frontal Thrust).

In contrast, Muñoz (1992) considers that the central South Pyrenean unit (the only unit on the ECORS profile) was initially located to the south of the Axial Zone with the Montsec unit covering the Rialp basement unit (the Lower Cretaceous basin present in the Boixiols-Cotiella and Upper Pedraforca units being initially above the Orri unit but no longer present in the central South Pyrenean unit). He invokes the rooting of South Pyrenean thrust sheets beneath the Axial Zone (floor thrust beneath the Axial Zone)

with an overall southward displacement of all units. By the means of (northward) backthrusting of the central South Pyrenean unit over the Hercynian basement, he restores the present day N-S succession (central South Pyrenean unit-Nogueres Zone-Orri thrust) and suggests that the Nogueres Zone and the Gavarnie thrust belong to the same unit (the so-called Nogueres thrust). In other words, the Nogueres Zone is the only unit to root into the Axial Zone. No gravity gliding is considered, only pure compressional tectonics. This implies that the Axial Zone basement has been highly shortened by the means of important Eocene thrusts, further steepened by doming. However, the model does not apply for neither the Boixols-Cotiella unit nor the Pedraforca unit (Vergés et al., 1995).

Another model was established in an attempt to tackle this problem and fit observations both in the central South Pyrenean unit and the Boixiols-Cotiella and Pedraforca units (Vergés et al., 1995; Vergés and Garcia-Senz, 2001). In this model, only the initial location of the Lower Cretaceous basin present in the Boixiols-Cotiella and Upper Pedraforca units changes, being initially set above the Nogueres unit, so further north compared to the model of Muñoz (1992). This model is therefore a composite model with an initial cover template similar to that of Séguret (1972) and an initial basement template similar to that of Muñoz (1992). It does not necessarily equaled the Nogueres Zone to the Gavarnie thrust.

More recently, Laumonier (2015) proposes that large allochtonous units (klippes) in the South Pyrenean Zone including the central South Pyrenean unit, the Pedraforca unit and the Emporda unit (Neogene unit) in the south-eastern Pyrenees, cannot be rooted into the Axial Zone"due to lack of suitable Alpine thrusts". Rather, they represent thrust sheets that overthrust the Axial Zone southward on thrusts rooted somewhere to the north of the Axial Zone and in the North Pyrenean Fault. This implies the following (Figure III.4.d): (1) the present-day horizontal basement-cover limit throughout most of the Axial Zone would be the expression of a basement-cover limit that remained horizontal at the scale of the Axial Zone (Laumonier, 2015) rather than that of a hinge zone within a dome structure that would have been up-to-20-km-high and made of Hercynian and Alpine thrust sheets (Muñoz, 1992), (2) much lower deformation and fewer tectonic units in the Axial Zone leading to both a drastic change in plaeogeographic reconstructions just south of what has become the present-day North Pyrenean Fault - the model of Muñoz (1992) is in favour of a 45-km motion rangeward (northward) while that of Laumonier (2015) suggests a 45-km motion basinward (southward). The basement would therefore be much less shortened in the Axial Zone, (3) post-Late Cretaceous structuration of the present-day Axial Zone results from south-vergant thrusting of both the Metamorphic Internal Zone and North Pyrenean Zone onto the proximal Iberian margin that was subsequently uplifted and erosed to form a tectonic window (the so-called Axial Zone), and (4) a much narrower Upper Cretaceous Iberian domain involved into the total accumulated crustal shortening seen in geology: 80 km (Laumonier, 2015) contrary to 165 km (Muñoz, 1992). However, his model involves southward movements only, while the tendency for consider both southward

and northward displacements is emerging (polyphased inversion of the Metamorphic Internal Zone according to geological observations; Ducoux et al., in prep; de Saint-Blaquat et al., in prep).

Recent work (Wang et al., 2016; Figure III.4.c), although carried out further west of the deep seismic reflexion Arize ECORS line, uses tomographic modelling on the western PYROPE seismic transect through the Mauléon-Arzacq basin. Geological interpretation of the tomographic model may open up new and promising exploration in the interpretation of the Pyrenean crustal thrust structure in central Pyrenees, as it seems to agree with the model proposed by Roure et al. (1989) and Roure and Choukroune (1998) (Figure III.4).

III.1.7 The Southern Pyrenean Zone

The South Pyrenean Zone is a south-verging thin-skinned fold-and-thrust belt with syn-orogenic thrust sheet-top basins. It developed on the lower, relatively thick Iberian plate and is flanked to the south by the Ebro foreland basin (Vergés et al., 1998; Vergés et al., 2002b; Figure III.1). It forms together with the Axial Zone a major pro-wedge thrust system. It structurally consists of southward-propagating imbricate thrust sheets that are made up of Mezosoic to Cenozoic (Paleogene) sediments (Séguret, 1972; Puigdefàbregas et al., 1986, 1992; Vergés and Muñoz, 1990; Muñoz, 1992). In contrast to the North Pyrenean Zone, no crystalline Paleozoic basement massifs occur in the South Pyrenean Zone. Pro-wedge deformation style is predominantly thin-skinned with thrust sheets decoupled and thrusted along the Triassic (Keuper) evaporite decollement.

The South Pyrenean Zone comprises a thin Mesozoic platform sequence and early syn-orogenic, Upper Cretaceous to Oligocene depocentres of the pro-foreland basin system (Jaca, Ainsa, Tremp, and Ripoll piggyback basins; Muñoz et al., 1986; Vergés and Muñoz, 1990; Huyghe et al., 2009; Filleaudeau, 2011; Whitchurch et al., 2011; Filleaudeau et al., 2012). Most of thrusting activity in the depositional wedge-top basin occured from Early Eocene (*ca.* 55 Ma; Vergés et al., 1995; Vergés and Burbank, 1996) to Late Oligocene (*ca.* 25 Ma; Hogan and Burbank, 1996; Meigs et al., 1996), with highest rates of thrust propagation during the Ypresian. The South Pyrenean Zone is separated from the Ebro pro-foreland basin to the south by the South Pyrenean Frontal Thrust.

III.1.8 The Ebro Basin

The Ebro Basin is the Pyrenean pro-foreland foredeep, (e.g. Salas et al., 2001; Whitchurch et al., 2011). It is overthrust by the South Pyrenean Zone on the South Pyrenean Fault. It is broader and shallower than the Aquitaine Basin and the maximum sediment thickness (up to 3-5 km) is observed toward the Pyrenean range (northernmost part of the basin). The basin is triangular in shape and is bordered to the east by the Catalan Coastal Ranges and to the southwest by the Iberian Range (Figure III.1). This basin mainly records the flexural response of the Iberian plate to Pyrenean orogenic loading (Brunet, 1986; Desegaulx et al., 1990) but also the less important loading (e.g. Riba et al., 1983; Puigdefàbregas et al., 1992) by the Catalan Coastal Ranges

to the east from the latest mid-Eocene - abrupt increase in tectonic subsidence at 41.5Ma (Lutetian-Bartonian) in the southernmost margin of the Ebro basin (Vergés et al., 1998) due to beginning tectonic activity (early to middle Eocene; e.g. Guimerá, 1984) related to the front of the range - and by the Iberian Range to the southwest - beginning tectonic activity (Late Eocene-Oligocene; e.g. Guimerá, 1984) -.

The basin started filling in the Paleocene with marine sediments whose deposition continued until the early Late Eocene (Costa et al., 2010). The Early Priabonian (Vergés et al., 1995, 1998; Costa et al., 2010) saw the the uplift of the western Pyrenees and the Ebro Basin subsequently turned into an endorheic basin in response to closure of the western connection toward the Altantic Ocean (e.g. Riba et al., 1983; Burbank et al., 1992; Puigdefàbregas et al., 1992; Vergés et al., 1995; Vergés and Burbank, 1996). This marked the end of marine deposition and the onset of a period of internal drainage that resulted in far higher sediment supply from the surrounding mountain belts (Sinclair et al., 2005), which in turn resulted in both progressive basin infill, onlap and burial of the South Pyrenean Zone (Vergés and Muñoz, 1990; Coney et al., 1996). Depositional environments changed from marine in Eocene times to continental in early Oligocene times (Vergés et al., 1995, 1998; Costa et al., 2010). This overfilling by non-marine clastic deposits continued until opening of the Ebro Basin to the Mediterranean Sea in the Late Miocene (Tortonian; e.g. Coney et al., 1996; Vergés et al., 2002a).

As in the European foreland basin, earliest sediment deposited in the Iberian depocentre (transition from platform carbonate and evaporite facies to distal, marly facies to alluvial fans and deltas) was supplied from an eastern source.

The Ebro basin is therefore the latest, syn- to post-orogenic, Upper Eocene to Lower Miocene depocentre (Canérot, 2008). Deposition was controlled by the South Pyrenean Frontal Thrust until contraction ceased in early Miocene (Teixell, 1996; Teixell and Muñoz, 2000).

III.2 Geodynamics

The oldest series (igneous and meta-sedimentary rocks) found throughout all the Pyrenean range are observed in the Axial Zone and the exernal massifs of the northern Pyrenees. They record the Variscan cycle (Carboniferous to Permian) and older orogenic cycles. These older cycles are not the focus of the present work. Nonetheless they will be discussed when considering the role of lithospheric inheritance and reactivation of Variscan structures during the Alpine cycle.

The breakup of *Pangaea*, formed by the Permian, bagan during Late Permian to Early Triassic time with the initial phase of the post-Hercynian opening of the North Atlantic Ocean and the splitting of the North American plate from the Eurasian and African plates (Uchupi et al., 1976; Ziegler, 1988; Lambiase, 1989). This phase continued until the Late Triassic-Early Jurassic times (200-180 Ma; Logar, 1983; Moulin et al., 2010; Nkoumbou et al., 2014). The final breakup of Africa and South America began in the Early Jurassic to the south of these continents, creating the southernmost part of the

South Atlantic Ocean (Uchupi, 1989; Binks and Fairhead, 1992; Guiraud and Maurin, 1992; Figure III.5). This gradually proceeded northward during Cretaceous time. However, the continental separation to the south was more complicated than that to the north. It is thought to occur in four tectonic phases including three periods of rotation (Aslanian et al., 2009; Moulin et al., 2010; Chaboureau et al., 2013; Granot and Dyment, 2015): (1) rifting/stretching during Middle to Late Jurassic times (165-135 Ma), (2) initial continental break-up between - read here leading to the formation of - Africa and South America in the southernmost part of the South Atlantic Ocean (first rotation) during Late Jurassic to Early Cretaceous times (135-120 Ma), (3) seafloor spreading in the southernmost part of the South Atlantic Ocean during Early to Late Cretaceous times (120-80 Ma), synchronous to continental break-up propagating northward toward the Equatorial Atlantic Ocean (second rotation, or divergent "drift" of Wegener), and finally (4) seafloor spreading propagating northward toward the Equatorial Atlantic Ocean (third rotation, or parallel "drift" of Wegener) during Cenozoic times to the present day (80-0 Ma).

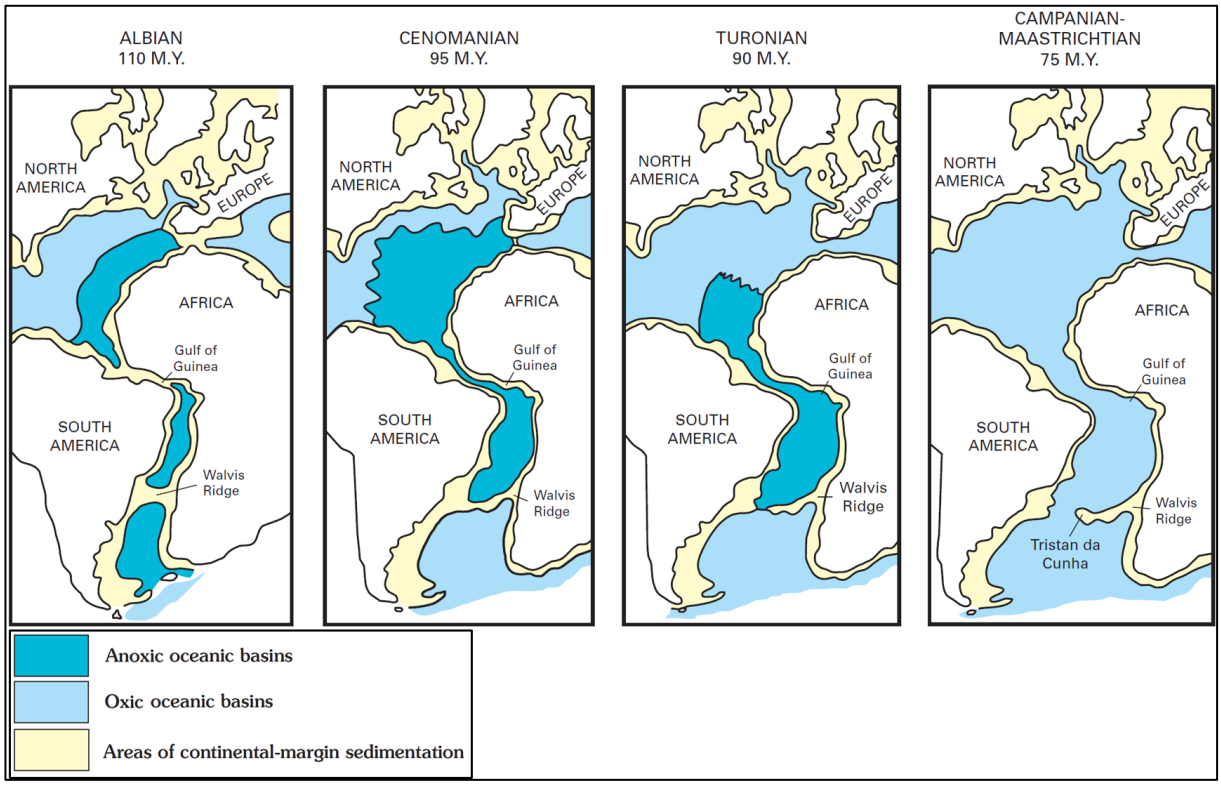

Figure III.5: Paleogeographic maps of the continental break-up of African and South America during the Cretaceous, showing diachronous seafloor spreading in the Atlantic Ocean from Late Albian-Mid Santonian to present (propagating rift and seafloor spreading from south to north). Modified from Brownfield and Charpentier (2006).

The rifting/stretching phase is synchronous with Triassic to Late Jurassic transtension in the Pyrenean realm in an E-W corridor linking the Tethys and Atlantic oceans (e.g. Vergés and Fernàndez, 2012, and reference therein). During early seafloor spreading in the Early to Late Cretaceous (Figure III.5), Africa and South America are juxtaposed in the Ivory Coast-Benin area, causing separation between the North and

South Atlantic oceans to the north of the West African margin. In Mid-Albian times, a widespread margin tilting occurs due to a dramatic tectonic event that links the Central and the South Atlantic oceans. Change in the relative motion direction of Africa and South America (propagating rift/seafloor spreading) coincides with their final separation in the Gulf of Guinea around 100 Ma (Granot and Dyment, 2015). This is at time, Aptian to early Cenomanian, that extension occured in the Pyrenean realm, synchronous to the opening of the Bay of Biscay (extreme continental thinning in the Bay of Biscay and Pyrenean rift systems- the Basque Cantabrian-Parentis and Pyrenean (Arzac-Mauléon) segments as defined in Tugend (2013) and Tugend et al. (2014)- (e.g. Choukroune and Mattauer, 1978; Olivet et al., 1983, 1984; Puigdefàbregas and Souquet, 1986; Debroas, 1987a, 1987b, 1990; Olivet, 1996; Vergés and Garcia-Senz, 2001; Sibuet et al., 2004, 2012, Gong et al., 2008, 2009; Lagabrielle and Bodinier, 2008; Jammes, 2009; Jammes et al., 2009, 2010a, 2010b; Lagabrielle et al., 2010; Clerc et al., 2012; Tugend, 2013; Tugend et al., 2014; Corre et al., 2016; Teixell et al., 2016).

Iberia plate movement in this time span is nonetheless controversial with three main models proposed to explain the synchronous openings (Figure III.6). These vary considerably regarding (1) the number and type of phases involved in the pre-orogenic motion of the Iberian plate with regard to the European plate, (2) the exact timing, location and amount of pre-orogenic motion, and (3) how they constrain the age, amount and direction of resulting crustal extension, and width of the thinned domain.

The first model (Figure III.6.a) involves senestral wrenching on the North Pyrenean Fault and a pole of plate rotation in northern France during Aptian, based on oceanic magnetic anomalies in the Bay of Biscay (chron M0; Olivet, 1996; based on Le Pichon et al. (1970) and Olivet et al. (1983, 1984)). This model proposes a progressive rotation of Iberia throughout Cretaceous resulting in an overall motion of Iberia toward southeast. It also considers the North Pyrenean Fault as a transform (so a strike-slip plate boundary) fault from Aptian to Late Santonian (chrons M0 to A33) that was reactivated and inverted with a significant dextral strike-slip component during Late Cretaceous oblique convergence (e.g. Choukroune and Mattauer, 1978). In this model, no hyperexended domain is considered, which result in a total convergence of 165 km, equaled to the 165 km of shortening geologically observed by Muñoz (1992).

The second model (Figure III.6.b), also based on oceanic magnetic anomalies in the Bay of Biscay (chron M0), consists in applying the scissor opening principle initiated by Carey (1959) with a pole of rotation in the Bay of Biscay (Srivastava et al., 1990a, 1990b, 2000; Sibuet et al., 2004; Vissers and Meijer, 2012a, 2012b). This model is constrained by maintaining the motion direction of plates along the Azores-Gibraltar fracture zone, based on plate kinematics of Srivastava et al. (1990a, 1990b, 2000). It is in favour of oblique convergence in Late Cretaceous and propose significant amount of oceanic subduction (up to 400 km) and continental subduction (up to 100 km). In the model of Sibuet et al. (2004), two subductions are invoked from early Aptian to present-day to accommodate a total eastward-increasing, SW-NE convergence of *ca.* 250-450 km: (1) the questionnable (Lacan, 2008) early Apto-Albian oceanic subduction of the neo-Tethys

crust formed during Late Jurassic-early Aptian N-S extension (350 km), synchronous to back-arc extension in the Pyrenean realm, followed by (2) the late Santonian-ealy Miocene continental subduction of the Iberian plate beneath the European plate. This results in significant thickening of the Iberian plate by wedging at depth and 130 km of crustal shortening in the Pyrenean realm. In the model of Vissers and Meijer (2012a, 2012b), a total convergence of 500 km (chron M0 to present-day) is proposed, including subduction of 320 km of hyperextended domain (neo-Tethys ocean floor) as a result of the single-phase 35° counterclockwise rotation of Iberia with respect to Europe in Aptian time (Gong et al., 2008, 2009, and reference therein for discussion on the number of rotation phases and amount of rotation) and 165 km of total crustal shortening.

In contrast to the two previous models, the third model supports pure extension during the Aptian to Cenomanian extension (Jammes, 2009; Jammes et al., 2009, 2010a, 2010b; Handy et al., 2010; Tugend, 2013; Tugend et al., 2014, 2015; Figure III.6.c). According to their restorations of the Bay of Biscay and Pyrenean domains, NNE-SSW- to NE-SW-trending Variscan faults compartmentalised rifting at least from late Aptian to early Albian. Although they cannot be traced with confidence across the Pyrenees, these fault systems are relatively continuous within European foreland and are locally sealed by Albian sediments (e.g. Pamplona fault; Razin, 1989). The authors argue that this implies that the transcurrent motion of Iberia with regard to Europe, associated with left-lateral strike-slip components- what Jammes et al. (2009) refers to as "most of the E-W directed movement"-, was already accounted (*ca.* 300 to 500 km of eastward motion of Iberia is accommodated) at some point between the latest Jurassic (Tithonian) to Early Cretaceous (Late Aptian). At chron A34 (Santonian), the north Iberia plate boundary was located in the Bay of Biscay (Boillot et al., 1989; Srivastava et al., 1990a, 1990b; Figure III.6.b). The northward movement of the newly formed Afro-Iberian plate coincides with the cessation of seafloor spreading in the Bay of Biscay (Olivet, 1996). This initiated inversion of the northern margin of Iberia. Convergence was accommodated by: (1) northward underthrusting of the eastern part of the Iberian plate beneath Europe, to a minimum depth of 80 km (ECORS deep seismic reflection profiles; Choukroune and Mattauer, 1978; Choukroune, 1988, 1989; Roure et al., 1989; seismic tomography data; Souriau and Granet, 1995) to create a N100°-110°-striking doubly wedged mountain, and (2) over-riding of the western part of Iberia, onto the European plate (souther margin Bay of Biscay) that subducts southward to depth of *ca.* 70 km leading to continent-ocean collision.

According to syn-orogenic stratigraphic records and plate kinematic reconstructions, the Pyrenean orogeny was generated from end Santonian-early Campanian (around 84-83 Ma) to Oligocene-Miocene (around 30 Ma) due to oblique and relatively consistent N-S to NNE-SSW convergence of the Iberian and European plates (Dewey et al., 1989a, 1989b; Srivastava et al., 1990a, 1990b; Vergés et al., 2002a, 2002b). The northward movement of Africa was largely controlled by the opening of the South and Central North Atlantic during the Late Cretaceous (e.g. Guiraud and Bosworth, 1997).

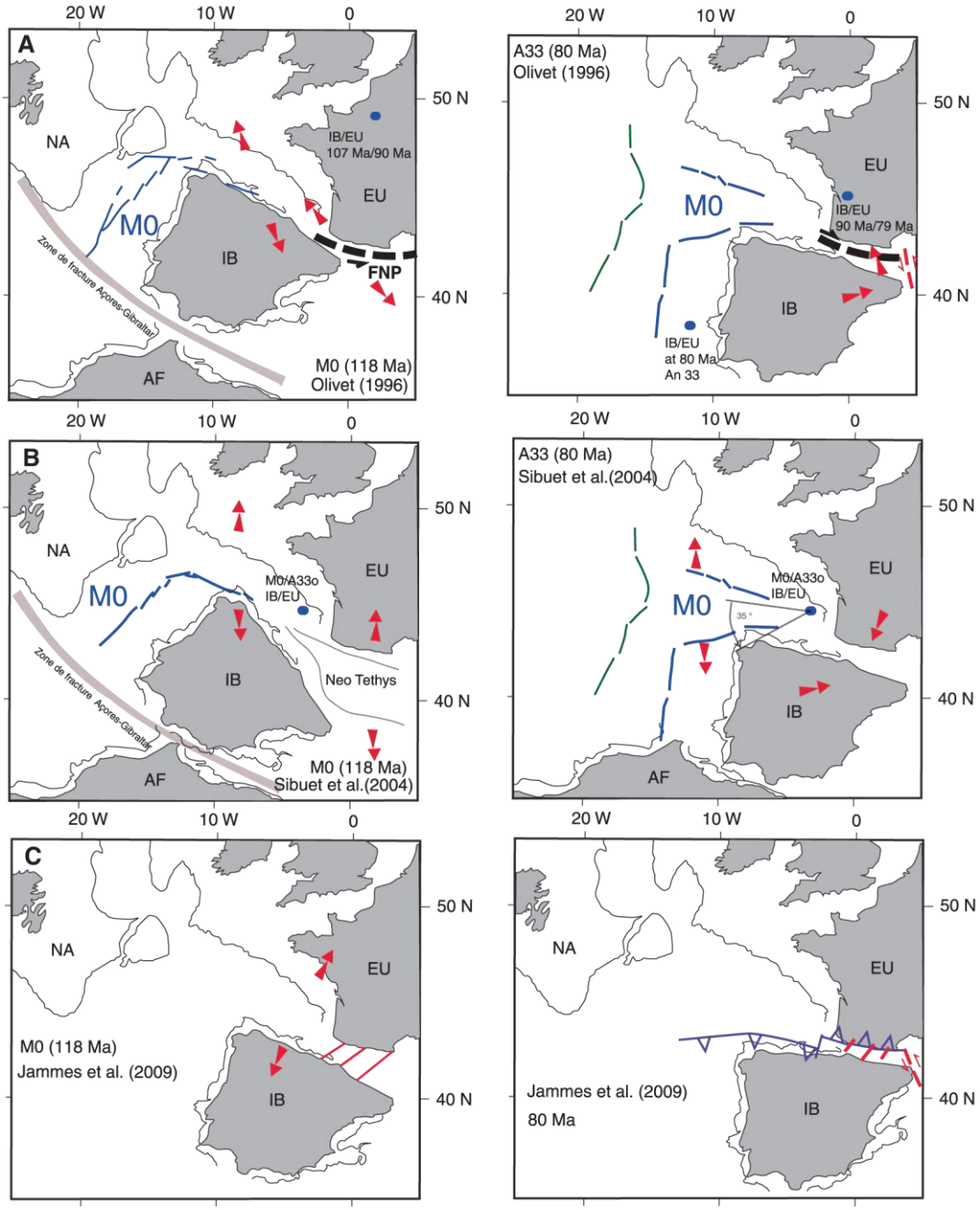

Figure III.6: Proposed Iberia plate movement kinematic reconstructions in Early Cretaceous (chron M0; ~118 Ma) and Late Cretaceous times (chron A33; 80Ma). From Mouthereau et al. (2014). "(a) Transtensional rift model after Olivet (1996), which accounts for dextral strike-slip reactivation and inversion of the Iberian and European margins during oblique convergence. (b) Scissor opening model after Srivastava et al. (2000) that implies large oceanic subduction beneath the Pyrenees during the Albian. (c) Kinematic reconstruction of Mesozoic motion of Iberia after Jammes et al. (2009) that includes transcurrent motion of Iberia during the Late Jurassic, followed by orthogonal stretching in the Middle-Late Cretaceous, and subsequent frontal convergence of Iberia. The position of NA = North America, AF = Africa, and IB = Iberia relative to fixed EU = Eurasia is shown as well as location of IB/EU rotation poles (blue circles). Anomaly A33 and M0 are shown as green and blue segments, respectively." (Mouthereau et al., 2014).

At the time of the transition from transtension (e.g. Olivet, 1996; Sibuet et al., 2004) or extension (e.g. Jammes et al., 2009) to convergence (chron A34; Santonian),

Iberia had just become "re-"attached to Africa, marking the end of a period (Early-Middle Cretaceous) throughout which Iberian Peninsula had acted as an independent microplate since it detached from Laurasia, formed by continental breakup of *Pangaea*.

The total amount of N-S plate convergence has been debated for a long time since its maximum value depends on whether the hyper-extended domain is or not considered into restorations and geological data are or not available (Choukroune et al., 1973; Deramond et al., 1985; Séguret and Daignieres, 1986; Roure et al., 1989; Muñoz, 1992; Vergés et al., 1995; Olivet, 1996; Teixell, 1996, 1998; Beaumont et al., 2000; Rosenbaum et al., 2002; Sibuet et al., 2004; Mouthereau et al., 2014). Although its maximum value ranges from 100-165 km (Olivet et al., 1984; Deramond et al., 1985; Roure et al., 1989; Muñoz, 1992; Vergés et al., 1995; Olivet, 1996; Beaumont et al., 2000) up to 400 km (Sibuet et al., 2004; Vissers and Meijer, 2012a, 2012b), values of 90 to 140 km of convergence between the two plates tend generally to be accepted (Muñoz, 1992; Mouthereau et al., 2014).

While most data supports the onset of Pyrenean inversion within the Cenomanian-Santonian time span there are several contradictory proposals: (1) Curnelle (1986) argues that the Pyrenean contraction began in the Cenomanian, mainly in the eastern part of the Pyrenean range as a transpressive event due to the continuation of the opening of the Bay of Biscay (Souquet, 1984), while the pull-apart-like Apto-Albian flysch basins merged into a wider North Pyrenean flysch basin westward from Albian-Cenomanian to Maastrichian (a two-phase merge: in Cenomanian and in mid-"Senonian"; Curnelle et al., 1980), (2) Bourrouilh et al. (1995) suggest that compression might initiate from late Turonian, and (3) Le Vot et al. (1996) propose that Pyrenean inversion may already start in Late Albian times given that brief periods of basin inversion are recorded in the overall highly subsiding, rhomb-shaped, en-echelon pull-apart-like Apto-Albian flysch basins (e.g. Debroas, 1990; Hiscott et al., 1990; Bourrouilh et al., 1995; Vergés and Garcia-Senz, 2001). The latter suggest that (1) these brief periods of basin inversion in late Aptian to late Albian might be linked to reactivation of pre-existing Variscan-inherited, NNE-SSW- to NE-SW-trending transfer faults that cross the Iberian-European plate boundary (e.g. the Santander, Hendaye, Pamplona, Toulouse and Cevennes basement fault systems; e.g. Choukroune and Mattauer, 1978; Boillot, 1986; Rat, 1988; Bourrouilh et al., 1995; Larrasoaña et al., 2003a, 2003b; Jammes, 2009; Jammes et al., 2009, 2010a, 2010b; Lagabrielle et al., 2010; Roca et al., 2011; Tavani and Muñoz, 2012; Chevrot et al., 2014), (2) subsequent tilting, folding, uplifting and erosion of overlying strata are a good sign for change in tectonic setting (inversion), and (3) these numerous transpressional episodes that briefly disrupted transtensional/extensional tectonic settings may already mark an Apto-Albian transition toward contractional setting. However, Canérot et al. (2005) consider that these episodes are only the result of minor changes or variations in plate motions or fault bend geometries.

In their crustal restoration along the central deep seismic ECORS profile, Ford et al. (2016) show that the onset of orogenesis is marked by acceleration of tectonic

subsidence in the distal basin (the Subpyrenean Zone) and a continuation of the post-rift subsidence rate in the more proximal basin toward the end of the Santonian (84-83 Ma). These authors have concurred that inversion started below the Late Cretaceous flexural basin, at some time in the Campanian or Maastrichtian. In other words, the Campano-Maastrichian sediments record the onset of flexure. This is in fairly good agreement with a whole continent-continent collision that initiated in the earliest Campanian (e.g. Roure et al., 1989; Muñoz, 1992; Schettino and Scotese, 2002; Canérot et al., 2005).

The evolution of the Pyrenean range can therefore be divided into four main phases (Sinclair et al., 2005; Ford et al., 2016): (1) a Late Cretaceous early contractional phase, (2) a Paleocene quiet phase, (3) an Eocene contractional phase, and (4) an Oligocene-Miocene, late to post-orogenic phase.

The growth of Pyrenean topography is thought to initiate in the east before propagating westward as a result of the oblique underthrusting of the Iberian plate beneath the Eurasian plate (e.g. Choukroune, 1972, 1974, 1989; Capote et al., 2002; Martín-Chivelet et al., 2002). Many authors suggest that the magnitude of both convergence and shortening decrease from east to west along the Pyrenees (e.g. low-temperature thermochronology record; Yelland, 1990, 1991, and references therein). Most shortening was accommodated by upper crustal thickening in the pro-wedge (e.g. Vergés et al., 2002a). Estimates of shortening include in the central Pyrenees along the deep seismic reflection ECORS profile from *ca.* 165 km with no hyper-extended domain (Muñoz, 1992; Fitzgerald et al., 1999; Beaumont et al., 2000; Rosenbaum et al., 2002) or 140 km with hyper-extended domain (Mouthereau et al., 2014); on western ECORS line 103 km in the west-central Pyrenees (Martinez-Peña and Casas-Sainz, 2003); in the Basque-Cantabrian Pyrenees along the Basque-Cantabrian Pyrenees ECORS section 80 km near the Pamplona fault and 90 km (Teixell, 1996, 1998); in the Cantabrian Mountains along the deep seismic reflection ESCI-N profiles 95 km (Alonso et al., 1996)). However, crustal restorations of Teixell (1996, 1998) in the western Pyrenees together with the more recent sequential restoration of Mouthereau et al. (2014) in the central Pyrenees indicate that the eastern and western Pyrenees may have accommodated similar crustal shortening (*ca.* 90 km). As noticed by Vergés et al. (2002a), large-scale shortening in both the pro- and retro-foreland basins started during the Paleocene.

The Early Miocene has seen the latest deformation observed within the Pyrenean range (Vergés et al., 2002b; Jolivet et al., 2007; Huyghe et al., 2009). Plate reconstructions suggest that at this time Iberia started moving as part of the Eurasian plate with its southern boundary along the Azores-Gibraltar Fracture Zone (Srivastava et al., 1990b; Roest and Srivastava, 1991).

III.3 Low-temperature thermochronology insight

Although the recognition of the importance for quantifying both syn-orogenic denudation and source-to-sink processes in understanding orogen development started quite a long time (30 years) ago, using low-temperature thermochronology to study the

orogenic development of the Pyrenees has been somewhat new when compared to the long-lived study of Pyrenean geology.

The first "thermochronological" (read radiometric or "geochronological" here; Reiners, 2005a) studies carried out in the Pyrenees used high-temperature thermochronometres with closure temperature range of 525 °C to 280 °C, but suffered from being carried out over both quite limited and specific areas (Jäger and Zwart, 1968; Vitrac-Michard and Allègre, 1975; Albarède and Michard-Vitrac, 1978; Michard-Vitrac et al., 1980; Respaut and Lancelot, 1983; McCaig and Miller, 1986; Montigny et al., 1986; Alibert et al., 1988; Costa and Maluski, 1988; Majoor, 1988). The only geochronological study that has been carried out regionally in the Pyrenees is that of Goldberg et al. (1986) to investigate the thermal regime on the orogen scale.

The first low-temperature study carried out in the Pyrenees is that of Garwin (1985) who performed fission-track analysis on apatite (AFT, 11 ages) and zircon (ZFT, 15 ages) mainly from the eastern and northeastern Pyrenees. In a larger, regional study that was designed to unravel the timing and dynamics of mountain building on the scale of the Pyrenean collision orogen ("to examine the low-temperature (230 °C) cooling history of the Pyrenean and Provence regions "), Yelland (1990, 1991) also provided AFT and ZFT age data and re-dated samples of Garwin (1985).

According to the age data he got throughout the Pyrenean range (AFT and ZFT age ranges of 16-48 Ma and 24-82 Ma, respectively), the author agreed with Garwin (1985) and already observed at that time "a major difference in style of uplift/cooling from north to south of the chain" that "is very probably the result of variable structural evolution during collision associated with the development of a Pyrenean accretionary wedge profoundly influenced by an inherited strike-slip margin buttress". He shows there are apparent age trends both converging and younging from north to south across the Pyrenean range.

Most of the subsequent low-temperature thermochronology studies have been first essentially carried out on the internal Paleozoic massifs of the Axial Zone (bedrock thermochronology; Morris et al., 1998; Fitzgerald et al., 1999; Sinclair et al., 2005; Gibson et al., 2007; Jolivet et al., 2007; Maurel et al., 2008; Gunnell et al., 2009; Metcalf et al., 2009; Figure III.7 and Figure III.8).

The bedrock low-temperature thermochronology record of the Axial Zone mostly spans the Eocene-Miocene period (Yelland, 1990, 1991; Morris et al., 1998; Fitzgerald et al., 1999; Sinclair et al., 2005; Gibson et al., 2007; Jolivet et al., 2007; Maurel et al., 2008; Metcalf et al., 2009; Figure III.7 and Figure III.8) and indicates an overall southward-younging tendency accross the Axial Zone from Late Cretaceous to Miocene (Yelland, 1990, 1991; Morris et al., 1998; Fitzgerald et al., 1999; Sinclair et al., 2005; Filleaudeau, 2011; Whitchurch et al., 2011; Filleaudeau et al., 2012; Mouthereau et al., 2014). In fact, the Axial Zone records the highest rates of Pyrenean exhumation in Paleogene times (Eocene-Early Oligocene; Fitzgerald et al., 1999; Sinclair et al., 2005; Metcalf et al., 2009; Beamud et al., 2011; Filleaudeau, 2011).

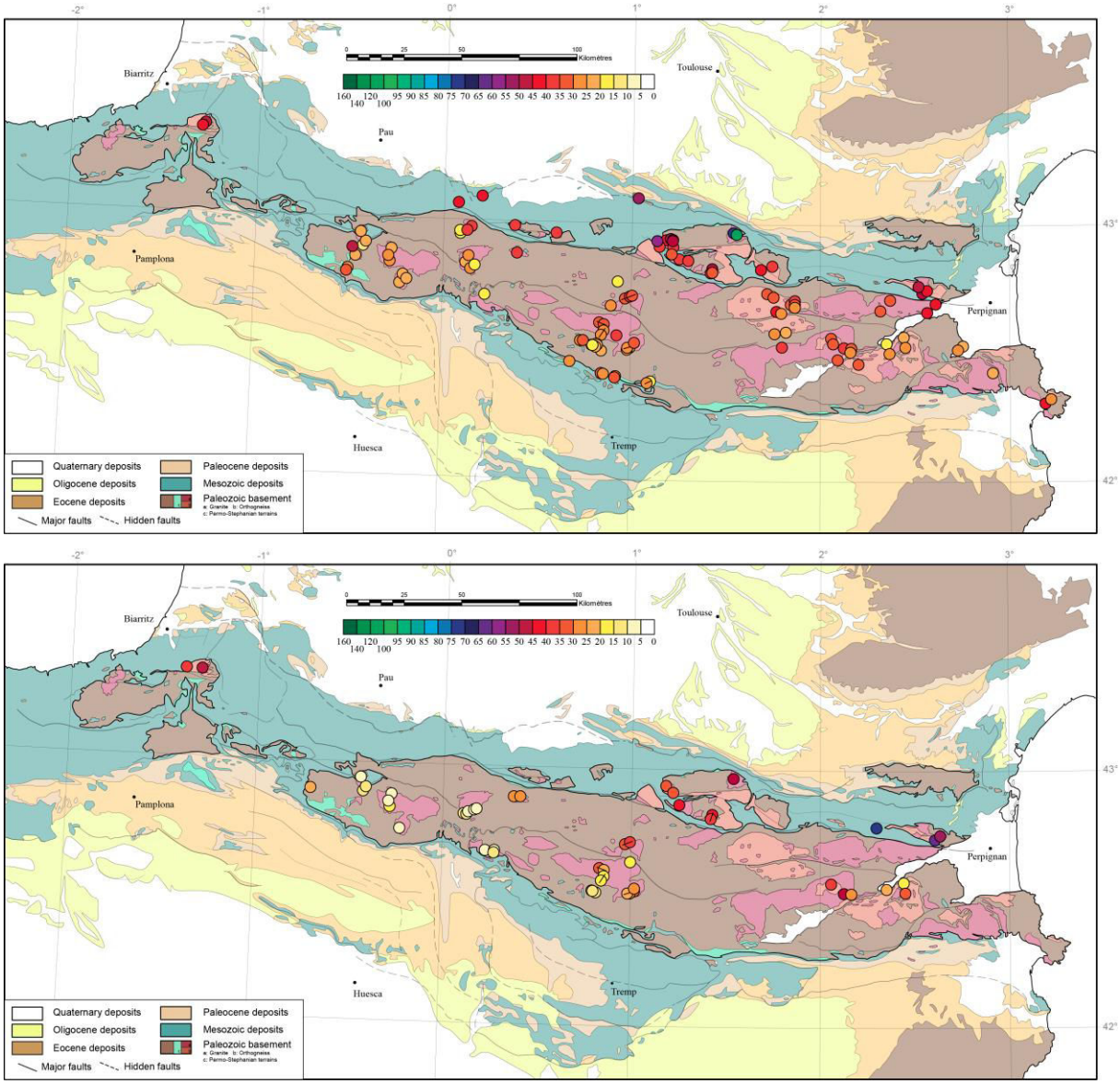

Figure III.7: Compilation of all apatite fission track age data (AFT, top) and apatite (U-Th)/He age data (AHe, bottom) in the Pyrenees. Modified after Vacherat (2016, PYRAMID workshop).

The earliest post-rift, syn-orogenic cooling events are mostly, if not only, recorded *in situ* in the north-central/north-eastern Pyrenean massifs where cooling ages fall into Late Cretaceous to Paleocene times (e.g. the Arize, Trois-Seigneur massifs: Vacherat, 2014; Vacherat et al., 2016; Agly Massif: Yelland, 1990; Figure III.8) and are relatively rare to non-existing in massifs further west (except the Ursuya pluton recording a Late Cretaceous cooling event in the westernmost Pyrenees; Whitchurch et al., 2011; Figure III.9).

The last decade has seen important developments and improvements in analytical techniques such as those involved in low-temperature thermochronology, especially in (U-Th)/He dating used to quantify both exhumation and mass flux in orogenic systems. Thus, many studies started investigating record of both sedimentary and bed rocks for the southern and northern fold-and-thrust belts (Meresse, 2010; Beamud et al., 2011; Filleaudeau, 2011; Whitchurch et al., 2011; Filleaudeau et al., 2012; Fillon and van der

Beek, 2012; Fillon et al., 2013; Rushlow et al., 2013; Mouthereau et al., 2014; Vacherat, 2014; Vacherat et al., 2014, 2016; Bosch et al., 2016; DeFelipe et al., 2019).

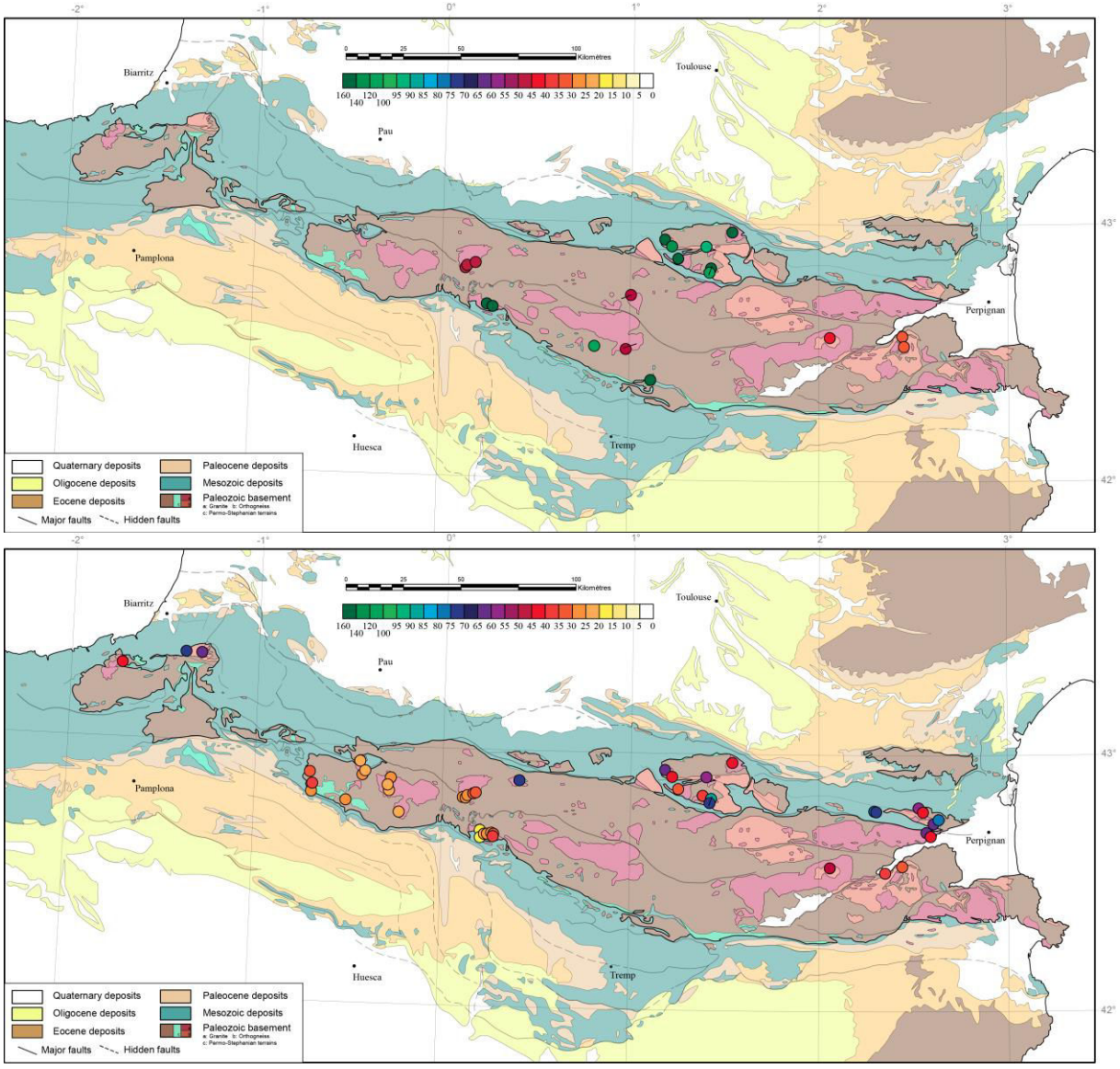

Figure III.8: Compilation of all zircon fission track age data (ZFT, top) and zircon (U-Th)/He age data (ZHe, bottom) in the Pyrenees. Modified after Vacherat (2016, PYRAMID workshop).

Nonetheless, with the exception of Bosch et al. (2016) and DeFelipe et al. (2019), most of these do have been focused on the eastern and central Pyrenees near or along the ECORS deep seismic reflection profile (see Whitchurch et al. (2011), Figure III.9, and Mouthereau et al. (2014), Figure III.10, for the most recent syntheses of both bedrock and detrital low-temperature thermochronology data available).

While the use of the bedrock archive allows deciphering an early cooling signal (Late Cretaceous) that is quite limited in space (in the north-eastern Pyrenees), detrital thermochronology has recently appeared to open up new and promising thinking about early orogen dynamics, especially when combining low-temperature (fission-track, helium, etc) data and U/Pb data, which allows documenting denudation dynamics and source provenance (Filleaudeau, 2011; Whitchurch et al., 2011; Filleaudeau et al., 2012).

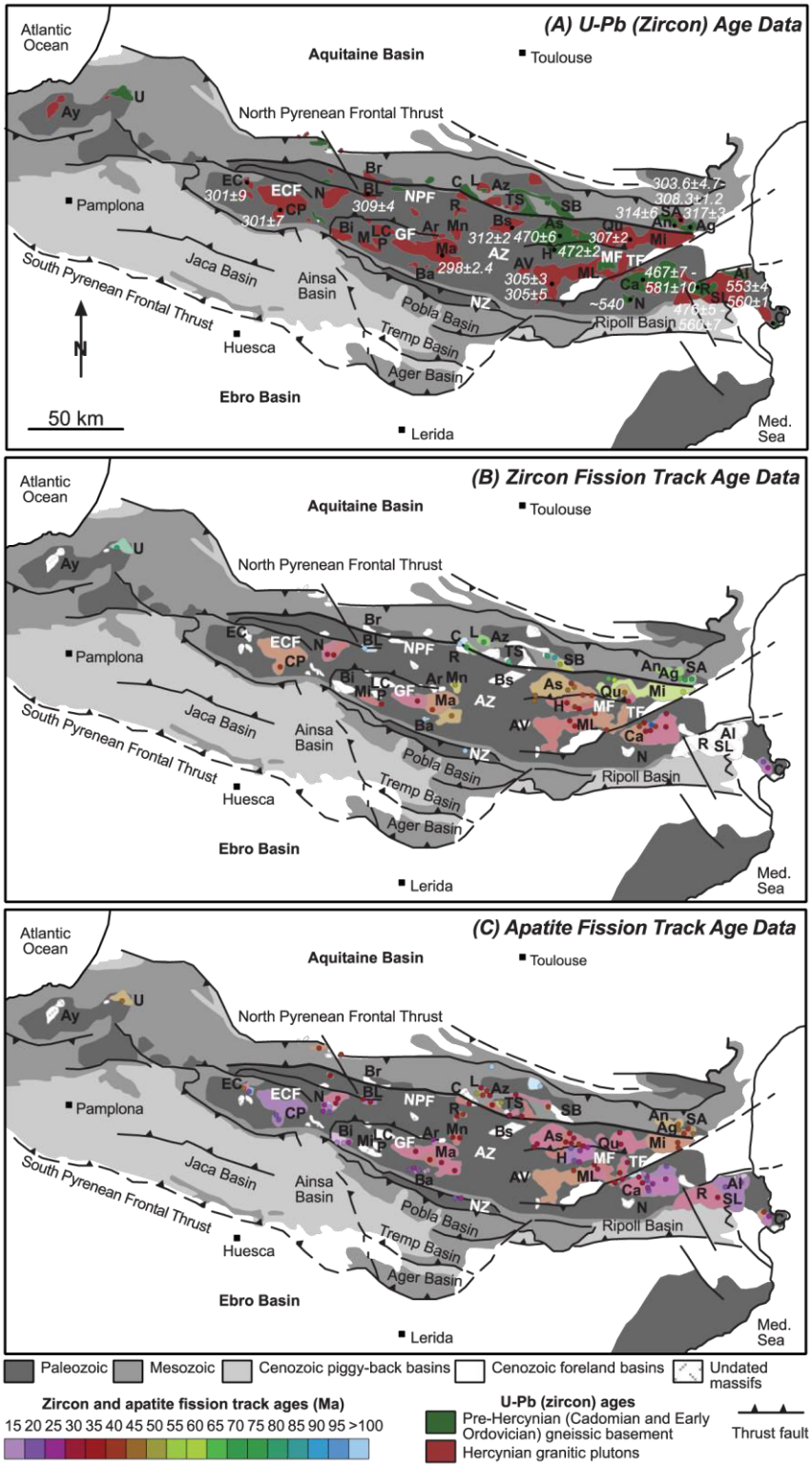

Figure III.9: Synthesis by Whitchurch et al. (2011) of: A) bedrock zircon U/Pb age data; B) bedrock zircon cooling ages (ZFT age data); and C) bedrock apatite cooling ages (AFT age data). The North Pyrenean basement massifs: U = Ursuya, Br = Barousse, C = Castillon, Az = Arize, TS = Trois Seigneurs, SB = Saint Barthelemy, Ag = Agly. Main plutons/gneiss domes: Ay = Aya, EC = Eaux Chaudes, CP = Cauterets-Panticosa, N = Neouvielle, Bi = Bielsa, BL = Borderes = Louron, Mi = Millares, P = Posets, LC = Lys = Caillaouas, Ba = Barruera, Ma = Maladeta, Ar = Arties, Mn = Marimańa, R = Riberot, L = Lacourt, Bs = Bassies, Av = Andorra, As = Aston, H = Hospitalet, ML = Mont-Louis, Qu = Querigut, Ca = Canigou, N = Nuria, An = Ansignan, SA = St-Arnac, Mi = Millas, R = Roc de Frausa, Al = Alberes, SL = Saint-Laurent-de-Cerdans, C = Cap de Creus.

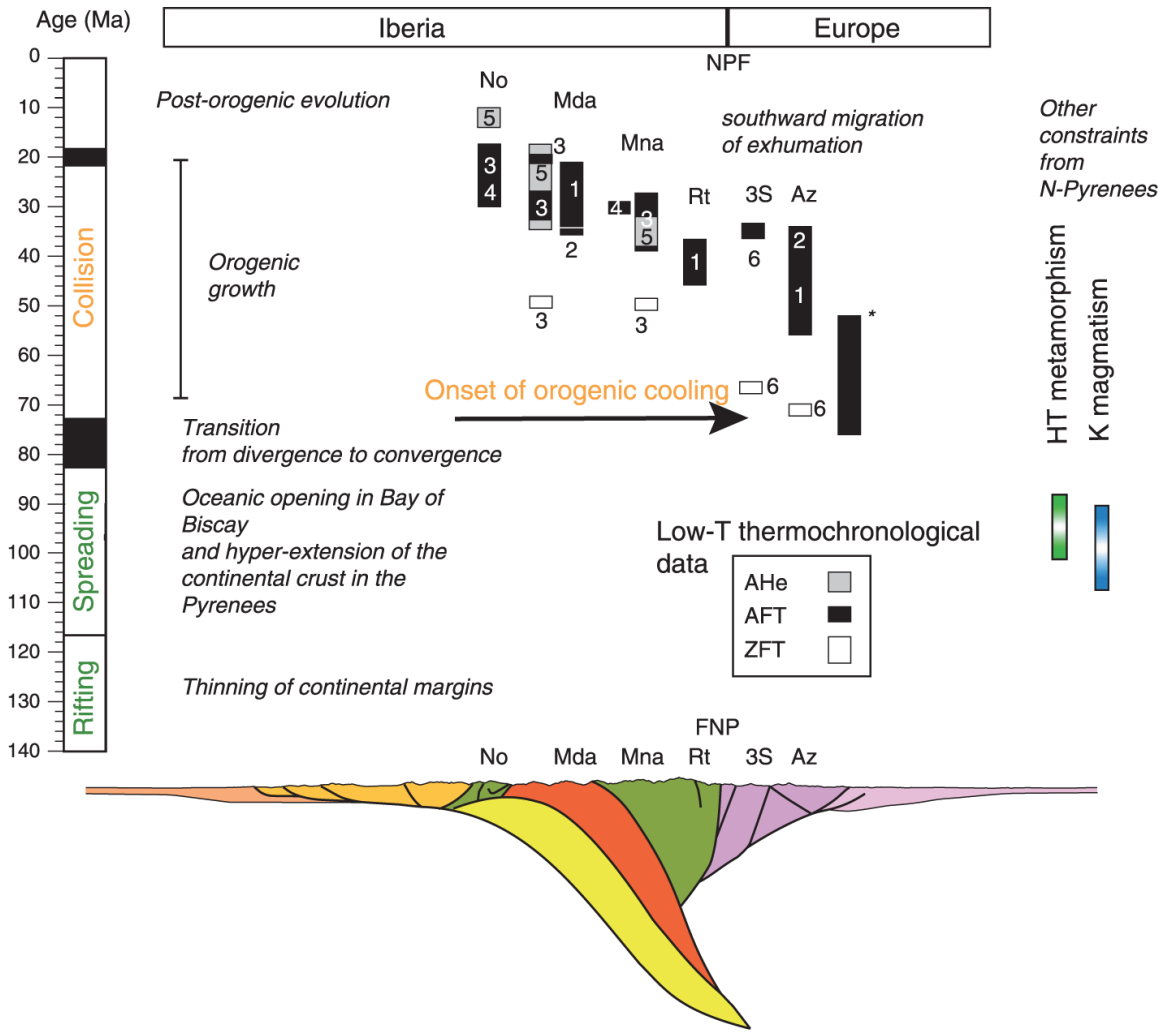

Figure III.10: Synthesis by Mouthereau et al. (2014) of bedrock cooling ages and ages of K-magmatism and high-temperature metamorphism plotted against main tectonic events. Thermochronometers: AHe = apatite (U-Th)/He dating, AFT = apatite fission track dating, and ZFT = zircon fission track dating. No = Nogueres; Mda = Maladeta; Mna = Marimaña; Rt = Riberot; 3S = Trois-Seigneurs; Az = Arize; NPF = FNP = North Pyrenean Fault. Age constraints from: (1) Fitzgerald et al. (1999), (2) Morris et al. (1998), (3) Sinclair et al. (2005), (4) Jolivet et al. (2007), (5) Gibson et al. (2007), and (6) Yelland (1991). * indicates detrital data, so data characterizing the cooling history of the source of the sediments.

The first study dealing with such a reconstruction in the Pyrenees is that of Whitchurch et al. (2011) in the south-central Pyrenees. These authors show that the detrital ZFT and U/Pb archive allows "*extending the thermal record back to the early stages of orogenesis*" (Figure III.9). In fact, detrital low-temperature data from this study record a progressive, westward-younging cooling phase of the sedimentary source: according to paleo-currents and depositional age of sediments within the sedimentary pile, zircon grains contained into Late Cretaceous to Oligocene sediments record exhumation that initiated in Late Cretaceous (cooling age of 78 Ma; Campanian) somewhere to the east and propagated westward until the Oligocene (younger cooling age).

Similarly to what is tectonically (accelerated subsidence from earliest Campanian to Late Maastrichian (84-68 Ma)), stratigraphically and lithologically (development of a large, westward-prograding deltaic system from Campanian to Late Maastrichian) recorded in the central North Pyrenean Zone (Ford et al., 2016), Whitchurch et al. (2011) show that, through time, sediments whose deposition in the south-central Pyrenees spans the Late Cretaceous-Middle Eocene period enrich progressively in Hercynian zircon grains while they get poorer in Cadomian zircon grains. They therefore argue that, during the Late Cretaceous to Middle Eocene, these sediments were not supplied directly from the central Pyrenees (Hercynian sources) by the means of orogen-transverse sediment dispersal, but from an eastern source (Cadomian sources) by the means of orogen-parallel sediment dispersal.

The authors also show that exhumation rates increased during the Late Cretaceous to Paleocene (lag times decrease with time). They therefore invoke that significant topography must have existed to the east during this time period, both to supply sediments toward foreland basins and to allow such exhumation rates.

However, it is worth noticing that each detrital single grain dataset (ZFT and zircon U/Pb ages) from this study, although extensive, was acquired separately, and so doing independently, from each other: no grain was dated for both fission-track and U/Pb ages while these rigorously characterize both cooling and crystallisation histories of the specific zircon single source rock.

Yet, these results have been confirmed by the more recently published detrital single-grain zircon U-He and U/Pb double dating study of Filleaudeau et al. (2012) that is the completion of the previous doctoral work of Filleaudeau (2011) on the reconstruction of thermo-tectonic evolution of the south-central Pyrenees. Double dating of detrital single zircon grains from the pro- and retro-wedge notably indicate that (1) a source must have existed in the eastern Pyrenees according to Cadomian U/Pb ages measured onto detrital single zircon grains from the Late Cretaceous (latest Maastrichian-earliest Danian) Tremp Formation, (2) the central (Hercynian bedrocks) and eastern (Cadomian bedrocks) Pyrenean massifs were never (re-)buried after being exhumed during the Campanian, (3) a sufficiently high-relief topography (2-3 km) must have formed in the early orogenic growth stage, and (4) the pro-wedge would be exhumed from Early Campanian (*ca.* 80 Ma in the Tremp Formation) to Maastrichian (*ca.* 68 Ma in the Escanilla Formation) by southward-thrusting tectonics that decelerated from Late Cretaceous to Middle Eocene while convergence accelerated.

This study (Filleaudeau, 2011; Filleaudeau et al., 2012), together with that of Whitchurch et al. (2011), indicates there must have been a significant westward-migrating growth of topography during the early Pyrenean orogenic wedge growth (Campano-Maastrichian).

Some detrital low-temperature thermochronology data (Albian sandstones in southern central Pyrenees) even record local, already rapid exhumation associated with propagating Apto-Albian rifting toward east (Filleaudeau et al., 2012; Fillon et al., 2013).

SUMMARY

Pyrenean geology has been a long-lived source of debate on topics ranging from mechanisms of exhumation of the lower crust and sub-continental mantle to plate tectonics in the region. Questions that are still unresolved include: (1) How many extensional phases did the Pyrenean crust undergo before convergence? (2) How much shortening has been involved in the Pyrenees? (3) What was the thermal regime during orogenesis? (4) What was the importance of strike-slip tectonics during extension and in the formation of the mountain range?

Offshore domains record the rifting phase that comprises an extensional to transtensional history with the formation of an oceanic lithosphere in the Bay of Biscay. Onshore domains record the second part of the rift-collision transition (the orogenic phase) and the post-orogenic stage. Altogether this allows observing what happens to extensional systems that are involved in subduction and subsequent collision, even involved into another extensional regime later on. In other words, it allows investigating processes of reactivation and of transfer that look like quite complicated, onshore as well as offshore, in a region where extensional even pre-extensional inheritance plays a key role in the next stage, and the relationships between inheritance and finale structure can be observed. Thus, what is the role of lithospheric inheritance in development of later structures?

The Pyrenean system is highly asymmetrical from a structural, sedimentological and evolutional point of view. When comparing basins to the north (French, retro-side) and to the south (Spanish, pro-side) of the chain, irrespective of a N-S transect or an E-W transect, timing of both deformation and sedimentation is drastically different. This is also exemplified when looking at petroleum discoveries that are far more numerous in southwestern France than in northern Spain.

Many deformation phases are observed, as well as deformation styles ranging from thin-skinned style during early convergence, Campanian to Maastrichian, to thick-skinned style during late convergence, Eocene to Oligocene-Miocene. How can an orogenic system pass to another? What are the processes involved? What are the implications for the system itself and what happens afterwards? How distributed is the deformation? Is there a link between the early convergent phase and the late convergent phase? What are the dynamic, mechanical, sedimentary, thermal and fluid transfers leading to dynamic topography creation?

Foreland basin history indicates that convergence took place in two phases, Campanian to Maastrichian and Eocene, separated by a quiet Paleocene phase. To the east of the Toulouse Fault, Upper Cretaceous sediments are directly overlying basement, which may suggest that this eastern crystalline basement was emergent and/or acted as a bypass zone from Triassic to Late Cretaceous times. Development of the deltaic system infilling progressively the Subpyrenean Trough from east to west (BRGM et al., 1974; Dubois and Seguin, 1978; Bilotte et al., 2005; Serrano et al., 2006) indicates sediment supply from an eastern source (Ford et al., 2016). Oldest subsidence appears near the

North Pyrenean Frontal Thrust and propagates toward the Aquitaine Platform, suggesting a first-order flexural signal for the retro-foreland basin development. Low-temperature thermochronological data indicate that the North Pyrenea Zone was buried below at least 2-km-thick Late Cretaceous sediments, suggesting that the Upper Cretaceous depocentre was larger and must have been located further south of its present-day location (Ford et al. 2016; Vacherat et al. 2016). Can these two phases of convergence be recognised in the fold-and-thrust belts? The t-T history of North Pyrenean basement massifs is of particular interest since preliminary low-temperature thermochronology results (Vacherat, 2014; Vacherat et al., 2016) indicate that central massifs (Trois-Seigneurs, Arize) record a faster and earlier cooling history (60-50 Ma) than western massifs (50-15 Ma). What about exhumation of eastern massifs and its significance for early orogenic evolution? Such lateral variations have implications for the distribution and timing of shortening along the range, in particular the location of early orogenic wedge growth.

Available data and pioneering thermochronology analysis indicate that the early Pyrenean foreland basin records accelerated denudation of the eastern orogen during Campanian times. Detailed subsidence analysis within the foreland basins and combined bedrock-detrital low-temperature thermochronology, both in basins and in bedrocks, indicate that exhumation is highly diachronous along and across the range, with overall southward- and westward-younging tendencies accross the Axial Zone from Late Cretaceous (Santonian) to Miocene (Yelland, 1990, 1991; Morris et al., 1998; Fitzgerald et al., 1999; Sinclair et al., 2005; Jammes et al., 2010a; Filleaudeau, 2011; Whitchurch et al., 2011; Filleaudeau et al., 2012; Mouthereau et al., 2014). This exhumation could be interpreted as due to crustal thickening while subsidence acceleration and deepening of environments could be more direct signals of early wedge growth. Nonetheless, little is known about the early thermal and dynamic evolution of the Pyrenees since there is a poor documentation of denudation dynamics in sediments from the mountain belt.

REFERENCES

Albarède, F., & Michard-Vitrac, A. (1978). Age and significance of the North Pyrenean metamorphism. Earth and Planetary Science Letters, 40(3), 327–332. https://doi.org/10.1016/0012-821X(78)90157-7

Alibert, C., Debon, F., & Ternet, Y. (1988). Le pluton à structure concentrique du Néouvielle (Hautes-Pyrénées): typologie chimique, âge et genèse. Comptes Rendus de l'Académie Des Sciences. Série 2, Mécanique, Physique, Chimie, Sciences de l'Univers, Sciences de La Terre, 306(1), 49–54.

Alonso, J., Pulgar, J., García-Ramos, J., & Barba, P. (1996). W5 Tertiary basins and Alpine tectonics in the Cantabrian Mountains (NW Spain). Tertiary Basins of Spain: The Stratigraphic Record of Crustal Kinematics. Retrieved from https://books.google.fr/books?hl=fr&lr=&id=3hwD5UjwjbEC&oi=fnd&pg=PA214&dq=Alonso+et+al.,+1996+cantabrian+mountains&ots=tIYtLPkj7f&sig=w6WIVCStN62DnkgeVH7WYCincKU

Angrand, P., Ford, M., & Watts, A. B. (2018). Lateral Variations in Foreland Flexure of a Rifted Continental Margin: The Aquitaine Basin (SW France). Tectonics, 37(2), 430–449. https://doi.org/10.1002/2017TC004670

Arthaud, F., & Matte, P. (1975). Les décrochements tardi-hercyniens du Sud-Ouest de l'Europe. Géométrie et essai de reconstitution des conditions de la déformation. Tectonophysics, 25(1), 139–171.

Arthaud, Francois, & Matte, P. (1977). Late Paleozoic strike-slip faulting in southern Europe and northern Africa: Result of a right-lateral shear zone between the Appalachians and the Urals. Geological Society of America Bulletin, 88(9), 1305–1320.

Aslanian, D., Moulin, M., Olivet, J.-L., Unternehr, P., Matias, L., Bache, F., et al. (2009). Brazilian and African passive margins of the Central Segment of the South Atlantic Ocean: Kinematic constraints. Tectonophysics, 468(1), 98–112.

Azambre, B., & Pozzi, J. P. (1982). Etude du magnetisme des roches eruptives de la region d'Arette (Pyrenees Atlantiques), preliminaire a l'analyse de l'evolution des contraintes regionales. Bulletin de La Société Géologique de France, 7(2), 255–263.

Azambre, Bernard, & Rossy, M. (1976). Le magmatisme alcalin d'age cretace, dans les Pyrenees occidentales et l'Arc basque; ses relations avec le metamorphisme et la tectonique. Bulletin de La Société Géologique de France, 7(6), 1725–1728.

Baby, P., Crouzet, G., Specht, M., Déramond, J., Bilotte, M., & DEBRAOS, E. (1988). Rôle des paléostructures albo-cénomaniennes dans la géométrie des chevauchements frontaux nord-pyrénéens. Comptes Rendus de l'Académie Des Sciences. Série 2, Mécanique, Physique, Chimie, Sciences de l'Univers, Sciences de La Terre, 306(4), 307–313.

Barbey, P., Cheilletz, A., & Laumonier, B. (2001). The Canigou orthogneisses (Eastern Pyrenees, France, Spain): an Early Ordovician rapakivi granite laccolith and its contact aureole. Comptes Rendus de l'Académie Des Sciences - Series IIA - Earth and Planetary Science, 332(2), 129–136. https://doi.org/10.1016/S1251-8050(00)01506-8

Beamud, E., Muñoz, J. A., Fitzgerald, P. G., Baldwin, S. L., Garcés, M., Cabrera, L., & Metcalf, J. R. (2011). Magnetostratigraphy and detrital apatite fission track thermochronology in syntectonic conglomerates: constraints on the exhumation of the South-Central Pyrenees. Basin Research, 23(3), 309–331.

Beaumont, C., Muñoz, J. A., Hamilton, J., & Fullsack, P. (2000). Factors controlling the Alpine evolution of the central Pyrenees inferred from a comparison of observations and geodynamical models. Journal of Geophysical Research: Solid Earth, 105(B4), 8121–8145.

Berger, G. M., Alabouvette, B., Bessière, G., Bilotte, M., Crochet, B., Dubar, M., et al. (1997). Notice explicative, Carte géol. France (1/50 000), feuille Tuchan (1078). Orléans: BRGM.

Bilotte, M. (2007). Permanence, au Crétacé supérieur, de la position de la limite plate-forme/basin dans la zone sous-pyrénéenne orientale (Aude, France). Géologie de La France, 1, 33–53.

Bilotte, M., Koess, L., & Debroas, E. J. (2005). Relations tectonique–sedimentation sur la marge nord-orientale du sillon sous-pyreneen au cours du Santonien superieur. Bulletin de La Société Géologique de France, 176(5), 443–456.

Bilotte, Michel, & Canerot, J. (2006). Rôles respectifs des tectoniques fini-crétacée et éocène dans la partie orientale de la chaîne des Pyrénées. Le «Garumnien» de Cucugnan et ses relations avec le Chevauchement Frontal Nord-Pyrénéen (Corbières méridionales, France). Eclogae Geologicae Helvetiae, 99(1), 17–27. https://doi.org/10.1007/s00015-006-1179-8

Binks, R. M., & Fairhead, J. D. (1992). A plate tectonic setting for Mesozoic rifts of West and Central Africa. Tectonophysics, 213(1–2), 141–151.

Biteau, J.-J., Le Marrec, A., Le Vot, M., & Masset, J.-M. (2006). The Aquitaine Basin. Petroleum Geoscience, 12(3), 247–273.

Boillot, G., Capdevilla, R., Hennequin-Marchand, I., Lamboy, M., & Lepretre, J. P. (1973). La zone nord-pyrénéenne, ses prolongements sur la marge continentale nord-espagnole et sa signification structurale. CR Acad Sci Paris, 277, 2692–2632.

Boillot, Gilbert, Mougenot, D., Girardeau, J., & Winterer, E. L. (1989). Rifting processes on the West Galicia margin, Spain. AAPG Memoir, (46), 363–378.

Bosch, G., Teixell, A., Jolivet, M., Labaume, P., Stockli, D., Domènech, M., & Monié, P. (2016). Timing of Eocene–Miocene thrust activity in the Western Axial Zone and Chaînons Béarnais (west-central Pyrenees) revealed by multi-method thermochronology. Comptes Rendus Geoscience, 348(3–4), 246–256. https://doi.org/10.1016/j.crte.2016.01.001

Boulvais, P., de Parseval, P., D'Hulst, A., & Paris, P. (2006). Carbonate alteration associated with talc-chlorite mineralization in the eastern Pyrenees, with emphasis on the St. Barthelemy Massif. Mineralogy and Petrology, 88(3–4), 499–526. https://doi.org/10.1007/s00710-006-0124-x

Boulvais, Philippe, Ruffet, G., Cornichet, J., & Mermet, M. (2007). Cretaceous albitization and dequartzification of Hercynian peraluminous granite in the Salvezines Massif (French Pyrénées). Lithos, 93(1–2), 89–106. https://doi.org/10.1016/j.lithos.2006.05.001

Bourrouilh, R., Richert, J.-P., & Zolnai, G. (1995). The north Pyrenean Aquitaine basin, France: evolution and hydrocarbons. AAPG Bulletin, 79(6), 831–853.

BRGM, Elf-Re, ESSO-REP, & SNPA. (1974). Géologie du Bassin d'Aquitaine. Bureau de Recherches Géologiques et Minières, Orléans.

Brownfield, M. E., & Charpentier, R. R. (2006). Geology and total petroleum systems of the west-central coastal province (7203), west Africa. Retrieved from https://pubs.er.usgs.gov/publication/b2207B

Brunet, M. F. (1986). The influence of the evolution of the Pyrenees on adjacent basins. Tectonophysics, 129(1–4), 343–354.

Brunet, M.-F. (1991). Subsidence et géodynamique du Bassin d'Aquitaine. Relations avec l'ouverture de l'Atlantique. Retrieved from http://cat.inist.fr/?aModele=afficheN&cpsidt=145956

Burbank, D. W., Vergés, J., MUNOZ, J. A., & Bentham, P. (1992). Coeval hindward-and forward-imbricating thrusting in the south-central Pyrenees, Spain: Timing and rates of shortening and deposition. Geological Society of America Bulletin, 104(1), 3–17.

Burg, J.-P., Van Den Driessche, J., & Brun, J.-P. (1994). Syn- to post-thickening extension : mode and consequences. Comptes Rendus de l'Académie Des Sciences. Série 2. Sciences de La Terre et Des Planètes, 319(9), 1019–1032.

Canérot, J. (1987). Evolution géodynamique jurassique et éocrétacée de la zone nord-pyrénéenne en Bigorre méridionale (région de Lourdes-Bagnères). Conséquences structurales. Comptes Rendus de l'Académie Des Sciences. Série 2, Mécanique, Physique, Chimie, Sciences de l'Univers, Sciences de La Terre, 305(4), 297–300.

Canérot, J. (1989). Rifting éocrétacé et halocinèse sur la marge ibérique des Pyrénées Occidentales (France). Conséquences structurales. Cent. Rech. Expl, 13, 87–99.

Canérot, J., & Delavaux, F. (1986). Tectonique et sédimentation sur la marge nord-ibérique des chaînons béarnais (Pyrénées-béarnaises). Remise en question de la signification des lherzolites du sommet

de Saraillé. Comptes Rendus de l'Académie Des Sciences. Série 2, Mécanique, Physique, Chimie, Sciences de l'Univers, Sciences de La Terre, 302(15), 951–956.

Canérot, J., Majesté-Menjoulas, C., & Ternet, Y. (2001). La faille Nord Pyrénéenne: Mythe ou réalité. Strata, 37, 36.

Canérot, Joseph. (2008). Les Pyrénées: Histoire géologique (Vol. 1). Atlantica.

Canérot, Joseph, Majesté-Menjoulas, C., & Ternet, Y. (2004). Nouvelle interprétation structurale de la « faille Nord- Pyrénéenne » en vallée d'Aspe (Pyrénées-Atlantiques). Remise en question d'un plutonisme ophitique danien dans le secteur de Bedous. Comptes Rendus Geoscience, 336(2), 135–142. https://doi.org/10.1016/j.crte.2003.11.004

Canérot, Joseph, Hudec, M. R., & Rockenbauch, K. (2005). Mesozoic diapirism in the Pyrenean orogen: Salt tectonics on a transform plate boundary. AAPG Bulletin, 89(2), 211–229. https://doi.org/10.1306/09170404007

Capote, R., Muñoz, J. A., Simón, J. L., Liesa, C. L., & Arlegui, L. E. (2002). Alpine tectonics I: the Alpine system north of the Betic Cordillera. The Geology of Spain, 367–400.

Carey, S. W. (1959). The tectonic approach to continental drift. Geology Dept., Univ. of Tasmania.

Castéras, M., Calvet, P., Guitard, G., Ovtracht, A., & Raguin, E. (1967). Notice explicative, Carte géol. France (1/80 000), feuille Quillan (254) (3rd ed.). Paris: Service de la Carte Géologique.

Chaboureau, A.-C., Guillocheau, F., Robin, C., Rohais, S., Moulin, M., & Aslanian, D. (2013). Paleogeographic evolution of the central segment of the South Atlantic during Early Cretaceous times: Paleotopographic and geodynamic implications. Tectonophysics, 604, 191–223.

Charrière, A., & Durand-Delga, M. (2004). Le jeu fini-Crétacé du front nord-pyrénéen aux environs de Cucugnan (Corbières méridionales, Aude, France). Comptes Rendus Geoscience, 336(13), 1199–1208. https://doi.org/10.1016/j.crte.2004.07.001

Chelalou, R., Nalpas, T., Bousquet, R., Prevost, M., Lahfid, A., Poujol, M., et al. (2016). New sedimentological, structural and paleo-thermicity data in the Boucheville Basin (eastern North Pyrenean Zone, France). Comptes Rendus Geoscience, 348(3–4), 312–321. https://doi.org/10.1016/j.crte.2015.11.008

Chevrot, S., Villaseñor, A., Sylvander, M., Benahmed, S., Beucler, E., Cougoulat, G., et al. (2014). High-resolution imaging of the Pyrenees and Massif Central from the data of the PYROPE and IBERARRAY portable array deployments. Journal of Geophysical Research: Solid Earth, 119(8), 6399–6420.

Choukroune, P. (1988). The ECORS deep reflection seismic survey across the Pyrenees. Nature, 331(6156), 508–511.

Choukroune, P. (1989). The Ecors Pyrenean deep seismic profile reflection data and the overall structure of an orogenic belt. Tectonics, 8(1), 23–39. https://doi.org/10.1029/TC008i001p00023

Choukroune, P., & Mattauer, M. (1978). Tectonique des plaques et Pyrenees; sur le fonctionnement de la faille transformante nord-pyreneenne; comparaisons avec des modeles actuels. Bulletin de La Société Géologique de France, 7(5), 689–700.

Choukroune, Pierre. (1974). Structure et évolution tectonique de la zone nord-pyrénéenne: analyse de la déformation dans une portion de chaîne à schistosité sub-verticale.

Choukroune, Pierre. (1992). Tectonic evolution of the Pyrenees. Annual Review of Earth and Planetary Sciences, 20, 143.

Choukroune, Pierre, Le Pichon, X., Seguret, M., & Sibuet, J.-C. (1973). Bay of Biscay and Pyrenees. Earth and Planetary Science Letters, 18(1), 109–118.

Christophoul, F., Soula, J.-C., Brusset, S., Elibana, B., Roddaz, M., Bessiere, G., & Déramond, J. (2003). Time, place and mode of propagation of foreland basin systems as recorded by the sedimentary fill: examples of the Late Cretaceous and Eocene retro-foreland basins of the north-eastern Pyrenees. Special Publication-Geological Society of London, 208, 229–252.

Clerc, C., Lahfid, A., Monié, P., Lagabrielle, Y., Chopin, C., Poujol, M., et al. (2015). High-temperature metamorphism during extreme thinning of the continental crust: a reappraisal of the North

Pyrenean passive paleomargin. Solid Earth, 6(2), 643–668. https://doi.org/10.5194/se-6-643-2015

Clerc, Camille. (2012). Evolution du domaine nord-pyrénéen au Crétacé : amincissement crustal extrême et thermicite élevée : un analogue pour les marges passives. Paris 6. Retrieved from http://www.theses.fr/2012PA066572

Clerc, Camille, & Lagabrielle, Y. (2014). Thermal control on the modes of crustal thinning leading to mantle exhumation: Insights from the Cretaceous Pyrenean hot paleomargins. Tectonics, 33(7), 1340–1359. https://doi.org/10.1002/2013TC003471

Clerc, Camille, Lagabrielle, Y., Neumaier, M., Reynaud, J.-Y., & de Saint Blanquat, M. (2012). Exhumation of subcontinental mantle rocks: evidence from ultramafic-bearing clastic deposits nearby the Lherz peridotite body, French Pyrenees. Bulletin de La Societe Geologique de France, 183(5), 443–459. https://doi.org/10.2113/gssgfbull.183.5.443

Cocherie, A., Baudin, T., Autran, A., Guerrot, C., Fanning, C. M., & Laumonier, B. (2005). U-Pb zircon (ID-TIMS and SHRIMP) evidence for the early ordovician intrusion of metagranites in the late Proterozoic Canaveilles Group of the Pyrenees and the Montagne Noire (France). Bulletin De La Societe Geologique De France, 176(3), 269–282. https://doi.org/10.2113/176.3.269

Combes, P. J., Peybernes, B., & Fondecave-Wallez, M. J. (2004). Repeated karstification, marine and continental facies in the Paleocene of the eastern Pyrenees of France. Eclogae Geologicae Helvetiae, 97(2), 155–174. https://doi.org/10.1007/s00015-004-1120-y

Combes, P.-J., Peybernès, B., & Leyreloup, A. F. (1998). Altérites et bauxites, témoins des marges européenne et ibérique des Pyrénées occidentales au Jurassique supérieur — Crétacé inférieur, à l'ouest de la vallée d'Ossau (Pyrénées-Atlantiques, France). Comptes Rendus de l'Académie Des Sciences - Series IIA - Earth and Planetary Science, 327(4), 271–278. https://doi.org/10.1016/S1251-8050(98)80085-2

Coney, P. J., Muñoz, J. A., McClay, K. R., & Evenchick, C. A. (1996). Syntectonic burial and post-tectonic exhumation of the southern Pyrenees foreland fold–thrust belt. Journal of the Geological Society, 153(1), 9–16.

Corre, B., Lagabrielle, Y., Labaume, P., Fourcade, S., Clerc, C., & Ballèvre, M. (2016). Deformation associated with mantle exhumation in a distal, hot passive margin environment: New constraints from the Saraillé Massif (Chaînons Béarnais, North-Pyrenean Zone). Comptes Rendus Geoscience, 348(3–4), 279–289. https://doi.org/10.1016/j.crte.2015.11.007

Costa, E., Garcés, M., López-Blanco, M., Beamud, E., Gómez-Paccard, M., & Larrasoaña, J. C. (2010). Closing and continentalization of the South Pyrenean foreland basin (NE Spain): magnetochronological constraints. Basin Research, 22(6), 904–917.

Costa, S., & Maluski, H. (1988). Use of the 40 Ar-39 Ar stepwise heating method for dating mylonite zones: An example from the St. Barthe\' le\' my massif (Northern Pyrenees, France). Chemical Geology: Isotope Geoscience Section, 72(2), 127–144.

Curnelle, R. (1986). Projet d'Implantation du profil "Structure profonde du Golfe de Gascogne", profil plateau Aquitaine. Internal Report IFP No. 33910, 16.

Curnelle, R., Dubois, P., & Seguin, J. C. (1980). Le bassin d'Aquitaine: Substratum anté-Tertiaire et bordures mésozoïques. La Chaîne Des Pyrénées et Son Avant-Pays Aquitano-Languedocien. Bulletin Des Centres de Recherches Exploration–Production Elf-Aquitaine, Mémoire, 3, 47–58.

Debroas, E. J. (1987a). Le flysch à fucoïdes d'Uchentein témoin d'un escarpement turono-sénonien inférieur de la paléofaille nord pyrénéenne. Pyrénées Centrales, France, Strata, 77–93.

Debroas, E. J. (1987b). Modèle de bassin triangulaire à l'intersection de décrochements divergents pour le fossé albo-cénomanien de la Ballongue (zone nord-pyrénéenne, France). Bull. Soc. Geol. Fr, 8, 887–898.

Debroas, E. J. (1990). Le Flysch noir albo-cénomanien témoin de la structuration albienne à sénonienne de la zone nord-pyrénéenne en Bigorre (Hautes-Pyrénées, France). Bulletin de La Société Géologique de France, 6(2), 283–285.

Debroas, E. J., Canérot, J., & Bilotte, M. (2010). Les brèches d'Urdach, témoins de l'exhumation du manteau pyrénéen dans un escarpement de faille vraconnien-cénomanien inférieur (Zone nord-pyrénéenne, Pyrénées-Atlantiques, France). Géologie de La France, 2, 53–63.

DeCelles, P. G., & Giles, K. A. (1996). Foreland basin systems. Basin Research, 8(2), 105–123.

DeFelipe, I., Pedreira, D., Pulgar, J. A., Beek, P. A. van der, Bernet, M., & Pik, R. (2019). Unraveling the Mesozoic and Cenozoic Tectonothermal Evolution of the Eastern Basque-Cantabrian Zone–Western Pyrenees by Low-Temperature Thermochronology. Tectonics, 0(0). https://doi.org/10.1029/2019TC005532

Demange, M., Lia-Aragnouet, F., Pouliguen, M., Perrot, X., & Sauvage, H. (1999). Les syénites du Castillet (massif de l'Agly, Pyrénées orientales, France): une roche exceptionnelle dans les Pyrénées. Comptes Rendus de l'Académie Des Sciences - Series IIA - Earth and Planetary Science, 329(5), 325–330.

Denèle, Y., Olivier, P., Gleizes, G., & Barbey, P. (2009). Decoupling between the middle and upper crust during transpression-related lateral flow: Variscan evolution of the Aston gneiss dome (Pyrenees, France). Tectonophysics, 477(3–4), 244–261. https://doi.org/10.1016/j.tecto.2009.04.033

Denèle, Y., Barbey, P., Deloule, E., Pelleter, E., Olivier, P., & Gleizes, G. (2009). Middle Ordovician U-Pb age of the Aston and Hospitalet orthogneissic laccoliths: their role in the Variscan evolution of the Pyrenees. Bulletin De La Societe Geologique De France, 180(3), 209–216.

Denèle, Y., Paquette, J.-L., Olivier, P., & Barbey, P. (2012). Permian granites in the Pyrenees: the Aya pluton (Basque Country). Terra Nova, 24(2), 105–113.

Denèle, Y., Laumonier, B., Paquette, J.-L., Olivier, P., Gleizes, G., & Barbey, P. (2014). Timing of granite emplacement, crustal flow and gneiss dome formation in the Variscan segment of the Pyrenees. In K. Schulmann, J. R. MartinezCatalan, J. M. Lardeaux, V. Janousek, & G. Oggiano (Eds.), Variscan Orogeny: Extent, Timescale and the Formation of the European Crust (Vol. 405, pp. 265–287). Bath: Geological Soc Publishing House.

Déramond, J., Graham, R. H., Hossack, J. R., Baby, P., & Crouzet, G. (1985). Nouveau modèle de la chaîne des Pyrénées. Comptes Rendus de l'Académie Des Sciences. Série 2, Mécanique, Physique, Chimie, Sciences de l'Univers, Sciences de La Terre, 301(16), 1213–1216.

Déramond, Joachim, Souquet, P., Fondecave-Wallez, M.-J., & Specht, M. (1993). Relationships between thrust tectonics and sequence stratigraphy surfaces in foredeeps: model and examples from the Pyrenees (Cretaceous-Eocene, France, Spain). Geological Society, London, Special Publications, 71(1), 193–219.

Desegaulx, P., Roure, F., & Villein, A. (1990). Structural evolution of the Pyrenees: tectonic inheritance and flexural behaviour in the continental crust. Tectonophysics, 182(3), 211–225.

Desegaulx, PASCAL, & Brunet, M.-F. (1990). Tectonic subsidence of the Aquitaine basin since Cretaceous times. Bulletin de La Société Géologique de France, 8, 295–306.

Dewey, J. F., Helman, M. L., Knott, S. D., Turco, E., & Hutton, D. H. W. (1989). Kinematics of the western Mediterranean. Geological Society, London, Special Publications, 45(1), 265–283.

Dewey, J. F., Cande, S., & Pitman, W. C. (1989). Tectonic evolution of the India/Eurasia collision zone. Eclogae Geologicae Helvetiae, 82(3), 717–734.

Dubois, P., & Seguin, J. C. (1978). Les flyschs crétacé et éocène de la zone commingeoise et leur environnement. Bulletin de La Société Géologique de France, 7(5), 657–671.

Fabriès, J., Lorand, J.-P., Bodinier, J.-L., & Dupuy, C. (1991). Evolution of the upper mantle beneath the Pyrenees: evidence from orogenic spinel lherzolite massifs. Journal of Petrology, (2), 55–76.

Fabriès, J., Lorand, J.-P., & Bodinier, J.-L. (1998). Petrogenetic evolution of orogenic lherzolite massifs in the central and western Pyrenees. Tectonophysics, 292(1), 145–167.

Fallourd, S., Poujol, M., Boulvais, P., Paquette, J.-L., de Saint Blanquat, M., & Rémy, P. (2014). In situ LA-ICP-MS U–Pb titanite dating of Na–Ca metasomatism in orogenic belts: the North Pyrenean example. International Journal of Earth Sciences, 103(3), 667–682.

Filleaudeau, P.-Y. (2011, April 29). Croissance et dénudation des Pyrénées du Crétacé supérieur au Paléogène : apports de l'analyse de bassin et thermochronométrie détritique (phdthesis). Université Pierre et Marie Curie - Paris VI. Retrieved from https://tel.archives-ouvertes.fr/tel-00642171/document

Filleaudeau, P.-Y., Mouthereau, F., & Pik, R. (2012). Thermo-tectonic evolution of the south-central Pyrenees from rifting to orogeny: insights from detrital zircon U/Pb and (U-Th)/He thermochronometry. Basin Research, 24(4), 401–417. https://doi.org/10.1111/j.1365-2117.2011.00535.x

Fillon, C., & van der Beek, P. (2012). Post-orogenic evolution of the southern Pyrenees: constraints from inverse thermo-kinematic modelling of low-temperature thermochronology data. Basin Research, 24(4), 418–436. https://doi.org/10.1111/j.1365-2117.2011.00533.x

Fillon, C., Gautheron, C., & van der Beek, P. (2013). Oligocene–Miocene burial and exhumation of the Southern Pyrenean foreland quantified by low-temperature thermochronology. Journal of the Geological Society, 170(1), 67–77.

Fitzgerald, P. G., Muñoz, J. A., Coney, P. J., & Baldwin, S. L. (1999). Asymmetric exhumation across the Pyrenean orogen: implications for the tectonic evolution of a collisional orogen. Earth and Planetary Science Letters, 173(3), 157–170. https://doi.org/10.1016/S0012-821X(99)00225-3

Ford, M. (2004). Depositional wedge tops: interaction between low basal friction external orogenic wedges and flexural foreland basins. Basin Research, 16(3), 361–375. https://doi.org/10.1111/j.1365-2117.2004.00236.x

Ford, M., Hemmer, L., Vacherat, A., Gallagher, K., & Christophoul, F. (2016). Retro-wedge foreland basin evolution along the ECORS line, eastern Pyrenees, France. Journal of the Geological Society, 173(3), 419–437.

Freytet, P. (1970). Les dépôts continentaux et marins du Crétacé supérieur et des couches de pass de l'Eocene en Languedoc. Univ. Paris Sud.

Garwin, L. J. (1985). Fission track dating and tectonics in the Eastern Pyrenees (Ph.D.). University of Cambridge. Retrieved from http://ethos.bl.uk/OrderDetails.do?did=1&uin=uk.bl.ethos.373658

Gibson, M., Sinclair, H. D., Lynn, G. J., & Stuart, F. M. (2007). Late- to post-orogenic exhumation of the Central Pyrenees revealed through combined thermochronological data and modelling. Basin Research, 19(3), 323–334. https://doi.org/10.1111/j.1365-2117.2007.00333.x

Golberg, J. M., & Leyreloup, A. F. (1990). High temperature-low pressure Cretaceous metamorphism related to crustal thinning (Eastern North Pyrenean Zone, France). Contributions to Mineralogy and Petrology, 104(2), 194–207.

Golberg, J. M., Maluski, H., & Leyreloup, A. F. (1986). Petrological and age relationship between emplacement of magmatic breccia, alkaline magmatism, and static metamorphism in the North Pyrenean Zone. Tectonophysics, 129(1–4), 275–290.

Golberg, Jean-Marc. (1987). Le métamorphisme mésozoïque dans la partie orientale des Pyrénées: relations avec l'évolution de la chaîne au Crétacé. Montpellier 2. Retrieved from http://www.theses.fr/1987MON20175

Golberg, J.-M., & Maluski, H. (1988). Données nouvelles et mise au point sur l'âge du métamorphisme pyrénéen. Comptes Rendus de l'Académie Des Sciences. Série 2, Mécanique, Physique, Chimie, Sciences de l'Univers, Sciences de La Terre, 306(6), 429–435.

Gong, Z., Langereis, C. G., & Mullender, T. A. T. (2008). The rotation of Iberia during the Aptian and the opening of the Bay of Biscay. Earth and Planetary Science Letters, 273(1–2), 80–93. https://doi.org/10.1016/j.epsl.2008.06.016

Gong, Zhihong, van Hinsbergen, D. J. J., Vissers, R. L. M., & Dekkers, M. J. (2009). Early Cretaceous syn-rotational extension in the Organyà basin—New constraints on the palinspastic position of Iberia during its rotation. Tectonophysics, 473(3–4), 312–323. https://doi.org/10.1016/j.tecto.2009.03.003

Granot, R., & Dyment, J. (2015). The Cretaceous opening of the South Atlantic Ocean. Earth and Planetary Science Letters, 414, 156–163.

Grool, A. R., Ford, M., Vergés, J., Huismans, R. S., Christophoul, F., & Dielforder, A. (2018). Insights Into the Crustal‐Scale Dynamics of a Doubly Vergent Orogen From a Quantitative Analysis of Its Forelands: A Case Study of the Eastern Pyrenees. Tectonics, 37(2), 450–476. https://doi.org/10.1002/2017TC004731

Guimerá, J. (1984). Palaeogene evolution of deformation in the northeastern Iberian Peninsula. Geological Magazine, 121(05), 413. https://doi.org/10.1017/S0016756800029940

Guiraud, Rene, & Bosworth, W. (1997). Senonian basin inversion and rejuvenation of rifting in Africa and Arabia: synthesis and implications to plate-scale tectonics. Tectonophysics, 282(1), 39–82.

Guiraud, René, & Maurin, J.-C. (1992). Early Cretaceous rifts of Western and Central Africa: an overview. Tectonophysics, 213(1–2), 153–168.

Gunnell, Y., Calvet, M., Brichau, S., Carter, A., Aguilar, J.-P., & Zeyen, H. (2009). Low long-term erosion rates in high-energy mountain belts: Insights from thermo- and biochronology in the Eastern Pyrenees. Earth and Planetary Science Letters, 278(3–4), 208–218. https://doi.org/10.1016/j.epsl.2008.12.004

Hall, C. A., & Bennett, V. C. (1979). Significance of lherzolite at the Etang de Lherz, central Pyrenees, southern France. Earth and Planetary Science Letters, 45(2), 349–354.

Handy, M. R., M. Schmid, S., Bousquet, R., Kissling, E., & Bernoulli, D. (2010). Reconciling plate-tectonic reconstructions of Alpine Tethys with the geological–geophysical record of spreading and subduction in the Alps. Earth-Science Reviews, 102(3–4), 121–158. https://doi.org/10.1016/j.earscirev.2010.06.002

Henry, P., Azambre, B., Montigny, R., Rossy, M., & Stevenson, R. K. (1998). Late mantle evolution of the Pyrenean sub-continental lithospheric mantle in the light of new 40 Ar–39 Ar and Sm–Nd ages on pyroxenites and peridotites (Pyrenees, France). Tectonophysics, 296(1), 103–123.

Hiscott, R. N., Wilson, R. C. L., Gradstein, F. M., Pujalte, V., Garcia-Mondejar, J., Boudreau, R. R., & Wishart, H. A. (1990). Comparative stratigraphy and subsidence history of mesozoic rift basins of North Atlantic (1). AAPG Bulletin, 74(1), 60–76.

Hogan, P. J., & Burbank, D. W. (1996). E14 Evolution of the Jaca piggyback basin and emergence of the External Sierra, southern Pyrenees. Tertiary Basins of Spain: The Stratigraphic Record of Crustal Kinematics, 6, 153.

Huyghe, D., Mouthereau, F., Castelltort, S., Filleaudeau, P. Y., & Emmanuel, L. (2009). Paleogene propagation of the southern Pyrenean thrust wedge revealed by finite strain analysis in frontal thrust sheets: Implications for mountain building. Earth and Planetary Science Letters, 288(3–4), 421–433. https://doi.org/10.1016/j.epsl.2009.10.002

Jäger, E., & Zwart, H. J. (1968). Rb-Sr age determinations of some gneisses and granites of the Aston-Hospitalet massif (Pyrenees). Geologie En Mijnbouw, 47(5), 249–358.

Jammes, S. (2009). Processus d'amincissement crustal en contexte transtensif: L'exemple du golfe de Gascogne et des Pyrénées basques. Strasbourg. Retrieved from http://www.theses.fr/2009STRA6067

Jammes, S., Manatschal, G., Lavier, L., & Masini, E. (2009). Tectonosedimentary evolution related to extreme crustal thinning ahead of a propagating ocean: Example of the western Pyrenees. Tectonics, 28(4), TC4012, 1–24. https://doi.org/10.1029/2008TC002406

Jammes, S., Tiberi, C., & Manatschal, G. (2010). 3D architecture of a complex transcurrent rift system: The example of the Bay of Biscay–Western Pyrenees. Tectonophysics, 489(1–4), 210–226. https://doi.org/10.1016/j.tecto.2010.04.023

Jammes, S., Lavier, L., & Manatschal, G. (2010). Extreme crustal thinning in the Bay of Biscay and the Western Pyrenees: From observations to modeling: MODELIZATION OF EXTREME CRUSTAL THINNING. Geochemistry, Geophysics, Geosystems, 11(10), n/a-n/a. https://doi.org/10.1029/2010GC003218

Jolivet, M., Labaume, P., Monié, P., Brunel, M., Arnaud, N., & Campani, M. (2007). Thermochronology constraints for the propagation sequence of the south Pyrenean basement thrust system (France-Spain). Tectonics, 26(5), TC5007. https://doi.org/10.1029/2006TC002080

de Jong, K. (1990). Alpine tectonics and rotation pole evolution of Iberia. Tectonophysics, 184(3–4), 279–296.

Kieken, M., & Winnock, E. (1973). Olistostromes dans le Lutétien du Bas-Adour à l'avant du Front nord-pyrénéen. Bull. BRGM, 4, 5–15.

Lagabrielle, Y., & Bodinier, J.-L. (2008). Submarine reworking of exhumed subcontinental mantle rocks: field evidence from the Lherz peridotites, French Pyrenees. Terra Nova, 20(1), 11–21.

Lagabrielle, Y., Labaume, P., & de Saint Blanquat, M. (2010). Mantle exhumation, crustal denudation, and gravity tectonics during Cretaceous rifting in the Pyrenean realm (SW Europe): Insights from the geological setting of the lherzolite bodies: PYRENEAN LHERZOLITES, GRAVITY TECTONICS. Tectonics, 29(4), n/a-n/a. https://doi.org/10.1029/2009TC002588

Lamare, P. (1936). Recherches géologiques dans les Pyrénées basques d'Espagne. Société géologique de France.

Lambiase, J. J. (1989). The framework of African rifting during the Phanerozoic. Journal of African Earth Sciences (and the Middle East), 8(2–4), 183–190.

Larrasoaña, J. C., Parés, J. M., Millán, H., Del Valle, J., & Pueyo, E. L. (2003). Paleomagnetic, structural, and stratigraphic constraints on transverse fault kinematics during basin inversion: The Pamplona Fault (Pyrenees, north Spain). Tectonics, 22(6). Retrieved from http://onlinelibrary.wiley.com/doi/10.1029/2002TC001446/full

Larrasoaña, J. C., Marí, J., Millán, H., & others. (2003). Triassic paleomagnetism from the Western Pyrenees revisited: implications for the Iberian–Eurasian Mesozoic plate boundary. Tectonophysics, 362(1), 161–182.

Laumonier, B. (2015). Les Pyrénées alpines sud-orientales (France, Espagne) – essai de synthèse. Revue de Géologie Pyrénéenne, 2(1). Retrieved from http://www.geologie-des-pyrenees.com/wp-content/uploads/2015/10/Laumonier-2015-Pyr%C3%A9n%C3%A9es-alpines-sud-orientales.pdf

Le Pichon, X., Sibuet, J.-C., & Bonnin, J. (1970). La faille nord-pyrénéenne: Faille transformante liée à l'ouverture du golfe de Gascogne. Comptes Rendus Académie Des Sciences de Paris, 271, 1941–1944.

Le Vot, M., Biteau, J. J., & Masset, J. M. (1996). The Aquitaine Basin : oil and gas production in the foreland of the Pyrenean fold-and-thrust belt New exploration perspectives. Mémoires Du Muséum National d'histoire Naturelle, 170, 159–171.

Logar, J. F. (1983). 1983 West Africa well evaluation conference, Part 1: Geology. (Schlumberger Paris).

Majoor, F. J. (1988). A geochronological study of the Axial Zone of the Central Pyrenees, with emphasis on Variscan events and Alpine resetting. Retrieved from https://inis.iaea.org/search/search.aspx?orig_q=RN:20036417

Martín-Chivelet, J., Berástegui, X., Rosales, I., Vilas, L., Vera, J. A., Caus, E., et al. (2002). Cretaceous. The Geology of Spain. Geological Society, London, 255, 292.

Martinez-Peña, M., & Casas-Sainz, A. (2003). Cretaceous–Tertiary tectonic inversion of the Cotiella Basin (southern Pyrenees, Spain). International Journal of Earth Sciences, 92(1), 99–113.

Masini, E., Manatschal, G., Tugend, J., Mohn, G., & Flament, J.-M. (2014). The tectono-sedimentary evolution of a hyper-extended rift basin: the example of the Arzacq–Mauléon rift system (Western Pyrenees, SW France). International Journal of Earth Sciences, 103(6), 1569–1596. https://doi.org/10.1007/s00531-014-1023-8

Mathey, B., Floquet, M., & Martînez-Torres, L. M. (1999). The Leiza palaeo-fault: role and importance in the Upper Cretaceous sedimentation and palaeogeography of the Basque Pyrenees (Spain). Comptes Rendus de l'Académie Des Sciences - Series IIA - Earth and Planetary Science, 328(6), 393–399.

Mattauer, M., & Choukroune, P. (1974). Les lherzolites des Pyrénées sont des extrusions de matériel ancien dans le Mésozoique nord Pyrénées. 2nd Réunion Annuelle Des Sciences de La Terre, Soc. Géol. de Fr., Paris.

Mattauer, M., & Proust, F. (1962). Sur la tectonique de la fin du Crétacé et du début du Tertiaire en Languedoc. Rev. Géol. Dyn. Géogr. Phys, 2, 5–11.

Mattauer, M., & Séguret, M. (1971). Les relations entre la chaîne des Pyrénées et le golfe de Gascogne. J. Debyser, X. Le Pichon, and L. Montadert. Technip, Paris, 1–24.

Mattauer, Maurice. (1968). Les traits structuraux essentiels de la chaîne Pyrénéenne. Revue de Géologie Dynamique et de Géographie Physique, 10, 3–11.

Matte, P. (2001). The Variscan collage and orogeny (480–290 Ma) and the tectonic definition of the Armorica microplate: a review. Terra Nova, 13(2), 122–128.

Maurel, O., Monié, P., Pik, R., Arnaud, N., Brunel, M., & Jolivet, M. (2008). The Meso-Cenozoic thermo-tectonic evolution of the Eastern Pyrenees: an 40Ar/39Ar fission track and (U–Th)/He thermochronological study of the Canigou and Mont-Louis massifs. International Journal of Earth Sciences, 97(3), 565–584. https://doi.org/10.1007/s00531-007-0179-x

McCaig, A. M., & Miller, J. A. (1986). 40 Ar-39 Ar age of mylonites along the Merens Fault, central Pyrenees. Tectonophysics, 129(1), 149–172.

Meigs, A. J., Vergés, J., & Burbank, D. W. (1996). Ten-million-year history of a thrust sheet. Geological Society of America Bulletin, 108(12), 1608–1625.

Meresse, F. (2010). Dynamique d'un prisme orogénique intracontinental: évolution thermochronologique (traces de fission sur apatite) et tectonique de la Zone Axiale et des piémonts des Pyrénées centro-occidentales. Université de Montpellier 2. Retrieved from https://tel.archives-ouvertes.fr/tel-00772154/

Metcalf, J. R., Fitzgerald, P. G., Baldwin, S. L., & Muñoz, J.-A. (2009). Thermochronology of a convergent orogen: Constraints on the timing of thrust faulting and subsequent exhumation of the Maladeta Pluton in the Central Pyrenean Axial Zone. Earth and Planetary Science Letters, 287(3–4), 488–503. https://doi.org/10.1016/j.epsl.2009.08.036

Michard-Vitrac, A., Albarede, F., Dupuis, C., & Taylor Jr, H. P. (1980). The genesis of Variscan (Hercynian) plutonic rocks: inferences from Sr, Pb, and O studies on the Maladeta igneous complex, Central Pyrenees (Spain). Contributions to Mineralogy and Petrology, 72(1), 57–72.

Minnigh, L. D., Van Calsteren, P. W. C., & Den Tex, E. (1980). Quenching: An additional model for emplacement of the Iherzolite at Lers (French Pyrenees). Geology, 8(1), 18–21.

Moine, B., Fortune, J. P., Moreau, P., & Viguier, F. (1989). Comparative mineralogy, geochemistry, and conditions of formation of two metasomatic talc and chlorite deposits; Trimouns (Pyrenees, France) and Rabenwald (Eastern Alps, Austria). Economic Geology, 84(5), 1398–1416.

Monchoux, P. (1970). Les lherzolites pyrénéennes: contribution à l'étude de leur minéralogie, de leur genèse et de leurs transformations. Toulouse.

Monod, B., Bourroullec, I., & others. (2014). Carte Géologique numérique à 1/250 000 de la région Midi–Pyrénées. Notice Technique, Bureau Des Recherches Géologiques et Minières, Orléans, France.

Montigny, R., Azambre, B., Rossy, M., & Thuizat, R. (1986). The Geological Evolution of the Pyrenees K-Ar Study of cretaceous magmatism and metamorphism in the pyrenees: Age and length of rotation of the Iiberian Peninsula. Tectonophysics, 129(1), 257–273. https://doi.org/10.1016/0040-1951(86)90255-6

Morris, R. G., Sinclair, H. D., & Yelland, A. J. (1998). Exhumation of the Pyrenean orogen: implications for sediment discharge. Basin Research, 10(1), 69–85.

Moulin, M., Aslanian, D., & Unternehr, P. (2010). A new starting point for the South and Equatorial Atlantic Ocean. Earth-Science Reviews, 98(1), 1–37.

Mouthereau, F., Filleaudeau, P.-Y., Vacherat, A., Pik, R., Lacombe, O., Fellin, M. G., et al. (2014). Placing limits to shortening evolution in the Pyrenees: Role of margin architecture and implications for the Iberia/Europe convergence: Plate convergence in the Pyrenees. Tectonics, 33(12), 2283–2314. https://doi.org/10.1002/2014TC003663

Muñoz, J. A. (1992). Evolution of a continental collision belt: ECORS-Pyrenees crustal balanced cross-section. In Thrust tectonics (pp. 235–246). Springer. Retrieved from http://link.springer.com/chapter/10.1007/978-94-011-3066-0_21

Naylor, M., & Sinclair, H. D. (2008). Pro- vs. retro-foreland basins: Pro- vs. retro-foreland basins. Basin Research, 20(3), 285–303. https://doi.org/10.1111/j.1365-2117.2008.00366.x

Nkoumbou, C., Barbey, P., Yonta-Ngouné, C., Paquette, J.-L., & Villiéras, F. (2014). Pre-collisional geodynamic context of the southern margin of the Pan-African fold belt in Cameroon. Journal of African Earth Sciences, 99, 245–260.

Olivet, J. L. (1996). Kinematics of the Iberian Plate. Bulletin Des Centres De Recherches Exploration-Production Elf Aquitaine, 20(1), 131–195.

Olivet, J. L., Auzende, J. M., & Beuzart, P. (1983). Western extension of the Iberian-European plate boundary during the Early Cenozoic (Pyrenean) convergence: A new model — Comment. Marine Geology, 53(3), 237–238. https://doi.org/10.1016/0025-3227(83)90078-6

Olivet, J.-L., Bonnin, J., Beuzart, P., & Auzende, J.-M. (1984). Cinématique de l'Atlantique nord et central. Centre océanologique de Bretagne.

Paris, J.-P., & Cavaillé, A. (1974). Carte géologique de France (1/50 000), feuille Le Fousseret (1033). Orléans: BRGM.

Peybernes, B., & Souquet, P. (1984). Basement blocks and tecto-sedimentary evolution in the Pyrenees during Mesozoic times. Geological Magazine, 121(05), 397–405.

Plaziat, J.-C. (1984). Le domaine pyrénéen de la fin du Crétacé à la fin de l'Eocène: stratigraphie, paléoenvironnements et évolution paléogéographique. Université de Paris-Sud. Retrieved from http://www.worldcat.org/title/stratigraphie-et-evolution-paleogeographique-du-domaine-pyreneen-de-la-fin-du-cretace-phase-maastrichtienne-a-la-fin-de-leocene-phase-pyreneenne/oclc/490767464?referer=di&ht=edition

Poujol, M., Boulvais, P., & Kosler, J. (2010). Regional-scale Cretaceous albitization in the Pyrenees: evidence from in situ U-Th-Pb dating of monazite, titanite and zircon. Journal of the Geological Society, 167(4), 751–767. https://doi.org/10.1144/0016-76492009-144

Puigdefàbregas, C., & Souquet, P. (1986). Tecto-sedimentary cycles and depositional sequences of the Mesozoic and Tertiary from the Pyrenees. Tectonophysics, 129(1–4), 173–203. https://doi.org/10.1016/0040-1951(86)90251-9

Puigdefàbregas, C., Muñoz, J. A., & Marzo, M. (1986). Thrust belt development in the eastern Pyrenees and related depositional sequences in the southern foreland basin. Foreland Basins, 229–246.

Puigdefàbregas, C., Muñoz, J. A., & Vergés, J. (1992). Thrusting and foreland basin evolution in the southern Pyrenees. In Thrust tectonics (pp. 247–254). Springer. Retrieved from http://link.springer.com/chapter/10.1007/978-94-011-3066-0_22

Rat, P. (1988). The Basque-Cantabrian basin between the Iberian and European plates: Some facts but still many problems. Revista de La Sociedad Geológica de España, 1(3–4), 327–348.

Razin, P. (1989). Evolution tecto-sédimentaire alpine des Pyrénées basques à l'ouest de la transformante de Pamplona, Province du Labourd. Bordeaux 3. Retrieved from http://www.theses.fr/1989BOR30202

Respaut, J., & Lancelot, J. (1983). U/Pb Dating on Zircons and Monazites of the Synmetamorphic Emplacement. Neues Jahrbuch Fur Mineralogie-Abhandlungen, 147(1), 21–34.

Riba, O., Reguant, S., & Villena, J. (1983). Ensayo de síntesis estratigráfica y evolutiva de la cuenca terciaria del Ebro. Geologica España, 2, 131–159.

Ricateau, R., & Villemin, J. (1973). Évolution au Crétacé supérieur de la pente séparant le domaine de plate-forme du sillon sous-pyrénéen en Aquitaine méridionale. Bulletin de La Societe Geologique de France, 7(1), 30–39.

Roca, E., Muñoz, J. A., Ferrer, O., & Ellouz, N. (2011). The role of the Bay of Biscay Mesozoic extensional structure in the configuration of the Pyrenean orogen: Constraints from the MARCONI deep seismic reflection survey. Tectonics, 30(2). Retrieved from http://onlinelibrary.wiley.com/doi/10.1029/2010TC002735/full

Roest, W. R., & Srivastava, S. P. (1991). Kinematics of the plate boundaries between Eurasia, Iberia, and Africa in the North Atlantic from the Late Cretaceous to the present. Geology, 19(6), 613–616.

Rosenbaum, G., Lister, G. S., & Duboz, C. (2002). Relative motions of Africa, Iberia and Europe during Alpine orogeny. Tectonophysics, 359(1–2), 117–129. https://doi.org/10.1016/S0040-1951(02)00442-0

Rougier, G., Ford, M., Christophoul, F., & Bader, A.-G. (2016). Stratigraphic and tectonic studies in the central Aquitaine Basin, northern Pyrenees: Constraints on the subsidence and deformation history of a retro-foreland basin. Comptes Rendus Geoscience, 348(3–4), 224–235. https://doi.org/10.1016/j.crte.2015.12.005

Roure, F., Choukroune, P., Berastegui, X., Munoz, J. A., Villien, A., Matheron, P., et al. (1989). ECORS deep seismic data and balanced cross sections: Geometric constraints on the evolution of the Pyrenees. Tectonics, 8(1), 41–50.

Roure, François, & Choukroune, P. (1998). Contribution of the Ecors seismic data to the Pyrenean geology: Crustal architecture and geodynamic evolution of the Pyrenees. Mémoires de La Société Géologique de France, 173, 37–52.

Rushlow, C. R., Barnes, J. B., Ehlers, T. A., & Vergés, J. (2013). Exhumation of the southern Pyrenean fold-thrust belt (Spain) from orogenic growth to decay. Tectonics, 32(4), 843–860.

Salas, R., Guimera, J., Mas, R., Martin-Closas, C., Melendez, A., & Alonso, A. (2001). Evolution of the Mesozoic Central Iberian Rift System and its Cainozoic inversion (Iberian chain). In P. A. Ziegler, W. Cavazza, A. H. F. Robertson, & S. CrasquinSoleau (Eds.), Peri-Tethys Memoir 6: Peri-Tethyan Rift/Wrench Basins and Passive Margins (Vol. 186, pp. 145–186). Paris: Publications Scientiques Du Museum.

Schärer, U., Parseval, P. de, Polvé, M., & de Saint Blanquat, M. (1999). Formation of the Trimouns talc-chlorite deposit (Pyrenees) from persistent hydrothermal activity between 112 and 97 Ma. Terra Nova, 11(1), 30–37.

Schettino, A., & Scotese, C. (2002). Global kinematic constraints to the tectonic history of the Mediterranean region and surrounding areas during the Jurassic and Cretaceous. Journal of the Virtual Explorer, 8, 149–168.

Seguret, M. (1972). Etude tectonique des nappes et séries décollées de la partie centrale du versant sud des Pyrénées: caractère synsédimentaire, rôle de la compression et de la gravité. Publications de l'Université des sciences et techniques du Languedoc (USTELA).

Seguret, M., & Daignieres, M. (1986). Crustal scale balanced cross-sections of the Pyrenees; discussion. Tectonophysics, 129(1–4), 303–318. https://doi.org/10.1016/0040-1951(86)90258-1

Serrano, O., Guillocheau, F., & Leroy, E. (2001). Évolution du bassin compressif Nord-Pyrénéen au Paléogène (bassin de l'Adour): contraintes stratigraphiques. Comptes Rendus de l'Académie Des Sciences - Series IIA - Earth and Planetary Science, 332(1), 37–44.

Serrano, O., Delmas, J., Hanot, F., Vially, R., Herbin, J.-P., Houel, P., & Tourlière, B. (2006). Le bassin d'Aquitaine: valorisation des données sismiques, cartographie structurale et potentiel pétrolier. BRGM.

Sibuet, J.-C., Srivastava, S. P., & Spakman, W. (2004). Pyrenean orogeny and plate kinematics. Journal of Geophysical Research: Solid Earth, 109(B8). Retrieved from http://onlinelibrary.wiley.com/doi/10.1029/2003JB002514/full

Sibuet, J.-C., Rouzo, S., Srivastava, S., Dehler, S., Deptuck, M., & Karim, A. (2012). Plate tectonic reconstructions and paleogeographic maps of the central and North Atlantic oceans 1, 2 1 This article is one of a series of papers published in this CJES Special Issue on the theme of Mesozoic–Cenozoic geology of the Scotian Basin . 2 Earth Sciences Sector Contribution 20120172. Canadian Journal of Earth Sciences, 49(12), 1395–1415. https://doi.org/10.1139/e2012-071

Sinclair, H. D., Gibson, M., Naylor, M., & Morris, R. G. (2005). Asymmetric growth of the Pyrenees revealed through measurement and modeling of orogenic fluxes. American Journal of Science, 305(5), 369–406. https://doi.org/10.2475/ajs.305.5.369

Souquet, P., & Peybernes, B. (1991). Sequence Stratigraphy of the Albian Cycle in the French and Spanish Pyrenees. Bulletin Des Centres De Recherches Exploration-Production Elf Aquitaine, 15(1), 195–213.

Souquet, P., Debroas, E.-J., Boirie, J.-M., Pons, P., Fixari, G., Roux, J.-C., et al. (1985). Le groupe du Flysch noir (albo-cénomanien) dans les Pyrénées. Bulletin Des Centres de Recherche Exploration-Production Elf Aquitaine, 9, 183–252.

Souriau, A., & Granet, M. (1995). A Tomographic Study of the Lithosphere Beneath the Pyrenees from Local and Teleseismic Data. Journal of Geophysical Research-Solid Earth, 100(B9), 18117–18134. https://doi.org/10.1029/95JB01053

Srivastava, S. P., Schouteni, H., Roest, W. R., Klitgordi, K. D., Kovacs, L. C., & Verhoef, J. (1990). lberian plate kinematics: a jumping plate boundary. Nature, 344, 19.

Srivastava, S. P., Roest, W. R., Kovacs, L. C., Oakey, G., Levesque, S., Verhoef, J., & Macnab, R. (1990). Motion of Iberia since the Late Jurassic: results from detailed aeromagnetic measurements in the Newfoundland Basin. Tectonophysics, 184(3–4), 229–260.

Srivastava, S. P., Sibuet, J.-C., Cande, S., Roest, W. R., & Reid, I. D. (2000). Magnetic evidence for slow seafloor spreading during the formation of the Newfoundland and Iberian margins. Earth and Planetary Science Letters, 182(1), 61–76.

Tavani, S., & Muñoz, J. A. (2012). Mesozoic rifting in the Basque–Cantabrian Basin (Spain): Inherited faults, transversal structures and stress perturbation. Terra Nova, 24(1), 70–76.

Teixell, A. (1996). The Ansó transect of the southern Pyrenees: basement and cover thrust geometries. Journal of the Geological Society, 153(2), 301–310.

Teixell, A., & Muñoz, J. A. (2000). Evolución tectonosedimentaria del Pirineo meridional durante el Terciario: una síntesis basada en la transversal del río Noguera Ribagorçana. Revista de La Sociedad Geológica de España, 13(2), 251–264.

Teixell, A., Labaume, P., Ayarza, P., Espurt, N., de Saint Blanquat, M., & Lagabrielle, Y. (2018). Crustal structure and evolution of the Pyrenean-Cantabrian belt: A review and new interpretations from recent concepts and data. Tectonophysics, 724–725, 146–170. https://doi.org/10.1016/j.tecto.2018.01.009

Teixell, Antonio. (1998). Crustal structure and orogenic material budget in the west central Pyrenees. Tectonics, 17(3), 395–406.

Teixell, Antonio, Labaume, P., & Lagabrielle, Y. (2016). The crustal evolution of the west-central Pyrenees revisited: Inferences from a new kinematic scenario. Comptes Rendus Geoscience, 348(3–4), 257–267. https://doi.org/10.1016/j.crte.2015.10.010

Tugend, J., Manatschal, G., Kusznir, N. J., Masini, E., Mohn, G., & Thinon, I. (2014). Formation and deformation of hyperextended rift systems: Insights from rift domain mapping in the Bay of Biscay-Pyrenees. Tectonics, 33(7), 1239–1276. https://doi.org/10.1002/2014TC003529

Tugend, Julie. (2013). Role of hyperextension for the formation of rift systems and its implication for reactivation processes and orogen formation : the example of the Bay of Biscay and Pyrenees. Strasbourg. Retrieved from http://www.theses.fr/2013STRAH019

Uchupi, E. (1988). The Mesozoic-Cenozoic geologic evolution of Iberia, a tectonic link between Africa and Europe. Rev. Soc. Geol. España, 1(3–4), 257–294.

Uchupi, Elazar, Emery, K. O., Bowin, C. O., & Phillips, J. D. (1976). Continental margin off western Africa: Senegal to Portugal. AAPG Bulletin, 60(5), 809–878.

Uchupi, Elezar. (1989). The tectonic style of the Atlantic Mesozoic rift system. Journal of African Earth Sciences (and the Middle East), 8(2), 143–164.

Vacherat, A., Mouthereau, F., Pik, R., Bernet, M., Gautheron, C., Masini, E., et al. (2014). Thermal imprint of rift-related processes in orogens as recorded in the Pyrenees. Earth and Planetary Science Letters, 408, 296–306. https://doi.org/10.1016/j.epsl.2014.10.014

Vacherat, Arnaud. (2014). Inversion d'une marge hyper-amincie: contexte thermo-cinématique et interactions tectonique-érosion au Nord des Pyrénées. Université Pierre et Marie Curie-Paris VI. Retrieved from https://tel.archives-ouvertes.fr/tel-01127615/

Vacherat, Arnaud, Mouthereau, F., Pik, R., Bellahsen, N., Gautheron, C., Bernet, M., et al. (2016). Rift-to-collision transition recorded by tectonothermal evolution of the northern Pyrenees: COOLING

HISTORY OF THE NORTHERN PYRENEES. Tectonics, 35(4), 907–933. https://doi.org/10.1002/2015TC004016

Vauchez, A., Clerc, C., Bestani, L., Lagabrielle, Y., Chauvet, A., Lahfid, A., & Mainprice, D. (2013). Preorogenic exhumation of the North Pyrenean Agly massif (Eastern Pyrenees-France). Tectonics, 32(2), 95–106. https://doi.org/10.1002/tect.20015

Vergés, J., & Burbank, D. W. (1996). Eocene-Oligocene thrusting and basin configuration in the eastern and central Pyrenees (Spain). Tertiary Basins of Spain. Cambridge University Press, World and Regional Geology E, 11, 120–133.

Vergés, J., Millán, H., Roca, E., Muñoz, J. A., Marzo, M., Cirés, J., et al. (1995). Eastern Pyrenees and related foreland basins: pre-, syn-and post-collisional crustal-scale cross-sections. Marine and Petroleum Geology, 12(8), 903–915.

Vergés, J., Marzo, M., Santaeularia, T., Serra-Kiel, J., Burbank, D. W., Munoz, J. A., & Gimenez-Montsant, J. (1998). Quantified vertical motions and tectonic evolution of the SE Pyrenean foreland basin. Geological Society, London, Special Publications, 134(1), 107–134. https://doi.org/10.1144/GSL.SP.1998.134.01.06

Vergés, J., Marzo, M., & Muñoz, J. A. (2002). Growth strata in foreland settings. Sedimentary Geology, 146(1), 1–9.

Vergés, Jaume, & Fernàndez, M. (2012). Tethys–Atlantic interaction along the Iberia–Africa plate boundary: The Betic–Rif orogenic system. Tectonophysics, 579, 144–172.

Vergés, Jaume, & García-Senz, J. (2001). Mesozoic evolution and Cainozoic inversion of the Pyrenean rift. Mémoires Du Muséum National d'histoire Naturelle, 186, 187–212.

Vergés, JAUME, & Muñoz, J. A. (1990). Thrust sequences in the southern central Pyrenees. Bulletin de La Société Géologique de France, 8(6), 265–271.

Vergés, JAUME, Fernàndez, M., & Martínez, A. (2002). The Pyrenean orogen: pre-, syn-, and post-collisional evolution. Journal of the Virtual Explorer, 8, 57–76.

Vielzeuf, D., & Kornprobst, J. (1984). Crustal splitting and the emplacement of Pyrenean lherzolites and granulites. Earth and Planetary Science Letters, 67(1), 87–96.

Villien, A., & Matheron, P. (1989). Géodynamique de la zone nord pyrénéenne: conséquences sur l'exploration pétrolière. Bulletin Technique Exploration-Production Elf Aquitaine, 131, 3–19.

Vissers, R. L. M., & Meijer, P. Th. (2012a). Iberian plate kinematics and Alpine collision in the Pyrenees. Earth-Science Reviews, 114(1–2), 61–83. https://doi.org/10.1016/j.earscirev.2012.05.001

Vissers, R. L. M., & Meijer, P. Th. (2012b). Mesozoic rotation of Iberia: Subduction in the Pyrenees? Earth-Science Reviews, 110(1–4), 93–110. https://doi.org/10.1016/j.earscirev.2011.11.001

Vitrac-Michard, A., & Allègre, C. J. (1975). 238 U-206 Pb, 235 U-207 Pb, systematics on Pyrenean basement. Contributions to Mineralogy and Petrology, 51(3), 205–212.

Wang, Y., Chevrot, S., Monteiller, V., Komatitsch, D., Mouthereau, F., Manatschal, G., et al. (2016). The deep roots of the western Pyrenees revealed by full waveform inversion of teleseismic P waves. Geology, 44(6), 475–478. https://doi.org/10.1130/G37812.1

Whitchurch, A. L., Carter, A., Sinclair, H. D., Duller, R. A., Whittaker, A. C., & Allen, P. A. (2011). Sediment routing system evolution within a diachronously uplifting orogen: Insights from detrital zircon thermochronological analyses from the South-Central Pyrenees. American Journal of Science, 311(5), 442–482.

Yelland, A. J. (1990). Fission track thermotectonics in the Pyrenean orogen. International Journal of Radiation Applications and Instrumentation. Part D. Nuclear Tracks and Radiation Measurements, 17(3), 293–299. https://doi.org/10.1016/1359-0189(90)90049-4

Yelland, Andrew John. (1991). Fission track thermotectonics of the Iberian-Eurasian plate collection. (Ph.D.). Birkbeck University of London, London. Retrieved from http://ethos.bl.uk/OrderDetails.do?uin=uk.bl.ethos.261137

Ziegler, Peter A. (1988). Evolution of the Arctic-North Atlantic and the western Tethys. A visual presentation of a series of paleogeographic-paleotectonic maps. AAPG Memoir, 43, 164–196.

Second Part

Methodology

Chapter 4
IV. Methodology and Analytical Procedures

FOREWORD

This Chapter covers a quite vast range of aspects of the methodology used in this thesis, going from the fundamentals of geo-thermochronology to the application of these dating tools for reconstructing dynamics in a collisional orogen, and passing through the various analytical techniques, approaches (bedrock and detrital) and statistical methods available. A particular focus will be made on the low-temperature zircon (U-Th)/He thermochronometer because it is used both alone and in combination with the zircon U/Pb geochronometer in this thesis. The choice for zircon dating has been highlighted in the previous Chapter. However, because the various aspects of (U-Th)/He dating cover a wide range of scientific disciplines (fundamental particle physics, radiation damage, advanced statistical methods and physical chemistry) it will be necessary to cover some of these aspects in a succinct but cursory way.

TABLE OF CONTENT

LIST OF FIGURES

LIST OF TABLES

IV.1 Geo-thermochronology: Definition and Fundamentals

IV.1.1 Brief Historical Summary

To serve a correct description of what is actually referred to as "thermochronology" and "geochronology" in the community, one might be tempted to say that "*In one form or another, geochronologists have been practicing thermochronology, the use of radioisotopic dating to constrain thermal histories of rocks and minerals, for over 40 years*" or also that "*Given that all radioisotopic systems are subject to disturbance and resetting at sufficiently high temperatures, it might be surmised that all radioisotopic dating is essentially thermochronology.*" (Reiners et al., 2005). Nonetheless, Reiners et al. (2005) end their introductory statement by the following formulation: "*Despite this overlap, the bottom line is that thermochronology is distinguished from geochronology by its ability to resolve both temporal and thermal aspects of geologic processes, and thus both timing and rates of processes.*" A classical example for such a fuzzy distinction between geochronology and thermochronology is found around the radioisotopic (U-Th)/He system on zircon. A brief overview is given in the next paragraph and will be developed in a much extensive way in later sections.

The possibility of dating minerals by the means of measuring a daughter/parent isotope ratio was first proposed by Rutherford (1906) and Strutt (1905). This consisted in measuring concentrations of daughter ^{4}He and parent U and Th nuclides in minerals at the time of analysis (see section IV.1.2.1). The reliability of such a dating system was investigated on several, various aspects until the second half of the 1970s (Strutt, 1908, 1909; Hurley, 1955; Damon and Kulp, 1957; Fanale and Kulp, 1962; Damon and Green, 1963; Fanale and Schaeffer, 1965; Turekian et al., 1970; Bender, 1973; Ferreira et al., 1975; Leventhal, 1975; Graham et al., 1987). From these investigations generally came up the observation that the technique yielded ages much younger than expected to represent rock formation ages as determined by U/Pb dating. This observation was not unique and similar observations were made for other radioisotopic systems (e.g. Evernden et al. 1960; Fechtig and Kalbitzer 1966; Musset 1969). Nonetheless, the degree of age discrepancy between measured and expected ages in the other systems was not as high as it was in the (U-Th)/He system. As a result, the (U-Th)/He technique, considered to be too obscure, was essentially abandoned and the apparent unreliability of the radioisotopic (U-Th)/He system to date rock formation was surmised to be due to diffusive He loss and thermal resetting possibly associated with radiation damage. In contrast, the dependence of fission-tracks with temperature was recognized quite early (Fleischer et al., 1965a). Fission-track ages, albeit also younger than U/Pb mineral formation ages, were accepted to define the moment when the fission-track system becomes closed, in particular when the fission-tracks become stable. Fleischer et al. (1965a) shows that such stability is attained at temperatures that may be far below those of mineral formation.

IV.1.2 The Closure Temperature Concept

While the use of (U-Th)/He dating was becoming sporadic, this is interestingly in the early 1970s that a major conceptual breakthrough for "thermochronology" was made by Dodson (1973). The author has formally established the concept of closure temperature that links for the first time on a theoretical basis a characteristic temperature of a given radioisotopic system to diffusivity and time. The closure temperature represents the temperature below which any decay product of a given cooling radioisotopic system accumulates within a mineral, i.e. the temperature at which diffusion of the daughter (and parent) isotopes out of a mineral has become thermally inactivated (Figure IV.1). In strict terms, accumulation of an isotope outpaces diffusion of this isotope through and out of the mineral below the effective closure temperature. The closure temperature is therefore defined by Dodson (1973) to be the temperature of the system at the time given by its apparent (cooling) age. It is effective and characteristic of the retention behaviour of the system:

Equation IV.1: $$T_c = \frac{R}{E.\ln\left(\frac{A\tau D_0}{a^2}\right)}$$

where:
- R is the gas constant,
- E is the activation energy,
- A is a numerical constant depending on geometry and decay constant of parent,
- τ is the time constant with which the diffusion coefficient D diminishes,
- D_0 is the diffusivity at infinite temperature, also known as the frequency factor or diffusion constant,
- a is a characteristic diffusion size.

Up to the time for introduction of Dodson's concept, the first paragraphs of review in this Chapter have shown that principles about radioactive decay were well established and that thermal effects on radioisotopic ages by diffusion were recognised. Nonetheless, it is fair to say that conceiving the one-way property of time ("time's arrow"; Eddington, 1928) has always been much easier, albeit with "no analogue in space", than understanding in every detail phenomena or processes that would seem realistic whether played forwards or backwards. This is all the more true when confronting purely time-dependent radioactivity on one side, and the complicated time-temperature histories that many samples have likely experienced at the relatively low temperatures found beneath our feet one the other side. As a matter of fact, as much more was known about the greater retentivity of minerals for Pb and Ar compared to He, larger focus in the community was first made on determining reliable formation ages rather than thermal histories. Below, I present the fundamental concept of Dodson (1973) for geo-thermochronology by following the general flow of this paragraph.

IV.1.2.1 Radioactive decay

Most (radio)chronometric methods rely on the "basic" principle of radioactive decay (also known as nuclear decay, radioactive disintegration, radioactivity, or nuclear radiation). Radioactive decay is the process by which an unstable atomic nucleus (the

parent element, (radio)nuclide or (radio)isotope) loses mass energy by emitting radiation and converts into another chemical nucleus (the daughter nuclide, element or isotope). Several modes of natural radioactivity exist and emitted radiation during decay may be either a decay particle or energy/light (or both): alpha decay (ejection of an alpha particle), beta decay (ejection of an electron and an antineutrino if beta-minus decay; a positron and a neutrino if beta-plus decay), gamma decay (emission of a gamma ray), electron capture and spontaneous fission.

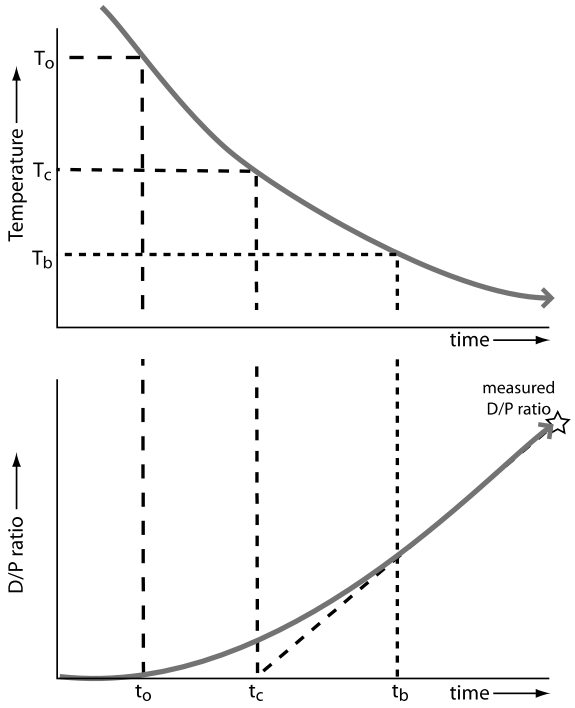

Figure IV.1: Definition of closure temperature according to Dodon (1973) (T_c, Equation IV.1) with regards to daughter to parent isotopic ratio (D/P) of the thermochronological system. Theoretical upper and lower temperature limits for the domain of intermediate behaviour where accumulation and diffusion processes are competing, defined as the "open-system" and blocking temperatures, are also represented (T_o and T_b, respectively). Above the former temperature, the thermochronological system is fully open (100% diffusion of daughter elements, D/P = 0). The daughter isotope produced by nuclear decay of a parent isotope is removed effectively immediately upon its production. Below the latter temperature, the system is closed (100% accumulation of daughter elements, D/P increases asymptotically). The daughter isotope is completely retained within the host mineral. The apparent thermochronological age of the system, t_c, is comprised between the time at which retention initiates, t_o, and the time at which diffusion stops, t_b. From Braun et al. (2006).

In case of the nuclear transmutation of a parent atom to a daughter atom, the decay of the parent nuclides is given by:

Equation IV.2: $$\frac{dN_p}{dt} = -\lambda_p N_p(t)$$

where:
- λ_p is the decay constant for the parent isotope, i.e. the rate at which the parent decays;
- $N_p(t)$ is the number of parent atoms that have not decayed yet, at any time.

The number of parent atoms at any time is obtained by integrating Equation IV.2 over time:

Equation IV.3: $$N_p(t) = N_p(0)\, e^{-\lambda_p t}$$

where:
- $N_p(0)$ is the initial parent isotopic abundance, and is thus largely unknown.

To calculate a radiometric age (time since decay started in a closed system), it is more robust (based on fewer unknowns and leading to lower uncertainties) to measure both the parent and daughter isotopic abundances. The production of daughter isotopes that results from decay can be expressed as follows:

Equation IV.4: $$N_d(t) = N_p(t)\left(e^{\lambda_p t} - 1\right)$$

The isotope ratio is a function of time:

Equation IV.5: $$\frac{N_d(t)}{N_p(t)} = e^{\lambda_p t} - 1$$

and the general age equation for any radioisotopic system is thus:

Equation IV.6: $$t = \frac{1}{\lambda_p} \ln\left[\frac{N_d(t)}{N_p(t)} + 1\right]$$

In the general case, a unique parent isotope can decay to a range of possible daughter isotopes i = 1, ..., n, at a specific rate defined by the partial decay constant λ_{p_i}. One daughter isotopic abundance $N_{d_i}(t)$ is therefore:

Equation IV.7: $$N_{d_i}(t) = \frac{\lambda_{p_i}}{\lambda} N_p(t)\left(e^{\lambda t} - 1\right)$$

where: $\lambda = \lambda_{p_1} + \cdots + \lambda_{p_n}$ is the total decay constant for the parent isotope.

and the age equation specific to the daughter branching:

Equation IV.8: $$t = \frac{1}{\lambda} \ln\left[\frac{\lambda}{\lambda_{p_i}} \frac{N_{d_i}(t)}{N_p(t)} + 1\right]$$

IV.1.2.2 Diffusion

A certain number of radiochronometric systems are particular, in the way that the parent isotope, which is generally an essential structural constituent of the lattice of a mineral, decays in a daughter isotope that is no longer geochemically compatible in the

mineral. The inability of daughter products to chemically bond allows them to migrate at relatively low energy cost through, and eventually out of, the mineral. Such a migration is referred to as diffusion and is made possible within a solid through a series of random jumps between equilibrium lattice sites.

IV.1.2.2.1 General laws

Diffusion of a particle obeys Fick's first law that postulates that for any cause, such as spatial concentration inhomogeneity (concentration gradient), a response such as a net movement of particles (diffusion flux) has to be proportional to and down the concentration gradient. Any element will therefore flow from a region of high concentration in this element to a region of low concentration across a concentration gradient, if present. The rate of transfer of mass per unit area per unit time is thus:

Equation IV.9: $$J_N = -D\left(\frac{\partial N(x,y,z)}{\partial x}x + \frac{\partial N(x,y,z)}{\partial y}y + \frac{\partial N(x,y,z)}{\partial z}z\right)$$

where:
- D is the diffusion coefficient,
- $N(x, y, z)$ is the concentration of the diffusing element,
- x, y, z are space vectors.

Fick's law, as Darcy's law for hydraulic flow, Ohm's law for charge transport, and Fourier's law for heat transport, describes the evolution of a system towards steady state. System equilibrium will be reached and respected if, and only if, net transport of material is null and the principle of charge-balance is not violated. The first condition postulates that the migration of an element through a unit area during a unit time interval is balanced by the migration of any other element(s) in the opposite direction through the same unit area during the same unit time interval. The second condition implies that the addition of any charged element must be compensated by the removal of an equal charge.

In a closed system where mass is conserved, i.e. in absence of any source for production or disappearance (e.g. radioactive decay, chemical reaction, loss), the concentration distribution of the diffusing element within a medium can be predicted as a function of the space coordinates and time (Fick's second law) as follows:

Equation IV.10: $$\frac{\partial N(x,y,z,t)}{\partial t} = D\nabla^2 N(x, y, z, t)$$

where:
- D is the diffusion coefficient,
- ∇^2 is the second order spatial derivative (Laplacian operator),
- $N(x, y, z, t)$ is the concentration of the diffusing element through time.

This expression is the diffusion equation, predicting how diffusion causes spatial concentration to change with time.

IV.1.2.2.2 Diffusion applied to solid-state medium

Within a mineral, i.e. a solid-state medium, the atoms (molecules or ions) are tightly bound to each other in a regular geometric lattice characterized by structural rigidity and resistance to changes of shape or volume. Four mechanisms of atomic diffusion transport are therefore possible (Harrison and Zeitler, 2005; Figure IV.2). (i) The exchange mechanism involves "*the exchange of two adjacent atoms*". (ii) The interstitial mechanism sees "*an interstitial atom sited in between normal lattice sites moving into a new interstitial location by squeezing past atoms in regular sites*". (iii) The interstitalcy mechanism involves "*an interstitial atom displacing a normally sited atom into another interstitial location*". (iv) The vacancy mechanism sees "*an atom moving into a neighboring vacant lattice site*". From these strict definitions it is relatively easy to realize that the exchange and interstitalcy mechanisms both involve motion of an atom, which requires a lot of energy and is therefore unlikely. Because of the rather narrow interstitial volume an atom (or interstitial defect) can occupy with low energy, the interstitial mechanism most likely applies to small nucleus only. The vacancy mechanism thus seems to be the best candidate to describe overall atomic diffusion within a perfect solid.

A vacancy, also known as a vacancy defect, is a type of point defect that occurs naturally in all crystalline materials and corresponds to an anomalously empty lattice site. It can form either during crystallization or as a result of deformation, ionization or any processes involving local atomic rearrangement for bounding or charge-balance. The concentration of the vacancy defects in a pure crystal may be intrinsically expressed as a function of temperature in an Arrhenius relationship (Ehrhart, 1992). Chemical impurities are additional sources for vacancy defects (charge balancing).

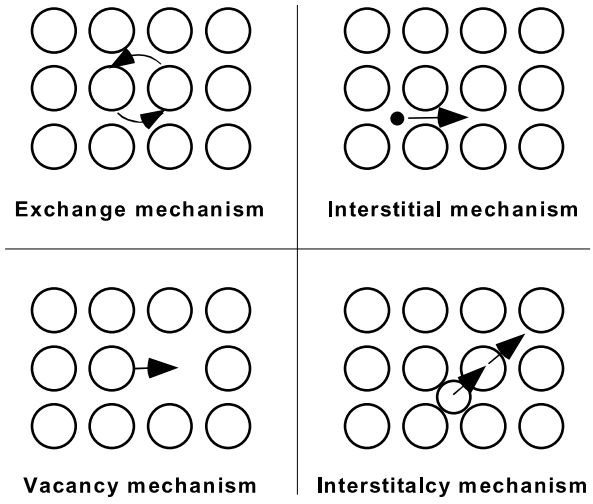

Figure IV.2: Schematic illustration of the four possible mechanisms of atomic diffusion transport: exchange, interstitial, interstitalcy, and vacancy (Harrison and Zeitler, 2005). Descriptions are provided in the text.

On this basis, it is interesting to note that diffusion of particles leads to "diffusion" of vacancy defects in the vacancy mechanism. In strict terms, the two phenomena are intrinsically connected and may be regarded as leading to or controlling each other. In a

stable crystal structure, as an atom moves to occupy the neighbouring vacant lattice site, the vacancy moves in the opposite direction to the site which used to be occupied by the moving atom. Diffusion of atoms within a solid-state medium therefore occurs at a rate that is a function of the energy needed for an atom to overcome the potential barrier and move from one site to another, and of the vacancy concentration which itself depends exponentially on the energy required for vacancy formation and temperature. As a matter of fact, both the rate of atom migration and defect formation have a first-order dependence on temperature. The overall diffusion coefficient (rate) for atom migration can thus be described by the following Arrhenius relationship:

Equation IV.11: $$\frac{D}{a^2} = \frac{D_0}{a^2} e^{-\frac{E}{RT}}$$

where:
- D_0 is the diffusivity at infinite temperature,
- E is the overall activation energy,
- R is the gas constant,
- T is absolute temperature,
- a is the dimension of the diffusion domain (the physical size (radius) of the grain or smaller size sub-grain structure),

Units for D are typically given in cm^2/s.

By definition, D is specific to an atom (size, energy) and a mineral (the tendency of a given mineral to form vacancy defects).

IV.1.2.3 Accumulation

Overall, the concentration of a given radioisotope in a closed-system mineral $N_i(x, y, z, t)$ varies through time as a function of its *in situ* production by radioactive decay within the mineral, $P_i(x, y, z, t)$, its reaction with surrounding constituents, $R_i(x, y, z, t)$, and its diffusion through, and ultimately out of, the mineral, $D_i(x, y, z, t)$ (Figure IV.1). The concentration distribution of this nuclide within a given mineral can therefore be derivated from Equation IV.10 and Equation IV.11, and expressed as follows:

Equation IV.12: $$\frac{dN_i(x,y,z,t)}{dt} = D_{0_i} e^{-\frac{E}{RT}} \nabla^2 N_i(x, y, z, t) + P_i(x, y, z, t) + R_i(x, y, z, t)$$

where:
- D_{0_i} is the diffusivity at infinite temperature, specific to the isotope and the mineral,
- $N_i(x, y, z, t)$ is the concentration of the isotope.

Two assumptions are generally made, the first one being of great concern: (i) Any decaying isotope is uniformly distributed within the grain, so that production is spatially uniform: $P_i(x, y, z, t) = P_i(t)$. (ii) As any (fast) diffusing isotope reaches grain boundaries, it is rapidly removed and lost from the system, so that its concentration on the mineral surface is zero. While the first assumption is applicable to the parent radioisotope, the second assumption mainly refers to the daughter isotope. For a parent radioisotope of

interest in a closed system, N_p, the concentration is assumed to be only driven by radioactive decay, so additional assumptions are $D_{0_p} \approx 0$, $P_p(t) = -\lambda_p N_p(t)$, and $R_p(x, y, z, t) = 0$. This is Equation IV.3. For a daughter radioisotope of interest, N_d, the concentration is initially zero and only depends on production by radioactive decay and subsequent diffusion, so $P_d(t) = \lambda_p N_p(t) = \lambda_p N_p(0)\, e^{-\lambda_p t}$ and $R_d(x, y, z, t) = 0$.

IV.1.2.4 Effective closure temperature

If diffusion of the daughter nuclide is zero, this brings us back to Equation IV.4 and the age of the radioisotopic system is given by Equation IV.6. Finding the effective temperature at which diffusion becomes negligible (diminishes by a factor e^{-1}, i.e. a 37% drop), so that Equation IV.5 and Equation IV.6 can be used and analytically solved, is the conceptual approach of Dodson (1973) for samples monotonically cooled from high to low temperatures ($T(t) \approx 1/t$) (Figure IV.1). The time taken for diffusion to verify such a drop is τ.

This approach implies the existence of only two domains for a given cooling radioisotopic system: a domain of full retention of decay products where the daughter/parent ratio increases steadily and a domain of full loss where the ratio is null. The limit between these two domains is defined as the closure temperature that is nominal and increases with cooling rate (Figure IV.3).

IV.1.3 From the closure temperature concept to thermochronology

It is fair to state that the closure temperature concept thereby defines the term "thermochronology", not because it is relevant to any sample but because it allows both grasping first-order principles about the retentivity of a system and predicting observables such as ages for a given, simple tectono-thermal scenario.

The mathematical formulation for calculating the closure temperature involves the diffusion kinetic properties of the system in a given mineral, the geometry and size of (or characteristic dimension of) the mineral and the cooling rate of the sample (Equation IV.1). The closure temperature is therefore specific to a particular cooling system and a mineral, also called a thermochronometer (Figure IV.3). This makes it possible to determine and/or constrain the thermal history of rocks within a framework of absolute time that is determined by dating various minerals for the same system or various systems for the same mineral. Dodson's work echoed, and probably influenced and was influenced by, results obtained through pioneering fission-track (e.g. Wagner and Reimer, 1972) and multi-dating method (e.g. Wagner et al., 1977) studies over the same time interval. These studies were made on bedrock samples in orogens dominated by erosional denudation (the Central and Southern Alps in Switzerland and Italy), where Dodson's concept is fairly easy to use for understanding exhumation processes. They represent the first applications of what we now refer to as *in situ* or bedrock thermochronology.

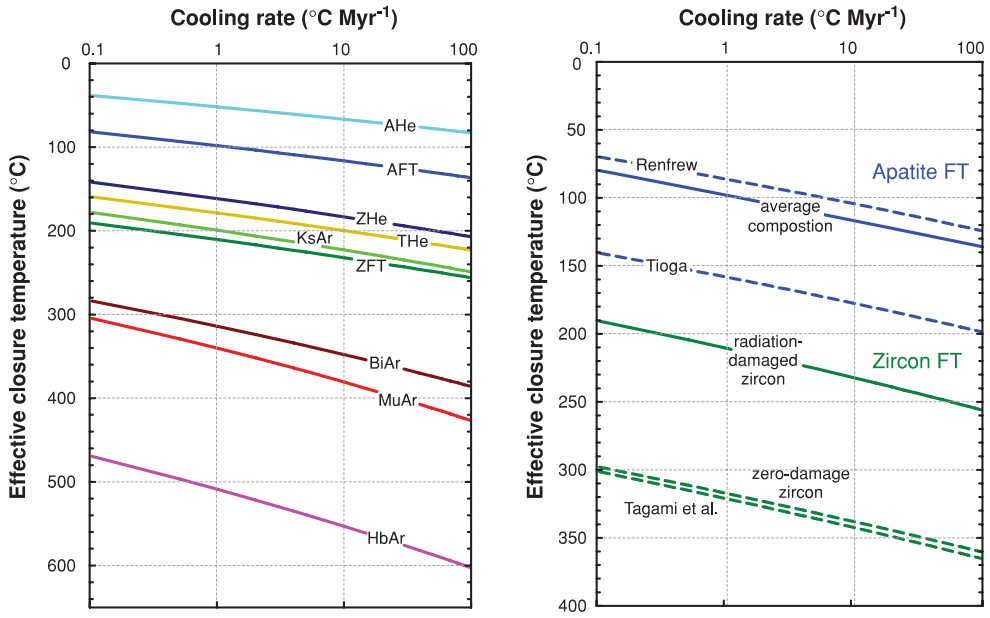

Figure IV.3: Effective closure temperature (Tc) as a function of cooling rate for the three commonly used thermochronometers for the study of orogenic processes (low-temperature (U-Th)/He, fission-track and medium-temperature ^{40}Ar-^{39}Ar). From Reiners and Brandon (2006).

The principal limitation of the analytical closure temperature solution given by Equation IV.1 is that it lacks time dependence, restricting the equation to describing the geological case of an isothermal history. As retention behaviour is controlled by thermally-activated diffusion (i.e. solid diffusion processes follow the Arrhenius equation), a third, rather diffuse, in-between domain of intermediate behaviour where accumulation and diffusion processes are competing is predicted. Upper and lower temperature limits for this domain are defined as the "open-system" and blocking temperatures (100% diffusion and 100% accumulation, respectively), but lack proper constrains in practice (Figure IV.1; Braun et al., 2006). They are indeed equalled to the closure temperature in Dodson's concept. In nature, this domain was clearly evidenced early in the 1980s (Gleadow and Duddy, 1981) while apparent fission-track age and track length were observed to decrease systematically with increasing depth, and so doing temperature. It was first called the partial stability field (Wagner and Reimer, 1972), then was commonly referred to as the partial annealing zone for fission-tracks (Gleadow and Fitzgerald, 1987; Wagner et al., 1989) and later called the partial retention zone in broader terms (Baldwin and Lister, 1998; Wolf et al., 1998; Figure IV.4). Within this zone, any radioisotopic decay products (e.g. fission-track or ^{4}He) are only partially retained owing to thermally-activated diffusion or annealing. Eventually, retention of decay products depends on grain-specific characteristics such as the composition (e.g. Green et al., 1985; Hourigan et al., 2005) and radiation damage (e.g. Hurley, 1955; Nasdala et al., 2005; Rahn et al., 2004; Reiners et al., 2004; Guenthner et al., 2013). This makes the retention process sometimes difficult to be represented by a first-order Arrhenius rate law, as highlighted in case of apatite fission-track by Green et al. (1988). It is therefore more reasonable to consider that a given thermochronometer has a range of closure temperatures and that any measured cooling age points to just a

single temperature on the cooling path of a sample through the so-called partial retention zone. This point will be discussed in more details later as it is one of the principal motivations of this thesis (see Chapter 5, for instance).

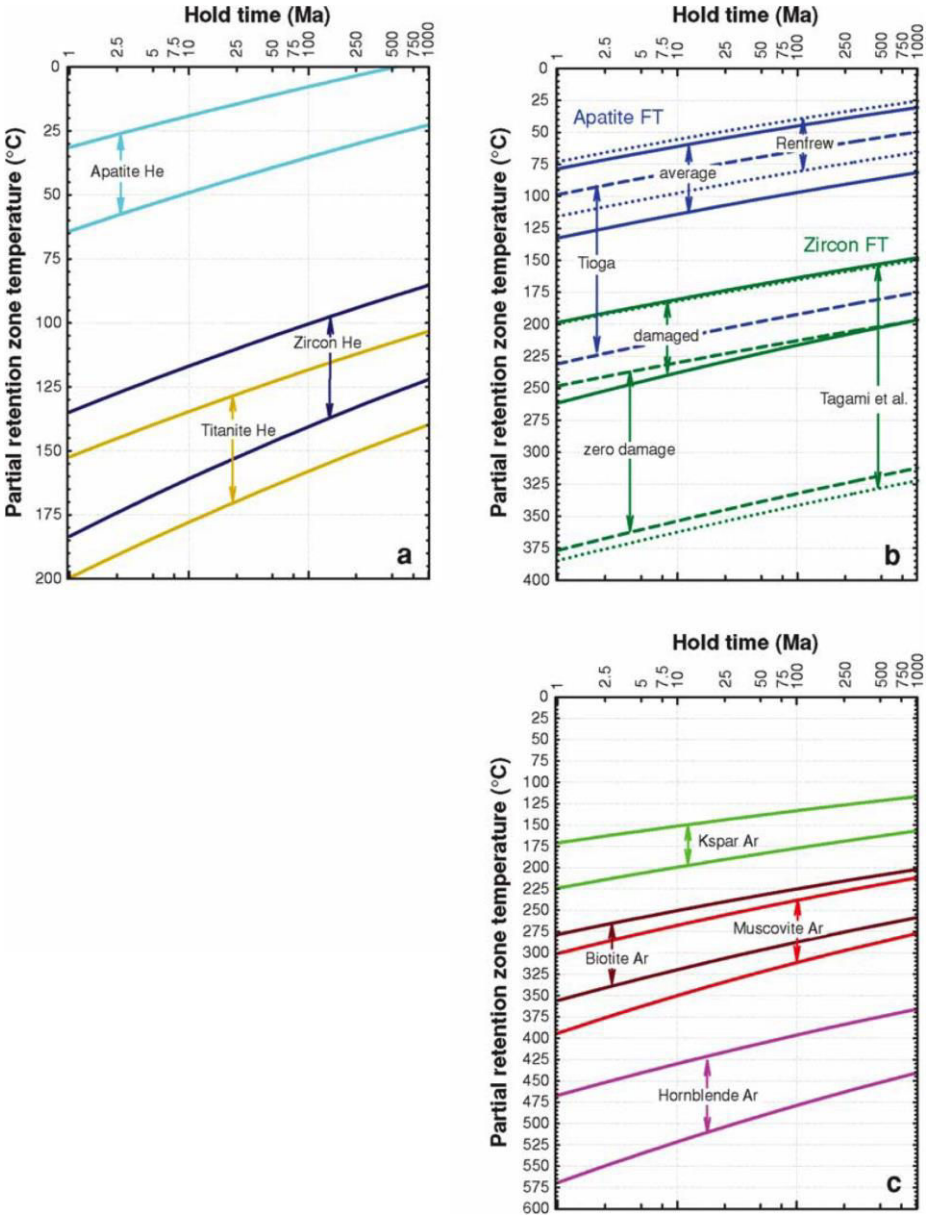

Figure IV.4: Partial retention zones as a function of time for the three commonly used thermochronometers for the study of orogenic processes (low-temperature (U-Th)/He, fission-track and medium-temperature ^{40}Ar-^{39}Ar). Upper and lower boundaries for each partial retention zone correspond to 90% and 10% retention, respectively. From Reiners and Brandon (2006).

In a general sense, thermochronology (or thermochronometry; see Reiners et al., 2005) therefore generally measures the timing and rates at which rocks move toward the surface and cool as the result of exhumation. Since exhumation is itself the result of tectonic (normal faulting, ductile thinning) or erosional denudation, thermochronology can be applied as a tool wherever there is a need for constraining the thermal history of a rock, a mineral or a geological terrane, and whatever the tectonic settings are (theory:

Ehlers, 2005; Reiners and Ehlers, 2005; applications in extensional context: e.g. Foster and John, 1999; Stockli, 2005; Wells et al., 2005; in contractional regions: e.g. Yelland, 1990; Witt et al., 2012; for hydrothermal fluid circulation in fault systems: e.g. Ault et al., 2016; etc). Because the focus of this thesis is made on the reconstruction of early orogen dynamics in a collisional orogen, the remainder of this Chapter, and more generally this thesis, will be about thermochronology in orogenic settings where there is a strong interplay of rock uplift, surface uplift, erosional denudation/exhumation and crustal thickening (as defined in Reiners and Brandon, 2006).

For a more complete, detailed review of the history of thermochronology, the reader may refer to Farley (2002), Reiners et al. (2005) and Ganguly and Tirone (2009).

IV.2 Application of Geo-thermochronology to Orogenic Evolution

IV.2.1 Available Thermochonometers

Based on the critical taper model that physically describes the mechanics underlying accretion and orogenic building (Chapter 2; Chapple, 1978; Davis et al., 1983; Dahlen et al., 1984; Dahlen, 1990), it has been shown that a wedge attempts to maintain mechanical equilibrium (criticality) by internal thickening/shortening or thinning/extension, depending on its taper angle with respect to criticality. From this model easily appears the fact that quantifying the timing and rates of vertical and lateral motion in orogenic belts requires from us to be interested mainly in the brittle portion of the crust, i.e. the upper 15 km of the crust. Typical erosion rates of 0.05-10 km/myr in active and decaying mountain ranges (Reiners and Brandon, 2006) also point out to these depths, “sucking up” rocks from depth and exhuming higher temperature and pressure rocks. Assuming a typical geothermal gradient of 35-40 °C/km for thermally equilibrated crust involved into collisional zones, at least before magmatic activity starts (Allen and Allen, 2013), the temperature window of interest to study upper crustal processes (exhumation) is therefore about 0 to 300-550 °C. As shown in Figure IV.5, this makes low- and medium-temperature thermochronometers well suited to this task because they are sensitive to temperature changes between about 0-300 °C and 300-500 °C, respectively (e.g. Carrapa, 2010; Peyton and Carrapa, 2013; and references therein).

Three dating methods are commonly used for the study of orogenic processes in terms of thermal history of rocks: the low-temperature (U-Th)/He, fission-track and medium-temperature ^{40}Ar-^{39}Ar methods. In contrast, the U/Pb method covers a much higher closure temperature range, providing information about crystallization or the growth of a crystal. As zircon is a very durable mineral phase surviving sedimentary transport and interaction with fluids that may affect sedimentary strata during burial and diagenesis, detrital U/Pb geochronology represents a powerful tool for provenance analysis and sediment routing reconstruction (e.g. Dickinson and Gehrels, 2008; Gehrels, 2012; Lawton, 2014). In particular, it can allow discriminating the origin of a detrital grain from the complex terrane assemblage that composes an orogen by correlating detrital zircon U/Pb ages within a sediment or sedimentary rock with the zircon

crystallization ages of the source terrains (lithologic units with characteristic ages within a larger source area; Brandon, 1992).

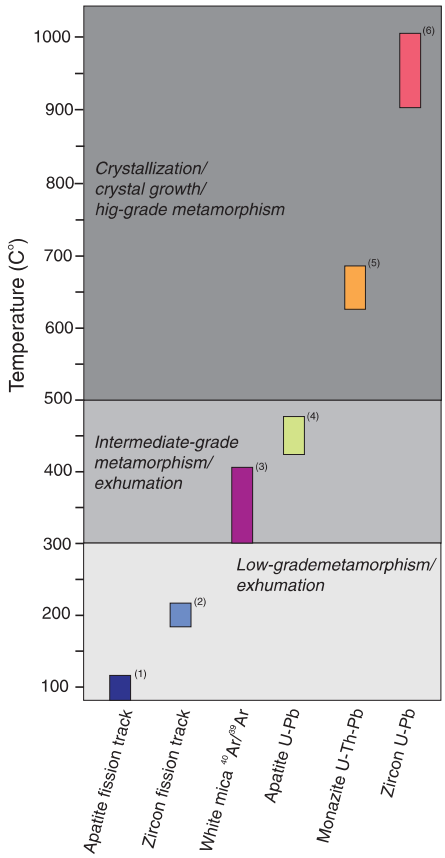

Figure IV.5: Characteristic partial retention zones of commonly used thermochronometers for the study of orogenic processes (low-temperature (U-Th)/He, fission-track and medium-temperature ^{40}Ar-^{39}Ar and apatite U/Pb) and provenance (monazite and zircon U/Pb). General interpretations of their thermochronological age significance are provided. From Carrapa (2010).

Because (U-Th)/He dating is the primary method of analysis used in this thesis in combination with U/Pb dating, an emphasis on these two methods will be made below. Also, because the fission-track method has been extensively used in the Pyrenees and use of the (U-Th)/He method in this thesis was the intimate consequence of this fact, the fission-track method must be introduced in this Chapter and will be presented below. Finally, as this will be discussed in later sections of this thesis, use of the ^{40}Ar-^{39}Ar method has admittedly proved to provide limited to no constraints regarding orogenic dynamics in the Pyrenees, unlike (U-Th)/He and fission-track datings (e.g. Maurel et al., 2008). Nonetheless, the potential of this method in constraining parts of the pre-orogenic thermal history to better understand the Pyrenean crustal template before orogenesis has been fully demonstrated (e.g. Albarède et al., 1978; Albarède and Michard-Vitrac, 1978; Goldberg et al., 1986; Montigny et al., 1986; Golberg and Maluski, 1988; Nicolas, 1998; Maurel et al., 2003, 2004, 2008; Boulvais et al., 2007). For this reason, I feel it necessary to cover some of the ^{40}Ar-^{39}Ar method aspects in a succinct but cursory way as well.

IV.2.1.1 The U/Pb system

IV.2.1.1.1 Dating principle

Uranium has three naturally occurring isotopes: ^{238}U, ^{235}U and ^{234}U. Only the first two isotopes are long-lived. Relative isotope abundances are reported in Table IV.1 and the present-day, average crustal $^{238}U/^{235}U$ composition is 137.818 ± 0.045 (2σ) (Hiess et al., 2012). This value reflects the average uranium isotopic composition and variability of terrestrial zircon, rejecting the previous value of 137.88 (Steiger and Jager, 1977) that was considered invariant but has been recently shown to depend on $^{238}U/^{235}U$ fractionation processes at magmatic temperatures.

Isotope	Relative isotope abundance (atom%)	Range of natural variations (atom%)	
238U	99.2745(106)	99.2752	99.2739
235U	0.7200(51)	0.7202	0.7198
234U	0.0055(2)	0.0059	0.005

Table IV.1: Relative isotope abundances for the three naturally occurring uranium isotopes (Rosman and Taylor, 1998).

By the mean of substitution some minerals incorporate non-formula elements (actinides and lanthanides) in minor to trace amounts in medium- to high-temperature processes (e.g. >750 °C for zircon; Finch and Hanchar, 2003). Uranium and Thorium, as part of these accommodated elements, decay through two modes: alpha-decay and spontaneous fission. While the former is the basis of (U-Th)/He dating, the latter is the rational of fission-track dating (see below).

Alpha-decay is the primary mechanism of decay for Uranium and Thorium. ^{238}U, ^{235}U and ^{232}Th decay to ^{206}Pb, ^{207}Pb and ^{208}Pb, respectively, through a series of intermediate daughter elements (series decays; Figure IV.6) associated with a certain amount of alpha particles (also known as ^{4}He nuclei) that depends on the radiogenic system considered (Table IV.2):

$$^{238}U \rightarrow {}^{206}Pb^{*} + 8\alpha + 4\beta^{-}$$
$$^{235}U \rightarrow {}^{207}Pb^{*} + 7\alpha + 4\beta^{-}$$
$$^{232}Th \rightarrow {}^{208}Pb^{*} + 6\alpha + 4\beta^{-}$$

where * indicates the radiogenic portion (formed in situ by decay of the parent nuclei) of the element or isotope.

Isotope	λ (Ga-1)	half-life time (Ga)
238U	0.155125	4.47
235U	0.98485 ± 0.00135 **	0.704
232Th	0.049475	14.01

Table IV.2: Half-life time values and radiogenic decay constants for decay of Uranium and Thorium (Jaffey et al., 1971). ** recently revised to 0.98571 ± 0.00012 Ga^{-1} by Mattison (2010).

Given the relatively short half-life time values (<1 myr) for intermediate daughter elements, it is common to assume that Uranium and Thorium instantaneously disintegrate into Lead when dating tens-to-thousands-myr-old grains.

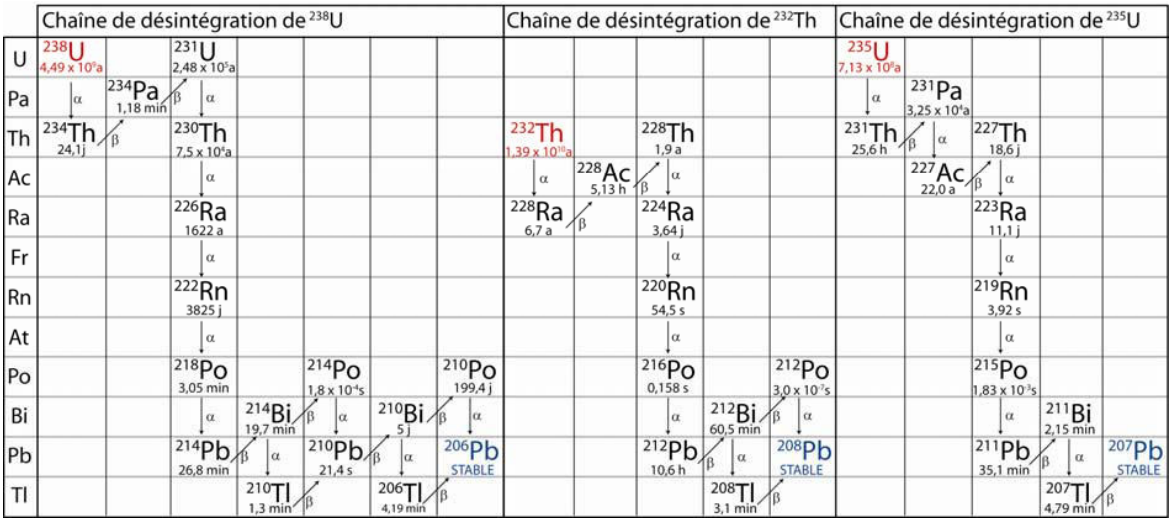

Figure IV.6: Series decays of ^{238}U, ^{235}U and ^{232}Th. The principal modes of natural radioactivity involved (alpha decay and beta decay) are presented in section IV.1.2.1.

Based on the well-established theoretical knowledge of radioactivity, the radiogenic daughter production equations for all the decay systems considered, are:

Equation IV.13: $$^{206}Pb^{*} = {}^{238}U\,(e^{\lambda_{238}t} - 1)$$

Equation IV.14: $$^{207}Pb^{*} = {}^{235}U\,(e^{\lambda_{235}t} - 1) \qquad \text{i.e., } {}^{207}Pb^{*} = \frac{^{238}U}{137.82}\,(e^{\lambda_{235}t} - 1)$$

Equation IV.15: $$^{208}Pb^{*} = {}^{232}Th\,(e^{\lambda_{232}t} - 1)$$

The age equations are thus:

Equation IV.16: $$t_{206/238} = \frac{1}{\lambda_{238}} \ln\left[\frac{^{206}Pb^{*}}{^{238}U} + 1\right]$$

Equation IV.17: $$t_{207/235} = \frac{1}{\lambda_{235}} \ln\left[\frac{^{207}Pb^{*}}{^{235}U} + 1\right] \qquad \text{i.e., } = \frac{1}{\lambda_{235}} \ln\left[137.82\,\frac{^{207}Pb^{*}}{^{238}U} + 1\right]$$

Equation IV.18: $$t_{208/232} = \frac{1}{\lambda_{232}} \ln\left[\frac{^{208}Pb^{*}}{^{232}Th} + 1\right]$$

where:
- λ_{238} is the decay constant for ^{238}U,
- λ_{235} is the decay constant for ^{235}U,
- λ_{232} is the decay constant for ^{232}Th,
- ^{238}U is the amount of parent ^{238}U nuclides in the mineral,
- ^{235}U is the amount of parent ^{235}U nuclides in the mineral,
- ^{232}Th is the amount of parent ^{232}Th nuclides in the mineral,
- t is the accumulation time.

^{238}U and ^{235}U decay at different rates to ^{206}Pb and ^{207}Pb, respectively, allowing the evaluation of closed-system behaviour. For systems that have been closed since the

formation of the mineral, the two calculated ages from Equation IV.16 and Equation IV.17 are strictly equal to one another and to the true age of the mineral. These ages are said to be concordant. On the contrary, if the systems have opened (perturbation after crystallization such as metamorphism), resulting in gains or losses of Uranium, of Lead or intermediate members of the radioactive decay scheme, for example, Radon or Ionium, during the time since the formation of the mineral, then the equilibrium condition between the two radiogenic systems is no longer satisfied. The two ages calculated for each decay scheme are unequal and said to be discordant.

In practice care must be taken when using the equations of radioactive decay as Lead concentrations considered must correspond to radiogenic lead formed *in situ* by decay of the parent nucleii only. If not, proper corrections have to be made for the initial concentration of ^{206}Pb and ^{207}Pb. In particular, some Lead (^{204}Pb) contained in the crust, referred to as "common Lead", may be present in the crystals when they formed, entering their crystal lattice during crystallization processes. Measured Lead concentrations have therefore to be corrected for initial, common Lead if any.

A graphical way to investigate whether the two radiogenic systems evolved under equilibrium conditions is to plot $^{206}Pb/^{238}U$ and $^{207}Pb/^{235}U$ ratios (or equivalents) in a concordia diagram, either Conventional (Figure IV.7; Wetherill, 1956) or Tera-Wasserburg (Tera and Wasserburg, 1972). If closure has occurred (crystallization) and the equilibrium condition has been satisfied since the formation of the mineral (no further perturbation after crystallization), these ratios are predictable from Equation IV.13 and Equation IV.14 and have unique values for any given time. All the $^{206}Pb/^{238}U$-$^{207}Pb/^{235}U$ pairs define an age curve, called concordia. On the contrary, if there have been isotopic gains or losses, the $^{206}Pb/^{238}U$-$^{207}Pb/^{235}U$ couples will plot outside of the age curve. Co-genetic crystals that have been variably perturbed will thus yield $^{206}Pb/^{238}U$-$^{207}Pb/^{235}U$ ratios that plot on a straight line, called discordia (generally $^{206}Pb/^{238}U$ age < $^{207}Pb/^{235}U$ age < $^{207}Pb/^{206}Pb$ age). The upper intercept between the concordia and the discordia reflects the original age of crystallization or closure, while the lower intercept reflects the age of the discrete episode that led to opened-system behaviour.

IV.2.1.1.2 Analytical procedure

Several analytical techniques were designed to date minerals for U/Pb. In the Pyrenees, Corsica and Sardinia, for instance, these include Pb evaporation (e.g. Cocherie et al., 1991), thermal ionization mass spectrometry (TIMS) and its various procedures (isotope dilution ID-, Pb evaporation or chemical abrasion CA-; e.g. Olivier et al., 2004; Frank et al., 2011; Pavanetto et al., 2012), sensitive high-resolution ion microprobe (SHRIMP) and its different versions (SHRIMP, SHRIMP-II and SHRIMP-RG; e.g. Casas et al., 2010; Aguilar et al., 2014; Martinez et al., 2016), secondary ion mass spectroscopy (SIMS; e.g. Deloule et al., 2002), and inductively coupled plasma mass spectrometry (ICP-MS) with its coupling to various laser ablation systems (excimer laser ablation ELA-, laser ablation microprobe LAM-, laser ablation sector field LA-SF-, laser ablation multi-

collector LA-MC-; e.g. Giacomini et al., 2006; Rossi et al., 2009; Carosi et al., 2012; Laurent et al., 2017; Vacherat et al., 2017). The latter technique has proved early to be fast, relatively inexpensive and easy to implement and use, while allowing determining precise U-Pb age and isotopic and trace element compositions (Feng et al., 1993; Fryer et al., 1993; Hirata and Nesbitt, 1995; Machado and Gauthier, 1996). For this reason, and based on the main objectives of this thesis, the LA-ICP-MS technique was used for detrital zircon U/Pb dating and trace element composition measurements (Chapter 6).

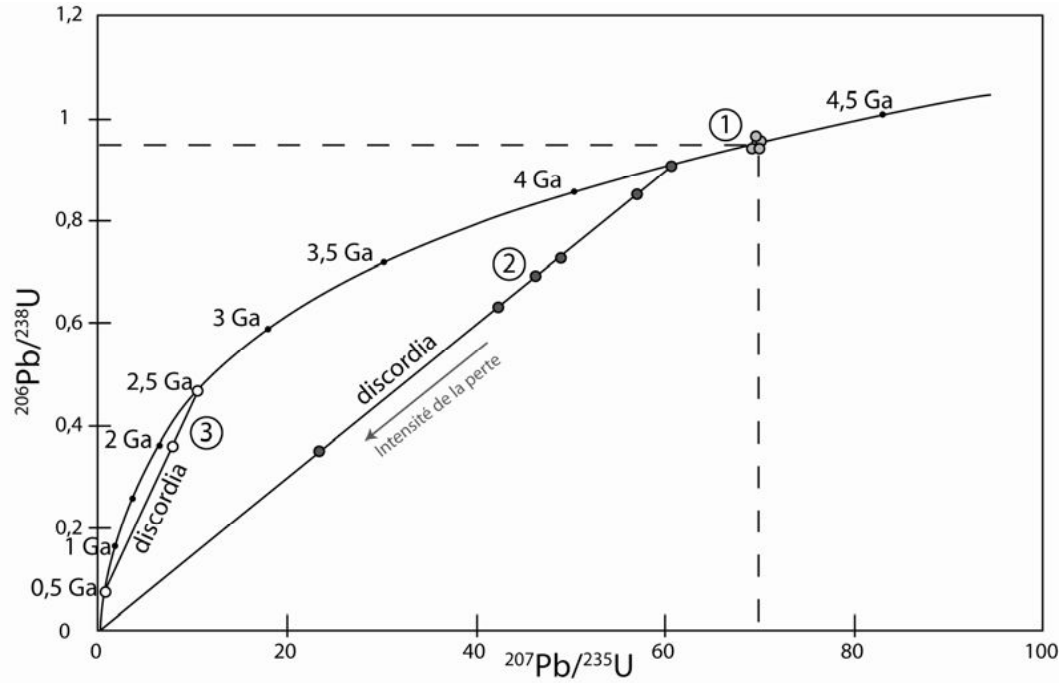

Figure IV.7: Conventional concordia diagram as proposed by Wetherill (1956). Three case studies are presented: 1) The U/Pb radiogenic systems have been closed since the formation of the mineral, so that they have evolved under equilibrium conditions through time. The $^{206}Pb/^{238}U$ and $^{207}Pb/^{235}U$ ratios plot on the concordia curve, and ages from Equation IV.16 and Equation IV.17 are strictly equal to one another and to the true age of the mineral: the crystallization age. 2) and 3) Several $^{206}Pb/^{238}U$-$^{207}Pb/^{235}U$ pairs plot on a discordia line. Grains are co-genetic and data can be regressed. Upper and lower intercepts would indicate ages of crystallization and ages of Pb-loss, overgrowth or any isotopic perturbation, respectively.

IV.2.1.2 The (U-Th)/He system

IV.2.1.2.1 Dating principle

The decay chains that produce radiogenic ^{4}He are the same as those that produce radiogenic Pb. A certain amount of ^{4}He, albeit generally insignificant, is also produced by the decay of ^{147}Sm to ^{143}Nd (Reiners et al., 2005).

$$^{147}Sm \rightarrow {}^{143}Nd^{*} + \alpha \qquad (\lambda_{147} = 6.539 \times 10^{-3}\ Ga^{-1};\ t_{half\text{-}life\ 147Sm} = 106\ Ga)$$

Because ^{4}He is an inert gas, it is unable to chemically bond in silicates. Due to this chemical property and the smaller size of ^{4}He nucleii compared to their parent atoms U and Th, ^{4}He nucleii will diffuse at a faster pace than the parent atoms and tend to be preferentially lost from U-Th-bearing minerals, resulting in (U-Th)/He ages much younger than the age of mineral formation (U/Pb age).

For all the decay systems considered, the radiogenic daughter production equations are:

Equation IV.19: $^{4}He^{*} = 8\ ^{238}U\ (e^{\lambda_{238}t} - 1)$

Equation IV.20: $^{4}He^{*} = 7\ ^{235}U\ (e^{\lambda_{235}t} - 1)$ i.e., $^{4}He^{*} = 7\ \frac{^{238}U}{137.82}\ (e^{\lambda_{235}t} - 1)$

Equation IV.21: $^{4}He^{*} = 6\ ^{232}Th\ (e^{\lambda_{232}t} - 1)$

Equation IV.22: $^{4}He^{*} = {}^{147}Sm\ (e^{\lambda_{147}t} - 1)$

As a result, the total production of ^{4}He nuclei can be described by the ^{4}He ingrowth equation that is:

Equation IV.23: $$^{4}He^{*} = 8\ ^{238}U\left(e^{\lambda_{238}t} - 1\right) + 7\ \frac{^{238}U}{137.82}\left(e^{\lambda_{235}t} - 1\right) + 6\ ^{232}Th\left(e^{\lambda_{232}t} - 1\right) + {}^{147}Sm\ (e^{\lambda_{147}t} - 1)$$

where:
- λ_{238} is the decay constant for ^{238}U,
- λ_{235} is the decay constant for ^{235}U,
- λ_{232} is the decay constant for ^{232}Th,
- ^{238}U is the amount of parent ^{238}U nuclides in the mineral,
- ^{235}U is the amount of parent ^{235}U nuclides in the mineral,
- ^{232}Th is the amount of parent ^{232}Th nuclides in the mineral,
- ^{147}Sm is the amount of parent ^{147}Sm nuclides in the mineral,
- t is the accumulation time or (U-Th)/He age.

As for U/Pb dating, the ingrowth Equation IV.23 assumes secular equilibrium among all short-lived actinide daughters in the decay chain. This condition is guaranteed for minerals that are fully crystallized (closed system) and not too U-Th-rich (lattice preservation). Farley et al. (2002) suggest that 350 kyr are required for secular equilibrium to establish after crystals have formed.

The ingrowth Equation IV.23 also assumes ^{4}He to be formed *in situ* by decay of the parent nucleii in the crystal. This assumption does not apply in presence of Helium "contamination". Four sources of helium excess can be mentioned: atmospheric helium, mineral inclusion, fluid inclusion, and alpha injection. Atmoshpere-derived ^{4}He is unlikely to be present in most minerals due to low He concentration in the atmosphere (5 ppm; Farley et al., 2002). The other sources, nevertheless, are of particular concern in U-Th-poor minerals like apatite as phases with higher U and Th may dramatically affect the He budget of the mineral (e.g. Lippolt et al., 1994; House et al., 1997; McInnes et al., 1999; Stockli et al., 2000; Axen et al., 2001; Spiegel et al., 2009; Gautheron et al., 2012; Murray et al., 2014; Janowski et al., 2017).

Another consideration to be made, that was not necessary for U/Pb given atomic sizes of parents and daughters at play, is the effect of alpha stopping distances on measured helium quantity. Because alpha particles of the ^{238}U, ^{235}U, and ^{232}Th decay series are emitted with high kinetic energies in minerals (4 to 9 MeV; Farley et al., 1996), they can travel over distances up to 40 µm, depending on the initial energy of the alpha particle and the elemental composition and density of the mineral (Farley et al., 1996; Farley et Stockli, 2002; Ketcham et al., 2011). Long stopping distances can thus cause substantial spatial, natural fractionation of the parent/daughter ratio, with abnormal He depletion (crystal zoning, alpha ejection from the outer rim) or enrichment (crystal zoning, inclusions, alpha injection into the outer rim; see sections IV.3.1 and IV.5.6.1).

IV.2.1.2.2 Analytical procedure

Because ^{4}He is an inert gas, measurements for parent ^{238}U, ^{235}U, ^{232}Th, ^{147}Sm and daughter ^{4}He concentrations in a grain are in general conducted with different analytical instruments. Only use of Laser Induced Breakdown Spectroscopy (LIBS; e.g. Gallou et al., 2011) could overcome this limitation since it allows measuring trace element compositions at the same time as ^{4}He is extracted by laser ablation in an ultra-high vaccum cell. As we did not have access to this technique during my thesis, it will not be discussed in this thesis. Two techniques are presented below.

IV.2.1.2.2.i Conventional, bulk technique

Most laboratories have, until recent, measured (U-Th)/He ages as bulk ages. Bulk ages reflect the total integrated ^{4}He content of the age-unknown sample. This way to analyse is thereafter referred to as conventional (U-Th)/He dating (see Chapter 5). It involves measurement of parent and daughter nuclides on the same aliquots since U and Th concentrations may vary significantly from one crystal to another. Conventional bulk (U-Th)/He dating typically consists in four steps, two for preparation and two for analysis.

Firstly, crystal sizes (length, width and thickness) are measured for any handpicked grain to be dated. They must be measured in at least two mutually perpendicular perspectives parallel to the a_1 and a_2 crystallographic axes for correct crystal volume estimation (Reiners, 2005). They are also used to calculate the alpha-ejection correction, accounting for ^{4}He lost from the crystal by long-stopping distances of alpha particles.

Secondly, grains are packed into Pt or Nb foil packets (aliquots) and subsequently placed into an ultra-high vacuum cell with a synthetic sapphire viewport for optical laser heating application. Depending on the ^{4}He content of some minerals (essentially very young or U-Th-poor samples) and the limits of detection of used analytical instruments, it has been common practice to sometimes analyse multi-crystals aliquots (e.g. Maurel, 2003; Gibson et al., 2007; Maurel et al., 2008; Denèle, 2007; Gautheron et al., 2009; Metcalf et al., 2009). Nevertheless, this procedure has never become standard practice since analysing multi-crystal aliquots prevents from confidently interpret ages as a

function of individual grain properties including closure temperature, radiation damage and chemistry (e.g. Flowers et al, 2009; Gautheron et al., 2009; Guenthner et al., 2013).

Thirdly, aliquots are degassed by in-vacuo heating and the released gases are purified in a dedicated high-vacuum system before measurement in a noble gas mass spectrometer. A ^{3}He spike may be added in case of analysis of the resulting mixture by a quadrupole mass spectrometer.

Finally, following complete ^{4}He extraction, Pt packets are retrieved for U, Th, and Sm measurements in solution by ICP-MS. Two main procedures are thus proposed in the litterature. In the first procedure, grains are dissolved along with their Pt packets in a N- or HF-HNO3 mixture for several hours or days, depending on the mineral analysed (for apatite: Gautheron et al., 2013; for zircon: Reiners et al., 2002; Tagami et al., 2003; Evans et al., 2005; Reiners, 2005; Wolfe and Stockli, 2010). In the other procedure, each grain is retrieved from its Pt packet, placed in a Pt crucible, mixed with a solution of LiBO2 - B(OH)3, fused at 990 °C for two hours and subsequently dissolved in HNO3 (Tibari et al., 2016). The latter procedure was used at the CRPG for the bedrock study presented in Chapter 5.

IV.2.1.2.2.ii *Laser ablation, in situ technique*

Over the last decade, on the basis of what was routinely done for U/Pb dating, a laser ablation microanalytical procedure has been developed for *in situ* (U-Th)/He thermochronology (Boyce et al., 2006, 2009; Tripathy-Lang et al., 2013; Evans et al., 2015; Horne et al., 2016). Implementing this recently developed, innovative technique is one of the main objectives of my thesis. As a result, I will dedicate a special section further in this Chapter to this technique (section IV.5). This analytical technique was used at the CRPG for the detrital study presented in Chapter 6.

IV.2.1.3 The fission-track system

IV.2.1.3.1 Dating principle

Spontaneous nuclear fission is a much less common process for the decay of Uranium and Thorium (Figure IV.8). In the case of Uranium in zircon, the process occurs 2 $x10^{6}$ times less frequently than alpha decay (Tagami, 2005). It results from the heavy and unstable nature of U and Th nucleii that spontaneously disintegrate in smaller and more stable nucleii. Spontaneous fission leads to two smaller and more stable fragments of the original atom that recoil away from one another through the crystal lattice, producing ionization damage along their repulsive paths. Such a motion causes disorder in the crystal lattice over a zone, called a fission-track (Price and Walker, 1962a, 1962b; Fleischer et al., 1964, 1965b), where atoms are dislocated from their stable position (Fleischer et al., 1975).

It is fair to say that the fission-track system has proved early to be one of those systems globally well explained by the closure temperature concept of Dodson (1973) without following the first-order law assumption made by this concept (Green et al.,

1988). In cause is probably our inability to understand properly yet how a track forms (and anneals). Indeed, thermally-activated diffusion allows the defects in the track to migrate and the damage to anneal (e.g. Green et al., 1985, 1986; Wagner et al 1989). However, fission-tracks are experimentally shown to anneal at temperatures found in the upper 5 km of the crust while it is known and observed that they are naturally preserved. Donelick et al. (1990) show that tracks can anneal at room temperature and track length reduction appears to depend on time, temperature and composition (Crowley et al., 1991; Barbarand et al., 2003). Altogether these observations suggest complex retention behaviour of fission-tracks, possibly due to the fact that defects composing a fission-track are diverse and that activation energy of defects for annealing is not unique (Ketcham et al., 1999).

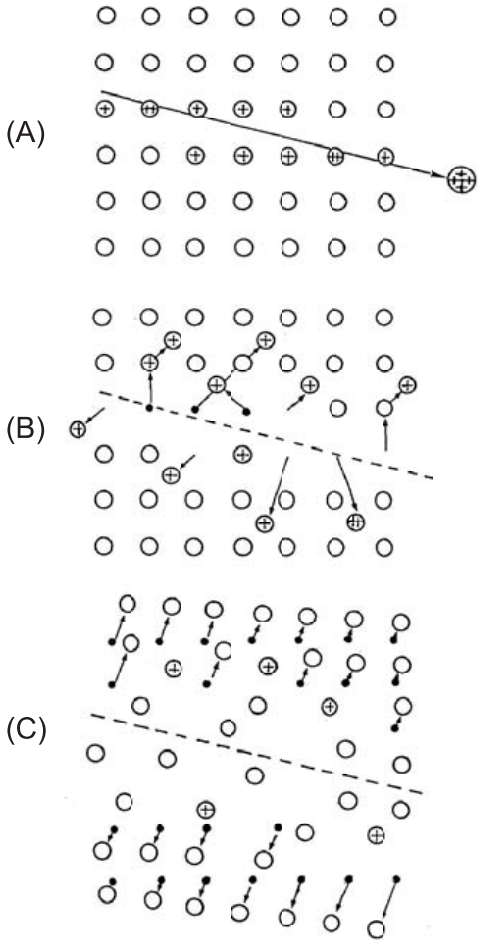

Figure IV.8: Spontaneous fission decay of a radioactive ^{238}U atom leading to latent (unetched) fission-track. From Tagami and O'Sullivan (2005).

As for any dating method based on radioactive decay, three parameters are required to estimate a fission-track age: the amounts of parent (^{238}U) and daughter (fission-tracks) nuclides in the mineral and the decay constant for the parent nuclide. Because ^{238}U decays by both spontaneous nuclear fission and α-emission - the latter mechanism occurring with a much greater decay constant (see Table IV.2) -, it is necessary to weight the amount of ^{238}U that actually produced tracks by spontaneous decay of ^{238}U.

Equation IV.24: $$FT = \frac{\lambda_F}{\lambda_F + \lambda_{238}} \, ^{238}U \left(e^{(\lambda_F + \lambda_{238})t} - 1\right)$$

where:
- λ_{238} is the decay constant for ^{238}U,
- λ_F is the spontaneous fission constant for ^{238}U, with estimates ranging from 7.9 to 8.7 x10^{-8} Ga^{-1} (Bigazzi, 1981; Van den Haute et al., 1998) and a recommended value of 8.45 x10^{-8} ± 0.10 x10^{-8} Ga^{-1} (Holden and Hoffman, 2000),
- ^{238}U is the amount of parent nuclides in the mineral.

One might notice that $\lambda_F \ll \lambda_{238}$ so $(\lambda_F + \lambda_{238}) \approx \lambda_{238}$. The fission-track age equation is thus (Tagami and O'Sullivan, 2005):

Equation IV.25: $$t = \frac{1}{\lambda_{238}} \ln\left[\frac{\lambda_{238}}{\lambda_F} \frac{FT}{^{238}U} + 1\right]$$

where:
- λ_{238} is the decay constant for ^{238}U,
- λ_F is the spontaneous fission decay constant for ^{238}U,
- FT is the amount of spontaneous fission tracks in the mineral,
- ^{238}U is the amount of parent nuclides in the mineral.

IV.2.1.3.2 Analytical procedure

To measure the amount of daughter nuclides, it is necessary to reveal the tracks to the human eye, aided by an optical microscope (Price and Walker, 1962a, 1962b). As tracks are zones of atomic disorder, atomic bounds within a track are weak and material that constitutes the track can be dissolved more easily than the surrounding undamaged crystal lattice. A specific chemical reagent is used, depending on the medium, and tracks are etched and enlarged for observation. After being revealed by acid etching, only spontaneous fission-tracks intersecting the etched surface are counted over a particular area under an optical microscope.

Regarding the amount of parent nuclides, its measurement has been, until recent, quite indirect. The only way to reliably estimate ^{238}U concentration has been by proxy, requiring use of thermal neutron irradiation to artificially induce nuclear fission of sample ^{235}U to fission-tracks (e.g. Gleadow, 1981; Hurford and Green, 1982, 1983; Galbraith, 1984; Hurford, 1990; Wagner and Van den Haute, 1992; Van den Haute et al., 1998). Current practice is use of a mica (or plastic) detector attached to the polished mount during irradiation to record these induced fission-tracks (the External Detector Method; Figure IV.9; Hurford and Green, 1983; Hurford, 1990). As for spontaneous fission-tracks, the induced fission-tracks are subsequently etched and those intersecting the etched surface of the mica are counted over the area that is mirror to that considered for spontaneous fission-track counting. The age equation is thus:

Equation IV.26: $$t = \frac{1}{\lambda_{238}} \ln\left[\frac{\lambda_{238}}{\lambda_F}\frac{\rho_s}{\rho_i}\frac{^{235}U}{^{238}U} QG\phi\sigma_F + 1\right]$$

where:
- λ_{238} is the decay constant for ^{238}U,
- λ_F is the spontaneous fission decay constant for ^{238}U,
- ρ_s is the surface density of etched spontaneous fission tracks in the sample,
- ρ_i is the surface density of etched induced fission tracks in the external mica detector,
- $\frac{^{235}U}{^{238}U}$ is the present-day, average crustal U isotopic composition (137.818 ± 0.045; Hiess et al., 2012),
- Q is the integrated factor of registration and observation efficiency of fission tracks,
- G is the integrated geometry factor of etched surface,
- ϕ is the thermal neutron fluence,
- σ_F is the cross section for induced nuclear fission of ^{235}U by thermal neutrons.

The method, given its technical design, requires measuring the thermal neutron fluence, ϕ, that might vary from one irradiation batch to another, or within a sample stack if the nuclear reactor is not well thermalised. Conventionally, as recommended by the IUGS subcommission on Geochronology (Hurford 1990), ϕ is implicitly estimated by counting induced fission-tracks in a dosimeter glass of known (and uniform) U concentration that is used as a standard glass irradiated together with the sample. Surface densities are thus normalized within the age equation, and remaining constants such as the spontaneous fission decay constant for ^{238}U and the cross section for induced nuclear fission of ^{235}U by thermal neutrons are included in a calibration constant, named the zeta age calibration factor (ζ). This factor is determined empirically by analyzing a set of standard materials of known ages (Hurford, 1990). The fission-track age equation can therefore be reformulated as follows:

Equation IV.27: $$t = \frac{1}{\lambda_{238}} \ln\left[\lambda_{238}\,\zeta\,\rho_d\frac{\rho_s}{\rho_i} QG + 1\right]$$

where:
- λ_{238} is the decay constant for ^{238}U,
- ρ_s is the surface density of etched spontaneous fission tracks in the sample,
- ρ_i is the surface density of etched induced fission tracks in the external mica detector,
- ρ_d is the surface density of the induced fission tracks in the U-doped standard glass,
- Q is the integrated factor of registration and observation efficiency of fission tracks (equal to 1 as long as the age standards and age-unknown samples are analyzed using identical experimental procedures and criteria),
- G is the integrated geometry factor of etched surface,
- $\zeta = \frac{1}{\lambda_{238}}\rho_d\left(\frac{\rho_s}{\rho_i}\right)_{standard} QG\left(e^{\lambda_{238}\,t_{standard}} - 1\right)$.

More recently, developments and analytical improvements made for the LA-ICP-MS technique have allowed routine determination of the ^{238}U concentration (Hasebe et al., 2004, 2009, 2013; Soares et al., 2014; Gleadow et al., 2015).

Describing characteristics of tracks (density, track length, Dpar, etc) is the basis of fission-track dating. Much more could be said about this method, but as the remainder of

this doctoral work will be mainly focused on the zircon (U-Th)/He and U/Pb dating methods, I invite any reader interested in the fission-track method to refer to Gallagher et al. (1998), Tagami and O'Sullivan (2005), Donelick et al. (2005), Tagami (2005), Ketcham (2005), Danhara and Iwano (2013), and Vermeesch (2017) for further information about the fission-track technique.

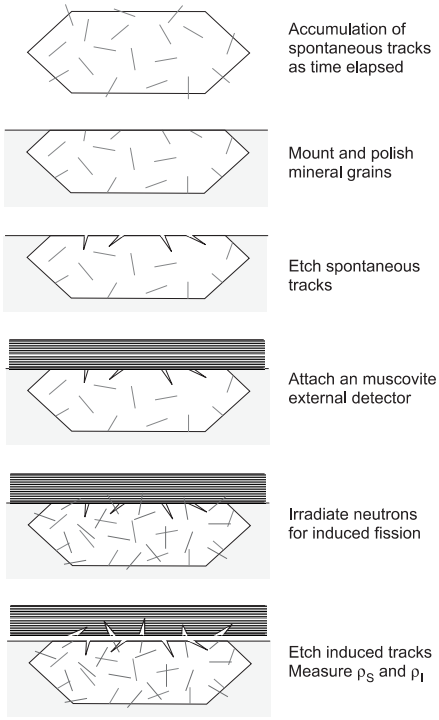

Figure IV.9: Schematic illustration of the procedure of the External Detector Method (Fleischer and Hart, 1972; Hurford and Green, 1983; Hurford, 1990). A mica (or plastic) detector is attached to the polished mount during irradiation to record induced fission-tracks from nuclear fission of ^{235}U. These are subsequently etched and those intersecting the etched surface of the mica are counted over the area mirror to that considered for spontaneous fission-track counting, allowing estimating ^{238}U concentration. From Tagami and O'Sullivan (2005).

IV.2.1.4 The ^{40}Ar-^{39}Ar system

IV.2.1.4.1 Dating principle

The ^{40}Ar-^{39}Ar method is based on the radioactive decay of ^{40}K to radiogenic ^{40}Ar and fast neutron irradiation of ^{39}K to radiogenic ^{39}Ar. Like He, Ar is a noble gas, and its retention behaviour is controlled by thermally-activated diffusion. Ar diffusion is slower than that of He, resulting in cooling ages generally older than He cooling ages.

Because ^{40}K decays to both ^{40}Ar and ^{40}Ca - the former mechanism occurring nine times less frequently than the latter -, it is necessary to weight the amount of ^{40}K that actually produced radiogenic ^{40}Ar. The total decay constant for ^{40}K (λ_{40} = 5.543 x10^{-10} yr^{-1}) is thus divided by the partial decay constants to the ^{40}Ar branch by electron capture (β+) to an excited state (λ_e = 0.572 x10^{-10} yr^{-1}) and electron capture (β+) to the ground state (λ_e' = 0.0088 x10^{-10} yr^{-1}) (McDougall and Harrison, 1999). The ^{40}K -^{40}Ar age equation is therefore ($\lambda_{40} \gg \lambda_e \gg \lambda_e'$ so $\lambda_{40} + \lambda_e + \lambda_e' \approx \lambda_{40}$):

Equation IV.28: $$t = \frac{1}{\lambda_{40}} \ln\left[\frac{\lambda_{40}}{\lambda_e+\lambda_{e'}} \frac{^{40}Ar}{^{40}K} + 1\right]$$

where:
- λ_{40} is the decay constant for ^{40}K,
- $\frac{\lambda_{40}}{\lambda_e+\lambda_{e'}}$ is the ^{40}Ar branching decay constant ratio,
- $\frac{^{40}Ar}{^{40}K}$ is the ratio of radiogenic ^{40}Ar to ^{40}K in the age-unknown sample.

IV.2.1.4.2 Analytical procedure

Because ^{40}K is an alkaline metal and ^{40}Ar is an inert gas, measurements for ^{40}K and ^{40}Ar concentrations cannot be made in another way than in separate analyses, leading to probable age discrepancies in case of sample inhomogeneity. Like fission-track dating, the concentration of parent nuclides is here estimated by proxy, requiring use of fast neutron irradiation of ^{39}K to ^{39}Ar. The sample of unknown age is irradiated together with a standard sample of accurately known K-Ar age. This technical design allows comparing the $^{40}Ar/^{39}Ar$ ratios from the age-unknown sample and age standard that are both analysed using identical experimental procedures, rather than determining the absolute dose of fast neutrons the sample has received during irradiation.

Following irradiation, both the sample and the age standard are placed in an ultrahigh vacuum system. $^{40}Ar/^{39}Ar$ ratios are measured with a mass spectrometer as materials are either degassed entirely or step-heated for argon release. The latter technique is performed to gain insights into the distribution of ^{40}Ar in the sample relative to that of ^{39}K (and ^{40}K as the $^{40}K/^{39}K$ ratio is essentially constant in nature; Humayun and Clayton, 1995). Isotopic abundances are corrected, notably for atmospheric ^{40}Ar (~1% of air). The ^{40}K -^{40}Ar age equation can therefore be reformulated and transformed into an ^{40}Ar-^{39}Ar age equation as follows:

Equation IV.29: $$t = \frac{1}{\lambda_{40}} \ln\left[J \frac{^{40}Ar}{^{39}Ar} + 1\right]$$

where:
- λ_{40} is the decay constant for ^{40}K,
- J is the irradiation parameter, determined experimentally from measuring the $^{40}Ar/^{39}Ar$ ratio of the irradiated age standard: $J = \frac{\left(e^{\lambda_{40}\, t_{standard}} - 1\right)}{\left(\frac{^{40}Ar}{^{39}Ar}\right)_{standard}}$,
- $\frac{^{40}Ar}{^{39}Ar}$ is the isotopic, radiogenic ratio of the age-unknown sample.

Again, much more could be said about this method; information is only given here to better understand the ^{40}Ar-^{39}Ar data taken from the literature and integrated into the first study presented in Chapter 5. I invite any reader interested in the ^{40}Ar-^{39}Ar method to refer to Harrison and Zeitler (2005) for further information about the technique.

IV.2.2 Conceptual approaches for constraining spatio-temporal changes in exhumation (mostly erosional)

IV.2.2.1 Bedrock thermochronology

Bedrock thermochronology represents the first, most common approach for directly applying thermochronological concepts (the " *in situ* " approach). Two main methods were proposed for bedrock thermochronology in orogenic settings and are described below.

IV.2.2.1.1 The vertical transect method

The first method proposed for bedrock thermochronology in orogenic settings is known as the vertical transect method and was first used by Wagner and Reimer (1972). The method consists in sampling a high topography, fast erosion area at various elevations over a short horizontal distance. As such, topographic relief may represent a vertical crustal transect and each sample a specific portion of the crust. Cooling ages are measured for each sample and used to construct an age-elevation profile. The slope of this profile represents the vertical velocity of the rocks crossing closure isotherms at time of closure on their path toward Earth's surface. As the movement of rocks toward the surface is the result of a denudational process, essentially erosional in active orogens, any change in the slope of the age-elevation profile is usually interpreted to represent change in erosion rate with time (Fitzgerald et al., 1993). This method, albeit proving to be very useful, nevertheless suffers from quite important assumptions that nature most likely does not respect in many situations (e.g. advection of mass and heat; Ehlers and Farley, 2003): (i) erosion rate was spatially uniform for the considered area at a given time; (ii) the depth of the closure isotherm has remained constant with time; and (iii) the closure isotherm was flat at the time of closure. Altogether these conditions would ensure that rock cooling reflect the true movement of rocks toward the surface, i.e. exhumation (Figure IV.10).

IV.2.2.1.1 The multi-dating method

Measuring cooling ages of systems with different closure temperatures in the same rock, now known as the multi-dating method, is another bedrock method to constraining temporal changes in erosion-related exhumation rates (Purdy and Jäger, 1976; Wagner et al., 1977). This method allows tracking cooling of a sample through crustal levels (cooling path) and estimating an average cooling rate by dividing the difference in the closure temperatures of two thermochronometers by the difference in their cooling ages (Figure IV.11). Assuming a vertical thermal gradient during erosion, an average erosion rate can be calculated. Nonetheless, this calculation is correct if, and only if, a steady-state thermal field has established as a result of long-term, steady erosion (Moore and England, 2001). Otherwise, the effective closure temperature has been shown to vary not only with cooling rate but also with erosion rate (Figure IV.12; Reiners and Brandon, 2006).

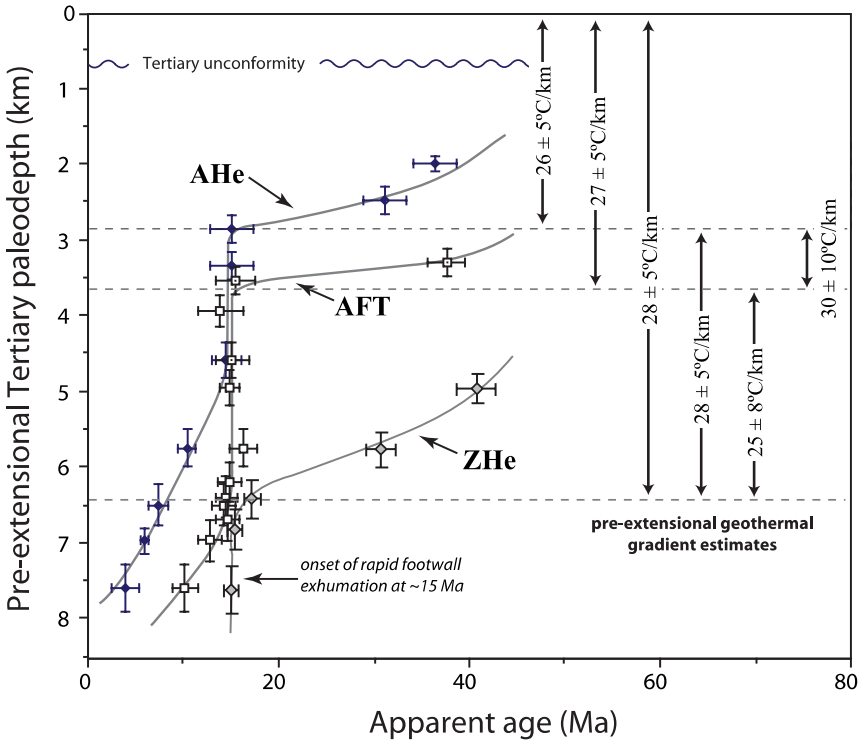

Figure IV.10: Age-elevation profile from Reiners (2005), showing change in slope at around 15 Ma for the apatite fission-track and apatite and zircon (U-Th)/He thermochronometers. This change is interpreted as record of the onset of footwall exhumation.

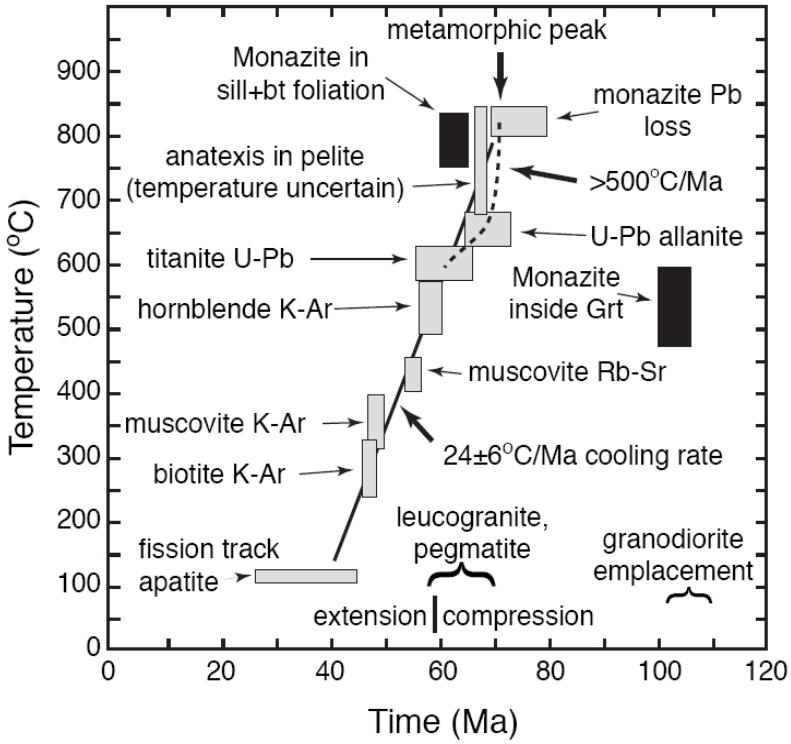

Figure IV.11: Case study example of a multi-dating study, tracking cooling of a sample or several samples through different crustal levels. From Ganguly and Tirone (2009).

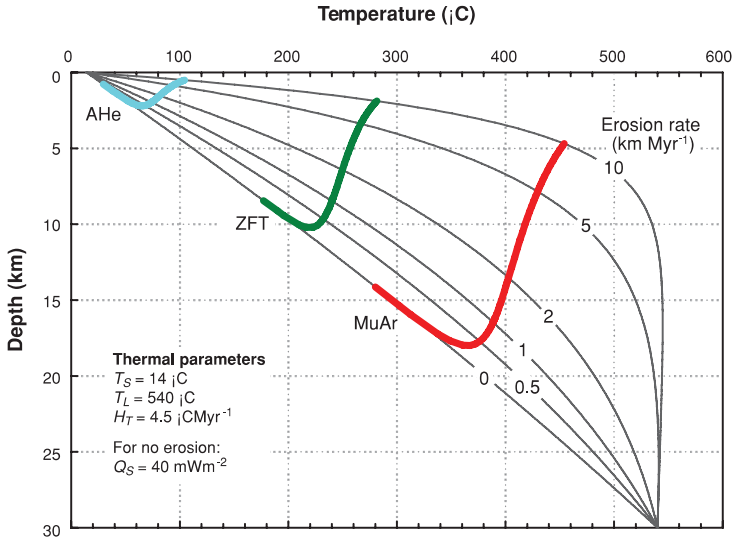

Figure IV.12: Influence of erosion rate on the thermal profile and closure temperatures at steady state. The colored lines show the evolution of effective closure (a depth for a specific closure temperature) for some commonly used thermochronometers for the study of orogenic processes as a function of erosion rate. Two competing effects determine the depth of the closure isotherm. Faster erosion causes all isotherms to migrate closer to the surface, so that the closure depth becomes shallower. On the other hand, the thermal gradient becomes steeper, so that cooling becomes faster and the closure temperature larger.

IV.2.2.2 Detrital geo-thermochronology

IV.2.2.2.1 Detrital U/Pb geochronometry

Identifying and characterizing source regions that eroded in the past within a specific geological province is one of the main objectives of detrital studies aiming at unravelling sediment provenance and basin source-to-sink histories. A widely-used and powerful tool for provenance analysis and sediment routing reconstruction is detrital zircon U/Pb geochronometry (e.g. Dickinson and Gehrels, 2008; Gehrels, 2012; Lawton, 2014). The method consists in correlating detrital zircon U/Pb ages within a sediment or sedimentary rock with the zircon crystallization ages of the source terrains (lithologic units with characteristic ages within a larger source area; Brandon, 1992). However, source region interpretations may be complicated by several factors, including differential source region zircon fertility, regional similarities of bedrock U/Pb signatures and protracted tectonic histories with sediment recycling and mixing, which all lead to complex, ambiguous and sometimes nondiagnostic detrital age distributions (e.g. Dickinson and Gehrels, 2009; Malusà et al., 2013).

IV.2.2.2.2 Detrital low-temperature thermochronology

Another standard tool for studying and quantifying the long-term thermal history of a mountain belt is detrital thermochronology, in particular detrital apatite and zircon low-temperature thermochronology. The general principle underpinning detrital thermochronology is the same as in bedrock thermochronology, except that we are looking at erosional products rather than bedrock exposures (Figure IV.13). The detrital approach therefore presents two main advantages over the bedrock approach. First, it

provides a longer-term record for an evolving orogen. Bedrock exposures very often reveal partial information about the entire evolution of an orogen, the spatial extent of bedrock exposures being limited and the rocks that record earlier tectonothermal events being probably already eroded away off the orogen into the sedimentary repository at the time of analysis. Second, detrital thermochronology provides a more complete view of the orogen. Because sediments deposited in one place are representative of the drained areas upstream, collecting sedimentary rocks amounts to sampling each potential source terrains in the orogen that contributed to detritus. Examining detrital low-temperature thermochronology record within continuous stratigraphic sequences thus allows getting a spatially integrated view of mountain building through time, and utlimately, identifying and charaterizing source regions in an orogen (e.g. Zeitler et al., 1982; Cerveny et al., 1988; Garver et al., 1999; Bernet et al., 2001, 2009; Whitchurch et al., 2011; Bermúdez et al., 2013, 2015).

Such examination has usually consisted in observing the temporal evolution of a variable, called lag time, through a vertical sedimentary succession (the lag-time concept; Figure IV.13; e.g. Brandon and Vance, 1992; Garver and Brandon, 1994; Garver et al., 1999; Bernet et al., 2001). Lag time is commonly defined as the time difference between the apparent cooling age of a detrital grain and the depositional age of the sedimentary rock that contains the grain. In other words, it integrates both the time needed for a crystal (a radioisotopic system) to be brought from the crustal levels where it crossed the closure isotherm to the surface and the time required to transfer (erode and transport) detritus containing the crystal to an adjacent sedimentary basin. Lag time is specific to the thermochronometer considered and is based on several, interrelated assumptions that it is crucial to be aware of. (i) The first assumption is undoubtedly the most important as it refers to the specific settings for which the lag-time concept was primarily established: in virtually all active orogens, there is a lag between closure and deposition, which is primarily a function of exhumation rates (Garver et al., 1999; Bernet and Garver, 2005; Reiners and Brandon, 2006). Cooling is thus assumed to be due to exhumation. (ii) Processes contributing in transferring cooling signals from the source to the sink are erosion and subsequent transport. In active orogens, recycling through multiple erosional and depositional cycles is unlikely, so that the time needed for transporting erosional products is likely very short (<1 myr) when compared to the amount of time associated with exhumation (Copeland and Harrison, 1990; Heller et al., 1992; Garver and Kamp, 2002; Bernet et al., 2004; Stewart and Brandon, 2004). This time is generally shorter than propagated errors in cooling ages and is therefore inferred to be geologically instantaneous, i.e. it is ignored in the lag-time calculation. (iii) Exhumation is slow enough not to lead to perturbation of isotherms towards the surface nor change in geothermal gradient, i.e. it is slow enough to allow the thermal field to be at steady sate. (iv) Cooling and erosion are slow enough not to lead to variations in the effective closure temperature, i.e. they are slow enough to allow the closure isotherm to closely follow steady state. (v) Lag time derivation from one detrital sample to another is performed on grains that are themselves derived from the same source, so that lag times allow characterizing the thermal history of a unique source.

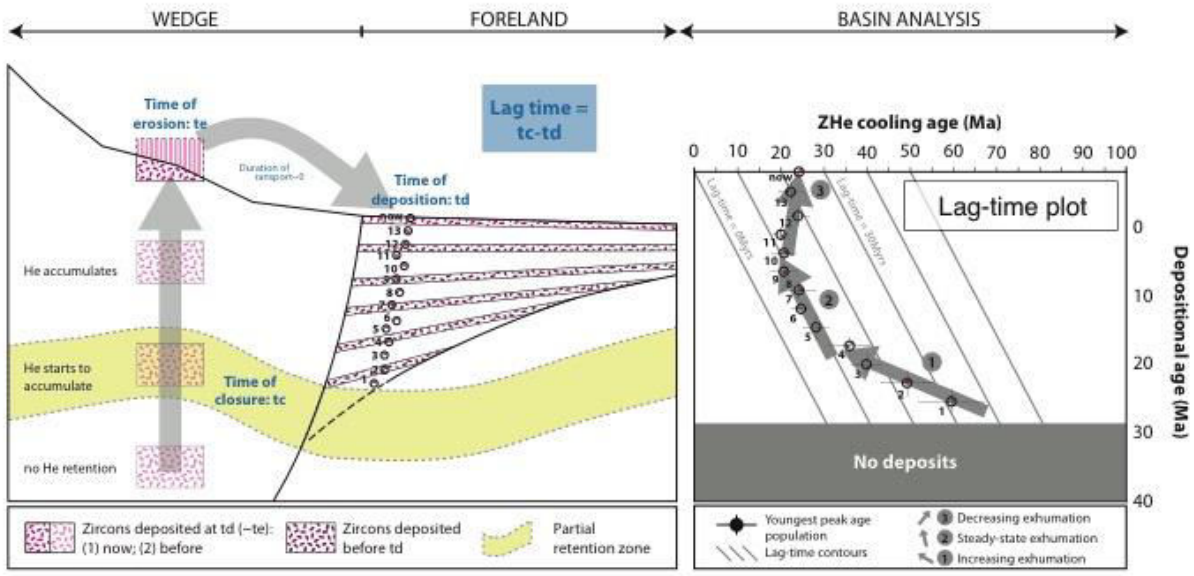

Figure IV.13: Lag-time concept. Lag time is defined as the time difference between the apparent cooling age of a detrital grain and the depositional age of the sedimentary rock that contains the grain. Time for transporting erosional products is assumed negligible compared to the amount of time associated with exhumation (Copeland and Harrison, 1990; Heller et al., 1992; Garver and Kamp, 2002; Bernet et al., 2004; Stewart and Brandon, 2004). Upsection trends in lag time of different components or peaks (here only the youngest peak for each sample is shown) are used to interpret the exhumational history of the source areas that have supplied sediments into the basin. Adapted for zircon (U-Th)/He dating after Bernet and Garver (2005) and Bernet et al. (2009).

In case these assumptions are all verified, the temporal evolution of lag time through a stratigraphic sequence can be interpreted as the evolution of spatially averaged cooling or exhumation rates in the source. Three main scenarios exist, each of them characterized by a typical lag-time trend (Figure IV.13): (1) decreasing lag times upsection suggest increasing exhumation rates/accelerating exhumation through time (i.e. constructional phase, orogenic wedge growth, growing topography); (2) increasing lag times upsection represent decreasing exhumation rates/slowing exhumation (i.e. post-orogeny, decaying orogen, reducing topography); and (3) constant lag times upsection indicate uniform, steady-state exhumation (i.e. exhumational steady state, typical of surface processes compensating tectonic processes). In the latter scenario, the exhumation rate and the closure depth can be said to have remained steady with time. It is wise to mention that such interpretations are common in orogens dominated by erosional denudation, so that exhumation is mostly erosional and the lag time can be used to estimate average erosion rates in the source region of the sediment. Complications to lag time interpretation will arise from any other origin for cooling (this will be discussed in later chapters at the sight of the results obtained during this thesis) or from thermal resetting/annealing by burial or hot fluid circulations.

Nonetheless, identifying and charaterizing source regions in an orogen on the basis of the low-temperature thermochronology record alone may be ambiguous (Garver and Brandon, 1994a, 1994b; Carter et al., 1995). Potential source terrains in the orogen that contributed to detritus can have similar thermal histories, making discrimination for

provenance difficult. At first order, this can even be generalized to any type of radioisotopic systems studied alone while looking at the detrital archive.

IV.2.2.3 Detrital multi-dating

To reduce uncertainty and misinterpretation of source, some provenance analysis studies were conducted by performing multi-dating on the same samples (e.g. Carter and Moss, 1999; Thomson and Hervé, 2002; Whitchurch et al., 2011; Mouthereau et al., 2014) and/or grains (e.g. Rahl et al., 2003; Campbell et al., 2005; Reiners et al., 2005; Bernet et al., 2006; Enkelmann et al., 2008; Perry et al., 2009; Carter et al., 2010; Filleaudeau et al., 2012; Jourdan et al., 2013; Stevens et al., 2013; Thomson et al., 2017). Advantages and limitations of the multi-dating method will be discussed in later sections.

IV.3 *In situ* vs. conventional dating

The power of any (single, double or multi-) dating method in pinpointing sediment sources depends on the precision of each individual dating as well as the degree of method-based bias that they introduce. The former refers to the ability of a dating method to clearly allow identifying peak age populations and distinguishing them from each other (e.g. Carter, 2019). The latter deals with the ability of a method to statistically represent sediment source(s) as a whole given notably sample size, grain dimensions and shape, zoning, inclusions and defects (e.g. Malùsa et al., 2013). In case of fission-track dating, additional potential bias includes dimensions of counting areas, etching and track density.

IV.3.1 Conventional methods: insights and shortcomings

Based on what has just been said in previous paragraphs, it is fair to write that studies that apply the single-grain double dating method have commonly done it on a limited number of grains (<50 grains) due to fastidious intrinsic analytical protocols for low-temperature thermochronology: difficulty in dating grains with very high track densities for fission-track dating, and need for handling and dissolution of the grains for conventional (U-Th)/He dating. While the latter limitation explains the low-resolution distribution of ages from a single sedimentary sample in itself, the former limitation has generally led to omission of zircon crystals with likely high U concentration and/or very old age, which skews detrital fission-track data sets toward low U concentration and young ages. This puts into question how representative of sediment source the data sets are. An example of this issue is provided for detrital zircon (U-Th)/He dating in Figure IV.14.

Regarding the zircon (U-Th)/He system, the conventional technique has proved to provide crucial insights into thermal histories of bed rocks, but suffers from a certain number of complexities intrinsic to the radioisotopic system that are presented below and might be an issue for detrital studies. The most obvious factor that can complicate the interpretation of conventional zircon (U-Th)/He data is the ejection of alpha particles produced by radioactive decay of ^{238}U, ^{235}U, and ^{232}Th nuclides. Given the

travelling distances of these particles within zircon (~16.7 µm, ~19.6 µm, and ~19.3 µm, respectively; Farley et al., 1996), these particles can be ejected from the outer ~20 µm of the grain. Such a distance represents a substantial portion of most crystals, which restricts the minimum grain size for proper ^{4}He measurement in laboratories and requires morphometrical correction for alpha ejection (F_T correction; Farley et al., 1996; Ketcham et al., 2011) not to underestimate the true closure age of the grain (e.g. Hurley, 1955).

Alpha correction is designed for crystals in which parent elements are ideally distributed homogeneously and for which geometry and dimensions are measured before chemical digestion for parent concentration measurements (Farley et al., 1996). First, as a consequence of the "already time-intensive" nature of the conventional approach, it must be acknowledged that measurement of the degree of zonation within each of the dated grains is not typical for conventional zircon (U-Th)/He dating studies (an example is provided in this thesis, in Chapter 5). Yet, parent nuclide zoning is among the most important known factors that influence helium diffusion, all the more exacerbated in zircon (Reiners et al., 2004; Hourigan et al., 2005; Dobson et al., 2008; Guenthner et al., 2013, 2015). While zoning may be simple, allowing relatively easy alpha ejection correction (Reiners et al., 2004; Hourigan et al., 2005; Herman et al., 2007), it is most of the time unpredictably complex, requiring more sophisticated computation (Gautheron et al., 2012). It is a potential source of age variation that has its strongest effect for grains with an ~60 µm equivalent spherical radius when high eU cores or high eU rims occupy the inner or outer third of the grain, respectively (the zircon impact index/factor/number; Guenthner et al., 2013, 2015). Second, despite the extremely durable nature of zircon during sedimentary transport (e.g. Kowalewski and Rimstidt, 2003), detrital zircon grains are quite frequently abraded, broken and/or fractured during transport from their source areas. Lack of information about their original size and shape hinders a proper correction for alpha ejection. This has, until recent, resulted in either employing additional approaches to estimate these unknowns (for zircon: Rahl et al., 2003; Reiners, 2005; Reiners et al., 2005; Thomson et al., 2013; for apatite: e.g. Brown et al., 2013) or simply discarding too suspicious grains from the detrital pool. Whatever the option chosen, this can significantly bias the distribution of conventional, bulk (U-Th)/He ages for a detrital sample.

Alpha injection is another potential source of bias to consider, implanting alpha particles ejected from neighbouring crystals into the grain of interest and leading to an erroneously old measured apparent closure age for this grain. Gautheron et al. (2012) model the effect of such a phenomenon on closure ages and show that it may significantly impact ages (even more than alpha ejection) in case of grains surrounded by neighboring alpha emitters richer in U and Th than the grain of interest. While this may be of great concern for apatite, this is probably of lesser significance in zircon because of its higher U and Th concentrations relative to apatite. The same can be concluded for the inclusion problem that represents the biggest hurdle to accurate and reliable apatite (U-Th)/He age determinations.

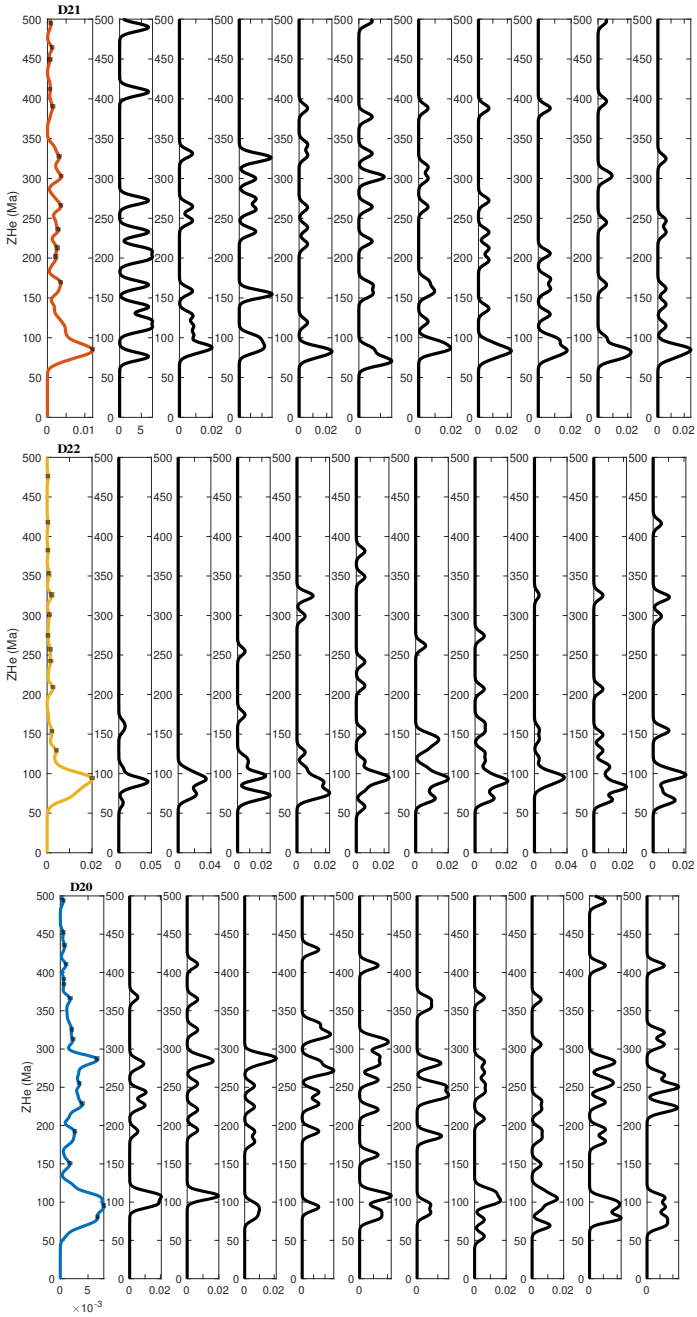

Figure IV.14: The sample size effect. It shows the results of 10 random samplings without replacement from the data of three of my detrital Pyrenean samples (n = 130 for D21, n = 157 for D22 and n = 154 for D20), using the datasample function in Matlab. As in the Pyrenees, typical sample size for conventional (U-Th)/He dating is 10-20 dated grains (Filleaudeau et al., 2012; Thomson et al., 2017; Vacherat et al., 2017; Odlum and Stockli, in revisions; Thomson et al., in review), the function is asked to return 15 ages (observations) sampled uniformly and at random from my detrital samples. Results demonstrate that the youngest peak age in an age distribution may be missed, distorting the estimation of lag times. They also show that interpreting data on the basis of component proportions is very likely to lead to a biased or misleading provenance interpretation, and so doing, should be reasonably avoided in absence of other constraints.

Altogether, issues related to sample size (number of grains dated) and age meaning represent the shortcomings of the conventional approach for (U-Th)/He dating in detrital samples.

IV.3.2 *In situ* methods: insights and modification of the closure concept

To tackle the first limitation about sample size, a laser ablation microanalytical procedure has been developed for *in situ* (U-Th)/He thermochronology on the basis of what was routinely done for U/Pb dating (Boyce et al., 2006, 2009; van Soest et al., 2008; Tripathy-Lang et al., 2013; Evans et al., 2015; Danišík et al., 2017; Horne et al., 2016, 2019). This technique consists in the use of a laser to ablate pits in a polished grain surface, leading to the release of gases contained into the ablated volume of material. These gases are subsequently purified and spiked for isotope-dilution measurement of radiogenic ^{4}He. The volume of the pits ablated for ^{4}He extraction is measured, allowing conversion of the measured quantities of ^{4}He to ^{4}He concentrations at the location of the pits. U, Th, and Sm concentration measurements are then made in or in close proximity to the first pits ablated for ^{4}He extraction using another microanalytical techniques such as LA-ICP-MS (laser-ablation inductively coupled plasma mass spectrometry).

An alternative to pit volume measurement, and so doing ^{4}He concentration estimation, which is the most time-consuming step in the protocol, has been proposed by Vermeesch et al. (2012). It consists in normalizing the raw U, Th, Sm and He signals of the grain of interest to the raw signals of a standard material independently dated for (U-Th)/He. By doing so, the authors argue that this avoids the use of a separate reference material (usually a NIST glass in which the elemental fractionation of U and Th is assumed to be the same as in zircon; Pearce et al., 1997) when estimating U, Th and Sm concentrations of the sample by LA-ICP-MS. The alternative technique assumes, nevertheless, that the age standard and the sample were ablated at identical laser ablation rates.

As the process of *in situ* measurements of parent content by LA-ICP-MS can be designed to measure at the exact same time U/Pb ages, single crystals can be double dated *in situ* by default (for zircon: Tripathy-Lang et al., 2013; Evans et al., 2015; Horne et al., 2016). There exist currently two different approaches. In the first procedure, developed by Tripathy-Lang et al. (2013) and Horne et al. (2016), a 25 µm-wide and 12.5 µm-deep pit is ablated for the ^{4}He analysis before the laser is centred over the same spot for a second, concentric, 40-45 µm-wider and 20 µm-deeper ablated pit for U-Th-Sm measurements. Despite the fact that the second spot completely erases the first pit, the two are concentric. In the second procedure, developed by Evans et al. (2015), positions of the spots are designed to measure theoretically the daughter and parent concentrations at the same place while reducing uncertainty of ^{4}He pit volume estimations. They employ a 50 µm-wide and extremely shallow (<2 µm-deep) ^{4}He pit that is followed by a concentric, narrower (33 µm-wide) and deeper (25 µm-deep) ablation for U, Th, and Sm analysis. To get a sense of the potential (U-Th)/He age differences we might obtain by applying either procedure, I will present some simulations in a later section of this chapter.

The single-grain *in situ* laser ablation techniques described above present therefore not only a way to considerably save analytical time and increase in turn

analysis capabilities, but also the opportunity for single grain U/Pb and (U-Th)/He double dating of individual accessory mineral crystals. Nonetheless, it is important to stress the fact that the meaning of the derived apparent cooling ages should vary. Indeed, we are no longer dealing with bulk crystals, and so with doing bulk closure ages and effective nominal closure temperatures that are considered in the closure temperature theory articulated by Dodson (1973) and presented in section IV.1.2. In fact, the *in situ* method implies to consider closure temperatures that are specific to the spots where ablation is performed within the crystal. In particular, it has been shown by Dodson (1986) that the closure temperature for silicate and oxide systems is not constant at different points in a cooling mineral: it varies as a function of the radial distance from the core of the mineral (Figure IV.15). The author introduces another term in its Equation IV.1 that he called "*the closure function*", *G*. This term is logarithmic, "*independent of cooling rate*" and "*depends upon the geometry of the system, the equilibrium concentration-temperature relationship, and the shape of the cooling curve*". The formulation of the closure temperature equation in the conceptual vision of Dodson (1973) can be revised as follows:

Equation IV.30: $$T_c = \frac{E/R}{\left[\ln\left(\frac{A\tau D_0}{a^2}\right)+G\right]}$$

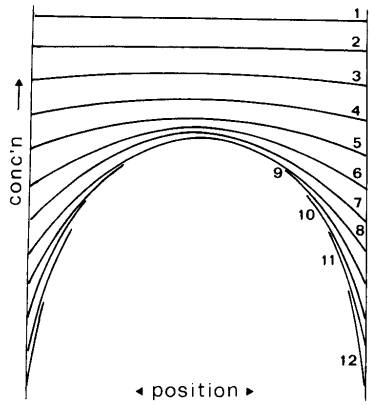

Figure IV.15: Successive concentration profiles (1-12) across a cooling body with changing equilibrium concentration (from Dodson, 1986). During cooling, the highest concentration value of the concentration profile in the grain (at the core) decreases. Dealing with concentration profile 1 will lead to very little age difference between calculated bulk and in situ (U-Th)/He cooling ages. In contrast, performing in situ (U-Th)/He dating at the interior of the grain when dealing with concentration profile 12 will lead to a much older age than in conventional dating (but younger than the in situ age for profile 1).

In other words, the difference between the nominal closure temperature of a crystal and a spot-specific closure temperature depends on the radial position of the spot (ablated ^{4}He pit) within the crystal, the relative sizes of this spot and the crystal itself, and how the cooling rate evolves through time. On this basis, it is therefore fair to stress the fact that zonation of U and Th (see previous section IV.3.1) is likely a potential source of age variation with a possibly even greater effect than it has in convential dating. I will discuss it and illustrate it with some sensitivity tests in later sections of this Chapter. Nevertheless, in case of unzoned crystal, such a difference in closure

temperatures obviously leads to differences between calculated bulk and *in situ* cooling ages for the same grain. In case of rapid cooling (no less than 5 °C/myr) as is generally the case in rapidly exhuming orogens (e.g. Dodson, 1973; Brandon et al., 1998; Bernet et al., 2006; Reiners and Brandon, 2006), such differences are shown to be equal to or less than typical *in situ* laser ablation analytical uncertainties (Tripathy-Lang et al., 2013). As temperature decreases rapidly, diffusion is thermally-activated at a specific temperature and falls rapidly to zero (exponential dependence on -1/T). As a consequence, it has no time to lead to significant variation in concentration accross the grain (flat concentration profile and flat closure profile; Dodson, 1986). The concentration thus stays close everywhere throughout the grain to the equilibrium value it had when diffusion was thermally-activated.

In contrast, differences between conventional and laser ablation (U-Th)/He dating may be significant in case of very slow cooling, with far higher *in situ* closure temperatures and older laser ablation (U-Th)/He ages for the same grain, as warned by Dodson (1986) and Tripathy-Lang et al. (2013). Such a slow cooling is expected in a situation where a grain spends some residence time in the partial retention zone. As temperature decreases slowly, diffusion generates variation in concentration accross the grain (concentration profile and closure profile; Dodson, 1986). The thermochonometric age obtained with conventional techniques for this grain is thus an apparent cooling age resulting from the complex interplay between diffusion and accumulation in the grain (sections IV.1.2 and IV.1.3). It usually does not date an event nor the time at which the closure isotherm was crossed. In contrast, targetting the interior of this grain with *in situ* laser ablation techniques aims to sample the highest concentration value of the concentration profile in the grain. This value represents the concentration that "*lag[s] behind that at the surface*" through diffusion (Dodson, 1986), i.e. the concentration that was at equilibrium with its environment when temperature started decreasing. The age calculated with this value thus dates a true cooling event that most likely occurred prior to the period of slow cooling.

In theory (simple case of unzoned grains), applying the *in situ* laser ablation technique therefore prevents from assuming that the closure temperature is constant for all zircon grains while this was previously done implicitly in studies using conventional detrital zircon (U-Th)/He thermochronology. In particular, performing ablation at the core of a detrital grain should lead to a cooling age pointing to a specific temperature on the cooling path of the grain/source region at which the ^{4}He concentration was at equilibrium with its environment before diffusion generates variation in concentration accross the grain. For unzoned grains, this thus brings us back to the scenario of rapid cooling for which diffusion has no time to lead to significant variation in concentration accross the grain. This point suggests that laser ablation *in situ* (U-Th)/He dating favours documentation of rapid cooling episodes and reduces "noise" due to slow cooling when determining a cooling age. In other words, this restricts the cooling record to portions of the cooling path out of the partial retention zone, which is fairly analogous to what lies in the closure temperature concept of

Dodson (1973): both the upper and lower temperature limits for the partial retention domain are equalled to the closure temperature (thickness of this domain tends toward zero). I therefore argue that if a sample/crystal in the source region were to cool steadily as a result of any marked tectonic event such as early orogenesis, the cooling age yielded by the core of the crystal would necessarily correspond to the age of the tectonic event. After transfer of the source signal into the sedimentary basin, the measured cooling age distribution would then probably seem more fragmentary as complex parts of the thermal history of the source region (residence in the partial retention zone) would have been removed or their signature minimized. This is illustrated in the next section.

IV.3.3 Contributions of single-grain *in situ* dating to early orogenesis

Early convergence processes and mechanisms responsible for the transition from rift to collision are, as yet, little known and quantified (Chapter 1 and Chapter 2). In the Pyrenees, two points need to be addressed: (i) a two-fold shortcoming in quantifying syn-orogenic denudation, and (ii) an issue with recognising the signature of early Pyrenean convergence in source-to-sink processes. Regarding the first point, most previous regional exhumation studies have focused on reconstructing thermal histories for currently exposed bedrock, which has led to sparse constraints on the initiation and early phase of convergence. Moreover, regional detrital double dating has, until recent years, been performed either on distinct batches of grains or statistically non-representative numbers of grains or samples. Regarding the second point, the delay between the end of rifting (and associated HT metamorphism, early Cenomanian) and the onset of convergence (end Santonian) is short in the Pyrenees, leading to difficulties in recognising a clear thermal signature of early orogenesis. Dealing with early orogenesis may thus require dealing with a non-steady thermal field in the crust and raises the questions: can we distinguish an early orogenic thermal signature from earlier thermal events such as those associated with preceding rifting? Which tool could help us to do so? While the first point is further developed in Chapter 5, the second is the focus of this section.

IV.3.3.1 *In situ* laser ablation vs. conventional bulk (U-Th)/He dating

To get a sense of the differences between *in situ* and conventional (U-Th)/He dating mentionned in sections IV.3.1 and IV.3.2, simple numerical modelling was performed using Matlab. We consider the evolution of a 2D continental crustal segment that would have undergone rifting and thermal reset (Albian; 110 Ma) before being exhumed during early convergence (Campanian-Maastrichtian; 75-65 Ma). In this simulation steady-state sawtooth topography (1-km-high) is assumed, i.e. vertical rock uplift is instantaneously balanced by erosion. The crust is totally reset at the beginning of the simulation (rifting) and has inherited, 35-myr-old vertical zircon (U-Th)/He age profiles at the onset of exhumation (onset of convergence). On the basis of the discussion in Chapter 5, vertical age profiles were obtained using HeFTy for three different populations of unzoned zircons (uniform radius), each of them with a specific closure temperature/eU concentration. Vertical rock uplift and erosion rates are kept

constant at 1 km/myr from the onset of exhumation to the end of the simulation 10 myrs later. The temperatures at the bottom and top of the crustal segment are fixed. At each time step, the thermal state of the crust is calculated, which allows updating zircon (U-Th)/He age profiles through simulation time. Modelling returns one distribution of erosional products (3000 zircon (U-Th)/He ages) for each synthetic deposit accounting for 2 myrs of deposition. Each distribution comes under the form of associated kernel density estimate (KDE) and histogram.

Two simulations were run, each of the two with a specific set of three vertical age profiles (Figure IV.16 and Figure IV.17). The first simulation and its associated set of profiles correspond to grains with a radius of 50 µm that would be dated in the conventional way. The second simulation and its associated set of profiles correspond to grains with a radius of 50 µm but the outer 35 µm abraded, illustrating what we could obtain with laser ablation *in situ* (U-Th)/He dating (spheric spot for He measurement with a diameter of 30 µm).

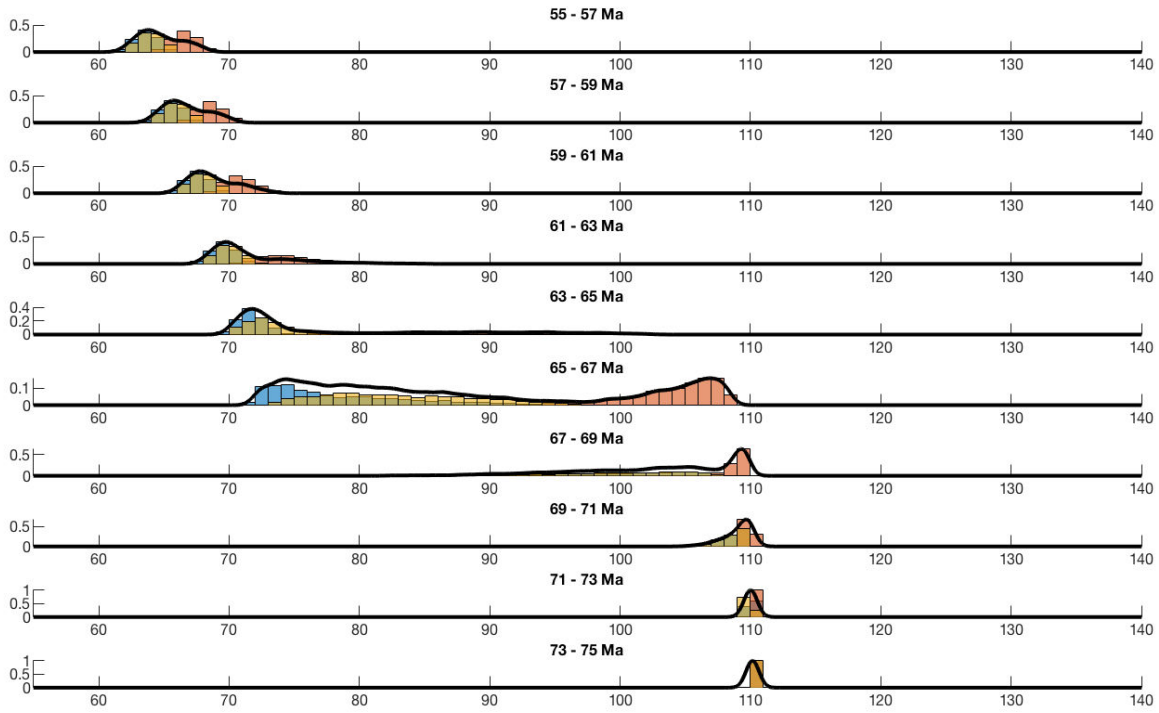

Figure IV.16: Results for the first simulation (conventional) without any error. Blue = high eU; Red = intermediate eU; Yellow = low eU.

When simulated ages come without any error (perfect data, infinite analytical precision) - which allows simple comparison between the detrital zircon (U-Th)/He age distributions returned by the two simulations -, it clearly appears that the simulation illustrating laser *in situ* dating favours documentation of rapid cooling episodes, with two well defined, spaced components at 65-72 Ma (Maastrichtian) and 110 Ma (Lower Cretaceous; Figure IV.17). These components are observed for each population of zircons, but "never" together within sediments. The Lower Cretaceous component defines a static peak up stratigraphic section from 75 to 65 Ma, with a constant peak age

and increasing lag times upsection (Garver and Brandon, 1994a, 1994b; Bernet and Garver, 2005). This indicates erosion of grains that were totally reset then rapidly cooled around 110 Ma. The Lower Cretaceous component dies out between 67 and 63 Ma, while the Maastrichtian component appears. In sediments deposited between 67 and 65 Ma, ages younger than 110 Ma are yielded by grains with low and high eU concentrations (lower closure temperature, see Chapter 5). In contrast, the few remaining ages of 110 Ma observed in sediments deposited between 65 and 63 Ma are only yielded by grains with intermediate eU concentration/higher closure temperature. In the latter sediments the Maastrichtian component dominates, then youngs upsection at the same rate at which the depositional age changes, leading to an approximately constant lag time. This indicates continuous exhumation at a constant rate (Bernet et al., 2001; Willett and Brandon, 2002; Bernet and Garver, 2005), which is consistent with our imposed condition regarding steady-state sawtooth topography during exhumation from 75 Ma to 65 Ma.

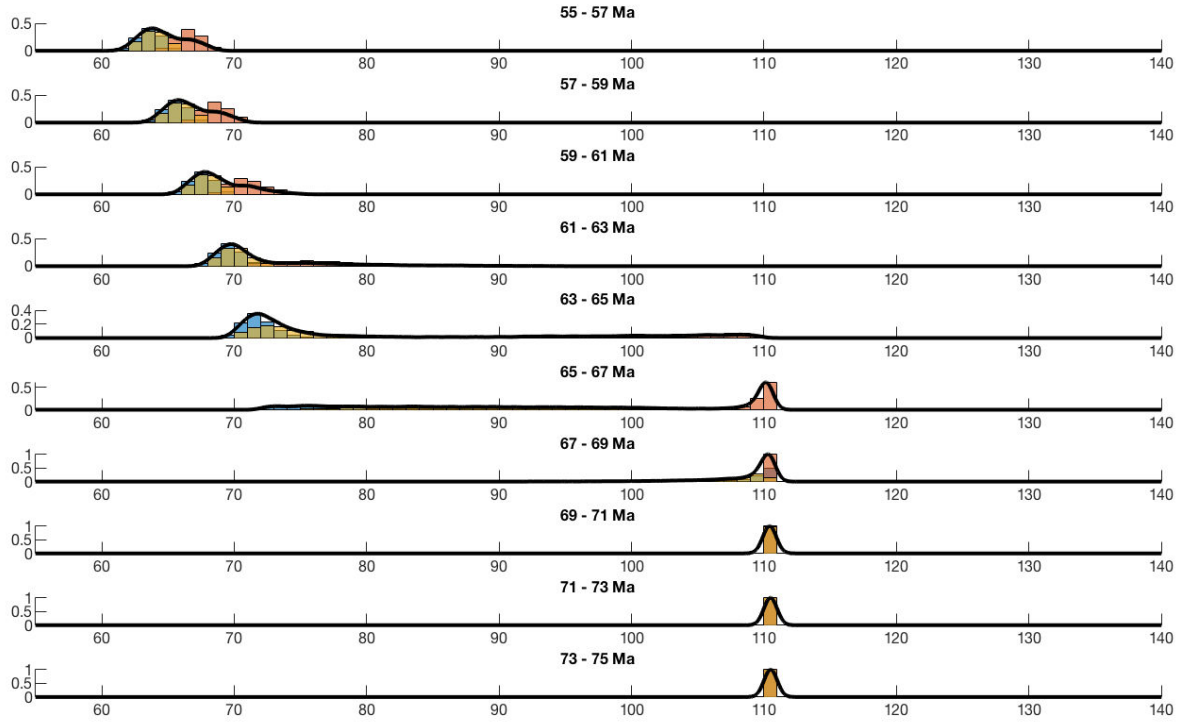

Figure IV.17: Results for the second simulation (in situ) without any error. Blue = high eU; Red = intermediate eU; Yellow = low eU.

In contrast, the simulation illustrating conventional dating returns a multimodal age distribution for sediments deposited between 67 and 65 Ma (Figure IV.16). The Lower Cretaceous and Maastrichtian components are still evident but they are clearly less well defined due to the presence of a complex cooling signature between 110 Ma and 72 Ma. This indicates erosion of grains that rapidly cooled at 110 and 75 Ma, but also grains that spent significant time in the partial retention zone between 110 and 75 Ma. These modelling results therefore further support the potential of laser *in situ* (U-Th)/He dating to better resolve age components related to true, rapid cooling events during early orogenesis.

However, as the laser *in situ* technique involves the analysis of a smaller amount of material than the conventional method that requires grains to be dissolved, it yields data with higher analytical uncertainties, typically 8-10% (1σ; Horne et al., 2016) instead of 6-8% (1σ; Wolfe and Stockli, 2010; Tibari et al., 2016) for Fish Canyon tuff zircon. Two other simulations integrating statistical noise were then run to account for these uncertainties (Figure IV.18 and Figure IV.19). A Gaussian distribution of a width that is twice the analytical uncertainties was attributed at each age of the vertical age profiles. When a grain is eroded, a value is randomly sampled within the Gaussian distribution and the age is added to the synthetic data set.

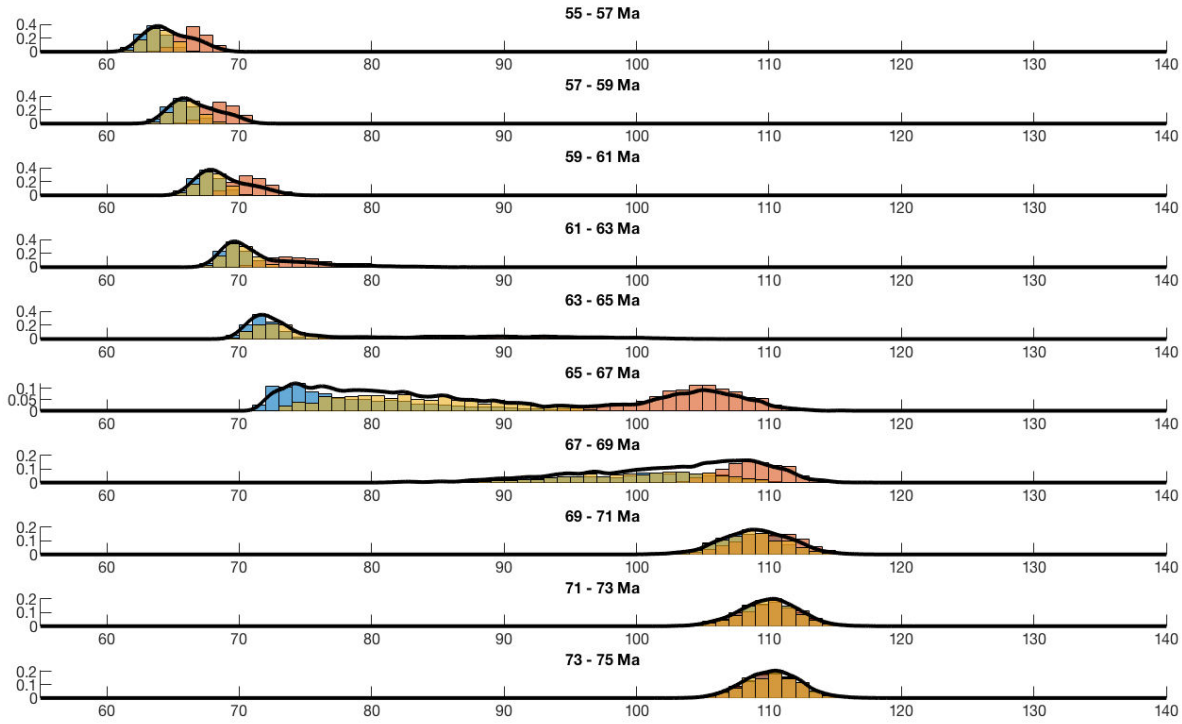

Figure IV.18: Results for the first simulation (conventional) with 6% error. Blue = high eU; Red = intermediate eU; Yellow = low eU.

As anticipated, given that the precision of the data is lower than previously considered, it leads to poorer definition of the components related to rapid cooling events in both simulations. Nevertheless, while this is clearly observed for the older, Lower Cretaceous component due to its larger width, it is less marked for the younger, Maastrichtian component. Moreover, the age distributions yielded by the two simulations are very comparable from one sample to another. As larger noise is considered in the simulation representing *in situ* dating but results of both simulations are similar, it is interesting to observe that the *in situ* technique, as currently developped, has a fairly equivalent resolution to that of the conventional method applied on the same number of grains. Figure IV.20 shows that this observation is still valid if analytical uncertainties go up to 15% for *in situ* dating (see next sections for discussion of this value).

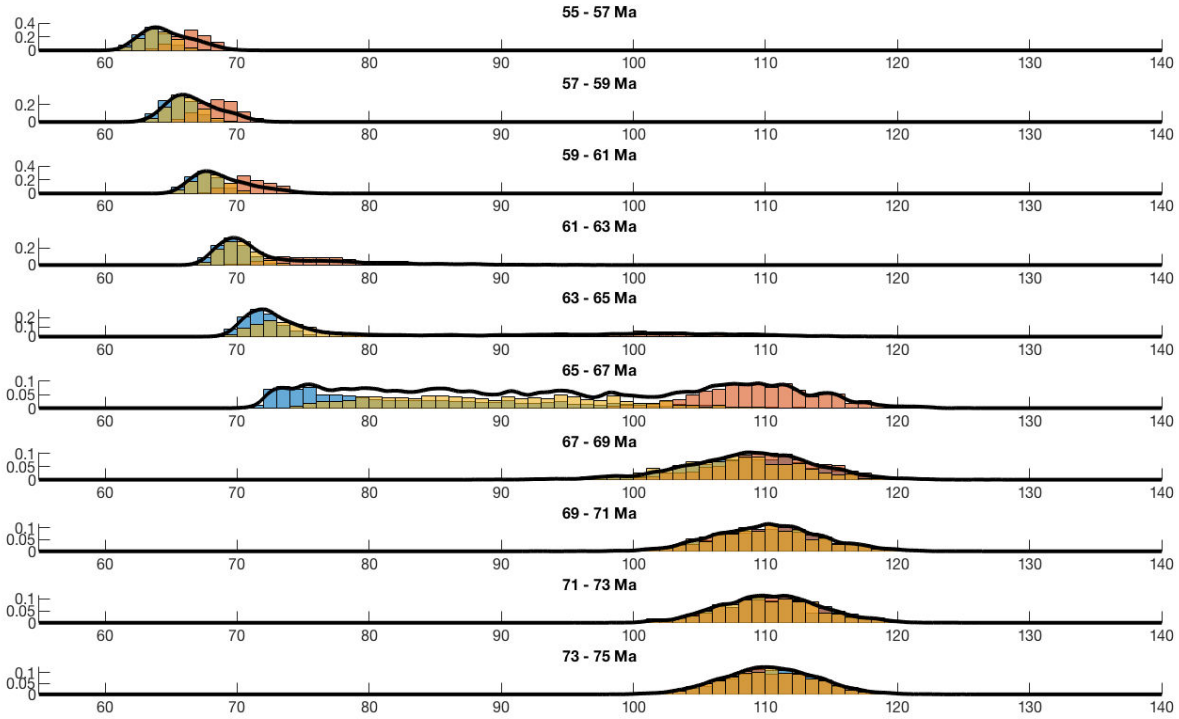

Figure IV.19: Results for the second simulation (in situ) with 10% error. Blue = high eU; Red = intermediate eU; Yellow = low eU.

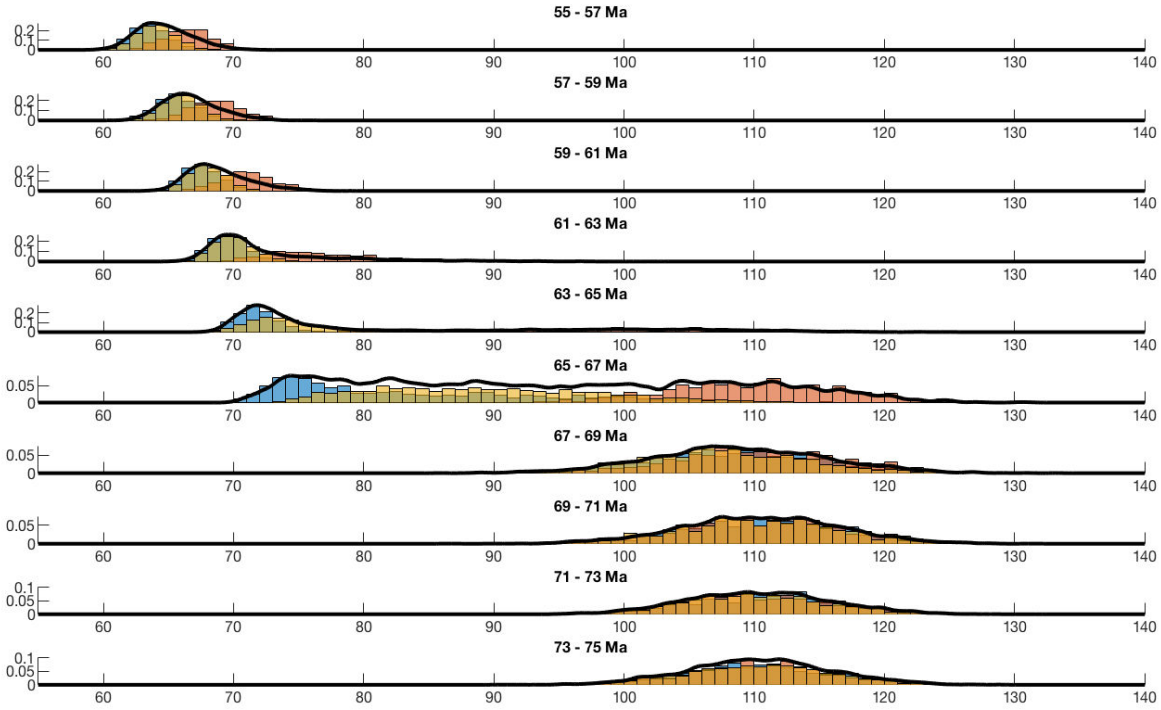

Figure IV.20: Results for the second simulation (in situ) with 15% error. Blue = high eU; Red = intermediate eU; Yellow = low eU.

Based on these modelling results and the fact that the laser ablation procedure simplifies and accelerates (U-Th)/He dating of detrital minerals, as well as reduces sampling biases related to selective picking of unbroken and little abraded crystals in the conventional method, I therefore argue that laser *in situ* (U-Th)/He dating should

allow better constraining the thermal and denudational evolution of the early Pyrenean orogen from extensional episodes to early orogenic stages. My work therefore aims to constrain the timing and rates of orogenic episodes as well as timescales for sediment transport from source to sink in the eastern Pyrenees. To do so, I needed to implement the *in situ* laser ablation (U-Th)/He technique at the CRPG lab during my doctoral project.

IV.3.3.2 *In situ* double dating vs. conventional double dating

Whitchurch et al. (2011) provide the community with two extensive U/Pb and fission-track data sets for the Pyrenees (the latter being the largest low-temperature thermochronology data set in the region). While U/Pb data show a major Hercynian component in syn-orogenic Late Cretaceous sediments, fission-track data show evidence for cooling during the Late Cretaceous. The authors thus suggest that sediment supply during early orogenesis was from an eastern source that was progressively exhumed, leading to removal of the non-to-partially-reset Paleozoic cover and progressive exhumation of previously deep-seated basement rocks (Hercynian granite plutons) in the eastern Pyrenees. Nevertheless, these two data sets were obtained on different zircon aliquots and it is fair to write that correlating the appearance of the early convergence cooling signal with that of the Hercynian crystallisation peak is ambiguous as we do not know for facts what is the thermal history associated with the Hercynian sources. Separate use of the fission-track and U/Pb methods may therefore result in a biased or misleading provenance interpretation. To solve this issue, Filleaudeau et al. (2012) adopt a single-grain detrital double dating approach, combining both (U-Th)/He and U/Pb analyses on zircon. These authors provide data that allow a conclusive decision on this point: Hercynian zircons cooled during the Late Cretaceous.

Since the only evidence we have for sure for a single detrital grain is that it comes from a single source, studies including single-grain multi-dating for a certain number of grains should allow statistically more robust and convincing revealing of populations with distinct combinations of ages in the sampled sediment (Figure IV.21). This is in this regard that the single-grain (U-Th)/He - U/Pb double dating approach has been used during my thesis. The next section presents the last but not least, key step that has to be conducted carefully to increase even further the benefits we can get from this approach: the statistical treatment of the data.

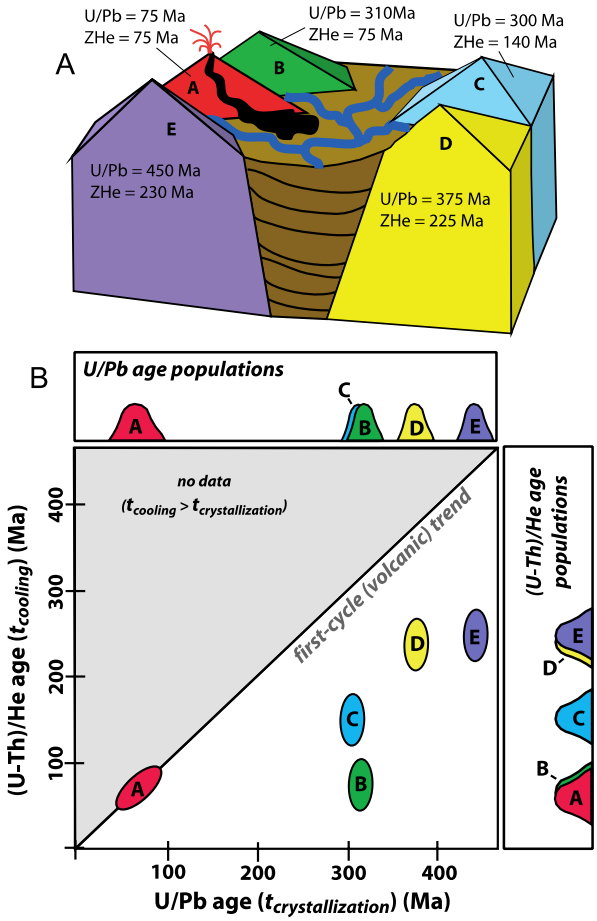

Figure IV.21: Schematic illustration of the single-grain (U-Th)/He - U/Pb double dating approach. By combining both (U-Th)/He and U/Pb analysis on zircon, one is able to resolve U/Pb-indistiguishable terrains B and C (same crystallization age, different cooling ages), and (U-Th)/He-indistiguishable terrains A and B, and D and E (same cooling age, different crystallization ages).

IV.4 Statistical Analysis Methods

I did state in the previous section IV.3 that "*the power of any (single, double or multi-) dating method in pinpointing sediment sources depends on the precision of each individual dating as well as the degree of method-based bias they introduce.*" In the present section, I add the reliability and consistency of the way we try to unbiasedly approximate the cooling history of the source areas from which the sediment originated.

IV.4.1 Geo-thermochronology data plots

In detrital geo-thermochronology, it is useful for any multi-grain data set to first be assessed visually, with a statistical goal that is shared by many other types of studies: estimating the probability density function (p.d.f.) of a random, continuous variable - here this is the cooling age -. In theory, the probability density function gives the relative likelihood of the different ages in the population and quantifies uncertainty associated with the true value of these ages: this is the true age distribution. In this view, uncertainty is not analytical; it only comes from the nature and duration of the

process/event that is described by the age. The probability of an event (an age interval) is the area under the p.d.f. curve and the total area under the p.d.f. curve is 1.

In reality, sampling is the main source for bias as we may miss or highlight portions of the true age interval. As age measurements are always convoluted with analytical uncertainty, the detrital age distribution we obtain is also somehow biased by the analytical technique we use. Nonetheless, it is fair to say that we generally know much more about how precisely we are measuring than how representative our sampling is. The best we can do is therefore to try to minimize these statistical artefacts, or noise, and estimate the age measurement distribution. Such a distribution can be seen as the ideal age distribution we can produce by measurement. It is always a smoothed version of the true age distribution (Figure IV.22). This fact is part of a much larger, vast field of research referred to as the density estimation problem (e.g. Silverman, 1986; Devroye, 1987; Devroye, 1991).

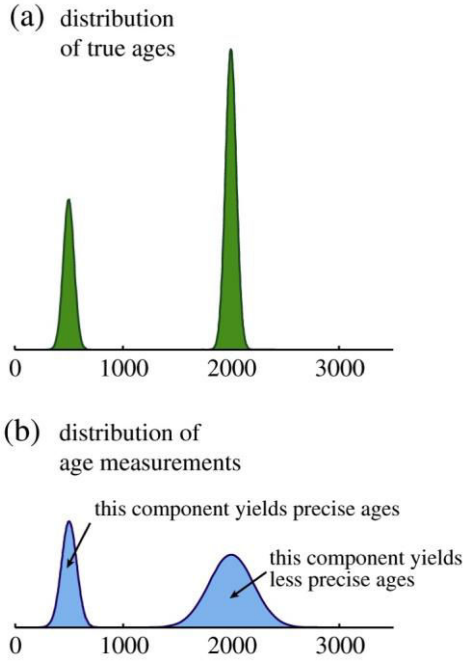

Figure IV.22: Illustration of the smoothing effect of the true age distribution by analytical measurement. (a) A synthetic example of a bimodal true age distribution displaying true ages with infinite precision (equivalent to the p.d.f. curve). (b) The ideal age distribution we can produce by measurement. Ages are true but with finite analytical precision, leading to a smoother age distribution than that shown in the upper plot. This highlights that the lower the analytical precision of measurements characterizing one component, the smoother the distribution of the component. From Vermeesch (2012).

IV.4.2 From the representation of ages of a detrital sample...

Regarding provenance studies, four approaches aiming at plotting detrital age distributions have been commonly used, but their integration within the community is variable. The first main practice involves the use of histograms as a density estimator for any type of detrital data (e.g. Bernet et al., 2006; Whitchurch et al., 2011; Filleaudeau et al., 2012; Mouthereau et al., 2014; Thomson et al., 2017). A histogram is discrete and

discontinuous ("binned"). It is effective at conveying frequency information but it does not consider analytical uncertainties, which is key in estimating the age measurement distribution (e.g. Hurford et al., 1984; Kowallis et al., 1986; Sircombe, 2004). The shape of the histogram depends on the bin width (how much it is binned) and the bin location (binning starting or not at 0 Ma, for instance). It can be mentionned that the binwidth is sometimes chosen to "reflect" analytical precision, but this is obviously not statistically robust.

The second common approach has been to use the probability density plot/distribution (e.g. Hurford et al., 1984; Kowallis et al., 1986; Brandon, 1996; Ireland et al., 1998; Ludwig, 2003; Sircombe, 2004) for visualising detrital age distributions (e.g. Whitchurch et al., 2011; Mouthereau et al., 2014). This visual representation accounts for analytical uncertainty, unlike the histogram. It is obtained by stacking a Normal or Gaussian density function on top of each age estimate to generate a continuous frequency curve or total probability density function (to be distinguished from the p.d.f.). The width of each individual Gaussian density function is determined by the analytical precision (or 60% of it, Brandon, 1996), so that the probability density plot has an arbitrary tendency to make precise measurements stand out and imprecise measurements die out (Figure IV.23). In other words, the frequency information is visually affected by the analytical uncertainty. This amounts to making the assumption that analytical uncertainties fit with the underlying functional form of the true density. While Sircombe (2004) recommended the use of both the histogram and probability density plot, Galbraith (1998) and more recently Vermeesch (2012) pointed out the unreliability of the probability density plot to be a true probability density estimator.

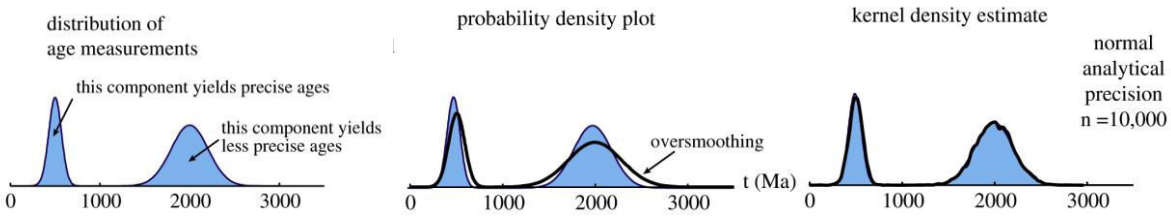

Figure IV.23: Illustration of two approaches to visually represent data. Left: the ideal age distribution we can produce by measurement, as shown in Figure IV.22. Middle: the probability density plot/distribution is a smooth version of the ideal measurement distribution shown on the left. Smoothing results from the fact that analytical uncertainty is taken into account. The older component of the bimodal distribution is dying out due to its lower analytical precision, so that it may seem less significant for provenance analysis and leads to a biased or misleading provenance interpretation. Right: the ideal measurement distribution estimated by the kernel densitiy estimation. The overall kernel density estimate reproduces quite well the age distribution we can produce by measurement, indicating that "*the kernel density estimator converges to the true measurement distribution with increasing sample size n*" (Vermeesch, 2012).

Due to (very) large and variable uncertainties associated with single-grain fission-track ages, a statistical tool known as the radial plot (Galbraith, 1988, 1990) was designed to avoid problems associated with the probability density plot approach when plotting detrital fission-track age distribution. The tool is graphical and allows representing data with the single grain precision on the X-axis and the standard

deviation of the measurement error of each data point on the Y-scale. In simple terms, precise measurements plot towards the right-hand side of the radial plot whilst imprecise measurements plot closer to the origin. A single grain age may be read on an additional, curved axis (the radial scale) on the right-hand side of the plot, by drawing a straight line from the origin of the plot through the data point to the radial scale. Given its design, it is fair to write that the radial plot is suited for luminescence data (Dietze et al., 2016), but of limited help when dealing with relatively precise ages (e.g. zircon U/Pb age data) and/or data with same analytical uncertainty (%).

Most recently, some detrital double dating studies (for instance in the Pyrenees: Vacherat et al., 2014, 2016, 2017; Thomson et al., 2017) used the Kernel Density Estimation. This approach has recently emerged in the geo-thermochronology community after being emphasised in the treatment of detrital data by Vermeesch (2012). This approach, albeit first presented as potential density estimator for U/Pb data by Vermeesch (Figure IV.22), is implemented in the Java-based visualisation tool he developed, the DensityPlotter program, for representation of any kind of data (Vermeesch, 2009, 2012). The Kernel Density Estimation is not new and has been one of the focuses of a large body of statistical literature regarding non-parametric density estimation and smoothing (e.g. Silverman, 1986; Müller, 1988; Härdle, 1990; Sheather and Jones, 1991; Green and Silverman, 1994; Bowman and Azzalini, 1997; Botev et al., 2010, and references therein). This estimation is produced by putting a kernel function of a certain width (or standard deviation, called the bandwidth of the estimator) on top of each age measurement, then attributing a probability mass 1/n (n = sample size) at each measurement for equal statistical weight, and finally summing kernel functions to create a continuous curve (Figure IV.24). In its simplest form, the Kernel Density Estimation is a smooth and continuous version of the histogram (an average histogram) which is determined by the density of the data. It makes no assumptions about the underlying functional form of the true density (i.e. is non-parametric) and takes no account of measurement error that is considered to be noise, unlike the probability density plot. In this view, only sampling matters and disregarding the measurement error aims to tend to the true ages (the ages had we been able to observe without measurement error). The bandwidth should thus be seen as sampling uncertainty (uncertainty on data density), rather than analytical uncertainty. The question of how good or optimal a bandwidth is falls outside the scope of this thesis but there are different approaches and bandwidth selection algorithms (e.g. Abramson, 1982; Silverman, 1986; Sheather and Jones, 1991; Botev et al., 2010; Shimazaki and Shinomoto, 2010; Vermeesch, 2012). A striking discussion on this point is made by Rudge (2008). I will come back to his point later.

IV.4.3 ... Towards the interpretation of these ages in terms of provenance

Applying detrital low-temperature thermochronology aims to infer erosion rates and track mountain belt evolution on the basis of the lag-time concept. Detrital grains from a sedimentary sample are dated and a cooling age distribution is obtained for the sample. This is reproduced for other samples upsection within a stratigraphic sequence.

As grains originate from erosion of a source region (*sensu lato*) where exhumation rates are likely to vary, the age distributions should record that variability. To identify and characterize specific areas of erosion within the source region, it is thus key to statistically invert detrital grains ages and model them in terms of a finite number of component distributions mixed together. The problem is to unmix the mixed, detrital age distribution of a sample into individual component distributions - each of them characteristic of an eroding source area at the time of deposition -, and identify the proportions and statistical properties of these distributions. This problem is called "mixture modelling" (see Peel and McLachlan, 2000; McLachlan et al., 2019) and consists, in its simplest form, in using population modelling to find a parsimonious set of population ages that explain the age distribution, i.e. the variance in the observed grain ages. This is the final and most critical step to convert data into lag times (see section IV.2.2.2.2). In other words, I would like to stress the fact that robustness of the interpretations of detrital data in terms of provenance is directly conditioned by the way data are modelled.

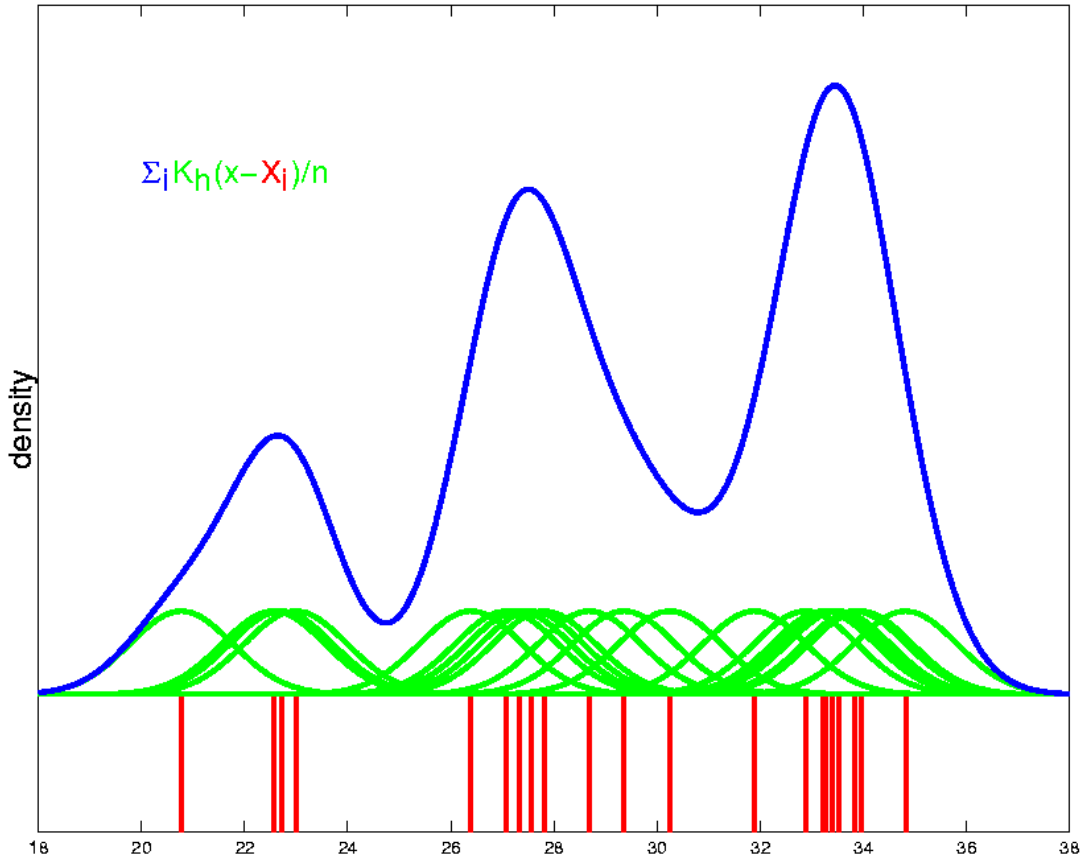

Figure IV.24: Schematic diagram illustrating how a kernel density estimate of a random variable, x, is built. The observations for/measurements of the variable are xi (red bars) with i = 1, ..., n, and n is the number of observations. A kernel of a certain width, h, is put on top of each measurement (green Gaussian curves) with a probability mass of 1/n. Kernels thus represent smooth pieces of "density". These pieces are subsequently summed according to their probability mass to estimate density and produce the kernel function of the variable, K(x) (blue curve). This shows that the kernel density estimate takes no account of measurement error and is determined by the density of the data: the smaller the data set, the poorer the estimate of the true measurement distribution.

There are currently three main methods used to model detrital grain age data. The two first are the most commonly applied methods: finite mixture and minimum age modelling with assumed normal/Gaussian component distributions/densities (Brandon, 1992; Galbraith, 1988, 2005; Galbraith and Green, 1990; Galbraith and Laslett, 1993; see Galbraith (2005) for the big picture) or Gaussian and non-Gaussian statistics (Sambridge and Compston, 1994). The third method is about continuous mixture modelling (Jasra et al., 2006) and uses Bayesian and Markov chain Monte Carlo approaches to fit the models (Gallagher et al, 2009). While the finite mixture modelling method is implemented in DensityPlotter (Vermeesch, 2009, 2012), the continuous mixture modelling method is implemented in BayesMix, a standalone application developed by Kerry Gallagher. I present below the mixture modelling results using these two programs on synthetic data and real Pyrenean data studied in this thesis (Chapter 6).

IV.4.4 Statistics for (U-Th)/He dating in early orogenic settings

The point I would like to stress in this section is the following: if one has no clue about the number of components that is needed for explaining the zircon (U-Th)/He age distribution of a detrital sample, which mixture modelling method is better than another? In the Pyrenees the onset of convergence during latest Santonian postdates by only 10 myrs the end of a phase of rifting (Aptian-Cenomanian), possibly hyperextension. The question that arises for the Pyrenean case study is therefore: can we statistically distinguish an early orogenic thermal signature from earlier thermal events such as those associated with preceding rifting in detrital age distributions of samples in the Pyrenees?

In an attempt to answer these questions, the mixture modelling methods implemented in DensityPlotter and BayesMix are applied first on two synthetic zircon (U-Th)/He age data sets obtained by numerical modelling in section IV.3.3.1, then on the data set of one of my detrital Pyrenean samples.

IV.4.4.1 Case study 1: synthetic detrital zircon (U-Th)/He data

As simulations presented in section IV.3.3.1 return 3000 data for each synthetic deposit, I reduce the number of data for the sediments presenting a complex cooling signature (those deposited from 67 to 65 Ma) to a typical size of 150 laser *in situ* (U-Th)/He ages (see the random sampling without replacement procedure presented in Figure IV.14). Two synthetic data sets are thereafter considered: first, *in situ* data with analytical uncertainties of 10%, and second, *in situ* data with analytical uncertainties of 15%. They both present bimodal kernel density estimates and histograms (bandwidth of 5 Ma and binwidth of 8 Ma, respectively). The two modes can be visually determined at 81 and 106 Ma for the first data set (Figure IV.25), and 84 and 105 Ma for the second (Figure IV.26).

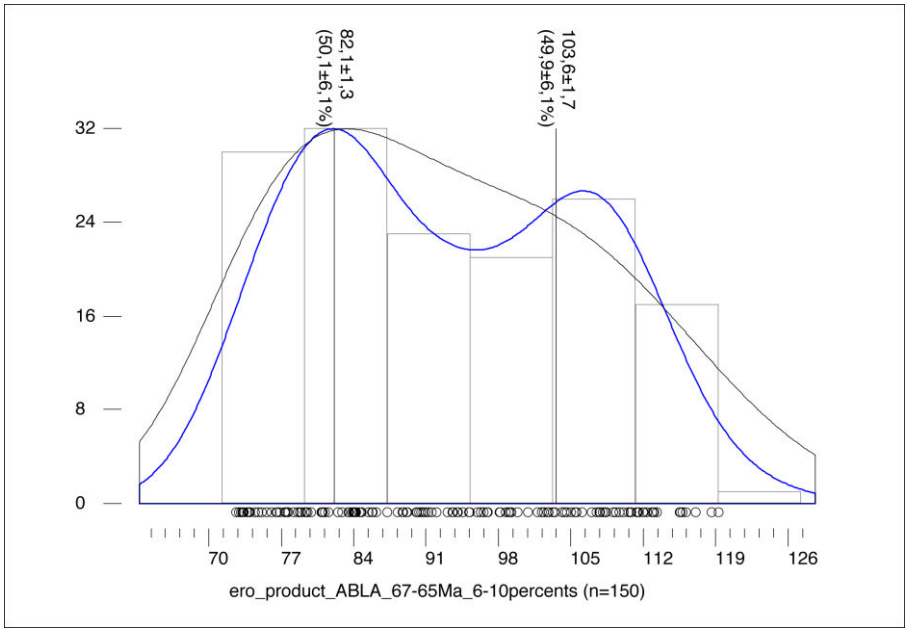

Figure IV.25:Visual representation (kernel density estimate in blue, bandwidth of 5 Ma; probability density plot in black; histogram, binwidth of 8 Ma) of and mixture modelling results ("auto" option selected) for the 150 *in situ* (U-Th)/He ages with analytical uncertainties of 10%, using DensityPlotter (Vermeesch, 2012). Two modes can be visually determined at 81 and 106 Ma. Likewise, the finite mixture modelling method in DensityPlotter returns two components at ca. 82 and 104 Ma. Both visual and inversion methods therefore agree with each other. They are consistent with the two tectono-thermal events at 75 and 110 Ma simulated to produce the data.

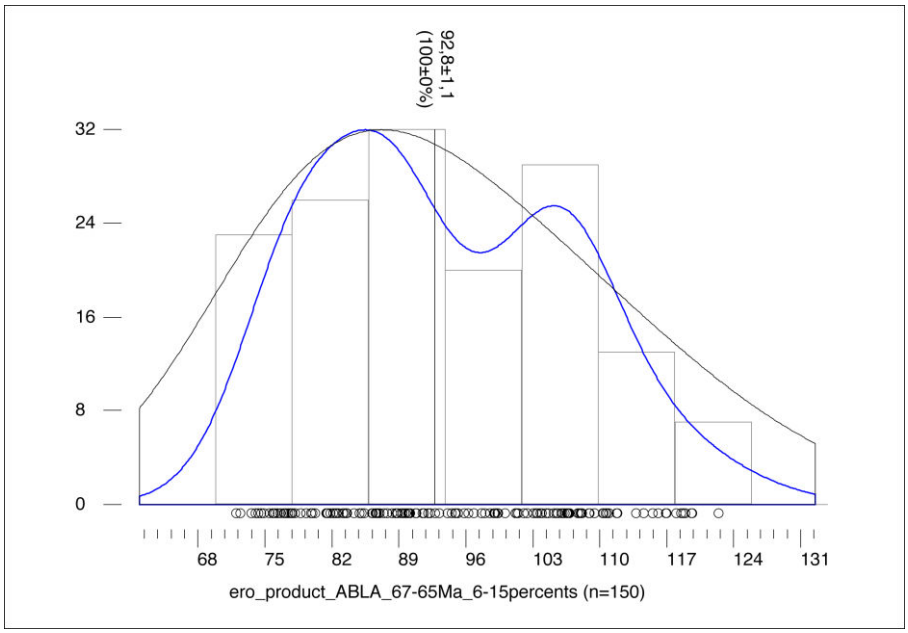

Figure IV.26: Visual representation (kernel density estimate in blue, bandwidth of 5 Ma; probability density plot in black; histogram, binwidth of 8 Ma) of and mixture modelling results ("auto" option selected) for the 150 *in situ* (U-Th)/He ages with analytical uncertainties of 15%, using DensityPlotter (Vermeesch, 2012). Two modes can be visually determined at 84 and 105 Ma. In contrast, the finite mixture modelling method in DensityPlotter returns only one component at *ca.* 93 Ma. While the kernel density estimate is consistent with the two tectono-thermal events at 75 and 110 Ma simulated to produce the data, the mixture modelling methods implemented in DensityPlotter are unable to identify age populations that explain the age distribution when uncertainties for data are too high.

For the 150 *in situ* (U-Th)/He ages with analytical uncertainties of 10%, the finite mixture modelling method in DensityPlotter returns two components at *ca.* 82 and 104 Ma by choosing the "auto" option (Figure IV.25). Likewise, under the same assumption of Normal (Gaussian) distributions as in DensityPlotter, the posterior distribution in BayesMix (burn-in = 200,000 iterations; post-burn-in = 200,000) clearly favours 2 components (P(2) = 0.7) at *ca.* 83 and 104 Ma, although a 3 component model may also statistically explain the data (Figure IV.27). These results are very close to the modes of the kernel density estimate and are consistent with the two tectono-thermal events at 75 and 110 Ma simulated to produce the data set.

In contrast, the mixture modelling methods implemented in DensityPlotter and Bayesmix return only one component at *ca.* 93 Ma and 91 Ma, respectively, for the 150 *in situ* (U-Th)/He ages with analytical uncertainties of 15% (Figure IV.26). While the posterior distribution in BayesMix clearly shows that more than one component is unlikely (Figure IV.28), any choice of more than one component in DensityPlotter leads to non-unique solutions (the algorithm actually gets stuck in local minima; Pieter Vermeesch, pers. com.). This result is not consistent with the thermal history simulated in section IV.3.3.1, suggesting the inability of both methods to identify age populations that explain the age distribution when uncertainties for (U-Th)/He data are too high.

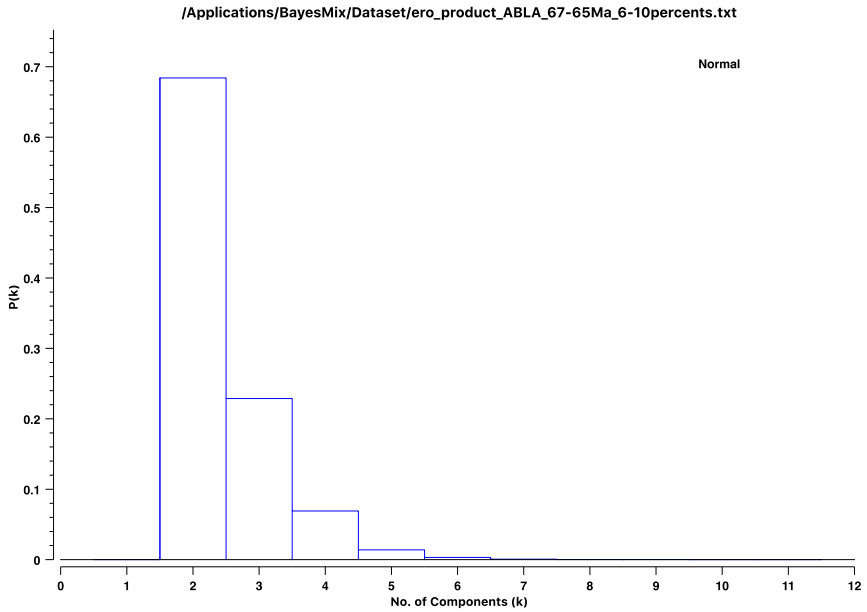

Figure IV.27: Posterior distribution (burn-in = post-burn-in = 200,000 iterations) for the 150 *in situ* (U-Th)/He ages with analytical uncertainties of 10% when modelled using BayesMix by Kerry Gallagher. The distribution clearly favours 2 components at *ca.* 83 and 104 Ma, although a 3 component model may also statistically explain the data. These results are very close to the modes of the kernel density estimate and are consistent with the two tectono-thermal events at 75 and 110 Ma simulated to produce the data.

Since numerical modelling I performed in section IV.3.3.1 was quite simple and aimed to decipher in the sediment archive the first-order response of the zircon (U-Th)/He system to two little spaced thermal events, I will now apply mixture modelling methods on one of my detrital Pyrenean sample, more complex by nature.

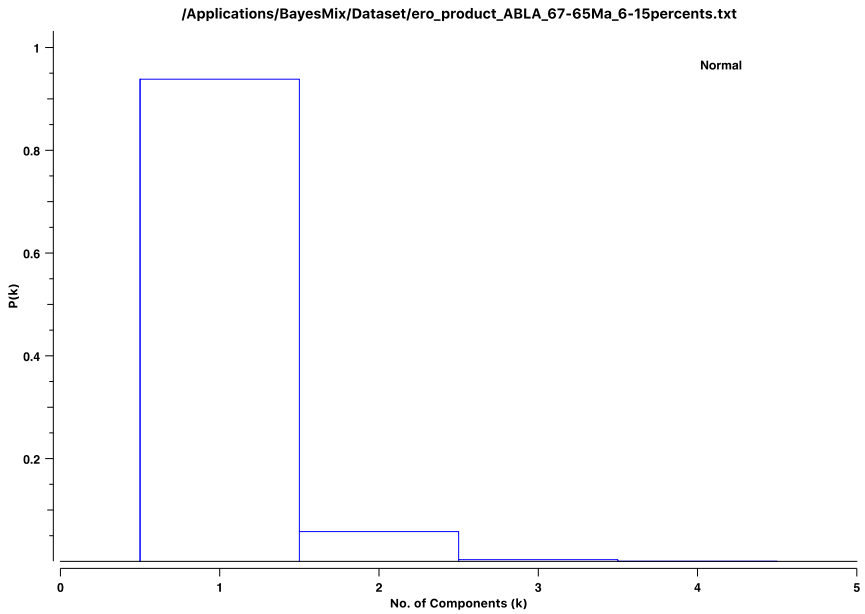

Figure IV.28: Posterior distribution (burn-in = post-burn-in = 200,000 iterations) for the 150 *in situ* (U-Th)/He ages with analytical uncertainties of 15% when modelled using BayesMix by Kerry Gallagher. The distribution shows that more than one component is unlikely. These results are not consistent with the two tectono-thermal events at 75 and 110 Ma simulated to produce the data, suggesting the inability of the inversion method to identify age populations that explain the age distribution when uncertainties for data are too high.

IV.4.4.2 Case study 2: detrital Pyrenean zircon (U-Th)/He data

As it will be discussed in Chapter 6, my detrital zircon (U-Th)/He results present strong age-eU similarities with bedrock data from the north-easternmost Pyrenean Agly-Salvezines massif over the time interval 130-0 Ma (Ternois et al., 2019; Chapter 5). This is particularly clear for one sample (the middle Maastrichtian sample D21) which presents similar kernel density estimate and histogram for (U-Th)/He ages over this interval. Based on the argumentation presented in Chapter 5, I therefore argue that this sample exhibits two cooling components, Lower Cretaceous (age peak at 105 Ma) and lower Campanian (age peak at 80 Ma), which I relate to Aptian-Cenomanian rifting and early orogenesis, respectively. This statement represents my working hypothesis to test to which extent mixture modelling methods allow (i) unmixing mixed, detrital (U-Th)/He age distributions of samples into individual component distributions, and (ii) identifying the proportions and statistical properties of these distributions.

When applied on the entire data set of sample D21 (n = 130 grains), the finite mixture modelling method in DensityPlotter returns the two expected age peaks at *ca.* 80 and 110 Ma if and only if the "auto" option (equivalent to the "5 components" option here) is chosen (Figure IV.29). The age peak at 80 Ma is nevertheless obtained as soon as the number of components chosen is superior to 3. Under the assumption of Normal (Gaussian) distributions, the posterior distribution obtained after a first simulation in BayesMix (burn-in = 200,000 iterations; post-burn-in = 200,000) favours 5 and 6 components (P(5) = P(6) = 0.15), although 4 and 7 component models have relatively similar support probabilistically (simulation #1a; Figure IV.30). In contrast, more than

10 components is inferred to be unlikely. A second simulation (same burn-in and post-burn-in) yields pretty similar results, indicating that 5, 6 and 7 component models are equiprobable, 4, 8 and 9 components are likely, but again, more than 10 components is unlikely (simulation #1b; Figure IV.31). In both simulations, however, 10 or 11 components are actually needed to obtain the expected age peaks at *ca.* 80 and 105-110 Ma (Figure IV.32). In contrast, under the assumption of Skew-t distributions, the posterior distribution clearly favours 2 components (P(2) = 0.5), although a 3 component models have relatively similar support probabilistically, while more than 5 components is inferred to be unlikely (Figure IV.33). Apart from the maximum posterior model which predicts the two expected age peaks with only 3 skewed components, there is a need for 7 or 8 components in general.

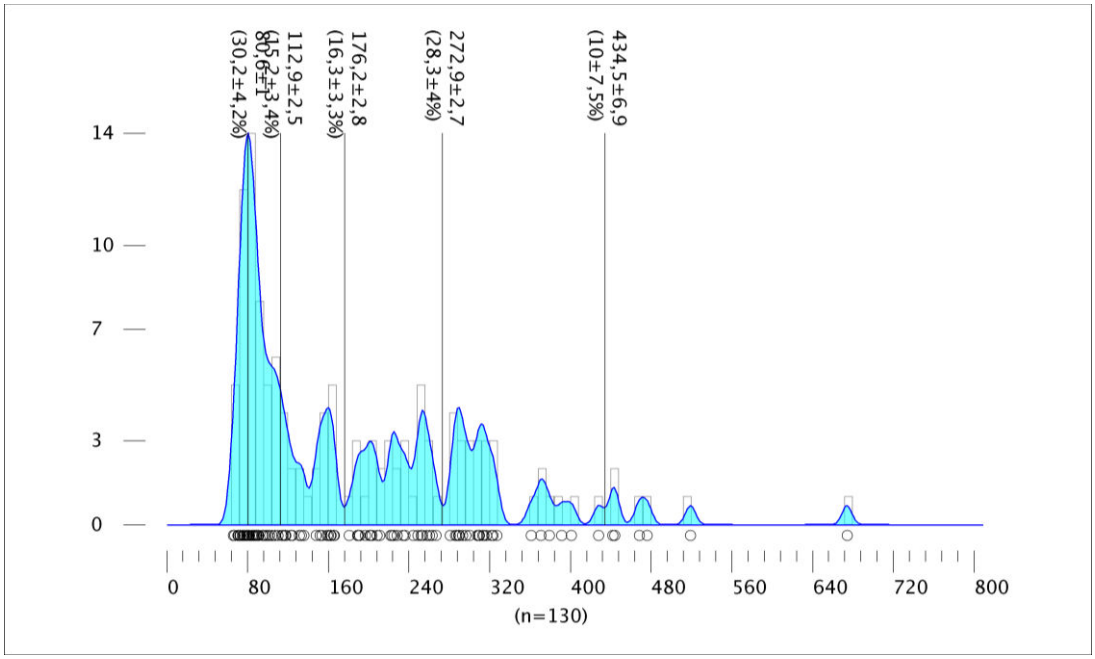

Figure IV.29: Visual representation (kernel density estimate in blue and filled, bandwidth of 5 Ma; histogram, binwidth of 8 Ma) of and mixture modelling results ("auto" option selected) for the 130 *in situ* (U-Th)/He ages of sample D21 (Chapter 6), using DensityPlotter (Vermeesch, 2012). The finite mixture modelling method in DensityPlotter returns the two expected age peaks at *ca.* 80 and 110 Ma if and only if the "auto" option (equivalent to the "5 components" option here) is chosen.

When applied to a subset of the data set of sample D21 (n = 70 grains), created by random sampling without replacement as presented in Figure IV.14, mixture modelling methods do not yield more satisfactory results. Overall, both mixture modelling methods resolve the lower Campanian component at *ca.* 80 Ma. However, while the kernel density estimation and histogram of the data subset are similar to those of the entire data set over the 130-0 Ma interval, the age peak for the expected Lower Cretaceous component is displaced at *ca.* 128 Ma when the "auto" option is chosen in DensityPlotter (Figure IV.34). With Bayesmix, 10 or 11 components under the assumption of either Normal or Skew-t distributions are needed to obtain the two expected age peaks for Lower Cretaceous and lower Campanian components while there is little probabilistical support for such a large number of components (Figure IV.35).

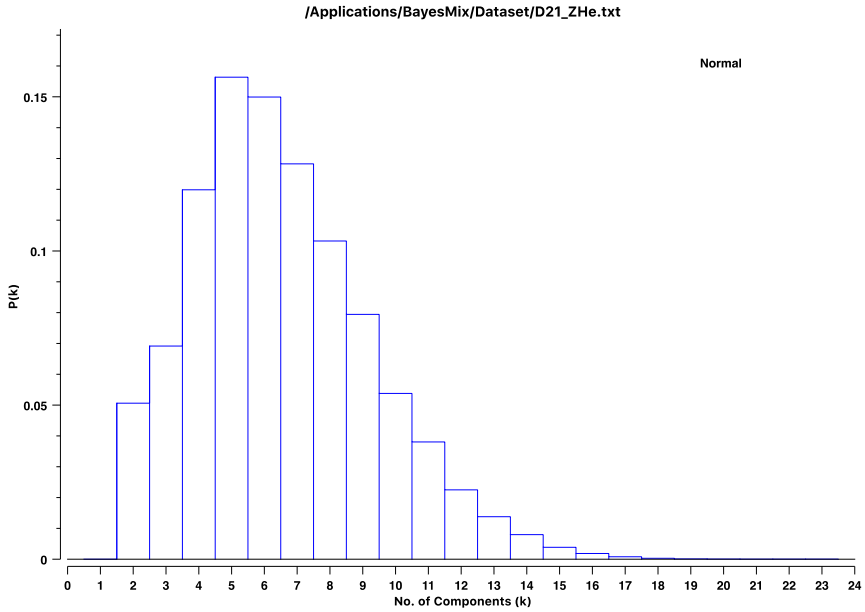

Figure IV.30: Posterior distribution (burn-in = post-burn-in = 200,000 iterations) for the 130 *in situ* (U-Th)/He ages of sample D21 when modelled using BayesMix under the assumption of Normal (Gaussian) distributions (simulation #1a). The distribution clearly favours 5 and 6 components, although 4 and 7 component models have relatively similar support probabilistically. In contrast, more than 10 components is inferred to be unlikely.

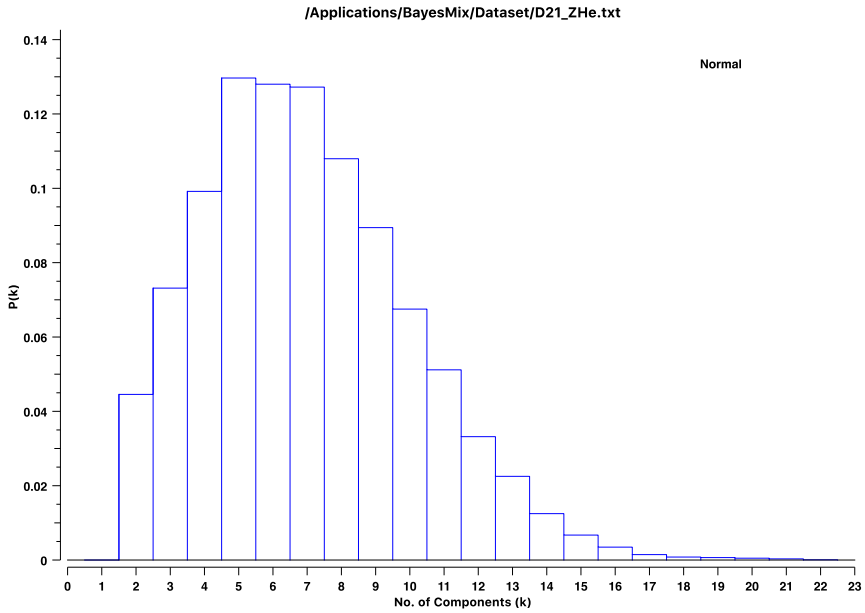

Figure IV.31: Posterior distribution (burn-in = post-burn-in = 200,000 iterations) for the 130 *in situ* (U-Th)/He ages of sample D21 when modelled using BayesMix under the assumption of Normal (Gaussian) distributions (simulation #1b). The distribution clearly favours 5, 6 and 7 components, although 4, 8 and 9 component models have relatively similar support probabilistically. More than 10 components is inferred to be unlikely, though.

Finally, another point to be made is that the range of data impacts mixture modelling results. A first example would be to consider an outlier at the upper end of the data range by adding artificially an age of 678 ± 37 Ma (but any older age works!) to the true data set of sample D21 (n = 131 grains). This inevitably results in ageing the Lower Cretaceous component (136 ± 2.5 Ma instead of 112.9 ± 2.5 Ma) with the mixture

modelling method implemented in DensityPlotter (Figure IV.36). In this example, nevertheless, no change in the output from BayesMix is noticed compared to previous situations: the posterior distributions and number of components to obtain the two expected age peaks under the assumption of either Normal or Skew-t distributions are still the same. The kernel density estimation and histogram do not change locally over the 130-0 Ma interval.

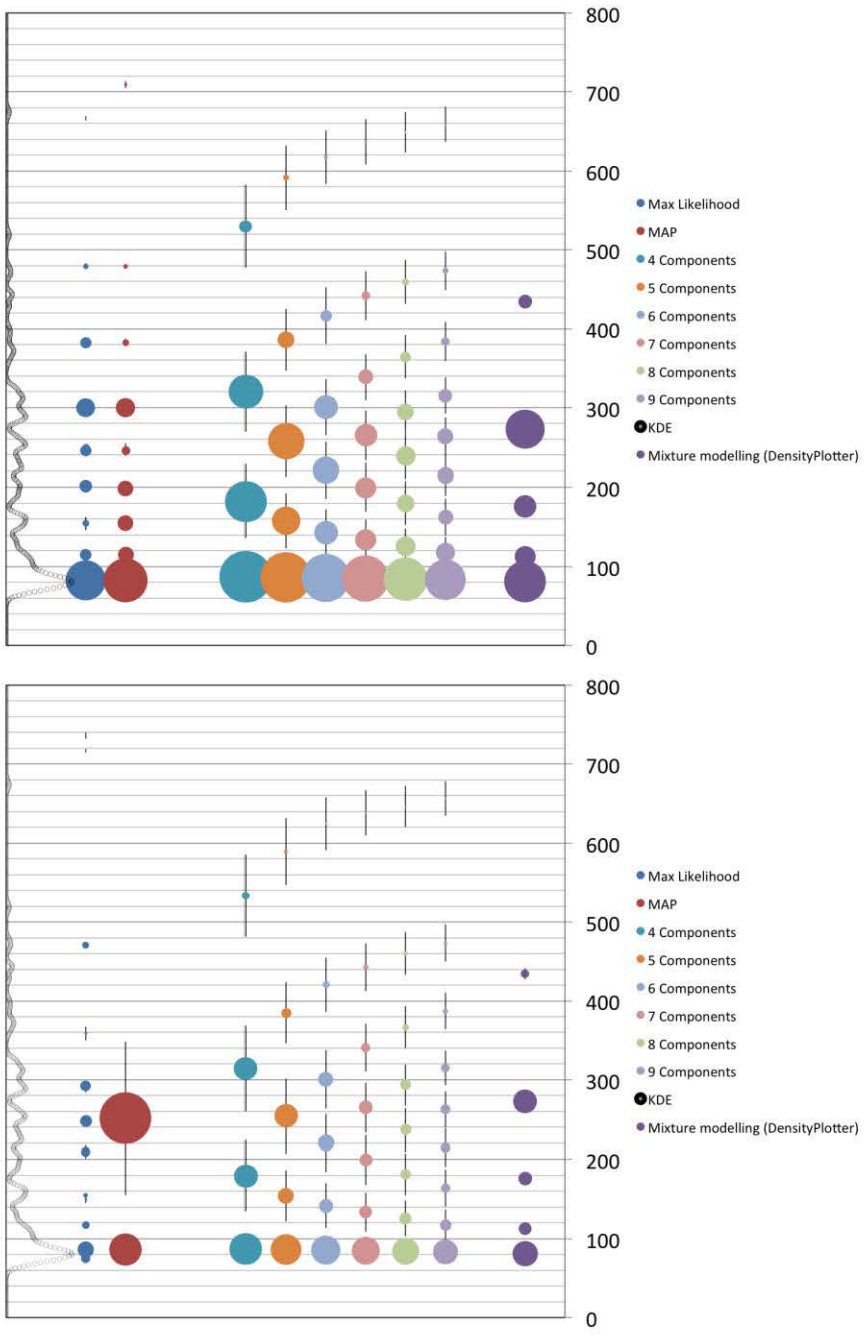

Figure IV.32: Compilations of the age modes (vertical scale is age in Ma) and their relatives proportions (data point size) obtained for different component models of the 130 *in situ* (U-Th)/He ages of sample D21 (top insert: simulation #1a; bottom insert: simulation #1b). Visual representation (KDE) is put for reference on the left. Results are obtained using BayesMix under the assumption of Normal (Gaussian) distributions if not specified otherly (e.g. "Mixture modelling (DensityPlotter)" obtained while selecting the "auto" option in DensityPlotter).

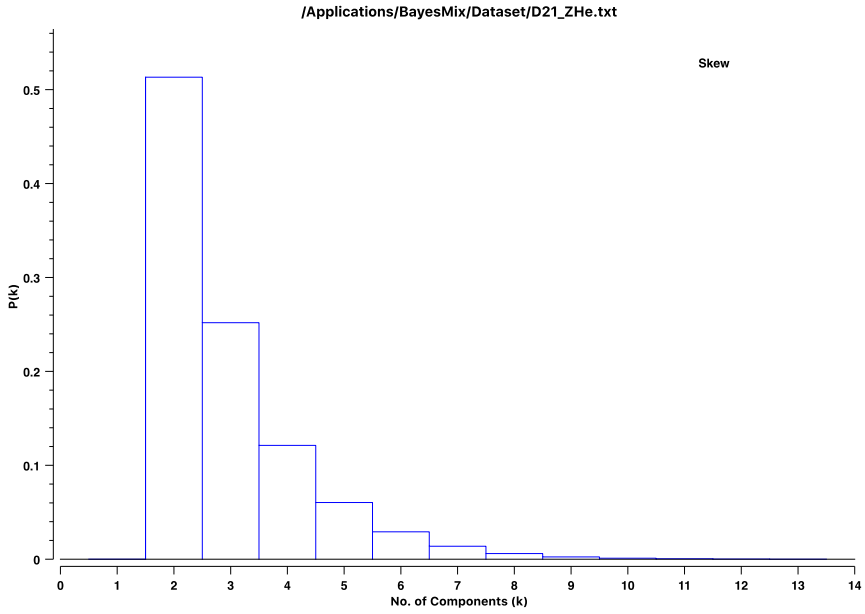

Figure IV.33: Posterior distribution (burn-in = post-burn-in = 200,000 iterations) for the 130 *in situ* (U-Th)/He ages of sample D21 when modelled using BayesMix under the assumption of Skew-t distributions (simulation #1b). The distribution clearly favours 2 components, although a 3 component models have relatively similar support probabilistically, while more than 5 components is inferred to be unlikely.

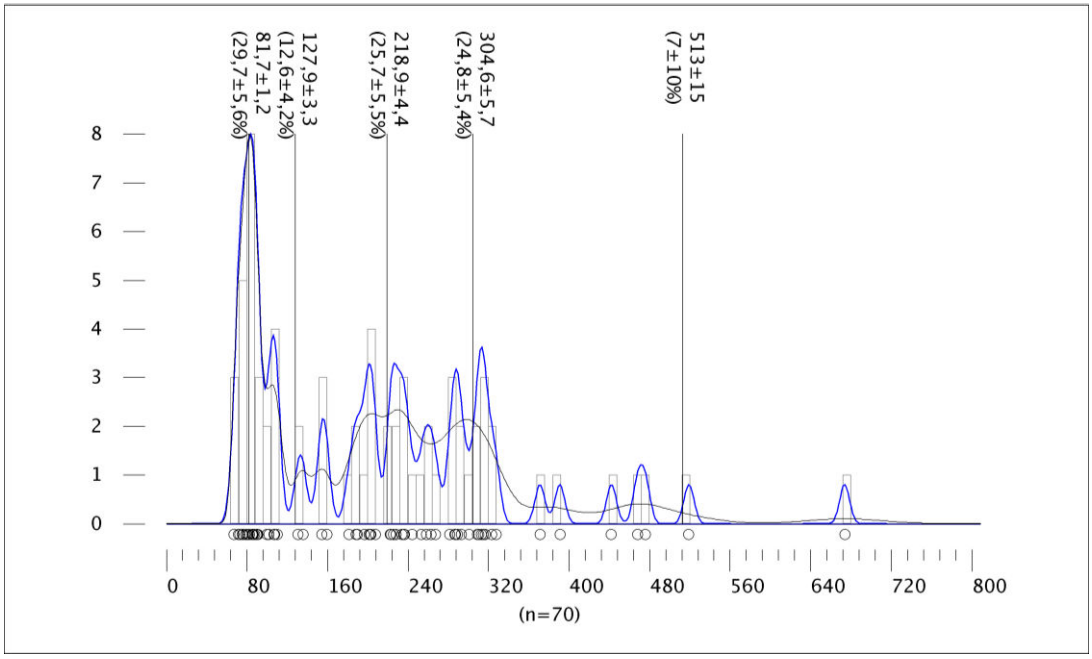

Figure IV.34: Visual representation (kernel density estimate in blue, bandwidth of 5 Ma; probability density plot in black; histogram, binwidth of 8 Ma) of and mixture modelling results ("auto" option selected) for the subset of 70 *in situ* (U-Th)/He ages of sample D21, using DensityPlotter (Vermeesch, 2012). The finite mixture modelling method in DensityPlotter returns the two expected age peaks at *ca.* 80 and 110 Ma if and only if the "auto" option (equivalent to the "5 components" option here) is chosen.

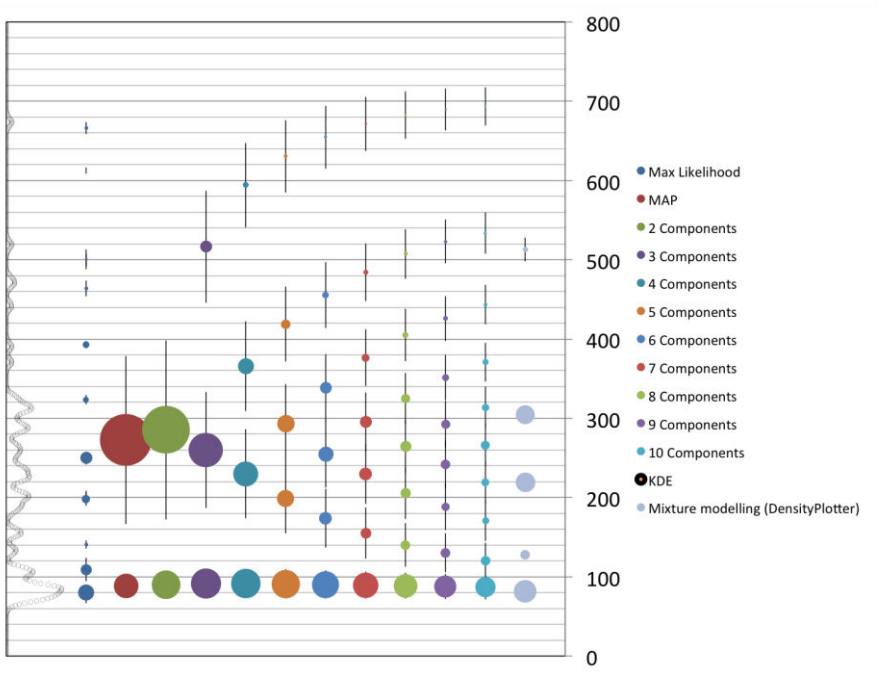

Figure IV.35: Compilation of the age modes (vertical scale is age in Ma) and their relatives proportions (data point size) obtained for different component models of the subset of 70 *in situ* (U-Th)/He ages of sample D21. Visual representation (KDE) is put for reference on the left. Results are obtained using BayesMix under the assumption of Normal (Gaussian) distributions if not specified otherly (e.g. "Mixture modelling (DensityPlotter)" obtained while selecting the "auto" option in DensityPlotter).

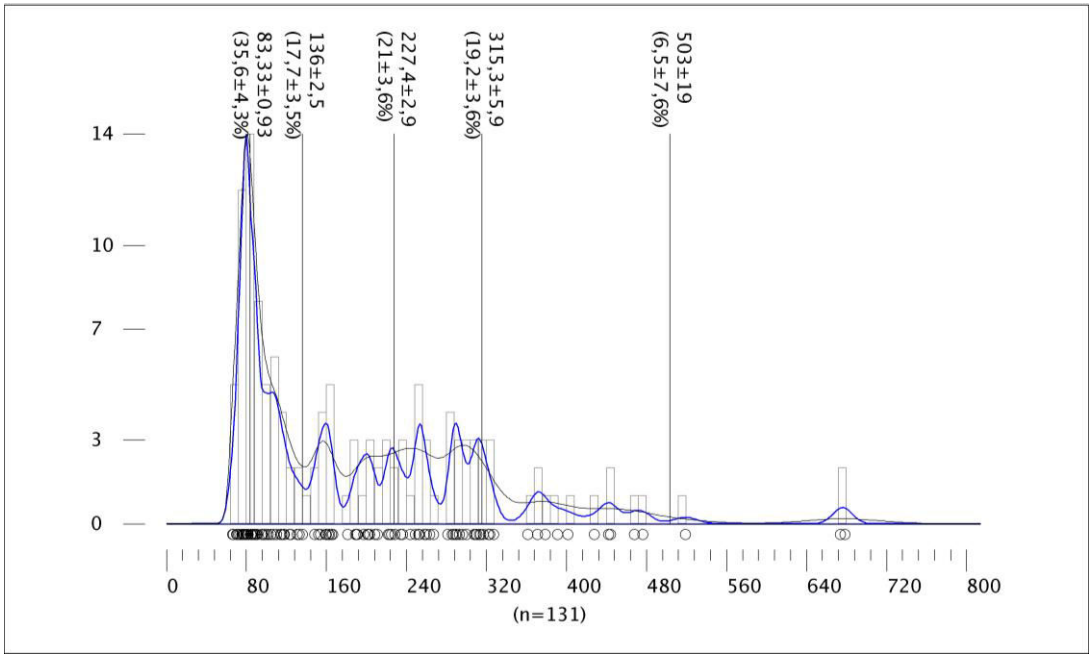

Figure IV.36: Visual representation (kernel density estimate in blue, bandwidth of 5 Ma; probability density plot in black; histogram, binwidth of 8 Ma) of and mixture modelling results ("auto" option selected) for the 130 *in situ* (U-Th)/He ages of sample D21 + an artificially added outlier at the upper end of the data range (678 ± 37 Ma). This leads to an older modelled Lower Cretaceous component (136 ± 2.5 Ma instead of 112.9 ± 2.5 Ma) and clearly shows that the range of data highly impacts mixture modelling results from current inversion methods implemented in DensityPlotter.

We may then also consider a subset with only ages between 0 and 130 Ma (n = 56 grains), drastically reducing the range of data. Again, the kernel density estimation and histogram do not change over the 130-0 Ma, preserving the peaks at 80 and 105 Ma. In contrast, the "auto" option in DensityPlotter yields 3 components at 75, 88 and 111 Ma, but these values are not unique, suggesting that fewer components are likely. The dangers of choosing the "auto" option have already been discussed by Vermeesch (2019) who warns that the solution returned by DensityPlotter gives the highest (log-) likelihood but may not be guaranteed to be the optimal solution. In this example, a 2-component model, indeed, exhibits peaks at 80 and 107 Ma. A number of 2 components is also favoured by the posterior distribution in BayesMix with the exact same ages.

IV.4.4.3 About the use of current mixture modelling methods to interpret (U-Th)/He data

In conclusion, it therefore seems quite challenging to compare mixture modelling results for two (U-Th)/He data sets if the latter have very different analytical uncertainties, different sizes or different natural complexities. This would be true if one compares results of two studies that would have used different methodologies (i.e. (U-Th)/He data with potentially different analytical uncertainties) or that would have been conducted in distinct areas. This should also be also true when comparing results from one sample to another in the same study. While mixture models appear to reasonably reproduce the observations (kernel density estimate and histogram) when measurement errors are typical of the *in situ* technique, as currently developped by Horne et al. (2016), they may lead to biased or misleading provenance interpretations when measurement errors are higher. Length of the data sets also appears to be of particular concern, especially when trying to resolve two closely spaced components in a naturally complex sample. Mixture models must therefore be used with caution, bearing in mind that robustness of the interpretations of detrital data in terms of provenance (notably lag time estimations) is directly conditioned by the way data are modelled. Ignoring the dependence of test statistics on uncertainties, for instance, may lead to statistical models which might make sense in a mathematical sense, but have little or no geological relevance. In particular, it is important to stress the facts that the tools currently available were primarily designed for fission-track analysis and U/Pb dating, and that the Bayesian Information Criterion (BIC) used in both DensityPlotter and BayesMix only seek to explain the variance in a dataset with a small number of model parameters (concept of statistical parsimony). As shown in the two case studies, the geological reality may be quite different, with a geological model providing a marginally worse statistical explanation of the data. This overall problem is actually not new, especially within the fission-track community where these points are well recognized. It has, however, drawn the attention of very few authors (Naylor et al., 2015).

In constrast, a kernel density estimation, by attributing a probability mass 1/n (n = sample size) at each measurement for equal statistical weight, by making no assumptions about the underlying functional form of the true density (non-parametric)

and by taking no account of measurement error that is considered to be noise, is fundamentally determined by the density of the data. Results of simulations in section IV.3.3.1 did show that the two components related to cooling events, albeit becoming poorly defined with larger uncertainties (*in situ* vs. conventional dating) or with consideration of slow cooling (conventional dating by nature), are supported by the denser fractions of the data. The geological reason for this is that rapid cooling leads to brutal changes in equilibrium conditions. The more rapid the cooling rates, the faster the changes, so that the consequences of these changes may outpace the effects of processes such as diffusion and thermal reset of radiation dammage that are slow and act at larger timescale (with typical larger time constant). This thus tends to reduce dispersion in the data that is mainly due to random grain-specific characteristics (for instance, composition and radiation damage) and is typical of what is expected for the partial retention zone. In absence of the tools to trade off statistical and geological parsimony in a routine manner, I therefore decide to use kernel density estimates as a tool not only to visually represent my detrital (U-Th)/He data, but also to visually identify peak age components (first-order interpretations).

As mentionned in section IV.4.2, the question to be addressed is: which bandwidth of the kernel to choose? This point is similar to what applies to the choice of binwidth in histograms. Choosing a too low bandwith will have a tendency to undersmooth the distribution while a too high bandwidth will lead to oversmoothing. This raises additional questions including: which modes/peaks/bumps/features observed in a smooth of data are really there? What is the important underlying structure as opposed to noise artefacts, or artefacts attributable to sampling variability? Should the bandwidth selection be a data-based choice? Should bandwidth selection algorithms be used whilst they sometimes make assumptions and approximations that contradict the non-parametric nature of the kernel density estimation method? Rudge (2008) highlights these points and shows why these questions should be considered: “There can be good reasons for manually choosing a smaller bandwidth: for example, if one is interested in small scale features of the density function, or if the density is thought to have well separated peaks. However, there is always the danger that many of the peaks found with a small bandwidth are artefacts of the sampling and do not reflect the true distribution. Even with an automatic choice of bandwidth, a few peaks may be seen that do not reflect the true distribution.” Building onto a large body of statistical literature regarding the statistical problem of feature significance (e.g. Chaudhuri and Marron, 1999), Rudge (2008) emphasises the complementary use of the tool SiZer (Significant Zero crossings of the derivative; Chaudhuri and Marron, 1999). He thus provides the community with an alternative solution: considering all possible bandwidths rather than choosing only one of them and looking at whole spectrum of smooths (the SiZer map; Figure IV.37). This gives the opportunity to rapidly explore the different structures that occur at different smoothing levels. Although a proper investigation of all the SiZer fundamentals falls outside the scope of this thesis, I used the SiZer technique as one way of deciding which peaks are significant and getting a sense of potential bias in my interpretations.

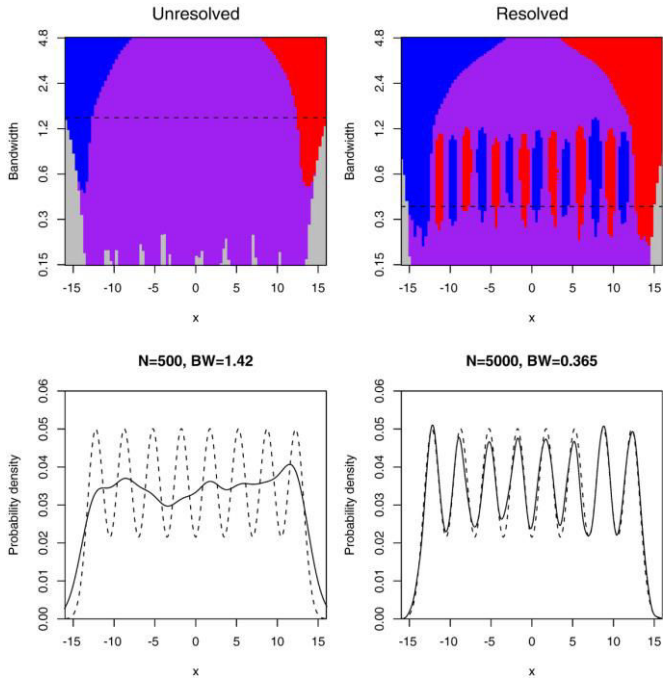

Figure IV.37: SiZer map (top) and kernel density estimate (bottom) for synthetic data (from Rudge, 2008). The SiZer analysis relies on the basic idea that a bump in a distribution is characterized by an increase followed by a decrease, so that the sign of the slope of the smooth can capture many features of interest. A SiZer map is built as a color map and represents statistical inference on slopes over a certain scale space defined by the range of bandwidths. The bandwidth is on a logarithmic scale. Blue, red and purple regions represent regions where slope is significantly upwards (strongly positive derivative), significantly downwards (strongly negative derivative) and insignificant (zero, or near zero, derivative), respectively. Gray regions indicate where there are not enough data for inference, based on computing thresholds. The dashed horizontal line shows the bandwidth used in the kernel density estimate below. Peaks and troughs are clearly identified from the blue-red-blue-red pattern for the cartoon on the right, showing that we are able to resolve the structure of the true density from the sample. Notice that the peaks and troughs in the density estimate lie in the purple regions between red and blue on the SiZer map.

IV.5 Lab implementation of the *in situ* laser (U-Th)/He technique

IV.5.1 General workflow and instrumentation

The workflow that I followed for *in situ* laser ablation dating during my doctoral work is:

(1) Isolating zircon grains from the 50- to 250-µm fraction using conventional mineral separation techniques, including crushing, grinding, sieving, and water table concentration, standard heavy-liquid density, and magnetic susceptibility separation techniques.

(2) Randomly handpicking grains for analysis according to the following conditions: (i) of any shape (euhedral, rounded, broken), (ii) of any size (length, width, and thickness) >60 µm, and (iii) of any transparency/opacity/colour. An additional condition applied to very small grains: having visibly fracture-free and inclusion-free "cores" when inspected under a binocular microscope. The latter condition may sound

contradictory with the fact that *in situ* laser ablation dating has the advantage to overcome grain selection bias inherent to conventional (bulk/whole grain) dating. Nonetheless, this condition only applied to grains that were so small that I would not have been able to avoid cracks and inclusions while still locating the laser pits in the core of the grains - which is the primary objective of the *in situ* dating method used in this thesis! -.

(3) Mounting grains in Teflon foils and polishing them by hand for laser ablation analyses. Sandpaper with grit sizes of 1,200 and 2,400 were used to grind the grains, which were subsequently polished using polishing clothes and diamond paste with 6-, 3-, 1- and 0.25-µm grain sizes.

(4) ^{4}He extraction and measurements were performed at CRPG (Vandoeuvre-les-Nancy, France), using a New Wave Research NWR213 Nd: YAG automated deep-UV 213 nm laser ablation system coupled to an MKS Microvision 2 quadrupole mass spectrometer equipped with an RGA (Residus Gas Analysis) sensor; we use the Ultra High Vacuum (UHV) cell developed with University College London (Pieter Vermeesch) that has a 52 mm sapphire window tested to $<10^{-10}$ arm-cc/sec.

(5) ^{4}He volume pit measurements were made at Institut Jean Lamour (Nancy, France), using a ZEISS LSM 510 laser scanning confocal microscope.

(6) U, Th, Sm and Pb analysis was conducted at Georessources (Vandoeuvre-les-Nancy, France), using a Geolas Pro automated high-end deep-UV 193 nm optical system equipped with a nanosecond excimer laser coupled to an Agilent 7500 quadrupole-based ICP-MS.

The workflow is similar to that described previously in the literature (Boyce et al., 2006, 2009; van Soest et al., 2008; Vermeesch et al., 2012; Tripathy-Lang et al., 2013; Evans et al., 2015; Horne et al., 2016). Nonetheless, we used a solid-state Nd: YAG laser rather than a 193 nm ArF excimer laser system. We also decided not to perform chemical characterization of crystals by backscattered electron, cathodoluminescence, and/or Raman mapping prior to dating. The reasons for both these choices will be shortly developed below.

Aiming at possibly conducting fission-track analysis in addition to (U-Th)/He - U/Pb double dating in the future, zircon grains were mounted in Teflon foil. I did try to use indium as Boyce et al. (2006) and Vermeesch et al. (2012) but I could not really polish grains once they were mounted in indium (they have to be polished beforehand and mounted flat- tough to do!). Moreover, polished grains were not flat in the indium, so that I had issues with pit volume calculations. I also had trouble tracking grains for laser ablation due to the high light reflectivity of indium. In contrast, although polishing Teflon is challenging because it is very thin, using Teflon has given me nice grains with flat, polished faces and simplified the ablation and pit volume measurement steps. The Teflon itself also has to be flat around the grains for good pit volume calculations. The indium and Teflon had roughly the same baseline.

IV.5.2 The New Wave NW213 Nd: YAG laser ablation system

IV.5.2.1 General overview about lasers

There are five general categories of lasers: gas, liquid, plasma, semiconductor, and solid-state. For decades, the gas type has been successfully used in a wide variety of applications as a result of its ability to both generate a large variety of excimer-dependent emission wavelengths in the ultraviolet range and deliver very stable and high energy density beams. In particular, 193 nm Argon-Fluorine excimer lasers were found to be perfectly suited for *in situ* (U-Th)/He dating of minerals commonly used in geo-thermochronology (monazite: Boyce et al., 2006, 2009; apatite: van Soest et al., 2008; and zircon: van Soest et al., 2008; Vermeesch et al., 2012; Tripathy-Lang et al., 2013; Evans et al., 2015; Horne et al., 2016). As shown by these authors, such lasers produce nice, well-defined cylindrical ablation pits, facilitating measurement of pit volume.

Solid-state lasers represent the other widely used, albeit a little bit on the side, type of lasers. These lasers use a solid medium that is typically made from crystal, glass, or ceramics, and acts as a host to which a dopant is added (ionic medium). This medium is excited by optical pumping to produce the light that powers the laser. Among solid-state lasers is the most powerful Nd: YAG system which uses a Nd: YAG crystal (Neodymium-doped: Yttrium, Aluminium Garnet) as active medium. This crystal is one of the very few solid-state crystals that can produce both continuous and pulsed outputs. Because it can resist the extreme heat generated by a continuous wave pumping source, it can pulse very rapidly (up to 200 pulses per second contrary to 2-3 pulses per second with other media; https://www.daenotes.com/electronics/microwave-radar/solid-state-lasers).

IV.5.2.2 Principal motivations for using solid-state lasers

Solid-state Nd: YAG lasers present many advantages over gas lasers. First, they are more rugged and compact than gas lasers. Second, they represent a cost-effective option in the long term. They lower operating costs by eliminating the use of gas and associated expensive gas logistics. Preliminary findings also show that solid-state lasers may offer up to twice the expected lifespan of gas lasers (10,000 hours; Rauscher, 2018). Finally, significant technical progress (about the power, accuracy, and beam quality, and emission wavelength generation) has been made in recent years regarding solid-state lasers, so that their efficiency and performance are now on a par with those of gas lasers.

In 2015, preliminary experiments were conducted to compare ablation pit shapes and bottoms obtained with the latest generation New Wave NW213 Nd: YAG laser ablation system and the previous New Wave UP213 Nd: YAG system used by Pieter Vermeesch for noble gas work at University College of London. These experiments showed that the new solid-state Tempest™ 213 nm laser has been engineered so that the beam from the fundamental (1st harmonic, 1064 nm) to the final (5th harmonic, 213

nm) output is completely flat-topped for the flattest craters at the sample surface. I will present below the drilling experiments I performed.

IV.5.2.3 Drilling experiments and choice of laser ablation settings

To measure pit volumes, I used a ZEISS LSM 510 laser scanning confocal microscope that was at disposal at the beginning of my doctoral project. This instrument had proved to be both accurate and precise at measuring ablation pit volumes since it had yielded similar pit volume estimations to those by X-rays tomography for a bunch of typical *in situ* ^{4}He holes drilled into a 1 cm^2 small Si wafer. Nevertheless, measuring pit volumes with such an instrument is quite time-consuming as good-resolution imaging takes 3 to 5 minutes with additional time for manual treatment. For typical amounts of grains that should be analysed to be statistically meaningful (>70, say; Vermeesch, 2004), I therefore aimed at measuring pit volumes with this technique for only one fourth of the grains.

I believed this to be reasonable in keeping the protocol relatively time-efficient without compromising the quality of the data. As this simplification requires volume estimations to be quite similar from one grain to another with the same laser ablation settings, it was crucial to test (1) the effect of the various laser settings (laser energy level, repetition rate, number of pulses and spot size) on ablation quality and (2) the ablation repeatability and reproducibility of the New Wave NW213 Nd: YAG laser ablation system.

IV.5.2.3.1 Spot size and ablated pit depth and volume

I first investigated ablation repeatability (10 ablations) by testing the effect of using 20-80 µm spot sizes in 10 µm steps on both the measured ablation depth and volume. Results are presented in Appendix 1 and Appendix 2 for a relatively homogeneous (in-house investigations), centimetre-scale zircon crystal, and in Appendix 3 and Appendix 4 for detrital zircon grains (Pyreneean detrital samples). Regarding depth, respective total errors are 2-3% and 3-5% (Appendix 1 and Appendix 3). Regarding volume, they are 2-3% and 3-6% (Appendix 2 and Appendix 4). For a given laser energy (20%), repetition rate (10 Hz) and pulse count (100 and 200 pulses for experiments on the homogenous crystal and the different grains, respectively), mean measured radii are found to be smaller than expected spot radii, except for spot sizes of 20, 30 and 40 µm for which measured and expected values are very close to each other (Figure IV.38 and Figure IV.39). These gaps are more pronounced for the homogeneous crystal, but this may be simply due to the lower pulse count used. For both ablated materials the measured volume to measured depth ratio increases linearly with increasing square measured radius. The proportionality coefficient is close to the expected value of the number π, albeit the more homogeneous the material, the closer to the π value the coefficient. Nonetheless, the measured volume to measured depth ratio is always found to be lower than that expected for perfectly cylindrical pits with similar diameters (solid straight line). It is important to notice that the smaller the spot size, the

closer to the ideal values our measurements on heterogeneous material. I thus chose to work with a spot size of 30 µm.

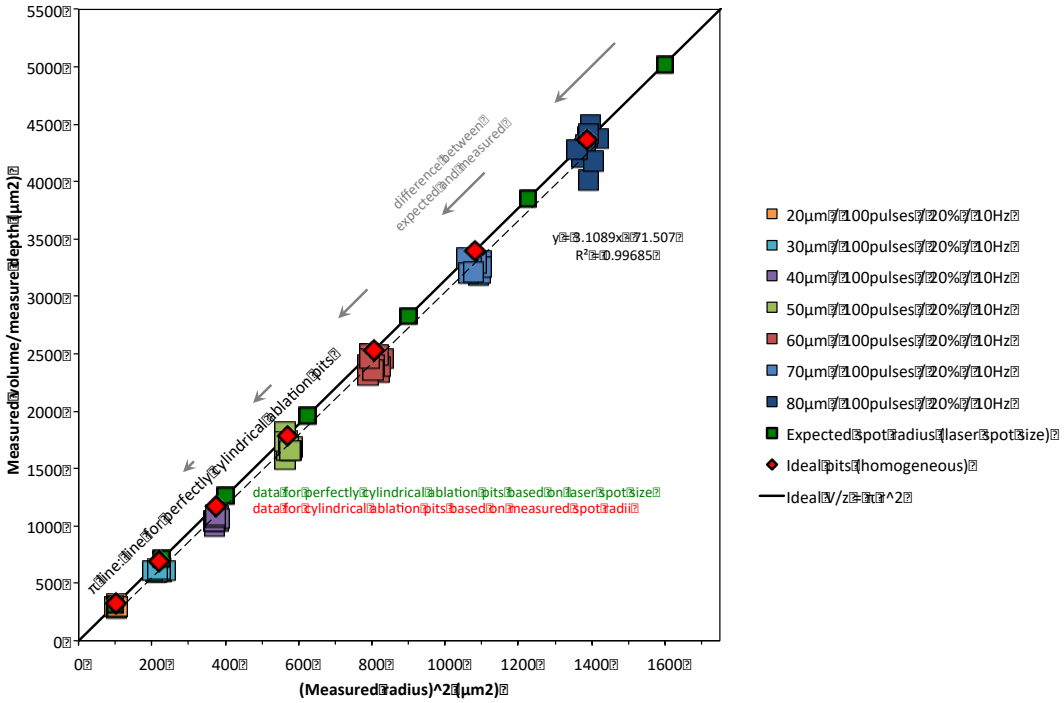

Figure IV.38: Laser ablation repetability results for variable spot sizes (20-80 µm spot sizes in 10 µm steps, fixed laser energy of 20%, fixed repetition rate of 10 Hz, fixed pulse count of 100) for a centimetre-scale zircon crystal considered as homogeneous. Results are displayed as measured volume to measured depth ratios vs square measured radii. The solid straight line represents the relationship satisfied by perfectly cylindrical ablation pits, with a slope equal to π. Dark green squares plot on this line and represent the volume to depth ratios we expect for perfectly cylindrical ablation pits based on our choice of laser ablation spot sizes. Red diamonds also plot on the line and represent the volume to depth ratios we should get for perfectly cylindrical ablation pits based on mean measured radii. Grey arrows highlight the fact that mean measured radii are found to be smaller than expected spot radii. Results show that the lower the laser spot size used, the lower this difference.

IV.5.2.3.2 Laser energy/pulse count and ablated pit depth and volume

I then investigated the effect of using 2-20% energies in 2% steps on the measured ablation depth. An equivalence output power (%)-fluence (J/cm²) is provided for two given repetition rates in Table IV.3 and Table IV.4. For the first series of experiments, the spot size and repetition rate were taken as constants (30 µm and 4 Hz, respectively) while the number of pulses varied (50-500 pulses, 50 pulses increment). Experiments were conducted on the homogeneous zircon crystal. Results are presented in Appendix 5 and Appendix 6. Appendix 5 shows that depth increases linearly with the number of pulses at a given energy, while Appendix 6 indicates that depth follows a logarithmic law with increasing energy at a constant pulse count.

A second series of experiments was conducted on naturally different grains (Fish Canyon Tuff zircons). Energy-pulse count combinations were derived from the

relationships in Appendix 5 and Appendix 6 to target a depth of 12-13 µm. For a given spot size (30 µm) and a fixed repetition rate (4 Hz), 6 energy settings (4, 6, 8, 12, 16 and 20%) and their corresponding pulse count to get pits about 12-13 µm deep (370, 300, 260, 220, 200 and 180 pulses) were tested. 30 grains were ablated per combination to test repeatability. Results are presented in Figure IV.40 and Figure IV.41. They show that for each combination the measured depth is close to the targeted one, ranging from 11 to 14 µm (Figure IV.40). Total errors are 5-10%. For a given energy level, results also suggest that the higher the ablated pit depth, the larger the pit volumes. But most importantly, results indicate that for a same depth, the higher the energy level used, the larger and closer the volume of the ablated pits to expected values for perfectly cylindrical pits. Figure IV.41 allows closer inspection on this point. Firstly, mean measured radii are systematically found to be far smaller than the expected spot radius when used energy is below 12%. On the contrary, they are very close to the expected value for 12, 16 and 20% energy levels. Secondly, it is important to notice that below 16% energy the measured volume to measured depth ratio plots far away from the ideal line, indicating underestimation of pit volumes. Only for 16% and 20% is indeed observed such a ratio to be very close to the ratio for perfectly cylindrical pits. Based on my observation of confocal microscopy images, this is consistent with the fact that ablated pit surface gets more circular and pit shape more cylindrical with increasing energy. I therefore chose to work with 20% energy.

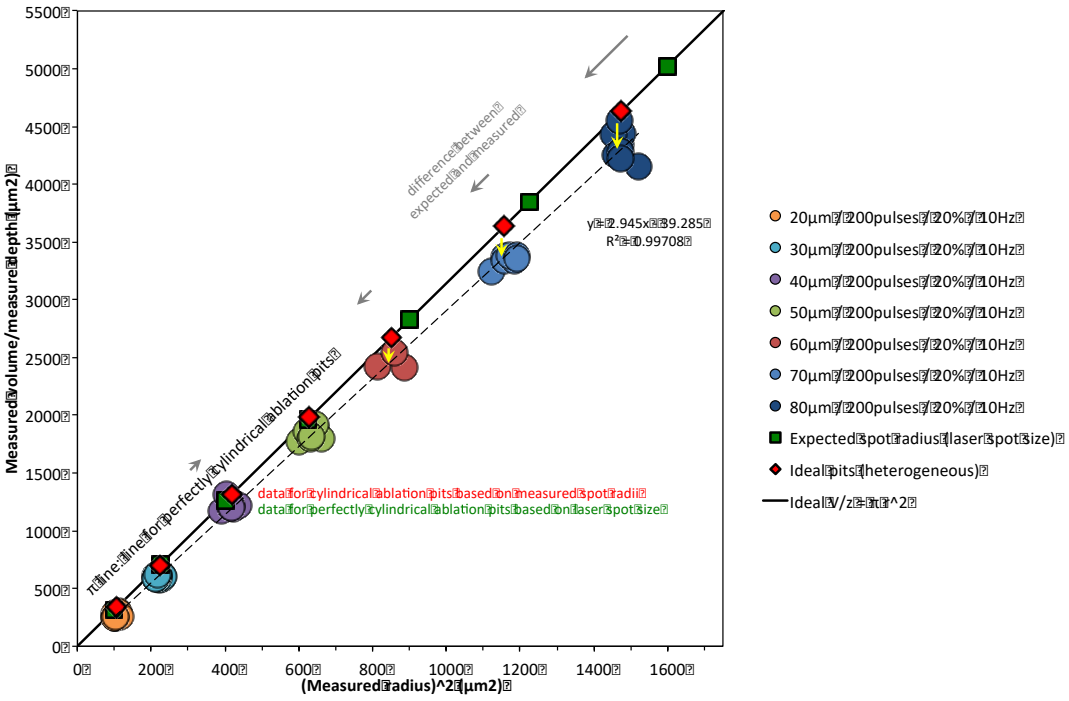

Figure IV.39: Laser ablation repetability results for variable spot sizes (20-80 µm spot sizes in 10 µm steps, fixed laser energy of 20%, fixed repetition rate of 10 Hz, fixed pulse count of 100) for different zircon grains. Results are displayed as measured volume to measured depth ratios vs square measured radii. Results show that the lower the laser spot size used, the lower the difference between expected and mean measured radii (grey arrows), and the more cylindrical the shape of the ablation pits (yellow arrows). See Figure IV.38 for description.

energy (%)	fluence (J/cm2)
2	0.9
4	1.6
5	2.25
6	2.85
8	3.7
10	4.55
12	5.5
14	6.5
16	7.6
18	8.4
20	9.5

Table IV.3: Equivalence output power (%)-fluence (J/cm²) for a repetition rate of 4 Hz.

energy (%)	fluence (J/cm2)
2	0.9
4	1.7
5	2.3
6	2.9
8	3.8
10	4.7
12	5.65
14	6.6
16	7.8
18	8.8
20	9.9

Table IV.4: Equivalence output power (%)-fluence (J/cm²) for a repetition rate of 10 Hz.

IV.5.2.3.3 Repetition rate and ablated pit depth and volume

Finally, I designed some experiments to test the effect of repetition rate on ablated pit volume and depth. A series of experiments was conducted on the homogeneous zircon crystal. Spot size is taken as a constant (30 μm). For a repetition rate of 1 Hz, the linear increase in depth as a function of the pulse count is observed (tests at 50-500 pulses, 50 pulses increment), irrespective of the energy level (2, 5, 8 and 10%; Appendix 7). Volume also increases linearly with increasing pulse count, and as a matter of fact, with depth (Appendix 8 and Appendix 9). Despite the much fewer measurements for repetition rates of 2 Hz and 4 Hz (only at 250 and 500 pulses) similar trends seem to be displayed, irrespective of the energy level (2, 5, 8 and 10%; Appendix 10 and Appendix 11). It can be finally noticed that the ablated pit volume and depth do not depend at first order on the repetition rate used (Appendix 12). Though, it may be argued that the higher the repetition rate, the slightly shallower the ablated pits for a similar volume. In other words, the higher the repetition rate, the slightly larger the pit volumes at a given depth. Figure IV.42 allows closer inspection on this point. Firstly, it seems that at higher repetition rates, mean measured radii get closer to the expected spot radius. Secondly, the measured volume to measured depth ratio gets closer to the ratio for perfectly cylindrical pits with increasing repetition rates. Based on my observation of confocal microscopy images, this suggests that the higher the repetition rate, the slightly more cylindrical the pit shape. Nonetheless, Figure IV.43 shows that no significant difference is observed when two different repetition rates (4 Hz and 10 Hz) are used at relatively high energy (20% energy, 180 pulses and 30 μm spot size). I chose to work with a repetition rate of 10 Hz (faster analysis).

Figure IV.40: (next page) Laser ablation repetability results for variable energy-pulse count combinations (fixed laser spot size of 30 μm, fixed repetition rate of 4 Hz) for different zircon grains. Results are displayed as measured volume vs measured depth. The solid straight line represents the relationship satisfied by perfectly cylindrical ablation pits, with a slope equal to π. The two yellow diamonds represent the volume we expect for perfectly cylindrical ablation pits with depths of 12.5 and 13.5 μm. The blue arrow highlights the fact that the higher the laser energy used, the lower the difference between expected and measured volumes, and the more cylindrical the shape of ablation pits.

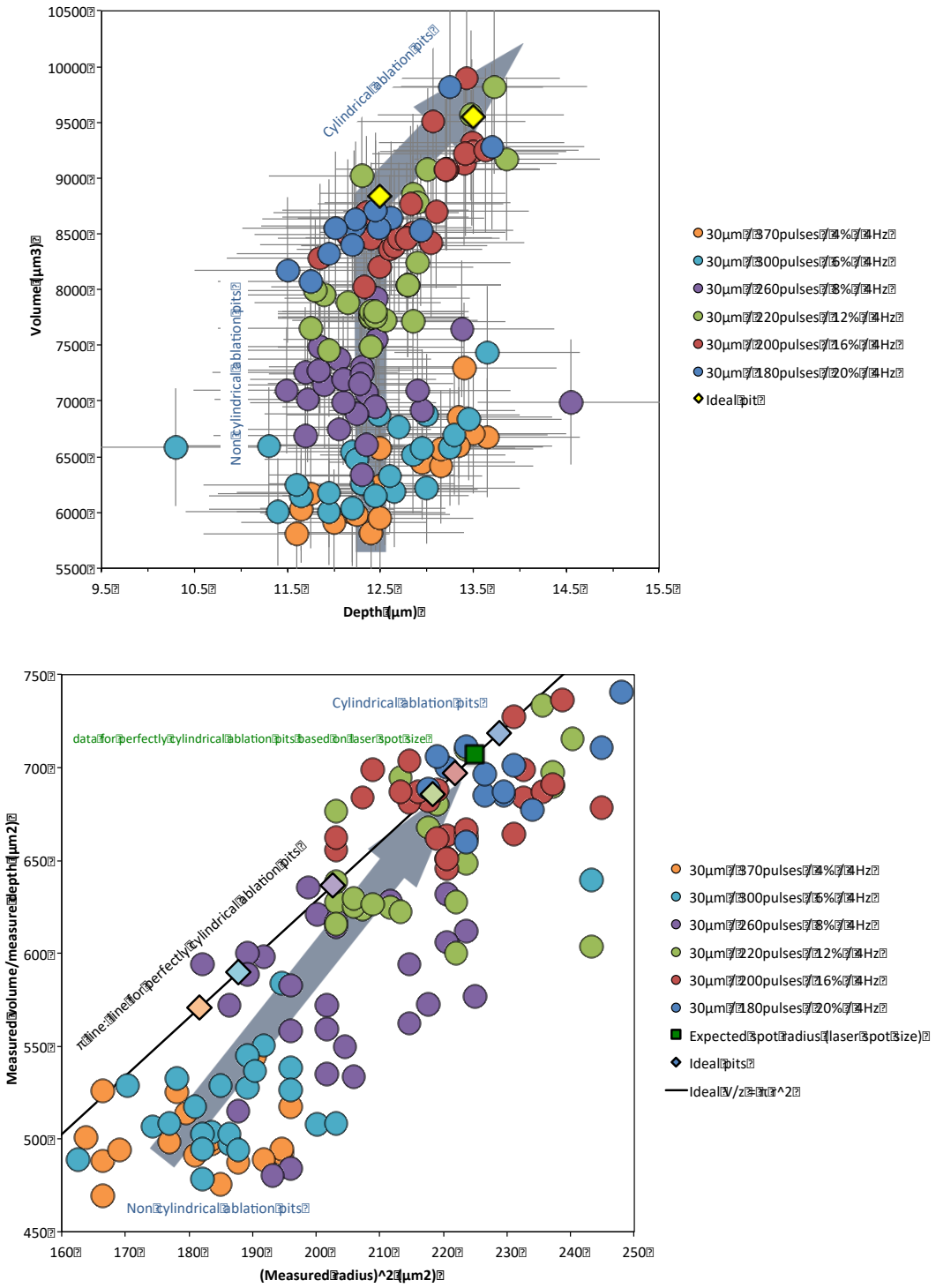

Figure IV.41: Laser ablation repetability results for variable energy-pulse count combinations (fixed laser spot size of 30 µm, fixed repetition rate of 4 Hz) for different zircon grains. Results are displayed as measured volume to measured depth ratios vs square measured radii. The solid straight line represents the relationship satisfied by perfectly cylindrical ablation pits, with a slope equal to π. The dark green square plots on this line and represents the volume to depth ratios we expect for perfectly cylindrical ablation pits with a radius of 30 µm (laser spot size). Coloured diamonds also plot on the line, each of them with the colour specific to the energy-pulse count combination tested. They represent the volume to depth ratios we should get for perfectly cylindrical ablation pits based on mean measured radii. The blue arrow highlights the fact that the higher the laser energy used, the lower the difference between expected and mean measured radii, and the more cylindrical the shape of ablation pits.

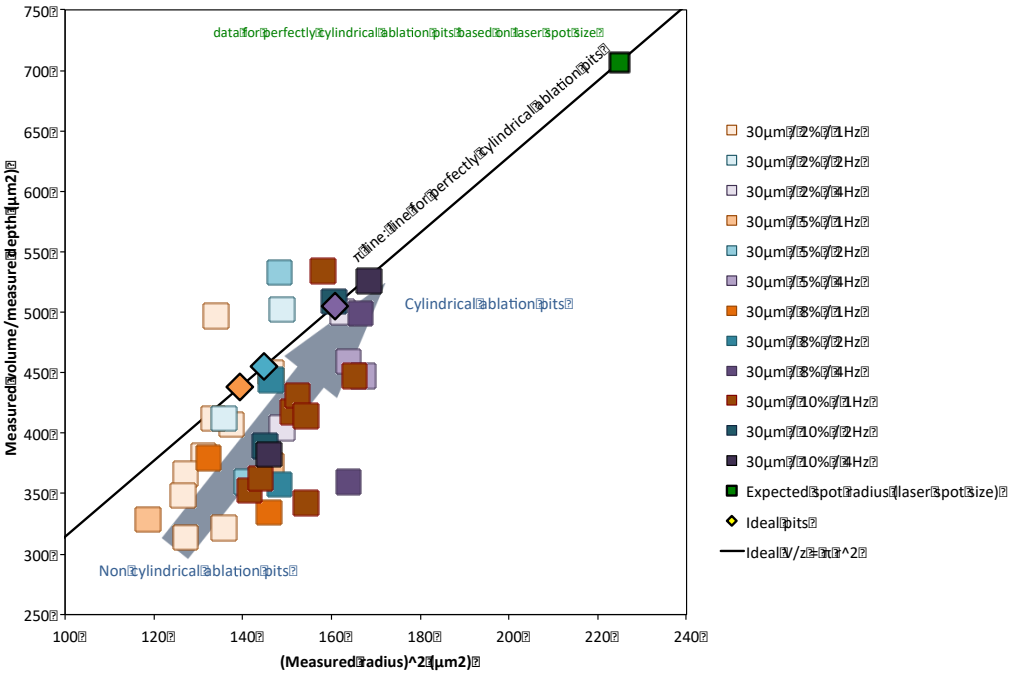

Figure IV.42: Laser ablation results for the homogeneous zircon with variable energy-repetition rate combinations (fixed laser spot size of 30 µm). For each combination, the number of pulses varied (50-500 pulses, 50 pulses increment). Results are displayed as measured volume to measured depth ratios vs square measured radii. The blue arrow highlights the facts that the shape of the ablation pits gets cylindrical and the mean measured radius gets closer to the expected spot size with increasing repetition rate (first order), but also energy and pulse count (second order). Symbols description is analogous to Figure IV.41.

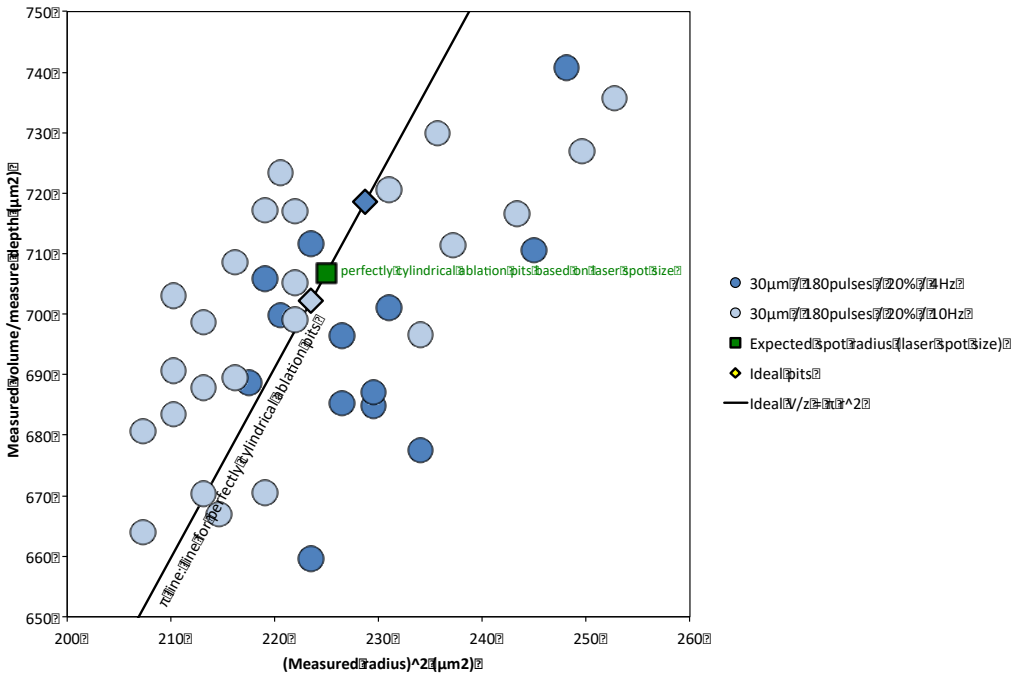

Figure IV.43: Laser ablation results for different zircon grains at repetition rates of 4 and 10 Hz (fixed laser spot size of 30 µm, fixed laser energy of 20%, fixed pulse count of 180). Results are displayed as measured volume to measured depth ratios vs square measured radii. At fixed laser energy of 20% and spot size of 30 µm, no significant difference is observed regarding ablation pit shape when working at either 4 Hz or 10 Hz. See Figure IV.41 for symbols description.

IV.5.3 Noble gas extraction/purification vacuum line and ^{4}He measurements

The noble gas extraction line implemented at the CRPG in the framework of my doctoral project is presented in Figure IV.44. In order to measure noble gas abundances by (quadrupole) mass spectrometry, in particular ^{4}He from ablated matrix, we used the isotope dilution method.

The isotope dilution method requires a noble gas spike to be prepared, enriched in the rare isotopes, such as ^{3}He in our case. Known amounts of this enriched isotope are stored in a reservoir attached to the extraction line (Figure IV.44). Before introducing an aliquot of gas samples through the gas inlet, a pipette of the ^{3}He spike is introduced into the system. Then the noble gases are extracted from the sample, with thorough mixing of the spike gas with the extracted gases. After mixing of the sample and spike noble gases, elemental fractionation of noble gases does not affect the analysis, since the mixed spikes behave identically to the natural isotopes. Precision of noble gas abundance measurements using the isotope dilution method is therefore limited to the accuracy of the isotopic ratio of the natural isotope to the spike isotope by the quadrupole mass spectrometer.

The noble gas extraction line used in this Thesis was initially built on previously existing purification facilities connected to a dedicated sector-type noble gas mass spectrometer for conventional (U-Th)/He dating (Chapter 5). Robust calibrations of the line and the ^{3}He spike to be used for laser ablation *in situ* (U-Th)/He dating were done by determining helium contents by the peak height method using two standard gases: a lab-made air standard (mixture of known amounts of isotopes) with He = 2 x10^{-9} mol per shot, and a tank helium standard with He = 3 x10^{-8} mol per shot.

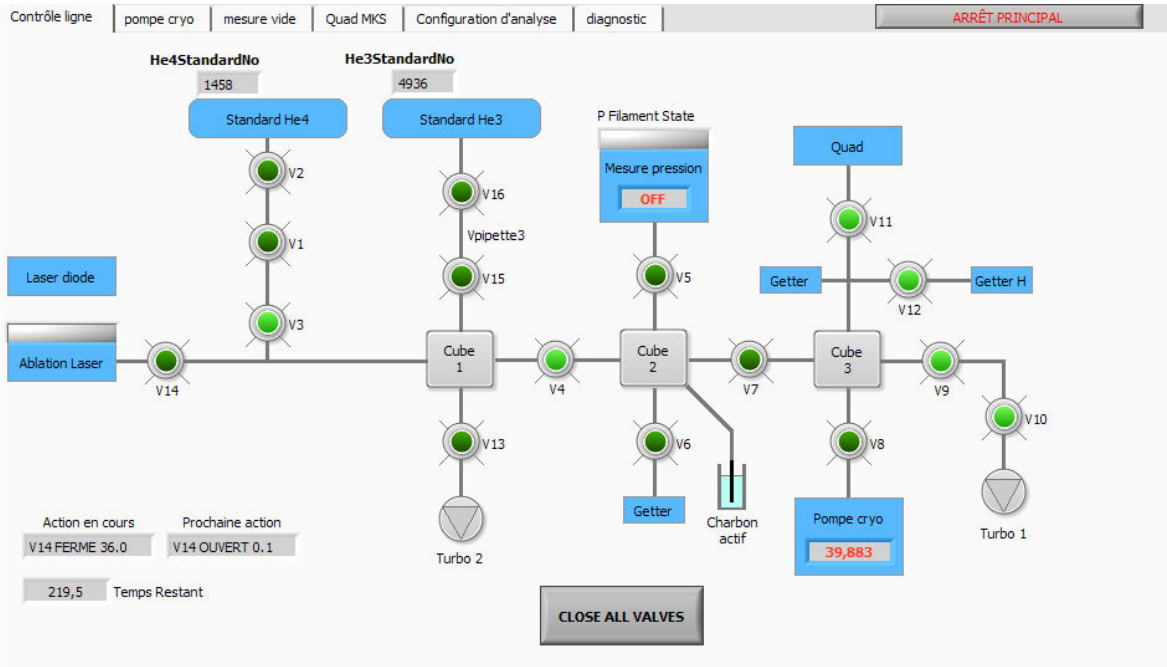

Figure IV.44: Schematic diagram of the noble gas extraction vacuum line implemented during this doctoral project.

Around the same time in 2017, we changed the sector-type mass spectrometer by a quadrupole mass spectrometer, modified the line geometry and connected the laser ablation system. As the line had changed, this required a new calibration. Through this operation, the lab-made air standard was partly pumped due to a technical problem on the valves isolating the standard from the line. As the Fish Canyon ash-flow tuff is used in many noble gas laboratories worldwide as a standard for (U-Th)/He dating (and other thermochronometric systems including $^{40}Ar/^{39}Ar$ and fission-track on various minerals; e.g. Tagami et al., 2003; Dobson et al., 2008; Danhara and Iwano, 2013; Gleadow et al., 2015; Horne et al., 2016), we decided to check line calibration using Fish Canyon Tuff (FCT) zircon standards and other fast-cooled in-house volcanic Ethiopian Chifra tuff (CHIFF) zircons. The calibration thus involved finding/adjusting the spike initial ^{3}He abundance for each analytical sequence of zircon standards in order to obtain the generally accepted age for Fish Canyon Tuff zircon standards (*ca.* 27.3 Ma; Dobson et al., 2008; Horne et al., 2016) and Chifra tuff zircons (*ca.* 8 Ma; Deiller and Pik, unpublished). This value was 4.6 $x10^{-13}$ spike initial ^{3}He moles.

Once calibration was successfully made early 2017, I started running ablations on detrital Pyrenean samples. A typical analysis sequence started with three gas standards (^{4}He measured over the same expanded volume as a sample) followed by a line blank (same measurement, without any ablation), a gas standard, a line blank, a gas standard, a line blank, a gas standard and a line blank (in total, 6 gas standards and 4 line blanks for quality check). Then ten unknown zircons were analysed, with a gas standard and a line blank run every ten unknown zircon ablations. Every detrital Pyrenean zircon ablation was run using the same laser settings for ^{4}He extraction and measurement: a laser spot size of 30 µm, a repetition rate of 10 Hz, a pulse count of 200 pulses, and an output laser power of 20%.

Some months after the end of my analytical work, early August 2018, the extraction line was connected to another analytical system: a diode laser system for conventional (U-Th)/He dating. First results on other Pyrenean zircons (thermal history relatively well-known) dated in the conventional way indicated ages far too young, raising questions and requiring further investigation. The line was therefore calibrated once again, but this time with a more precise and robust material: the reference pyroxene material CRONUS-P used by the cosmogenic noble gas community for cosmogenic ^{3}He and radiogenic ^{4}He measurements (Blard et al., 2015). The calibration process revealed that the value being used for the ^{3}He spike until then in all my age calculations (4.6 $x10^{-13}$ spike initial ^{3}He moles) was incorrect and underestimated by a factor of about 1.5 compared to the true, newly calibrated value (7.36 $x10^{-13}$ moles). A batch of Fish Canyon Tuff zircon standards was thus analysed in the conventional way for quality control. The generally accepted conventional age for Fish Canyon Tuff zircons was indeed obtained when analysing a dozen of spiked Fish Canyon Tuff zircon standards with a value of 7.36 $x10^{-13}$ moles for the ^{3}He spike. Using this value in the age Equation IV.23 for laser *in situ* (U-Th)/He dating thus led to too old ages. At this point, we therefore evidenced that there was something wrong with the laser ablation

procedure implemented at the CRPG, releasing too much ^{4}He compared to measured parent abundances. Unfortunately, this issue was noticed after all my detrital samples were analysed.

The simplest explanation for this issue was lying in the use of a "nonconventional" solid-state Nd: YAG laser ablation system, possibly causing overextraction of ^{4}He when running ablations. Based on discussions with the New Wave Research team, it is known that nanosecond lasers do cause heating of the sample around the ablation site due to phonon release after incomplete bond cleavage during the multi-photon absorption stage. A way to modulate these effects is to ablate at lower fluence (below 20%, 8 J/cm^2) although there is a lower limit to this due to the ablation threshold of the matrix (typically 0.75-1 J/cm^2). Reducing the repetition rate (below 10 Hz) would also limit the heat energy gradient set up when the sample is hit with a large absolute energy (due to a combination of fluence, repetition rate and spot size). This would thereby reduce the size and temperature of the heat affected zone, and therefore the volume of He-bearing material we are heating. However, experiments exploring very low fluence and low repetition rates as the “best cases” for reducing laser energy escaping from the ablation site were already run (sections IV.5.2.3.2 and I.1.1.1.1, respectively), and proved not to yield promising results regarding pit shape. As shorter-wavelength pulsed lasers (typically, some of the gas lasers we tried to "avoid") have been shown to generate little or no heating of the surrounding material while producing nice pits, there is the urgent need for another ablation system of this type (basically a 193 nm ArF excimer laser system). In particular, this will allow providing the community with more accurate, viable and robust data.

This is in progress at the time of writing this thesis. Until this happens, all the *in situ* data presented thereafter have been corrected for ^{4}He over-extraction. Justifications are provided in section IV.5.5 and results will be shown and discussed in Chapter 6.

IV.5.4 U/Pb dating and U, Th and Sm measurements

U/Pb dating, U, Th, Sm and trace elements measurements made during this doctoral project were performed using a 193 nm Geolas ArF nanosecond excimer laser coupled to an Agilent 7500c quadrupole-based ICP-MS at Georessources (Vandoeuvre-les-Nancy, France). Fixed 60 µm diameter spots were used with a laser frequency of 8 Hz and a fluence of around 4.5 J/cm^2 by focussing the beam at the sample surface. The ablated material was transported from the ablation cell to the ICP-MS by a flow of 0.5 L/min of He, added to 1.1 L/min of Ar just before reaching the torch to facilitate the ionization of the particles.

Each analysis consisted of 20 seconds of collection of a gas blank (plasma on but laser not firing) to define the baseline, followed by 90 seconds of ablation of the material of interest. The Agilent 7500c was tuned before each analytical session using the NIST610 glass standard to maximize signal intensity and stability, keeping Th/U ratio ~ 1 and ThO/Th ratio < 0.5%. All operating parameters, including ICP-MS and laser settings, were held constant for standards and unknowns to minimize any potential bias

between samples and standards. At the beginning of each analytical session, four analyses on Plešovice zircon standard (Sláma et al., 2008) and three analyses on NIST612 glass (Pearce et al., 1997) were performed (considered both as unknown sample to tests the precision and accuracy of the analyses), coupled to 6 analyses of 91500 zircon (Wiedenbeck et al., 1995) and 4 analyses of NIST610 glass (Pearce et al., 1997), both used as external standards. U/Pb ages and U, Th and Sm concentrations were subsequently estimated using data reduction schemes in the Iolite™ plugin for Igor Pro™: U/Pb geochronology and trace elements (Paton et al., 2011; Petrus and Kamber, 2012). The 91500 zircon reference material is used to calibrate the different ratios of interest and to correct analyses from U/Pb and Th-Pb down-hole fractionation during the analysis of zircon. The calculation of the concentrations and limit of detections for U, Th, Sm were calculated using ^{29}Si as internal standard (14.76 wt% for perfect zircon crystals; 33.55 wt% for NIST612 glass) and NIST610 glass as external standard, using the equations proposed by Longerich et al. (1996). During a typical analytical session the 91500 zircon reference material, the Plesovice zircon, and the NIST610 and NIST612 glasses were analyzed two to three times each every 15 to 25 unknown analyses. For NIST612, the accuracy and precision were in the range of -10 to 10% and 0.1 to 10% for the considered elements, respectively.

For each analytical session, all the $^{206}Pb/^{238}U$, $^{207}Pb/^{235}U$ and $^{207}Pb/^{206}Pb$ data were plotted in an error vs. age diagram to find the cross-over for the uncertainties from $^{206}Pb/^{238}U$ to $^{207}Pb/^{206}Pb$ ages (precision cutoff, 1500 Ma). The $^{206}Pb/^{238}U$ ages were chosen as the best ages when younger than the cross-over, and the $^{207}Pb/^{206}Pb$ ages were chosen otherwise. Data were then filtered on the basis of the percentage of discordancy, 5% using as a cut-off. Abnormal U concentration, U/Th ratio, $^{206}Pb/^{204}Pb$ ratio, ^{202}Hg abundance and age uncertainty were carefully looked at in order to understand discordance (Pb loss, igneous/metamorphic, common lead and analytical issue) and limit biasing data by discordance filtering. Regressing data was considered but did not provide much more constraints since grains were not proved to be cogenetic. Nevertheless, upper and lower intercepts would indicate ages of crystallization older than Mesoproterozoic (>1500 Ma) and mostly Hercynian ages of Pb-loss, respectively. In this thesis, discordant ages represent around 20-30% of ages for data sets with more than 100 U/Pb ages (6 samples); they account for 20% to 50% otherwise (4 samples). These were not further considered for provenance interpretations.

IV.5.5 Laser *in situ* zircon (U-Th)/He analyses

All analytical sequences were conducted using pretty similar laser settings for $^{4}He/U$, Th and Sm measurements:

- Laser spot size: 30 µm/60 µm (40 µm/60 and occasionally 90 µm for Fish Canyon Tuff zircons);
- Repetition rate: 10 Hz/8 Hz;
- Pulse count: 200/450 pulses;
- Output laser power or fluence: 20%/4.4 J/cm^2

As stressed in section IV.5.3, laser ablation *in situ* (U-Th)/He data obtained during this thesis (standard material and detrital Pyrenean samples) were acquired with excess of ^{4}He. Table IV.5 synthesizes in a chronological order the analytical sequences conducted over my 3-year doctoral project, showing (i) used laser settings, (ii) He pit volume measurements, (iii) mean measured ages and sample size, (iv) generally accepted ages for the two zircon standards, and (v) the correction factor to be applied to the mean measured age for each analytical sequence of zircon standards in order to obtain the generally accepted age for Fish Canyon Tuff zircon standards. Table IV.5 shows that every analytical sequence of zircon standards gives the same mean age in the error bars: *ca.* 43-44 Ma for Fish Canyon Tuff zircon standards and *ca.* 13 Ma for Chifra tuff zircons. The correction factor is fairly constant (1.55 ± 0.07). This suggests somehow that ^{4}He overextraction was quite systematic over time and can be reasonably corrected. Figure IV.45 shows standardized age reproducibility for Fish Canyon Tuff and Chifra tuff zircon standards through time.

By applying such a correction, it is important to stress the fact that one produces a standardized, average age that takes into account and corrects from ^{4}He overextraction within an analytical session. This is quite unusual: the common practice in many laboratories worldwide is to calibrate the ^{4}He, U, Th and Sm concentrations of an unknown sample (the data) on the known ^{4}He, U, Th and Sm concentrations of a standard material (gas standard for ^{4}He and NIST610-612 glass for U, Th and Sm), then calculate an age (the output). Some variations exist (for instance, Vermeesch et al., 2012; see section IV.3.2). In our case, these are therefore not the measurements allowing calculating an age that are calibrated, but the age itself (on a standard age, that of Fish Canyon Tuff zircons), and so doing overextraction. The best analogy to this is the use of the zircon reference material 91500 to correct from down-hole fractionation within an analytical LA-ICP-MS session. The data from individual analyses of the reference standard are combined to generate an average pattern of changes in the elemental ratio with ablation time. This allows modelling down-hole fractionation within an analytical session based on the expected age of the reference material. Obviously, this is not ideal, preventing from any absolute dating, but I argue that this is reasonable.

As my detrital Pyrenean samples were analysed between analytical sessions of Fish Canyon Tuff zircon standards, using the same laser settings, I argue that detrital sample age data can be corrected by the same mean correction factor of 1.55. The consistency of this correction can be chalenged for a couple of bedrock samples that were already dated using conventional techniques. Conventional and *in situ* laser ablation data for 6 different samples are plotted on the same graph (Figure IV.46 and Figure IV.47). These figures show that dispersion and age range for conventional and corrected laser ablation data are almost exactly the same. This suggests that correcting my *in situ* detrital data by a factor of 1.55 is reasonable and robust

Table IV.5: (next page) Synthesis of all analytical sessions.

Operator	Name	Type	Date	Spot size for He	Spot Size for U-Th-Sm	inferred fluence level - laser output power (He)	rep rate (He)	pulse (He)	He pit volume	%error	%difference He pit volume mean-intercept	Non corrected age (true spike initial 3He moles = 7.36e-13)	+/-	%error	n =	Correction factor to get standard FCT ZHe age	+/-	Corrected age (arbitrarily adjusted spike initial 3He moles to get standard FCT ZHe age)	+/-	%error	Reference ZHe age value (conventional)	+/-	%error	n =	Reference
(-)	(-)	(-)	(-)	(µm)	(µm)	(J/cm2) - (%)	(Hz)	(-)	(µm3)	(%)	(%)	(Ma)	(Ma)	(%)	(-)	(-)	(Ma)	(Ma)	(Ma)	(%)	(Ma)	(Ma)	(Ma)	(-)	(-)
ST	FCT #1	Internal std	02/06/17	40	60-90	13 - 20	10	200	16578	2%	1%	44.6	5.7	13%	37	1.58	+0.22 / -0.37	28.3	3.6	13%	28.3	3.1	10.9%	127; 9	Dodson et al., 2008; CRPG
ST	CHIFF #1	Internal std	04/06/17	40	60-90	13 - 20	10	200	15669	2%	1%	13.4	0.9	7%	21			8.6	0.6	7%	7.0	2.3	33%	34	CRPG
ST	B6b2	Sample	05/06/17	30	60-90	13 - 20	10	200	9731-12375	6%	4%														
ST	B4b2	Sample	08/06/17	30	60	13 - 20	10	200	12315	6%	1%														
ST	B4b1	Sample	16/06/17	30	60	13 - 20	10	200	10418	2%	1%														
ST	B6b1	Sample	17/06/17	30	60	13 - 20	10	200	10813	5%	1%														
ST	B1b1	Sample	20/06/17	30	60	13 - 20	10	200	10082-11454	4%	2%														
ST	B2b1	Sample	21/06/17	30	60	13 - 20	10	200	11027	2%	1%														
ST	B3b1	Sample	23/06/17	30	60	13 - 20	10	200	12110	3%	1%														
ST	A8b1	External std	25/06/17	30	60	13 - 20	10	200	10022	7%	1%														Chapter 5 (Ternois et al., 2019)
ST	A11b1	External std	25/06/17	30	60	13 - 20	10	200	10965	2%	1%														Chapter 5 (Ternois et al., 2019)
ST	2Ab1	External std	26/06/17	30	60	13 - 20	10	200	11008	3%	1%														Chapter 5 (Ternois et al., 2019)
ST	D17b1	Sample	26/06/17	30	60	13 - 20	10	200	8750-10826	6%	4%														
ST	FCTirr #1	Internal std	06/10/17	40	60	13 - 20	10	200	9521-11887	6%	4%	41.6	5.0	12%	39	1.47	+0.21 / -0.16	28.3	3.4	12%	28.3	3.1	10.9%	127; 9	Dodson et al., 2008; CRPG
ST	CHIFF #2	Internal std	28/11/17	40	60	13 - 20	10	200	11754-13049	3%	3%	12.4	0.8	6%	9	1.51	+0.2 / -0.16	8.2	0.5	6%	7.0	2.3	33%	34	CRPG
ST	FCT #2	Internal std	02/12/17	40	60	13 - 20	10	200	12798-15145	5%	9%	42.7	4.9	11%	32			28.3	3.2	11%	28.3	3.1	10.9%	127; 9	Dodson et al., 2008; CRPG
ST	D15b1	Sample	12/01/18	30	60	13 - 20	10	200	7022-8591	4%	8%														
ST	D21b1	Sample	17/01/18	30	60	13 - 20	10	200	8101-9557	4%	5%														
JL	LM1	Sample	21/02/18	30	60	13 - 20	10	200	9739	3%	1%														
JL	MF5	Sample	22/02/18	30	60	13 - 20	10	200	10403	2%	1%														
ST	D22b1	Sample	26/02/18	30	60	13 - 20	10	200	8172-9936	5%	6%														
ST	D20b1	Sample	01/03/18	30	60	13 - 20	10	200	8270-10510	6%	7%														
MW	ZA16-50	External std	03/05/18	30	60	13 - 20	10	200	*11263-11743*	*2%*	*3%*														Waldner et al., in prep
MW	ZA16-15	External std	05/05/18	30	60	13 - 20	10	200	*7213-8418*	*8%*	*4%*														Waldner et al., in prep
MW	ZA16-16	External std	05/05/18	30	60	13 - 20	10	200	*8736-9802*	*5%*	*3%*														Waldner et al., in prep
MW	ZA16-62	External std	08/05/18	30	60	13 - 20	10	200	*9620-11636*	*10%*	*2%*														Waldner et al., in prep
ST	FCTirr #2	Internal std	08/05/18	30	60	13 - 20	10	200	10612-12831	5%	8%	45.9	3.1	7%	28	1.62	+0.12 / -0.1	28.3	1.9	7%	28.3	3.1	10.9%	127; 9	Dodson et al., 2008; CRPG
JL	MF5	Sample	10/05/18	30	60	13 - 20	10	200	*12351*	*3%*	*1%*														
CRPG	FCT	Internal std	08/2018	Conventional + spiked								28.3	3.1	10.9%	9	1					28.3	3.1	10.9%	127	Dodson et al., 2008
CRPG	CHIFF	Internal std	08/2018	Conventional + spiked								7.0	2.3	33%	8	1									CRPG

Mean correction factor	+/- (non propagated)
1.55	0.07

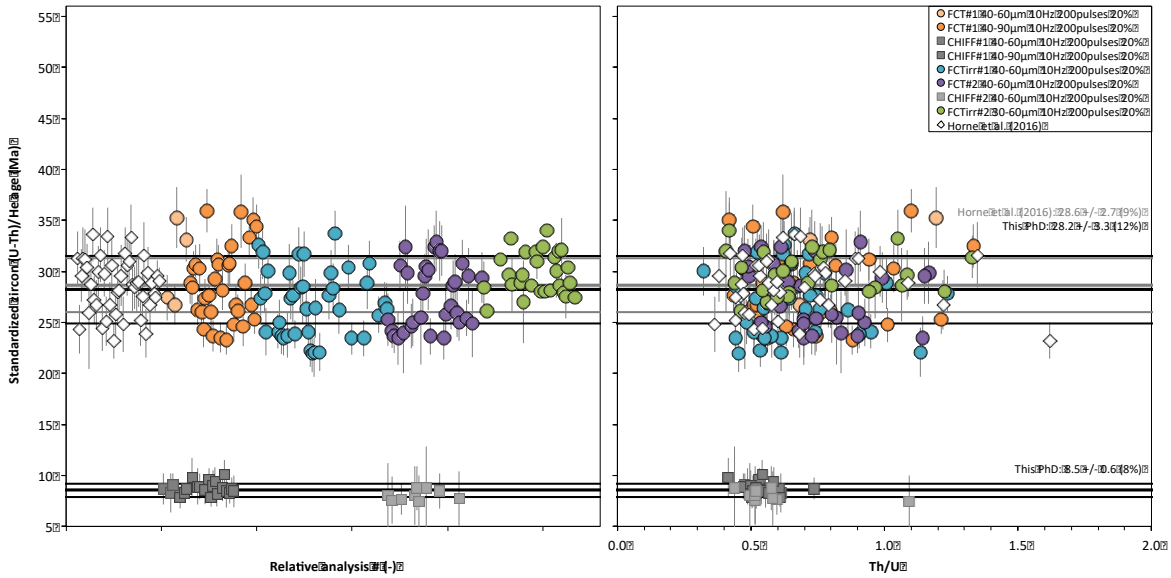

Figure IV.45: Standardized in situ single-grain (U-Th)/He age reproducibility for Fish Canyon Tuff (FCT) and Chifra tuff (CHIFF) zircon standards through time (left) and as a function of Th/U (right). All measured ages were corrected by a factor of 1.55. In situ single-grain age data of Horne et al. (2016) are plotted for comparison (white diamonds). The in situ age value for FCT zircon standards of these authors (28.6 ± 2.7 Ma) is also reported, along with the standardized in situ age values for FCT and CHIFF zircon standards obtained during this Thesis. Laser settings are reported in the key.

IV.5.6 "Proof-of-concepts" study of Fish Canyon tuff and Ethiopian tuff zircons

First laser ablation analyses for He measurement started beginning Spring 2017. These were performed on Fish Canyon Tuff zircon standards and Ethiopian Chifra tuff zircons.

Figure IV.46: (next page) Comparison between conventional (cicles) and standardized in situ (squares) single-grain (U-Th)/He data for one granitic (St-Arnac) and two gneissic samples (Belesta and Caramany) from the Agly-Salvezines Massif in the North Pyrenean Zone. Conventional data are presented, interpreted and discussed in Chapter 5. The two types of data show a similar range, intra-sample age variation and distribution across the eU spectrum (effective uranium concentration eU [ppm] = U [ppm] + 0.235 * Th [ppm]) for each sample. The younger, Late Cretaceous ages obtained using each analytical technique plot at opposite ends of the eU concentration spectrum for the St-Arnac and Belesta samples, in particular at relatively low (<600 ppm) and high (>1,000 ppm) eU concentrations. These are confined to only low eU in the Caramany sample. The older, Early Cretaceous ages obtained using each analytical technique plot also at similar eU concentrations, in particular at intermediate eU concentrations (300-400 ppm). In the Caramany sample, these ages are only obtained with the in situ technique, which is consistent with theoretical considerations made in section IV.3.2. Both data sets therefore suggest the same thermal history for the Agly-Salvezines Massif (see Chapter 5 for more details).

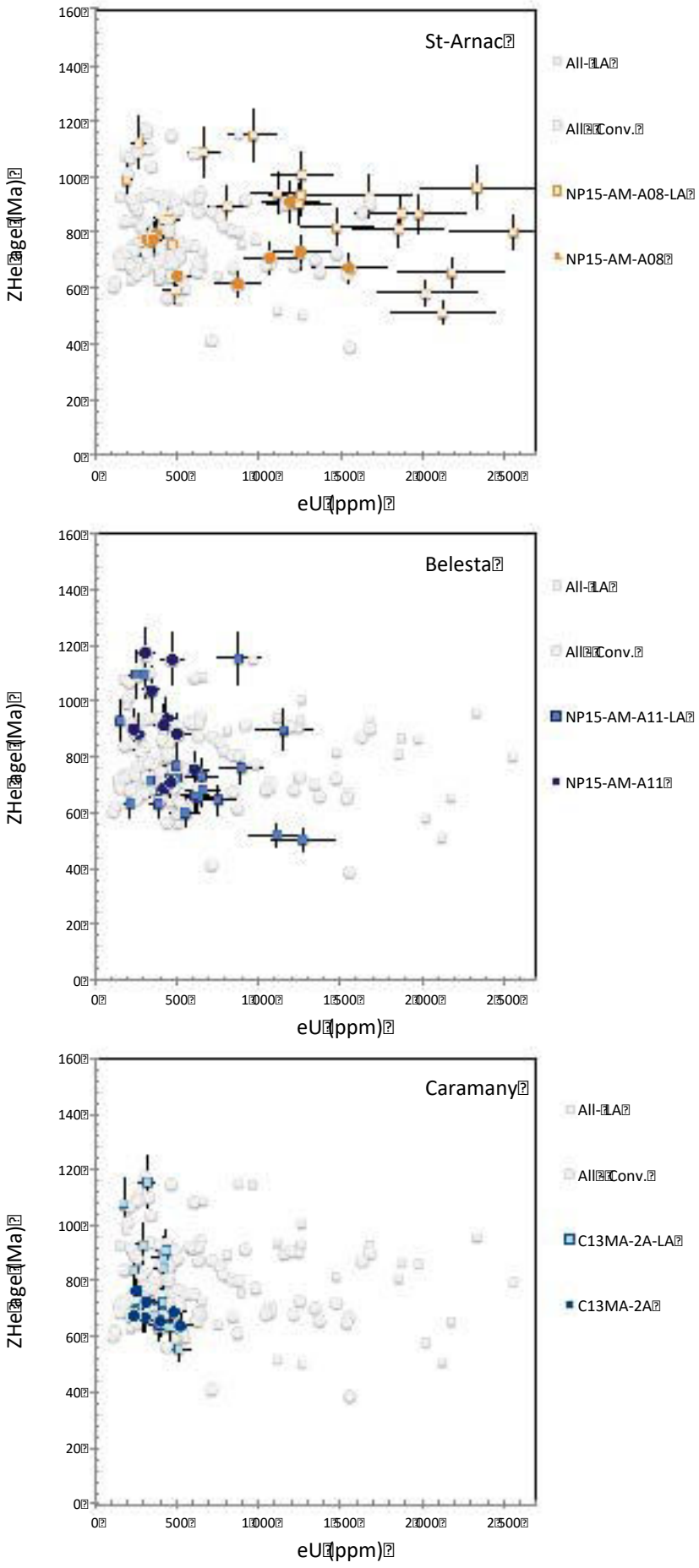
St-Arnac
All-LA
All Conv.
NP15-AM-A08-LA
NP15-AM-A08
Belesta
All-LA
All Conv.
NP15-AM-A11-LA
NP15-AM-A11
Caramany
All-LA
All Conv.
C13MA-2A-LA
C13MA-2A
ZHe age (Ma)
eU (ppm)
0
20
40
60
80
100
120
140
160
500
1000
1500
2000
2500

IV.5.6.1 Choice of the *in situ* single grain (U-Th)/He dating technique

The analytical procedure I used during this thesis was inspired from that described by Tripathy-Lang et al. (2013) and Horne et al. (2016). The procedure of these authors is considered to minimize measurement decoupling between the daughter and its parents in a better way than that of Evans et al. (2015). Because U, Th and Sm nuclides produce, by radioactive decay, alpha particles that are stopped within a distance of 20 µm in the zircon lattice (Farley et al., 1996; Ketcham et al., 2011), most of the ^{4}He measured in the innermost part of the grain (the "core") may be argued to be produced by U, Th and Sm nuclides contained in the surrounding, outer 20 µm-wide area. To get a sense of the potential differences we might obtain by applying either procedure, I used the HeFTy software developed by Richard Ketcham (2005) to simulate ages for Fish Canyon Tuff zircon crystals with a radius of 45 µm. The spherical model is here a strong assumption since pits are cylindrical in reality.

Fish Canyon Tuff zircon crystals are known to be zoned in a quite complex fashion (Dobson et al., 2008). Zoning patterns simulated are presented in Figure IV.48 and Figure IV.49 and cover simple and oscillatory zonation with variable zone widths and enrichments as described by Dobson et al. (2008). The software output includes a normalized 1D He concentration profile (513 dots) and the absolute maximum value of He concentration, which allows calculation of the absolute He concentration at a particular (one out of 513) radius within the grain. Based on the zoning pattern defined by the user, the absolute U, Th and Sm concentrations at a particular radial position within the grain can also be derived. Under the assumption of sphericity, 3D weighted mean daughter and parent concentrations for specific portions of the grain can be calculated. The age is subsequently estimated with usual age equations (Equation IV.23 in section IV.2.1.2.1).

Figure IV.47: (next page) Comparison between conventional (cicles) and standardized in situ (squares) single-grain (U-Th)/He data for four massifs (Bethmal, Ribeirot, Marimanya and Artiès) in the central Axial Zone of the Pyrenees (Waldner et al., 2017). Conventional zircon (U-Th)/He data for the Agly-Salvezines Massif further northeast in the North Pyrenean Zone are also shown for further comparison (Chapter 5). The two types of data from Waldner et al. show a similar range, intra-sample age variation and distribution across the eU spectrum for each sample. The younger, Eocene ages obtained using each analytical technique plot at opposite ends of the eU concentration spectrum, in particular at relatively low (<600 ppm) and high (>1,000 ppm) eU concentrations. These ages are younger than the youngest zircon (U-Th)/He ages recorded in the Agly-Salvezines Massif, but similar to the apatite (U-Th)/He ages for this massif (see Chapter 5 for more details). They therefore fit well with a thermal history showing some delay between early inversion in the North Pyrenean Zone during Late Cretaceous and main collision starting in early Eocene times. They are also consistent with the main, second phase of convergence generally recorded as Eocene-Oligocene in low-temperature thermochronology studies (e.g. Mouthereau et al., 2014; Whitchurch et al., 2011, and references therein). The older, Early Cretaceous ages found at intermediate eU concentrations (300-400 ppm) also fit well with the observations made in the Agly-Salvezines Massif and most likely record the late Aptian-Cenomanian rifting phase and associated postrift cooling.

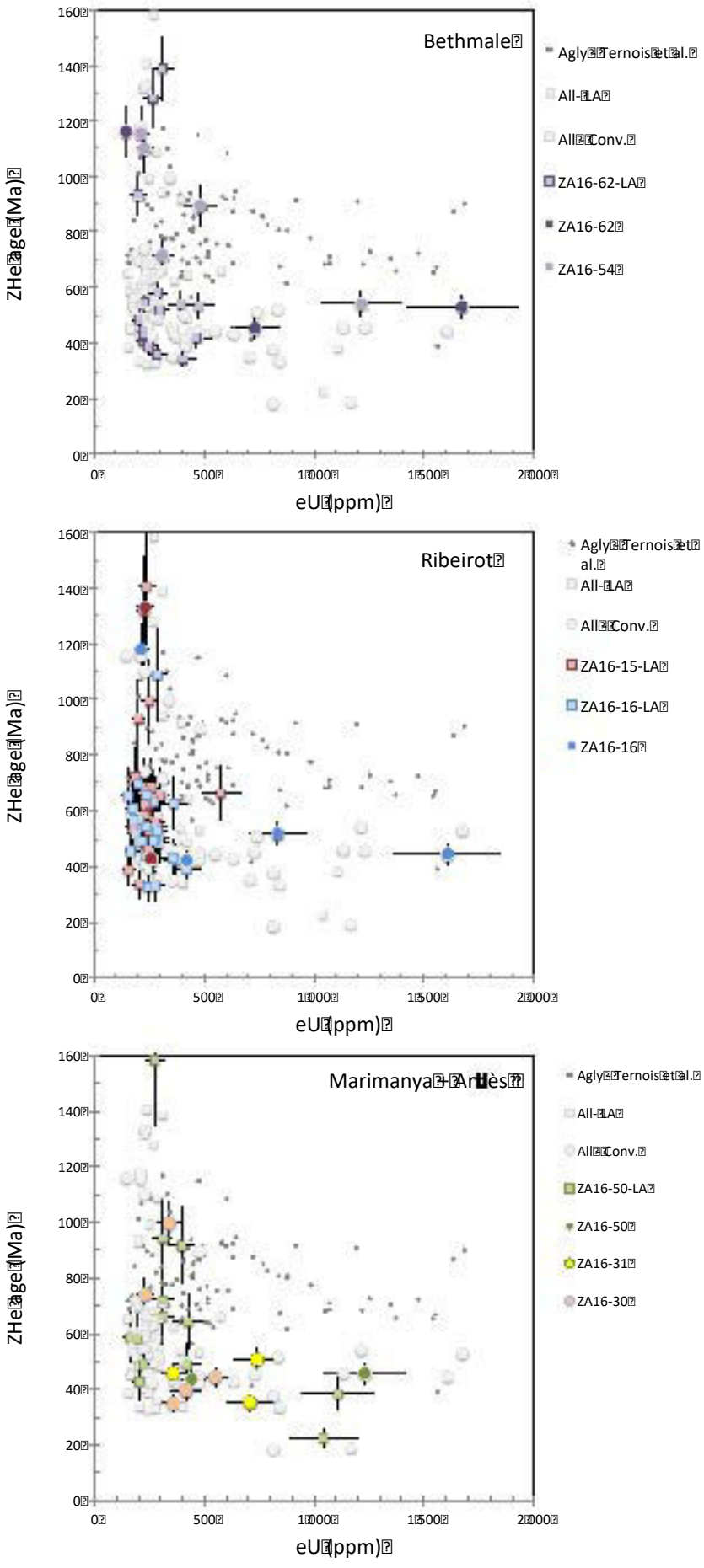
Bethmale
Agly Ternois et al.
All-LA
All Conv.
ZA16-62-LA
ZA16-62
ZA16-54
Ribeirot
Agly Ternois et al.
All-LA
All Conv.
ZA16-15-LA
ZA16-16-LA
ZA16-16
Marimanya - Arrès
Agly Ternois et al.
All-LA
All Conv.
ZA16-50-LA
ZA16-50
ZA16-31
ZA16-30
ZHe age (Ma)
eU (ppm)
0
20
40
60
80
100
120
140
160
500
1000
1500
2000

To model results one might obtain when using the procedure developed by Horne et al. (2016), 3D weighted mean daughter and parent concentrations for the core (a sphere with a 12.5 µm radius) and an outer, spherical 20 µm-thick envelope (volume obtained by subtracting the volume of a sphere with a 65 µm-radius and the volume of the core) can be easily calculated. Regarding the procedure developed by Evans et al. (2015), 3D weighted mean daughter and parent concentrations can be estimated for the same sphere with a radius of 25 µm.

Modelling results are summarized in Appendix 13 for the various zoning patterns tested. As a way to check the validity of these simulations, the conventional age calculated in a similar manner (total integrated volume and concentrations) is also reported in Appendix 13. F_T correction factors are obtained by dividing the HeFTy uncorrected age by the HeFTy corrected age. Calculated *in situ* zircon (U-Th)/He ages are plotted as a function of the radial extent of the innermost zone (the "core" as defined by Dobson et al., 2008) in Figure IV.50. These results show that the two analytical techniques yield similar age dispersion for simple zoning patterns (enriched and depleted core; Figure IV.50.a). However, they suggest that the technique developed by Horne et al. (2016) yields ages much closer to the generally accepted conventional value for Fish Canyon Tuff zircon standards (28.3 ± 3.1 Ma; Dobson et al., 2008) when zonation is oscillatory (Figure IV.50.b). This type of zonation represents more than 80% of the zoning patterns observed in the Fish Canyon Tuff zircons (Dobson et al., 2008), and is typical in zircon over a range of scales (Fowler et al., 2002).

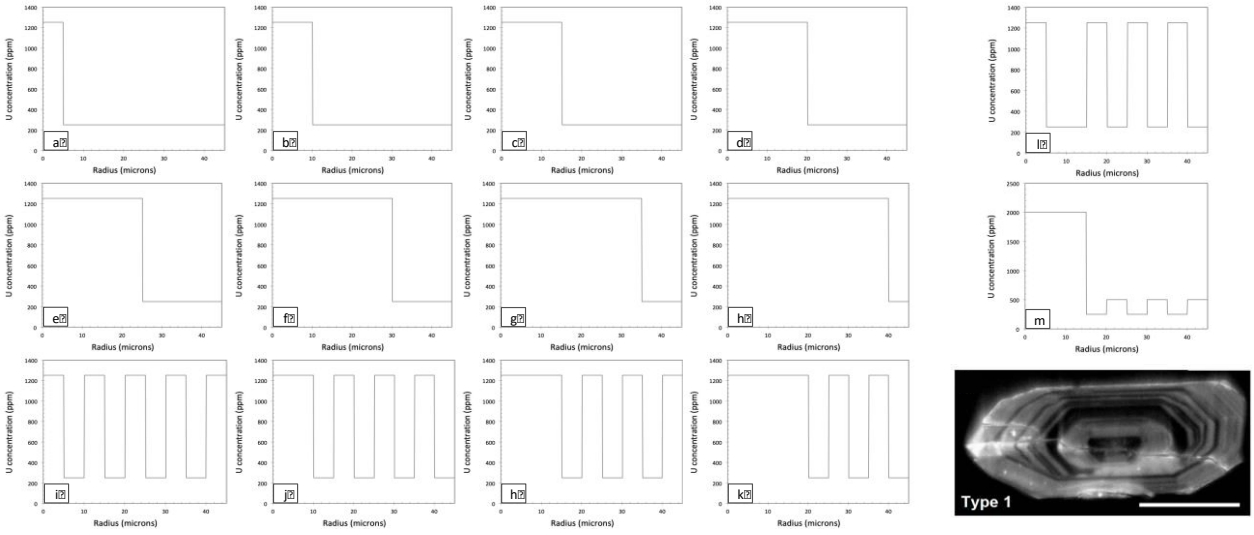

Figure IV.48: Zoning patterns that were simulated in HeFTy and cover simple (a-h) and oscillatory (i-m) zonation with variable zone widths for grains with cores enriched in uranium, as described by Dobson et al. (2008). For each graph, the horizontal axis represents radius from 0 to 45 µm with 10 µm increment. For graphs a-l, the vertical axis represents U concentration from 0 to 1400 ppm with 200 ppm increment. For graph m, the vertical axis represents U concentration from 0 to 2500 ppm with 500 ppm increment.

Because the aim of these *in situ* techniques is primarily to permit the rapid dating of crystals, it seems a bit contradictory to spend a lot of effort on chemical characterization of crystals if there is no need for it in the first place. Especially, these

techniques have been designed to overcome the principal limitation of the conventional methods for age frequency distribution characterization in a sediment or sedimentary rock: the limited number of crystals one could date. As traditional methods have avoided measurement of the degree of zonation in most - if not any cases -, it is fair to write that one might just keep going as it is, use the *in situ* technique without chemical characterization of crystals, see what happens and make scientific decisions in consequence (see below).

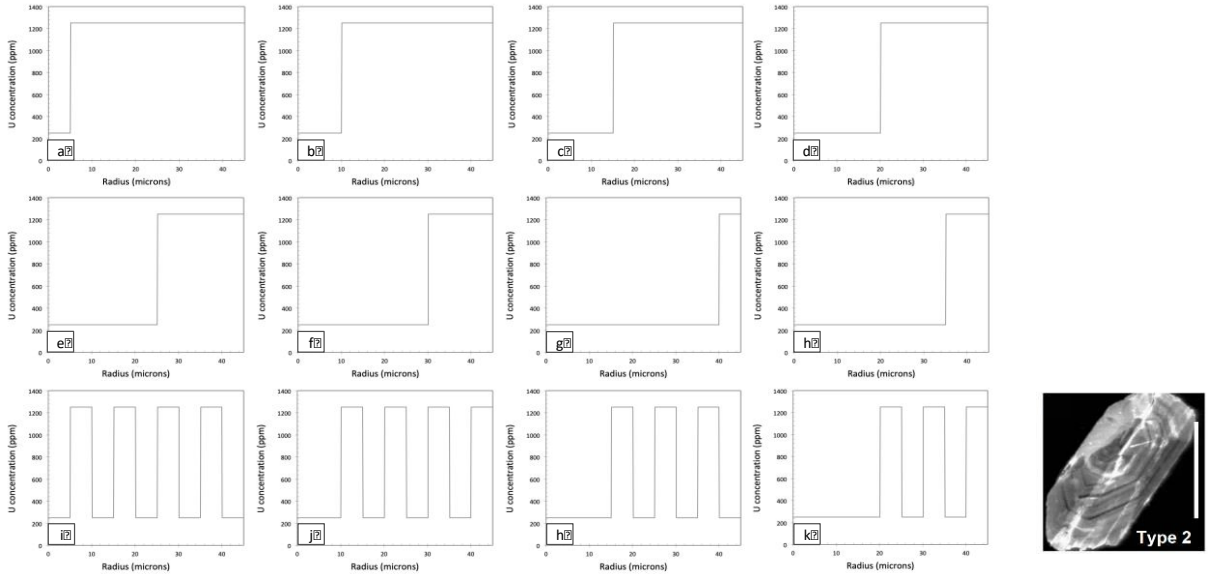

Figure IV.49: Zoning patterns that were simulated in HeFTy and cover simple (a-h) and oscillatory (i-k) zonation with variable zone widths for grains with rims enriched in uranium, as described by Dobson et al. (2008). For each graph, the horizontal axis represents radius from 0 to 45 µm with 10 µm increment. The vertical axis represents U concentration from 0 to 1400 ppm with 200 ppm increment.

IV.5.6.2 Zircon (U-TH)/He results

Standardized *in situ* single grain zircon He ages obtained for Fish Canyon Tuff zircon crystals in this thesis (28.2 ± 3.3 Ma; Figure IV.47) are in good agreement with published *in situ* data (28.6 ± 2.7 Ma; Horne et al., 2016). *In situ* ages for the Ethiopian tuff are similar to those obtained previsouly either in the conventional way or with another ablation system at the CRPG (Deiller and Pik, unpublished). Standard deviation for Fish Canyon tuff data obtained with the newly implemented laser *in situ* dating technique is larger than that for conventional dating (Dodson et al., 2008; Tibari et al., 2016), but it was somehow expected (previous section). The same conclusion can be made about analytical uncertainties that are higher for *in situ* dating due to smaller amounts of material used for dating compared to conventional methods. These observations are similar to those already made by Horne et al. (2016).

Nonetheless, the age scatter we obtain is a bit larger than that of Horne et al. (2016), resulting in higher errors for the mean Fish Canyon Tuff ZHe age. This was investigated through modelling, using once again HeFTy. Results are presented below.

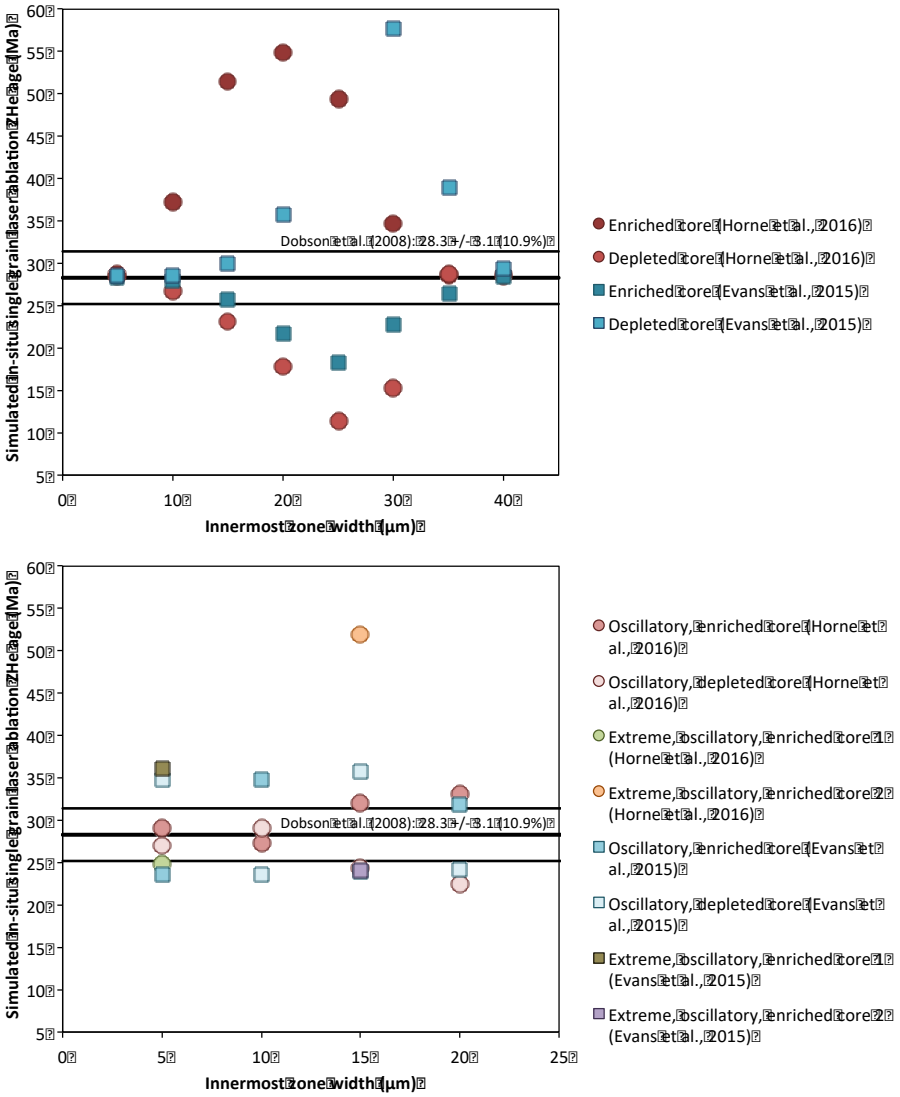

Figure IV.50: HeFTy modelling results showing ages that can be obtained when using the procedures of Horne et al. (2016) and Evans et al. (2015) for grains with various zoning patterns. Simulations were run under the assumption of sphericity in HeFTy. The generally accepted conventional value for Fish Canyon Tuff (FCT) zircon standards (28.3 ± 3.1 Ma; Dobson et al., 2008) is reported. Top: Simple zonation with variable zone widths and enrichments as described by Dobson et al. (2008) and shown in Figure IV.48.a-h and Figure IV.49.a-h. Bottom: Oscillatory zonation with variable zone widths and enrichments as described by Dobson et al. (2008) and shown in Figure IV.48.i-m and and Figure IV.49.i-k.

IV.5.6.3 Comparison with published procedures

It is fair to stress the fact that through my doctoral project I applied about the same procedure of Horne et al. (2016). "About the same procedure" means that ablated pits for daughter and parents were 30 µm- and 60 µm-large in my procedure, respectively, while they were 25 µm- and 65 µm-large in the procedure of these authors. The value of 30 µm was derived from calculations aimed to find ablated pit volumes that would be needed to extract a ^{4}He quantity at least 10 times the extraction vaccum line blank (10-16 moles) and its standard deviation. The spot size for U, Th, Sm analysis was taken as a lesser evil due to limited aperture selection allowed by the Geolas Pro automated high-

end deep-UV 193 nm optical system (36, 60, 90 µm, etc). Given the 20 µm travelling distance of alpha particles within zircon lattice, we expect Horne et al. (2016) to better take into account such a process by choosing an at least 20 µm large outer volume for U, Th and Sm measurements. Let's investigate what the dimension differences between our procedure and that of Horne et al. (2016) could imply depending on the zoning pattern. In other words, are these procedure differences causing the larger standard deviation for Fish Canyon tuff data we obtain compared to results of Horne et al. (2016)?

Zoning patterns simulated are those presented in Figure IV.50 and Figure IV.51 and calculations are similar to those made for the procedure of Horne et al. (2016). 3D weighted mean daughter and parent concentrations for the core (a sphere with a 15 µm radius) and an outer, spherical 15 µm-thick envelope were calculated. Volume, concentration and age estimates are reported in Appendix 14 and ages obtained with both our procedure and that of Horne et al. (2016) are plotted together for comparison in Figure IV.51. Modelling results reproduce the larger standard deviation yielded by our procedure compared to that of Horne et al. (2016). This standard deviation is equivalent to that yielded by the procedure of Evans et al. (2015).

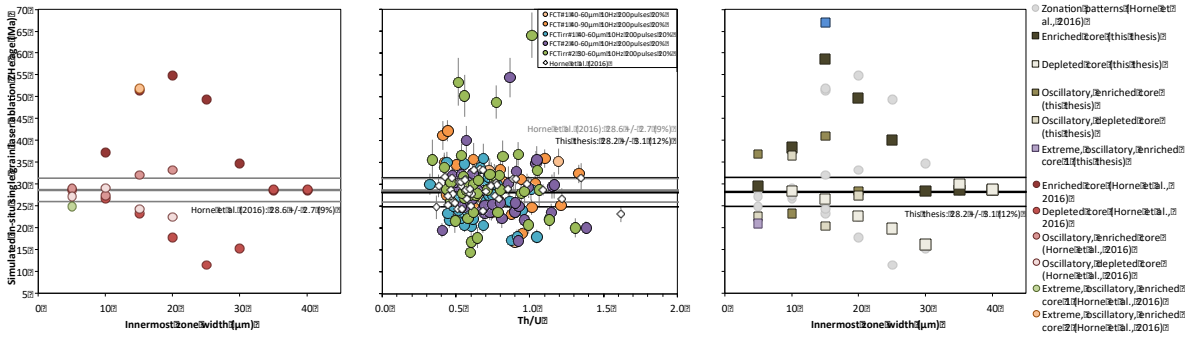

Figure IV.51: Comparision between HeFTy modelling results showing ages that can be obtained with the procedure of Horne et al. (2016) (left) and that implemented at the CRPG during this thesis (right). Middle: all the data for Fish Canyon Tuff (FCT) zircon standards acquired during this Thesis ("outliers" were discarded for the estimation of the correction factor in section IV.5.5).

IV.5.6.4 Conclusions and Perspectives

Throughout this Thesis, it has appeared that nanosecond solid-state lasers such as the New Wave Reasearch NW213 Nd: YAG laser ablation system cause heating of the sample around the ablation site and overextraction of ^{4}He. A way to modulate these effects would be to ablate at lower fluence (below 20%, 8 J/cm^2) and lower repetition rate (below 10 Hz) but experiments exploring very low fluence and low repetition rates as the “best cases” for reducing laser energy escaping from the ablation site proved not to yield promising results. In particular, the lower the energy level used, the smaller and farther to expected values for perfectly cylindrical pits the volume of the ablated pits. Pit volumes are in fact systematically underestimated below 16% energy (measured radii far smaller than the expected spot radius and measured volume to measured depth ratios far away from the line for perfectly cylindrical pits), reducing ablation quality,

repeatability and reproducibility. Performing (U-Th)/he analyses with these laser ablation settings would have thus required measuring pit volumes for any single grain, making very little sense given the instruments available during my thesis.

There is therefore the urgent need for another ablation system (basically a 193 nm ArF excimer laser system) to provide the community with more accurate, viable and robust data. This is in progress at the time of writing this thesis. Until this happens, all the *in situ* detrital data presented thereafter have been corrected for ^{4}He over-extraction. The correction to apply to data has been presented and discussed, and seems pretty constant with analytical time and geologically reasonable. I therefore argue that the data acquired during my doctoral work can, as they are, help clarify early orogenic dynamics in the Pyrenees, providing key first-order constraints on dynamic coupling between range and foreland basin(s), and contributing to the debate on the role of rift inheritance into early orogenic processes.

REFERENCES

Abramson, I. S., 1982, On Bandwidth Variation in Kernel Estimates-A Square Root Law: The Annals of Statistics, v. 10, no. 4, p. 1217-1223.

Aguilar, C., M. Liesa, P. Castiñeiras, and M. Navidad, 2014, Late Variscan metamorphic and magmatic evolution in the eastern Pyrenees revealed by U-Pb age zircon dating: Journal of the Geological Society, v. 171, no. 2, p. 181-192, doi:10.1144/jgs2012-086.

Albarede, F., G. Feraud, I. Kaneoka, and C. J. Allegre, 1978, ^{39}Ar-^{40}Ar Dating: The Importance of K-Feldspars on Multi-Mineral Data of Polyorogenic Areas: The Journal of Geology, v. 86, no. 5, p. 581-598.

Albarède, F., and A. Michard-Vitrac, 1978, Age and significance of the North Pyrenean metamorphism: Earth and Planetary Science Letters, v. 40, no. 3, p. 327-332, doi:10.1016/0012-821X(78)90157-7.

Allen, P. A., and J. R. Allen, 2013, Basin Analysis: Principles and Application to Petroleum Play Assessment: John Wiley & Sons, 1206 p.

Ault, A. K., M. Frenzel, P. W. Reiners, N. H. Woodcock, and S. N. Thomson, 2016, Record of paleofluid circulation in faults revealed by hematite (U-Th)/He and apatite fission-track dating: An example from Gower Peninsula fault fissures, Wales: Lithosphere, v. 8, no. 4, p. 379-385, doi:10.1130/L522.1.

Axen, G. J., P. S. Lam, M. Grove, D. F. Stockli, and J. Hassanzadeh, 2001, Exhumation of the west-central Alborz Mountains, Iran, Caspian subsidence, and collision-related tectonics: Geology, v. 29, no. 6, p. 559-562, doi:10.1130/0091-7613(2001)029<0559:EOTWCA>2.0.CO;2.

Baldwin, S. L., and G. S. Lister, 1998, Thermochronology of the South Cyclades Shear Zone, Ios, Greece: Effects of ductile shear in the argon partial retention zone: Journal of Geophysical Research: Solid Earth, v. 103, no. B4, p. 7315-7336, doi:10.1029/97JB03106.

Barbarand, J., A. Carter, I. Wood, and T. Hurford, 2003, Compositional and structural control of fission-track annealing in apatite: Chemical Geology, v. 198, no. 1-2, p. 107-137, doi:10.1016/S0009-2541(02)00424-2.

Bender, M. L., 1973, Helium-uranium dating of corals: Geochimica et Cosmochimica Acta, v. 37, no. 5, p. 1229-1247, doi:10.1016/0016-7037(73)90058-6.

Bermúdez, M. A., P. A. van der Beek, and M. Bernet, 2013, Strong tectonic and weak climatic control on exhumation rates in the Venezuelan Andes: Lithosphere, v. 5, no. 1, p. 3-16, doi:10.1130/L212.1.

Bermúdez, M. A., C. Hoorn, M. Bernet, E. Carrillo, P. A. van der Beek, J. I. Garver, J. L. Mora, and K. Mehrkian, 2017, The detrital record of late-Miocene to Pliocene surface uplift and exhumation of the Venezuelan Andes in the Maracaibo and Barinas foreland basins: Basin Research, v. 29, no. S1, p. 370-395, doi:10.1111/bre.12154.

Bernet, M., P. van der Beek, R. Pik, P. Huyghe, J.-L. Mugnier, E. Labrin, and A. Szulc, 2006, Miocene to Recent exhumation of the central Himalaya determined from combined detrital zircon fission-track and U/Pb analysis of Siwalik sediments, western Nepal: Basin Research, v. 18, no. 4, p. 393-412.

Bernet, M., M. Brandon, J. Garver, M. L. Balestieri, B. Ventura, and M. Zattin, 2009, Exhuming the Alps through time: clues from detrital zircon fission-track thermochronology: Basin Research, v. 21, no. 6, p. 781-798, doi:10.1111/j.1365-2117.2009.00400.x.

Bernet, M., M. T. Brandon, J. I. Garver, and B. R. Molitor, 2004, Fundamentals of detrital zircon fission-track analysis for provenance and exhumation studies with examples from the European Alps, in Special Paper 378: Detrital thermochronology - Provenance analysis, exhumation, and landscape evolution of mountain belts: Geological Society of America, p. 25-36, doi:10.1130/0-8137-2378-7.25.

Bernet, M., and J. I. Garver, 2005, Fission-track Analysis of Detrital Zircon: Reviews in Mineralogy and Geochemistry, v. 58, no. 1, p. 205-237, doi:10.2138/rmg.2005.58.8.

Bernet, M., M. Zattin, J. I. Garver, M. T. Brandon, and J. A. Vance, 2001, Steady-state exhumation of the European Alps: Geology, v. 29, no. 1, p. 35-38, doi:10.1130/0091-7613(2001)029<0035:SSEOTE>2.0.CO;2.

Bigazzi, G., 1981, The problem of the decay constant λf of ^{238}U: Nuclear Tracks, v. 5, no. 1, p. 35-44, doi:10.1016/0191-278X(81)90024-X.

Blard, P.-H. et al., 2015, An inter-laboratory comparison of cosmogenic ^{3}He and radiogenic ^{4}He in the CRONUS-P pyroxene standard: Quaternary Geochronology, v. 26, p. 11-19, doi:10.1016/j.quageo.2014.08.004.

Botev, Z. I., J. F. Grotowski, and D. P. Kroese, 2010, Kernel density estimation via diffusion: The Annals of Statistics, v. 38, no. 5, p. 2916-2957, doi:10.1214/10-AOS799.

Boulvais, P., G. Ruffet, J. Cornichet, and M. Mermet, 2007, Cretaceous albitization and dequartzification of Hercynian peraluminous granite in the Salvezines Massif (French Pyrénées): Lithos, v. 93, no. 1-2, p. 89-106, doi:10.1016/j.lithos.2006.05.001.

Bowman, A. W., and A. Azzalini, 1997, Applied Smoothing Techniques for Data Analysis.

Boyce, J. W., K. V. Hodges, D. King, J. L. Crowley, M. Jercinovic, N. Chatterjee, S. A. Bowring, and M. Searle, 2009, Improved confidence in (U-Th)/He thermochronology using the laser microprobe: An example from a Pleistocene leucogranite, Nanga Parbat, Pakistan: IMPROVED CONFIDENCE IN (U-Th)/He THERMOCHRONOLOGY: Geochemistry, Geophysics, Geosystems, v. 10, no. 9, p. n/a-n/a, doi:10.1029/2009GC002497.

Boyce, J. W., K. V. Hodges, W. J. Olszewski, M. J. Jercinovic, B. D. Carpenter, and P. W. Reiners, 2006, Laser microprobe (U-Th)/He geochronology: Geochimica et Cosmochimica Acta, v. 70, no. 12, p. 3031-3039, doi:10.1016/j.gca.2006.03.019.

Brandon, M. T., 1992, Decomposition of fission-track grain-age distributions: American Journal of Science, v. 292, no. 8, p. 535-564, doi:10.2475/ajs.292.8.535.

Brandon, M. T., 1996, Probability density plot for fission-track grain-age samples: Radiation Measurements, v. 26, no. 5, p. 663-676, doi:10.1016/S1350-4487(97)82880-6.

Brandon, M. T., M. K. Roden-Tice, and J. I. Garver, 1998, Late Cenozoic exhumation of the Cascadia accretionary wedge in the Olympic Mountains, northwest Washington State: GSA Bulletin, v. 110, no. 8, p. 985-1009, doi:10.1130/0016-7606(1998)110<0985:LCEOTC>2.3.CO;2.

Brandon, M. T., and J. A. Vance, 1992, Tectonic evolution of the Cenozoic Olympic subduction complex, Washington State, as deduced from fission-track ages for detrital zircons: American Journal of Science, v. 292, no. 8, p. 565-636, doi:10.2475/ajs.292.8.565.

Braun, J., P. Van Der Beek, and G. Batt, 2006, Quantitative thermochronology: numerical methods for the interpretation of thermochronological data: Cambridge University Press.

Brown, R. W., R. Beucher, S. Roper, C. Persano, F. Stuart, and P. Fitzgerald, 2013, Natural age dispersion arising from the analysis of broken crystals. Part I: Theoretical basis and implications for the apatite (U-Th)/He thermochronometer: Geochimica et Cosmochimica Acta, v. 122, p. 478-497, doi:10.1016/j.gca.2013.05.041.

Campbell, I. H., P. W. Reiners, C. M. Allen, S. Nicolescu, and R. Upadhyay, 2005, He-Pb double dating of detrital zircons from the Ganges and Indus Rivers: Implication for quantifying sediment recycling and provenance studies: Earth and Planetary Science Letters, v. 237, no. 3-4, p. 402-432, doi:10.1016/j.epsl.2005.06.043.

Carosi, R., C. Montomoli, M. Tiepolo, and C. Frassi, 2012, Geochronological constraints on post-collisional shear zones in the Variscides of Sardinia (Italy): Terra Nova, v. 24, no. 1, p. 42-51, doi:10.1111/j.1365-3121.2011.01035.x.

Carrapa, B., 2010, Resolving tectonic problems by dating detrital minerals: Geology, v. 38, no. 2, p. 191-192, doi:10.1130/focus022010.1.

Carter, A., 2019, Thermochronology on Sand and Sandstones for Stratigraphic and Provenance Studies, in Fission-Track Thermochronology and its Application to Geology: Springer, Cham, Springer Textbooks in Earth Sciences, Geography and Environment, p. 259-268, doi:10.1007/978-3-319-89421-8_14.

Carter, A., C. S. Bristow, and A. J. Hurford, 1995, The application of fission-track analysis to the dating of barren sequences: examples from red beds in Scotland and Thailand: Geological Society, London, Special Publications, v. 89, no. 1, p. 57-68, doi:10.1144/GSL.SP.1995.089.01.05.

Carter, A., and S. J. Moss, 1999, Combined detrital-zircon fission-track and U/Pb dating: A new approach to understanding hinterland evolution: Geology, v. 27, no. 3, p. 235, doi:10.1130/0091-7613(1999)027<0235:CDZFTA>2.3.CO;2.

Carter, A., Y. Najman, A. Bahroudi, P. Bown, E. Garzanti, and R. D. Lawrence, 2010, Locating earliest records of orogenesis in western Himalaya: Evidence from Paleogene sediments in the Iranian Makran region and Pakistan Katawaz basin: Geology, v. 38, no. 9, p. 807-810, doi:10.1130/G31087.1.

Casas, J. M., P. Castiñeiras, M. Navidad, M. Liesa, and J. Carreras, 2010, New insights into the Late Ordovician magmatism in the Eastern Pyrenees: U-Pb SHRIMP zircon data from the Canigó massif: Gondwana Research, v. 17, no. 2, p. 317-324, doi:10.1016/j.gr.2009.10.006.

Cerveny, P. F., N. D. Naeser, P. K. Zeitler, C. W. Naeser, and N. M. Johnson, 1988, History of uplift and relief of the Himalaya during the past 18 million years: Evidence from fission-track ages of detrital zircons from sandstones of the Siwalik Group, in New perspectives in basin analysis: Springer, p. 43-61.

Chapple, W. M., 1978, Mechanics of thin-skinned fold-and-thrust belts: Geological Society of America Bulletin, v. 89, no. 8, p. 1189-1198, doi:10.1130/0016-7606(1978)89<1189:MOTFB>2.0.CO;2.

Chaudhuri, P., and J. S. Marron, 1999, SiZer for Exploration of Structures in Curves: Journal of the American Statistical Association, v. 94, no. 447, p. 807-823, doi:10.1080/01621459.1999.10474186.

Cocherie, A., C. Guerrot, and P. Rossi, 1991, Single-zircon dating by step-wise Pb evaporation: Comparison with other geochronological techniques applied to the Hercynian granites of Corse.ca,France: p. 11.

Copeland, P., and T. M. Harrison, 1990, Episodic rapid uplift in the Himalaya revealed by $^{40}Ar/^{39}Ar$ analysis of detrital K-feldspar and muscovite, Bengal fan: Geology, v. 18, no. 4, p. 354-357, doi:10.1130/0091-7613(1990)018<0354:ERUITH>2.3.CO;2.

Crowley, K. d, M. Cameron, and R. l Schaefer, 1991, Experimental studies of annealing of etched fission-tracks in fluorapatite: Geochimica et Cosmochimica Acta, v. 55, no. 5, p. 1449-1465, doi:10.1016/0016-7037(91)90320-5.

Dahlen, F. A., 1990, Critical taper model of fold-and-thrust belts and accretionary wedges: Annual Review of Earth and Planetary Sciences, v. 18, p. 55.

Dahlen, F. A., J. Suppe, and D. Davis, 1984, Mechanics of fold-and-thrust belts and accretionary wedges: Cohesive Coulomb Theory: Journal of Geophysical Research: Solid Earth, v. 89, no. B12, p. 10087-10101, doi:10.1029/JB089iB12p10087.

Damon, P. E., and W. D. Green, 1963, Investigations of the helium age dating method by stable isotope dilution technique: Radioactive Dating, p. 55-71.

Damon, P. E., and J. L. Kulp, 1957, Determination of radiogenic helium in zircon by stable isotope dilution technique: Transactions, American Geophysical Union, v. 38, no. 6, p. 945, doi:10.1029/TR038i006p00945.

Danhara, T., and H. Iwano, 2013, A review of the present state of the absolute calibration for zircon fission-track geochronometry using the external detector method: Island Arc, v. 22, no. 3, p. 264-279, doi:10.1111/iar.12035.

Danišík, M., B. I. A. McInnes, C. L. Kirkland, B. J. McDonald, N. J. Evans, and T. Becker, 2017, Seeing is believing: Visualization of He distribution in zircon and implications for thermal history reconstruction on single crystals: Science Advances, v. 3, no. 2, p. e1601121, doi:10.1126/sciadv.1601121.

Davis, D., J. Suppe, and F. A. Dahlen, 1983, Mechanics of fold-and-thrust belts and accretionary wedges: Journal of Geophysical Research: Solid Earth, v. 88, no. B2, p. 1153-1172, doi:10.1029/JB088iB02p01153.

Deloule, E., P. Alexandrov, A. Cheilletz, B. Laumonier, and P. Barbey, 2002, *In situ* U-Pb zircon ages for Early Ordovician magmatism in the eastern Pyrenees, France: the Canigou orthogneisses: International Journal of Earth Sciences, v. 91, no. 3, p. 398-405, doi:10.1007/s00531-001-0232-0.

Denèle, Y., 2007, Formation des dômes gneissiques hercyniens dans les Pyrénées : exemple du massif de l'Aston-Hospitalet: Toulouse 3.

Devroye, L., 1987, A Course in Density Estimation: Cambridge, MA, USA, Birkhauser Boston Inc.

Devroye, L., 1991, Exponential Inequalities in Nonparametric Estimation, in G. Roussas, ed., Nonparametric Functional Estimation and Related Topics: Dordrecht, Springer Netherlands, NATO ASI Series, p. 31-44, doi:10.1007/978-94-011-3222-0_3.

Dickinson, W. R., and G. E. Gehrels, 2008, Sediment delivery to the Cordilleran foreland basin: Insights from U/Pb ages of detrital zircons in Upper Jurassic and Cretaceous strata of the Colorado Plateau: American Journal of Science, v. 308, no. 10, p. 1041-1082, doi:10.2475/10.2008.01.

Dickinson, W. R., and G. E. Gehrels, 2009, U/Pb ages of detrital zircons in Jurassic eolian and associated sandstones of the Colorado Plateau: Evidence for transcontinental dispersal and intraregional recycling of sediment: Geological Society of America Bulletin, v. 121, no. 3-4, p. 408-433, doi:10.1130/B26406.1.

Dietze, M., S. Kreutzer, C. Burow, M. C. Fuchs, M. Fischer, and C. Schmidt, 2016, The abanico plot: Visualising chronometric data with individual standard errors: Quaternary Geochronology, v. 31, p. 12-18, doi:10.1016/j.quageo.2015.09.003.

Dobson, K. J., F. M. Stuart, and T. J. Dempster, 2008, U and Th zonation in Fish Canyon Tuff zircons: Implications for a zircon (U-Th)/He standard: Geochimica et Cosmochimica Acta, v. 72, no. 19, p. 4745-4755, doi:10.1016/j.gca.2008.07.015.

Dodson, M. H., 1986, Closure Profiles in Cooling Systems: doi:10.4028/www.scientific.net/MSF.7.145: <https://www.scientific.net/MSF.7.145> (accessed March 12, 2019).

Dodson, M. H., 1973, Closure temperature in cooling geochronological and petrological systems: Contributions to Mineralogy and Petrology, v. 40, no. 3, p. 259-274.

Donelick, R. A., P. B. O'Sullivan, and R. A. Ketcham, 2005, Apatite Fission-Track Analysis: Reviews in Mineralogy and Geochemistry, v. 58, no. 1, p. 49-94, doi:10.2138/rmg.2005.58.3.

Donelick, R. A., M. K. Roden, J. D. Mooers, B. S. Carpenter, and D. S. Miller, 1990, Etchable length reduction of induced fission-tracks in apatite at room temperature (≈ 23 °C): Crystallographic orientation effects and "initial" mean lengths: International Journal of Radiation Applications and Instrumentation. Part D. Nuclear Tracks and Radiation Measurements, v. 17, no. 3, p. 261-265, doi:10.1016/1359-0189(90)90044-X.

Eddington, A. S., 1928, The Nature of the Physical World: Cambridge, England, 1929EddingtonThe Nature of the Physical World1929.

Ehlers, T. A., 2005, Crustal Thermal Processes and the Interpretation of Thermochronometer Data: Reviews in Mineralogy and Geochemistry, v. 58, no. 1, p. 315-350, doi:10.2138/rmg.2005.58.12.

Ehlers, T. A., and K. A. Farley, 2003, Apatite (U-Th)/He thermochronometry: methods and applications to problems in tectonic and surface processes: Earth and Planetary Science Letters, v. 206, no. 1, p. 1-14.

Ehrhart, P., 1992, Properties and interactions of atomic defects in metals and alloys, PhD Thesis: Verlag nicht ermittelbar.

Enkelmann, E., J. I. Garver, and T. L. Pavlis, 2008, Rapid exhumation of ice-covered rocks of the Chugach-St. Elias orogen, Southeast Alaska: Geology, v. 36, no. 12, p. 915, doi:10.1130/G2252A.1.

Evans, N. J., J. P. Byrne, J. T. Keegan, and L. E. Dotter, 2005, Determination of uranium and thorium in zircon, apatite, and fluorite: Application to laser (U-Th)/He thermochronology: Journal of Analytical Chemistry, v. 60, no. 12, p. 1159-1165.

Evans, N. J., B. I. A. McInnes, B. McDonald, M. Danišík, T. Becker, P. Vermeesch, M. Shelley, E. Marillo-Sialer, and D. B. Patterson, 2015, An *in situ* technique for (U-Th-Sm)/He and U-Pb double dating: J. Anal. At. Spectrom., v. 30, no. 7, p. 1636-1645, doi:10.1039/C5JA00085H.

Evernden, J. F., G. H. Curtis, R. W. Kistler, and J. D. Obradovich, 1960, Argon diffusion in glauconite, microcline, sanidine, leucite and phlogopite: American Journal of Science, v. 258, no. 8, p. 583-604, doi:10.2475/ajs.258.8.583.

Fanale, F. P., and J. L. Kulp, 1962, The helium method and the age of the Cornwall, Pennsylvania magnetite ore: Economic Geology, v. 57, no. 5, p. 735-746, doi:10.2113/gsecongeo.57.5.735.

Fanale, F. P., and O. A. Schaeffer, 1965, Helium-Uranium Ratios for Pleistocene and Tertiary Fossil Aragonites: Science, v. 149, no. 3681, p. 312-316, doi:10.1126/science.149.3681.312.

Farley, K. A., 2002, (U-Th)/He Dating: Techniques, Calibrations, and Applications: Reviews in Mineralogy and Geochemistry, v. 47, no. 1, p. 819-844, doi:10.2138/rmg.2002.47.18.

Farley, K. A., and D. F. Stockli, 2002, (U-Th)/He Dating of Phosphates: Apatite, Monazite, and Xenotime: Reviews in Mineralogy and Geochemistry, v. 48, no. 1, p. 559-577, doi:10.2138/rmg.2002.48.15.

Farley, K. A., R. A. Wolf, and L. T. Silver, 1996, The effects of long alpha-stopping distances on (U-Th)/He ages: Geochimica et Cosmochimica Acta, v. 60, no. 21, p. 4223-4229, doi:10.1016/S0016-7037(96)00193-7.

Fechtig, H., and S. Kalbitzer, 1966, The Diffusion of Argon in Potassium-Bearing Solids, in O. A. Schaeffer, and J. Zähringer, eds., Potassium Argon Dating: Berlin, Heidelberg, Springer Berlin Heidelberg, p. 68-107, doi:10.1007/978-3-642-87895-4_4.

Feng, R., N. Machado, and J. Ludden, 1993, Lead geochronology of zircon by LaserProbe-inductively coupled plasma mass spectrometry (LP-ICPMS): Geochimica et Cosmochimica Acta, v. 57, no. 14, p. 3479-3486, doi:10.1016/0016-7037(93)90553-9.

Ferreira, M. P., R. Macedo, V. Costa, J. H. Reynolds, J. E. Riley, and M. W. Rowe, 1975, Rare-gas dating, II. Attempted uranium-helium dating of young volcanic rocks from the madeira archipelago: Earth and Planetary Science Letters, v. 25, no. 2, p. 142-150, doi:10.1016/0012-821X(75)90190-9.

Filleaudeau, P.-Y., F. Mouthereau, and R. Pik, 2012, Thermo-tectonic evolution of the south-central Pyrenees from rifting to orogeny: insights from detrital zircon U/Pb and (U-Th)/He thermochronometry: Basin Research, v. 24, no. 4, p. 401-417, doi:10.1111/j.1365-2117.2011.00535.x.

Finch, R. J., and J. M. Hanchar, 2003, Structure and Chemistry of Zircon and Zircon-Group Minerals: Reviews in Mineralogy and Geochemistry, v. 53, no. 1, p. 1-25, doi:10.2113/0530001.

Fitzgerald, P. G., E. Stump, and T. F. Redfield, 1993, Late Cenozoic uplift of Denali and its relation to relative plate motion and fault morphology: Science, v. 259, no. 5094, p. 497-499.

Fleischer, R. L., P. B. Price, E. M. Symes, and D. S. Miller, 1964, Fission-Track Ages and Track-Annealing Behavior of Some Micas: Science, v. 143, no. 3604, p. 349-351, doi:10.1126/science.143.3604.349.

Fleischer, R. L., P. B. Price, and R. M. Walker, 1965a, Effects of temperature, pressure, and ionization of the formation and stability of fission-tracks in minerals and glasses: Journal of Geophysical Research, v. 70, no. 6, p. 1497-1502, doi:10.1029/JZ070i006p01497.

Fleischer, R. L., P. B. Price, and R. M. Walker, 1965b, Ion explosion spike mechanism for formation of charged-particle tracks in solids: Journal of applied Physics, v. 36, no. 11, p. 3645-3652.

Fleischer, R. L., P. B. Price, and R. M. Walker, 1975, Nuclear Tracks in Solids: University of California Press.

Flowers, R. M., R. A. Ketcham, D. L. Shuster, and K. A. Farley, 2009, Apatite (U-Th)/He thermochronometry using a radiation damage accumulation and annealing model: Geochimica et Cosmochimica Acta, v. 73, no. 8, p. 2347-2365, doi:10.1016/j.gca.2009.01.015.

Foster, D. A., and B. E. John, 1999, Quantifying tectonic exhumation in an extensional orogen with thermochronology: examples from the southern Basin and Range Province: Geological Society, London, Special Publications, v. 154, no. 1, p. 343-364, doi:10.1144/GSL.SP.1999.154.01.16.

Fowler, A., A. Prokoph, R. Stern, and C. Dupuis, 2002, Organization of oscillatory zoning in zircon: analysis, scaling, geochemistry, and model of a zircon from Kipawa, Quebec, Canada: Geochimica et Cosmochimica Acta, v. 66, no. 2, p. 311-328, doi:10.1016/S0016-7037(01)00774-8.

Franke, W., M. P. Doublier, K. Klama, S. Potel, and K. Wemmer, 2011, Hot metamorphic core complex in a cold foreland: International Journal of Earth Sciences, v. 100, no. 4, p. 753-785, doi:10.1007/s00531-010-0512-7.

Fryer, B. J., S. E. Jackson, and H. P. Longerich, 1993, The application of laser ablation microprobe-inductively coupled plasma-mass spectrometry (LAM-ICP-MS) to *in situ* (U)-Pb geochronology: Chemical Geology, v. 109, no. 1, p. 1-8, doi:10.1016/0009-2541(93)90058-Q.

Galbraith, R. F., 2005, Statistics for Fission-track Analysis: <https://www.crcpress.com/Statistics-for-Fission-Track-Analysis/Galbraith/p/book/9781584885337> (accessed May 11, 2019).

Galbraith, R. F., 1990, The radial plot: Graphical assessment of spread in ages: International Journal of Radiation Applications and Instrumentation. Part D. Nuclear Tracks and Radiation Measurements, v. 17, no. 3, p. 207-214, doi:10.1016/1359-0189(90)90036-W.

Galbraith, R. F., 1998, The trouble with "probability density" plots of fission-track ages: Radiation Measurements, v. 29, no. 2, p. 125-131, doi:10.1016/S1350-4487(97)00247-3.

Galbraith, R. F., and P. F. Green, 1990, Estimating the component ages in a finite mixture: International Journal of Radiation Applications and Instrumentation. Part D. Nuclear Tracks and Radiation Measurements, v. 17, no. 3, p. 197-206, doi:10.1016/1359-0189(90)90035-V.

Galbraith, R. F., and G. M. Laslett, 1993, Statistical models for mixed fission-track ages: Nuclear Tracks and Radiation Measurements, v. 21, no. 4, p. 459-470, doi:10.1016/1359-0189(93)90185-C.

Gallagher, K., R. Brown, and C. Johnson, 1998, Fission-track Analysis and Its Applications to Geological Problems: Annual Review of Earth and Planetary Sciences, v. 26, no. 1, p. 519-572, doi:10.1146/annurev.earth.26.1.519.

Gallagher, K., K. Charvin, S. Nielsen, M. Sambridge, and J. Stephenson, 2009, Markov chain Monte Carlo (MCMC) sampling methods to determine optimal models, model resolution and model choice for Earth Science problems: Marine and Petroleum Geology, v. 26, no. 4, p. 525-535, doi:10.1016/j.marpetgeo.2009.01.003.

Gallou, G., J. B. Sirven, C. Dutouquet, O. L. Bihan, and E. Frejafon, 2011, Aerosols Analysis by LIBS for Monitoring of Air Pollution by Industrial Sources: Aerosol Science and Technology, v. 45, no. 8, p. 918-926, doi:10.1080/02786826.2011.566899.

Ganguly, J., and M. Tirone, 2009, Closure temperature, cooling age and high temperature thermochronology, in Physics and Chemistry of the Earth's Interior: Springer, p. 89-99.

Garver, J. I., and M. T. Brandon, 1994a, Erosional denudation of the British Columbia Coast Ranges as determined from fission-track ages of detrital zircon from the Tofino basin, Olympic Peninsula, Washington: Geological Society of America Bulletin, p. 16.

Garver, J. I., and M. T. Brandon, 1994b, Fission-track ages of detrital zircons from Cretaceous strata, southern British Columbia: Implications for the Baja BC hypothesis: Tectonics, v. 13, no. 2, p. 401-420, doi:10.1029/93TC02939.

Garver, J. I., M. T. Brandon, M. Roden-Tice, and P. J. J. Kamp, 1999, Exhumation history of orogenic highlands determined by detrital fission-track thermochronology: Geological Society, London, Special Publications, v. 154, no. 1, p. 283-304, doi:10.1144/GSL.SP.1999.154.01.13.

Gautheron, C., J. Barbarand, R. A. Ketcham, L. Tassan-Got, P. van der Beek, M. Pagel, R. Pinna-Jamme, F. Couffignal, and M. Fialin, 2013, Chemical influence on α-recoil damage annealing in apatite: Implications for (U-Th)/He dating: Chemical Geology, v. 351, p. 257-267.

Gautheron, C., L. Tassan-Got, J. Barbarand, and M. Pagel, 2009, Effect of alpha-damage annealing on apatite (U-Th)/He thermochronology: Chemical Geology, v. 266, no. 3, p. 157-170.

Gautheron, C., L. Tassan-Got, R. A. Ketcham, and K. J. Dobson, 2012, Accounting for long alpha-particle stopping distances in (U-Th-Sm)/He geochronology: 3D modeling of diffusion, zoning, implantation, and abrasion: Geochimica et Cosmochimica Acta, v. 96, p. 44-56, doi:10.1016/j.gca.2012.08.016.

Giacomini, F., R. Maria Bomparola, C. Ghezzo, and H. Guldbransen, 2006, The geodynamic evolution of the Southern European Variscides: Constraints from the U/Pb geochronology and geochemistry of the lower Palaeozoic magmatic-sedimentary sequences of Sardinia (Italy): Contributions to Mineralogy and Petrology, v. 152, p. 19-42, doi:10.1007/s00410-006-0092-5.

Gibson, M., H. D. Sinclair, G. J. Lynn, and F. M. Stuart, 2007, Late- to post-orogenic exhumation of the Central Pyrenees revealed through combined thermochronological data and modelling: Basin Research, v. 19, no. 3, p. 323-334, doi:10.1111/j.1365-2117.2007.00333.x.

Gleadow, A. J. W., 1981, Fission-track dating methods: what are the real alternatives? Nuclear Tracks, v. 5, no. 1, p. 3-14.

Gleadow, A. J. W., and P. G. Fitzgerald, 1987, Uplift history and structure of the Transantarctic Mountains: new evidence from fission-track dating of basement apatites in the Dry Valleys area, southern Victoria Land: Earth and Planetary Science Letters, v. 82, no. 1, p. 1-14, doi:10.1016/0012-821X(87)90102-6.

Gleadow, A., M. Harrison, B. Kohn, R. Lugo-Zazueta, and D. Phillips, 2015, The Fish Canyon Tuff: A new look at an old low-temperature thermochronology standard: Earth and Planetary Science Letters, v. 424, p. 95-108, doi:10.1016/j.epsl.2015.05.003.

Golberg, J.-M., and H. Maluski, 1988, Données nouvelles et mise au point sur l'âge du métamorphisme pyrénéen: Comptes Rendus de l'Académie des Sciences. Série 2, Mécanique, Physique, Chimie, Sciences de l'Univers, Sciences de la Terre, v. 306, no. 6, p. 429-435.

Golberg, J.-M., H. Maluski, and A. F. Leyreloup, 1986, Age de 95 Ma (méthode ^{39}Ar-^{40}Ar) d'une shonkinite des Corbières, de la brèche magmatique du col d'Agnes, et du métamorphisme statique dans la zone nord-pyrénéenne: Bull. Soc. géol. Fr, p. 623-628.

Graham, D. W., W. J. Jenkins, M. D. Kurz, and R. Batiza, 1987, Helium isotope disequilibrium and geochronology of glassy submarine basalts: Nature, v. 326, no. 6111, p. 384-386, doi:10.1038/326384a0.

Green, P. F., I. R. Duddy, A. J. W. Gleadow, P. R. Tingate, and G. M. Laslett, 1985, Fission-track annealing in apatite: Track length measurements and the form of the Arrhenius plot: Nuclear Tracks and Radiation Measurements (1982), v. 10, no. 3, p. 323-328, doi:10.1016/0735-245X(85)90121-8.

Green, P. F., I. R. Duddy, A. J. W. Gleadow, P. R. Tingate, and G. M. Laslett, 1986, Thermal annealing of fission-tracks in apatite: 1. A qualitative description: Chemical Geology: Isotope Geoscience section, v. 59, p. 237-253, doi:10.1016/0168-9622(86)90074-6.

Green, P. F., I. R. Duddy, and G. M. Laslett, 1988, Can fission-track annealing in apatite be described by first-order kinetics? Earth and Planetary Science Letters, v. 87, no. 1-2, p. 216-228, doi:10.1016/0012-821X(88)90076-3.

Green, P. J., and B. W. Silverman, 1993, Nonparametric Regression and Generalized Linear Models.

Guenthner, W. R., P. W. Reiners, P. G. DeCelles, and J. Kendall, 2015, Sevier belt exhumation in central Utah constrained from complex zircon (U-Th)/He data sets: Radiation damage and He inheritance effects on partially reset detrital zircons: Geological Society of America Bulletin, v. 127, no. 3-4, p. 323-348.

Guenthner, W. R., P. W. Reiners, R. A. Ketcham, L. Nasdala, and G. Giester, 2013, Helium diffusion in natural zircon: Radiation damage, anisotropy, and the interpretation of zircon (U-Th)/He thermochronology: American Journal of Science, v. 313, no. 3, p. 145-198.

Härdle, W., 1990, Applied Nonparametric Regression: Cambridge university press.

Harrison, T. M., and P. K. Zeitler, 2005, Fundamentals of Noble Gas Thermochronometry: Reviews in Mineralogy and Geochemistry, v. 58, no. 1, p. 123-149, doi:10.2138/rmg.2005.58.5.

Hasebe, N., J. Barbarand, K. Jarvis, A. Carter, and A. J. Hurford, 2004, Apatite fission-track chronometry using laser ablation ICP-MS: Chemical Geology, v. 207, no. 3, p. 135-145, doi:10.1016/j.chemgeo.2004.01.007.

Hasebe, N., A. Carter, A. J. Hurford, and S. Arai, 2009, The effect of chemical etching on LA-ICP-MS analysis in determining uranium concentration for fission-track chronometry: Geological Society, London, Special Publications, v. 324, no. 1, p. 37-46, doi:10.1144/SP324.3.

Hasebe, N., A. Tamura, and S. Arai, 2013, Zeta equivalent fission-track dating using LA-ICP-MS and examples with simultaneous U-Pb dating: Island Arc, v. 22, no. 3, p. 280-291, doi:10.1111/iar.12040.

van den Haute, P., F. de Corte, R. Jonckheere, and F. Bellemans, 1998, The Parameters That Govern the Accuracy of Fission-Track Age Determinations: A Re-Appraisal, in Peter van den Haute, and Frans de Corte, eds., Advances in Fission-Track Geochronology: A selection of papers presented at the International Workshop on Fission-Track Dating, Ghent, Belgium, 1996: Dordrecht, Springer Netherlands, Solid Earth Sciences Library, p. 33-46, doi:10.1007/978-94-015-9133-1_3.

Heller, P. L., R. W. Tabor, J. R. O'neil, D. R. Pevear, M. Shafiqullah, and N. S. Winslow, 1992, Isotopic provenance of Paleogene sandstones from the accretionary core of the Olympic Mountains,

Washington: GSA Bulletin, v. 104, no. 2, p. 140-153, doi:10.1130/0016-7606(1992)104<0140:IPOPSF>2.3.CO;2.

Herman, F., J. Braun, T. J. Senden, and W. J. Dunlap, 2007, (U-Th)/He thermochronometry: Mapping 3D geometry using micro-X-ray tomography and solving the associated production-diffusion equation: Chemical Geology, v. 242, no. 1, p. 126-136, doi:10.1016/j.chemgeo.2007.03.009.

Hiess, J., D. J. Condon, N. McLean, and S. R. Noble, 2012, $^{238}U/^{235}U$ Systematics in Terrestrial Uranium-Bearing Minerals: v. 335, p. 6.

Hirata, T., and R. W. Nesbitt, 1995, U/Pb isotope geochronology of zircon: evaluation of the laser probe-inductively coupled plasma mass spectrometry technique: Geochimica et Cosmochimica Acta, v. 59, no. 12, p. 2491-2500, doi:10.1016/0016-7037(95)00144-1.

Horne, A. M., M. C. van Soest, and K. V. Hodges, 2019, U/Pb and (U-Th-Sm)/He "double" dating of detrital apatite by laser ablation: A critical evaluation: Chemical Geology, v. 506, p. 40-50, doi:10.1016/j.chemgeo.2018.12.004.

Horne, A. M., M. C. van Soest, K. V. Hodges, A. Tripathy-Lang, and J. K. Hourigan, 2016, Integrated single crystal laser ablation U/Pb and (U-Th)/He dating of detrital accessory minerals - Proof-of-concept studies of titanites and zircons from the Fish Canyon tuff: Geochimica et Cosmochimica Acta, v. 178, p. 106-123, doi:10.1016/j.gca.2015.11.044.

Hourigan, J. K., P. W. Reiners, and M. T. Brandon, 2005, U-Th zonation-dependent alpha-ejection in (U-Th)/He chronometry: Geochimica et Cosmochimica Acta, v. 69, no. 13, p. 3349-3365, doi:10.1016/j.gca.2005.01.024.

House, M. A., B. P. Wernicke, K. A. Farley, and T. A. Dumitru, 1997, Cenozoic thermal evolution of the central Sierra Nevada, California, from (UTh)/He thermochronometry: Earth and Planetary Science Letters, v. 151, no. 3, p. 167-179, doi:10.1016/S0012-821X(97)81846-8.

Humayun, M., and R. N. Clayton, 1995, Potassium isotope cosmochemistry: Genetic implications of volatile element depletion: Geochimica et Cosmochimica Acta, v. 59, no. 10, p. 2131-2148, doi:10.1016/0016-7037(95)00132-8.

Hurford, A. J., 1990, Standardization of fission-track dating calibration: Recommendation by the Fission-track Working Group of the I.U.G.S. Subcommission on Geochronology: Chemical Geology: Isotope Geoscience section, v. 80, no. 2, p. 171-178, doi:10.1016/0168-9622(90)90025-8.

Hurford, A. J., F. J. Fitch, and A. Clarke, 1984, Resolution of the age structure of the detrital zircon populations of two Lower Cretaceous sandstones from the Weald of England by fission-track dating: Geological Magazine, v. 121, no. 04, p. 269, doi:10.1017/S0016756800029162.

Hurford, A. J., and P. F. Green, 1982, A users' guide to fission-track dating calibration: Earth and Planetary Science Letters, v. 59, no. 2, p. 343-354, doi:10.1016/0012-821X(82)90136-4.

Hurford, A. J., and P. F. Green, 1983, The zeta age calibration of fission-track dating: Chemical Geology, v. 41, p. 285-317, doi:10.1016/S0009-2541(83)80026-6.

Hurley, P. M., 1955, The helium age method and the distribution and migration of helium in rocks: Massachusetts Institute of Technology, Department of Geology and Geophysics.

Ireland, T. R., T. Flöttmann, C. M. Fanning, G. M. Gibson, and W. V. Preiss, 1998, Development of the early Paleozoic Pacific margin of Gondwana from detrital-zircon ages across the Delamerian orogen: Geology, v. 26, no. 3, p. 243-246, doi:10.1130/0091-7613(1998)026<0243:DOTEPP>2.3.CO;2.

Jaffey, A. H., K. F. Flynn, L. E. Glendenin, W. C. Bentley, and A. M. Essling, 1971, Precision Measurement of Half-Lives and Specific Activities of $^{235}\mathrm{U}$ and $^{238}\mathrm{U}$: Physical Review C, v. 4, no. 5, p. 1889-1906, doi:10.1103/PhysRevC.4.1889.

Janowski, M., N. Loget, C. Gautheron, J. Barbarand, N. Bellahsen, J. Van Den Driessche, J. Babault, and B. Meyer, 2017, Neogene exhumation and relief evolution in the eastern Betics (SE Spain): Insights from the Sierra de Gador: Terra Nova, v. 29, no. 2, p. 91-97, doi:10.1111/ter.12252.

Jasra, A., D. A. Stephens, K. Gallagher, and C. C. Holmes, 2006, Bayesian Mixture Modelling in Geochronology via Markov Chain Monte Carlo: Mathematical Geology, v. 38, no. 3, p. 269-300, doi:10.1007/s11004-005-9019-3.

Jourdan, S., M. Bernet, P. Tricart, E. Hardwick, J.-L. Paquette, S. Guillot, T. Dumont, and S. Schwartz, 2013, Short-lived, fast erosional exhumation of the internal western Alps during the late early Oligocene: Constraints from geothermochronology of pro- and retro-side foreland basin sediments: Lithosphere, v. 5, no. 2, p. 211-225, doi:10.1130/L243.1.

Ketcham, R. A., R. A. Donelick, and W. D. Carlson, 1999, Variability of apatite fission-track annealing kinetics; III, Extrapolation to geological time scales: American Mineralogist, v. 84, no. 9, p. 1235-1255, doi:10.2138/am-1999-0903.

Ketcham, R. A., C. Gautheron, and L. Tassan-Got, 2011, Accounting for long alpha-particle stopping distances in (U-Th-Sm)/He geochronology: refinement of the baseline case: Geochimica et Cosmochimica acta, v. 75, no. 24, p. 7779-7791.

Kowalewski, M., and J. D. Rimstidt, 2003, Average Lifetime and Age Spectra of Detrital Grains: Toward a Unifying Theory of Sedimentary Particles: The Journal of Geology, v. 111, no. 4, p. 427-439, doi:10.1086/375284.

Kowallis, B. J., J. S. Heaton, and K. Bringhurst, 1986, Fission-track dating of volcanically derived sedimentary rocks: Geology, v. 14, no. 1, p. 19, doi:10.1130/0091-7613(1986)14<19:FDOVDS>2.0.CO;2.

Laurent, O., S. Couzinié, A. Zeh, O. Vanderhaeghe, J.-F. Moyen, A. Villaros, V. Gardien, and C. Chelle-Michou, 2017, Protracted, coeval crust and mantle melting during Variscan late-orogenic evolution: U-Pb dating in the eastern French Massif Central: International Journal of Earth Sciences, v. 106, no. 2, p. 421-451, doi:10.1007/s00531-016-1434-9.

Lawton, T. F., 2014, Small grains, big rivers, continental concepts: Geology, v. 42, no. 7, p. 639-640, doi:10.1130/focus072014.1.

Leventhal, J. S., 1975, An evaluation of the uranium-thorium-helium method for dating young basalts: Journal of Geophysical Research (1896-1977), v. 80, no. 14, p. 1911-1914, doi:10.1029/JB080i014p01911.

Lippolt, H. J., M. Leitz, R. S. Wernicke, and B. Hagedorn, 1994, (Uranium + thorium)/helium dating of apatite: experience with samples from different geochemical environments: Chemical Geology, v. 112, no. 1, p. 179-191, doi:10.1016/0009-2541(94)90113-9.

Longerich, H. P., S. E. Jackson, and D. Günther, 1996, Inter-laboratory note. Laser ablation inductively coupled plasma mass spectrometric transient signal data acquisition and analyte concentration calculation: Journal of Analytical Atomic Spectrometry, v. 11, no. 9, p. 899-904, doi:10.1039/JA9961100899.

Ludwig, K. R., 2003, User's Manual for Isoplot 3.00 - A Geochronological Toolkit for Microsoft Excel: Berkeley Geochronology Center Special Publication.

Ludwig, K. R., 2012, User's Manual for Isoplot 3.75 - A Geochronological Toolkit for Microsoft Excel: Berkeley Geochronology Center Special Publication.

Machado, N., and G. Gauthier, 1996, Determination of $^{207}Pb/^{206}Pb$ ages on zircon and monazite by laser-ablation ICPMS and application to a study of sedimentary provenance and metamorphism in southeastern Brazil: Geochimica et Cosmochimica Acta, v. 60, no. 24, p. 5063-5073, doi:10.1016/S0016-7037(96)00287-6.

Malusà, M. G., A. Carter, M. Limoncelli, I. M. Villa, and E. Garzanti, 2013, Bias in detrital zircon geochronology and thermochronometry: Chemical Geology, v. 359, p. 90-107, doi:10.1016/j.chemgeo.2013.09.016.

Martínez, F. J., C. Dietsch, J. Aleinikoff, J. Cirés, M. L. Arboleya, J. Reche, and D. Gómez-Gras, 2016, Provenance, age, and tectonic evolution of Variscan flysch, southeastern France and northeastern Spain, based on zircon geochronology: GSA Bulletin, v. 128, no. 5-6, p. 842-859, doi:10.1130/B31316.1.

Mattinson, J. M., 2010, Analysis of the relative decay constants of ^{235}U and ^{238}U by multi-step CA-TIMS measurements of closed-system natural zircon samples: Chemical Geology, v. 275, no. 3, p. 186-198, doi:10.1016/j.chemgeo.2010.05.007.

Maurel, O., 2003, L'exhumation de la Zone Axiale des Pyrénées orientales: Une approche thermo-chronologique multi-méthodes du rôle des failles.: p. 264.

Maurel, O., P. Moniè, R. Pik, N. Arnaud, M. Brunel, and M. Jolivet, 2008, The Meso-Cenozoic thermo-tectonic evolution of the Eastern Pyrenees: an $^{40}Ar/^{39}Ar$ fission-track and (U-Th)/He thermochronological study of the Canigou and Mont-Louis massifs: International Journal of Earth Sciences, v. 97, no. 3, p. 565-584, doi:10.1007/s00531-007-0179-x.

Maurel, O., P. Monié, J. P. Respaut, A. F. Leyreloup, and H. Maluski, 2003, Pre-metamorphic $^{40}Ar/^{39}Ar$ and U-Pb ages in HP metagranitoids from the Hercynian belt (France): Chemical Geology, v. 193, no. 3, p. 195-214, doi:10.1016/S0009-2541(02)00351-0.

Maurel, O., J.-P. Respaut, P. Monié, N. Arnaud, and M. Brunel, 2004, U/Pb emplacement and $^{40}Ar/^{39}Ar$ cooling ages of the eastern Mont-Louis granite massif (Eastern Pyrenees, France): Comptes Rendus Geoscience, v. 336, no. 12, p. 1091-1098, doi:10.1016/j.crte.2004.04.005.

McDougall, I., and T. M. Harrison, 1999, Geochronology and Thermochronology by the $^{40}Ar/^{39}Ar$ Method.

McInnes, B. I. A., K. A. Farley, R. H. Sillitoe, and B. P. Kohn, 1999, Application of apatite (U-Th)/He thermochronometry to the determination of the sense and amount of vertical fault displacement at the Chuquicamata porphyry copper deposit, Chile: Economic Geology, v. 94, no. 6, p. 937-947, doi:10.2113/gsecongeo.94.6.937.

McLachlan, G. J., S. X. Lee, and S. I. Rathnayake, 2019, Finite Mixture Models: Annual Review of Statistics and Its Application, v. 6, no. 1, p. 355-378, doi:10.1146/annurev-statistics-031017-100325.

Metcalf, J. R., P. G. Fitzgerald, S. L. Baldwin, and J.-A. Muñoz, 2009, Thermochronology of a convergent orogen: Constraints on the timing of thrust faulting and subsequent exhumation of the Maladeta Pluton in the Central Pyrenean Axial Zone: Earth and Planetary Science Letters, v. 287, no. 3-4, p. 488-503, doi:10.1016/j.epsl.2009.08.036.

Montigny, R., B. Azambre, M. Rossy, and R. Thuizat, 1986, The Geological Evolution of the Pyrenees K-Ar Study of cretaceous magmatism and metamorphism in the pyrenees: Age and length of rotation of the Iiberian Peninsula: Tectonophysics, v. 129, no. 1, p. 257-273, doi:10.1016/0040-1951(86)90255-6.

Mouthereau, F., P.-Y. Filleaudeau, A. Vacherat, R. Pik, O. Lacombe, M. G. Fellin, S. Castelltort, F. Christophoul, and E. Masini, 2014, Placing limits to shortening evolution in the Pyrenees: Role of margin architecture and implications for the Iberia/Europe convergence: Plate convergence in the Pyrenees: Tectonics, v. 33, no. 12, p. 2283-2314, doi:10.1002/2014TC003663.

Müller, H. G., 1988, Nonparametric Regression Analysis of Longitudinal Data.

Murray, K. E., D. A. Orme, and P. W. Reiners, 2014, Effects of U-Th-rich grain boundary phases on apatite helium ages: Chemical Geology, v. 390, p. 135-151, doi:10.1016/j.chemgeo.2014.09.023.

Mussett, A. E., 1969, Diffusion Measurements and the Potassium-Argon Method of Dating: Geophysical Journal International, v. 18, no. 3, p. 257-303, doi:10.1111/j.1365-246X.1969.tb03569.x.

Nasdala, L., J. M. Hanchar, A. Kronz, and M. J. Whitehouse, 2005, Long-term stability of alpha particle damage in natural zircon: Chemical Geology, v. 220, no. 1-2, p. 83-103, doi:10.1016/j.chemgeo.2005.03.012.

Naylor, M., H. D. Sinclair, M. Bernet, P. van der Beek, and L. A. Kirstein, 2015, Bias in detrital fission-track grain-age populations: Implications for reconstructing changing erosion rates: Earth and Planetary Science Letters, v. 422, p. 94-104, doi:10.1016/j.epsl.2015.04.020.

Nicolas, R., 1998, Etude géochronologique et pétrostructurale des mylonites du massif de l'Agly, PhD Thesis.

Olivier, P., G. Gleizes, and J. L. Paquette, 2004, Gneiss domes and granite emplacement in an obliquely convergent regime: New interpretation of the Variscan Agly Massif (Eastern Pyrenees, France), in D. L. Whitney, C. Teyssier, and C. S. Siddoway, eds., Gneiss Domes in Orogeny: Boulder, Geological Soc Amer Inc, p. 229-242.

Paton, C., J. Hellstrom, B. Paul, J. Woodhead, and J. Hergt, 2011, Iolite: Freeware for the visualisation and processing of mass spectrometric data: Journal of Analytical Atomic Spectrometry, v. 26, no. 12, p. 2508-2518, doi:10.1039/C1JA10172B.

Pavanetto, P., A. Funedda, C. J. Northrup, M. Schmitz, J. Crowley, and A. Loi, 2012, Structure and U/Pb zircon geochronology in the Variscan foreland of SW Sardinia, Italy: STRUCTURE AND U/PB GEOCHRONOLOGY IN THE SARDINIAN VARISCAN FORELAND: Geological Journal, v. 47, no. 4, p. 426-445, doi:10.1002/gj.1350.

Pearce, N. J. G., W. T. Perkins, J. A. Westgate, M. P. Gorton, S. E. Jackson, C. R. Neal, and S. P. Chenery, 1997, A Compilation of New and Published Major and Trace Element Data for NIST SRM 610 and NIST SRM 612 Glass Reference Materials: Geostandards Newsletter, v. 21, no. 1, p. 115-144, doi:10.1111/j.1751-908X.1997.tb00538.x.

Peel, D., and G. J. McLachlan, 2000, Robust mixture modelling using the t distribution: Statistics and Computing, v. 10, no. 4, p. 339-348, doi:10.1023/A:1008981510081.

Perry, S. E., J. I. Garver, and K. D. Ridgway, 2009, Transport of the Yakutat Terrane, Southern Alaska: Evidence from Sediment Petrology and Detrital Zircon Fission-Track and U/Pb Double Dating: The Journal of Geology, v. 117, no. 2, p. 156-173, doi:10.1086/596302.

Petrus, J. A., and B. S. Kamber, 2012, VizualAge: A Novel Approach to Laser Ablation ICP-MS U/Pb Geochronology Data Reduction: Geostandards and Geoanalytical Research, v. 36, no. 3, p. 247-270, doi:10.1111/j.1751-908X.2012.00158.x.

Peyton, S. L., and B. Carrapa, 2013, An Introduction to Low-temperature Thermochronologic Techniques, Methodology, and Applications: p. 15-36, doi:10.1306/13381688St653578.

Price, P. B., and R. M. Walker, 1962a, Chemical Etching of Charged-Particle Tracks in Solids: Journal of Applied Physics, v. 33, no. 12, p. 3407-3412, doi:10.1063/1.1702421.

Price, P. B., and R. M. Walker, 1962b, Observations of Charged-Particle Tracks in Solids: Journal of Applied Physics, v. 33, no. 12, p. 3400-3406, doi:10.1063/1.1702420.

Rahl, J. M., P. W. Reiners, I. H. Campbell, S. Nicolescu, and C. M. Allen, 2003, Combined single-grain (U-Th)/He and U/Pb dating of detrital zircons from the Navajo Sandstone, Utah: Geology, v. 31, no. 9, p. 761, doi:10.1130/G19653.1.

Rahn, M. K., M. T. Brandon, G. E. Batt, and J. I. Garver, 2004, A zero-damage model for fission-track annealing in zircon: American Mineralogist, v. 89, no. 4, p. 473-484, doi:10.2138/am-2004-0401.

Reiners, P. W., 2005, Zircon (U-Th)/He Thermochronometry: Reviews in Mineralogy and Geochemistry, v. 58, no. 1, p. 151-179, doi:10.2138/rmg.2005.58.6.

Reiners, P. W., and M. T. Brandon, 2006, Using Thermochronology to Understand Orogenic Erosion: Annual Review of Earth and Planetary Sciences, v. 34, no. 1, p. 419-466, doi:10.1146/annurev.earth.34.031405.125202.

Reiners, P. W., T. A. Ehlers, and P. K. Zeitler, 2005, Past, Present, and Future of Thermochronology: Reviews in Mineralogy and Geochemistry, v. 58, no. 1, p. 1-18, doi:10.2138/rmg.2005.58.1.

Reiners, P. W., K. A. Farley, and H. J. Hickes, 2002, He diffusion and (U-Th)/He thermochronometry of zircon: initial results from Fish Canyon Tuff and Gold Butte: Tectonophysics, v. 349, no. 1, p. 297-308.

Reiners, P. W., T. L. Spell, S. Nicolescu, and K. A. Zanetti, 2004, Zircon (U-Th)/He thermochronometry: He diffusion and comparisons with (40)Ar/(39)Ar dating: Geochimica Et Cosmochimica Acta, v. 68, no. 8, p. 1857-1887, doi:10.1016/J.GCA.2003.10.021.

Rosman, K. J. R., and P. D. P. Taylor, 1998, Isotopic compositions of the elements 1997 (Technical Report): Pure and Applied Chemistry, v. 70, no. 1, p. 217-235, doi:10.1351/pac199870010217.

Rossi, P., G. Oggiano, and A. Cocherie, 2009, A restored section of the "southern Variscan realm" across the Corsica-Sardinia microcontinent: Comptes Rendus Geoscience, v. 341, no. 2, p. 224-238, doi:10.1016/j.crte.2008.12.005.

Rudge, J. F., 2008, Finding peaks in geochemical distributions: A re-examination of the helium-continental crust correlation: Earth and Planetary Science Letters, v. 274, no. 1-2, p. 179-188, doi:10.1016/j.epsl.2008.07.021.

Rutherford, E., 1906, Present Problems of Radioactivity: Houghton Mifflin.

Sambridge, M. S., and W. Compston, 1994, Mixture modeling of multi-component data sets with application to ion-probe zircon ages: Earth and Planetary Science Letters, v. 128, no. 3, p. 373-390, doi:10.1016/0012-821X(94)90157-0.

Sheather, S. J., and M. C. Jones, 1991, A Reliable Data-Based Bandwidth Selection Method for Kernel Density Estimation: Journal of the Royal Statistical Society: Series B (Methodological), v. 53, no. 3, p. 683-690, doi:10.1111/j.2517-6161.1991.tb01857.x.

Shimazaki, H., and S. Shinomoto, 2010, Kernel bandwidth optimization in spike rate estimation: Journal of Computational Neuroscience, v. 29, no. 1, p. 171-182, doi:10.1007/s10827-009-0180-4.

Silverman, B. W., 1986, Density Estimation for Statistics and Data Analysis: Density Estimation for Statistics and Data Analysis, p. 22.

Sircombe, K. N., 2004, AgeDisplay: an EXCEL workbook to evaluate and display univariate geochronological data using binned frequency histograms and probability density distributions: Computers & Geosciences, v. 30, no. 1, p. 21-31, doi:10.1016/j.cageo.2003.09.006.

Sláma, J. et al., 2008, Plešovice zircon — A new natural reference material for U-Pb and Hf isotopic microanalysis: Chemical Geology, v. 249, no. 1, p. 1-35, doi:10.1016/j.chemgeo.2007.11.005.

Soares, C. J., S. Guedes, J. C. Hadler, R. Mertz-Kraus, T. Zack, and P. J. Iunes, 2014, Novel calibration for LA-ICP-MS-based fission-track thermochronology: Physics and Chemistry of Minerals, v. 41, no. 1, p. 65-73, doi:10.1007/s00269-013-0624-2.

van Soest, M. C., B. D. Monteleone, J. W. Boyce, and K. V. Hodges, 2008, Advances in Laser Microprobe (U-Th)/He Geochronology: AGU Fall Meeting Abstracts, v. 53, p. V53B-2161.

Spiegel, C., B. Kohn, D. Belton, Z. Berner, and A. Gleadow, 2009, Apatite (U-Th-Sm)/He thermochronology of rapidly cooled samples: The effect of He implantation: Earth and Planetary Science Letters, v. 285, no. 1, p. 105-114, doi:10.1016/j.epsl.2009.05.045.

Steiger, R. H., and E. Jäger, 1977, Subcommission on geochronology: Convention on the use of decay constants in geo- and cosmochronology: Earth and Planetary Science Letters, v. 36, no. 3, p. 359-362, doi:10.1016/0012-821X(77)90060-7.

Stevens, T., A. Carter, T. P. Watson, P. Vermeesch, S. Andò, A. F. Bird, H. Lu, E. Garzanti, M. A. Cottam, and I. Sevastjanova, 2013, Genetic linkage between the Yellow River, the Mu Us desert and the Chinese Loess Plateau: Quaternary Science Reviews, v. 78, p. 355-368, doi:10.1016/j.quascirev.2012.11.032.

Stewart, R. J., and M. T. Brandon, 2004, Detrital-zircon fission-track ages for the "Hoh Formation": Implications for late Cenozoic evolution of the Cascadia subduction wedge: GSA Bulletin, v. 116, no. 1-2, p. 60-75, doi:10.1130/B22101.1.

Stockli, D. F., 2005, Application of Low-Temperature Thermochronometry to Extensional Tectonic Settings: Reviews in Mineralogy and Geochemistry, v. 58, no. 1, p. 411-448, doi:10.2138/rmg.2005.58.16.

Stockli, D. F., K. A. Farley, and T. A. Dumitru, 2000, Calibration of the apatite (U-Th)/He thermochronometer on an exhumed fault block, White Mountains, California: Geology, v. 28, no. 11, p. 983-986, doi:10.1130/0091-7613(2000)28<983:COTAHT>2.0.CO;2.

Strutt, R. J., 1908, On the accumulation of helium in geological time: Proceedings of the Royal Society of London. Series A, Containing Papers of a Mathematical and Physical Character, v. 81, no. 547, p. 272-277, doi:10.1098/rspa.1908.0079.

Strutt, R. J., 1905, On the Radio-Active Minerals: Proceedings of the Royal Society of London. Series A, Containing Papers of a Mathematical and Physical Character, v. 76, no. 508, p. 88-101.

Strutt, R. J., 1909, The leakage of helium from radio-active minerals: Proceedings of the Royal Society of London. Series A, Containing Papers of a Mathematical and Physical Character, v. 82, no. 553, p. 166-169, doi:10.1098/rspa.1909.0019.

Tagami, T., 2005, Zircon Fission-Track Thermochronology and Applications to Fault Studies: Reviews in Mineralogy and Geochemistry, v. 58, no. 1, p. 95-122, doi:10.2138/rmg.2005.58.4.

Tagami, T., K. A. Farley, and D. F. Stockli, 2003, (U-Th)/He geochronology of single zircon grains of known Tertiary eruption age: Earth and Planetary Science Letters, v. 207, no. 1, p. 57-67, doi:10.1016/S0012-821X(02)01144-5.

Tagami, T., and P. B. O'Sullivan, 2005, Fundamentals of Fission-Track Thermochronology: Reviews in Mineralogy and Geochemistry, v. 58, no. 1, p. 19-47, doi:10.2138/rmg.2005.58.2.

Tera, F., and G. J. Wasserburg, 1972, U-Th-Pb systematics in lunar highland samples from the Luna 20 and Apollo 16 missions: Earth and Planetary Science Letters, v. 17, no. 1, p. 36-51, doi:10.1016/0012-821X(72)90257-9.

Ternois, S., M. Odlum, M. Ford, R. Pik, D. Stockli, B. Tibari, A. Vacherat, and V. Bernard, 2019, Thermochronological evidence of early orogenesis, eastern Pyrenees, France: Tectonics, doi:10.1029/2018TC005254.

Thomson, S. N., and F. Hervé, 2002, New time constraints for the age of metamorphism at the ancestral Pacific Gondwana margin of southern Chile (42-52°S): Revista geológica de Chile, v. 29, no. 2, p. 255-271, doi:10.4067/S0716-02082002000200007.

Thomson, S. N., P. W. Reiners, S. R. Hemming, and G. E. Gehrels, 2013, The contribution of glacial erosion to shaping the hidden landscape of East Antarctica: Nature Geoscience, v. 6, no. 3, p. 203-207, doi:10.1038/ngeo1722.

Thomson, K. D., D. F. Stockli, J. D. Clark, C. Puigdefàbregas, and A. Fildani, 2017, Detrital zircon (U-Th)/(He-Pb) double-dating constraints on provenance and foreland basin evolution of the Ainsa Basin, south-central Pyrenees, Spain: Tectonics, v. 36, no. 7, p. 2017TC004504, doi:10.1002/2017TC004504.

Tibari, B., A. Vacherat, M. Stab, R. Pik, D. Yeghicheyan, and P. Hild, 2016, An Alternative Protocol for Single Zircon Dissolution with Application to (U-Th-Sm)/He Thermochronometry: Geostandards and Geoanalytical Research, p. n/a-n/a, doi:10.1111/j.1751-908X.2016.00375.x.

Tripathy-Lang, A., K. V. Hodges, B. D. Monteleone, and M. C. van Soest, 2013, Laser (U-Th)/He thermochronology of detrital zircons as a tool for studying surface processes in modern catchments: Detrital zircon thermochronology: Journal of Geophysical Research: Earth Surface, v. 118, no. 3, p. 1333-1341, doi:10.1002/jgrf.20091.

Turekian, K. K., D. P. Kharkar, J. Funkhouser, and O. A. Schaeffer, 1970, An evaluation of the uranium-helium method of dating of fossil bones: Earth and Planetary Science Letters, v. 7, no. 5, p. 420-424, doi:10.1016/0012-821X(70)90084-1.

Vacherat, A. et al., 2016, Rift-to-collision transition recorded by tectonothermal evolution of the northern Pyrenees: Cooling history of the northern Pyrenees: Tectonics, v. 35, no. 4, p. 907-933, doi:10.1002/2015TC004016.

Vacherat, A., F. Mouthereau, R. Pik, M. Bernet, C. Gautheron, E. Masini, L. Le Pourhiet, B. Tibari, and A. Lahfid, 2014, Thermal imprint of rift-related processes in orogens as recorded in the Pyrenees: Earth and Planetary Science Letters, v. 408, p. 296-306, doi:10.1016/j.epsl.2014.10.014.

Vacherat, A., F. Mouthereau, R. Pik, D. Huyghe, J.-L. Paquette, F. Christophoul, N. Loget, and B. Tibari, 2017, Rift-to-collision sediment routing in the Pyrenees: A synthesis from sedimentological, geochronological and kinematic constraints: Earth-Science Reviews, v. 172, p. 43-74, doi:10.1016/j.earscirev.2017.07.004.

Vermeesch, P., 2012, On the visualisation of detrital age distributions: Chemical Geology, v. 312-313, p. 190-194, doi:10.1016/j.chemgeo.2012.04.021.

Vermeesch, P., 2009, RadialPlotter: A Java application for fission-track, luminescence and other radial plots: Radiation Measurements, v. 44, no. 4, p. 409-410, doi:10.1016/j.radmeas.2009.05.003.

Vermeesch, P., 2017, Statistics for LA-ICP-MS based fission-track dating: Chemical Geology, v. 456, p. 19-27, doi:10.1016/j.chemgeo.2017.03.002.

Vermeesch, P., S. C. Sherlock, N. M. W. Roberts, and A. Carter, 2012, A simple method for *in situ* U-Th-He dating: Geochimica et Cosmochimica Acta, v. 79, p. 140-147, doi:10.1016/j.gca.2011.11.042.

Wagner, G. A., A. J. W. Gleadow, and P. G. Fitzgerald, 1989, The significance of the partial annealing zone in apatite fission-track analysis: Projected track length measurements and uplift chronology of the

transantarctic mountains: Chemical Geology: Isotope Geoscience section, v. 79, no. 4, p. 295-305, doi:10.1016/0168-9622(89)90035-3.

Wagner, G. A., and P. van den Haute, 1992, Fission-Track Dating: Dordrecht, Kluwer Academic Publishers.

Wagner, G. A., and G. M. Reimer, 1972, Fission-track tectonics: The tectonic interpretation of fission-track apatite ages: Earth and Planetary Science Letters, v. 14, no. 2, p. 263-268, doi:10.1016/0012-821X(72)90018-0.

Wagner, G. A., G. M. Reimer, and E. Jaeger, 1977, Cooling Ages Derived by Apatite Fission-track: Mica Rb-Sr, and K-Ar Dating: The Uplift and Cooling History of the Central Alps: Societa Cooperativa Tipografica, Padova.

Waldner, M., Bellahsen, N., Mouthereau, F., Pik, R., Bernet, M., Scaillet, S., & Rosenberg, C. (2017). New Constraints for Tectono-Thermal Alpine Evolution of the Pyrenees: Combining Zircon Fission-Track and (U-Th)/He Analyses with Raman Spectrometry and In-Situ K-Ar Geochronology. AGU Fall Meeting Abstracts, 13. Retrieved from http://adsabs.harvard.edu/abs/2017AGUFM.T13A0493W

Wells, M. L., M. A. Beyene, T. L. Spell, J. L. Kula, D. M. Miller, and K. A. Zanetti, 2005, The Pinto shear zone; a Laramide synconvergent extensional shear zone in the Mojave Desert region of the southwestern United States: Journal of Structural Geology, v. 27, no. 9, p. 1697-1720, doi:10.1016/j.jsg.2005.03.005.

Wetherill, G. W., 1956, Discordant uranium-lead ages, I: Eos, Transactions American Geophysical Union, v. 37, no. 3, p. 320-326, doi:10.1029/TR037i003p00320.

Whitchurch, A. L., A. Carter, H. D. Sinclair, R. A. Duller, A. C. Whittaker, and P. A. Allen, 2011, Sediment routing system evolution within a diachronously uplifting orogen: Insights from detrital zircon thermochronological analyses from the South-Central Pyrenees: American Journal of Science, v. 311, no. 5, p. 442-482.

Wiedenbeck, M., P. Allé, F. Corfu, W. L. Griffin, M. Meier, F. Oberli, A. V. Quadt, J. C. Roddick, and W. Spiegel, 1995, Three Natural Zircon Standards for U-Th-Pb, Lu-Hf, Trace Element and Ree Analyses: Geostandards Newsletter, v. 19, no. 1, p. 1-23, doi:10.1111/j.1751-908X.1995.tb00147.x.

Willett, S. D., and M. T. Brandon, 2002, On steady states in mountain belts: Geology, v. 30, no. 2, p. 175-178.

Witt, C., S. Brichau, and A. Carter, 2012, New constraints on the origin of the Sierra Madre de Chiapas (south Mexico) from sediment provenance and apatite thermochronometry: ORIGIN OF SIERRA MADRE DE CHIAPAS: Tectonics, v. 31, no. 6, p. n/a-n/a, doi:10.1029/2012TC003141.

Wolf, R. A., K. A. Farley, and D. M. Kass, 1998, Modeling of the temperature sensitivity of the apatite (U-Th)/He thermochronometer: Chemical Geology, v. 148, no. 1-2, p. 105-114, doi:10.1016/S0009-2541(98)00024-2.

Wolfe, M. R., and D. F. Stockli, 2010, Zircon (U-Th)/He thermochronometry in the KTB drill hole, Germany, and its implications for bulk He diffusion kinetics in zircon: Earth and Planetary Science Letters, v. 295, no. 1-2, p. 69-82, doi:10.1016/j.epsl.2010.03.025.

Yelland, A. J., 1990, Fission-track thermotectonics in the Pyrenean orogen: International Journal of Radiation Applications and Instrumentation. Part D. Nuclear Tracks and Radiation Measurements, v. 17, no. 3, p. 293-299, doi:10.1016/1359-0189(90)90049-4.

Zeitler, P. K., N. M. Johnson, C. W. Naeser, and R. A. K. Tahirkheli, 1982, Fission-track evidence for Quaternary uplift of the Nanga Parbat region, Pakistan: Nature, v. 298, no. 5871, p. 255-257, doi:10.1038/2

Third Part

Results

Chapter 5

V. Thermochronological Evidence of Early Orogenesis, Eastern Pyrenees, France

FOREWORD

This Chapter has led to a publication in Tectonics:

AGU100 ADVANCING EARTH AND SPACE SCIENCE

Tectonics

RESEARCH ARTICLE
10.1029/2018TC005254

Thermochronological Evidence of Early Orogenesis, Eastern Pyrenees, France

Sébastien Ternois[1], Margaret Odlum[2], Mary Ford[1], Raphaël Pik[1], Daniel Stockli[2], Bouchaïb Tibari[1], Arnaud Vacherat[1], and Vincent Bernard[1]

[1]Centre de Recherches Pétrographiques et Géochimiques, UMR 7358 CNRS-Université de Lorraine, Vandoeuvre-lès-Nancy, France, [2]Department of Geological Sciences, Jackson School of Geosciences, University of Texas, Austin, TX, USA

Key Points:
- Zircon (U-Th)/He data record a cooling phase during early convergence in the Pyrenean low-relief retrowedge (Agly-Salvezines block)
- Forward and inverse thermal history modeling reveals limitations in current radiation damage-annealing models for He diffusion in zircon
- Crustal section sequential restoration demonstrates that tectonic processes alone can generate rapid cooling during early orogenesis

Supporting Information:
- Supporting Information S1
- Data Set S1

Correspondence to:
S. Ternois,
seb.ter@hotmail.fr

Citation:
Ternois, S., Odlum, M., Ford, M., Pik, R., Stockli, D., Tibari, B., et al. (2019). Thermochronological evidence of early orogenesis, eastern Pyrenees, France. *Tectonics*, *38*. https://doi.org/10.1029/2018TC005254

Received 26 JUL 2018
Accepted 24 JAN 2019
Accepted article online 2 FEB 2019

Abstract In collisional orogens, distinguishing the thermal signature of early orogenesis from the preceding rift or from subsequent thermal events is a major challenge. We present an integrated geological and low-temperature thermochronology study of the Paleozoic Agly-Salvezines crustal block in the retrowedge of the eastern Pyrenees (France). The northern Pyrenees preserves one of the best geological records of a rift-to-collision transition. The Agly-Salvezines block represents the inverted distal European margin of an Aptian–Cenomanian rift system. Seventeen samples were collected throughout the external orogenic massif and analyzed for low-temperature thermochronology: zircon (U-Th)/He dating documents the cooling history of the massif during the initiation and early phase of Pyrenean convergence, while apatite (U-Th)/He dating completes the record of plate collision. Using inverse and forward modeling of new low-temperature thermochronology data, we show that the Pyrenean retrowedge records two clear phases of orogenic cooling, Late Campanian–Maastrichtian and Ypresian–Bartonian, which we relate to early inversion of the distal rifted margin and main collision, respectively. An earlier, late Aptian–Turonian cooling history is detected, possibly related to rifting and/or postrift. No cooling is evidenced during the Paleocene during which tectonic quiescence is recorded in the adjacent Aquitaine retroforeland basin. Using our low-temperature thermochronology data and geological constraints, we propose a crustal-scale sequentially restored model for the tectonic and thermal transition from extension to peak orogenesis in the eastern Pyrenees, which suggests that both thrusting and underplating processes contributed to early inversion of the Aptian–Cenomanian rift system.

1. Introduction

The Pyrenean orogen was generated from late Santonian–early Campanian to middle Miocene by N-S convergence of the Iberian and European plates (Choukroune, 1989; Muñoz, 1992; Macchiavelli et al., 2017). External orogenic zones and foreland basins record two distinct periods of low but accelerating tectonic shortening and subsidence, latest Santonian–Danian and Thanetian–Oligocene, separated by a quiet (very low to near-zero subsidence) period during the Paleocene (Ford et al., 2016). These two periods are recognized to be synorogenic and mark two phases of convergence, the second generally recorded as Eocene–Oligocene in low-temperature thermochronology studies. Significantly, the orogen's three-phase convergence history does not correspond to behavior predicted by foreland dynamic models (Naylor & Sinclair, 2008; Sinclair et al., 2005; Sinclair & Naylor, 2012). While the evolution of crustal thickening, thermicity, orogen relief, and erosion during the main Eocene–Oligocene collisional phase are well studied and show a clear link to foreland basin dynamics (Fillon et al., 2013; Sinclair, 2011), the early Pyrenean history of convergence and the subsequent phase of quiescence are poorly constrained. In particular, there are few data on the thermal and dynamic behavior of the orogen during the earliest phase of Pyrenean convergence. The record of early orogenesis is best observed in the retrowedge where shortening and translation values are low (Naylor & Sinclair, 2008) and where the main Aptian–Cenomanian rifting phase is preserved. In this paper we present new zircon and apatite (U-Th-Sm)/He (ZHe and AHe, respectively) data from an external Paleozoic crustal block, Agly-Salvezines (Figures 1 and 2), in the eastern Pyrenean retrowedge. By integrating these data with new and published geological data, we address the following questions: Can we recognize a thermal signature for the onset of Pyrenean convergence and for Paleocene quiescence? Are early crustal thermal events contemporaneous with early foreland tectonic events, or is there a lag time between these two phenomena? Can we distinguish an early orogenic thermal signature from other thermal events such as those associated with preceding rifting or later collision?

TABLE OF CONTENT

LIST OF FIGURES

V.1 Abstract

In collisional orogens, distinguishing the thermal signature of early orogenesis from the preceding rift or from subsequent thermal events is a major challenge. We present an integrated geological and low-temperature thermochronology study of the Paleozoic Agly-Salvezines crustal block in the retro-wedge of the eastern Pyrenees (France). The northern Pyrenees preserves one of the best geological records of a rift-to-collision transition. The Agly-Salvezines block represents the inverted distal European margin of an Aptian-Cenomanian rift system. Seventeen samples were collected throughout the external orogenic massif and analyzed for low-temperature thermochronology: zircon (U-Th)/He dating documents the cooling history of the massif during the initiation and early phase of Pyrenean convergence, while apatite (U-Th)/He dating completes the record of plate collision. Using inverse and forward modeling of new low-temperature thermochronology data, we show that the Pyrenean retro-wedge records two clear phases of orogenic cooling, Late Campanian-Maastrichtian and Ypresian-Bartonian, which we relate to early inversion of the distal rifted margin and main collision, respectively. An earlier, late Aptian-Turonian cooling history is detected, possibly related to rifting and/or postrift. No cooling is evidenced during the Paleocene during which tectonic quiescence is recorded in the adjacent Aquitaine retroforeland basin. Using our low-temperature thermochronology data and geological constraints, we propose a crustal-scale sequentially restored model for the tectonic and thermal transition from extension to peak orogenesis in the eastern Pyrenees, which suggests that both thrusting and underplating processes contributed to early inversion of the Aptian-Cenomanian rift system.

Key Points:

- Zircon (U-Th)/He data record a cooling phase during early convergence in the Pyrenean low-relief retro-wedge (Agly-Salvezines block)
- Forward and inverse thermal history modeling reveals limitations in current radiation damage-annealing models for He diffusion in zircon
- Crustal section sequential restoration demonstrates that tectonic processes alone can generate rapid cooling during early orogenesis

V.2 Introduction

The Pyrenean orogen was generated from late Santonian-early Campanian to middle Miocene by N-S convergence of the Iberian and European plates (Choukroune, 1989; Muñoz, 1992; Macchiavelli et al., 2017). External orogenic zones and foreland basins record two distinct periods of low but accelerating tectonic shortening and subsidence, latest Santonian-Danian and Thanetian-Oligocene, separated by a quiet (very low to near-zero subsidence) period during the Paleocene (Ford et al., 2016). These two periods are recognized to be synorogenic and mark two phases of convergence, the second generally recorded as Eocene-Oligocene in low-temperature thermochronology studies. Significantly, the orogen's three-phase convergence history does not correspond to behavior predicted by foreland dynamic models (Naylor &

Sinclair, 2008; Sinclair et al., 2005; Sinclair & Naylor, 2012). While the evolution of crustal thickening, thermicity, orogen relief, and erosion during the main Eocene-Oligocene collisional phase are well studied and show a clear link to foreland basin dynamics (Fillon et al., 2013; Sinclair, 2011), the early Pyrenean history of convergence and the subsequent phase of quiescence are poorly constrained. In particular, there are few data on the thermal and dynamic behavior of the orogen during the earliest phase of Pyrenean convergence. The record of early orogenesis is best observed in the retro-wedge where shortening and translation values are low (Naylor & Sinclair, 2008) and where the main Aptian-Cenomanian rifting phase is preserved. In this paper we present new zircon and apatite (U-Th-Sm)/He (ZHe and AHe, respectively) data from an external Paleozoic crustal block, Agly-Salvezines (Figure V.1 and Figure V.2), in the eastern Pyrenean retro-wedge. By integrating these data with new and published geological data, we address the following questions: Can we recognize a thermal signature for the onset of Pyrenean convergence and for Paleocene quiescence? Are early crustal thermal events contemporaneous with early foreland tectonic events, or is there a lag time between these two phenomena? Can we distinguish an early orogenic thermal signature from other thermal events such as those associated with preceding rifting or later collision?

The Pyrenean case study has both advantages and challenges for the study of early orogenesis. Advantages include a low total convergence (92-165 km; Beaumont et al., 2000; Mouthereau et al., 2014; Muñoz, 1992; Roure et al., 1989; Teixell et al., 2018, 2016) allowing better preservation of early phases than in high-convergence orogens. There is also no thermal signature of subduction preceding collision, as is the case in many orogens, because no true oceanic crust was formed before the onset of convergence (Clerc & Lagabrielle, 2014; Jammes et al., 2009; Lagabrielle et al., 2010; Lagabrielle & Bodinier, 2008; Masini et al., 2014; Tugend et al., 2014). On the other hand, the Aptian-Cenomanian rifting generated a major thermal pulse that had not reequilibrated before the onset of convergence some 10 myrs later (Angrand et al., 2018). This inherited thermal perturbation may have been present during the first 30-35 myrs of orogenesis (Angrand et al., 2018; Vacherat et al., 2014), maintaining temperatures during early orogenesis above the sensitivity limit of low-temperature thermochronometers (40-300 °C; e.g. Carrapa, 2010; Peyton & Carrapa, 2013) and thus delaying any cooling record until the main Eocene collision (Vacherat et al., 2016). However, previous limited low-temperature thermochronology data (Yelland, 1991) indicate that the massifs at the eastern end of the external Pyrenean orogenic system, Agly-Salvezines, record a Campanian-Maastrichtian cooling signal, synchronous with the first period of accelerating subsidence in the retroforeland (Ford et al., 2016). This signature is absent in more proximal crystalline massifs further west, which only record Eocene exhumation (e.g. Vacherat et al., 2016), with the exception of the Labourd-Ursuya Massif at the extreme western end of the orogen (Figure V.1; Yelland, 1991; Vacherat et al., 2014). As paleotemperature data obtained by Raman spectroscopy on carbonaceous material (RSCM; Clerc et al., 2015; Chelalou et al., 2016, and references therein) and radiometric data (Clerc et al., 2015, and references therein) for Mesozoic

sediments suggest higher postrift cooling rates from end of rifting to the onset of convergence in the eastern Pyrenean retro-wedge, we can expect paleotemperatures at the onset of orogenesis to be lower in this region. A clear low-temperature thermochronology signal of the onset and early phase of orogenesis is therefore most likely to be preserved in the east, specifically in the Agly-Salvezines block.

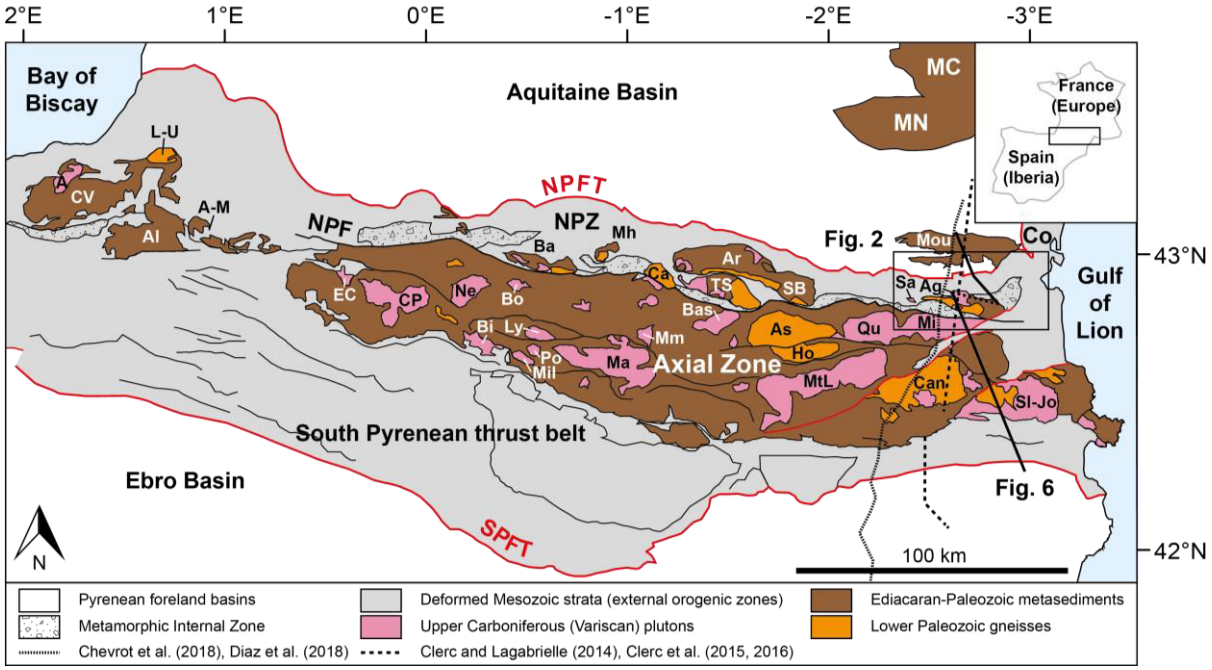

Figure V.1: Simplified tectonic map of the Pyrenees showing the main tectonic units, the location of the study area (Figure V.2), the position of the crustal-scale crosssectional model proposed in this paper (Figure V.6), and the location of (i) the North Pyrenean basement massifs and (ii) the main plutons/gneiss domes in the Axial Zone. NPFT = North Pyrenean Frontal Thrust; NORTH PYRENEAN ZONE = North Pyrenean Zone; NPF = North Pyrenean Fault; SPFT = South Pyrenean Fault; MN = Montagne Noire; MC = Massif Central; Mou = Mouthoumet; Co = Corbières. (i) L-U = Labourd-Ursuya; CV = Cinco Villas; Al = Aldudes; A-M = Arbailles-Mendibelza; Ba = Barousse; Mh = Milhas; Ca = Castillon; Ar = Arize; TS = Trois Seigneurs; SB = Saint-Barthélémy; Ag = Agly; Sa = Salvezines. (ii) A = Aya; EC = Eaux Chaudes; CP = Cauterets-Panticosa; Ne = Néouvielle; Bi = Bielsa; Bo = Bordères; Mil = Millares; Po = Posets; Ly = Lys-Caillaouas; Ma = Maladeta; Mm= Marimanha; Bas = Bassiès; As = Aston; Ho = Hospitalet; MtL = Mont-Louis; Qu = Quérigut; Mi = Millas; Can = Canigou-Carança; Sl-Jo = Saint Laurent-La Jonquera.

Campanian-to-Maastrichtian successions of the early Pyrenean foreland basins record sediment supply from a main eastern source area (Bilotte, 1985; Monod, 2014; Plaziat, 1981), which has since been destroyed by the Oligocene-Miocene opening of the Gulf of Lion (Séranne, 1999; Gunnell et al., 2008, 2009). The early orogenic wedge supplied little or no sediment at this time and therefore was of low relief, probably largely submarine (Ford et al., 2016). During the Eocene main collision, the growth of major orogen relief then migrated from east to west (Whitchurch et al., 2011, and references therein). Mass balance models predict that orogen relief will grow as long as topographic uplift (due to crustal thickening) is not balanced by erosion (growth phase; Willett et al., 1993; Willett & Brandon, 2002). Once this balance is achieved, the orogen passes to a steady state phase. Numerical models that use thermochronology data to constrain the thermal evolution of a growing orogen (e.g. Batt et al., 2001; Batt & Braun,

1997, 1999) have always evoked uplift and erosion to interpret cooling events. However, in the case of early orogenic wedge growth, erosion is expected to be nonsignificant. This could result in a negligible perturbation in thermal gradients at closure temperature depths, therefore questioning the potential of low-temperature thermochronology to record cooling related to the onset of orogenesis. However, as the recent work of Mesalles et al. (2014) has highlighted, crustal thickening by early underthrusting alone may lower the geotherm of distal rifted margins due to the downward deflection of isotherms. This implies that low-temperature thermochronology data may indeed record the initial stage of convergence.

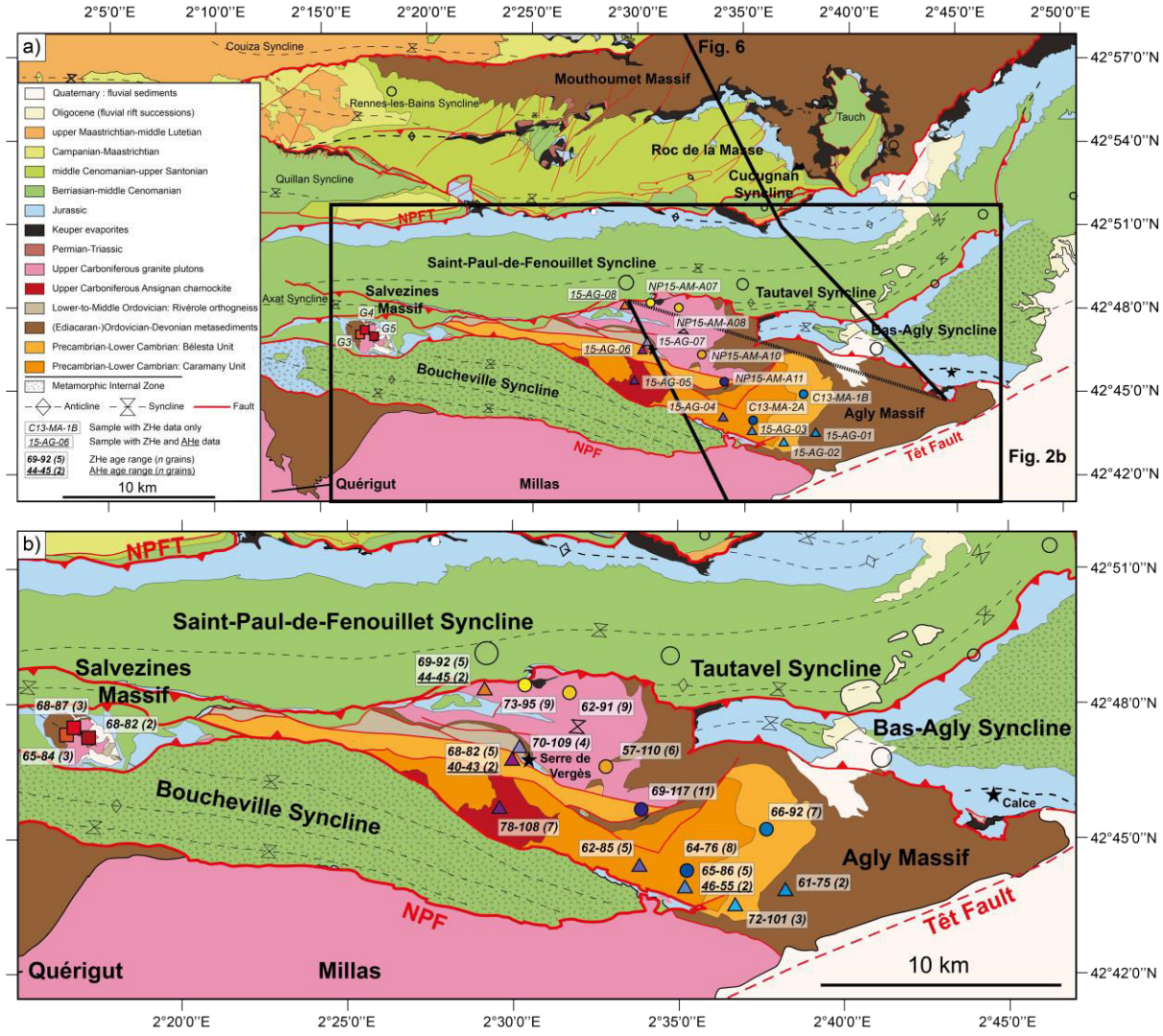

Figure V.2: Geological map of the Agly-Salvezines area, based on maps published by the BRGM (Bureau de Recherches Géologiques et Minières; Quillan: Bessière et al., 1989; Crochet et al., 1989; Tuchan: Berger, Alabouvette, et al., 1997; Berger, Bessière, et al., 1997; Rivesaltes: Berger et al., 1993; Fonteilles et al., 1993), showing the main structural elements and lithologies. The position of the crustal-scale sequentially restored cross-sectional model proposed in this paper Figure V.6) is indicated. Samples analyzed in this study are grouped into igneous/northern compartment rocks (yellow-red symbol colors) and metamorphic/southern compartment rocks (purple-blue symbol colors). Corresponding model results are shown in Figure V.4, Figure V.5, Appendix 17, Appendix 19, and Appendix 20. Sample names underlined have been dated by both ZHe and AHe methods.

Campanian-to-Maastrichtian successions of the early Pyrenean foreland basins record sediment supply from a main eastern source area (Bilotte, 1985; Monod, 2014; Plaziat, 1981), which has since been destroyed by the Oligocene-Miocene opening of the Gulf of Lion (Séranne, 1999; Gunnell et al., 2008, 2009). The early orogenic wedge supplied little or no sediment at this time and therefore was of low relief, probably largely submarine (Ford et al., 2016). During the Eocene main collision, the growth of major orogen relief then migrated from east to west (Whitchurch et al., 2011, and references therein). Mass balance models predict that orogen relief will grow as long as topographic uplift (due to crustal thickening) is not balanced by erosion (growth phase; Willett et al., 1993; Willett & Brandon, 2002). Once this balance is achieved, the orogen passes to a steady state phase. Numerical models that use thermochronology data to constrain the thermal evolution of a growing orogen (e.g. Batt et al., 2001; Batt & Braun, 1997, 1999) have always evoked uplift and erosion to interpret cooling events. However, in the case of early orogenic wedge growth, erosion is expected to be nonsignificant. This could result in a negligible perturbation in thermal gradients at closure temperature depths, therefore questioning the potential of low-temperature thermochronology to record cooling related to the onset of orogenesis. However, as the recent work of Mesalles et al. (2014) has highlighted, crustal thickening by early underthrusting alone may lower the geotherm of distal rifted margins due to the downward deflection of isotherms. This implies that low-temperature thermochronology data may indeed record the initial stage of convergence.

In this paper we present a detailed low-temperature thermochronology record of early convergence in the eastern Pyrenees, more precisely in the Agly-Salvezines region where the inverted distal margin of the Aptian-Cenomanian hyperextended rift system is preserved. We show that the easternmost massifs of the northern Pyrenees, unlike their more westerly counterparts, record two distinct cooling events during convergence, Campanian-Maastrichtian (ZHe data) and Ypresian-Bartonian (AHe data), separated by a period of very little cooling in the Paleocene. We argue that the early convergence cooling was due to early orogenic wedge thickening by underplating of the Iberian distal margin beneath the Agly-Salvezines crustal block and coeval northward thrusting of this block onto the colder, northern European crust. Exhumation of the thickening crust (wedge thickening by basal accretion coupled with erosion) is evoked as the principal cooling mechanism for the Eocene main convergence cooling event. Erosion-related exhumation then progressively migrated south. We discuss the implications of these new results for models of orogenic growth in the Pyrenees and for early convergence in general.

V.3 Geological Setting

The Pyrenean mountain belt is a relatively narrow (100-km-wide), double-wedged orogenic system trending N110° and extending over 1,500 km from the Cantabrian platform in northern Spain to the Mediterranean Sea (Languedoc-Provence) in southwestern France (Figure V.1). The orogen is divided into five tectonostratigraphic

zones. The external orogenic zone on the southern Iberian plate comprises the South Pyrenean fold-and-thrust belt and the Ebro (foreland) Basin (Vergés et al., 1995, 1998). The South Pyrenean Frontal Thrust (SPFT) separates the two systems. The Axial Zone in the core of the Pyrenean range consists of south-verging thrust sheets of Variscan metasediments and basement (Barnolas et al., 1996; Muñoz, 1992, and references therein). The Aquitaine (foreland) Basin and the North Pyrenean Zone form the retroforeland system on the northern European plate separated by the North Pyrenean Frontal Thrust (NPFT; Biteau et al., 2006; Souquet et al., 1977).

The Pyrenean chain was built on a complex crustal template. Basement blocks of the North Pyrenean Zone, namely, the North Pyrenean basement massifs (Choukroune, 1974), and the Axial Zone consist of Ediacaran-Paleozoic metasedimentary and Ordovician-to-Early Permian plutonic rocks recording the Variscan orogeny (e.g. Barnolas et al., 1996, and references therein). This orogeny was followed by two phases of Mesozoic extension or transtension, the first occurring from Triassic to Late Jurassic in an east-west zone linking the Tethys and Central Atlantic oceans (e.g. Curnelle et al., 1980). Rifting from late Aptian to early-to-middle Cenomanian (114-97 Ma) then created deep marine depocenters (Debroas, 1987, 1990), adjacent to the North Pyrenean basement massifs and associated with exhumation of mantle rocks (Azambre & Ravier, 1978; Clerc et al., 2012; Lagabrielle et al., 2010; Lagabrielle & Bodinier, 2008).

V.4 Thermal History of the Pyrenean Orogeny

V.4.1 Pyrenean Thermal History

Extensive low-temperature thermochronology studies in the Pyrenees over the last 20 years have produced a world-class data set to constrain crustal thermal behavior during orogenesis (Bosch et al., 2016; Hart et al., 2017; Labaume et al., 2016; Mouthereau et al., 2014, and references therein; Rushlow et al., 2013; Thomson et al., 2017; Vacherat et al., 2014, 2016). Bedrock low-temperature thermochronology (AHe and apatite fission-track [AFT]) data from the Axial Zone and the basement massifs in the central North Pyrenean Zone record only the Eocene-Oligocene (50-20 Ma) main collision cooling history, younging from east to west and from north to south (Mouthereau et al., 2014; Whitchurch et al., 2011).

In contrast, relatively little is known about the thermal history of the early phase of Pyrenean convergence (latest Santonian to Danian). Sparse detrital AFT, ZHe and zircon fission-track (ZFT) data from early, synorogenic depocenters (southern Pyrenees: Filleaudeau et al., 2012; Fillon et al., 2013; Whitchurch et al., 2011) indicate that significant relief already supplied southern depocenters. However, foreland basin sedimentary records show that up to the Eocene, this relief lay to the east of the present-day mountain range (Bilotte, 1985; Monod, 2014; Plaziat, 1981). This suggests that an active orogenic zone existed further east for which two early cooling events are probably recorded by limited detrital low-temperature thermochronology data (95-135 and 60-80 Ma; Filleaudeau et al., 2012; Whitchurch et al., 2011; 85-110 and 60-85 Ma;

Mouthereau et al., 2014; Vacherat et al., 2017). The early Pyrenean orogen itself (Central Pyrenees) probably formed a low relief or even submarine edifice (Ford et al., 2016; Vacherat et al., 2017), with slow exhumation (0.2 km/myr) and little sediment yield until the late Eocene (Fillon & van der Beek, 2012; Fitzgerald et al., 1999). We would therefore expect that any sediments sourced from this area would be restricted to the upper, thermally non-reset levels of the crust.

Nevertheless, an early (Campanian to Maastrichtian) cooling event is recorded in sparse bedrock ZFT and ZHe data from Variscan basement massifs of the western (Labourd-Ursuya; Vacherat et al., 2014; Yelland, 1991) and eastern (Agly; Yelland, 1991) North Pyrenean Zone. Several factors may contribute to the lack of a clear record of early orogenic cooling. It is possible that sampling has been, as yet, too sparse to detect this early event. However, early crustal thickening probably affected only the distal rifted margin, migrating outward to the proximal areas with time (definition of "distal" and "proximal" according to Sutra et al., 2013). Another reason could be simply that the early record of convergence in the Central Pyrenees was eroded away off the Axial Zone sometime from the Late Cretaceous to present (e.g. Filleaudeau et al., 2012; Rushlow et al., 2013; Thomson et al., 2017; Whitchurch et al., 2011). Only the more distal areas would have preserved the record of early orogeny. In any case, basement of the distal margin is poorly preserved in the orogen. Basement massifs in the eastern North Pyrenean Zone are, however, recognized as representing the distal upper plate (Agly and Salvezines; e.g. Clerc & Lagabrielle, 2014; Clerc et al., 2016).

V.4.2 The North Pyrenean Zone

The North Pyrenean Zone is a 10-to-40-km-wide, north-verging thrust system (Figure V.1). This zone lies between the NPFT to the north and the steeply dipping North Pyrenean Fault (NPF) to the south that is generally accepted as the surface trace of the plate boundary (Choukroune, 1989). It consists of a deformed Triassic to Turonian sedimentary succession, overlying Variscan basement that is exposed in the North Pyrenean basement massifs (Baby et al., 1988; Barnolas et al., 1996; Choukroune, 1974, and references therein).

The eastern North Pyrenean basement massifs show widespread hydrothermal alteration (250-550 °C) in the form of albitization, dequartzification, and massive talc-chlorite deposits dated middle Aptian to early Turonian (117-92 Ma; Boutin et al., 2016, and references therein). Along its southern margin the North Pyrenean Zone includes the Metamorphic Internal Zone, a narrow (0.5-10-km-wide) area of high-temperature (HT)-low-pressure (LP) metamorphism affecting Mesozoic sedimentary rocks (Choukroune, 1974; Ravier, 1957; Ravier & Thiébaut, 1982; Figure V.1). The thermal perturbation is dated 113-85 Ma over the whole Pyrenean realm, encompassing a major phase of extension and associated magmatic activity (Golberg & Leyreloup, 1990; Montigny et al., 1986, and references therein). Centimeter-scale fragments to kilometer-scale blocks of subcontinental mantle rocks and slices of granulitic crustal rocks occur throughout the Metamorphic Internal Zone, often associated with, or encased in,

carbonate breccias (Azambre & Ravier, 1978; Clerc et al., 2012; Lagabrielle et al., 2010; Lagabrielle & Bodinier, 2008). It is argued that this zone represents an area of extreme crustal thinning, possibly hyperextension, where exhuming mantle provided the heat source that caused metamorphism of the overlying Mesozoic strata (Chelalou et al., 2016; Clerc & Lagabrielle, 2014; Clerc et al., 2015, 2016; Vauchez et al., 2013).

V.4.3 The Agly-Salvezines Area

V.4.3.1 Structure and Stratigraphy

The Agly Massif is a N110° trending lens-shaped half-dome (35 km by 8 km), consisting in two main assemblages, hereafter referred to as the southern (mainly middle crust) and northern (middle-upper crust) compartments, separated by steep faults (Berger et al., 1993; Fonteilles et al., 1993; Figure V.2). The Salvezines Massif outcrops as a 3 km by 2 km tectonic window trending N110° and represents the western continuation of the northern Agly compartment. Together, the two massifs are hereafter referred to as the Agly-Salvezines block.

The Agly Massif preserves the most complete, albeit tectonically reduced (less than 10-km-thick), section of Variscan crust outcropping in the Pyrenees (Barnolas et al., 1996, and references therein). The crustal section is characterized by an overall apparent tilting NNE of its northern, upper compartment that may be Variscan in age (Olivier et al., 2004, 2008). From south to north (or bottom to top) the massif consists of the following: (i) the granulite facies Caramany Unit (paragneisses, marbles, orthogneisses, granitoids; Precambrian-to-Lower Cambrian protoliths), typical of the base of the middle crust; (ii) the amphibolite facies Bélesta Unit (partly migmatized paragneisses, orthogneisses, granitoids, and pegmatites; Precambrian-to-Lower Cambrian protoliths), typical of the middle crust; and (iii) a metasedimentary cover of greenschist to amphibolite facies rocks (Cambro-Ordovician-to-Devonian protoliths), typical of the upper crust (Althoff et al., 1994; Berger et al., 1993; Delay, 1989; Olivier et al., 2004, 2008; Tournaire Guille et al., 2018). Plutonic intrusions include Lower-to-Middle Ordovician granitic laccoliths in the Paleozoic cover (Rivérole orthogneiss) and upper Carboniferous granitic bodies at the base of the Caramany Unit (Ansignan charnockite, 5-6 kbar, 20-to-23-km depth; Andrieux, 1982; Vielzeuf, 1996) and in the Paleozoic cover (Saint-Arnac granite, 5-to-10-km depth). Late Carboniferous plutonism is recognized to be closely linked to a well-known, albeit poorly dated, Carboniferous HT-LP metamorphism (e.g. Barnolas et al., 1996). The Salvezines Massif comprises from bottom to top the following: (i) upper Carboniferous granite and gneiss in its central and southern part and (ii) Devonian-Visean metasedimentary rocks in its NNW sector. Salvezines gneisses present facies and textural similarities to the Rivérole orthogneiss (Demange & Pascal, 1979; Pascal, 1979).

The Agly-Salvezines block is surrounded by three N090°-to-N110° trending regional synforms of Keuper to Apto-Albian strata (Figure V.2; Fonteilles et al., 1993). (i) The Boucheville synform to the SSW, immediately north of the NPF, is separated from the oldest and highest-grade units cropping out along the southern edge of the Agly

Massif by a very steep tectonic contact and from the southern Salvezines Mesozoic cover by a complex and highly deformed tectonic zone (Demange & Pascal, 1979; Pascal, 1979) incorporating a 400-m-wide body of serpentinized mantle peridotite. (ii) The Bas-Agly syncline to the ENE is in tectonic contact with the Agly Massif on its southwesternmost limb. (iii) The Saint-Paul-de-Fenouillet synform to the north is overthrust by the Agly Massif on its southern limb and by the Bas-Agly syncline in the Tautavel region (Tautavel syncline).

V.4.3.2 Mesozoic Metamorphism and Metasomatism

The Bas-Agly and Boucheville synforms, which lie to the north and south of the Agly-Salvezines block (Figure V.2), are assigned to the Metamorphic Internal Zone as both record HT metamorphism (400 to 600 °C; Chelalou, 2015; Ducoux, 2017; Golberg & Leyreloup, 1990; Vauchez et al., 2013). The most recent radiometric dating studies of this metamorphism in the Liassic-Albian strata (Albarède & Michard-Vitrac, 1978; Golberg & Maluski, 1988; Montigny et al., 1986) present ages of 95-90 Ma (late Cenomanian-late Turonian), coeval with magmatic activity in the Corbières region, further northeast. On the basis of RSCM paleotemperature data in the Boucheville synform, Chelalou et al. (2016) propose that temperature increases downward through the complexly folded and poorly dated succession, giving an estimated vertical geothermal gradient of 80 °C/km for the Cenomanian-Turonian peak HT-LP event. In contrast, in the simpler structure of the Bas-Agly syncline, highest temperatures are recorded in the youngest strata (Berriasian to Albian) with lower temperatures in older strata (350-500 °C; Chelalou, 2015; Ducoux, 2017; Golberg & Leyreloup, 1990; Vauchez et al., 2013) and underlying pre-Mesozoic rocks of the Agly Massif (maximum temperatures of 350 °C in the Calce region, Figure V.2; Clerc et al., 2015; Ducoux, 2017). Small pockets of lower Liassic to lowermost Cretaceous marbles, scapolite-bearing limestones, and breccias occur along fault zones within the Agly Massif itself (Berger et al., 1993; Fonteilles et al., 1993), recording temperatures as high as 400-450 °C (Serre de Vergès, Figure V.2; Ducoux, 2017). In contrast, further north, the Barremian-Albian sediments of the Saint-Paul-de-Fenouillet syncline record markedly lower temperature metamorphism (<260 °C) with temperatures increasing downward (Chelalou, 2015). No clear dating for this low-temperature metamorphism exists, so that it may be attributed either to synrift events or to Pyrenean orogenesis.

Albitization is almost exclusively confined to the northern Agly-Salvezines compartment (Boulvais et al., 2007; Pascal, 1979). Upper crustal granites of this compartment show hydrothermal alteration to albitite dated at 117-96 Ma (1.5-2 kbar and 350-450 °C; Boulvais et al., 2007; Demange & Pascal, 1979; Guinault et al., 2016; Pascal, 1979; Poujol et al., 2010). This precedes the Cenomanian-Turonian peak HT-LP event in the surrounding Boucheville and Bas-Agly synforms. The pressure conditions for albitization suggest a crustal depth of 5 to 8 km. If one considers that temperature conditions correspond to background temperatures, estimates ranging from 40 to 90 °C/km are derived for the geothermal gradient that prevailed over the Agly-Salvezines block during the Aptian to Cenomanian.

The reduced crustal profile of the Agly-Salvezines block has been alternatively interpreted as due to (i) late Variscan to post-Variscan extension, following either orogenic crustal thickening (Bouhallier et al., 1991) or transpressive thermal doming (Olivier et al., 2004, 2008), or (ii) Early Cretaceous extension based on directional similarities of basement stretching to Early Cretaceous stretching of the Agly Mesozoic cover (Delay, 1989; Delay & Paquet, 1989; Paquet & Delay, 1989; Paquet & Mansy, 1991, 1992). While not favoring either interpretation, the work by R. Nicolas cited in Clerc et al. (2015) shows that partial (re)activation of Variscan mylonitic extensional shear zones under greenschist facies conditions in the southern Agly compartment (300-400 °C, 2-3 kbar) was synchronous with Early Cretaceous rifting. These pressure conditions suggest a crustal depth of 8 to 12 km for the Agly southern compartment, which is consistent with its expected structural position with respect to the northern granitic compartment at that time. However, if one considers that the temperature conditions of shear zone recrystallization correspond to background temperatures during the Early Cretaceous, this gives estimates of only 30-50 °C/km for the geothermal gradient that prevailed over the Agly-Salvezines block. These estimates are lower than but overlapping with those obtained for albitization in the northern Agly-Salvezines compartment over the same period of time.

V.4.3.3 Thermal State of the Agly-Salvezines Block at Onset of Pyrenean Convergence

Although the Agly Massif lies between two sectors of the Metamorphic Internal Zone, which both record temperatures of up to 500-600 °C, the basement rocks of the massif did not record any post-Variscan temperature higher than the greenschist facies temperature conditions reached during the Variscan. Moreover, the vertical geothermal gradient that prevailed specifically over the Agly-Salvezines block during the Early Cretaceous (rifting, albitization, and mylonitic reactivation) is poorly constrained, with overall estimates ranging from 30 to 80 °C/km and varying between the northern and southern compartments.

Many processes have been proposed as the heat source for HT conditions recorded in Mesozoic strata: (i) exhumed mantle (Clerc & Lagabrielle, 2014; Clerc et al., 2015, 2016; Chelalou et al., 2016; Vauchez et al., 2013), and/or (ii) high thermal fluxes along deeply rooted strike-slip faults (Clerc et al., 2015, 2016; Vaudin, 1982), and/or (iii) heat transfer by fluid circulation (Boulvais, 2016; Clerc et al., 2015, 2016; Dauteuil & Ricou, 1989). Along with evidence of extensional shear zones possibly active during the Cretaceous on the northern side of the Agly Massif (Paquet & Mansy, 1991), the reduced crustal section of the Agly Massif, and the presence of a block of mantle peridotite in the Boucheville synform, these features have led recent workers to position the Agly-Salvezines block at the distal edge of the Aptian-Cenomanian rift system, where deep crustal levels and subcontinental mantle rocks were exhumed (Chelalou et al., 2016; Clerc et al., 2016; Clerc & Lagabrielle, 2014; Ducoux, 2017; Vauchez et al., 2013). While all models of these authors consider the Boucheville and Bas-Agly synforms as autochtonous depocenters to the north and south of the Agly Massif, they differ in that

they propose either (i) unroofing of the Agly-Salvezines basement by Albian times (Clerc & Lagabrielle, 2014; Ravier, 1957; Vauchez et al., 2013) or (ii) burial of the massif below a continuous and thick Apto-Albian depocenter (Chelalou et al., 2016; Clerc et al., 2015, 2016; Ducoux, 2017; Olivier, 2013). The former implies that the allochthonous Agly Mesozoic cover in the Calce region has been almost fully preserved since the Albian. In contrast, the latter is supported by the absence of any recorded clasts of Mesozoic or pre-Mesozoic lithologies in the upper Aptian-to-lower Cenomanian fine-grained distal clastic marine sediments in either the Bas-Agly or Saint-Paul-de-Fenouillet depocenter that could have been locally derived from the emerging massif (Berger et al., 1993). It also favors the proposition of Clerc and Lagabrielle (2014) who argue that Albian sediments in Bas-Agly and Boucheville experienced HT conditions below a possibly 3- to 6-km-thick cover of Albo-Cenomanian flysch. As highlighted by Olivier (2013), currently available field and geochemical data do not allow a conclusive decision on this point.

New data are therefore required to constrain the structural and thermal evolution of the Agly-Salvezines block during early orogenesis and to define the thermal state of the crustal block before the onset of orogenesis. If the block was part of the distal margin of an Aptian-Cenomanian rift system, possibly hyperextended, we would expect rift-related heating and subsequent postrift cooling. However, we do not know the depth of burial of the Agly-Salvezines block during the Early Cretaceous, nor do we know the extent of the HT-LP metamorphic event affecting the block. With low-temperature thermochronology we aim to distinguish between burial below a thin sedimentary cover (relatively cold signature) or a thick cover (relatively hot signature). We also aim to get a better sense of background temperatures through time and investigate whether the Early Cretaceous metamorphism was focused in fault zones and/or localized in certain areas. The data presented in this study aim to answer some of these critical issues regarding the rift-to-collision transition.

V.5 (U-Th)/He Thermochronology Analyses

V.5.1 Sampling Strategy

We collected a total of 17 samples from the Agly and Salvezines massifs: 10 granitic samples, mostly in the northern, upper compartment, and 1 detrital and 6 gneissic samples in the southern, lower compartment (Figure V.2). Four granitic samples (15-AG-08, NP15-AM-A07, NP15-AM-A08, and NP15-AM-A10) were collected in the Upper Carboniferous Saint-Arnac granite pluton in order to document the top, center, and base of the pluton (Olivier et al., 2004, 2008). Three samples with similar facies (G3, G4 and G5) were collected in the Salvezines albitized granite pluton. Sample 15-AG-01 was collected from sillimanite- and muscovitebearing Ordovician micaschists, and sample 15-AG-07 was collected in the Rivérole orthogneiss. Four samples were collected in the Bélesta Unit: samples C13MA-1B and 15-AG-06 are gneissic, and samples NP15-AM-A11 and 15-AG-02 present granitic textures. Finally, three gneissic samples (C13MA-2A, 15-AG-03, and 15-AG-04) were collected in the Caramany Unit, and

sample 15-AG-05 was collected in the Upper Carboniferous Ansignan charnockitic pluton.

V.5.2 Zircon (U-Th)/He Methodology

Zircon grains from the 50- to 250-µm fraction were isolated for (U-Th)/He dating analyses using conventional mineral separation techniques, including crushing, grinding, sieving, and water table concentration, standard heavy-liquid density, and magnetic susceptibility separation techniques. Zircon grains were subsequently handpicked for analysis according to the following conditions: (i) of bipyramidal shape (euhedral), unbroken and visibly fracture free, (ii) of any size (length, width, and thickness) >60 µm, (iii) of any transparency/opacity, and (iv) inclusion free when inspected under a binocular microscope.

The (U-Th)/He dating method is based on the radioactive decay of ^{238}U, ^{235}U, and ^{232}Th (decay series) into ^{4}He or alpha particles. Conventional bulk single-grain ZHe analyses were performed conjointly at the Centre de Recherches Pétrographiques et Géochimiques (CRPG; Nancy, France) and at the UTChron facilities at the Jackson School of Geosciences (University of Texas, Austin, USA). A bulk (U-Th)/He age is derived from measurements of parent and daughter nuclide abundances in a single, entire crystal (aliquot). It must be acknowledged that as is typical for most, if not all, conventional bulk ZHe dating studies, the degree of zonation within each of our dated grains was not measured due to intrinsic analytical protocol limitations. This will be discussed in section V.6. Nine samples were analyzed at the CRPG following procedures described in Pik et al. (2003) and Godard et al. (2009) for ^{4}He extraction and Tibari et al. (2016) for bulk parent U, Th, and Sm concentration measurements. The other eight samples were analyzed at the Jackson School of Geosciences following the procedures described in Wolfe and Stockli (2010). Based on replicate analysis of the Fish Canyon Tuff ZHe age standard, analytical uncertainties arising from the two protocols for uncorrected ZHe ages are estimated at 6% (1σ) and 4% (1σ), respectively.

Given the traveling distances of ^{4}He or alpha particles produced by radioactive decay of ^{238}U, ^{235}U, and ^{232}Th (~16.7, ~19.6, and ~19.3 µm, respectively; Farley et al., 1996), these particles can be ejected from the outer ~20 µm of the grain. As a result, ZHe ages were morphometrically corrected for alpha-ejection (the ejection correction parameter F_T) according to Ketcham et al. (2011). We considered our zircon grains as equidimensional bipyramidal solids, with width, a, equal to thickness, b, and the number of pyramids, Np, equal to 2. Polynomial fit parameters for surface-area-to-volume ratio, β, were those of Hourigan et al. (2005) for prisms with pyramids. As the Agly-Salvezines rocks are known to have experienced Carboniferous HT-LP metamorphism, we expected ZHe ages younger than 500 Ma. Therefore, we considered that the contribution of ^{235}U to the total ^{4}He concentration measured was negligible, and we decided to keep using F_T as the linear correction to the measured age as expressed by Farley et al. (1996).

V.5.3 Apatite (U-Th)/He Methodology

After mineral separation, apatite grains were handpicked for analysis according to the following conditions: (i) hexagonal shape (euhedral), unbroken and visibly fracture free, (ii) of sufficient size (width and thickness) >70 μm, and (iii) absolutely inclusion free when carefully inspected under a binocular microscope at ×180 immersed in alcohol. Selection of apatite absolutely free of U- and Th-bearing inclusions represents the biggest hurdle to accurate and reliable AHe age determinations. All conventional single-grain AHe analyses were performed at the UTChron facilities at the University of Texas, following procedures described in Prior et al. (2016).

Similar to ZHe ages, AHe ages were corrected morphometrically for alpha-ejection (F_T correction) according to Ketcham et al. (2011) due to long attenuation distances of radiogenic ^{4}He or alpha particles produced from ^{238}U, ^{235}U, and ^{232}Th (~19.7, ~22.8, and ~22.5 μm, respectively; Farley et al., 1996). After in vacuo totalfusion degassing by UV-laser heating for 5 min at 1070 °C and cryogenic purification, ^{4}He concentrations of single-grain apatite were determined using quadrupole mass spectrometry by isotope dilution (^{3}He spike). Degassed apatite aliquots are retrieved, dissolved in 30% nitric acid, spiked with an isotopically enriched tracer, and analyzed for U, Th, and Sm concentrations using a Thermo Element2 inductively coupled plasma mass spectrometer fitted with a microcentric nebulizer. Based on replicate analysis of the Fish Canyon Tuff AHe age and other fast-cooled in-house volcanic apatite standards, analytical uncertainties for uncorrected AHe ages are estimated at 3% (1σ).

V.6 (U-Th)/He Results

Our 17 samples provided a total of 94 zircon crystals satisfying the suitability tests for further investigation. Three of these samples also provided two suitable apatite crystals each. Our (U-Th)/He data are reported in Data Set S1 in the supporting information. Zircon grains yield F_T-corrected He ages ranging from 39.0 ± 2.3 to 117.1 ± 7.0 Ma with intrasample grain age variation from ~19% to ~93%. Our AHe ages range from 40.1 ± 2.4 to 55.0 ± 3.3 Ma. ZHe ages older than the Paleocene account for ~87% of the Agly-Salvezines data set. Ten samples yield middle Aptian to late Turonian (117-90 Ma) ZHe ages, hereafter referred to as middle Cretaceous ages. These ages account for ~22% of the data set. Only 2 zircons (~2% of the data set) yield Eocene ages, which fall into the range of our AHe ages and the AFT ages of Yelland (1991) and Gunnell et al. (2009) for the Agly Massif (40.3 ± 2.6 to 49.0 ± 1.8 Ma for mean track lengths of 13.19-14.18 μm).

Our ZHe and AHe data set shows a high degree of age variability due to significant intrasample variation, which is larger than would be expected given the analytical precision. It has been demonstrated that this could result from the inability of a single set of kinematic parameters for He diffusion to describe the natural thermochronometric behavior of zircon (Cherniak et al., 2009; Guenthner et al., 2013; Ketcham et al., 2013; Reiners et al., 2002, 2004) and apatite (Flowers et al., 2007; Gautheron et al., 2009; Shuster et al., 2006). Grain-specific characteristics such as grain

size, parent nuclide zoning, and radiation damage are among the most important known factors that influence helium diffusivity, all the more exacerbated in zircon (Dobson et al., 2008; Guenthner et al., 2013; Hourigan et al., 2005; Reiners et al., 2004; Wolfe & Stockli, 2010). It is therefore not unreasonable to expect outliers for crystals with very low helium retentivity. As the two Eocene ZHe ages fall into the range of both previously published AFT data and our AHe data, they are considered as outlier data points and will subsequently be ignored.

Systematic correlations between ZHe ages and equivalent spherical radius (an approximation of grain size) are not apparent in any of our individual sample zircon data sets (Appendix 15). Although no clear relationships between these two variables are found for zircon, we will nevertheless consider the grain size effect in later discussions. Regarding our AHe ages, it is not reasonable to search for any correlation with only two ages per sample, and we will therefore focus mainly on zircon ages. Given that zonation of U and Th is a potential source of age variation that has its strongest effect for grains with an ~60 μm equivalent spherical radius when high eU cores or high eU rims occupy the inner or outer third of the grain, respectively (the zircon impact index/factor/number; Guenthner et al., 2013, 2015), our lack of observations of zircon zonation for grains with a similar equivalent spherical radius on average (~65 μm) may appear to be an issue. In particular, Tournaire Guille et al. (2018) have recently shown that typical zircons collected from some of our sample locations show pre-Variscan-inherited cores and Upper Carboniferous metamorphic overgrowths that may occupy one third of the grains. However, Odlum and Stockli (2017), who analyzed zircons from eight of the samples presented in our study for U/Pb dating (solid triangles in Figure V.2 and Figure V.3), show that zircon zonation is only observed in gneissic samples 15-AG-06 and 15-AG-03. In addition, the U and Th abundance data for zoned grains presented in the two previously mentioned studies give a good sense of the style of zonation in all the grains analyzed. First, very few metamorphic overgrowths have been documented in typical zircons collected from the igneous sample locations. Second, these data indicate rim eU enrichment of less than an order of magnitude on average for zoned grains in the Bélesta and Caramany units, therefore likely placing the level of zonation for our equivalent grains between the "mildly problematic and worst case" scenarios of Guenthner et al. (2015; factor of enrichment of 2 and 10, respectively, for zircon grains systematically zoned in the same fashion with high eU rims occupying the outer third of the grain). These observations suggest that heterogeneous distribution of U and Th in our zircons, albeit likely contributing to some of the observed age irreproducibility in each sample, cannot alone explain the large spread in our ZHe ages. The remainder of this results section, and more generally this study, will therefore be mainly focused on the third main source of age variation in our ZHe data set: radiation damage (Guenthner et al., 2013, 2014, 2015, 2017).

Single-grain He ages are plotted against the bulk effective uranium concentration, eU, in Figure V.3.a (eU [ppm] = U [ppm] + 0.235 * Th [ppm]). Bulk eU is calculated for each grain, providing a proxy for both the production rate of alpha particles from decay

of U, Th, and their daughter products (Sm being a minor contributor to the alpha particle production budget) and the relative amount of radiation damage accumulated in each crystal of a sample that has not experienced annealing (for apatite: Flowers et al., 2007; Shuster et al., 2006; for zircon: Guenthner et al., 2013).

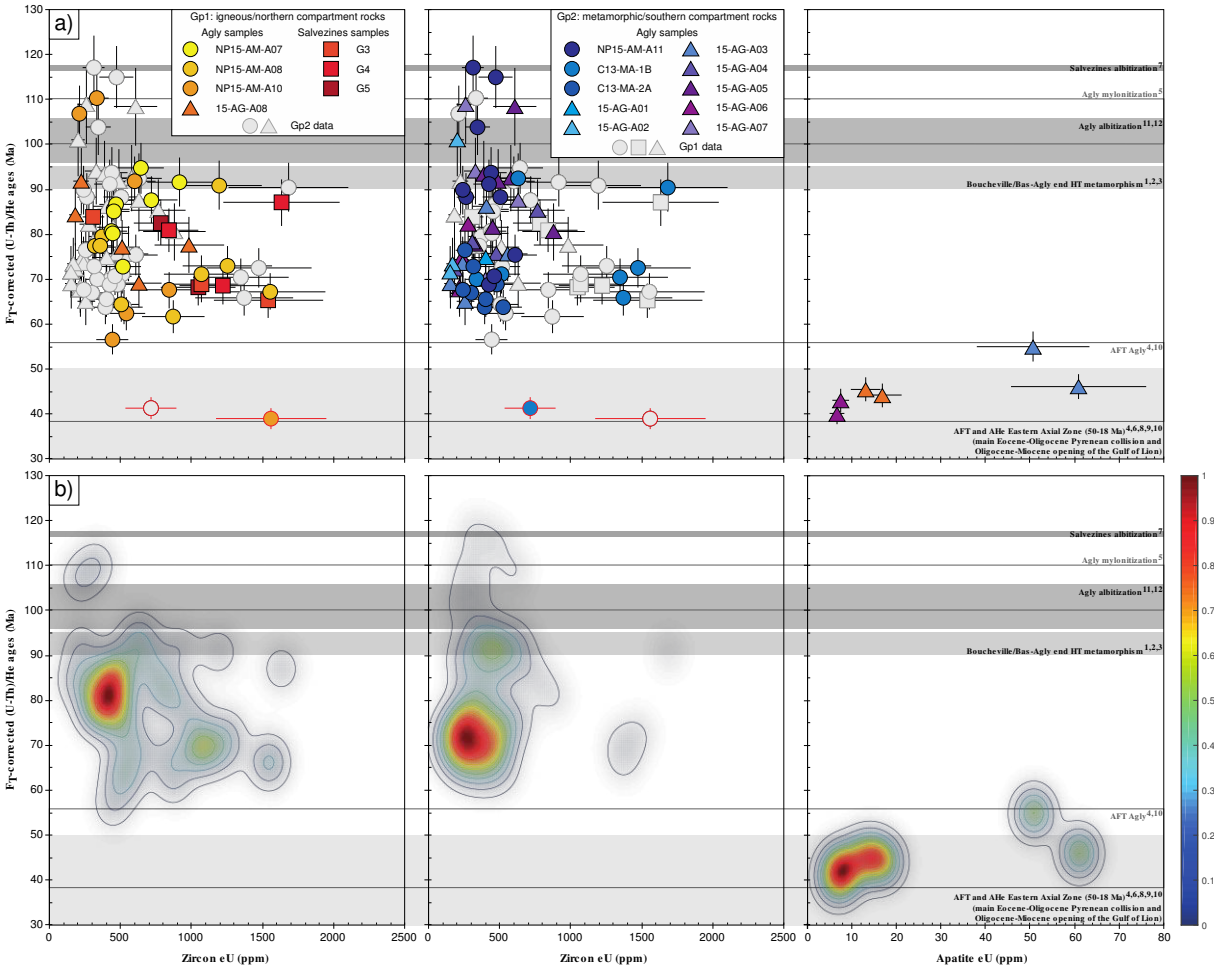

Figure V.3: (a) Zircon (left and middle inserts) and apatite (right insert) He age-eU correlations for the Agly-Salvezines data set, divided with the sample and group color scheme used in Figure V.2. ZHe age data for Gp1 and Gp2 are plotted separately. Gray bars indicate the ages of major thermal and structural events from literature. (b) Density graphs of the single-grain (U-Th)/He ages obtained in this study (2-D Kernel density estimation via the Parzen-Rosenblatt window method). 1: Albarède and Michard-Vitrac (1978); 2: Montigny et al. (1986); 3: Golberg and Maluski (1988); 4: Yelland (1991); 5: work by R. Nicolas cited in Clerc et al. (2015); 6: Maurel (2003); 7: Boulvais et al. (2007); 8: Denèle (2007); 9: Maurel et al. (2008); 10: Gunnell et al. (2009); 11: Poujol et al. (2010); 12: Guinault et al. (2016).

Our AHe ages are older at higher bulk eU. The age variability in our AHe data set is similar to that previously reported in other geological settings (Gautheron et al., 2009, and references therein). In particular, AHe ages at high eU concentrations may be found to be as old as or even a little older than AFT ages for the same geological province. It has been demonstrated that alpha-recoil damage induced by recoil of U and Th decay series during emission of alpha particles and eU concentration govern He diffusion within apatite crystals, and thus the resulting AHe ages (Flowers et al., 2007; Gautheron et al., 2009; Shuster et al., 2006). The amount of alpha-recoil damage increases with eU,

enhancing He retention for apatite crystals with higher eU and extending crystal temperature sensitivity from ~40-80 °C (Crowley et al., 2002; Farley, 2000; Farley et al., 1996; Stockli et al., 2000) up to (sometimes even higher than) that of the AFT system (~100 °C; Gallagher et al., 1998).

Similar age variability to that in our ZHe data set is reported in other data sets from the Pyrenees and from other similar orogenic settings (e.g. Guenthner et al., 2014, 2015, 2017; Vacherat et al., 2014, 2016). It has been demonstrated that this results from the inability of a single set of kinematic parameters for He diffusion to describe the natural thermochronometric behavior of zircon (Cherniak et al., 2009; Guenthner et al., 2013; Ketcham et al., 2013; Reiners et al., 2002, 2004). In particular, Guenthner et al. (2013) have recently proposed that such age variation in data sets illustrates the damage-dependent sensitivity of He in zircon to thermal processes. Similarly to the AHe system, these authors have established a zircon radiation-damage and annealing model that quantitatively describes the effects of radiation damage on He diffusion in zircon as a function of time and temperature. They show the clear dependency of He diffusivity on radiation damage by parameterizing the relationship between damage and diffusivity. Their model considers a partial annealing zone of 310-223 °C and the 8-orders-of-magnitude variation in diffusivity across the radiation dose spectrum. It also integrates the damage-based diffusion kinetics to calculate ZHe closure temperature as a function of the alpha dose. The model thus predicts that the ZHe system in damaged zircons (damage amounts ranging from 1 x1016 to 1 x1018 α/g) is sensitive to temperatures of 140 to 200-250 °C. This is in good agreement with previously documented temperature ranges for the ZHe partial retention zone (Reiners et al., 2002; Stockli, 2005; Tagami et al., 2003; Wolfe & Stockli, 2010).

In the case of ZHe thermochronology, age-eU plots have recently proved to be very useful to gain insight into the thermal history of a sample or a group of samples in several studies. It has been demonstrated that a sample or a group of samples may yield specific age-eU correlations, positive or negative, even both, as a result of its entire thermal history (e.g. Anderson et al., 2017; Guenthner et al., 2013, 2014, 2015, 2017; Hart et al., 2017; Johnson et al., 2017; Powell et al., 2016; Thomson et al., 2017; Vacherat et al., 2014, 2016). In our He age-eU plots (Figure V.3) we split the Agly-Salvezines sample collection into two distinct sample groups (Gp1 and Gp2) based on the sample rock type (igneous or metamorphic) and sample location (or inferred pre-Early Cretaceous sample depth: northern, upper compartment versus southern, lower compartment), irrespective of either the intrasample variation criterion or grain characteristics. This aimed at separating rocks that had, as a first approximation, distinct pre-Early Cretaceous history and therefore crystals with distinct grain-specific characteristics. Considerations of eU and sample groups are discussed in more detail in later sections of this chapter. Error bars shown here represent the 1σ analytical uncertainty for each singlegrain aliquot. Results for the two massifs, Agly and Salvezines, are presented together.

The first group (Gp1) comprises the seven igneous samples located in the northern compartment of Agly-Salvezines (Figure V.2). It is characterized by ZHe ages ranging from 56.6 ± 3.4 to 110.2 ± 6.6 Ma. Intrasample age variability is the same as that of the whole ZHe data set. ZHe ages are associated with bulk eU concentrations ranging from 183 to 1,633 ppm. Individual age and eU ranges are similar in the error bars from one sample to another, with the exception of sample NP15-AM-A10, which yields the oldest (Apto-Albian) ZHe ages for this group. Four samples (NP15-AM-A10, 15-AG-08, G3, and G5) have a clear negative age-eU correlation as ages decrease from ~90 ± 5 Ma to ~65 ± 5 with increasing eU (Appendix 16). Sample NP15-AM-A07 may have a positive age-eU correlation, as ages increase from ~75 ± 5 Ma to ~95 ± 5 with increasing eU.

The second group (Gp2) comprises the 10 samples from the southern compartment of Agly (Figure V.2). Both the intrasample grain variations and the ZHe age range of these samples are similar to those of Gp1 (age variability of ~19% to ~71%; ages of 63.8 ± 3.8 to 117.1 ± 7.0 Ma). Nonetheless, the ZHe age range is mostly confined to relatively low bulk eU concentrations (152-879 ppm) and a larger proportion of ages clustering around 60-75 Ma is found compared with Gp1. Five samples (15-AG-02, 15-AG-03, 15-AG-04, 15-AG-05, and 15-AG-06) have a positive age-eU correlation as ages increase from ~70 ± 5 to ~100 ± 5 Ma with increasing eU (Appendix 16). Three samples (NP15-AM-A11, C13-MA-2A, and 15-AG-07) may have a negative ageeU correlation.

Second-order scatter along the dominant age-eU trends is observed and likely results from the combined effects of grain size and, more importantly, intragranular U and Th heterogeneities within each grain. Nonetheless, it is clear that samples from the same group show similar individual zircon eU ranges and age-eU correlations (first-order negative correlations for Gp1 samples and positive correlations for Gp2 samples). We therefore argue that all samples of Gp1 experienced the same thermal history since the ZHe clock started. The same can be concluded for all samples of Gp2.

For each group, we combined individual sample data sets into a group data set and generated a twodimension (age and eU) kernel density estimation of the data (Figure V.3.b). The statistical distribution of Gp1 ages (37 ZHe ages) highlights two significant age clusters. The main age cluster (80 Ma) is found at eU concentrations of ~400 ppm. The second age cluster (70 Ma) corresponds to zircon crystals with eU concentrations ranging from ~1,000 to ~1,600 ppm. An additional age cluster, although poorly defined, may be centered on 110 Ma and 300-400 ppm. The age distribution in Gp2 (55 ZHe ages) suggests two age clusters at low eU concentrations (<500 ppm). The main cluster is found around 70 Ma at eU concentrations of ~300 ppm. The second cluster is centered on 90-95 Ma and eU concentrations of ~500 ppm. This cluster may be argued to encompass ages ranging from 90 to 117 Ma. An additional age cluster, although poorly defined, may be centered on 70 Ma and 1,500 ppm, corresponding to the rare ZHe ages plotting at high eU (>1,000 ppm). Both sample groups yield overlapping single-grain ZHe ages over the whole spread in bulk eU concentrations. Although 82-95% of ages from the Gp1 data set are younger than 90-95 Ma (compared with 64-79% for Gp2), arguing for distinct maximum ZHe ages of Gp1 and Gp2 is hazardous. Age distributions

(Figure V.3.b) do show an age cluster centered on 117-90 Ma (eU of ~300-500 ppm) for both groups. The situation is the same for most of ZHe ages around 65-75 Ma at low eU (~300-400 ppm) for Gp2 compared with Gp1 and around 70 Ma at high eU (1,000-1,500 ppm) for Gp1 compared with Gp2. These clusters are the cornerstones of the overall ZHe age-eU correlations observed for each group. First, these slight proportional differences could simply be the result of undersampling. Second, Odlum and Stockli (2017) and Tournaire Guille et al. (2018) have shown that incorporation of U and Th into zircon grains of the Agly Massif depends on the complexity of the grain crystallization history. In particular, typical zircons collected from the southern sample locations show systematic rim eU enrichment, so that they may have distinct domains with variable radiation damage, and therefore variable diffusivities. Consequently, this not only suggests that the ages these grains yield will be more dispersed or randomly distributed than ages of unzoned grains (igneous, northern compartment), but it also implies that they will probably plot at lower eU than their counterparts. One has then statistically more chance of handpicking zircon crystals with low bulk eU concentrations (or less chance in case of high bulk eU) in rocks from the southern compartment than in plutonic rocks from the northern compartment. Taken together, these two arguments could explain the better documentation of positive age-eU correlations for Gp2 and the poorer documentation of negative correlations in Gp1. On another note, based on the Guenthner et al. (2013) model, one can expect older crystals with longer exhumation histories to accumulate more radiation damage in the absence of annealing, shifting maximum retentivity for He and associated older ZHe ages at lower eU concentrations. All our samples yield older ages at similar bulk eU concentrations, most likely indicating homogeneous annealing (310-223 °C and above) of radiation damage of zircons at some point in their thermal history (the Variscan orogeny and the Aptian-middle Cenomanian HT-LP event are the best candidates; see below). We therefore argue that the reverse trends of age-eU correlations for Gp1 and Gp2 do not necessarily arise from distinct thermal histories for the two groups but may be simply due to some kind of sampling bias, as described above. The age clusters at low eU (~300-400 ppm) around 70 Ma for Gp2 and 80 Ma for Gp1 are most likely equivalent, possibly suggesting that rocks lying at different depths reached a particular closure temperature depth with some 10 myrs of delay. In a wider perspective, our AHe ages are very close to each other and display as a whole a positive age-eU correlation, consistent with apatite radiation-damage and annealing models. On the basis of all the low-temperature thermochronology similarities presented by the two groups, we expect all samples from this study to have experienced the same thermal history, at least since the middle Cretaceous.

V.7 Numerical (U-Th)/He Age Modeling

Recent studies (e.g. Anderson et al., 2017; Guenthner et al., 2014, 2015, 2017; Johnson et al., 2017; Powell et al., 2016; Vacherat et al., 2014, 2016) have shown that numerical modeling, incorporating apatite and zircon radiation-damage and annealing models for both the fission-track and (U-Th)/He systems, is extremely valuable for understanding and interpreting data. It allows exploration of the response of different

thermochronometers to various thermal histories and ultimately provides more quantitative constraints on the thermal history of a sample. To constrain the range of plausible t-T paths producing either model age-eU correlations or single-grain He ages that most closely match the data presented in this study, we performed both inverse modeling and forward modeling using the software program HeFTy (Ketcham, 2005).

V.7.1 Data Inverse Modeling Approach Using HeFTy

The new ZHe and AHe data presented in this study complete, and agree with, the sparse AFT data obtained by Yelland (1991) and Gunnell et al. (2009) for the Agly-Salvezines block. Altogether, these data document the time-temperature history of the crustal block in the overall temperature range of 45-250 °C (lower bound of the AHe partial retention zone-upper bound of the ZHe partial retention zone; e.g. Guenthner et al., 2013; Stockli et al., 2000).

V.7.1.1 HeFTy Thermochronology Model Parameterization

To explore plausible t-T spaces consistent with our data, we first used the inverse modeling approach. The number of thermochronometric models that can be input into HeFTy for inverse modeling is relatively limited. In particular, as already mentioned in Vacherat et al. (2014) and Powell et al. (2016), the full range of single-grain eU-dependent He ages cannot be used, so that representative individual ZHe and AHe ages must be chosen. All the model inputs and constraints used for our inverse modeling simulations are reported in Appendix 21, following the model input reporting protocol of Flowers et al. (2015).

Three ZHe age-eU couples were used as parameterizations of three HeFTy ZHe models, each of them representing one of the three age clusters shared by the two groups. The first cluster is defined around 75 Ma (± 9.4 Ma, 12%, 2σ analytical uncertainty) at low eU concentrations (300-500 ppm; HeFTy ZHe model 1). The second cluster concerns ZHe ages around 70 Ma (± 12%, 2σ analytical uncertainty) at relatively high eU concentrations (1,500 ppm; HeFTy ZHe model 2). The last cluster represents middle Cretaceous ages (105 Ma, ±12%, 2σ analytical uncertainty, ~400 ppm; HeFTy ZHe model 3). A similar reasoning was applied for AHe data with two AHe models characterizing ages either at low or at high eU concentrations (HeFTy AHe models 1 and 2). Finally, two AFT models were considered, based on Gunnell et al. (2009; HeFTy AFT models AGLY1 and AGLY5).

To reproduce the range of our ZHe ages (~70-110 Ma), our AHe ages (~43-50 Ma), and published AFT ages (~40-50 Ma), the post-Barremian time-temperature history was first left free within a t-T space limited by the upper bound of the partial annealing zone of the Guenthner et al. (2013) model (~300 °C) and surface temperature (shallow- to middle-crustal temperatures). The number of thermal constraints was then increased and t-T space limits modified according to the results of the first inverse modeling simulation to see whether this helps the software to search t-T paths consistent with our data.

V.7.1.2 Inverse Modeling Results

After randomly testing 300,000 t-T paths, the HeFTy software clearly fails to return thermal histories consistent with the required inputs (no acceptable or good solutions). In our case, such a failure occurs when more than five HeFTy inputs are used. The comparison of our AHe age data with the AFT age data present in the literature for the Agly Massif indicates that the AHe system encompasses a larger range of crystal temperature sensitivities than does the AFT system in this geological province. Therefore, we chose to keep performing inverse modeling with the five ZHe and AHe models only. Results of the first inverse modeling simulations are presented in Appendix 17.

The modeling returned only 142 acceptable and 4 good solutions. All the t-T paths obtained show that heating had to occur between 200 and 70-60 Ma, followed by rapid cooling. However, the timing of transition from heating to cooling is poorly constrained by inverse modeling. Overall, good fits place the onset of cooling around 60 Ma, whereas acceptable fits show a large range of possibilities (100-60 Ma). This result further illustrates that the pre-Eocene thermal history experienced by individual zircons is a variable that is difficult to constrain a priori in our data set. Nonetheless, these differences are intimately linked to the maximum temperature reached in the Cretaceous (and the total amount of heating). The good solutions involve a minimum temperature increase (~120 °C) and a fairly low heating rate (1 °C/Ma), but a large proportion of acceptable solutions suggest that heating may have generated temperatures as high as the upper bound of the partial annealing zone of the Guenthner et al. (2013) model in the Early Cretaceous (relatively short-lived heat pulse). This second result is striking on two aspects. First, the good t-T paths show that peak temperatures are not reached before the Late Cretaceous, which seems counterintuitive with regard to the HT conditions recorded by sediments in the Early Cretaceous. Second, a non-negligible number of paths do predict peak temperatures over the period that saw HT-LP metamorphism and/or hydrothermal alteration in the study area, but they only present an acceptable fit to the data. We therefore further constrained the software to search t-T paths incorporating an increasing number of thermal constraints during the Cretaceous (Appendix 17). To envision scenarios in which any heat pulse occurring in the Early Cretaceous may have been strong (peak temperatures higher than the ZHe partial retention zone, as constrained with the RSCM technique or estimated for albitization) but short-lived enough not to reset appreciably the ZHe system, we also ran simulations that allowed the software to search t-T paths within larger t-T spaces for the post-Barremian time-temperature history (Appendix 18).

The second generation of inverse modeling returned very few good solutions for each set of simulations. On the one hand, good fits obtained when increasing parsimoniously the number of constraints without contradicting geological observations (Appendix 17) show more rapid heating up to the ZHe partial retention zone in the Early Cretaceous and also more rapid cooling in the Late Cretaceous. The acceptable fits of representative data with a more complex model suggest that the data may not exclude a

short-lived heating pulse in the Early Cretaceous. Nonetheless, it should be acknowledged that this approach is close to the forward modeling approach that would consider the whole data set. For this reason, we performed more detailed forward modeling of our ZHe data that we present in the next section. On the other hand, the good t-T paths found over a larger, allowed temperature range in the Cretaceous are similar in every respect to those obtained when peak temperatures are not allowed to exceed the upper bound of the partial annealing zone of the Guenthner et al. (2013) model in the Cretaceous. In this set of simulations, the timing of transition from heating to cooling is no better constrained, again spanning the 100- to 60-Ma time range. A negative result is obtained if the number of constraints is increased, leading to fewer to no good t-T paths. Nonetheless, all t-T paths found further highlight the fact that the higher the peak temperature is in the Cretaceous, the earlier or shorter-lived the heat pulse has to be to fit the data. By doing so, the predicted ZHe age variability is always lower than the input ZHe age variability, with younger ages at intermediate eU and older ages at low and high eU. Yet the input age variation results from our choice of representative ages, so that it is itself already lower than that in our whole ZHe data set.

Taken together, these observations therefore suggest the peak temperatures proposed in the literature for both the HT-LP metamorphic event and albitization/shear zone recrystallization most likely do not reflect the background temperatures that existed in the Agly-Salvezines crustal block. In particular, if these maximum temperatures existed, they would have been very short-lived (less than 20 myrs) and probably localized as hydrothermal activity in fault zones. For this reason, we do not further simulate this option with forward modeling.

V.7.2 ZHe Data Forward Modeling Approach Using HeFTy

Guenthner et al. (2013) have shown that first-order correlations between age and eU for single samples are highly valuable to constrain thermal histories. As the degree of radiation damage in a crystal is a function of alpha production and annealing, themselves functions of the crystal's eU concentration and thermal history, each crystal from a single sample will act as an individual thermochronometer with its own temperature sensitivity, helium diffusivity (or retentivity), and (U-Th)/He age. As long as it is impossible to describe the full range of single-grain ZHe ages of a data set (specific to a single sample or a collection of samples with the same thermal history as expected here) in HeFTy, pertinent information on burial temperatures and cooling rates will probably be removed, making it impossible to properly constrain thermal histories. We therefore expect the forward modeling approach to better recognize the complexity manifested in our ZHe age-eU correlations.

V.7.2.1 Thermal Histories Tested

Given the thermal histories returned by inverse modeling, we used the forward modeling approach to produce zircon age-eU predictions for two distinct geologically plausible t-T paths from 305 Ma to present (first and second families; Figure V.4, Figure V.5, Appendix 19 and Appendix 20). Any specific characteristics of one or other family

are described in next sections of this chapter. These t-T paths represent a wide range of sensitivity for the ZHe system and allow us to evaluate the absolute and relative viability of many geologically reasonable but relatively simple thermal scenarios/options shown in Appendix 17 (residence in the ZHe partial retention zone during the Cretaceous, inverse modeling simulation #2; two-phase cooling, simulations #1-3). Unknowns such as the prevailing vertical geothermal gradient and burial depth of the crustal block during rifting led us to vary the Early Cretaceous maximum temperature in each of the two model families.

Forward t-T paths were constrained with the same data as for inverse modeling:

(1) The initial time constraint in our forward models is placed at 305 Ma. As the Guenthner et al. (2013) model considers a partial annealing zone of 310-223 °C, placing any initial temperature constraint above this temperature range does not significantly affect the prediction results. Thus, the initial temperature constraint is placed at 600 °C, regardless of the samples. As relatively little is known about cooling of the Agly-Salvezines rocks from Variscan times to the end Permian, samples are assumed to cool at a constant cooling rate from 305 to 250 Ma.

(2) Berger et al. (1993) indicate that the Saint-Arnac granite, and possibly the gneisses, may have been at or near the surface around Late Triassic times. Pressure estimates for albitization and Early Cretaceous mylonitisation in the massif (1.5-3 kbar; Pascal, 1979; work by R. Nicolas cited in Clerc et al., 2015) suggest that the lower part of the Saint-Arnac granite body was at around 4- to 5-km depth during the Early Cretaceous. The Bas-Agly and Saint-Paul-de-Fenouillet synclines record an Upper Triassic-to-lower Aptian sedimentary succession as thick as ~1 km. Assuming a vertical thermal gradient of 30 °C/km during Triassic (post-Variscan orogeny relaxation), t-T paths must reflect a temperature increase of ~30 °C from 250 Ma to 125 Ma. As the vertical repartition of our samples over post-Variscan times is largely unknown, we tested two end-members for sample depth from the end Permian to the early Aptian (see section V.7.2.1.1).

(3) AHe and AFT data document a time-temperature history of our samples in the overall temperature range of 45-110 °C. Two temperature constraints are therefore arbitrarily placed at 110 and 20 °C at 45 and 40 Ma, respectively. Near-surface temperatures (20 °C) were then retained from this time until present.

Because all the samples present similar ranges of single-grain ZHe ages and age-eU correlations, irrespective of their rock type or location, we expect that they most likely experienced the same post-Early Cretaceous thermal history. To test this prediction, we generated for each t-T path model an age-eU envelope that encompasses the 2-standard-deviation grain sizes measured as the equivalent spherical radius for the whole data set (69 ± 18 μm). These envelopes represent the range of age-eU curves that would be produced individually for a specific grain size in the 50- to 87-μm range. This aims to depict the age variation for a single sample resulting from the combined effects of radiation damage and grain size, that is, intrasample variation within our data set. The

zonation effect, albeit not accurately characterized, could be here considered as part of the radiation damage effect for the reasons mentioned in section V.6.

Both groups of middle Cretaceous ZHe ages fall within error into the time span over which heating is expected to occur over the whole Pyrenean realm based on the following: (i) stratigraphically constrained rifting (114-97 Ma; Debroas, 1987, 1990), (ii) the HT-LP event recorded in the eastern Metamorphic Internal Zone (113-95 Ma; Albarède & Michard-Vitrac, 1978; Golberg & Leyreloup, 1990; Montigny et al., 1986), (iii) the widespread hydrothermal fluid circulation in North Pyrenean basement massifs (117-92 Ma; Boutin et al., 2016, and references therein), (iv) partial to total resetting of the ^{40}Ar -^{39}Ar isotopic system in biotite and muscovite in mylonitic zones of the Agly basement (110-100 Ma; work by R. Nicolas cited in Clerc et al., 2015), and (v) mantle exhumation in the northwestern Pyrenees (108-105 Ma; Masini et al., 2014). On the other hand, temperatures inferred from the ZHe system in this study (140-250 °C and inverse modeling results) are far below (i) estimated RSCM temperatures in strata of Boucheville and Bas-Agly synforms (350-600 °C; Chelalou, 2015; Chelalou et al., 2016; Ducoux, 2017; Vauchez et al., 2013) as well as in pockets of similar lithologies within the Agly Massif (400-450 °C; Ducoux, 2017) and (ii) temperature conditions for albitization (350-450 °C; Boulvais et al., 2007; Pascal, 1979; Poujol et al., 2010). Overall, either the middle Cretaceous ages may therefore be due to partial resetting of the (U-Th)/He system in zircon (heating up to the ZHe partial retention zone) or they may strictly date cooling that followed heating of the crustal block above the ZHe partial retention zone (total reset) during middle Cretaceous times. The significance of the sample groups' ZHe ages around the maximum of age-eU correlations therefore requires consideration and is investigated by testing a second family of slightly more complex t-T path models.

V.7.2.1.1 First Family of t-T Path Models (Single-Phase Cooling History)

The first family of t-T path models simulates five simple thermal histories (scenarios 1 to 10) based on the maximum temperature (160, 180, 190, 200, and 250 °C) reached during rifting (at 115 Ma in simulations) and the relative amount of cooling that occurred starting at either 75 or 50 Ma (Figure V.4). Thus, we test end-member scenarios with a phase of synorogenic cooling starting either in the Late Cretaceous (75 Ma, scenarios 1-5), implying rapid and full cooling of the Agly-Salvezines block during early orogenesis, or in the Eocene (50 Ma, scenarios 6-10), implying a long period of quiescence before orogenic cooling. Additionally, we present variants in Appendix 19 and Appendix 20 that consider the following: (i) samples lay at 4- to 5-km depth before rifting and experienced temperatures of 120 to 150 °C (Appendix 19) or (ii) maximum temperature is reached during rifting at 100 Ma (Appendix 20).

V.7.2.1.2 Second Family of t-T Path Models (Two-Phase Cooling History)

Four thermal histories with two distinct phases of cooling were tested (scenarios 11 to 15; Figure V.5). These are variants of scenario 1 of the first family of t-T path

models, with a cooling event from structural levels at 160 °C starting in the Late Cretaceous (75 Ma). An earlier phase of cooling is added in the middle Cretaceous (100 Ma) that follows a 20-myr period of relatively high temperatures since 120 Ma (180, 190, 200, and 250 °C).

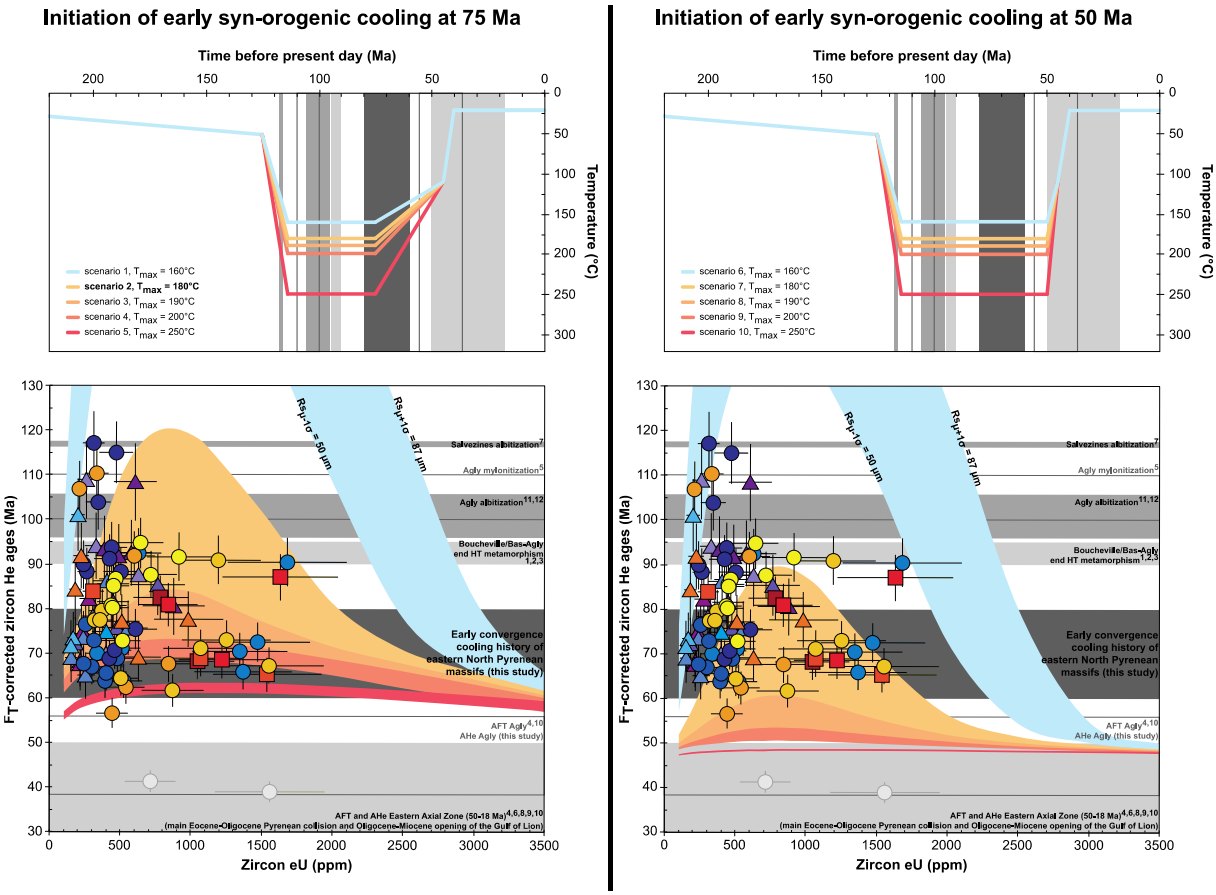

Figure V.4: Comparison of the Agly-Salvezines age-eU data set with first family forward models assuming (i) shallow-crustal depths from the end Permian to the early Aptian followed by (ii) rapid heating during Early Cretaceous rifting. The top two panels show five different t-T scenarios with either (left) Late Cretaceous cooling at 75 Ma or (right) Eocene cooling at 50 Ma. The resulting age-eU envelopes are plotted in the two bottom graphs with the color of each age-eU envelope matching a specific t-T path. Envelopes encompass the 2-standard-deviation grain sizes (69 ± 18 µm), so that the upper and lower bounds of the color envelopes correspond to the age-eU curve that would be produced for a grain size of 87 and 50 µm, respectively. Gray bars indicate the ages of major thermal and tectonic events from literature. See Figure V.3 for references 1-12.

V.7.2.2 HeFTy Forward Modeling Results

In the single-phase cooling models, samples of both groups lie within the ZHe partial retention zone from Early Cretaceous to Campanian times. The t-T paths models assuming a cooling phase starting at 75 Ma appear to predict model age-eU curves that explain a high percentage of the observed ages over the whole spread in eU, while those assuming a cooling phase starting at 50 Ma always predict ages at very low eU and very high eU that are far younger than almost all observed ZHe ages in the Agly-Salvezines data set. This is verified irrespective of the depth of our samples before the Early

Cretaceous and the timing of end of heating before convergence (Figure V.4, Appendix 19, and Appendix 20). In particular, scenario 2 is best able to reproduce the two groups' maximum cooling ages. The structural levels of Gp1 and Gp2 samples are not distinguishable over the period of modeling, although we might reasonably expect that the slightly different age clusters at low eU for Gp2 and Gp1 indicate that rocks lying at different vertical depths reached a particular closure temperature depth with some delay (section V.6).

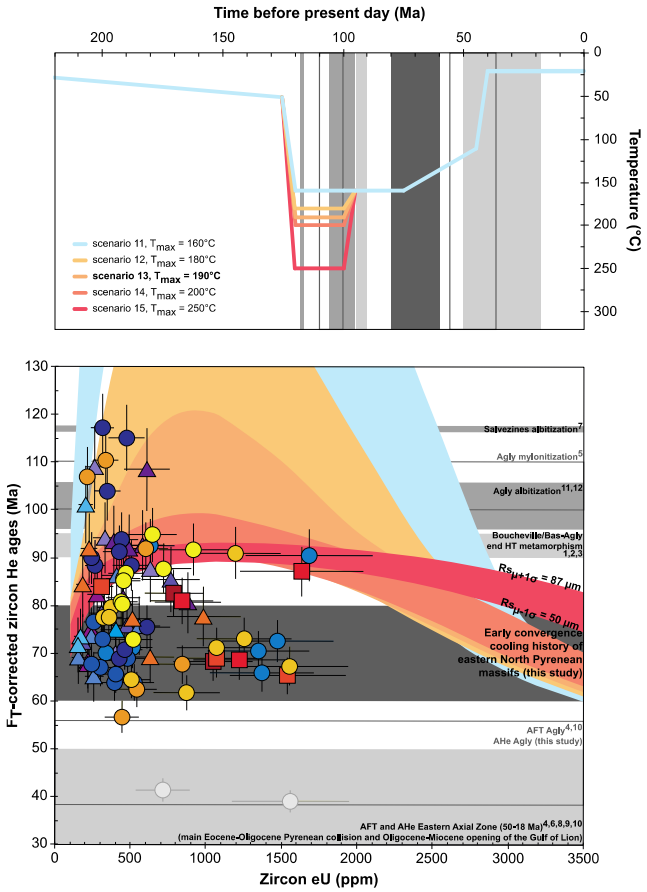

Figure V.5: Second family t-T path forward model results for the Agly-Salvezines data set integrating two thermal cooling events. The top panel shows the five different t-T scenarios tested, with Late Cretaceous cooling at 75 Ma from structural levels at 160 °C. The resulting age-eU envelopes are plotted in the bottom panel, with the color of each age-eU envelope matching a specific t-T path. Envelopes encompass the 2-standard-deviation grain sizes (69 ± 18 µm) so that the upper and lower bounds of the color envelopes correspond to the age-eU curve that would be produced for a grain size of 87 and 50 µm, respectively. Gray bars indicate the ages of major thermal and tectonic events from literature. See Figure V.3 for references 1-12.

In the two-phase cooling models, samples of both groups lie within or deeper than the ZHe partial retention zone from mid-late Aptian to mid-late Cenomanian times (~120-95 Ma in simulations). Most retentive zircon crystals (with higher closure temperatures) of both sample groups thus record cooling during this time (see age distributions in Figure V.3.b). One viable t-T path is found, producing the only age-eU envelope that encompasses a high percentage of the observed ZHe ages over the whole spread in eU (scenario 13; Figure V.5). In this scenario, the structural levels of Gp1 and Gp2 samples are not clearly distinguishable over the time of modeling.

V.8 Discussion

V.8.1 Interpretation of Data and Age-eU Correlations

The age variability in our AHe data set and the higher AHe age values at high eU compared with those in published AFT data (Gunnell et al., 2009; Yelland, 1991) indicate fairly rapid cooling of our samples below temperatures of 110-45 °C during early-middle Eocene (Ypresian-Lutetian) times. The overall positive AHe age-eU correlation illustrates the damage-dependent sensitivity of He in apatite to thermal processes as proposed and modeled by Flowers et al. (2007) and Gautheron et al. (2009). We interpret this cooling signature as due to denudation of the Agly-Salvezines block at the beginning of the main Eocene phase of orogenesis. Exhumation-related cooling is observed over the whole Pyrenees, propagating southward from the North Pyrenean basement massifs into the Axial Zone from the early Eocene to the late Oligocene (Bosch et al., 2016; Hart et al., 2017; Labaume et al., 2016; Mouthereau et al., 2014, and references therein; Rushlow et al., 2013; Thomson et al., 2017; Vacherat et al., 2014, 2016).

As with the AHe system, the clear age variation in our ZHe data set illustrates the damage-dependent sensitivity of He in zircon to thermal processes (Guenthner et al., 2013). Plotting single-grain ZHe ages against bulk eU clearly demonstrates the lack of a simple, straight correlation between age and radiation damage, which is likely due to grain size and zonation effects. Nonetheless, overall first-order positive and negative age-eU correlations seem to be displayed by ZHe ages as these increase from ~75 ± 5 to ~110 ± 5 Ma and then decrease down to ~70 ± 5 Ma with increasing eU.

None of the predicted ZHe age-eU envelopes (Figure V.4, Figure V.5, Appendix 19, and Appendix 20) explain all observed ages in the Agly-Salvezines data set. This result also clearly illustrates the difficulty in identifying a single t-T history using ZHe ages plotted against eU. As recently noted by some authors in other geologic settings (Anderson et al., 2017; Johnson et al., 2017; Powell et al., 2016; Vacherat et al., 2016), forward modeling suggests that the damage-dependent model of diffusion is able to reproduce only qualitatively, not quantitatively, the range of single-grain ZHe ages and both positive and negative age-eU correlations. This probably also explains the failure of the HeFTy software to produce plausible thermal histories when performing inverse modeling with too many input data.

Nevertheless, all our modeling results clearly concur with Guenthner et al. (2013), in that age-eU correlations yielded by a sample or a group of samples are the result of its entire history and are not only shaped by the most recent cooling event. They indicate to first order that the deeper the paleostructural level, the flater the predicted age-eU correlation and the younger the predicted maximum ZHe ages (scenarios 5 and 10, Figure V.4; scenario 15, Figure V.5). The most recent, rapid cooling history of a sample or a group of samples is dated at opposite ends of the eU concentration spectrum, irrespective of any earlier history. Any earlier thermal histories shape age-eU correlations for maximum predicted ages and constrain any positive and/or negative

correlation trends for these older ages (referred to as the ZHe inheritance curve; Guenthner et al., 2015; Powell et al., 2016). This point is illustrated with some sensitivity tests in Appendix 19 and Appendix 20 and will be discussed below.

The non-random distribution of the Agly-Salvezines single-grain ZHe ages, together with the closure temperature predictions of the Guenthner et al. (2013) model, allow us to suggest that the young ZHe ages (75-70 ± 5 Ma) at relatively low (<600 ppm) and high (>1,000 ppm) eU concentrations may correspond to zircon grains with He closure temperatures of 160 and <140 °C, respectively. Zircon grains that yield older, middle Cretaceous ZHe ages may have had higher closure temperatures (*ca.* 200-250 °C) due to higher He retentivity and required a longer residence time in the partial retention zone to be partially or totally reset.

V.8.2 New Insights Into Retro-wedge Thermal History

Inverse and forward modeling of t-T paths shows that ZHe ages of igneous and metamorphic rocks can be reproduced by assuming the same structural level and thus a common t-T history for the two groups from the Triassic onward. Gp1 and Gp2 samples belonged to either (1) a single and unique block from the Triassic onward while lying at the same depth or (2) two different blocks (northern granite block and southern granulite block) lying at the same depth that joined (necessarily before the Late Cretaceous) and cooled together thereafter. The geographical proximity of samples yielding middle Cretaceous cooling ages and the absence of conclusive field evidence for two separate blocks in Mesozoic times (Berger et al., 1993; Olivier et al., 2004, 2008) support the first option. This confirms our premodeling expectations and justifies the individualization of three representative age clusters for inverse modeling.

V.8.2.1 Campanian-Maastrichtian Convergence-Related Cooling

Based on closure temperature predictions of the Guenthner et al. (2013) model, we argue that similarity of mean ZHe ages for clusters at very low and high eU concentrations (75 and 70 Ma, respectively) shows near synchroneity in crossing multiple isotherms in the range <140-160 °C from 70 to 75 Ma (Figure V.3.b). This indicates a marked cooling event starting at 75 Ma. This is further supported by forward modeling, which indicates that the best fit of both positive and negative age-eU correlations to our data over the whole spread of eU values is obtained if we assume that the Agly-Salvezines crustal block was cooled from 75 Ma (Figure V.4).

This cooling event (below 120-160 °C) postdates by some 10 myrs the onset of tectonic inversion (Choukroune, 1989; Muñoz, 1992), itself postdating by some 10 myrs the end of Aptian-Cenomanian rifting. Angrand et al. (2018) have shown that the major thermal pulse generated by Early Cretaceous rifting was not reequilibrated before the onset of convergence. Thermal cooling thus contributed to foreland basin subsidence, particularly in the central and, even more so, in the western Aquitaine Basin. Their results concur with Vacherat et al. (2014, 2016) who propose that in western parts of the North Pyrenean Zone, temperatures of 400-200 °C (Clerc et al., 2015) persisted

during the first 30-35 myrs of orogenesis due to an inherited thermal perturbation. As yet, no clear cooling event older than 50 Ma has been documented in the western and central North Pyrenean basement massifs. In contrast, in the east the Agly-Salvezines crustal block had cooled to below 250 °C by the end of rifting (95-90 Ma) and clearly records a cooling event during early convergence. This difference in thermal histories along the orogen can be related to several causes. First, the rift may have been wider in the west (Tugend et al., 2014) than in the east, leading to a broader and more persistent thermal perturbation. Although higher in the eastern basins, the thermal perturbation was short-lived, cooling to 400-250 °C (Spear, 1993) by 95-90 Ma (Albarède & Michard-Vitrac, 1978; Golberg & Maluski, 1988; Montigny et al., 1986). Second, assuming a constant convergence rate along the orogen, it would have taken longer to close the wider rift to the west, thus preserving the thermal perturbation for longer. A faster convergence rate in the east as documented recently by Macchiavelli et al. (2017) would further promote this trend.

Given this tectonic history, the cooling event at 75 Ma may have been caused by either postrift cooling or early Pyrenean orogenesis. From the end of rifting, thermal reequilibration causes a gradual cooling over, typically, 50 myrs (thermal time constant for a standard continental lithosphere; Allen & Allen, 2013). It cannot therefore explain in an acceptable way a marked cooling event starting at 75 Ma, some 15-20 myrs after the end of rifting. We thus interpret the cooling signal as evidence for early orogenic inversion of the distal rifted margin. This agrees with Ford et al. (2016) and Grool et al. (2018) in identifying an early phase of distributed gentle inversion of rifted structures of the European plate (North Pyrenean Zone) due to thickskinned convergence during Campanian-Maastrichtian times.

In collisional settings an erosion-related exhumation of thickening crust is most commonly evoked as the principal cooling mechanism. However, early convergent margins are typically low relief and often submarine (e.g. Platt, 1986; Simpson, 2006). Based on foreland basin evolution, the early Pyrenean orogen also probably formed a low relief, possibly submarine edifice (Ford et al., 2016). This concurs with evidence of little or no erosion in the Axial Zone during this period (e.g. Fitzgerald et al., 1999). In such a setting, only continental underplating and/or thrusting can explain the rock cooling indicated by our data. These processes will be discussed further in a later section of this chapter. Similar processes are invoked early in orogenesis for the active arc-continent collision of southern Taiwan (Mesalles et al., 2014).

V.8.2.2 Preorogenic Thermal History of the Agly-Salvezines Area

We investigated the whole post-Barremian thermal history using both inverse and forward modeling approaches. As inverse modeling results indicate partial to total reset of the ZHe system over the period of time considered, we attempted to decipher the significance of the middle Cretaceous ZHe ages by testing two families of t-T path forward models (section V.7.2.1). One model from each family provides an acceptable fit for both positive and negative age-eU correlations of our data over the whole spread in

eU (Figure V.4 and Figure V.5): scenario 2 (single-phase history, Tmax 180 °C) and scenario 13 (two-phase history, Tmax 190 °C). Nonetheless, the two scenarios are so similar that the current calibration of the Guenthner et al. (2013) model does not allow us to differentiate between them. It is important to stress that here we have reached the model's limitations emanating from its parameterization requirements, as already detected by previous authors (Powell et al., 2016; Vacherat et al., 2016). We note that this model cannot simulate the older ages of our data set for any thermal history with maximum temperatures during rifting (120-95 Ma in simulations) higher than 190 °C (e.g. scenarios 4, 5, 9, 10, 14, and 15). This observation is consistent with inverse modeling results for any shorter-lived heat pulse within this time window. This is of particular concern because the peak paleotemperatures constrained with the RSCM technique (Serre de Vergès; Figure V.2) or the temperature estimates of albitization can reach 400-450 °C between 117 and 96 Ma (Boulvais et al., 2007; Demange et al., 1999; Ducoux, 2017; Poujol et al., 2010). Moreover, as highlighted in section V.4.3.2, radiometric data from Mesozoic sediments indicate that the HT-LP event took place between 113 and 95 Ma, peaking at 95-90 Ma in the eastern Pyrenees. Whatever the heat source for HT conditions recorded in Mesozoic strata, it had to occur contemporaneously with local metasomatism in basement by middle Cenomanian (95 Ma). One might expect that peaking HT metamorphism on both sides of the Agly-Salvezines block would have heated the massif's edges. Middle Cretaceous ZHe ages obtained in this study are mainly yielded by samples from the southern block, directly north of the Boucheville syncline. These ages potentially record cooling below 250 °C during and after the HT/albitization event. This may therefore indicate that maximum temperatures inferred from the RSCM analysis were localized due to HT fluid circulation (Boulvais, 2016; Dauteuil & Ricou, 1989) or were very short-lived (less than 20 myrs as indicated by inverse modeling). In both cases, they probably do not reflect background temperatures. This subsequently suggests that another cause has to be found to explain cooling in the middle Cretaceous in the two-phase cooling history (Figure V.5), possibly rift-related exhumation. In the absence of medium-temperature thermochronology data it is not possible to further constrain the thermal histories of the northern and southern Agly compartments during the preorogenic stage.

Although our t-T path models do not have the necessary sensitivity and resolution to quantify cooling rates, they can reproduce data when involving temperatures higher than 160 °C during the overall heat perturbation (115-95 Ma in simulations). If the Agly-Salvezines block had seen a maximum vertical geothermal gradient of 80 °C/km during the HT-LP event (113-95 Ma, peaking at 95-90 Ma) as proposed in Boucheville (Chelalou et al., 2016), it must have been buried below at least 2 km of Triassic-to-middle Cenomanian strata during the heating period. Our low-temperature thermochonology models therefore support the proposition of a continuous Albian-Cenomanian basin overlying the Agly basement (Clerc et al., 2015, 2016; Olivier, 2013). Our models also support middle Cretaceous exhumation that would be necessarily involved in the proposed, albeit extreme, unroofing of the Agly Massif by early Cenomanian times by some authors (Clerc & Lagabrielle, 2014; Ravier, 1957; Vauchez et al., 2013).

V.8.3 Crustal-Scale Model of Orogenic Tectonothermal Evolution for the Eastern

Pyrenean Retro-wedge We here combine our low-temperature thermochronology results with geological and geophysical data from literature to propose a model for the evolution of the eastern Pyrenean orogen and in particular the retro-wedge from the Santonian to present day. This model is based on the sequential restoration of a crustal-scale N-S cross-section through the central Agly Massif (Figure V.6) assuming constant crustal area and compressional pure shear. However, given the Oligocene-Miocene crustal thinning during the opening of the western Mediterranean (e.g. Faccenna et al., 2014; Gunnell et al., 2008), there is a high uncertainty associated with the assumption of constant crustal area. We use 32, 20, and 28 km for present-day Iberian, eastern North Pyrenean, and European crustal thicknesses, respectively (Chevrot et al., 2018; Diaz et al., 2018). Following Clerc et al. (2016) and inspired by modern analogs (Chenin et al., 2017; Reston, 2009; Sutra et al., 2013), we restore the eastern Pyrenees to a hyperextended rift in which the Agly-Salvezines block is surrounded by depocenters recording high temperatures (113-95 Ma) and with mantle exhumation below the more distal Boucheville basin. Key thermal events integrated into this model are that the Agly-Salvezines block (i) was affected by metasomatism from late Aptian to middle Cenomanian times followed by rapid cooling to 200-250 °C by 90 Ma and (ii) was cooled at 75 Ma during early convergence and again at 50 Ma during main collision. Total retro-wedge shortening on this cross section is estimated at 15 km; total pro-wedge shortening is 31 km based on Laumonier et al. (2015). This model is consistent with recent numerical modeling studies (Dielforder et al., 2017).

V.8.3.1 Preconvergence Phases (114-84 Ma): Early Cretaceous Crustal Template

Figure V.6.a shows the preorogenic configuration (late Santonian). Using the work of Vergés et al. (1995) and Laumonier (2015), we propose a first-order restoration of the Iberian crust between the SPFT and the NPF to an 81-km-wide preorogenic margin with a narrow distal domain (33 km wide). A more detailed restoration of the European margin (from the NPF to the northern edge of the Mouthoumet Massif) is constrained by published geological maps and new field data and inspired by previous schematic reconstructions in that area (Figure V.1; Choukroune, 1974; Chelalou et al., 2016; Clerc et al., 2016). The European margin is restored to a 66-km-wide rifted margin comprising an 11-km-wide proximal domain (Mouthoumet Massif), a 29-km-wide necking zone, a 17-km-wide zone of hyperthinned crust (the Agly-Salvezines block and Bas-Agly synform), and a 9-km-wide zone of exhumed mantle below the Boucheville depocenter. Major uncertainty is associated with the unknown amount of mantle exhumation. We therefore exclude closure of the exhumed mantle domain from all estimates of shortening given hereafter. The North Pyrenean Zone is restored to a 47-km-wide rifted margin, giving a minimum shortening of ~12 km. Following Grool et al. (2018) we assume that shortening in the retro-wedge was accommodated equally between the two orogenic phases. The model shows major Aptian-Cenomanian rift depocenters

controlled by basement faults at depth. Keuper evaporites and diapirs act as a decoupling layer between basement and cover. The crust is thinned to 0 km below the Boucheville depocenter and to 4 km below the Bas-Agly depocenter. The intervening Agly-Salvezines crustal block is thinned to 8 km (Clerc & Lagabrielle, 2014; Clerc et al., 2015, 2016) and buried below at least 2 km of Mesozoic sediments (section V.8.2.2).

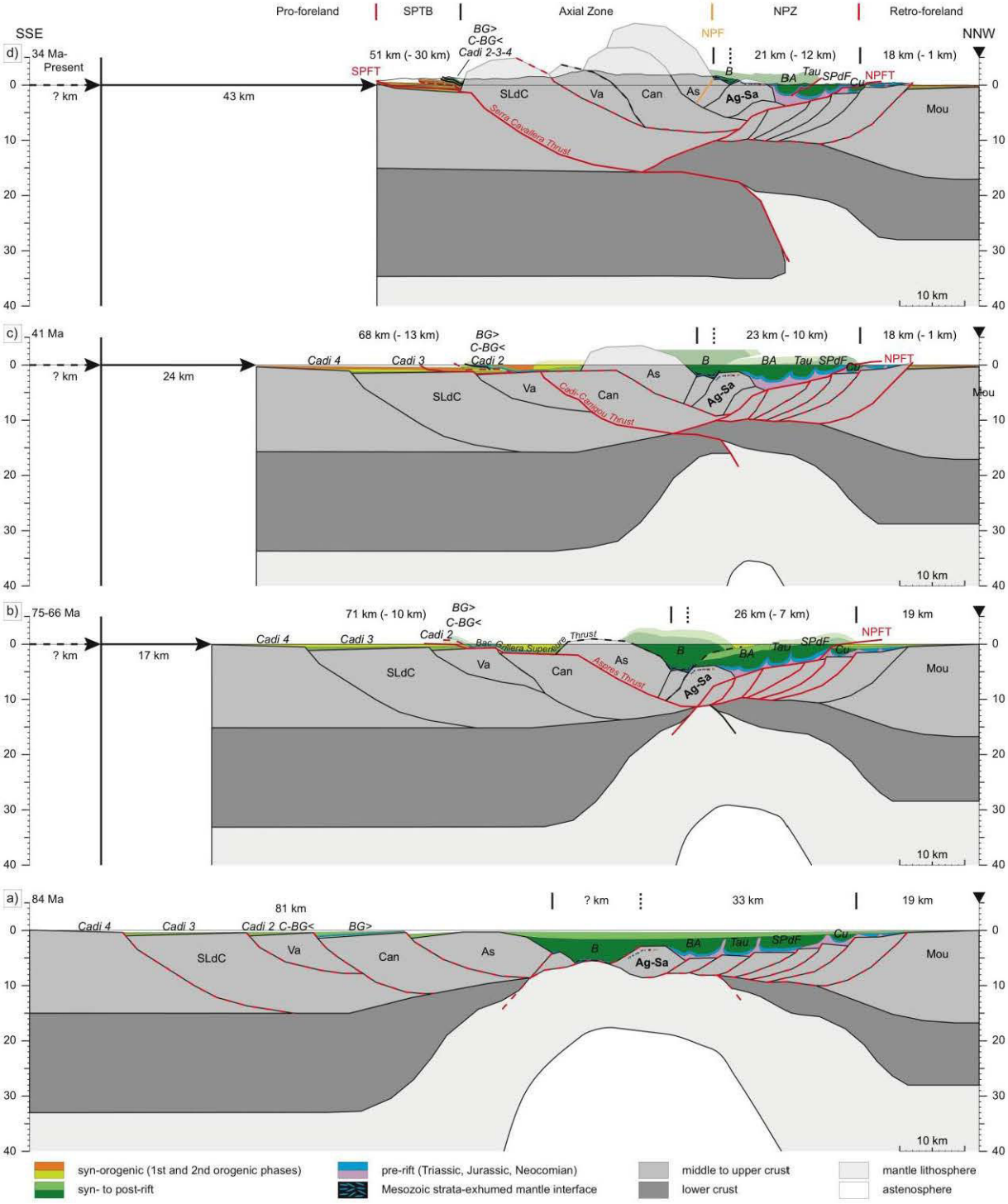

Figure V.6: (previous page) Sequentially balanced evolution of the eastern Pyrenees along a N-S section line located in Figure V.1 and Figure V.2. Shortening amounts are cumulative. Solid red lines indicate faults that are active. Dashed red lines indicate faults that were active during the preceding step (those in black being abandoned before those in red). Black lines indicate abandoned faults. Approximate sample location is indicated on the Agly-Salvezines crustal block. The present-day Moho is that along the deep seismic tomography line E-E′ passing though the Agly Massif of Chevrot et al. (2018) and Diaz et al. (2018; Figure V.1). Width of the North Pyrenean Zone (NPZ) on the present-day cross section Figure V.6.d) is larger than that on line E-E′ due to characteristics of the transect reconstructed in this study (Figure V.1 and Figure V.2). NPFT = North Pyrenean Frontal Thrust; NPF = North Pyrenean Fault; SPTB = South Pyrenean thrust belt (South Pyrenean Zone); SPFT = South Pyrenean Frontal Thrust;SLdC = Saint-Laurent-de-Cerdans; Va = Vallespir; Can = Canigou; As = Aspres; Ag-Sa = Agly-Salvezines; Mou = Mouthoumet; BG> = Bac Grillera Superieure; CBG< = Coustouge-Bac Grillera Inferieure; B = Boucheville; BA = Bas-Agly; Tau = Tautavel; SPdF = Saint-Paul-de-Fenouillet; Cu = Cucugnan.

V.8.3.2 First Orogenic Phase (84-66 Ma): Early Rift Inversion and Northward Underplating

During early convergence (Campanian-Maastrichtian; Figure V.6.b), a minimum of ~17 km shortening is accommodated across the orogen. The mantle domain is closed, and the overlying Boucheville basin is transported northward and southward onto the continental margins. The Bac Grillera Superieure Thrust (or supra-axial thrust of Laumonier, 2015) is then activated to accommodate ~5 km of thin-skinned shortening verging southward. It transports the Bac Grillera Superieure unit southward onto the Coustouge-Bac Grillera Inferieure unit. By middle Campanian times, the distal Iberian and European rifted crusts are in contact. The early orogenic edifice is a low-relief double wedge supplying little sediment into the early foreland basins. In this context, three structural scenarios could produce the cooling event recorded in the Agly-Salvezines crustal block: northward thrusting of the block onto the cooler proximal margin, northward underplating by the distal Iberian margin, or a combination of these two. The first two options would require amounts of shortening and structural geometries that are incompatible with present-day surface geology. The first scenario would require overthrusting of the entire Saint-Paul-de-Fenouillet synform by the Bas-Agly synform, while the second scenario would result in unrealistic mechanical deformation within the crust. In contrast, by combining more modest amounts of both overthrusting and underplating in the third option, we can reproduce present-day surface geometries. Faults across the distal margins are reactivated to accommodate ~7 and ~5 km shortening in the northern retro-wedge and southern pro-wedge, respectively. The NPFT and the Aspres Thrust become active at this time. The former links southward to the main crustal fault that carries the Agly-Salvezines block northward (similar to models of Ford et al., 2016; Rougier et al., 2016; and Grool et al., 2018). The latter carries the Agly-Salvezines block southward and further transports the Bac Grillera Superieure unit southward onto the Coustouge-Bac Grillera Inferieure unit.

V.8.3.3 Retro-wedge Quiescence Phase (66-59 Ma)

During the Paleocene, convergence appears to stop (Grool et al., 2018; Macchiavelli et al., 2017). The absence of cooling indicates that the massif remains beneath 2-4 km of

overburden, with no significant underplating-related or thrusting-related wedge thickening. Clastic supply from the orogen into the retroforeland basin is still minimal (Ford et al., 2016), indicating the absence of significant denudation of the orogen.

V.8.3.4 Second Orogenic Phase (59-34 Ma): Main Collision and Pro-wedge Deformation

In the early Eocene (Ypresian) the main continent-continent collision starts. By middle Eocene (Lutetian, 41 Ma; Figure V.6.c), continuing crustal thickening leads to emergence of the orogenic edifice and subaerial erosion. The Agly-Salvezines block is rapidly exhumed to near surface as the North Pyrenean Zone continues to shorten and deformation migrates northward. The NPFT is reactivated to accommodate ~6-km shortening, linking southward to the main crustal fault that carries the Agly-Salvezines block and the crustal imbricate it overthrusts. Thick-skinned shortening (3 km; only 1 km is shown in Figure V.6 as 2 km is accommodated further north) affects the retroforeland, exploiting weak horizons in underlying Variscan nappes (e.g. uplift of the Mouthoumet Massif; Christophoul et al., 2003). Shortening is progressively transferred to the pro-wedge to the south (Axial Zone and southern foreland) with reactivation of the Aspres Thrust and activation of the Cadi-Canigou Thrust to accommodate a total ~13-km shortening. The Aspres Thrust accommodates much more shortening than it did during the first phase of orogenesis, transporting the Coustouge-Bac Grillera (Inferieure and Superieure) unit southward onto the Cadi 2 unit (Laumonier, 2015; Laumonier et al., 2015; Pujadas et al., 1989, and references therein). From the middle Eocene to the early Oligocene, exhumation rates for the Axial Zone increase (Bosch et al., 2016; Labaume et al., 2016; Mouthereau et al., 2014, and references therein; Rushlow et al., 2013; Whitchurch et al., 2011, and references therein) while the Agly exhumation ceased (Gunnell et al., 2009). The SPFT (or Vallfogona thrust in Laumonier, 2015) is activated to accommodate ~7-km shortening, linking northward to the Serra Cavallera Thrust (Laumonier, 2015). A total shortening of ~26 km is therefore estimated during the second orogenic phase (Figure V.6.d).

V.9 Conclusions

We present new single-grain AHe and ZHe data for the North Pyrenean Agly-Salvezines block in the eastern Pyrenean retro-wedge that provide new insight into collisional wedge growth. We use inverse modeling and forward modeling of these new results to better constrain the tectonic and thermal evolution of the distal European rifted margin during early convergence. By integrating our low-temperature data with published data, we propose a sequentially balanced crustal-scale model for the tectonic and thermal evolution of the eastern inverted rift through collision.

Applying both a dating technique to multiple grains from a single sample and multiple dating techniques to the same sample reduces uncertainties in investigating the time-temperature history of our samples within the crust. We find that ZHe and AHe ages from the Agly-Salvezines block display correlations between age and eU. Using available radiation damage-He diffusivity models for apatite and zircon (Flowers et al.,

2009; Guenthner et al., 2013), we interpret these correlations to be the result of grain-specific He diffusivities and closure temperatures. This allows us to investigate the thermal history of the crustal block in a larger and less discretized temperature range (45-250 °C), and therefore over a longer period of time, than previously attempted.

In this study, we provide one of the largest bedrock ZHe data sets for the Pyrenean system. Zircon grains with the lowest closure temperatures (<140-160 °C) represent half the grain population we analyzed for (U-Th)/He thermochronology. They yield the youngest ages (75-70 Ma), which are significantly older than the youngest ages obtained by the same dating technique in basement massifs further west, where the riftinherited thermal perturbation has been proved to be broad and persistent until the Eocene (Hart et al., 2017; Vacherat et al., 2014). We therefore interpret our Campanian-Maastrichtian bedrock ZHe ages to date a marked cooling event associated with early orogenic crustal thickening. Previously, the thermal signature of such an early phase of orogenesis has been only detected in synorogenic deposits from the central Pyrenees (Beamud et al., 2011; Filleaudeau et al., 2012; Mouthereau et al., 2014; Rahl et al., 2011; Thomson et al., 2017; Whitchurch et al., 2011). Cooling occurred while the early orogen was probably forming a low relief or even submarine edifice with little to no erosion (Ford et al., 2016). In this context and in the absence of additional data to further constrain early inversion mechanisms in the North Pyrenean Zone, we limit ourselves to a structural scenario that can explain Campanian-Maastrichtian rock cooling: a combination of northward thrusting of the Agly-Salvezines crustal block onto the cooler proximal margin and northward underplating by the distal Iberian margin. On the other hand, zircon grains with the highest closure temperatures (200-250 °C) yield the oldest ages (117-90 Ma) for the Agly-Salvezines block. These ages are argued to record synrift to postrift cooling, suggesting that peak temperatures proposed in the literature for both the HT-LP metamorphic event and albitization/shear zone recrystallization most likely do not reflect the background temperatures that existed in the Agly-Salvezines crustal block during rifting. If these maximum temperatures existed, they would have been very short-lived (less than 20 myrs) and probably localized as hydrothermal activity in fault zones. Moreover, should a true cooling event have been recorded by the ZHe system in middle Cretaceous times (no partial reset), it would have been related to tectonic processes during Aptian-Cenomanian rifting. Medium-temperature thermochronology data are needed to further constrain the thermal histories of the Agly-Salvezines block during the preorogenic stage.

By showing the contemporaneity of crustal thermal events (cooling) with foreland tectonic events (subsidence) during convergence, this study provides new evidence for intimate coupling between the mountain belt and its foreland basin(s) even during earliest convergence. The insights gained into early orogenic wedge development also demonstrate the power that low-temperature thermochronology offers in detecting earliest crustal thickening.

V.10 Acknowledgments

This work was funded by the OROGEN research project, Geological Society of America, American Association of Petroleum Geologists, Jackson School of Geosciences at the University of Texas (grants awarded to M. Odlum), and the UTChron Laboratory at the University of Texas. New lowtemperature thermochronology data are presented in the supporting information (Data Set S1). We thank two anonymous reviewers for their very constructive feedback and remarks that greatly helped clarify the manuscript. We thank Tectonics Editor T. Schildgen and Associate Editor J. Cottle for their comments and editorial support. We thank P. Olivier and B. Laumonier for invaluable assistance in the field, helpful insights, and intriguing discussions. We thank C. Gautheron, D. Marquer, P. Goncalves, P. Trap, M. de Saint Blanquat, F. Galster, K. Thomson, T. Capaldi, and current and former colleagues at the CRPG and the OROGEN team, in particular Emmanuel Masini and Thierry Baudin, for their help and fruitful discussions. Many thanks to A. Carter and S. Brichaud for providing us with raw AFT data for the Agly Massif. We would also like to thank P. Hild, D. Yeghicheyan (SARM, Nancy, France), and D. Patterson and L. Stockli for their assistance with data acquisition. CRPG publication number 2680.

REFERENCES

Albarède, F., & Michard-Vitrac, A. (1978). Age and significance of the North Pyrenean metamorphism. Earth and Planetary Science Letters, 40(3), 327-332. https://doi.org/10.1016/0012-821X(78)90157-7

Allen, P. A., & Allen, J. R. (2013). Basin Analysis: Principles and application to petroleum play assessment (3rd ed.). West Sussex, UK: John Wiley & Sons.

Althoff, F., Barbey, P., & Pons, J. (1994). Hercynian age of an extensional tectonics in the Agly Massif (Pyrénées Orientales, France)—Evidence from the Ansignan charnockite and Saint-Arnac granite. Comptes Rendus de l'Académie des Sciences: Série 2, Mécanique, Physique, Chimie, Sciences de l'Univers, Sciences de la Terre, 319(2), 239-246.

Anderson, A. J., Hodges, K. V., & van Soest, M. C. (2017). Empirical constraints on the effects of radiation damage on helium diffusion in zircon. Geochimica et Cosmochimica Acta, 218(Supplement C), 308-322. https://doi.org/10.1016/j.gca.2017.09.006

Andrieux, P. (1982). Crystallization conditions and evolution of an Hercynian charnockite—The Ansignan granulite complex (Agly Massif, French Pyrenees). Bulletin de Minéralogie, 105(3), 253-266.

Angrand, P., Ford, M., &Watts, A. B. (2018). Lateral variations in foreland flexure of a rifted continental margin: The Aquitaine Basin (SW France). Tectonics, 37, 430-449. https://doi.org/10.1002/2017TC004670

Azambre, B., & Ravier, J. (1978). Les écailles de gneiss du faciès granulite du Port de Saleix et de la région de Lherz (Ariege), nouveaux témoins du socle profond des Pyrénées. Bulletin de la Société Géologique de France, S7-XX(3), 221-228. https://doi.org/10.2113/gssgfbull.S7-XX.3.221

Baby, P., Crouzet, G., Specht, M., Déramond, J., Bilotte, M., & Debroas, E.-J. (1988). Rôle des paléostructures albo-cénomaniennes dans la géométrie des chevauchements frontaux nord-pyrénéens. Comptes Rendus de l'Académie Des Sciences. Série 2, Mécanique, Physique, Chimie, Sciences de l'Univers, Sciences de La Terre, 306(4), 307-313.

Barnolas, A., Chiron, J.-C., Guérangé, B., Autran, A., Durand-Delga, M., & Fonboté, J. M. (Eds.) (1996). Synthèse Géologique et Géophysique Des Pyrénées. Introduction. Géophysique. Cycle Hercynien (Vol. 1). Orléans: BRGM.

Batt, G. E., Brandon, M. T., Farley, K. A., & Roden-Tice, M. (2001). Tectonic synthesis of the Olympic Mountains segment of the Cascadia wedge, using two-dimensional thermal and kinematic modeling of thermochronological ages. Journal of Geophysical Research, 106(B11), 26,731-26,746. https://doi.org/10.1029/2001JB000288

Batt, G. E., & Braun, J. (1997). On the thermomechanical evolution of compressional orogens. Geophysical Journal International, 128(2), 364-382. https://doi.org/10.1111/j.1365-246X.1997.tb01561.x

Batt, G. E., & Braun, J. (1999). The tectonic evolution of the Southern Alps, New Zealand: Insights from fully thermally coupled dynamical modelling. Geophysical Journal International, 136(2), 403-420. https://doi.org/10.1046/j.1365-246X.1999.00730.x

Beamud, E., Muñoz, J. A., Fitzgerald, P. G., Baldwin, S. L., Garcés, M., Cabrera, L., & Metcalf, J. R. (2011). Magnetostratigraphy and detrital apatite fission-track thermochronology in syntectonic conglomerates: constraints on the exhumation of the south-central Pyrenees. Basin Research, 23(3), 309-331. https://doi.org/10.1111/j.1365-2117.2010.00492.x

Beaumont, C., Muñoz, J. A., Hamilton, J., & Fullsack, P. (2000). Factors controlling the Alpine evolution of the central Pyrenees inferred from a comparison of observations and geodynamical models. Journal of Geophysical Research, 105(B4), 8121-8145. https://doi.org/10.1029/1999JB900390

Berger, G. M., Alabouvette, B., Bessière, G., Bilotte, M., Crochet, B., Dubar, M., et al. (1997). Notice explicative, Carte géol. France (1/50 000), feuille Tuchan (1078). Orléans: BRGM.

Berger, G. M., Bessière, G., Bilotte, M., & Viallard, P. (1997). Carte géologique de France (1/50 000), feuille Tuchan (1078). Orléans: BRGM.

Berger, G. M., Fonteilles, M., Leblanc, D., Clauzon, G., Marchal, J. P., & Vautrelle, C. (1993). Notice explicative, Carte géol. France (1/50 000), feuille Rivesaltes (1090). Orléans: BRGM.

Bessière, G., Bilotte, M., Crochet, B., Peybernès, B., Tambareau, Y., & Villatte, J. (1989). Notice explicative, Carte géol. France (1/50 000), feuille Quillan (1077). Orléans: BRGM.

Bilotte, M. (1985). Le Crétacé supérieur des plates-formes est-pyrénénnes (Vol. 5). Toulouse: Laboratoire de géologie sédimentaire et paléontologie, Université Paul Sabatier. Retrieved from https://strata.fr/libre-acces.html

Biteau, J.-J., Le Marrec, A., Le Vot, M., & Masset, J.-M. (2006). The Aquitaine Basin. Petroleum Geoscience, 12(3), 247-273. https://doi.org/10.1144/1354-079305-674

Bosch, G., Teixell, A., Jolivet, M., Labaume, P., Stockli, D., Domènech, M., & Monié, P. (2016). Timing of Eocene-Miocene thrust activity in the Western Axial Zone and Chaînons Béarnais (west-Central Pyrenees) revealed by multi-method thermochronology. Comptes Rendus Geoscience, 348(3-4), 246-256. https://doi.org/10.1016/j.crte.2016.01.001

Bouhallier, H., Choukroune, P., & Ballèvre, M. (1991). Structural evolution of the deep Hercynian crust—The example of the Agly Massif (eastern Pyrenees, France). Comptes Rendus de l'Académie des Sciences. Série 2, Mécanique, Physique, Chimie, Sciences de l'Univers, Sciences de la Terre, 312(6), 647-654.

Boulvais, P. (2016). Fluid generation in the Boucheville Basin as a consequence of the North Pyrenean metamorphism. Comptes Rendus Geoscience, 348(3-4), 301-311. https://doi.org/10.1016/j.crte.2015.06.013

Boulvais, P., Ruffet, G., Cornichet, J., & Mermet, M. (2007). Cretaceous albitization and dequartzification of Hercynian peraluminous granite in the Salvezines Massif (French Pyrénées). Lithos, 93(1-2), 89-106. https://doi.org/10.1016/j.lithos.2006.05.001

Boutin, A., de Saint Blanquat, M., Poujol, M., Boulvais, P., de Parseval, P., Rouleau, C., & Robert, J.-F. (2016). Succession of Permian and Mesozoic metasomatic events in the eastern Pyrenees with emphasis on the Trimouns talc-chlorite deposit. International Journal of Earth Sciences, 105(3), 747-770. https://doi.org/10.1007/s00531-015-1223-x

Carrapa, B. (2010). Resolving tectonic problems by dating detrital minerals. Geology, 38(2), 191-192.

Chelalou, R. (2015). Formation et évolution du bassin de Boucheville, implication sur l'évolution tectonique, métamorphique et sédimentaire des bassins sédimentaires mésozoïques du Nord-Est des Pyrénées. Thèse de doctorat. Rennes: Université Rennes 1. Retrieved from http://www.theses.fr/2015REN1S164

Chelalou, R., Nalpas, T., Bousquet, R., Prevost, M., Lahfid, A., Poujol, M., et al. (2016). New sedimentological, structural and paleothermicity data in the Boucheville Basin (eastern North Pyrenean Zone, France). Comptes Rendus Geoscience, 348(3-4), 312-321. https://doi.org/10.1016/j.crte.2015.11.008

Chenin, P., Manatschal, G., Picazo, S., Müntener, O., Karner, G., Johnson, C., & Ulrich, M. (2017). Influence of the architecture of magmapoor hyperextended rifted margins on orogens produced by the closure of narrow versus wide oceans. Geosphere, 13(2), 559-576. https://doi.org/10.1130/GES01363.1

Cherniak, D. J., Watson, E. B., & Thomas, J. B. (2009). Diffusion of helium in zircon and apatite. Chemical Geology, 268(1-2), 155-166. https://doi.org/10.1016/j.chemgeo.2009.08.011

Chevrot, S., Sylvander, M., Diaz, J., Martin, R., Mouthereau, F., Manatschal, G., et al. (2018). The non-cylindrical crustal architecture of the Pyrenees. Scientific Reports, 8(1), 9591. https://doi.org/10.1038/s41598-018-27889-x

Choukroune, P. (1974). Structure et évolution tectonique de la zone nord-pyrénéenne: analyse de la déformation dans une portion de chaîne à schistosité sub-verticale. Thèse de doctorat. Montpellier: Université des Sciences et Techniques du Languedoc.

Choukroune, P. (1989). The Ecors Pyrenean deep seismic profile reflection data and the overall structure of an orogenic belt. Tectonics, 8(1), 23-39. https://doi.org/10.1029/TC008i001p00023

Christophoul, F., Soula, J.-C., Brusset, S., Elibana, B., Roddaz, M., Bessière, G., & Déramond, J. (2003). Time, place and mode of propagation of foreland basin systems as recorded by the sedimentary fill: Examples of the Late Cretaceous and Eocene retro-foreland basins of the north-eastern Pyrenees.

Special Publication-Geological Society of London, 208(1), 229-252. https://doi.org/10.1144/GSL.SP.2003.208.01.11

Clerc, C., & Lagabrielle, Y. (2014). Thermal control on the modes of crustal thinning leading to mantle exhumation: Insights from the Cretaceous Pyrenean hot paleomargins. Tectonics, 33, 1340-1359. https://doi.org/10.1002/2013TC003471

Clerc, C., Lagabrielle, Y., Labaume, P., Ringenbach, J.-C., Vauchez, A., Nalpas, T., et al. (2016). Basement-cover decoupling and progressive exhumation of metamorphic sediments at hot rifted margin. Insights from the Northeastern Pyrenean analog. Tectonophysics, 686, 82-97. https://doi.org/10.1016/j.tecto.2016.07.022

Clerc, C., Lagabrielle, Y., Neumaier, M., Reynaud, J.-Y., & de Saint Blanquat, M. (2012). Exhumation of subcontinental mantle rocks: Evidence from ultramafic-bearing clastic deposits nearby the Lherz peridotite body, French Pyrenees. Bulletin de la Société Géologique de France, 183(5), 443-459. https://doi.org/10.2113/gssgfbull.183.5.443

Clerc, C., Lahfid, A., Monié, P., Lagabrielle, Y., Chopin, C., Poujol, M., et al. (2015). High-temperature metamorphism during extreme thinning of the continental crust: A reappraisal of the North Pyrenean passive paleomargin. Solid Earth, 6(2), 643-668. https://doi.org/10.5194/se-6-643-2015

Crochet, B., Villatte, J., Tambareau, Y., Bilotte, M., Bousquet, J. P., Kuhfuss, A., et al. (1989). Carte géologique de France (1/50 000), feuille Quillan (1077). Orléans: BRGM.

Crowley, P. D., Reiners, P. W., Reuter, J. M., & Kaye, G. D. (2002). Laramide exhumation of the Bighorn Mountains, Wyoming: An apatite (U-Th)/He thermochronology study. Geology, 30(1), 27-30. https://doi.org/10.1130/0091-7613(2002)030<0027:LEOTBM>2.0.CO;2

Curnelle, R., Dubois, P., & Seguin, J. C. (1980). Le bassin d'Aquitaine: Substratum anté-Tertiaire et bordures mésozoïques. In La Chaîne Des Pyrénées et Son Avant-Pays Aquitano-Languedocien, Bulletin Des Centres de Recherches Exploration-Production Elf-Aquitaine, Mémoire (Vol. 3, pp. 47-58).

Dauteuil, O., & Ricou, L.-E. (1989). Hot-fluid circulation as an origin for the North Pyrenean cretaceous metamorphism. Geodinamica Acta, 3(3), 237-249. https://doi.org/10.1080/09853111.1989.11105190

Debroas, E.-J. (1987). Modèle de bassin triangulaire à l'intersection de décrochements divergents pour le fossé albo-cénomanien de la Ballongue (Zone Nord-Pyrénéenne, France). Bulletin de la Société Géologique de France, 8, 887-898.

Debroas, E.-J. (1990). Le Flysch noir albo-cénomanien témoin de la structuration albienne à sénonienne de la zone nord-pyrénéenne en Bigorre (Hautes-Pyrénées, France). Bulletin de la Société Géologique de France, 6(2), 283-285.

Delay, F. (1989). Le massif nord-pyrénéen de l'Agly (Pyrénées orientales): Évolution tectono-métamorphique et exemple d'un amincissement crustal polyphasé. Thèse de doctorat. Lille: Université Lille 1. Retrieved from http://www.theses.fr/1989LIL10175

Delay, F., & Paquet, J. (1989). Tectonique ductile en extension dans le massif hercynien de l'Agly (Zone Nord-Pyrénéenne). Comptes Rendus de l'Académie des Sciences. Série 2, Mécanique, Physique, Chimie, Sciences de l'Univers, Sciences de la Terre, 308(18), 1637-1643.

Demange, M., Lia-Aragnouet, F., Pouliguen, M., Perrot, X., & Sauvage, H. (1999). Les syénites du Castillet (massif de l'Agly, Pyrénées orientales, France): Une roche exceptionnelle dans les Pyrénées. Comptes Rendus de l'Académie des Sciences - Series IIA - Earth and Planetary Science, 329(5), 325-330. https://doi.org/10.1016/S1251-8050(00)88582-1

Demange, M., & Pascal, M.-L. (1979). Structure du massif nord-pyrénéen de Salvezines (Aude). Comptes Rendus Académie Des Sciences de Paris, 289, 711-714.

Denèle, Y. (2007). Formation des dômes gneissiques hercyniens dans les Pyrénées: Exemple du massif de l'Aston-Hospitalet. Thèse de doctorat. Toulouse: Université Toulouse 3. Retrieved from http://www.theses.fr/2007TOU30274

Diaz, J., Vergés, J., Chevrot, S., Antonio-Vigil, A., Ruiz, M., Sylvander, M., & Gallart, J. (2018). Mapping the crustal structure beneath the eastern Pyrenees. Tectonophysics, 744, 296-309. https://doi.org/10.1016/j.tecto.2018.07.011

Dielforder, A., Frasca, G., & Ford, M. (2017). Initiation of the Pyrenean plate boundary fault and its effect on the near- and far-field deformation of the European plate (Vol. 19, p. 5144). Presented at the EGU General Assembly Conference Abstracts. Retrieved from http://adsabs.harvard.edu/abs/2017EGUGA..19.5144D

Dobson, K. J., Stuart, F. M., & Dempster, T. J. (2008). U and Th zonation in Fish Canyon Tuff zircons: Implications for a zircon (U-Th)/He standard. Geochimica et Cosmochimica Acta, 72(19), 4745-4755.

Ducoux, M. (2017). Structure et évolution tectonique de la Zone Interne Métamorphique des Pyrénées. Thèse de doctorat. Orléans: Institut des Sciences de la Terre d'Orléans.

Faccenna, C., Becker, T. W., Auer, L., Billi, A., Boschi, L., Brun, J. P., et al. (2014). Mantle dynamics in the Mediterranean. Reviews of Geophysics, 52, 283-332. https://doi.org/10.1002/2013RG000444

Farley, K. A. (2000). Helium diffusion from apatite: General behavior as illustrated by Durango fluorapatite. Journal of Geophysical Research, 105(B2), 2903-2914. https://doi.org/10.1029/1999JB900348

Farley, K. A., Wolf, R. A., & Silver, L. T. (1996). The effects of long alpha-stopping distances on (U-Th)/He ages. Geochimica et Cosmochimica Acta, 60(21), 4223-4229. https://doi.org/10.1016/S0016-7037(96)00193-7

Filleaudeau, P.-Y., Mouthereau, F., & Pik, R. (2012). Thermo-tectonic evolution of the south-central Pyrenees from rifting to orogeny: Insights from detrital zircon U/Pb and (U-Th)/He thermochronometry. Basin Research, 24(4), 401-417. https://doi.org/10.1111/j.1365-2117.2011.00535.x

Fillon, C., Huismans, R. S., & van der Beek, P. (2013). Syntectonic sedimentation effects on the growth of fold-and-thrust belts. Geology, 41(1), 83-86. https://doi.org/10.1130/G33531.1

Fillon, C., & van der Beek, P. (2012). Post-orogenic evolution of the southern Pyrenees: Constraints from inverse thermo-kinematic modelling of low-temperature thermochronology data. Basin Research, 24(4), 418-436. https://doi.org/10.1111/j.1365-2117.2011.00533.x

Fitzgerald, P. G., Muñoz, J. A., Coney, P. J., & Baldwin, S. L. (1999). Asymmetric exhumation across the Pyrenean orogen: Implications for the tectonic evolution of a collisional orogen. Earth and Planetary Science Letters, 173(3), 157-170. https://doi.org/10.1016/S0012-821X(99)00225-3

Flowers, R. M., Farley, K. A., & Ketcham, R. A. (2015). A reporting protocol for thermochronologic modeling illustrated with data from the Grand Canyon. Earth and Planetary Science Letters, 432, 425-435. https://doi.org/10.1016/j.epsl.2015.09.053

Flowers, R. M., Ketcham, R. A., Shuster, D. L., & Farley, K. A. (2009). Apatite (U-Th)/He thermochronometry using a radiation damage accumulation and annealing model. Geochimica et Cosmochimica Acta, 73(8), 2347-2365. https://doi.org/10.1016/j.gca.2009.01.015

Flowers, R. M., Shuster, D. L., Wernicke, B. P., & Farley, K. A. (2007). Radiation damage control on apatite (U-Th)/He dates from the Grand Canyon region, Colorado Plateau. Geology, 35(5), 447-450. https://doi.org/10.1130/G23471A.1

Fonteilles, M., Leblanc, D., Clauzon, G., Vaudin, J. L., & Berger, G. M. (1993). Carte géologique de France (1/50 000), feuille Rivesaltes (1090) Orléans: BRGM.

Ford, M., Hemmer, L., Vacherat, A., Gallagher, K., & Christophoul, F. (2016). Retro-wedge foreland basin evolution along the ECORS line, eastern Pyrenees, France. Journal of the Geological Society, 173(3), 419-437. https://doi.org/10.1144/jgs2015-129

Gallagher, K., Brown, R., & Johnson, C. (1998). Fission-track analysis and its applications to geological problems. Annual Review of Earth and Planetary Sciences, 26(1), 519-572. https://doi.org/10.1146/annurev.earth.26.1.519

Gautheron, C., Tassan-Got, L., Barbarand, J., & Pagel, M. (2009). Effect of alpha-damage annealing on apatite (U-Th)/He thermochronology.Chemical Geology, 266(3-4), 157-170. https://doi.org/10.1016/j.chemgeo.2009.06.001

Godard, V., Pik, R., Lavé, J., Cattin, R., Tibari, B., de Sigoyer, J., et al. (2009). Late Cenozoic evolution of the central Longmen Shan, eastern Tibet: Insight from (U-Th)/He thermochronometry. Tectonics, 28, TC5009. https://doi.org/10.1029/2008TC002407

Golberg, J.-M., & Leyreloup, A. F. (1990). High temperature-low pressure Cretaceous metamorphism related to crustal thinning (Eastern North Pyrenean Zone, France). Contributions to Mineralogy and Petrology, 104(2), 194-207. https://doi.org/10.1007/BF00306443

Golberg, J.-M., & Maluski, H. (1988). Données nouvelles et mise au point sur l'âge du métamorphisme pyrénéen. Comptes Rendus de l'Académie Des Sciences. Série 2, Mécanique, Physique, Chimie, Sciences de l'Univers, Sciences de La Terre, 306(6), 429-435.

Grool, A. R., Ford, M., Vergés, J., Huismans, R. S., Christophoul, F., & Dielforder, A. (2018). Insights into the crustal-scale dynamics of a doubly vergent orogen from a quantitative analysis of its forelands: A case study of the eastern Pyrenees. Tectonics, 37, 450-476. https://doi.org/10.1002/2017TC004731

Guenthner, W. R., Reiners, P. W., DeCelles, P. G., & Kendall, J. (2015). Sevier belt exhumation in central Utah constrained from complex zircon (U-Th)/He data sets: Radiation damage and He inheritance effects on partially reset detrital zircons. Geological Society of America Bulletin, 127(3-4), 323-348. https://doi.org/10.1130/B31032.1

Guenthner, W. R., Reiners, P. W., Drake, H., & Tillberg, M. (2017). Zircon, titanite, and apatite (U-Th)/He ages and age-eU correlations from the Fennoscandian Shield, southern Sweden: Fennoscandian Zirc He age-eU correlation. Tectonics, 36, 1254-1274. https://doi.org/10.1002/2017TC004525

Guenthner, W. R., Reiners, P. W., Ketcham, R. A., Nasdala, L., & Giester, G. (2013). Helium diffusion in natural zircon: Radiation damage, anisotropy, and the interpretation of zircon (U-Th)/He thermochronology. American Journal of Science, 313(3), 145-198. https://doi.org/10.2475/03.2013.01

Guenthner, W. R., Reiners, P. W., & Tian, Y. (2014). Interpreting date-eU correlations in zircon (U-Th)/He datasets: A case study from the Longmen Shan, China. Earth and Planetary Science Letters, 403, 328-339. https://doi.org/10.1016/j.epsl.2014.06.050

Guinault, M., Hallot, E., Boulvais, P., Poujol, M., de Saint Blanquat, M., & Rémy, P. (2016). L'albitisation dans le granite de Lansac-St Arnac: paroxysme de la métasomatose sodique pyrénéenne au Crétacé. In 25ème Réunion des sciences de la Terre (RST 2016) (p. 152).

Gunnell, Y., Calvet, M., Brichau, S., Carter, A., Aguilar, J.-P., & Zeyen, H. (2009). Low long-term erosion rates in high-energy mountain belts: Insights from thermo- and biochronology in the eastern Pyrenees. Earth and Planetary Science Letters, 278(3-4), 208-218. https://doi.org/10.1016/j.epsl.2008.12.004

Gunnell, Y., Zeyen, H., & Calvet, M. (2008). Geophysical evidence of a missing lithospheric root beneath the eastern Pyrenees: Consequences for post-orogenic uplift and associated geomorphic signatures. Earth and Planetary Science Letters, 276(3-4), 302-313. https://doi.org/10.1016/j.epsl.2008.09.031

Hart, N. R., Stockli, D. F., Lavier, L. L., & Hayman, N. W. (2017). Thermal evolution of a hyperextended rift basin, Mauléon Basin, western Pyrenees. Tectonics, 36, 1103-1128. https://doi.org/10.1002/2016TC004365

Hourigan, J. K., Reiners, P. W., & Brandon, M. T. (2005). U-Th zonation-dependent alpha-ejection in (U-Th)/He chronometry. Geochimica et Cosmochimica Acta, 69(13), 3349-3365. https://doi.org/10.1016/j.gca.2005.01.024

Jammes, S., Manatschal, G., Lavier, L., & Masini, E. (2009). Tectonosedimentary evolution related to extreme crustal thinning ahead of a propagating ocean: Example of the western Pyrenees. Tectonics, 28, TC4012. https://doi.org/10.1029/2008TC002406

Johnson, J. E., Flowers, R. M., Baird, G. B., & Mahan, K. H. (2017). "Inverted" zircon and apatite (U-Th)/He dates from the Front Range, Colorado: High-damage zircon as a low-temperature (<50 °C) thermochronometer. Earth and Planetary Science Letters, 466(supplement C), 80-90. https://doi.org/10.1016/j.epsl.2017.03.002

Ketcham, R. A. (2005). Forward and inverse modeling of low-temperature thermochronometry data. Reviews in Mineralogy and Geochemistry, 58(1), 275-314. https://doi.org/10.2138/rmg.2005.58.11

Ketcham, R. A., Gautheron, C., & Tassan-Got, L. (2011). Accounting for long alpha-particle stopping distances in (U-Th-Sm)/He geochronology: Refinement of the baseline case. Geochimica et Cosmochimica Acta, 75(24), 7779-7791. https://doi.org/10.1016/j.gca.2011.10.011

Ketcham, R. A., Guenthner, W. R., & Reiners, P. W. (2013). Geometric analysis of radiation damage connectivity in zircon, and its implications for helium diffusion. American Mineralogist, 98(2-3), 350-360. https://doi.org/10.2138/am.2013.4249

Labaume, P., Meresse, F., Jolivet, M., & Teixell, A. (2016). Exhumation sequence of the basement thrust units in the west-central Pyrenees. Constraints from apatite fission-track analysis. Geogaceta, 60, 11-14.

Lagabrielle, Y., & Bodinier, J.-L. (2008). Submarine reworking of exhumed subcontinental mantle rocks: Field evidence from the Lherz peridotites, French Pyrenees. Terra Nova, 20(1), 11-21. https://doi.org/10.1111/j.1365-3121.2007.00781.x

Lagabrielle, Y., Labaume, P., & de Saint Blanquat, M. (2010). Mantle exhumation, crustal denudation, and gravity tectonics during Cretaceous rifting in the Pyrenean realm (SW Europe): Insights from the geological setting of the lherzolite bodies: Pyrenean lherzolites, gravity tectonics. Tectonics, 29, TC4012. https://doi.org/10.1029/2009TC002588

Laumonier, B. (2015). Les Pyrénées alpines sud-orientales (France, Espagne) - essai de synthèse. Revue de Géologie Pyrénéenne, 2(1). Retrieved from http://www.geologie-des-pyrenees.com/wp-content/uploads/2015/10/Laumonier-2015-Pyr%C3%A9n%C3%A9esalpines-sud-orientales.pdf

Laumonier, B., Calvet, M., Wiazemsky, M., Barbey, P., Marignac, C., Lambert, J., & Lenoble, J.-L. (2015). Notice explicative, Carte géol. France (1/50 000), feuille Céret (1096). Orléans: BRGM.

Macchiavelli, C., Vergés, J., Schettino, A., Fernàndez, M., Turco, E., Casciello, E., et al. (2017). A new southern North Atlantic isochron map: Insights into the drift of the Iberian Plate since the Late Cretaceous. Journal of Geophysical Research: Solid Earth, 122, 9603-9626.https://doi.org/10.1002/2017JB014769

Masini, E., Manatschal, G., Tugend, J., Mohn, G., & Flament, J. M. (2014). The tectono-sedimentary evolution of a hyper-extended rift basin: The example of the Arzacq-Mauléon rift system (western Pyrenees, SW France). International Journal of Earth Sciences, 103(6), 1569-1596. https://doi.org/10.1007/s00531-014-1023-8

Maurel, O. (2003). L'exhumation de la Zone Axiale des Pyrénées orientales: Une approche thermo-chronologique multi-méthodes du rôle des failles. Thèse de doctorat. Montpellier: Université Montpellier II-Sciences et Techniques du Languedoc.

Maurel, O., Monié, P., Pik, R., Arnaud, N., Brunel, M., & Jolivet, M. (2008). The Meso-Cenozoic thermo-tectonic evolution of the eastern Pyrenees: An $^{40}Ar/^{39}Ar$ fission-track and (U-Th)/He thermochronological study of the Canigou and Mont-Louis massifs. International Journal of Earth Sciences, 97(3), 565-584. https://doi.org/10.1007/s00531-007-0179-x

Mesalles, L., Mouthereau, F., Bernet, M., Chang, C.-P., Lin, A. T.-S., Fillon, C., & Sengelen, X. (2014). From submarine continental accretion to arc-continent orogenic evolution: The thermal record in southern Taiwan. Geology, 42(10), 907-910. https://doi.org/10.1130/G35854.1

Monod, B. (2014). Carte géologique numérique à 1/250 000 de la région Midi-Pyrénées. Notice technique. BRGM/RP-63650-FR, 160p., 23fig., 1pl. hors-texte. Orléans, France.

Montigny, R., Azambre, B., Rossy, M., & Thuizat, R. (1986). The geological evolution of the Pyrenees K-Ar study of Cretaceous magmatism and metamorphism in the Pyrenees: Age and length of rotation of the Iberian Peninsula. Tectonophysics, 129(1-4), 257-273. https://doi.org/10.1016/0040-1951(86)90255-6

Mouthereau, F., Filleaudeau, P.-Y., Vacherat, A., Pik, R., Lacombe, O., Fellin, M. G., et al. (2014). Placing limits to shortening evolution in the Pyrenees: Role of margin architecture and implications for the Iberia/Europe convergence: Plate convergence in the Pyrenees. Tectonics, 33, 2283-2314. https://doi.org/10.1002/2014TC003663

Muñoz, J. A. (1992). Evolution of a continental collision belt: ECORS-Pyrenees crustal balanced cross-section. In Thrust tectonics (pp. 235-246). Dordrecht, Netherlands: Springer.

Naylor, M., & Sinclair, H. D. (2008). Pro- vs. retro-foreland basins. Basin Research, 20(3), 285-303. https://doi.org/10.1111/j.1365-2117.2008.00366.x

Odlum, M., & Stockli, D. F. (2017). Thermotectonic evolution of the North Pyrenean Agly Massif from hyperextension through inversion using multi-mineral thermochronometry (Vol. 19, p. 11277). Presented at the EGU General Assembly Conference abstracts.

Olivier, P. (2013). Comment on "Preorogenic exhumation of the North Pyrenean Agly Massif (eastern Pyrenees-France)" by A. Vauchez et al. Tectonics, 32, 821-822. https://doi.org/10.1002/tect.20049

Olivier, P., Gleizes, G., Paquette, J.-L., & Muñoz Sáez, C. (2008). Structure and U-Pb dating of the Saint-Arnac pluton and the Ansignan charnockite (Agly Massif): A cross-section from the upper to the middle crust of the Variscan eastern Pyrenees. Journal of the Geological Society, 165(1), 141-152. https://doi.org/10.1144/0016-76492006-185

Olivier, P., Gleizes, G., & Paquette, J. L. (2004). Gneiss domes and granite emplacement in an obliquely convergent regime: New interpretation of the Variscan Agly Massif (eastern Pyrenees, France). In D. L. Whitney, C. Teyssier, & C. S. Siddoway (Eds.), Gneiss Domes in Orogeny (Vol. 380, pp. 229-242). Boulder, CO: Geological Soc Amer Inc. https://doi.org/10.1130/0-8137-2380-9.229

Paquet, J., & Delay, F. (1989). Electron-microscope study of North Pyrenean mylonites (St Barthelemy and Agly Massifs, France) and discussion of their ages. Bulletin de la Société Géologique de France, 5(6), 1111-1122.

Paquet, J., & Mansy, J.-L. (1992). Alpine evolution of the North-Pyrenean Agly Massif (eastern Pyrenees). Comptes Rendus de l'Académie des Sciences. Série 2, Mécanique, Physique, Chimie, Sciences de l'Univers, Sciences de la Terre, 315(4), 487-494.

Paquet, J., & Mansy, J.-L. (1991). La structure de l'Est des Pyrénées (transversales du massif de l'Agly) : un exemple d'amincissement crustal. Comptes Rendus de l'Académie des Sciences. Série 2, Mécanique, Physique, Chimie, Sciences de l'Univers, Sciences de la Terre, 312(8), 913-919.

Pascal, M.-L. (1979). Les albitites du Massif de l'Agly (Pyrénées-Orientales). Thèse de doctorat. Paris: ENSMP.

Peyton, S. L., & Carrapa, B. (2013). An introduction to low-temperature thermochronologic techniques, methodology, and applications. In C. Knight & J. Cuzella (Eds.), Application of structural methods to Rocky Mountain hydrocarbon exploration and development: AAPG Studies in Geology 65 (pp. 15-36).

Pik, R., Marty, B., Carignan, J., & Lavé, J. (2003). Stability of the Upper Nile drainage network (Ethiopia) deduced from (U-Th)/He thermochronometry: Implications for uplift and erosion of the Afar plume dome. Earth and Planetary Science Letters, 215(1-2), 73-88. https://doi.org/10.1016/S0012-821X(03)00457-6

Platt, J. P. (1986). Dynamics of orogenic wedges and the uplift of high-pressure metamorphic rocks. Geological Society of America Bulletin, 97(9), 1037-1053. https://doi.org/10.1130/0016-7606(1986)97<1037:DOOWAT>2.0.CO;2

Plaziat, J.-C. (1981). Late Cretaceous to late Eocene palaeogeographic evolution of southwest Europe. Palaeogeography, Palaeoclimatology, Palaeoecology, 36(3-4), 263-320. https://doi.org/10.1016/0031-0182(81)90110-3

Poujol, M., Boulvais, P., & Kosler, J. (2010). Regional-scale Cretaceous albitization in the Pyrenees: Evidence from *in situ* U-Th-Pb dating of monazite, titanite and zircon. Journal of the Geological Society, 167(4), 751-767. https://doi.org/10.1144/0016-76492009-144

Powell, J., Schneider, D., Stockli, D., & Fallas, K. (2016). Zircon (U-Th)/He thermochronology of Neoproterozoic strata from the Mackenzie Mountains, Canada: Implications for the Phanerozoic exhumation and deformation history of the northern Canadian Cordillera. Tectonics, 35, 663-689. https://doi.org/10.1002/2015TC003989

Prior, M. G., Stockli, D. F., & Singleton, J. S. (2016). Miocene slip history of the Eagle Eye detachment fault, Harquahala Mountains metamorphic core complex, west-central Arizona. Tectonics, 35, 1913-1934. https://doi.org/10.1002/2016TC004241

Pujadas, J., Casas, J. M., Muñoz, J. A., & Sabat, F. (1989). Thrust tectonics and paleogene syntectonic sedimentation in the Empordà area, southeastern Pyrenees. Geodinamica Acta, 3(3), 195-206. https://doi.org/10.1080/09853111.1989.11105186

Rahl, J. M., Haines, S. H., & van der Pluijm, B. A. (2011). Links between orogenic wedge deformation and erosional exhumation: Evidence from illite age analysis of fault rock and detrital thermochronology of syn-tectonic conglomerates in the Spanish Pyrenees. Earth and Planetary Science Letters, 307(1-2), 180-190. https://doi.org/10.1016/j.epsl.2011.04.036

Ravier, J. (1957). Le métamorphisme des terrains secondaires des Pyrénées. Dans: Mém. Soc. Géol. de France, NS, T. 38 (Mém. N° 86). Thèse de doctorat.

Ravier, J., & Thiébaut, J. (1982). Sur l'origine lagunaire des marbres et cornéennes mésozoïques du col d'Agnès (Ariège). Comptes Rendus. Académie des Sciences, 294, 127-130.

Reiners, P. W., Farley, K. A., & Hickes, H. J. (2002). He diffusion and (U-Th)/He thermochronometry of zircon: Initial results from Fish Canyon Tuff and Gold Butte. Tectonophysics, 349(1-4), 297-308. https://doi.org/10.1016/S0040-1951(02)00058-6

Reiners, P. W., Spell, T. L., Nicolescu, S., & Zanetti, K. A. (2004). Zircon (U-Th)/He thermochronometry: He diffusion and comparisons with $^{40}Ar/^{39}Ar$ dating. Geochimica et Cosmochimica Acta, 68(8), 1857-1887. https://doi.org/10.1016/j.gca.2003.10.021

Reston, T. J. (2009). The structure, evolution and symmetry of the magma-poor rifted margins of the North and Central Atlantic: A synthesis. Tectonophysics, 468(1-4), 6-27. https://doi.org/10.1016/j.tecto.2008.09.002

Rougier, G., Ford, M., Christophoul, F., & Bader, A.-G. (2016). Stratigraphic and tectonic studies in the central Aquitaine Basin, northern Pyrenees: Constraints on the subsidence and deformation history of a retro-foreland basin. Comptes Rendus Geoscience, 348(3-4), 224-235. https://doi.org/10.1016/j.crte.2015.12.005

Roure, F., Choukroune, P., Berastegui, X., Muñoz, J. A., Villien, A., Matheron, P., et al. (1989). ECORS deep seismic data and balanced cross sections: Geometric constraints on the evolution of the Pyrenees. Tectonics, 8(1), 41-50. https://doi.org/10.1029/TC008i001p00041

Rushlow, C. R., Barnes, J. B., Ehlers, T. A., & Vergés, J. (2013). Exhumation of the southern Pyrenean fold-thrust belt (Spain) from orogenic growth to decay. Tectonics, 32, 843-860. https://doi.org/10.1002/tect.20030

Séranne, M. (1999). The Gulf of Lion continental margin (NW Mediterranean) revisited by IBS: An overview. Geological Society, London, Special Publications, 156(1), 15-36. https://doi.org/10.1144/GSL.SP.1999.156.01.03

Shuster, D. L., Flowers, R. M., & Farley, K. A. (2006). The influence of natural radiation damage on helium diffusion kinetics in apatite. Earth and Planetary Science Letters, 249(3-4), 148-161. https://doi.org/10.1016/j.epsl.2006.07.028

Simpson, G. D. H. (2006). How and to what extent does the emergence of orogens above sea level influence their tectonic development? Terra Nova, 18(6), 447-451. https://doi.org/10.1111/j.1365-3121.2006.00711.x

Sinclair, H. D. (2011). Thrust wedge/foreland basin systems. In C. Busby & A. Azor (Eds.), Tectonics of Sedimentary Basins: Recent Advances (pp. 522-537). Chichester, UK: John Wiley & Sons.

Sinclair, H. D., Gibson, M., Naylor, M., & Morris, R. G. (2005). Asymmetric growth of the Pyrenees revealed through measurement and modeling of orogenic fluxes. American Journal of Science, 305(5), 369-406. https://doi.org/10.2475/ajs.305.5.369

Sinclair, H. D., & Naylor, M. (2012). Foreland basin subsidence driven by topographic growth versus plate subduction. Geological Society of America Bulletin, 124(3-4), 368-379. https://doi.org/10.1130/B30383.1

Souquet, P., Peybernès, B., Bilotte, M., & Debroas, E.-J. (1977). La chaîne alpine des Pyrénées. Géologie Alp, 53, 193-216.

Spear, F. (1993). Metamorphic phase equilibria and pressure-temperature-time paths (pp. 352-356). Mineralogical Society of America.

Stockli, D. F. (2005). Application of low-temperature thermochronometry to extensional tectonic settings. Reviews in Mineralogy and Geochemistry, 58(1), 411-448. https://doi.org/10.2138/rmg.2005.58.16

Stockli, D. F., Farley, K. A., & Dumitru, T. A. (2000). Calibration of the apatite (U-Th)/He thermochronometer on an exhumed fault block, White Mountains, California. Geology, 28(11), 983-986. https://doi.org/10.1130/0091-7613(2000)28<983:COTAHT>2.0.CO;2

Sutra, E., Manatschal, G., Mohn, G., & Unternehr, P. (2013). Quantification and restoration of extensional deformation along the Western Iberia and Newfoundland rifted margins: Strain distribution along rifted margins. Geochemistry, Geophysics, Geosystems, 14, 2575-2597. https://doi.org/10.1002/ggge.20135

Tagami, T., Farley, K. A., & Stockli, D. F. (2003). (U-Th)/He geochronology of single zircon grains of known Tertiary eruption age. Earth and Planetary Science Letters, 207(1-4), 57-67. https://doi.org/10.1016/S0012-821X(02)01144-5

Teixell, A., Labaume, P., Ayarza, P., Espurt, N., de Saint Blanquat, M., & Lagabrielle, Y. (2018). Crustal structure and evolution of the Pyrenean-Cantabrian belt: A review and new interpretations from recent concepts and data. Tectonophysics, 724-725, 146-170. https://doi.org/10.1016/j.tecto.2018.01.009

Teixell, A., Labaume, P., & Lagabrielle, Y. (2016). The crustal evolution of the west-central Pyrenees revisited: Inferences from a new kinematic scenario. Comptes Rendus Geoscience, 348(3-4), 257-267. https://doi.org/10.1016/j.crte.2015.10.010

Thomson, K. D., Stockli, D. F., Clark, J. D., Puigdefàbregas, C., & Fildani, A. (2017). Detrital zircon (U-Th)/(He-Pb) double-dating constraints on provenance and foreland basin evolution of the Ainsa Basin, south-central Pyrenees, Spain. Tectonics, 36, 1352-1375. https://doi.org/10.1002/2017TC004504

Tibari, B., Vacherat, A., Stab, M., Pik, R., Yeghicheyan, D., & Hild, P. (2016). An alternative protocol for single zircon dissolution with application to (U-Th-Sm)/He thermochronometry. Geostandards and Geoanalytical Research https://doi.org/10.1111/j.1751-908X.2016.00375.x, 40(3), 365-375.

Tournaire Guille, B. T., Olivier, P., Paquette, J.-L., Bosse, V., & Guillaume, D. (2018). Evolution of the middle crust of the Pyrenees during the Paleozoic: New data on the plutonic rocks from the North Pyrenean Agly massif. International Journal of Earth Sciences. https://doi.org/10.1007/s00531-018-1652-4

Tugend, J., Manatschal, G., Kusznir, N. J., Masini, E., Mohn, G., & Thinon, I. (2014). Formation and deformation of hyperextended rift systems: Insights from rift domain mapping in the Bay of Biscay-Pyrenees. Tectonics, 33, 1239-1276. https://doi.org/10.1002/2014TC003529

Vacherat, A., Mouthereau, F., Pik, R., Bellahsen, N., Gautheron, C., Bernet, M., et al. (2016). Rift-to-collision transition recorded by tectonothermal evolution of the northern Pyrenees: Cooling history of the northern Pyrenees. Tectonics, 35, 907-933. https://doi.org/10.1002/2015TC004016

Vacherat, A., Mouthereau, F., Pik, R., Bernet, M., Gautheron, C., Masini, E., et al. (2014). Thermal imprint of rift-related processes in orogens as recorded in the Pyrenees. Earth and Planetary Science Letters, 408, 296-306. https://doi.org/10.1016/j.epsl.2014.10.014

Vacherat, A., Mouthereau, F., Pik, R., Huyghe, D., Paquette, J.-L., Christophoul, F., et al. (2017). Rift-to-collision sediment routing in the Pyrenees: A synthesis from sedimentological, geochronological and kinematic constraints. Earth-Science Reviews, 172, 43-74. https://doi.org/10.1016/j.earscirev.2017.07.004

Vauchez, A., Clerc, C., Bestani, L., Lagabrielle, Y., Chauvet, A., Lahfid, A., & Mainprice, D. (2013). Preorogenic exhumation of the North Pyrenean Agly Massif (eastern Pyrenees-France). Tectonics, 32, 95-106. https://doi.org/10.1002/tect.20015

Vaudin, J.-L. (1982). Etude géologique de la couverture mésozoïque du massif de l'Agly (entre Estagel et Baixas, Pyrénées orientales). Thèse de doctorat. Toulouse: Université Paul Sabatier.

Vergés, J., Marzo, M., Santaeulària, T., Serra-Kiel, J., Burbank, D. W., Muñoz, J. A., & Giménez-Montsant, J. (1998). Quantified vertical motions and tectonic evolution of the SE Pyrenean foreland basin. Geological Society, London, Special Publications, 134(1), 107-134. https://doi.org/10.1144/GSL.SP.1998.134.01.06

Vergés, J., Millán, H., Roca, E., Muñoz, J. A., Marzo, M., Cirés, J., et al. (1995). Eastern Pyrenees and related foreland basins: Pre-, synand post-collisional crustal-scale cross-sections. Marine and Petroleum Geology, 12(8), 903-915. https://doi.org/10.1016/0264-8172(95)98854-X

Vielzeuf, D. (1996). Les massifs nord-pyrénéens à soubassement granulitique. In BRGM-ITGE (Ed.), Synthèse Géologique et GéophysiqueDes Pyrénées. Introduction. Géophysique. Cycle Hercynien (Vol. 1, pp. 502-521). Orléans: BRGM.

Whitchurch, A. L., Carter, A., Sinclair, H. D., Duller, R. A., Whittaker, A. C., & Allen, P. A. (2011). Sediment routing system evolution within a diachronously uplifting orogen: Insights from detrital zircon thermochronological analyses from the south-central Pyrenees. American Journal of Science, 311(5), 442-482. https://doi.org/10.2475/05.2011.03

Willett, S., Beaumont, C., & Fullsack, P. (1993). Mechanical model for the tectonics of doubly vergent compressional orogens. Geology, 21(4), 371-374. https://doi.org/10.1130/0091-7613(1993)021<0371:MMFTTO>2.3.CO;2

Willett, S. D., & Brandon, M. T. (2002). On steady states in mountain belts. Geology, 30(2), 175-178. https://doi.org/10.1130/0091-7613(2002)030<0175:OSSIMB>2.0.CO;2

Wolfe, M. R., & Stockli, D. F. (2010). Zircon (U-Th)/He thermochronometry in the KTB drill hole, Germany, and its implications for bulk He diffusion kinetics in zircon. Earth and Planetary Science Letters, 295(1-2), 69-82. https://doi.org/10.1016/j.epsl.2010.03.025

Yelland, A. J. (1991). Fission-track thermotectonics of the Iberian-Eurasian plate collection. PhD thesis. Birkbeck College University of London, London. Retrieved from http://ethos.bl.uk/OrderDetails.do?uin=uk.bl.ethos.261137

Chapter 6

VI. Thermo-tectonic evolution of the eastern Pyrenees from Rifting to Collision: insights from *in situ* laser detrital zircon (U-Th)/He - U/Pb data

FOREWORD

This Chapter will lead to paper submission once new data will be aquired with the new laser ablation system.

TABLE OF CONTENT

LIST OF FIGURES

LIST OF TABLES

VI.1 Introduction

Identifying and characterizing source regions that eroded in the past within a specific geological province is one of the main objectives of detrital studies aiming at unravelling sediment provenance and basin source-to-sink histories. A widely-used and powerful tool for provenance analysis and sediment routing reconstruction is detrital zircon geochronometry, consisting in correlating detrital zircon U/Pb ages within a sediment or sedimentary rock with the zircon crystallization ages of the source terrains (e.g. Dickinson and Gehrels, 2008; Gehrels, 2012, 2014; Lawton, 2014). However, source region interpretations may be complicated by several factors, including differential zircon fertility between source regions, regional similarities of bedrock U/Pb signatures and protracted tectonic histories with sediment recycling and mixing, which all lead to complex, ambiguous and sometimes non-diagnostic detrital age distributions (e.g. Dickinson and Gehrels, 2009; Malusà et al., 2013). Similarly, conducting detrital studies on the basis of the low-temperature thermochronology record alone may lead to ambiguous results (Garver and Brandon, 1994a, 1994b; Carter et al., 1995). Potential source terrains that contributed detritus can have similar thermal histories, making discrimination of provenance terrains difficult. Provenance studies using multi-dating methods on the same sample can therefore reduce uncertainty and misinterpretation of source data (e.g. Rahl et al., 2003; Campbell et al., 2005; Reiners et al., 2005).

In the classic Wilson plate-tectonic cycle, plate convergence and orogenesis follow plate divergence, expressed as rifting and, eventually, seafloor spreading (Wilson, 1966). Tectonic inversion of an Aptian-Cenomanian rift system, where mantle rocks were exhumed (Lagabrielle and Bodinier, 2008; Jammes et al., 2009; Lagabrielle et al., 2010; Clerc and Lagabrielle, 2014; Masini et al., 2014; Tugend et al., 2014), resulted in the asymmetric doubly vergent collisional Pyrenean orogen. This orogen has a pro-foreland system to the south on the lower Iberian plate (South Pyrenean fold-and-thrust belt, Ebro Basin) and a retro-foreland system to the north on the upper, European plate (North Pyrenean Zone, Aquitaine Basin; Figure VI.1). The retro-foreland basin records two distinct periods of low but accelerating tectonic subsidence (latest Santonian-Danian and Thanetian-Oligocene), separated by a quiet (very low to near-zero subsidence) period during the Paleocene (Ford et al., 2016; Rougier et al. 2016). These two periods have recently been shown to be contemporaneous with two distinct crustal cooling events recorded in the Pyrenean retro-wedge, where the Aptian-Cenomanian rift is best preserved. The first is related to early inversion of the distal European rifted margin and the second to main collision (Ternois et al., 2019). While detrital low-temperature thermochronology studies have clearly established a direct coupling between growth of the Pyrenean range and sedimentation patterns in adjacent foreland basins (Sinclair et al., 2005; Beamud et al., 2011; Rahl et al., 2011; Fillon, Gautheron et al., 2013; Thomson et al., 2017), data on foreland dynamics and sediment routing during initiation and early growth of Pyrenean topography has so far been incomplete (Whitchurch et al., 2011; Filleaudeau et al., 2012; Mouthereau et al., 2014; Thomson et al., 2017; Vacherat et al., 2017; Odlum and Stockli, in revision; Thomson et al., in review).

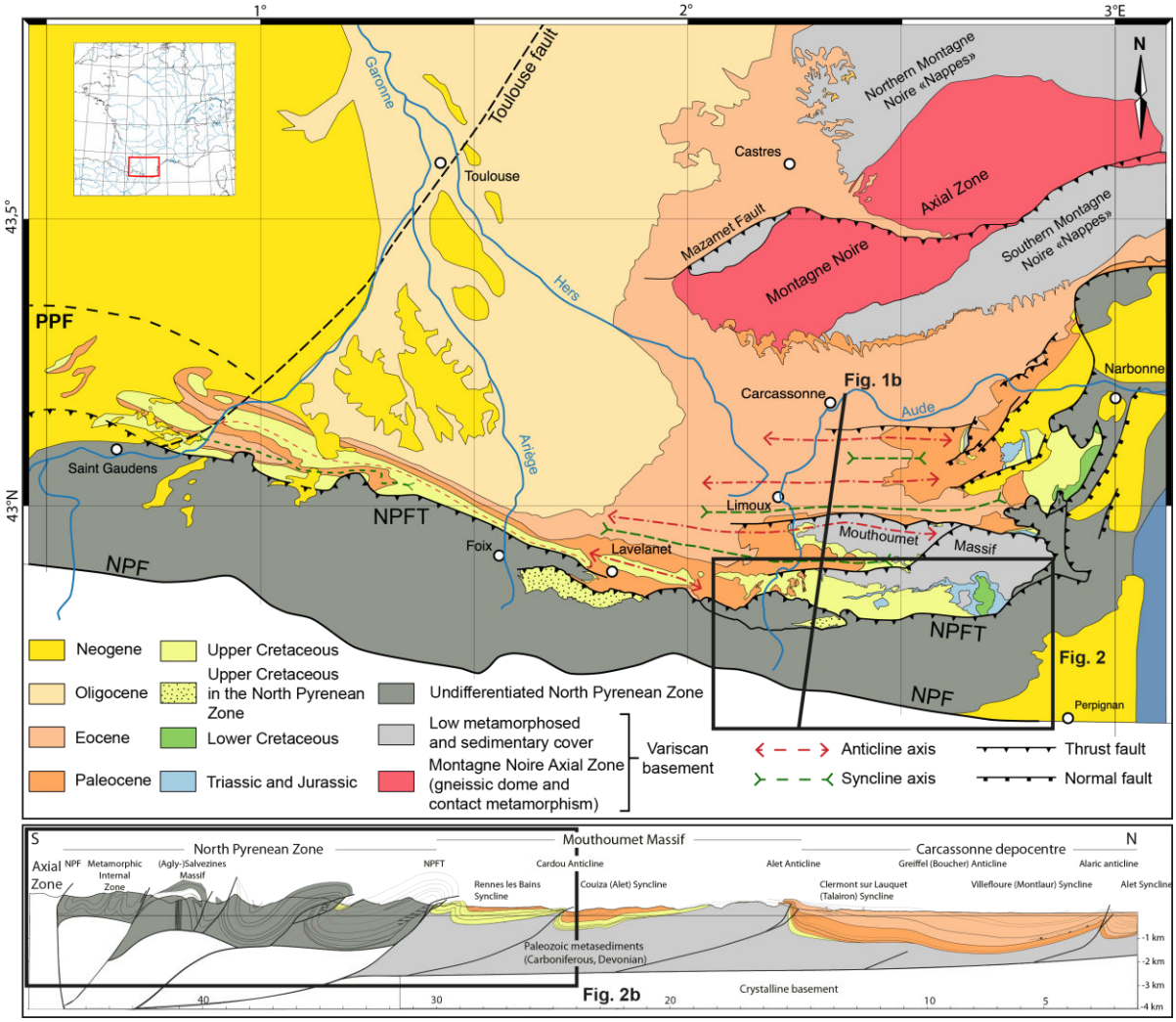

Figure VI.1: (a) Geological map of the central and eastern retroforeland Aquitain basin, based on maps published by the BRGM (Bureau de Recherches Géologiques et Minières; Castelnaudary: Cavaillé et al., 1975; Mirepoix: Cavaillé, 1976; Limoux: Bessière et al., 1978; Capendu: Ellenberger et al., 1987; Lavelanet: Bilotte et al., 1988; Quillan: Bessière et al., 1989; Crochet et al., 1989; Lezignan-Corbières: Berger et al., 1990; Tuchan: Berger, Alabouvette, et al., 1997; Berger, Bessière, et al., 1997; Rivesaltes: Berger et al., 1993; Fonteilles et al., 1993; Carcassonne: Berger et al., 1993), showing the main tectonic units, the location of the study area (Figure VI.2) and the position of the cross-section in Figure VI.1.b (modified from Christophoul et al., in prep). (b) Cross-section through the eastern retro-wedge (grey) and the eastern retroforeland basin showing the early convergence and main collision depocentres. NPF = North Pyrenean Fault; NPFT = North Pyrenean Frontal Thrust.

We here aim to investigate the evolution of synorogenic sediment routing systems during early convergence and the transition to main collision in the Pyrenean orogen in the Agly area of the eastern North Pyrenees. In this paper we present and interpret the first *in situ* single-grain detrital double dating dataset for the early Pyrenean orogen (1081 detrital zircon U/Pb ages and 902 detrital zircon (U-Th)/He ages) from the eastern Aquitaine foreland basin in the area of Rennes-les-Bains/Couiza (Figure VI.1 and Figure VI.2). By integrating these data with published geological data and various scale reconstructions, we address the following questions: What governs topographic growth during early inversion of rifted margins? Is the initiation of topographic growth

synchronous with onset of convergence or is there a lag time between these two processes? How precisely can we recognise tectonic events in the basin? Can we decipher patterns of exhumation, erosion and deposition through time and space that may be typical of laterally diachronous convergence zone? Can we distinguish differing styles of deformation and topographic growth between retro- and pro-wedge through time?

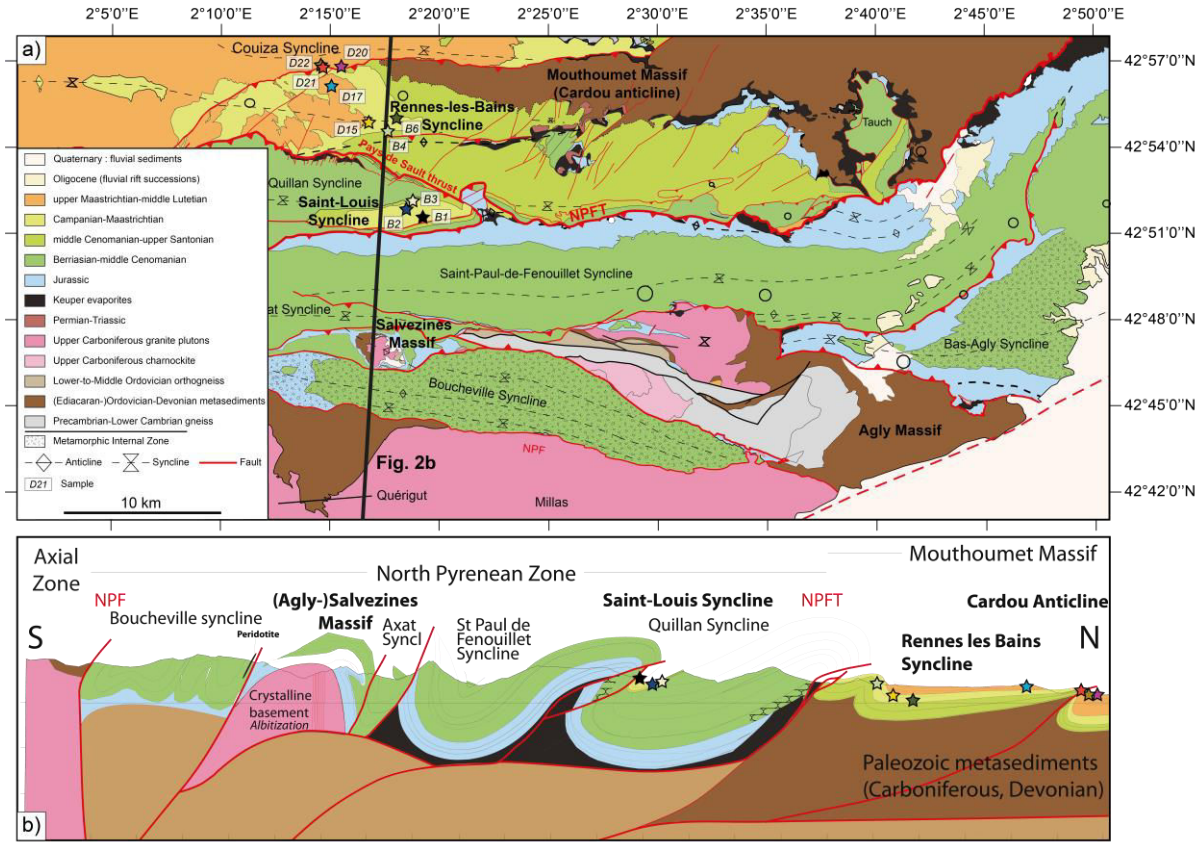

Figure VI.2: (a) Geological map of the Rennes-les-Bains/Couiza and Agly-Salvezines areas, based on maps published by the BRGM (Quillan: Bessière et al., 1989; Crochet et al., 1989; Tuchan: Berger, Alabouvette, et al., 1997; Berger, Bessière, et al., 1997; Rivesaltes: Berger et al., 1993; Fonteilles et al., 1993), showing the main structural elements and lithologies and the location of the 10 samples analyzed in this study (stars). The position of the cross-section presented in Figure VI.2.b is indicated. (b) Cross-section through the North Pyrenean Zone (inverted Aptian-Cenomian rift domain) and the early retroforeland basin. The stratigraphic position of the 10 samples analyzed in this study is indicated by stars (same colours as in Figure VI.2.a). NPF = North Pyrenean Fault; NPFT = North Pyrenean Frontal Thrust.

We show that the early eastern retroforeland basin preserves the full thermal and denudational evolution of the Pyrenean orogen from extensional episodes during the Early Cretaceous to early orogenic stages of the Late Cretaceous to early Eocene. In particular, our data suggest that the early Pyrenean edifice and the Early Cretaceous rift extended further east, in an area which has since been destroyed by the Oligocene-Miocene opening of the Gulf of Lion. We refer to this area as the Lion Pyrenees. Our work highlights the dominant role of rift inheritance into the distribution and magnitude of early orogenic inversion of distal rifted margins, allows better understanding of sediment routing during the initiation of Pyrenean topography, and shows fairly

instantaneous exhumation and erosion response to the onset of early orogenesis. We discuss the implications of these new results for models of orogenic growth in the Pyrenees, for early convergence in general, and for paleogeographic reconstructions.

VI.2 Geological background

VI.2.1 Regional setting, tectonic history and potential sources

A general overview of the Pyrenean system has been provided in Chapter 2. For convenience, the reader is kindly invited to refer to Chapter 2 for details. However, it is important to here introduce some key considerations we will be working with in this Chapter 6.

For each sample analysed in this detrital double dating study, concordant U/Pb ages are subdivided into groups reflecting the major tectonic-magmatic events recognised in the zircons of the northwestern Mediterranean region (Figure VI.3): post-Variscan (0-280 Ma), Variscan (280-330 Ma), Silurian-Devonian (330-440 Ma), Ordovician (440-480 Ma), Cadomian (480-700 Ma), and pre-Cadomian (>700 Ma). These groups are characteristic of zircons from Ediacaran-Paleozoic metasedimentary and Ordovician-to-Early Permian plutonic rocks recording the Variscan orogeny in the Axial Zone, the Mouthoumet Massif, the Montagne Noire (e.g. Cocherie, Baudin et al., 2005; Denèle et al., 2009a, 2009b, 2012, 2014; Hart et al., 2016; Margalef et al., 2016; Martínez et al., 2016), and Corsica and Sardinia (e.g. Cocherie, Rossi et al., 2005; Giacomini et al., 2005, 2006; Casini et al., 2012; Li et al., 2014, 2015; Martínez et al., 2016; Gaggero et al., 2017; Avigad et al., 2018). Such zircons may have been further recycled into Mesozoic deposits (e.g. Hart et al., 2016; Lin et al., 2016, 2018; Gaggero et al., 2017; Vacherat et al., 2017).

Likewise, (U-Th)/He ages are subdivided into time bins reflecting cooling associated with the major tectonic and thermal events recognised in the Pyrenees. These bins are defined as follows: post-orogenic phase (0-34 Ma), main collision (34-59 Ma), quiet period (59-66 Ma), early orogenesis (66-84 Ma), Cretaceous rifting (84-130 Ma), post-Variscan orogeny (130-320 Ma) and pre-Variscan orogeny (>320 Ma). The Pyrenean chain was built on a complex crustal template initiating mainly during the Variscan orogeny (e.g. Barnolas et al., 1996, and references therein). This orogeny was followed by two phases of Mesozoic extension or transtension, the first occurring from Triassic to Late Jurassic in an east-west zone linking the Tethys and Central Atlantic oceans (e.g. Curnelle et al., 1980). Rifting from late Aptian to early-to-middle Cenomanian (114-97 Ma) then created deep marine depocentres (Debroas, 1987, 1990) associated with exhumation of mantle rocks along the southern margin of the North Pyrenean Zone (Figure VI.1; Azambre and Ravier, 1978; Lagabrielle and Bodinier, 2008; Lagabrielle et al., 2010; Clerc et al., 2012). The thermal signature of early orogenesis (Late Campanian-Maastrichitian) has been distinguished from the preceding rift and subsequent thermal events related to main collision and later opening of the Gulf of Lion in the eastern Pyrenean retro-wedge (Chapter 5: Ternois et al., 2019).

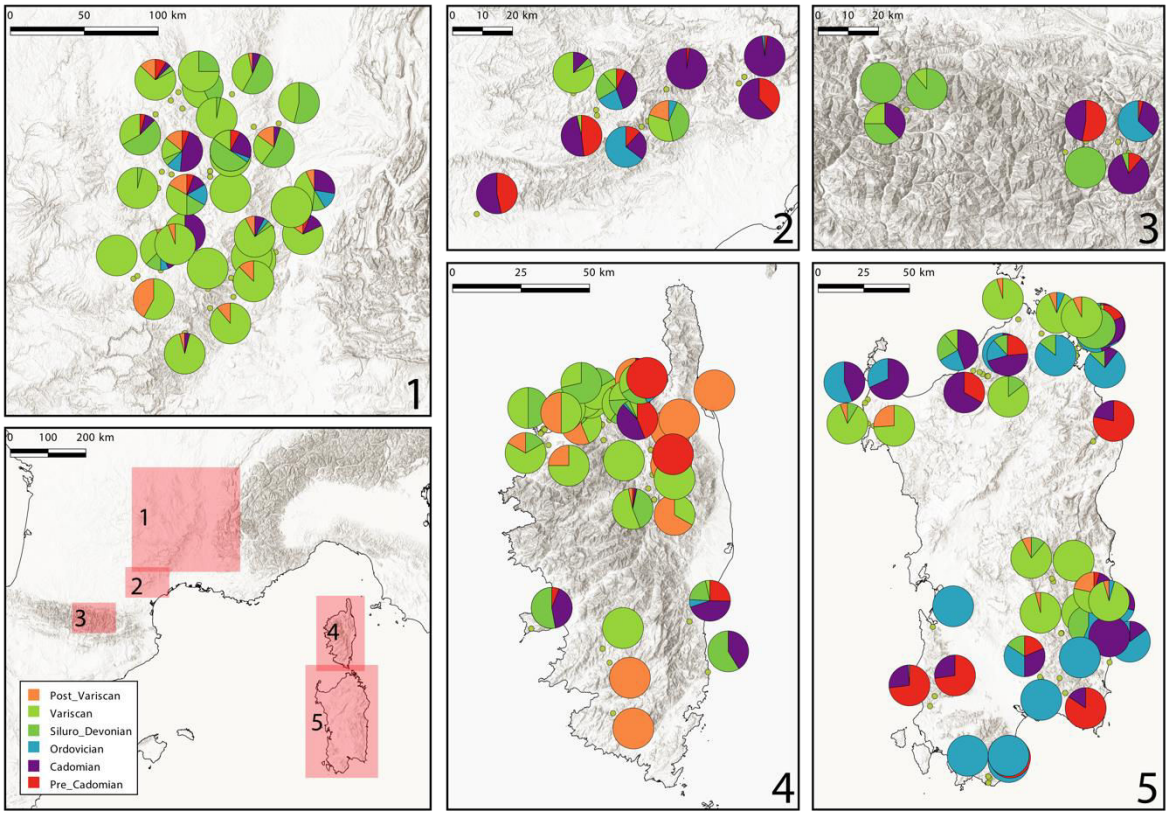

Figure VI.3: Zircon concordant U/Pb ages from potential source areas in the northwestern Mediterranean region, including the Massif Central (1), the Montagne Noire (2), the central Pyrenees (3), Corsica (4) and Sardinia (5) (Deloule et al., 2002; Maurel et al., 2003; Paquette et al., 2003; Olivier et al., 2004, 2008; Giacomini et al., 2005, 2006; Rossi et al., 2006, 2009; Denèle et al., 2009; Navidad et al., 2010; Oggiano et al., 2010; Franke et al., 2011; Poilvet et al., 2011; Avigad et al., 2012, 2018; Carosi et al., 2012; Casini et al., 2012; Pavanetto, 2011; Pavanetto et al., 2012; Li et al., 2014, 2015; Roger et al., 2015; Hart et al., 2016; Lin et al., 2016, 2018; Margalef et al., 2016; Mezger and Gerdes, 2016; Chelle-Michou et al., 2017; Gaggero et al., 2017; Laurent et al., 2017; Lotout et al., 2017; Padel et al., 2017; Poujol et al., 2017; Van Lichtervelde et al., 2017). It has to be stressed that some data, especially from the eastern Pyrenees, are currently missing in this figure due to the lack of GPS coordinates in several papers. By the time of submission of this work, this issue will be fixed.

VI.2.2 The north-eastern Pyrenees

In the eastern Pyrenean retro-wedge the North Pyrenean Frontal Thrust is recognized to be the inverted, northernmost or breakaway fault of the Aptian-Cenomanin rift (Souquet et al., 1977; Clerc et al., 2016; Ford, Hemmer et al., 2016; Grool et al., 2018; Ternois et al., 2019). North of this fault, small extent early detachment normal faults such as the Pays de Sault fault were reactivated as thrusts (Ford, Christophoul et al., 2016). Upper Cretaceous to Eocene strata of the Aquitaine foreland basin onlap directly onto Paleozoic basement and thick-skinned shortening affected the foreland generating several E-W basement-cored anticlines (Christophoul et al., 2003; Ternois et al., 2019), the most prominent of which is the Mouthoumet Massif.

The Mouthoumet Massif is generally represented as the proximal, northern margin of the Aptian-Cenomanin hyperextended rift (e.g. Clerc and Lagabrielle, 2014; Clerc et

al., 2016; Ternois et al., 2019), preserving the proximal breakaway zone of the Aptian-Albian extensional system along its southern border (Bilotte, 1985; Bilotte et al., 1999; Ford, Christophoul et al., 2016). This basement-cored anticline plunges to the west and separates into two branches, each defined by a smaller anticline cut by a north vergent thrust. These folds controlled the northward migration of synorogenic depocentres (Bilotte, 1985, 2007; Bessière et al., 1989; Crochet et al., 1989; Bilotte et al., 1999, 2005; Christophoul et al., 2003).

The northern Alet anticline separates the Campanian-Eocene Couiza depocentre to the south from the Campanian-Oligocene Carcassonne depocentre to the north. The southern Cardou anticline separates the Couiza synclinal depocentre to the north from the Cenomanian to early Eocene Rennes-les-Bains synclinal depocentre to the south. To the south of the Pays de Sault thrust, the Saint-Louis depocentre preserves the mid Cenomanian to latest Santonian stratigraphic record. We here focus on the Rennes-les-Bains and Saint-Louis sections that, between them, preserve a complete geological record of the rift-to-collision transition in the easternmost or Agly Pyrenees (Figure VI.2).

VI.2.3 Rennes-les-Bains and Saint-Louis area: stratigraphy and provenance studies

In this section, stratigraphy of the Rennes-les-Bains and Saint-Louis synclines (Figure VI.4) is presented on the basis of key paper references, sometimes resulting from the lifetime work of their authors. Regarding upper Cretaceous stratigraphy, these include Bilotte (1985), Bilotte et al. (1999), Bilotte et al. (2005), and Bilotte (2007). Regarding Paleogene stratigrathy, we can cite Freytet (1970), Freytet (1971), Freytet (1975), Freytet and Plaziat (1982).

VI.2.3.1 Post-rift stratigraphy

The Rennes-les-Bains and Saint-Louis successions record the Cenomanian to Eocene development of the eastern Aquitaine basin. Post-rift deposition started during the middle Cenomanian with shallow marine carbonates, and mixed carbonate-siliciclastic shelf deposits. These deposits thicken southwards from zero to *ca.* 500 m and onlap progressively northwards onto the Mouthoumet Massif that was a paleo-high between two depocentres at that time. No major tectonic activity is recorded and facies distribution was controlled by the interplay between accommodation space and sedimentation. Transgression continued with the deposition of the Blanque Sequence, including the Saint-Louis marls (Saint-Louis lower mals Formation), until late Turonian when a major regression cycle established (Figure VI.4). Late Turonian regression was marked by the deposition of the Lacal Sequence, including slumps in prodelta, the continued deposition of the Saint-Louis marls into the basin (Saint-Louis upper marls Formation), and thin delta front sandstones and limestones (Montplaisir Limestone Formation; Kennedy et al., 2015). During the Coniacian and early Santonian, the carbonate platform was drowned. Transgression initiated with deposition of thin deep-water limestones (Montferrand Limestone Formation; Rennes-les-Bains) then was fully expressed by deposition of hemipelagic shales (mainly Gauthiericeras Marl Formation;

Rennes-les-Bains and Saint-Louis). The overlying Micraster Marl Formation records the transition from transgression to regression in latest Coniacian-earliest Santonian. Platform carbonates were deposited to the north (Rennes-les-Bains) while deeper slope/basin sediments were deposited further south (Saint-Louis).

During the late Santonian, stratigraphic evidence of differential tectonically-driven subsidence and uplift are recorded in the Rennes-les-Bains area (Bilotte et al., 2005). The origin of such vertical movements is currently debated, with some authors invoking basement-involved tectonics (Bilotte et al., 2005; Bilotte, 2007) while recent workers suggest salt tectonics (Ford, Christophoul et al., 2014, 2016). Two successive deltaic to reefal systems developed (the Rennes-les-Bains and Montagne des Cornes deltas) with sandstone-rich gravity flow deposits in marine marls (Labastide Sandstone Formation). These slump deposits reached the distal slope domain. The first system is characterised by reworked Turonian to lower Santonian material as olistoliths (Ferrière Conglomerate; Saint-Louis) encased in blue, prodelta marls (Saint-Louis blue marls Formation) and sandy facies, delta front deposits (Rennes-les-Bains deltaic sandstone Formation). The second deltaic system followed a similar depositional succession with debris flow and intrabasinal reworked deposits (Gascous Conglomerate; Saint-Louis) encased in blue prodelta marls (Sougraigne Marl Formation), and sandy facies, delta front deposits (Sougraigne Sandstone Formation; Rennes-les-Bains). Gravity flows and paleocurrents are oriented NE-SW and/or E-W (Bessière et al., 1989), indicating that sediment was sourced at this time from east or NE as recorded regionally (e.g. Plaziat, 1981).

VI.2.3.2 Early orogenesis and tectonic quiescence

During the early Campanian, depositional environments evolved from tidal/estuarine to fluvial settings (around 83 Ma, basal Alet Sandstone Formation). This change coincides with the onset of N-S convergence of the Iberian and European plates in latest Santonian-early Campanian times (84 Ma; Macchiavelli et al., 2017). It is also synchronous with accelerating tectonic subsidence in the central Aquitaine retroforeland basin (Ford, Hemmer et al., 2016). Braided-meandering fluvial systems progressively established with multi-storey channels of coarse grained quartz-rich sandstone and a low proportion of overbank fines that are partially to totally reworked. Paleocurrents indicate sediment supply from a main eastern and/or northeastern source (Bessière et al., 1989). During accelerating creation of accommodation space, larger proportions of floodplain fines were preserved with progressive development and preservation of palaeosols by end Campanian (Campagne Red Marl Formation). During the early Maastrichtian, braided and meandering fluvial environments comprised small sand-filled channels confined by vegetated, fine-grained red overbank deposits (Estous Sandstone Formation and Maurine Red Marl Formation) containing dinosaur eggshells (Bilotte, 1985). No change in sourcing is noticed in this second fining-upward fluvial succession (Bilotte et al., 1999).

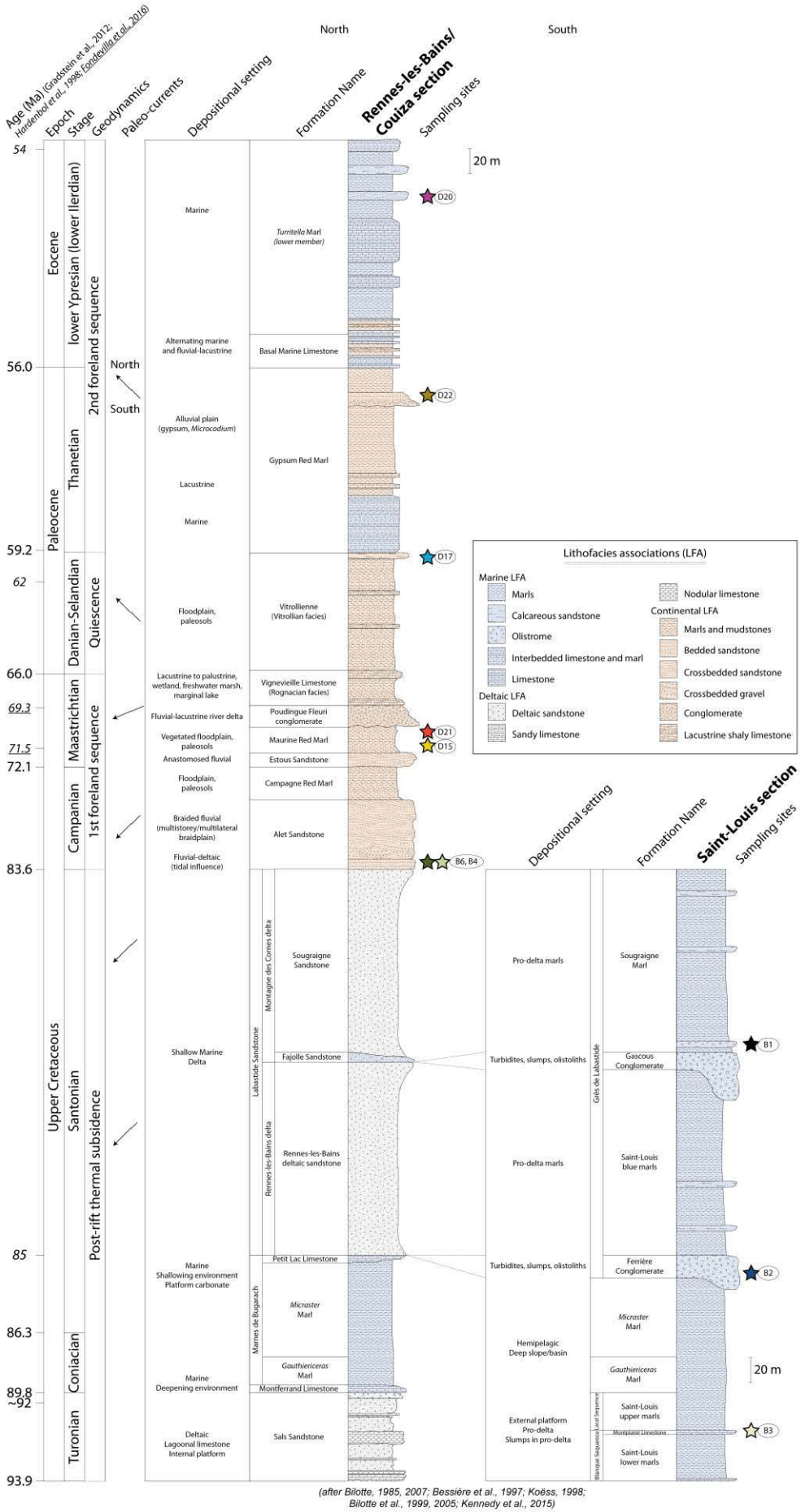

(after Bilotte, 1985, 2007; Bessière et al., 1997; Koëss, 1998; Bilotte et al., 1999, 2005; Kennedy et al., 2015)

Figure VI.4: (previous page) Stratigraphic overview of the Rennes-les-Bains/Couiza region showing two composite sections modified from Bilotte (1985), Bessière et al. (1989), Bilotte et al. (1999), Bilotte et al. (2005), and Bilotte (2007). Major formations, tectonic history, and depositional system evolution with paleocurrents are synthesized.

During the middle Maastrichtian (70 to 69 Ma; Fondevilla et al., 2016), the polygenic Poudingue Fleuri conglomerate was deposited as a small delta building into a lake. It was sourced from the same quartz-rich regions to the ENE as Campanian-Maastrichtian deposits and, in larger proportion, from calcareous regions also to the ENE with lithologies similar to lower Cretaceous formations of the North Pyrenean Zone (Bessière et al., 1989; Bilotte, 2014). No Paleozoic rocks originating from the North Pyrenean basement massifs have been observed in this formation.

Late Maastrichtian deposition is characterized by the palustrine-lacustrine Vignevieille Limestone Formation. This formation is very thin (5-15 m-thick) and made of two prominent, few meters thick, karstified limestone intervals separated by eggshell-bearing red marls. While the lower limestone yielded, along with the marls directly overlying it, charophyte species typical of lower to middle Maastrichtian deposits (Bessière et al., 1989; Marty, 2004; Marty and Meyer, 2006), the upper limestone yielded Danian charophyte (Marty, 2004; Marty and Meyer, 2006). Based on these biochronological markers, Fondevilla et al. (2016) propose a magnetostratigraphic correlation scheme for Maastrichtian continental deposits in the area and show that either upper Maastrichtian sediments are reduced or most of the late Maastrichtian is missing.

Continental conditions continued during the Danian-Selandian with deposition of the Vitrollienne Formation. Strong development of paleosols with microcodium and plant debris indicates a very low clastic supply to the foreland basin during the Paleocene. These conditions prevailed over the whole central Aquitaine retroforeland (negligible tectonic subsidence, no outward basin migration, very low sediment supply; Ford, Hemmer et al., 2016).

VI.2.3.3 Main collision stratigraphy

During the early Thanetian, a marine transgression is recorded in the Rennes-les-Bains and Couiza synclines by shallow marine limestones in a lacustrine limestone succession (Bessière et al., 1989). During the upper Thanetian, alluvial plain environments dominated with brown to red mudstones and with narrow channels of fine quartz sand to pebbly sand (Gypsum Red Marl Formation). Pebble lithologies indicate an emergent sedimentary source to the SSE (Bessière et al., 1989). Gypsum and Microcodium are present, but the latter is found in lower proportions than in earlier Vitrollian facies deposits (Bessière et al., 1989). Conglomeratic sedimentation increases in volume and grain size toward the west (Bilotte et al., 1988).

During the late Thanetian to early Ypresian (Illerdian) a second period of low but accelerating tectonic subsidence started in the central Aquitaine basin (Ford, Hemmer et al., 2016) and a major marine transgression from the west reached the eastern foreland

both north and south of the Mouthoumet Massif (Cavaillé et al., 1975; Cavaillé, 1976; Bessière et al., 1978; Ellenberger et al., 1987; Berger et al., 1990; Berger et al., 1993). The Rennes-les-Bains and Couiza synclines record alternating marine and fluvial-lacustrine deposits (Bessière et al., 1989). The basal shallow marine limestones unit (Basal Marine Limestone Formation; lower Ilerdian; Plaziat, 1981; Bessière et al., 1989) is overlain by the deeper water Turritella Marl Formation which consists of grey to yellow marls and cross-bedded sandstone and sandy limestone (lower to middle Illerdian; Bessière et al., 1989) and marks the transition from transgression to regression in its upper levels (diachronous top recording progradation from the east; Ford, Hemmer et al., 2016). Upper Illerdian deposition marked the onset of regression with increasing sandy content (sandy limestone, sandstones and pebbly sandstones) in the Couiza region. Areas of sedimentation then migrated westward from upper Ypresian (Cuisian) to Bartonian (Carcassonne Molasse Formation; Cavaillé et al., 1975; Cavaillé, 1976; Bessière et al., 1978; Ellenberger et al., 1987; Bilotte et al., 1988; Bessière et al., 1989; Berger et al., 1990; Berger et al., 1993), synchronously to the westward migration of growth of major orogen relief (e.g. Whitchurch et al., 2011, and references therein).

VI.2.3.4 Provenance studies in the early retroforeland basin

Based on classic basin analysis tools that combine sandstone petrographic analysis with sedimentological observations from paleocurrents measurements and detailed stratigraphic analysis of the retroforeland basin sedimentary fill, sourcing has been inferred to progressively evolve from ENE during the Santonian to SSE during the Illerdian (e.g. Combes et al., 1975; Plaziat, 1981; Freytet and Plaziat, 1982; Plaziat, 1984). Large quantities of Upper Devonian-Carboniferous slates and phyllites (lydite) in the upper Santonian Labastide Sandstone Formation together with paleocurrent data indicate local sourcing from the Paleozoic Mouthoumet Massif during the Santonian (Berger et al., 1997). However, the source of a small volume of granite pebbles in these deposits remains unidentified (Bilotte, 1985; Bessière et al., 1989) as no granitic rocks outcrop in the massif (Berger et al., 1997). Similarly, the source of the quartzitic material in Campanian and lower Maastrichtian siliciclastic sediments is poorly constrained since the amount of quartz that could be derived from the Paleozoic low-grade metasediments of the Mouthoumet Massif is considered insufficient (Bilotte, 2017). Finally, the recrystallized nature of limestone clasts in the middle Maastrichtian polygenic Poudingue Fleuri conglomerate has made many authors consider the Agly-Salvezines area, southeast of Rennes-les-Bains/Couiza, as a main source region for sediments during the Maastrichtian. However, the position of this area is incompatible with ENE-WSW paleocurrents for that period (Bilotte, 1985; Bessière et al., 1989).

To better identify and pinpoint the source regions for Pyrenean foreland basin sediment, recent studies have used modern techniques such as combining geochronology data with low-temperature thermochronology data (Whitchurch et al., 2011; Filleaudeau et al., 2012; Mouthereau et al., 2014; Thomson et al., 2017; Vacherat et al., 2017; Odlum and Stockli, in revision; Thomson et al., in review). These studies have revealed large-scale longitudinal drainage patterns in the southern pro-wedge

during early convergence in Late Cretaceous times while sediment dispersal in the northern retro-wedge was controlled by the inherited architecture of the former rifted margins. They also show that the first transverse drainage network to establish was in the southern Pyrenees occurred during the Paleocene, followed by a change from dominant longitudinal to transverse drainage in the central northern Pyrenees during the middle Eocene. However, these studies were hampered by either ambiguities of source tracers used independently (Whitchurch et al., 2011) or the limited number of samples (Filleaudeau et al., 2012; Mouthereau et al., 2014) or double-dated grains (Thomson et al., 2017; Vacherat et al., 2017; Odlum and Stockli, in revision; Thomson et al., in review), which were inadequate to describe the source of siliciclastic material. Moreover, the recent study of Fondevilla et al. (2016) in the northeastern Pyrenees allows comparison with sedimentation to the south (Galbrun et al., 1993; López-Martínez et al., 2001; Oms et al., 2007; Vila et al., 2012; Canudo et al., 2016) and shows that continental conditions during the Maastrichtian were established earlier in the retro-wedge, suggesting that a significant part of the evolution of sediment routing systems during the earliest orogenic stages of the Late Cretaceous is still poorly constrained.

New data are therefore required to constrain sediment provenance and sediment routing systems in the northeastern Pyrenees. With *in situ* laser ablation (U-Th)/(He-Pb) double dating on detrital zircons, this study revisits the source area problem of the eastern Pyrenees, providing a larger double dating data set with higher temporal and statistical resolution for the initiation of orogenesis in the Pyrenees. We also aim to get a better sense of Late Cretaceous paleogeography in the Mediterranean region and better understand the role of rift inheritance into the distribution and magnitude of early orogenic inversion of distal rift margins, as well as into the growth of topography. In particular, three different areas of the orogen will be considered further in the text, namely Corsica-Sardinia (CS), the Lion Pyrenees, and the Agly Pyrenees.

VI.3 Detrital zircon geo- and thermo-chronology analyses

VI.3.1 Sampling strategy

We collected a total of ten sandstone samples from Upper Santonian to Ypresian deposits from the Rennes-les-Bains and Saint-Louis sections (Figure VI.2 and Figure VI.4). Where possible, sandstone samples (3-9 kg) were collected targeting well-sorted sandstones with a consistent fine to coarse sand grain size to minimize effects of hydrodynamic grain size fractionation (e.g. Malusà et al., 2016). All samples are summarised in Table VI.1.

VI.3.1.1 Pre-convergence samples

Sample B3 was collected in the middle-to-upper Turonian Montplaisir Limestone Formation in a coarser level (fine-to-medium sands) of a glauconitic condensed siltstone to sandstone unit on the northern flank of the Saint-Louis syncline (Table VI.1; Figure VI.2).

Sample	Latitude (N)	Longitude (E)	Stratigraphic age	Stratigraphic epoch	Further information about location
NP17-QB-D20	42.94025421	2.278697014	lower Ypresian (lower Ilerdian)	Eocene	Right beneath the castle of Coustaussa
NP17-QB-D22	42.93698502	2.261810064	upper Thanetian	Paleocene	Along the road to Couiza, some 250 metres north of the sample D21
NP17-QB-D17	42.9270668	2.267273903	Danian-Selandian (Vitrollian facies)	Paleocene	Along the road to the village of Rennes-le-Château
NP17-QB-D21	42.93481445	2.264214993	middle Maastrichien	Upper Cretaceous	Along the road to Couiza (the steeply dipping northern limb of the Rennes-les-Bains syncline, north of the village of Rennes-le-Château)
NP17-QB-D15	42.90492249	2.298872948	lower Maastrichien	Upper Cretaceous	Near the village of Valdieu
NP15-QB-B4	42.90039063	2.312673092	basal lower Campanian	Upper Cretaceous	From the steeply dipping southern limb of the Rennes-les-Bains syncline
NP15-QB-B6	42.90841675	2.319375992	basal lower Campanian	Upper Cretaceous	From the gently S-dipping northern limb of the Rennes-les-Bains syncline
NP15-QB-B1	42.85133743	2.339293003	Turonian to Santonian	Upper Cretaceous	Near the Jean-Marie barn
NP15-QB-B2	42.85651016	2.326571941	Turonian to Santonian	Upper Cretaceous	Near the Richou barn
NP15-QB-B3	42.8595047	2.328347921	middle Turonian	Upper Cretaceous	On the northern flank of the Saint-Louis syncline, near Montplaisir

Table VI.1: Sample information.

Sample B2 was collected on the northern flank of the Saint Louis Syncline in a medium-to-coarse-grained decametre-scale sandstone block encased in the upper Santonian Saint-Louis blue marls and exhibiting planar lamination and cross-bedding (Labastide Sandstone Formation). This block is described as an olistolith whose age is Turonian or lower Santonian (Bilotte et al., 2005; Bilotte, 2007).

Sample B1 was collected in the upper Santonian Labastide Sandstone Formation, stratigraphically above the Gascous Conglomerate. This sample is a medium-to-coarse-grained sandstone with millimetre-scale components including angular to rounded quartz gravels, lydite and fragments of crinoids. Like sample B2, the quality/certainty associated with the stratigraphic age assigned to sample B1 is relatively poor, spanning a time interval between the Turonian and the late Santonian.

VI.3.1.2 Early-convergence samples

Samples B6 and B4 were both collected in the lower Campanian Alet Sandstone Formation, the former from the gently S-dipping northern limb of the Rennes-les-Bains syncline and the latter from the syncline's steeply dipping southern limb. Sample B6 is a quartz-rich, medium-to-coarse-grained cross-bedded sandstone. It was taken few centimetres above levels of poorly bedded conglomerate containing millimetre- to centimetre-scale rounded quartz pebbles and lydite clasts that are typical of the uppermost deltaic levels of the Sougraigne Sandstone Formation. Sample B4 is a parallel-laminated, fine-to-medium-grained, well-sorted sandstone with carbonate matrix. It is stratigraphically positioned some 50 metres above the marine Sougraigne Marl Formation. Since the samples were taken from one or the other limb of the Rennes-les-Bains syncline and facies vary from north to south, the stratigraphic position of the two samples relative to each other is uncertain.

Samples D15 and D21 were collected in the lower-middle Maastrichtian red beds of the Maurine Red Marl Formation. Sample D15 is a very fine-to-fine-grained sandstone with silty to muddy matrix taken from an isolated sand channel body within red marls. Bedding is roughly horizontal. Sample D21 is a medium-to-coarse-grained sandstone with silty to muddy reddish matrix taken few centimetres above levels of poorly bedded conglomerate containing millimetre- to decimetre-scale angular and rounded pebbles (pure quartz, brown sandstone, limestone). It is stratigraphically positioned some 5-10 metres below the Poudingue Fleuri conglomerate on the steeply dipping northern limb of the Rennes-les-Bains syncline.

VI.3.1.3 Quiescence to main collision samples

Sample D17 was collected in the Danian-Selandian Vitrollian Formation in the core of the Rennes-les-Bains Syncline. The sample is from a red, very fine-grained sandstone unit (channel) within a red marl succession deposited in fluvial floodplain environments. The sample contains Microcodium within its muddier parts and presents reddish, greyish and greenish colours that indicate fossil redox conditions.

Sample D22 was taken from upper Thanetian fine-to-medium-grained sandstones in the Gypsum Red Marl Formation, some 250 metres north of the sample D21. The base of this sandstone succession consists of pebble conglomerate with centimetre- to decimetre-scale rounded, elongated and locally imbricated pebbles (brown and red sandstone, pebbly sandstone, recrystallized limestone, slate).

Sample D20 is a cross-bedded, fine-grained sandstone containing brown to dark plant debris. It is interbedded with yellowish to blue-greyish silty marls of the lower Ypresian (lower to middle Illerdian) Turritella Marl Formation.

VI.3.2 *In situ* single-grain detrital zircon (U-Th)/(He-Pb) double dating methodology

As this has been thoroughly discussed in Chapter 4, results presented in this chapter are corrected for He overextraction. For more details, please refer to Chapter 4.

VI.4 Results

Our ten samples provided a total of 1081 zircon crystals dated by U/Pb. Among these crystals, 902 zircons satisfied the conditions suitable for *in situ* laser ablation (U-Th)/He dating. Samples D21, D22 and D20 yielded more than 120 concordant U/Pb ages (104-125 double-dated grains). Samples B4, D15 and D17 yielded between 60 and 95 concordant U/Pb ages (61-76 double-dated grains). The four other samples yielded less than 50 concordant U/Pb ages (samples B1, B2, B3 and B6; 4-45 double-dated grains). Following the recommendations of Vermeesch (2004) for provenance studies based on geochronological data, there is 95% confidence that no fraction with proportions higher than 8.5% was missed for two thirds of our samples (samples B4, D15, D17, D21, D22 and D20). The estimate rises to 10-20% for samples B1, B2, and B6 (and above for sample B3).

Due to the uncertainty associated with the depositional age of samples B2 and B1 (Turonian or Santonian), and the low to very low concordant zircon yield for these samples and sample B3 (Turonian), we decided to compile the three individual sample data sets into a single data set representing pre-convergence deposits (149 concordant U/Pb ages, 112 ZHe ages and 75 double-dated grains). The composite sample Bequ123 is given a mean depositional age of 89.5 ± 5 Ma, which serves as a reference age distribution for pre-convergence sediments.

Due to the uncertain stratigraphic position of samples B6 and B4 relative to each other, but a pretty similar depositional age, we also decided to compile these two data

sets into a characteristic data set for basal lower Campanian sandstones (196 concordant U/Pb ages, 166 ZHe ages and 109 double-dated grains). The composite sample Bequ46 is assigned an approximate depositional age of 82 ± 1 Ma, which serves as a reference age distribution for earliest convergence sediments. Results are described accordingly below.

VI.4.1 Detrital zircon (U-Th)/He results

Our detrital zircon (U-Th)/He results are reported in Appendix 23, Appendix 25, Appendix 27, Appendix 29, Appendix 31, Appendix 33, Appendix 35, Appendix 37, Appendix 39, Appendix 41. These are summarized as kernel density estimates (KDEs), and histograms in Figure VI.5. The proportion of each time bin in the individual total age distribution for each sample is tabulated in Table VI.2, summarized as pie charts in Figure VI.5 and plotted in Figure VI.6. As suggested in Chapter 4, the youngest peak age component of a sample or composite sample is obtained from its individual KDE. This component is also reported in Table VI.2.

Our results show only slight differences in the (U-Th)/He age distributions of the pre-convergence and basal lower Campanian composite samples. Both composite samples exhibit a broad spectrum of post-Variscan (U-Th)/He ages, with ages spanning the range ~150 Ma to ~350 Ma (Figure VI.5). Nevertheless, sample Bequ123 is dominated by a component around 230 Ma, while sample Bequ46 exhibits a dominant older, Variscan component at ~290 Ma (Figure VI.5).

Sample	post-orogenic phase (0-34 Ma)	main collision (34-59 Ma)	quiet period (59-66 Ma)	early orogenesis (66-84 Ma)	Cretaceous rifting (84-130 Ma)	post-Variscan orogeny (130-320 Ma)	pre-Variscan orogeny (>320 Ma)	Youngest component age (Ma)
D20	0%	1%	1%	10%	26%	22%	24%	75
D22	0%	1%	4%	27%	44%	14%	6%	68
D17	0%	0%	0%	7%	30%	19%	25%	81
D21	0%	0%	1%	19%	23%	26%	18%	80
D15	0%	0%	0%	0%	8%	32%	36%	110
Bequ46	0%	0%	0%	0%	2%	33%	42%	130
Bequ123	0%	0%	0%	0%	1%	49%	36%	155

Table VI.2: Detrital zircon (U-Th)/He results summarized in component percentages. Main results are plotted in Figure VI.6.

A gradual increase in the proportion of the Cretaceous rifting signal is observed upsection from the pre-convergence composite sample Bequ123 to the upper Thanetian sample D22 (from 0.9% to 43.9%; Table VI.2 and Figure VI.6). This increase significantly accelerates from the lower Maastrichtian sample D15 upward (Figure VI.6). The broad spectrum of post-Variscan (U-Th)/He ages exhibited by the basal lower Campanian composite sample Bequ46 is still evident in the lower Maastrichtian sample D15 (Figure VI.5). Similarly, the proportion of the early orogenesis signal increases upsection from lower Maastrichtian sample D15 to the upper Thanetian sample D22 (from 0% to 26.8%; Table VI.2 and Figure VI.6), albeit with some delay (~10 myrs) and more pronounced fluctuations. This increase is particularly sharp between D15 and the stratigraphically adjacent middle Maastrichtian sample D21 (from 0% and 18.9%). An abrupt younging of the youngest peak age component from 110 Ma to 80 Ma is also noticed in sample D21 (Table VI.2 and Figure VI.5). The proportion of the early orogenesis signal decreases by 11.8% in the lower Paleocene sample D17. After reaching a maximum value in the upper Thanetian sample D22, proportions in the Cretaceous

rifting and early orogenesis signals decrease by approximately half in the lower Ypresian sample D20.

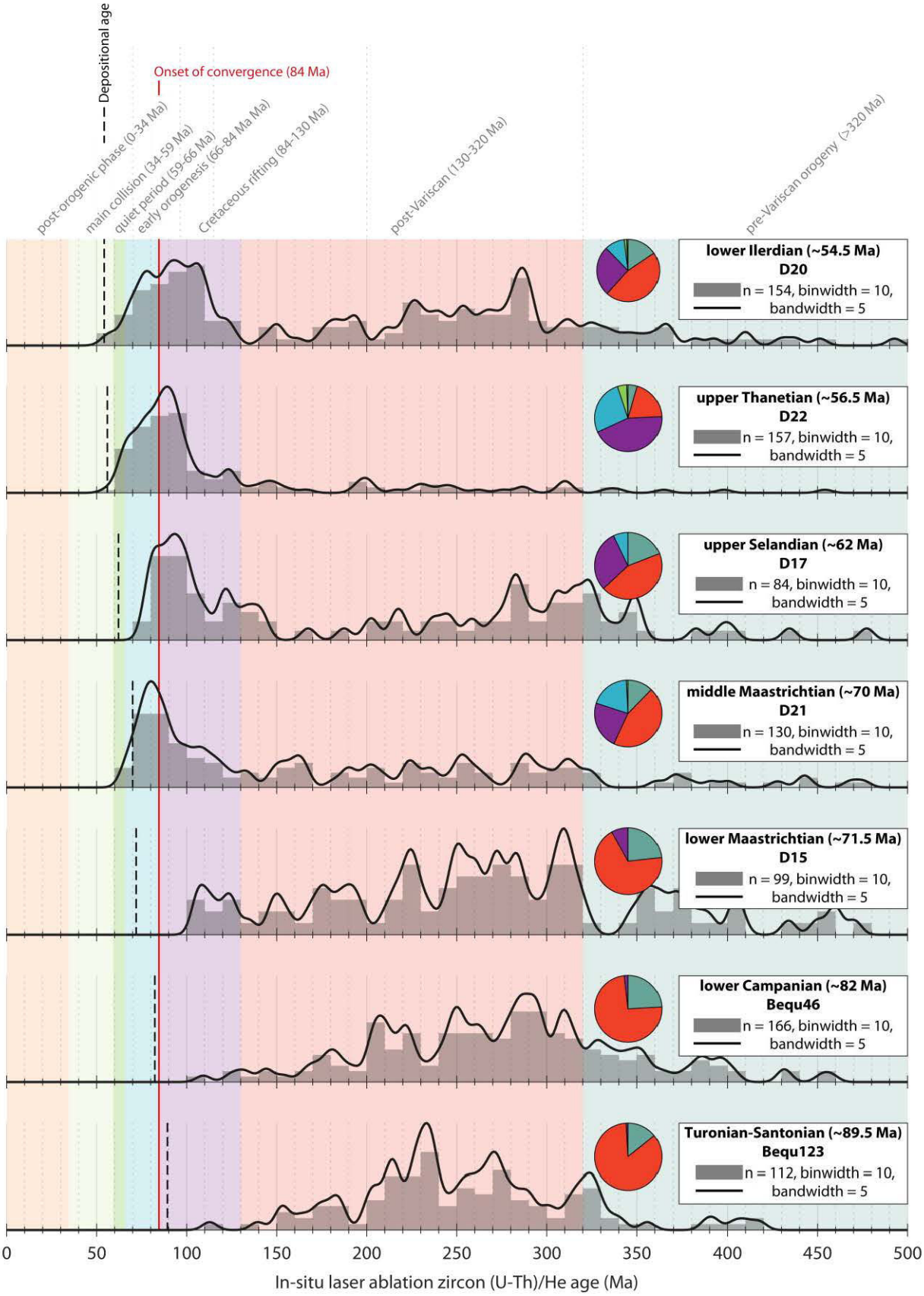

Figure VI.5: (previous page) Detrital zircon (U-Th)/He results displayed as kernel density estimates (KDE) and histograms (Vermeesch, 2012) from 0 to 500 Ma. Nonadaptive KDE bandwidth of 5 Ma; histogram binwidth of 10 Ma. The colored bars indicate time bins used for component definition. These time bins are also used for pie chart representations.

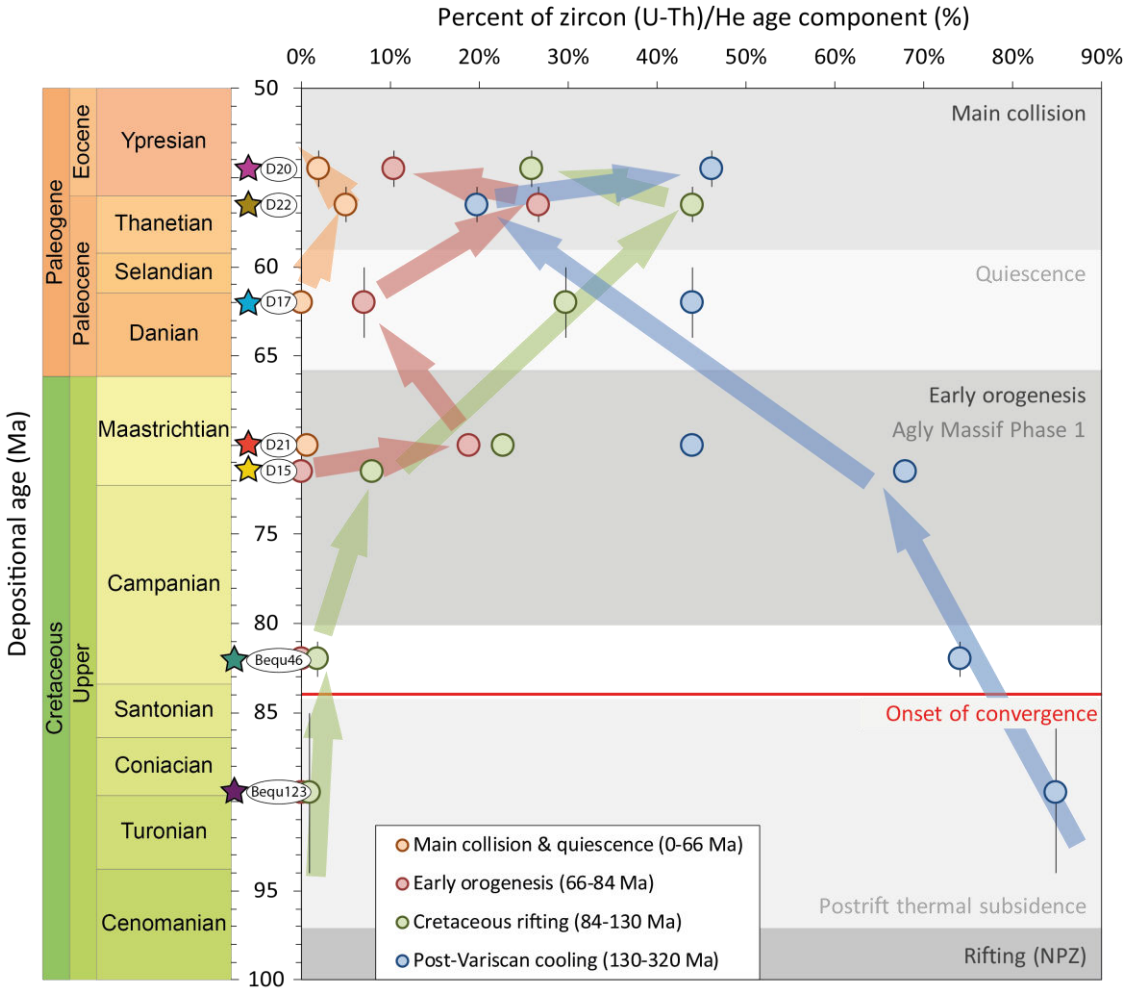

Figure VI.6: Proportions of the main detrital zircon (U-Th)/He components. Depositional age versus component percentages. Main trends are indicated by arrows. Over the complete stratigraphic interval, the proportion of the post-Variscan orogeny signal follows the exact opposite trend to those presented above (Figure VI.6), so that there is a compensatory relationship between early orogenesis/Cretaceous rifting and post-Variscan orogeny signals, with grains cooled during early orogenesis/Cretaceous rifting increasing as grains cooled after the Variscan orogeny decrease upsection.

The lag time is the difference between the youngest peak age obtained from the KDE of a sample and the depositional age of the sample, assuming instantaneous transport of detrital grains from source to sink (see section IV.2.2.2.2 for justification). Our results show that the lag time history can be divided into three main phases (Figure VI.7): (1) rapid decrease in lag times (~65 to ~10 myrs) during early orogenesis, (2) short but unstable lag times of ~10-19 myrs during the quiet phase, and (3) short but unstable (~12-21 myrs) lag times during the earliest stages of main collision.

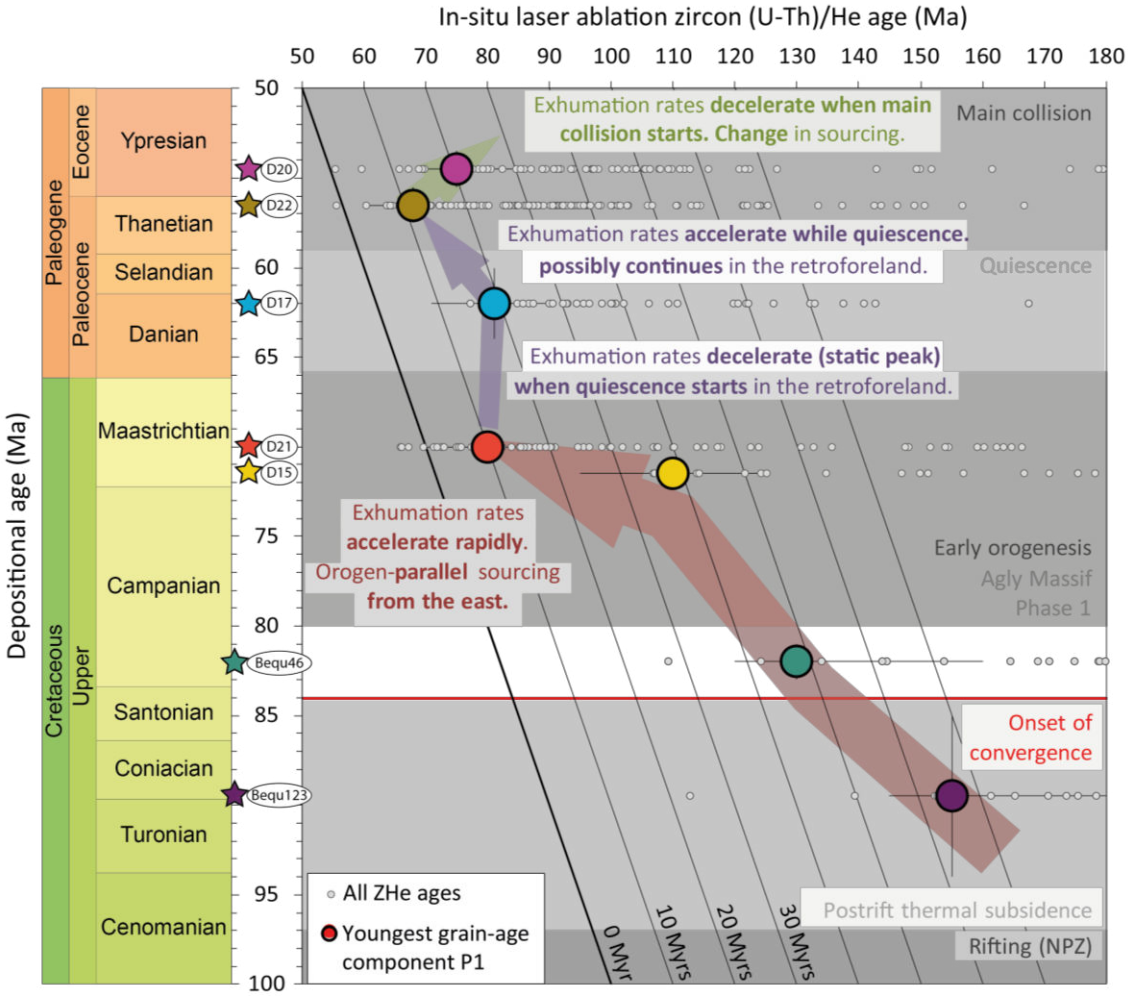

Figure VI.7: Lag-time plot. Depositional age versus zircon (U-Th)/He age. Large coloured circles represent the age of the youngest component P1 obtained from individual sample KDE. These are superimposed with sample data sets (small grey circles).

VI.4.2 Detrital zircon U/Pb results

Our detrital zircon U/Pb results are reported in Appendix 24, Appendix 26, Appendix 28, Appendix 30, Appendix 32, Appendix 34, Appendix 36, Appendix 38, Appendix 40 and Appendix 42. These are summarized as kernel density estimates (KDEs), and histograms in Figure VI.8. Only concordant U/Pb data are plotted in Figure VI.8. Concordia diagrams are provided in Appendix 43, Appendix 44, Appendix 45, Appendix 46, Appendix 47, Appendix 48, Appendix 49, Appendix 50, Appendix 51 and Appendix 52. Proportions of each group in the total age distribution for each sample are tabulated in Table VI.3, summarized as pie charts in Figure VI.8 and plotted in Figure VI.9.

No concordant U/Pb age data younger than ~220 Ma were recorded in any of the detrital samples. The pre-convergence composite sample Bequ123, the basal lower Campanian composite sample Bequ46 and the upper Thanetian sample D22 yield minor populations of post-Variscan (Permian-Triassic) concordant U/Pb ages (less than 3% of each individual data set). Overall, three main U/Pb age peaks stand out, albeit found in different proportions within each sample: ~300 Ma, ~450-480 Ma and ~540-650 Ma.

The latter can sometimes be clearly subdivided into two components at ~540-580 Ma and ~640-650 Ma (samples Bequ123, Bequ46, D15, D17 and D20).

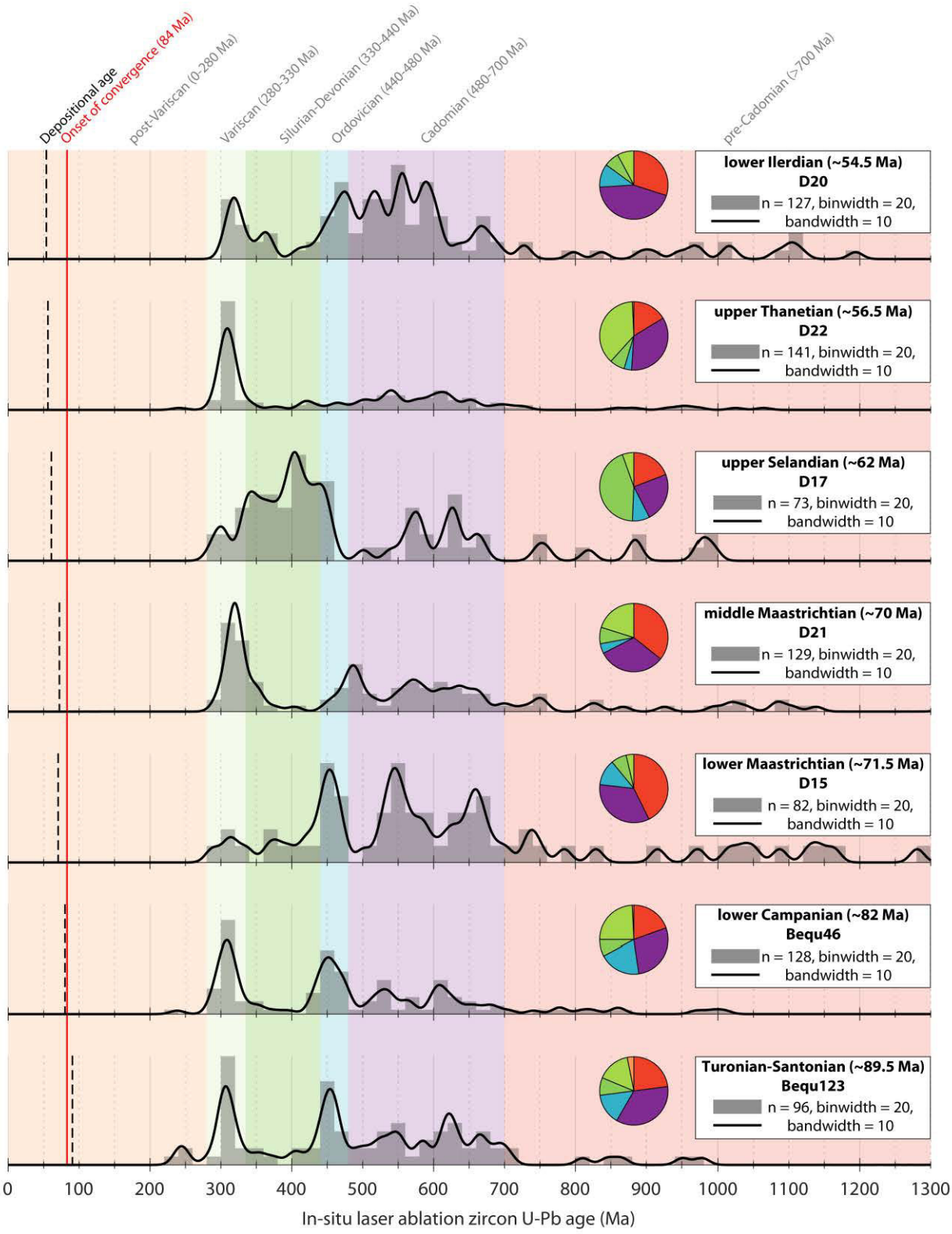

Figure VI.8: Detrital zircon U/Pb results displayed as kernel density estimates (KDE) and histograms (Vermeesch, 2012) from 0 to 1300 Ma. Nonadaptive KDE bandwidth of 10 Ma; histogram binwidth of 20 Ma. The colored bars indicate time bins used for component definition. These time bins are also used for pie chart representations.

Sample	Post-Variscan (0-280 Ma)	Variscan (280-330 Ma)	Silurian-Devonian (330-440 Ma)	Ordovician (440-480 Ma)	Cadomian (480-700 Ma)	pre-Cadomian (>700 Ma)
D20	0%	8%	7%	11%	44%	30%
D22	1%	38%	7%	4%	35%	16%
D17	0%	5%	44%	8%	23%	19%
D21	0%	20%	8%	5%	32%	36%
D15	0%	4%	7%	12%	34%	43%
Bequ46	1%	24%	8%	20%	28%	20%
Bequ123	3%	16%	8%	15%	35%	23%

Table VI.3: Detrital zircon concordant U/Pb results summarized in component percentages. Main results are plotted in Figure VI.9.

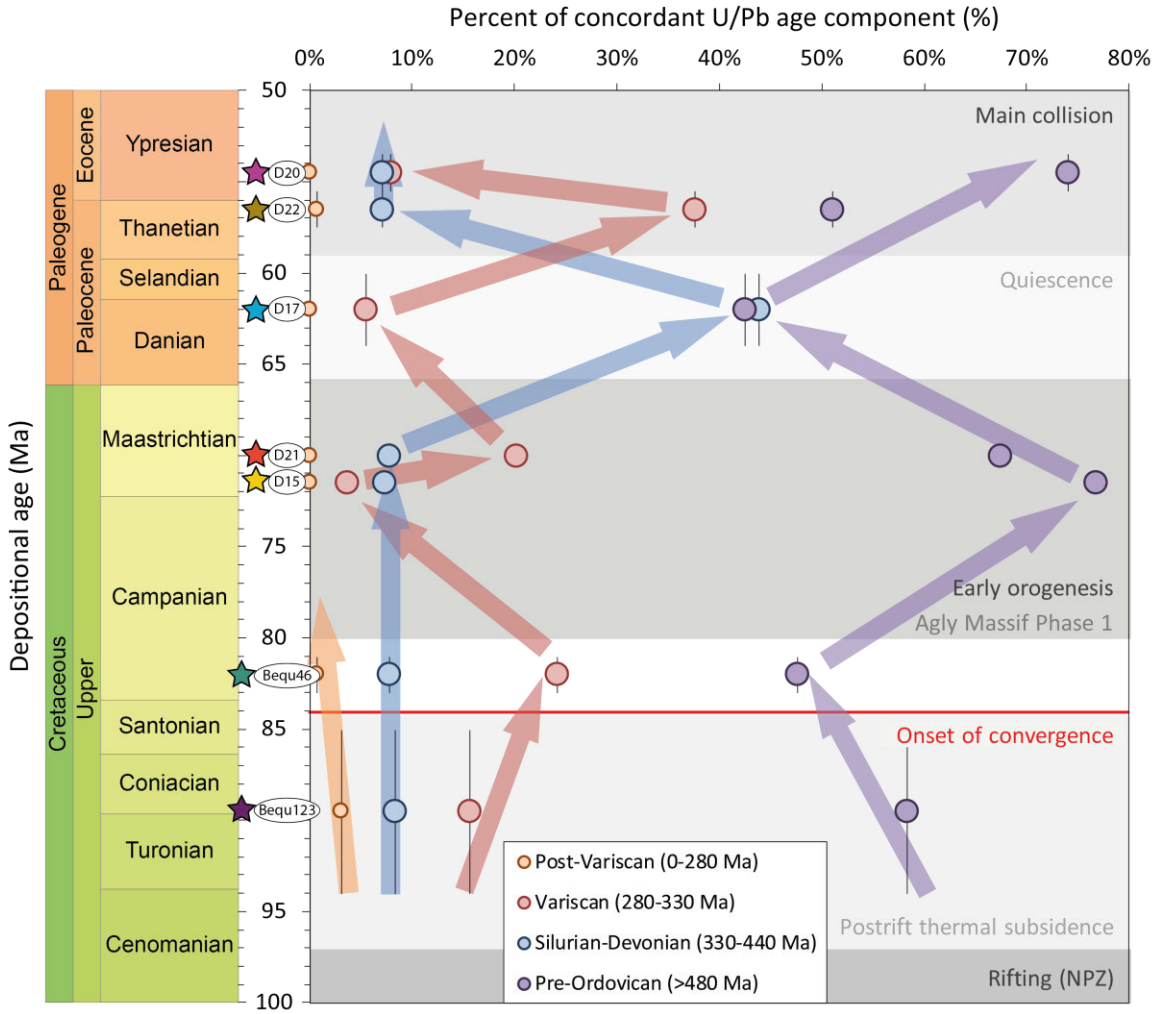

Figure VI.9: Proportions of the main detrital zircon concordant U/Pb components. Depositional age versus component percentages. Main trends are indicated by arrows.

The pre-convergence sample Bequ123, the basal lower Campanian sample Bequ46, the middle Maastrichtian sample D21, and the upper Thanetian sample D22 are all dominated by component peaks of ~300 Ma, with an additional major peak at ~450-480 Ma for the first three samples. Our results show that age distributions of samples Bequ123 and Bequ46, and samples D21 and D22 are very similar (Figure VI.8). Nevertheless, the proportion of the Variscan component is always higher in the stratigraphically younger sample (Figure VI.9). Conversely, the total proportion of the Cadomian and pre-Cadomian (i.e. pre-Ordovician) components is lower in the younger sample. A similar observation can be made between the two stratigraphically adjacent

samples D15 and D21, although their age distributions are different. The lower Maastrichtian sample D15 exhibits two major components of similar proportions at ~450-480 Ma, and ~540-580 Ma, with an additional peak at ~640-650 Ma. A Variscan signal is evident, but in a much lower proportion than the other components. The Ypresian sample D20 exhibits a broad spectrum of U/Pb ages, with ages spanning the range ~300 Ma to ~700 Ma.

Overall, upsection trends observed in all U/Pb data of Rennes-les-Bains/Saint-Louis reveal a compensatory relationship between Cadomian/pre-Cadomian and Variscan components: grains crystallized during the Variscan orogeny increase between two stratigraphically adjacent samples when Cadomian/pre-Cadomian grains decrease (Figure VI.9). The lower Paleocene sample D17 is the only sample that does not follow this trend, setting itself apart from the other samples by yielding the only zircon grains with concordant U/Pb ages spanning the range ~330 Ma to ~450 Ma (Silurian-Devonian signal; Figure VI.8 and Figure VI.9).

VI.5 Reconstruction of the thermo-tectonic evolution of the eastern Pyrenees from the detrital record

Whatever the samples, no cooling ages younger than the time of their deposition are observed. This clearly indicates that no sample experienced post-depositional thermal resetting, which allows us to confidently interpret our zircon (U-Th)/He data in terms of the thermal history of the source area(s). Moreover, no concordant U/Pb ages younger than 220 Ma were recorded, indicating that any (U-Th)/He ages younger than 220 Ma can be interpreted in terms of tectono-thermal events, such as periods of cooling through orogenic crustal thickening (e.g. Ternois et al., 2019) or normal fault- or erosion-induced exhumation (e.g. Reiners and Brandon, 2006).

In studies interested in unravelling the thermal history of rocks from bedrock exposures using (U-Th)/He thermochronometers such as zircon and apatite, it has been shown that data sets show a high degree of age variability due to significant intrasample variation, which is larger than would be expected given the analytical precision (e.g. Guenthner et al., 2014, 2015, 2017; Vacherat et al., 2014, 2016; Ternois et al., 2019). In Chapter 5, we used this age variability, resulting from the inability of a single set of kinematic parameters for He diffusion to describe the natural thermochronometric behavior of zircon (Reiners et al., 2002, 2004; Cherniak et al., 2009; Guenthner et al., 2013; Ketcham et al., 2013) and apatite (Shuster et al., 2006; Flowers et al., 2007; Gautheron et al., 2009), to investigate the thermal history of the Agly-Salvezines crustal block in a larger and less discretized temperature range (45-250 °C) than previously attempted with zircon and apatite fission-track methods. We found that AHe and ZHe ages display correlations between age and eU concentrations (eU [ppm] = U [ppm] + 0.235*Th [ppm]), which allowed us to propose a thermal and structural scenario accounting for closure temperature predictions of available radiation damage-He diffusivity models for apatite and zircon (Flowers et al., 2009; Guenthner et al., 2013). However, we highlighted that it is quite difficult to identify a single thermal history using

ages plotted against eU concentrations, suggesting that damage-dependent models of diffusion are able to reproduce only qualitatively, not quantitatively, the range of single-grain ages and age-eU correlations. This prevents us from attributing an accurate, specific closure temperature to a single grain, and in case of detrital studies, subsequently splitting any detrital data set into distinct grain populations based on eU concentrations of grains. Bearing this in mind, the following paragraphs will therefore be mainly focused on considering the multi-thermochronometric behaviour of the zircon (U-Th)/He system as evidenced in the Agly-Salvezines block by checking that a specific age distribution is not supported by grains with eU concentrations falling within a specific concentration range.

Zircon (U-Th)/He data for the four samples yielding a Late Cretaceous cooling age peak as the youngest cooling component in samples' age distributions (D21, D17, D22 and D20) are plotted against eU concentration in Figure VI.10. This shows that grains with the highest eU concentrations (>1,000 ppm) yielded exclusively young ages that mostly belong to the Late Cretaceous cooling age peak. This result is consistent with the fact that grains with higher eU concentrations are expected to have higher degree of radiation damage in absence of annealing, and so doing, have lower closure temperatures (very low helium retentivity; Shuster et al., 2006; Flowers et al., 2007; Guenthner et al., 2013), making them able to record only the late phases of a cooling event when temperatures are low enough for their specific (U-Th)/He clock to start (temperatures typical of the upper portions of the cooling path of a sample, <140 °C; e.g. Ternois et al., 2019). This observation, taken alone, may bring into question the significance of the youngest, Late Cretaceous cooling component that postdates by only 20 myrs the end of Aptian-Cenomanian rifting. However, Figure VI.10 also shows that grains with eU concentrations inferred to be typical of closure temperatures of 160-220 °C (100-800 ppm; Guenthner et al., 2013; Ternois et al., 2019) yielded ages that are non-specific and may belong to any statistical component of the age distributions, especially the Late Cretaceous peak age. This result therefore indicates that the Late Cretaceous cooling age peak is not restricted to grains with high eU concentrations only and can be interpreted as a major cooling event. Being unable to split detrital data sets on the basis of eU concentration as would usually be done in bedrock studies is therefore not an obstacle to investigating early orogenesis in the Pyrenees. The remainder of this discussion section will be mainly focused on interpreting the whole (U-Th)/He data set presented in this study, taking advantage of the multi-thermochronometric behaviour of the zircon (U-Th)/He system, as evidenced in the Agly-Salvezines block (Ternois et al., 2019).

Our detrital zircon (U-Th)/He results present strong age-eU similarities with published data from the Agly-Salvezines massif over the time interval 130-0 Ma as presented in Chapter 5 (Figure VI.10 and Figure VI.11; Ternois et al., 2019): (i) the young ZHe ages (80-60 ± 5 Ma) plot at opposite ends of the eU concentration spectrum, (ii) the grains yielding ZHe ages between 100 and 120 Ma have eU of 100-600 ppm, and interestingly (iii) some Variscan- zircon grains with relatively high (>800 ppm) eU

concentrations have ZHe ages between 84 and 95 Ma. Following the reasoning presented in Chapter 5, we argue that the young ZHe ages in our detrital data set at relatively low (<600 ppm) and high (>1,000 ppm) eU concentrations correspond to zircon grains with He closure temperatures of 160 and <140 °C, respectively, which record a rapid cooling event during early convergence.

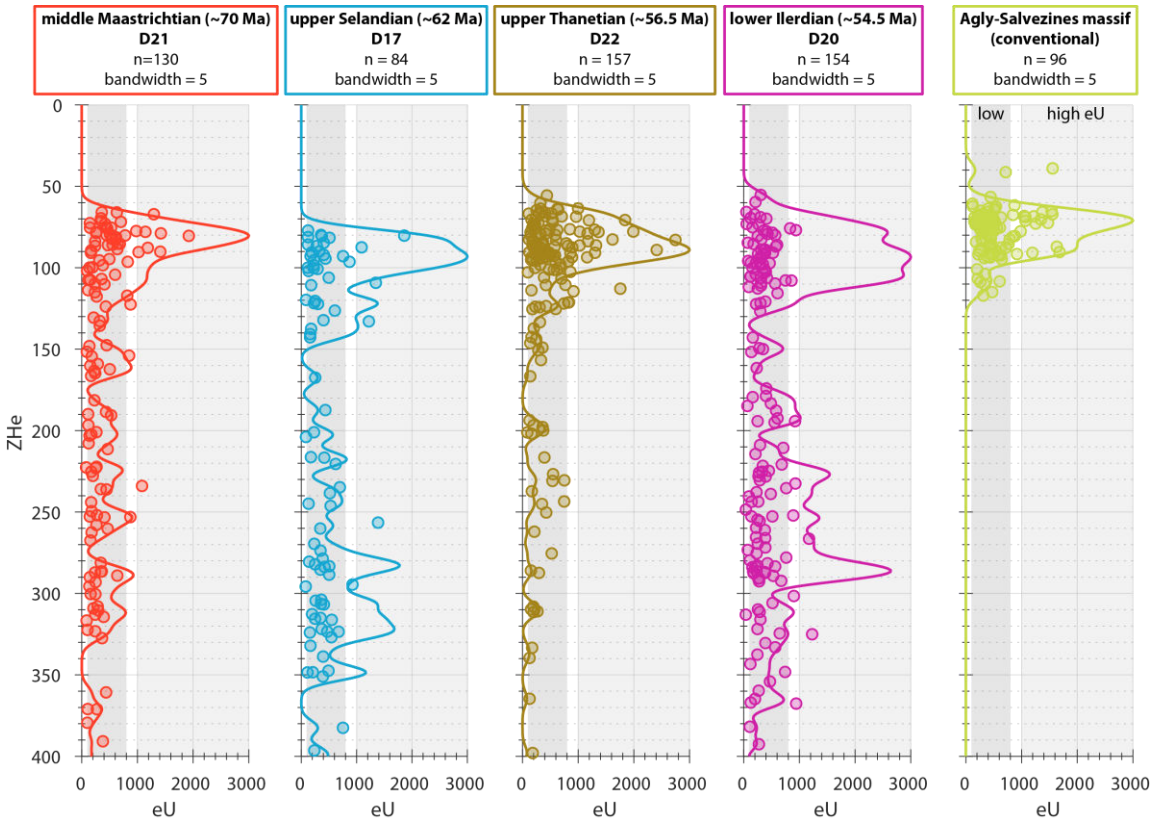

Figure VI.10: Zircon (U-Th)/He age versus eU concentration plots for four syn-orogenic samples analysed in this study and the Agly-Salvezines crustal block (Chapter 5).

In addition, Ternois et al. (2019) show that, assuming their middle Cretaceous ZHe ages are true cooling ages (no partial reset), they can only be related to Aptian-Cenomanian rifting and/or postrift cooling. Odlum and Stockli (2019) provide medium temperature thermochronology data (apatite U/Pb ages) that overlap with these zircon (U-Th)/He ages, thus supporting this model. This shows that the ZHe system can record two shortly spaced (<20 Ma) cooling events, namely Aptian-Cenomanian rifting and Late Cretaceous early orogenesis. We therefore propose that any Early Cretaceous ZHe component exhibited by our detrital samples can be interpreted as true cooling related to Aptian-Cenomanian rifting.

Whilst our detrital samples present age peak similarities in concordant U/Pb signatures (~300 Ma, ~440-450 Ma, ~530-540 Ma and ~600-660 Ma), overall upsection trends of our concordant U/Pb results show fluctuations in the proportions of U/Pb components between stratigraphically adjacent samples over the Turonian-Santonian to Ypresian stratigraphic interval (Figure VI.9). The Variscan component varies by 10-30%, and is similar to that observed by Thomson et al. (2017) for the Ainsa Basin in the south-central Pyrenees. As most of our samples yielded more than 70 concordant U/Pb ages

and the proportion of the Variscan component exceeds 5%, we argue that these fluctuations are not artefacts. Increases in the proportion of the Variscan component are recorded in samples with lower proportions of pre-Ordovician ages. Conversely, decreases in the proportion of the Variscan signal are recorded where pre-Ordovician components are predominant. These fluctuations may be attributed to (1) episodes of progressive unroofing of Variscan plutons due to erosion of overlying Paleozoic-Mesozoic strata (in possibly 3 different source areas) and/or (2) changes in source region from a predominantly granitic source to a predominantly sedimentary source (6 source switches, so possibly 6 different source areas).

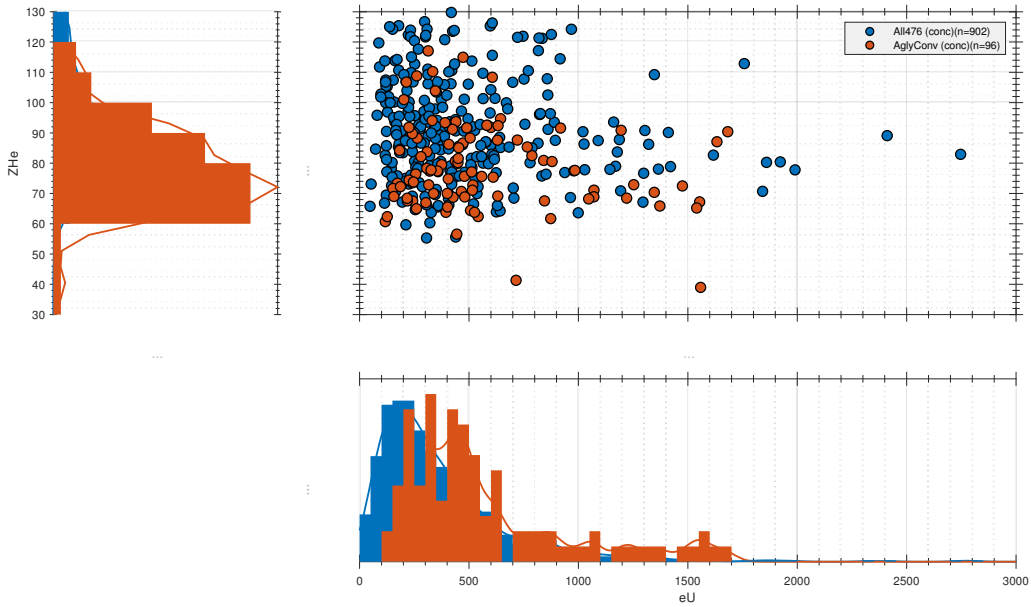

Figure VI.11: Zircon (U-Th)/He age versus eU concentration plots for all samples analysed in this study (blue) and the Agly-Salvezines crustal block (red, Chapter 5). This better allow seeing the strong age-eU similarities with published data from the Agly-Salvezines massif (Ternois et al., 2019) over the time interval 130-0 Ma.

In the first scenario, Mesozoic and Paleozoic cover rocks are eroded before deeper structural levels such as Variscan plutons, and eventually Ordovician and Cadomian metamorphic rocks intruded by Variscan plutons beneath (e.g. Agly Massif; Olivier et al., 2004, 2008). Any grains that would have experienced Carboniferous HT-LP metamorphism would show pre-Variscan inherited cores and Upper Carboniferous metamorphic overgrowths (e.g. Odlum and Stockli, 2017, 2019; Tournaire Guille et al., 2018). Consequently, grain cores would yield exclusively pre-Variscan concordant or discordant U/Pb ages, the latter type of U/Pb data being not considered here. Upsection detrital concordant U/Pb distributions would thus exhibit dominant pre-Variscan components (pre-Cadomian, Cadomian, Ordovician and Silurian-Devonian grains in cover rocks), replaced by a Variscan-dominated signature (Variscan plutons), and ultimately show the return of dominant Ordovician-Cadomian peaks (deep crustal levels). Further complexity for this scenario can be mentioned if one assumes that some Variscan plutons were already outcropping before the Late Cretaceous. Early Mesozoic rocks could thus contain not only multicycle zircons with pre-Cadomian, Cadomian,

Ordovician and Silurian-Devonian U/Pb age signatures, but also Variscan signatures, making it difficult to differentiate the latter from erosion of Variscan plutons only. In the second scenario, resulting age distributions would be quite similar but less cyclical, requiring much more differential vertical movements and/or rapid change in drainage pattern.

While these two options are not mutually exclusive, they would lead to differences in drainage evolution that have major implications for sediment routing systems evolution during the initiation of Pyrenean topography, for models of orogenic growth in the Pyrenees and for paleogeographic reconstructions in the Northwestern Mediterranean region. Based on the compilation of published U/Pb age data from present-day outcropping rocks in the Pyrenees, the Mouthoumet Massif, the Montagne Noire, the Massif Central, Corsica and Sardinia (Figure VI.3), it clearly appears that U/Pb data alone cannot differentiate between the two scenarios, or a combination of these two in the Pyrenean region. While Whitchurch et al. (2011), based on the absence of Cadomian magmatic rocks in the central Axial Zone but the presence of Cadomian orthogneiss bodies in the exposed basement of the eastern Axial Zone, suggest that sediment supply was from an eastern Pyrenean source during the Late Cretaceous-Paleocene, recent detrital studies have revealed the potential of Mesozoic sedimentary and Paleozoic metasedimentary units at different locations along strike of the range to provide similar zircon U/Pb age signatures to that observed in the eastern Pyrenean crystalline basement (e.g. Margalef et al., 2016; Hart et al., 2016). Likewise, Filleaudeau et al. (2012) propose the coeval exhumation of the central and eastern Pyrenees during the Campanian based on (i) limited detrital single-grain zircon (U-Th)/He and U/Pb double dating data (Variscan U/Pb signature, early Campanian cooling), (ii) the presence of basement clasts, and (iii) the very different U/Pb age signatures (Cadomian-dominated and Variscan-dominated) of two stratigraphically adjacent sandstone samples (Maastrichtian and lower Paleocene, respectively). However, Whitchurch et al. (2011) admit, "Because Hercynian age plutons are distributed throughout the Axial Zone it is difficult to speculate further on a precise source". The most recent detrital studies in the southern Pyrenean foreland (Thomson et al., 2017; Odlum and Stockli, in revision; Thomson et al., in review) actually show contributions from the southeastern Variscan sources of the Ebro Massif, Iberian Range, and Catalan Coastal Ranges during the earliest stages of orogenesis recorded in the Pyrenees (Ternois et al., 2019).

These studies use a similar approach to Filleaudeau et al., (2012), albeit conducted in a more extensive way. The (U-Th)/(He-Pb) double dating approach has been shown to overcome limitations of (U-Th)/He analysis alone if one considers the two previously mentioned scenarios. In the scenario of progressive unroofing of Variscan plutons and associated removal of overlying strata, one might expect a shift in the (U-Th)/He signatures from inherited, post-Variscan ages typical of the Paleozoic and Mesozoic cover rocks to Early Cretaceous ages yielded by rocks affected by Aptian-Cenomanian rifting. Ultimately Late Cretaceous ages would become dominant if even deeper rifted crustal levels are eroded during early orogenesis. In the scenario of change in source

region, a provenance shift from non-Pyrenean sources with inherited cooling ages to exhuming Pyrenean source regions with Cretaceous rifting and early orogenesis cooling ages would lead to similar detrital (U-Th)/He spectra, although this would depend on the rate and frequency of changes in sourcing. To reduce provenance ambiguities and discriminate between these two, possibly three, options we will therefore base our argumentation and interpretations in the remainder of this discussion section on combined U/Pb and (U-Th)/He results for each sample or composite sample.

VI.5.1 Turonian-middle Maastrichtian convergence onset and early phase

The overall upsection decrease in lag times from ~65 myrs to ~10 myrs in the Turonian to middle Maastrichtian succession and the gradual increase in the proportions of Early Cretaceous rifting and early orogenesis cooling signals suggest a rapid acceleration in denudation rates and progressive, first-order unroofing of thermally reset rifted Pyrenean crust in the early orogenic edifice to the east. In south central Pyrenean depocentes, Whitchurch et al. (2011) report ZFT lag times decreasing from ~60 myrs to ~15 myrs between the late Campanian (*ca.* 73 Ma) and late Paleocene (*ca.* 57 Ma). These data are similarly interpreted to record accelerating exhumation during early orogenesis. However, the timing of this decrease in ZFT lag times is later than that detected in our ZHe results, which is consistent with the time needed to erode through the deeper ZFT partial annealing zone. Our results also agree with short ZHe lag times (8 myrs) recorded by upper Campanian-lower Maastrichtian (*ca.* 72 Ma) sandstones in the easternmost basin of the South Pyrenean Zone, (Ripoll basin; Odlum and Stockli, in revision). Finally, they agree with an overall Campanian-Maastrichtian early orogenic cooling recorded by bedrock ZHe in the eastern Pyrenean retro-wedge (Agly-Salvezines crustal block; Ternois et al., 2019).

The two composite samples Bequ123 and Bequ46 have strong similarities in their (U-Th)/He and U/Pb age distributions. These similarities include (1) post-Variscan ZHe ages ranging from ~150 Ma to ~350 Ma, (2) very few Early Cretaceous cooling ages, (3) a Variscan-dominated signature with an additional major Ordovidician component, and (4) a minor population of Permian-Triassic concordant U/Pb ages. Slight differences in U/Pb components are, from Turonian-Santonian (Bequ123) to early Campanian (Bequ46), (1) a slight increase in the proportions of the Variscan and Ordovician U/Pb components, (2) a decrease in the pre-Ordovician component and (3) a decrease in the number of post-Variscan (Permian-Triassic) grains (Figure VI.9). Slight differences in ZHe components are (1) an increase in the number of Early Cretaceous grains, (2) a decrease in the post-Variscan component and (3) a dominant older post-Variscan component (~290 Ma compared to around 230 Ma). Combining both dating information (Figure VI.12), it appears that (1) Ordovician grains in the older sample (Bequ123) have Permo-Triassic (U-Th)/He cooling ages but can have Variscan to post-Variscan cooling ages in the younger sample (Bequ46), and (2) there is an increased contribution from Variscan rocks cooled during the Permian-Triassic in the younger sample. While either scenario proposed earlier in this section could explain the latter, the former does not support the scenario of unroofing. Together, these results might thus favour the scenario

of a change in sourcing. However, more grains were dated for the basal lower Campanian composite sample (128 compared to 96), suggesting that the slight differences observed between the two composite samples could be simply due to sample size and sampling bias. Moreover, these differences seem very minor compared to the strong similarities of the samples. All in all, our data indicate that Variscan plutons were at the surface and eroding in an eastern source area from the Turonian-Santonian to Campanian. Any changes in sourcing were therefore minor at the onset of convergence. This result is consistent with the presence of a small volume of granite pebbles in the upper Santonian Labastide Sandstone Formation (Bilotte, 1985; Bessière et al., 1989) for which no provenance explanation has been given yet. As no granitic rocks outcrop in the near Paleozoic Mouthoumet Massif (Berger et al., 1997), a major Variscan source area must be found to the E or ENE of the Mouthoumet Massif according to all published stratigraphically-based paleogeographic reconstructions (Combes et al., 1975; Plaziat, 1981; Freytet and Plaziat, 1982; Vacherat et al., 2017). This further suggests that published paleocurrent data in Rennes-les-Bains (Bilotte, 1985; Bessière et al., 1989) preferentially document the rather minor and local nature of the sediment supply from the Mouthoumet Massif to the NNE.

The only two land areas located E-ENE of the Mouthoumet Massif at present day are Corsica and Sardinia. Although published U/Pb age data from these two regions only characterize present-day outcropping rocks (Figure VI.3), they may help investigate provenance for Turonian-Santonian to Campanian sediments. Also, although the only existing low-temperature data for these two regions are ZFT, AFT and AHe ages (e.g. Danišík et al., 2007, 2012; Malusa et al., 2016; Figure VI.13), first-order correlations with our detrital ZHe ages for the pre-convergence and early convergence samples Bequ123 and Bequ46 can be made. On the one hand, compiled U/Pb data show a major, bimodal Variscan/Ordovician average concordant U/Pb signature (components at 295 and 459 Ma with proportions of ~35% and ~39%) in Sardinia and a major bimodal Variscan/Cadomian average signature (components at 331-286 and 557 Ma with proportions of ~53% and ~33%) in Corsica. The Cadomian signal (~555 Ma) is evident in Sardinia but in a much smaller proportion (~10%). A similar observation is made for the Ordovician component (~450 Ma; <10%) in Corsica. Corsica is the only region to exhibit an Upper Jurassic component (~160 Ma). On the other hand, the oldest cooling history for outcropping rocks in Corsica and Sardinia recorded by low-temperature data is a Permian to Jurassic ZFT cooling history in northwestern Corsica and eastern Sardinia. AFT and AHe data indicate that rocks in eastern Sardinia have been at shallow crustal depths since the Jurassic while rocks in northwestern Corsica remained at deeper depths until the late Oligocene-Miocene. Taken together, published U/Pb and low-temperature data better support a provenance from Sardinia from Turonian-Santonian to Campanian. Shorter lag times in the lower Campanian composite sample Bequ46 favours a scenario that involves accelerated removal of material from a pre-existing and already eroding relief (CS source area) consisting of crystalline basement at the onset of convergence. ZHe data from Sardinia would aid in confirming this interpretation.

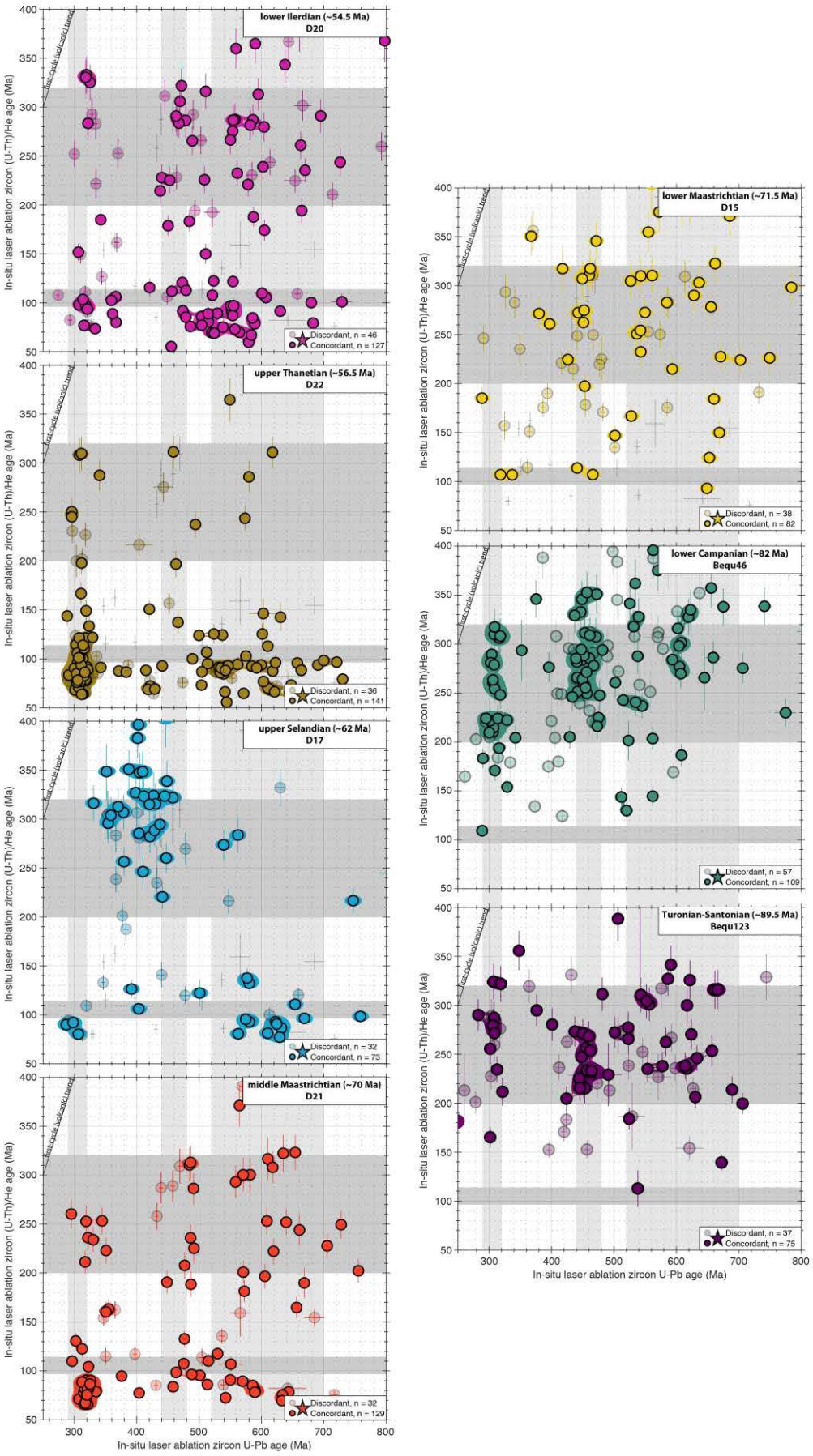

Figure VI.12: Sample zircon ages by the in situ laser (U-Th)/He - U/Pb double dating method.

During the Campanian to middle Maastrichtian, two fluctuations in the proportions of U/Pb components are noted. Firstly, from Campanian (Bequ46) to early Maastrichtian (D15) a strong decrease in the proportion of the Variscan U/Pb component is observed coupled with an increase in the pre-Ordovician components. This implies that the sediment sources of these samples are significantly different, with preferential material derivation from Variscan basement (Paleozoic-Mesozoic cover and Variscan plutons) for the former and from Paleozoic-Mesozoic sediments that were not reset during their pre-Pyrenean burial history for the latter. Along with the increase in the proportion of the Cretaceous rifting cooling signal between the two samples, our data suggest progressive inversion and erosion of the Pyrenean rift during the Campanian. In this region, Variscan plutons remained below a significant thickness of sediments and metasediments, preventing them from being eroded during the Campanian. This scenario of change in source region can explain the slight slowing down of exhumation rates (slower increase in lag times) observed between samples Bequ46 and D15.

The second fluctuation in the proportions of U/Pb components is observed between lower Maastrichtian (D15) and middle Maastrichtian (D21). The Variscan source signal has again increased in sample D21 and the lag times sharply increase between the two stratigraphically adjacent samples. In sample D15, almost all multicycle grains with pre-Variscan U/Pb ages have Variscan to Permian-Triassic cooling ages (Figure VI.12). In sample D21, pre-Variscan grains with Permian-Triassic cooling ages are still present but a large number of these multicle grains yield (U-Th)/He ages between 66 and 84 Ma. The grains with Variscan U/Pb crystallization ages show similar cooling signature. Taken together, these results support a scenario of rapid unroofing of Variscan rocks during the lower Maastrichtian. Through exhumation and erosional processes non to partially reset inherited zircon grains in Paleozoic-Mesozoic sediments were progressively transferred toward the basin during the Campanian (sample D15) before Variscan plutons reached the erosive surface by middle Maastrichtian (sample D21).

Figure VI.13: (next page) Combined published zircon U/Pb and fission-track data for Corsica (1) and Sardinia (2). 1a: Corsica apatite (U-Th)/He and fission-track data from Danisik et al. (2012). 1b: Corsica zircon fission-track data from Danisik et al. (2007) (modified from Malusa et al., 2016) superimposed with zircon U/Pb pie charts. 1c: Corsica U/Pb age distribution (Vermeesch, 2012) for the 1000 youngest concordant U/Pb ages (0-610 Ma) available from litterature (with GPS coordinates). 2a: Sardinia zircon fission-track data from Malusa et al. (2016) superimposed with zircon U/Pb pie charts 2b: Sardinia U/Pb age distribution (Vermeesch, 2012) for the 1000 youngest concordant U/Pb ages available from litterature (with GPS coordinates). For easier comparison with Corsica, horizontal axis is kept the same (0-610 Ma), so that only the 839 youngest ages are displayed.

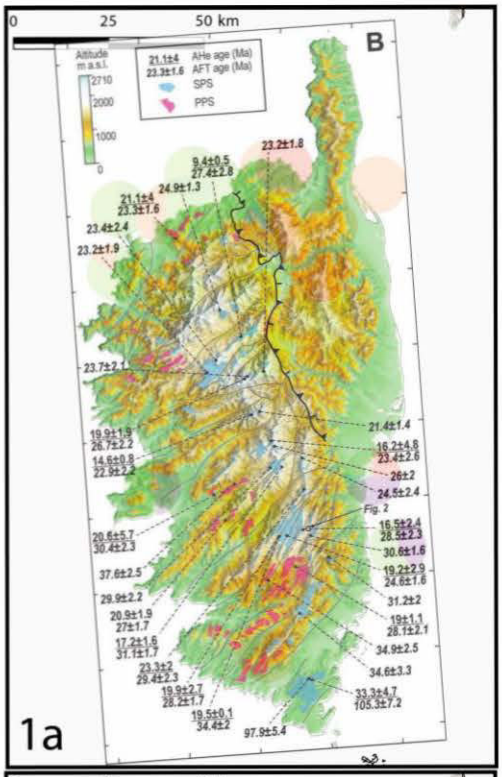
0 25 50 km
B
Altitude m a.s.l.
2710
2000
1000
0
21.1±4 AHe age (Ma)
23.3±1.6 AFT age (Ma)
SPS
PPS
1a

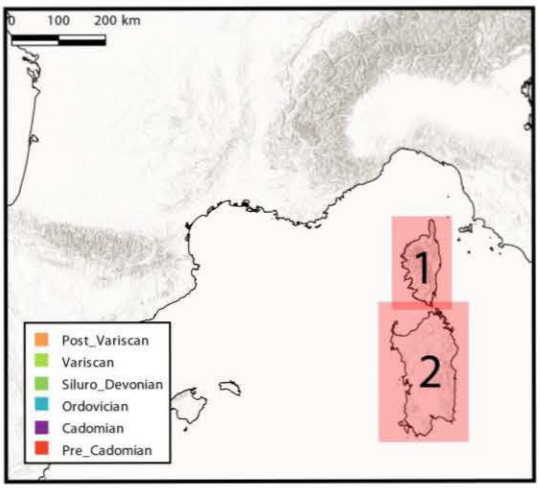
0 100 200 km
1
2
Post_Variscan
Variscan
Siluro_Devonian
Ordovician
Cadomian
Pre_Cadomian

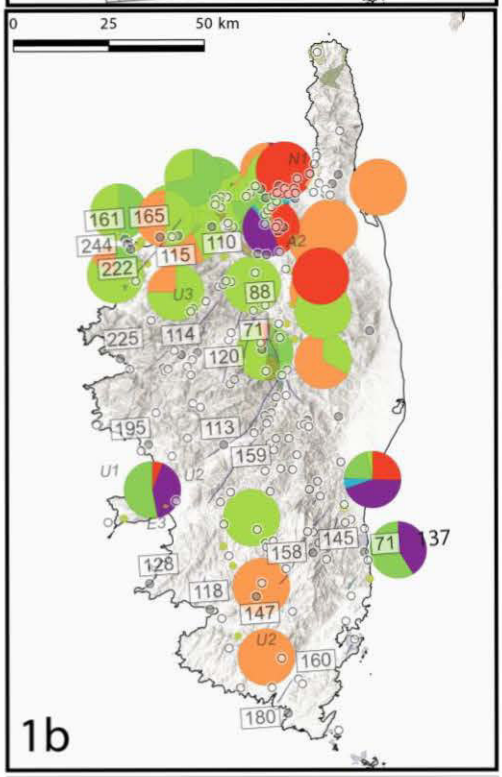
0 25 50 km
1b

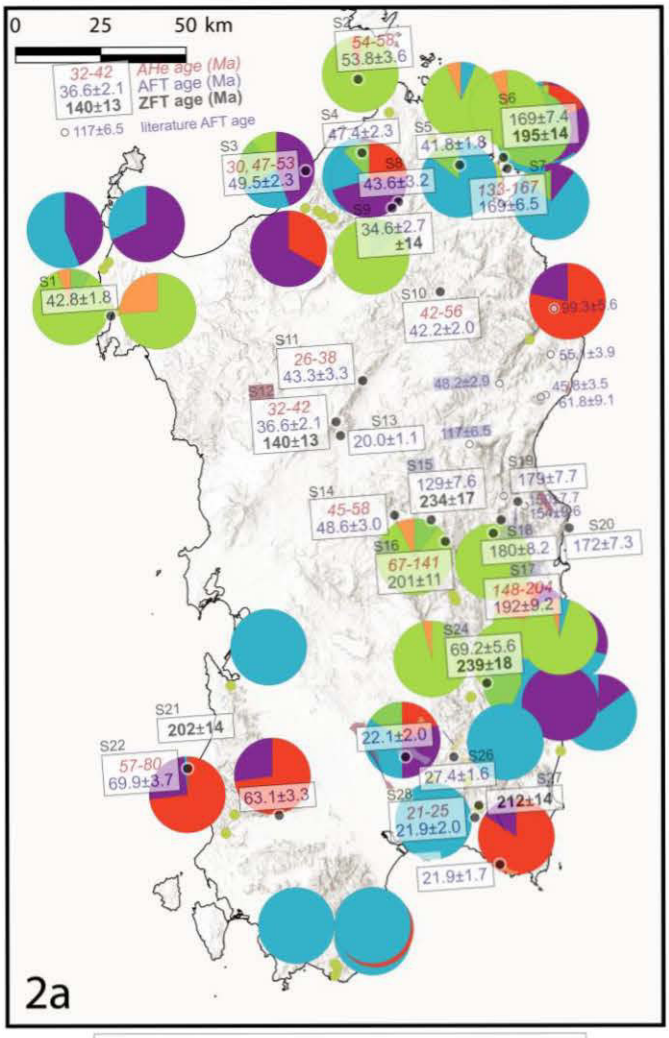
0 25 50 km
32-42
36.6±2.1
140±13
AHe age (Ma)
AFT age (Ma)
ZFT age (Ma)
117±6.5 literature AFT age
2a

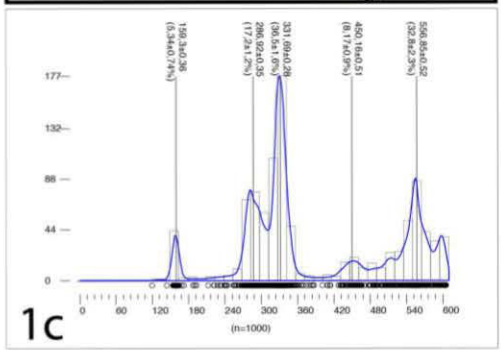
1c
(n=1000)

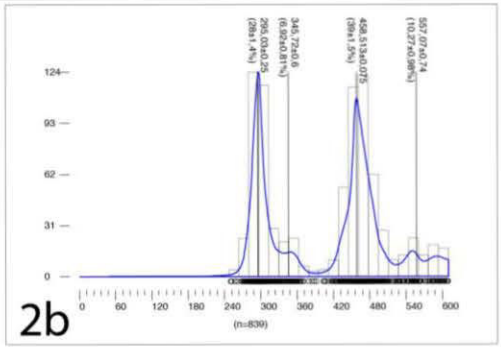
2b
(n=839)

In summary the key features of the Turonian to middle Maastrichtian phase are fluctuations in sample U/Pb signatures and the gradual upsection increase in the proportion of thermally reset detrital grains from Early Cretaceous rifting. We interpret these results as recording the onset of orogenesis and initiation of topographic growth in the Lion Pyrenees. Our data record the westward migration of inversion from a slightly rifted and thermally non-to-partially-reset region of Variscan basement in the east (tip of the rift domain) to more strongly extended and thermally reset regions further west. Rapid erosion through the zircon helium retention zone occurred in the eastern source area (Lion Pyrenees) during the early Maastrichtian (D15 and D21) while rapidly exhuming basement further west (Agly-Salvezines in the Agly Pyrenees) still lay beneath 2-4 km of synrift strata before final exhumation to the surface from Paleocene onwards (Ternois et al., 2019). This scenario is consistent with the younging of cooling histories from east to west and from north to south in the Axial Zone and in the basement massifs in the North Pyrenean Zone (Whitchurch et al., 2011; Mouthereau et al., 2014 and references therein; Vacherat et al., 2016; Ternois et al., 2019). In the westernmost orogen (Mauleon) Tugend et al. (2014) propose that the rift may have been wider than further east (study area). Assuming a constant convergence rate along the orogen, it would have taken shorter to close the narrow rift to the east, leading to creation of topography earlier in the east. A faster convergence rate in the east as documented recently by Macchiavelli et al. (2017) would further promote this trend. A scenario of initiation of Pyrenean topography due to early orogenic inversion of distal rifted margins during the early Maastrichtian is also consistent with the earlier establishment of continental conditions favourable to the development of dinosaur faunas in the northern Pyrenees (early Maastrichtian) compared to the south (late Maastrichtian to Danian; Fondevilla et al., 2016).

During the middle Maastrichtian to Danian, continental conditions were established with the deposition of the polygenic Poudingue Fleuri conglomerate as a small delta building into a lake and the palustrine-lacustrine Vignevieille Limestone Formation. Detailed petrographical study of the conglomerate (Bilotte, 1985; Bessière et al., 1989; Bilotte, 2014) indicates derivation of material from the same, local northeastern quartz-rich regions as during Campanian-Maastrichtian times (Plaziat, 1981; Bilotte, 1985; Monod et al., 2014; Ford et al., 2016) and, in larger proportion, from calcareous regions similar to the Lower Cretaceous terranes in the North Pyrenean Zone. These calcareous regions were located to the ESE, close enough for the limestone clasts they deliver to the early retroforeland basin to be preserved. No Paleozoic rocks originating from the North Pyrenean basement massifs have been observed in this formation, suggesting absence of these rocks at the surface. This provenance constraint supports our scenario of westward migration of inversion from a slightly rifted region (likely thin to absent Aptian-Cenomanian deposits overlying Paleozoic metasedimentary, Permian-Triassic sedimentary and Jurassic carbonate rocks; Lion Pyrenees) to more strongly extended regions further west (thicker, metamorphic Lower Cretaceous strata covering Paleozoic to Jurassic rocks; Agly Pyrenees). In their crustal-scale sequentially restored model for the tectonic and thermal transition from extension

to peak orogenesis in the Agly Pyrenees, Ternois et al. (2019) show that Campanian-Maastrichtian exhumation of the Agly-Salvezines crustal block (peaking early on orogenesis), southeast of the Rennes-les-Bains/Couiza area, most likely caused syn- to post-rift sediments within the North Pyrenean Zone to be eroded by late Maastrichtian times.

VI.5.2 Early Paleocene tectonic quiescence

Low tectonic subsidence, no basin migration, and very low sediment supply prevailed during the whole period of tectonic quiescence during the Danian and Selandian (Ford et al., 2016). The lower Paleocene (D17) records a lag-time of *ca.* 20 myrs, which is twice that recorded in the middle Maastrichtian (D21). Synchronous but even more significant slowing is observed in the southern Ripoll Basin (Odlum and Stockli, in revision; 8 to 43 myrs). Whitchurch et al. (2011) show a similar but delayed increase in ZFT lag times (early Ypresian) in the southern Pyrenees (15 to 50-70 myrs). The implied decrease in exhumation rate would result in lower clastic supply during the early Paleocene, which is supported by facies and thicknesses of the fluvio-lacustrine to palustrine Vignevieille and Vitrollian formations in the Rennes-les-Bains/Couiza area (Bessière et al., 1989; Marty and Meyer, 2006).

D17 (*ca.* 62 Ma) grains show a very distinctive U/Pb signature with a broad, dominant multimodal age spectrum between 300-320 Ma (Lower Carboniferous) and 440-460 Ma (Silurian) while recording ZHe post-Variscan cooling (Figure VI.12). This source signal is unique in our dataset and corresponds to an as-yet unknown source area to the east. To date, only an upper Paleocene-lower Eocene sample (*ca.* 56 Ma) from the Ripoll Basin has yielded a similar U/Pb signature (Odlum and Stockli, in revision). We interpret this as a true change in the main sediment source area, consistent with an observed change in paleo-current directions (from NE-SW to ESE-WNW) sometime between the middle-to-late Maastrichtian and late Selandian (Bilotte, 1985; Bilotte et al., 1999). Whilst the proportion of early orogenesis cooling signal is lower in D17, this sample yields zircon grains with clear double dating similarities to grains in D21 (Figure VI.12). Our results therefore indicate that sediment contribution from terranes eroded during early orogenesis (the emerging eastern Pyrenean edifice during the early Maastrichtian; Lion Pyrenees), albeit minor, probably continued during the early Paleocene. A marked decrease in the proportions of pre-Silurian zircons cooled during Variscan and Permian-Triassic times compared to sample D21 supports this interpretation, suggesting continued removal of Paleozoic to Mesozoic sediments and progressive exhumation of thermally reset rifted crustal levels by the end of the early Paleocene. We propose a change in sourcing during this period of slow deposition and tectonic quiescence. We argue that the dominant, new source was probably local, and supplied the early southern Pyrenean foreland basin with some delay (this study; Odlum and Stockli, in revision). This is consistent with migration of Pyrenean shortening and topographic growth into the south vergent pro-wedge during the Paleocene in eastern and central Pyrenees (Mouthereau et al., 2014; Grool et al., 2018; Ternois et al., 2019).

VI.5.3 Late Paleocene-early Eocene onset of main collision

The upper Thanetian sample D22 records a short lag time of *ca.* 12 myrs. This suggests that rapid exhumation rates resumed by end Paleocene. The proportions of the Cretaceous rifting and early orogenesis signals reach their maximum values in this sample while the low yield in non-reset pre-Silurian zircons observed in sample D17 is still present. Taken together, these results suggest that when shortening resumed in Thanetian times (Ford et al., 2016; Grool et al., 2018; Ternois et al., 2019), local sourcing from the as-yet unknown source area to the east stopped and erosion was exclusively concentrated again in the source region that supplied the early retroforeland basin with sediments before the quiescent phase (Lion Pyrenees). Variscan plutons that started exhuming during the early Maastrichtian clearly reached the erosive surface by early Ypresian times. Nevertheless, the rather large spacing between the lower Paleocene sample D17 (*ca.* 62 Ma) and the upper Thanetian sample D22 (*ca.* 56.5 Ma) does not allow constraining the exact timing of convergence resumption in the eastern orogen. Investigating whether shortening resumed earlier in the eastern orogen than generally accepted in the Pyrenean forelands (*ca.* 59 Ma; Ford et al., 2016; Grool et al., 2018) should provide important constraints for paleogeographic and plate kinematic reconstructions.

In contrast with the middle Maastrichtian to late Paleocene stratigraphic interval, a marked increase in the proportions of non-reset pre-Silurian zircons is observed in the lower Ypresian sample D20. Conversely, the proportions of Cretaceous rifting and early orogenesis signals sharply decrease during the early Ypresian. These results indicate an abrupt change in source areas with renewed erosion of Paleozoic to Mesozoic sediments. Based on spatial trends in bedrock cooling ages over the North Pyrenean Zone and the Axial Zone (Whitchurch et al., 2011; Mouthereau et al., 2014, and references therein; Vacherat et al., 2016; Ternois et al., 2019), we interpret our results as recording the continued westward migration of Pyrenean shortening and topographic growth during the early Eocene. This interpretation is consistent with previous detrital studies in the southern Pyrenees (Beamud et al., 2011; Rahl et al., 2011; Whitchurch et al., 2011; Filleaudeau et al., 2012; Fillon et al., 2013; Michael, 2013; Clark et al., 2017; Thomson et al., 2017; Thomson et al., in review; Odlum and Stockli, in revision) which interpret their Eocene-Oligocene cooling ages for all the low-temperature thermochronology systems (ZFT, ZHe, AFT and AHe) as evidence for rapid uplift of the central Pyrenees and transition from orogen-parallel to orogen-transverse sediment routing systems from the Eocene onward.

VI.5.4 Implications for the Northwestern Mediterranean paleogeography

We here combine our detrital geo-thermochronology results with geological data and paleogeographic reconstructions from literature to propose a model for the evolution of the eastern Pyrenean orogen and in particular the Northwestern Mediterranean region from postrif (Turonian-Santonian) to main collision (Eocene) (Figure VI.14).

The new constraints on the provenance of sediments in the early retroforeland basin (Rennes-les-Bains) coupled with the stratigraphic evolution of this basin highlight the existence of a major source area to the E or ENE of the Mouthoumet Massif before the onset of convergence in late Santonian times (Turonian-Santonian). This source area (CS) was essentially composed of Variscan plutons close to or at the surface and would look like present-day Sardinia, where U/Pb and low-temperature thermochronology signatures are very similar to our detrital age distributions for Turonian-Santonian sediments in the early retroforeland basin.

When N-S convergence between the Iberian and European plates initiates in late Santonian-early Campanian times (Choukroune, 1989; Muñoz, 1992; Macchiavelli et al., 2017), sediment supply from the CS Variscan-dominated source area in the east continued but accelerated. Sediment routing systems are orogen-parallel from the east. Cooling was not recorded yet in the eastern Agly Pyrenean retro-wedge (Ternois et al., 2019), most likely due to the time needed to close a wider exhumed mantle domain before inversion (Clerc and Lagabrielle, 2014; Tugend et al., 2014; Clerc et al., 2016), and/or slower convergence rates (Macchiavelli et al., 2017).

During early convergence (Campanian-middle Maastrichtian), distal rifted margins were progressively inverted, leading to initiation of topographic growth in the Lion Pyrenees and distributed gentle inversion of rifted structures (thick-skinned convergence) in the eastern Pyrenees (Ford et al., 2016; Grool et al., 2018; Ternois et al., 2019). Sediment routing systems are still orogen-parallel from the east. The early Pyrenean edifice and the Aptian-Cenomanian rift extended further east. Continental conditions established in the Pyrenean retro-wedge (early Maastrichtian) before the pro-wedge (late Maastrichtian-Danian; Fondevilla et al., 2016) where sediment supplies are mainly from the Catalan Coastal Ranges and/or the Ebro Massif to the southeast (Thomson et al., 2017; Odlum and Stockli, in revision; Thomson et al., in review).

During the late Maastrichtian to early Paleocene convergence slowed down, leading to low tectonic subsidence, no basin migration, and very low sediment supply in the retroforeland (Ford et al., 2016). Exhumation of the Agly Pyrenean retro-wedge stopped (Ternois et al., 2019) and sediment supply became local (minimal Variscan yield, reworked Mesozoic material typical of the North Pyrenean Zone, as-yet unknown Silurian-Devonian source area). Pyrenean shortening and topographic growth migrated into the south vergent pro-wedge in eastern and central Pyrenees (Mouthereau et al., 2014; Grool et al., 2018; Ternois et al., 2019). Shortening rates in the Iberian plate were, however, slow (Grool et al., 2018).

By late Thanetian times shortening resumed, leading to renewed exhumation of deeply seated Variscan rocks in areas exhuming during early orogenesis (Lion Pyrenees) and minor to no local sourcing. Variscan plutons clearly reached the erosive surface by early Ypresian times. Sediment routing systems are still orogen-parallel from the east.

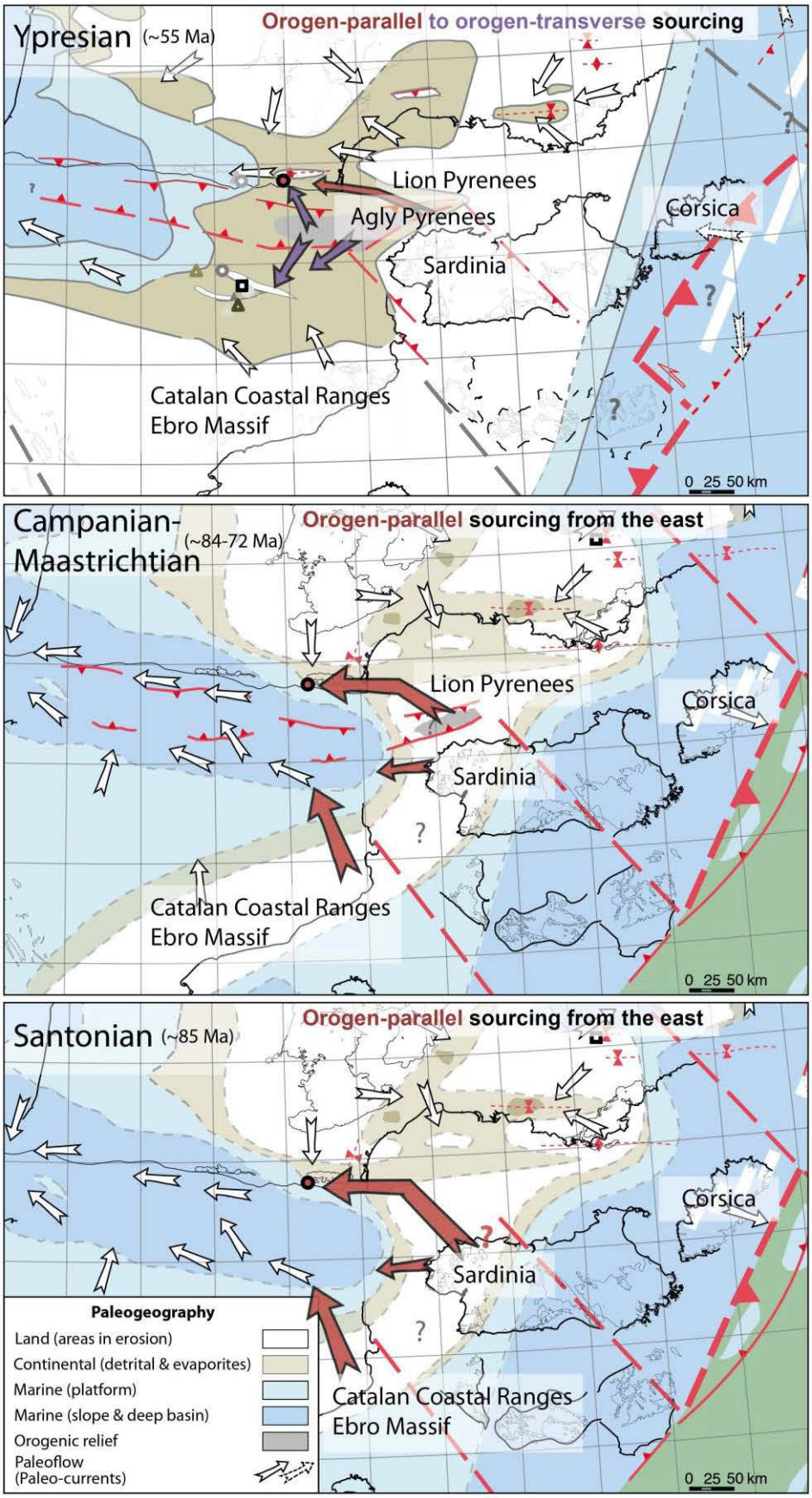

Figure VI.14: Paleogeographic reconstruction of the Northwestern Mediterranean region based on the thermo-tectonic evolution of the eastern Pyrenees from the detrital record. Grids indicate direction of the North. Adapted from Frasca et al. (in prep).

During the early Ypresian, a drastic change in source region occurred due to continued westward migration of Pyrenean convergence and topographic growth. Both the early retro- and pro-forelands record this abrupt change (this study; Odlum and Stockli, in revision). In the southern Pyrenees this change is characterized by the first appearance of Eocene ZHe cooling ages and by near-zero ZHe lag times in the early proforeland (change from dominantly Variscan SSE source region to Pyrenean, multimodal age distributions NNE source region at *ca.* 52 Ma), marking orogen-transverse sediment routing systems. In the early retroforeland of the northern Pyrenees the transition from orogen-parallel to orogen-transverse sediment routing systems is indicated by continued denudation of rocks cooled during early orogenesis and erosion of a new portion of Paleozoic-Mesozoic sedimentary cover (*ca.* 54 Ma). Nevertheless, we lack resolution between 54 and 52 Ma to pinpoint the exact timing of onset of orogen-transverse sediment routing systems in the north and south.

We present the first *in situ* single-grain detrital zircon (U-Th)/He and U/Pb double dating data set for the early Pyrenean orogen (1081 detrital zircon U/Pb ages and 902 detrital zircon (U-Th)/He ages) from the eastern Aquitaine foreland basin that provides new insight into topographic growth in a collision orogen. By applying an *in situ* approach for provenance analysis, we reduce ambiguities of source tracers used independently or based on a limited number of samples or grains dated with both geochronometric and low-temperature thermochronometric methods.

In this study, we provide the largest detrital ZHe data set for the Pyrenean system (902 ages). These data complete the detrital record of foreland dynamics and sediment routing during initiation and early growth of Pyrenean topography (Figure VI.15) by showing dominance of eastern sources like the Lion Pyrenees and Sardinia at the transition from rifting to early orogenesis. Inherited drainage patterns established before convergence continued for at most ~10 myrs after the onset of convergence (Sardinia). During early convergence (Campanian to Maastrichtian), an increase in denudation rates (decreasing ZHe lag times) is for the first time clearly evidenced, indicating a provenance shift from non-Pyrenean sources with inherited (pre-Variscan, Variscan, Permian-Triassic; Sardinia) cooling ages to exhuming Pyrenean source regions with Early Cretaceous and Late Cretaceous cooling ages. The increase in denudation rates is even more pronounced during the early Maastrichtian (over <2 myrs), with a sharp decrease in lag times from 40 to 10 myrs and the first appearance of Variscan grains cooled during the Late Cretaceous. It is synchronous with (1) cooling in the early Pyrenean retro-wedge (Agly-Salvezines; Ternois et al., 2019) and (2) establishment of continental conditions in the northeastern Pyrenees (Fondevilla et al., 2016). We therefore interpret these results as recording the onset of orogenesis and initiation of topographic growth in the Lion Pyrenees. From middle Maastrichtian onward, whatever the sample, the Late Cretaceous cooling component (moving peak, early orogenesis) is always associated with an Early Cretaceous cooling component (static peak, Aptian-Cenomanian rifting), demonstrating the dominant role of rift inheritance to the distribution and magnitude of early orogenic inversion of distal rifted margins (Figure

VI.16). Combined with geochronology, our low-temperature thermochronology data record the westward migration of inversion from a slightly rifted and thermally non-to-partially-reset region of Variscan basement in the east (Sardinia and Lion Pyrenees) to more strongly extended and thermally reset regions further west (Agly Pyrenees). In particular, our data suggest that the early Pyrenean edifice and the Early Cretaceous rift extended further east. Transition from orogen-parallel to orogen-transverse sediment routing systems in the retro-wedge is shown to occur at the onset of main collision, sometime between the late Thanetian and early Ypresian.

VI.6 Conclusions

By showing fairly instantaneous exhumation and erosion response to the onset of convergence, this study shows that the early eastern retroforeland basin preserves the full thermal and denudational evolution of the Pyrenean orogen from extensional episodes during the Early Cretaceous to early orogenic stages of the Late Cretaceous to early Eocene. Our work clarifies early growth in the Pyrenees, providing new evidence for dynamic coupling between range and foreland basin(s), and contributing to the debate on the role of rift inheritance into early orogenic processes.

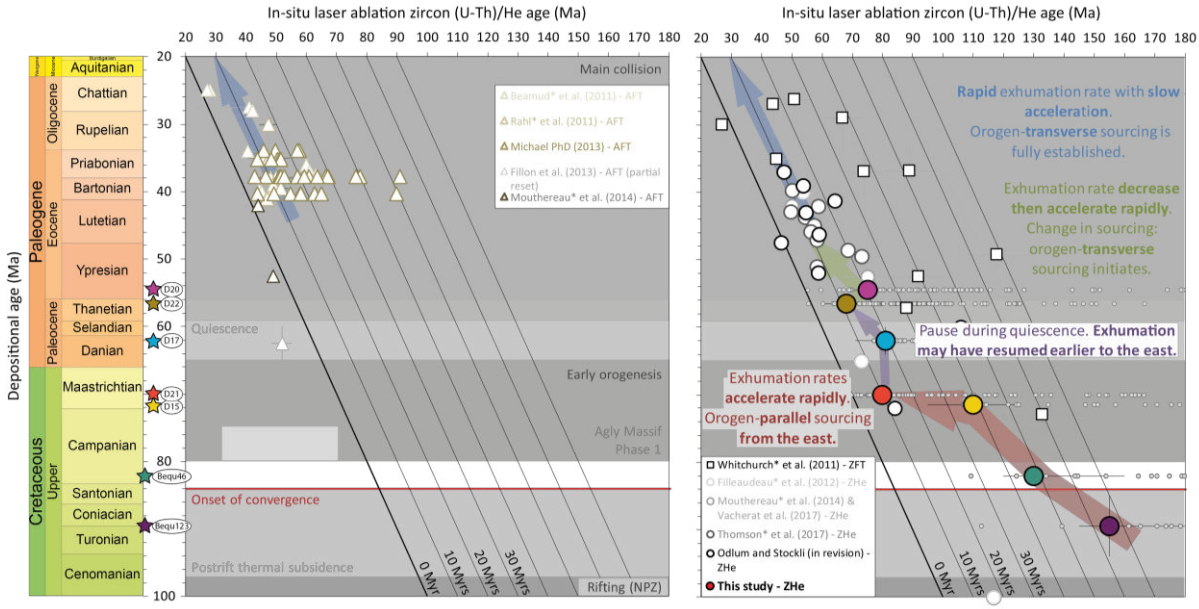

Figure VI.15: Lag-time plots. Left: Published apatite fission-track data. Right: Comparison between our in situ laser abation zircon (U-Th)/He data and published zircon fission-track and (U-Th)/He data.

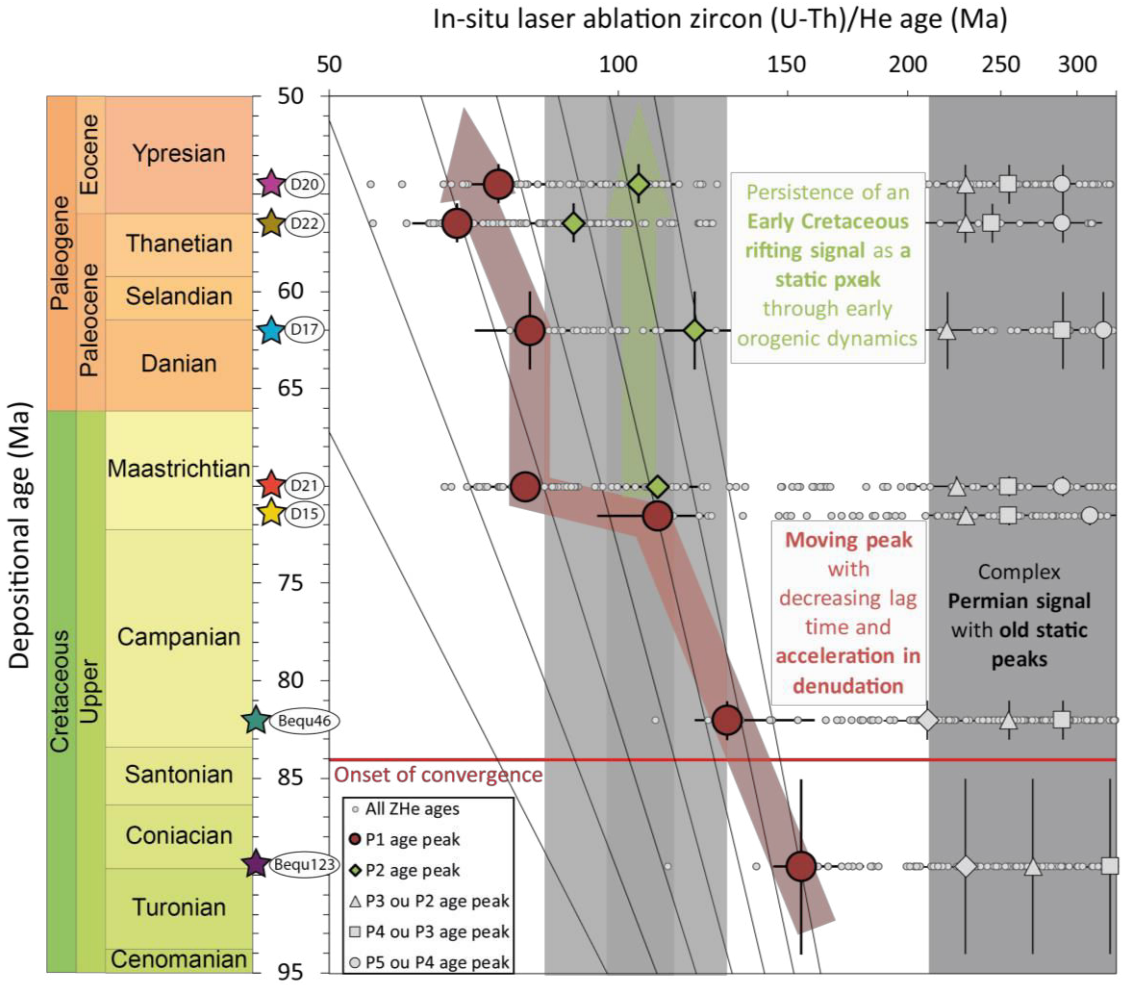

Figure VI.16: General lag-time plot synthesis of the low-temperature data provided by this study for the transition rifting-to-collision in the Pyrenees. From middle Maastrichtian onward, whatever the sample, the Late Cretaceous cooling component (moving peak, early orogenesis) is always associated with an Early Cretaceous cooling component (static peak, Aptian-Cenomanian rifting), demonstrating the dominant role of rift inheritance to the distribution and magnitude of early orogenic inversion of distal rifted margins in the eastern Pyrenees.

REFERENCES

Avigad, D., A. Gerdes, N. Morag, and T. Bechstädt, 2012, Coupled U-Pb-Hf of detrital zircons of Cambrian sandstones from Morocco and Sardinia: Implications for provenance and Precambrian crustal evolution of North Africa: Gondwana Research, v. 21, no. 2, p. 690-703, doi:10.1016/j.gr.2011.06.005.

Avigad, D., P. Rossi, A. Gerdes, and A. Abbo, 2018, Cadomian metasediments and Ordovician sandstone from Corsica: detrital zircon U-Pb-Hf constrains on their provenance and paleogeography: International Journal of Earth Sciences, doi:10.1007/s00531-018-1629-3.

Azambre, B., and J. Ravier, 1978, Les ecailles de gneiss du facies granulite du Port de Saleix et de la region de Lherz (Ariege), nouveaux temoins du socle profond des Pyrenees: Bulletin de la Société Géologique de France, v. S7-XX, no. 3, p. 221-228, doi:10.2113/gssgfbull.S7-XX.3.221.

Beamud, E., J. A. Muñoz, P. G. Fitzgerald, S. L. Baldwin, M. Garcés, L. Cabrera, and J. R. Metcalf, 2011, Magnetostratigraphy and detrital apatite fission-track thermochronology in syntectonic conglomerates: constraints on the exhumation of the South-Central Pyrenees: Basin Research, v. 23, no. 3, p. 309-331.

Berger, G. M., B. Alabouvette, G. Bessière, M. Bilotte, B. Crochet, M. Dubar, J. P. Marchal, Y. Tambareau, J. Villatte, and P. Viallard, 1997, Notice explicative, Carte géol. France (1/50 000), feuille Tuchan (1078): Orléans, BRGM, Carte géologique par Berger G.M., Bessière G., Bilotte M., Viallard P. (1997), 113 p.

Berger, G. M., G. Bessière, M. Bilotte, and P. Viallard, 1997, Carte géologique de France (1/50 000), feuille Tuchan (1078): Orléans, BRGM, 113 p.

Berger, G. M., F. Boyer, P. Debat, M. Demange, P. Freytet, J. P. Marchal, H. Mazéas, and C. Vautrelle, 1993, Notice explicative, Carte géol. France (1/50 000), feuille Carcassonne (1037): Orléans, BRGM, Carte géologique par.

Berger, G. M., M. Fonteilles, D. Leblanc, G. Clauzon, J. P. Marchal, and C. Vautrelle, 1993, Notice explicative, Carte géol. France (1/50 000), feuille Rivesaltes (1090): Orléans, BRGM, Carte géologique par Fonteilles M., Leblanc D., Clauzon G., Vaudin J.L., Berger G.M. (1993), 119 p.

Bessière, G., M. Bilotte, B. Crochet, B. Peybernès, Y. Tambareau, and J. Villatte, 1989, Notice explicative, Carte géol. France (1/50 000), feuille Quillan (1077): Orléans, BRGM, Carte géologique par Crochet B., Villatte J., Tambareau Y., Bilotte M., Bousquet J.P., Kuhfuss A., Bouillin J.P., Gélard J.P., Bessière G., Paris J.P. (1989), 98 p.

Bessière, G., M. Lenguin, J. P. Marchal, and J. Barruol, 1978, Notice explicative, Carte géol. France (1/50 000), feuille Limoux (1059): Orléans, BRGM, Carte géologique par.

Bilotte, M., 1985, Le Crétacé supérieur des plates-formes est-pyrénénnes: Laboratoire de géologie sédimentaire et paléontologie, Université Paul-Sabatier, Strata, 438 p.

Bilotte, M., 2014, Le gisement campanien du Ressec et les conglomérats maastrichtiens du Col del Teil (Anticlinal de Dreuilhe, Ariège, France). Intérêt géologique.: Bull. Soc. Hist. Nat. Toulouse, v. 150, p. 101-110.

Bilotte, M., 2017, Livret-guide AGSO d'excursion Corbières.

Bilotte, M., 2007, Permanence, au Crétacé supérieur, de la position de la limite plate-forme/basin dans la zone sous-pyrénéenne orientale (Aude, France): Géologie de la France, v. 1, p. 33-53.

Bilotte, M., J. Cosson, B. Crochet, B. Peybernes, J. Roche, F. Taillefer, Y. Tambareau, Y. Ternet, and J. Villatte, 1988, Notice explicative, Carte géol. France (1/50 000), feuille Lavelanet (1076): Orléans, BRGM, Carte géologique par.

Bilotte, M., L. Koess, and E. J. Debroas, 2005, Relations tectonique-sedimentation sur la marge nord-orientale du sillon sous-pyreneen au cours du Santonien superieur: Bulletin de la Société Géologique de France, v. 176, no. 5, p. 443-456.

Bilotte, M., L. Koess, and J. Le Loeuf, 1999, -96 Ma à -65 Ma autour de la vallée de l'Aude: Laboratoire de Géologie sedimentaire et paleontologie de l'université Paul Sabatier, Strata, 116 p.

Campbell, I. H., P. W. Reiners, C. M. Allen, S. Nicolescu, and R. Upadhyay, 2005, He-Pb double dating of detrital zircons from the Ganges and Indus Rivers: Implication for quantifying sediment recycling and provenance studies: Earth and Planetary Science Letters, v. 237, no. 3-4, p. 402-432, doi:10.1016/j.epsl.2005.06.043.

Canudo, J. I. et al., 2016, The upper Maastrichtian dinosaur fossil record from the southern Pyrenees and its contribution to the topic of the Cretaceous-Palaeogene mass extinction event: Cretaceous Research, v. 57, p. 540-551, doi:10.1016/j.cretres.2015.06.013.

Carosi, R., C. Montomoli, M. Tiepolo, and C. Frassi, 2012, Geochronological constraints on post-collisional shear zones in the Variscides of Sardinia (Italy): Terra Nova, v. 24, no. 1, p. 42-51, doi:10.1111/j.1365-3121.2011.01035.x.

Carter, A., C. S. Bristow, and A. J. Hurford, 1995, The application of fission-track analysis to the dating of barren sequences: examples from red beds in Scotland and Thailand: Geological Society, London, Special Publications, v. 89, no. 1, p. 57-68, doi:10.1144/GSL.SP.1995.089.01.05.

Casini, L., S. Cuccuru, M. Maino, G. Oggiano, and M. Tiepolo, 2012, Emplacement of the Arzachena Pluton (Corsica-Sardinia Batholith) and the geodynamics of incoming Pangaea: Tectonophysics, v. 544-545, p. 31-49, doi:10.1016/j.tecto.2012.03.028.

Cavaillé, A., 1976, Notice explicative, Carte géol. France (1/50 000), feuille Mirepoix (1058): Orléans, BRGM, Carte géologique par.

Cavaillé, A., P. Debat, and G. Calas, 1975, Notice explicative, Carte géol. France (1/50 000), feuille Castelnaudary (1036): Orléans, BRGM, Carte géologique par.

Chelle-Michou, C., O. Laurent, J.-F. Moyen, S. Block, J.-L. Paquette, S. Couzinié, V. Gardien, O. Vanderhaeghe, A. Villaros, and A. Zeh, 2017, Pre-Cadomian to late-Variscan odyssey of the eastern Massif Central, France: Formation of the West European crust in a nutshell: Gondwana Research, v. 46, p. 170-190, doi:10.1016/j.gr.2017.02.010.

Cherniak, D. J., E. B. Watson, and J. B. Thomas, 2009, Diffusion of helium in zircon and apatite: Chemical Geology, v. 268, no. 1, p. 155-166, doi:10.1016/j.chemgeo.2009.08.011.

Choukroune, P., 1989, The Ecors Pyrenean deep seismic profile reflection data and the overall structure of an orogenic belt: Tectonics, v. 8, no. 1, p. 23-39, doi:10.1029/TC008i001p00023.

Christophoul, F., J.-C. Soula, S. Brusset, B. Elibana, M. Roddaz, G. Bessiere, and J. Déramond, 2003, Time, place and mode of propagation of foreland basin systems as recorded by the sedimentary fill: examples of the Late Cretaceous and Eocene retro-foreland basins of the north-eastern Pyrenees: Special Publication-Geological Society of London, v. 208, p. 229-252.

Clark, J., S. Castelltort, C. Puigdefàbregas, D. F. Stockli, M. L. Dykstra, L. Honegger, K. Thomson, M. Odlum, and A. Fildani, 2017, Controls on Sediment Delivery to the Deep-Water in Eocene Source-to-Sink Clastic Systems of the South Pyrenean Foreland Basin, Spain.

Clerc, C., and Y. Lagabrielle, 2014, Thermal control on the modes of crustal thinning leading to mantle exhumation: Insights from the Cretaceous Pyrenean hot paleomargins: Tectonics, v. 33, no. 7, p. 1340-1359, doi:10.1002/2013TC003471.

Clerc, C., Y. Lagabrielle, P. Labaume, J.-C. Ringenbach, A. Vauchez, T. Nalpas, R. Bousquet, J.-F. Ballard, A. Lahfid, and S. Fourcade, 2016, Basement - Cover decoupling and progressive exhumation of metamorphic sediments at hot rifted margin. Insights from the Northeastern Pyrenean analog: Tectonophysics, v. 686, p. 82-97, doi:10.1016/j.tecto.2016.07.022.

Clerc, C., Y. Lagabrielle, M. Neumaier, J.-Y. Reynaud, and M. de Saint Blanquat, 2012, Exhumation of subcontinental mantle rocks: evidence from ultramafic-bearing clastic deposits nearby the Lherz peridotite body, French Pyrenees: Bulletin de la Societe Geologique de France, v. 183, no. 5, p. 443-459, doi:10.2113/gssgfbull.183.5.443.

Cocherie, A., T. Baudin, A. Autran, C. Guerrot, C. M. Fanning, and B. Laumonier, 2005, U/Pb zircon (ID-TIMS and SHRIMP) evidence for the early ordovician intrusion of metagranites in the late Proterozoic Canaveilles Group of the Pyrenees and the Montagne Noire (France): Bulletin De La Societe Geologique De France, v. 176, no. 3, p. 269-282, doi:10.2113/176.3.269.

Cocherie, A., Ph. Rossi, C. M. Fanning, and C. Guerrot, 2005, Comparative use of TIMS and SHRIMP for U-Pb zircon dating of A-type granites and mafic tholeiitic layered complexes and dykes from the Corsican Batholith (France): Lithos, v. 82, no. 1-2, p. 185-219, doi:10.1016/j.lithos.2004.12.016.

Combes, J.-P., F. Crouzel, P. Freytet, M. Gottis, M. Lenguin, M. P. Mouline, and J.-P. Plaziat, 1975, Du cône torrentiel au grand fleuve - Sédimentation continentale du crétacé inférieur au néogéne dans le midi de la France: Institut de Géodynamique, Université de Bordeaux III.

Crochet, B., J. Villatte, Y. Tambareau, M. Bilotte, J. P. Bousquet, A. Kuhfuss, J. P. Bouillin, J. P. Gélard, G. Bessière, and J. P. Paris, 1989, Carte géologique de France (1/50 000), feuille Quillan (1077): Orléans, BRGM.

Curnelle, R., P. Dubois, and J. C. Seguin, 1980, Le bassin d'Aquitaine: Substratum anté-Tertiaire et bordures mésozoïques: La chaîne des Pyrénées et son avant-pays Aquitano-languedocien. Bulletin des Centres de Recherches Exploration-Production Elf-Aquitaine, Mémoire, v. 3, p. 47-58.

Danisik, M., J. Kuhlemann, I. Dunkl, N. Evans, B. Székely, and W. Frisch, 2012, Survival of Ancient Landforms in a Collisional Setting as Revealed by Combined Fission-track and (U-Th)/He Thermochronometry: A Case Study from Corsica (France): The Journal of Geology, v. 120, p. 155-173, doi:10.1086/663873.

Danišík, M., J. Kuhlemann, I. Dunkl, B. Székely, and W. Frisch, 2007, Burial and exhumation of Corsica (France) in the light of fission-track data: Tectonics, v. 26, no. 1, doi:10.1029/2005TC001938.

Debroas, E. J., 1990, Le Flysch noir albo-cénomanien témoin de la structuration albienne à sénonienne de la zone nord-pyrénéenne en Bigorre (Hautes-Pyrénées, France): Bulletin de la Société géologique de France, v. 6, no. 2, p. 283-285.

Debroas, E. J., 1987, Modèle de bassin triangulaire à l'intersection de décrochements divergents pour le fossé albo-cénomanien de la Ballongue (zone nord-pyrénéenne, France): Bull. Soc. Geol. Fr, v. 8, p. 887-898.

Deloule, E., P. Alexandrov, A. Cheilletz, B. Laumonier, and P. Barbey, 2002, *In situ* U-Pb zircon ages for Early Ordovician magmatism in the eastern Pyrenees, France: the Canigou orthogneisses: International Journal of Earth Sciences, v. 91, no. 3, p. 398-405, doi:10.1007/s00531-001-0232-0.

Denèle, Y., P. Barbey, E. Deloule, E. Pelleter, P. Olivier, and G. Gleizes, 2009, Middle Ordovician U/Pb age of the Aston and Hospitalet orthogneissic laccoliths: their role in the Variscan evolution of the Pyrenees: Bulletin De La Societe Geologique De France, v. 180, no. 3, p. 209-216.

Denèle, Y., B. Laumonier, J.-L. Paquette, P. Olivier, G. Gleizes, and P. Barbey, 2014, Timing of granite emplacement, crustal flow and gneiss dome formation in the Variscan segment of the Pyrenees, in K. Schulmann, J. R. MartinezCatalan, J. M. Lardeaux, V. Janousek, and G. Oggiano, eds., Variscan Orogeny: Extent, Timescale and the Formation of the European Crust: Bath, Geological Soc Publishing House, p. 265-287.

Denèle, Y., P. Olivier, G. Gleizes, and P. Barbey, 2009, Decoupling between the middle and upper crust during transpression-related lateral flow: Variscan evolution of the Aston gneiss dome (Pyrenees, France): Tectonophysics, v. 477, no. 3-4, p. 244-261, doi:10.1016/j.tecto.2009.04.033.

Denèle, Y., J.-L. Paquette, P. Olivier, and P. Barbey, 2012, Permian granites in the Pyrenees: the Aya pluton (Basque Country): Terra Nova, v. 24, no. 2, p. 105-113.

Dickinson, W. R., and G. E. Gehrels, 2008, Sediment delivery to the Cordilleran foreland basin: Insights from U/Pb ages of detrital zircons in Upper Jurassic and Cretaceous strata of the Colorado Plateau: American Journal of Science, v. 308, no. 10, p. 1041-1082, doi:10.2475/10.2008.01.

Dickinson, W. R., and G. E. Gehrels, 2009, U/Pb ages of detrital zircons in Jurassic eolian and associated sandstones of the Colorado Plateau: Evidence for transcontinental dispersal and intraregional recycling of sediment: Geological Society of America Bulletin, v. 121, no. 3-4, p. 408-433, doi:10.1130/B26406.1.

Ellenberger, F., P. Freytet, J.-P. Plaziat, G. Bessière, P. Viallard, G. M. Berger, and J. P. Marchal, 1987, Notice explicative, Carte géol. France (1/50 000), feuille Capendu (1060): Orléans, BRGM, Carte géologique par.

Filleaudeau, P.-Y., F. Mouthereau, and R. Pik, 2012, Thermo-tectonic evolution of the south-central Pyrenees from rifting to orogeny: insights from detrital zircon U/Pb and (U-Th)/He thermochronometry: Basin Research, v. 24, no. 4, p. 401-417, doi:10.1111/j.1365-2117.2011.00535.x.

Fillon, C., C. Gautheron, and P. van der Beek, 2013, Oligocene-Miocene burial and exhumation of the Southern Pyrenean foreland quantified by low-temperature thermochronology: Journal of the Geological Society, v. 170, no. 1, p. 67-77.

Flowers, R. M., D. L. Shuster, B. P. Wernicke, and K. A. Farley, 2007, Radiation damage control on apatite (U-Th)/He dates from the Grand Canyon region, Colorado Plateau: Geology, v. 35, no. 5, p. 447-450, doi:10.1130/G23471A.1.

Fondevilla, V., J. Dinarès-Turell, B. Vila, J. Le Loeuff, R. Estrada, O. Oms, and À. Galobart, 2016, Magnetostratigraphy of the Maastrichtian continental record in the Upper Aude Valley (northern Pyrenees, France): Placing age constraints on the succession of dinosaur-bearing sites: Cretaceous Research, v. 57, p. 457-472, doi:10.1016/j.cretres.2015.08.009.

Fonteilles, M., D. Leblanc, G. Clauzon, J. L. Vaudin, and G. M. Berger, 1993, Carte géologique de France (1/50 000), feuille Rivesaltes (1090): Orléans, BRGM.

Ford, M., F. Christophoul, L. Menzer, J. Simonis, E. Saura, and J. Vergés, 2016, The role of salt tectonics in the evolution of the northeastern Pyrenees: p. EPSC2016-6047.

Ford, M., L. Hemmer, A. Vacherat, K. Gallagher, and F. Christophoul, 2016, Retro-wedge foreland basin evolution along the ECORS line, eastern Pyrenees, France: Journal of the Geological Society, v. 173, no. 3, p. 419-437.

Franke, W., M. P. Doublier, K. Klama, S. Potel, and K. Wemmer, 2011, Hot metamorphic core complex in a cold foreland: International Journal of Earth Sciences, v. 100, no. 4, p. 753-785, doi:10.1007/s00531-010-0512-7.

Freytet, P., 1975, Le Danien (Dano-Montien) des Petites Pyrénées et du Plantaurel : étude pétrographique et paléogéographique des faciès “lacustres”: Géologie Méditerranéenne, v. 2, no. 4, p. 159-177, doi:10.3406/geolm.1975.952.

Freytet, P., 1971, Le Languedoc au Cretace superieur et a l’Eocene inferieur; evolution des principaux elements structuraux (rides et sillons) migration des aires de sedimentation, role des phases precoces dans la tectogenese: Bulletin de la Société Géologique de France, v. S7-XIII, no. 5-6, p. 464-474, doi:10.2113/gssgfbull.S7-XIII.5-6.464.

Freytet, P., 1970, Les dépôts continentaux et marins du Crétacé supérieur et des couches de pass de l’Eocene en Languedoc: Univ. Paris Sud.

Freytet, P., and J.-C. Plaziat, 1982, Continental Carbonate Sedimentation and Pedogenesis - Late Cretaceous and Early Tertiary of Southern France: Contributions to Sedimentary Geology, v. 12, p. 213.

Gaggero, L., N. Gretter, A. Langone, and A. Ronchi, 2017, U-Pb geochronology and geochemistry of late Palaeozoic volcanism in Sardinia (southern Variscides): Geoscience Frontiers, v. 8, no. 6, p. 1263-1284, doi:10.1016/j.gsf.2016.11.015.

Galbrun, B., M. Feist, F. Colombo, R. Rocchia, and Y. Tambareau, 1993, Magnetostratigraphy and biostratigraphy of Cretaceous-Tertiary continental deposits, Ager Basin, Province of Lerida, Spain: Palaeogeography, Palaeoclimatology, Palaeoecology, v. 102, no. 1, p. 41-52, doi:10.1016/0031-0182(93)90004-3.

Garver, J. I., and M. T. Brandon, 1994a, Erosional denudation of the British Columbia Coast Ranges as determined from fission-track ages of detrital zircon from the Tofino basin, Olympic Peninsula, Washington: Geological Society of America Bulletin, p. 16.

Garver, J. I., and M. T. Brandon, 1994b, Fission-track ages of detrital zircons from Cretaceous strata, southern British Columbia: Implications for the Baja BC hypothesis: Tectonics, v. 13, no. 2, p. 401-420, doi:10.1029/93TC02939.

Gautheron, C., L. Tassan-Got, J. Barbarand, and M. Pagel, 2009, Effect of alpha-damage annealing on apatite (U-Th)/He thermochronology: Chemical Geology, v. 266, no. 3, p. 157-170.

Gehrels, G., 2012, Detrital Zircon U/Pb Geochronology: Current Methods and New Opportunities, in Tectonics of Sedimentary Basins: Wiley-Blackwell, p. 45-62, doi:10.1002/9781444347166.ch2.

Giacomini, F., R. M. Bomparola, and C. Ghezzo, 2005, Petrology and geochronology of metabasites with eclogite facies relics from NE Sardinia: constraints for the Palaeozoic evolution of Southern Europe: Lithos, v. 82, no. 1-2, p. 221-248, doi:10.1016/j.lithos.2004.12.013.

Giacomini, F., R. Maria Bomparola, C. Ghezzo, and H. Guldbransen, 2006, The geodynamic evolution of the Southern European Variscides: Constraints from the U/Pb geochronology and geochemistry of the lower Palaeozoic magmatic-sedimentary sequences of Sardinia (Italy): Contributions to Mineralogy and Petrology, v. 152, p. 19-42, doi:10.1007/s00410-006-0092-5.

Grool, A. R., M. Ford, J. Vergés, R. S. Huismans, F. Christophoul, and A. Dielforder, 2018, Insights Into the Crustal-Scale Dynamics of a Doubly Vergent Orogen From a Quantitative Analysis of Its Forelands: A Case Study of the Eastern Pyrenees: Tectonics, v. 37, no. 2, p. 450-476, doi:10.1002/2017TC004731.

Guenthner, W. R., P. W. Reiners, P. G. DeCelles, and J. Kendall, 2015, Sevier belt exhumation in central Utah constrained from complex zircon (U-Th)/He data sets: Radiation damage and He inheritance effects on partially reset detrital zircons: Geological Society of America Bulletin, v. 127, no. 3-4, p. 323-348.

Guenthner, W. R., P. W. Reiners, H. Drake, and M. Tillberg, 2017, Zircon, titanite, and apatite (U-Th)/He ages and age-eU correlations from the Fennoscandian Shield, southern Sweden: Fennoscandian Zirc He Age-eU Correlation: Tectonics, v. 36, no. 7, p. 1254-1274, doi:10.1002/2017TC004525.

Guenthner, W. R., P. W. Reiners, R. A. Ketcham, L. Nasdala, and G. Giester, 2013, Helium diffusion in natural zircon: Radiation damage, anisotropy, and the interpretation of zircon (U-Th)/He thermochronology: American Journal of Science, v. 313, no. 3, p. 145-198.

Guenthner, W. R., P. W. Reiners, and Y. Tian, 2014, Interpreting date-eU correlations in zircon (U-Th)/He datasets: A case study from the Longmen Shan, China: Earth and Planetary Science Letters, v. 403, p. 328-339, doi:10.1016/j.epsl.2014.06.050.

Hart, N. R., D. F. Stockli, and N. W. Hayman, 2016, Provenance evolution during progressive rifting and hyperextension using bedrock and detrital zircon U/Pb geochronology, Mauléon Basin, western Pyrenees: Geosphere, v. 12, no. 4, p. 1166-1186, doi:10.1130/GES01273.1.

Jammes, S., G. Manatschal, L. Lavier, and E. Masini, 2009, Tectonosedimentary evolution related to extreme crustal thinning ahead of a propagating ocean: Example of the western Pyrenees: Tectonics, v. 28, no. 4, p. TC4012, 1-24, doi:10.1029/2008TC002406.

Kennedy, W. J., M. Bilotte, and P. Melchior, 2015, Turonian ammonite faunas from the southern Corbières, Aude, France: Acta Geologica Polonica, v. 65, no. 4, p. 437-494, doi:10.1515/agp-2015-0020.

Ketcham, R. A., W. R. Guenthner, and P. W. Reiners, 2013, Geometric analysis of radiation damage connectivity in zircon, and its implications for helium diffusion: American Mineralogist, v. 98, no. 2-3, p. 350-360.

Lagabrielle, Y., and J.-L. Bodinier, 2008, Submarine reworking of exhumed subcontinental mantle rocks: field evidence from the Lherz peridotites, French Pyrenees: Terra Nova, v. 20, no. 1, p. 11-21.

Lagabrielle, Y., P. Labaume, and M. de Saint Blanquat, 2010, Mantle exhumation, crustal denudation, and gravity tectonics during Cretaceous rifting in the Pyrenean realm (SW Europe): Insights from the geological setting of the lherzolite bodies: PYRENEAN LHERZOLITES, GRAVITY TECTONICS: Tectonics, v. 29, no. 4, p. n/a-n/a, doi:10.1029/2009TC002588.

Laurent, O., S. Couzinié, A. Zeh, O. Vanderhaeghe, J.-F. Moyen, A. Villaros, V. Gardien, and C. Chelle-Michou, 2017, Protracted, coeval crust and mantle melting during Variscan late-orogenic evolution: U-Pb dating in the eastern French Massif Central: International Journal of Earth Sciences, v. 106, no. 2, p. 421-451, doi:10.1007/s00531-016-1434-9.

Lawton, T. F., 2014, Small grains, big rivers, continental concepts: Geology, v. 42, no. 7, p. 639-640, doi:10.1130/focus072014.1.

Li, X.-H., M. Faure, and W. Lin, 2014, From crustal anatexis to mantle melting in the Variscan orogen of Corsica (France): SIMS U-Pb zircon age constraints: Tectonophysics, v. 634, p. 19-30, doi:10.1016/j.tecto.2014.07.021.

Li, X.-H., M. Faure, P. Rossi, W. Lin, and D. Lahondère, 2015, Age of Alpine Corsica ophiolites revisited: Insights from *in situ* zircon U-Pb age and O-Hf isotopes: Lithos, v. 220-223, p. 179-190, doi:10.1016/j.lithos.2015.02.006.

Lin, W., M. Faure, X. Li, Y. Chu, W. Ji, and Z. Xue, 2016, Detrital zircon age distribution from Devonian and Carboniferous sandstone in the Southern Variscan Fold-and-Thrust belt (Montagne Noire, French Massif Central), and their bearings on the Variscan belt evolution: Tectonophysics, v. 677-678, p. 1-33, doi:10.1016/j.tecto.2016.03.032.

Lin, W., P. Rossi, M. Faure, X.-H. Li, W. Ji, and Y. Chu, 2018, Detrital zircon age patterns from turbidites of the Balagne and Piedmont nappes of Alpine Corsica (France): Evidence for an European margin source: Tectonophysics, v. 722, p. 69-105, doi:10.1016/j.tecto.2017.09.015.

López-Martínez, N., J. I. Canudo, L. Ardèvol, X. P. Suberbiola, X. Orue-Etxebarria, G. Cuenca-Bescós, J. I. Ruiz-Omeñaca, X. Murelaga, and M. Feist, 2001, New dinosaur sites correlated with Upper Maastrichtian pelagic deposits in the Spanish Pyrenees: implications for the dinosaur extinction pattern in Europe: Cretaceous Research, v. 22, no. 1, p. 41-61, doi:10.1006/cres.2000.0236.

Lotout, C., P. Pitra, M. Poujol, and J. Van Den Driessche, 2017, Ordovician magmatism in the Lévézou massif (French Massif Central): tectonic and geodynamic implications: International Journal of Earth Sciences, v. 106, no. 2, p. 501-515, doi:10.1007/s00531-016-1387-z.

Macchiavelli, C., J. Vergés, A. Schettino, M. Fernàndez, E. Turco, E. Casciello, M. Torne, P. P. Pierantoni, and L. Tunini, 2017, A New Southern North Atlantic Isochron Map: Insights Into the Drift of the Iberian Plate Since the Late Cretaceous: Journal of Geophysical Research: Solid Earth, v. 122, no. 12, p. 9603-9626, doi:10.1002/2017JB014769.

Malusà, M. G., A. Carter, M. Limoncelli, I. M. Villa, and E. Garzanti, 2013, Bias in detrital zircon geochronology and thermochronometry: Chemical Geology, v. 359, p. 90-107, doi:10.1016/j.chemgeo.2013.09.016.

Malusà, M. G., M. Danišík, and J. Kuhlemann, 2016, Tracking the Adriatic-slab travel beneath the Tethyan margin of Corsica-Sardinia by low-temperature thermochronometry: Gondwana Research, v. 31, p. 135-149, doi:10.1016/j.gr.2014.12.011.

Malusà, M. G., A. Resentini, and E. Garzanti, 2016, Hydraulic sorting and mineral fertility bias in detrital geochronology: Gondwana Research, v. 31, p. 1-19, doi:10.1016/j.gr.2015.09.002.

Margalef, A., P. Castiñeiras, J. M. Casas, M. Navidad, M. Liesa, U. Linnemann, M. Hofmann, and A. Gärtner, 2016, Detrital zircons from the Ordovician rocks of the Pyrenees: Geochronological constraints and provenance: Tectonophysics, v. 681, p. 124-134, doi:10.1016/j.tecto.2016.03.015.

Martínez, F. J., C. Dietsch, J. Aleinikoff, J. Cirés, M. L. Arboleya, J. Reche, and D. Gómez-Gras, 2016, Provenance, age, and tectonic evolution of Variscan flysch, southeastern France and northeastern Spain, based on zircon geochronology: GSA Bulletin, v. 128, no. 5-6, p. 842-859, doi:10.1130/B31316.1.

Marty, D., 2004, Sedimentology, palaeoenvironment, and stratigraphy of the palustrine Facies Rognacien at the K/T-Boundary in Southern France.

Marty, D., and C. A. Meyer, 2006, Depositional conditions of carbonate-dominated palustrine sedimentation around the K-T boundary (Faciès Rognacien, northeastern Pyrenean foreland, southwestern France), in Special Paper 416: Paleoenvironmental Record and Applications of Calcretes and Palustrine Carbonates: Geological Society of America, p. 169-187, doi:10.1130/2006.2416(11).

Masini, E., G. Manatschal, J. Tugend, G. Mohn, and J.-M. Flament, 2014, The tectono-sedimentary evolution of a hyper-extended rift basin: the example of the Arzacq-Mauléon rift system (Western Pyrenees, SW France): International Journal of Earth Sciences, v. 103, no. 6, p. 1569-1596, doi:10.1007/s00531-014-1023-8.

Maurel, O., P. Monié, J. P. Respaut, A. F. Leyreloup, and H. Maluski, 2003, Pre-metamorphic $^{40}Ar/^{39}Ar$ and U-Pb ages in HP metagranitoids from the Hercynian belt (France): Chemical Geology, v. 193, no. 3, p. 195-214, doi:10.1016/S0009-2541(02)00351-0.

Mezger, J. E., and A. Gerdes, 2016, Early Variscan (Visean) granites in the core of central Pyrenean gneiss domes: implications from laser ablation U/Pb and Th-Pb studies: Gondwana Research, v. 29, no. 1, p. 181-198, doi:10.1016/j.gr.2014.11.010.

Michael, N. A., 2013, Functioning of an ancient routing system, the Escanilla Formation, South Central Pyrenees: London, Imperial College London.

Monod, B., I. Bourroullec, and others, 2014, Carte Géologique numérique à 1/250 000 de la région Midi-Pyrénées: Notice Technique, Bureau des Recherches Géologiques et Minières, Orléans, France.

Mouthereau, F., P.-Y. Filleaudeau, A. Vacherat, R. Pik, O. Lacombe, M. G. Fellin, S. Castelltort, F. Christophoul, and E. Masini, 2014, Placing limits to shortening evolution in the Pyrenees: Role of margin architecture and implications for the Iberia/Europe convergence: Plate convergence in the Pyrenees: Tectonics, v. 33, no. 12, p. 2283-2314, doi:10.1002/2014TC003663.

Muñoz, J. A., 1992, Evolution of a continental collision belt: ECORS-Pyrenees crustal balanced cross-section, in Thrust tectonics: Springer, p. 235-246.

Navidad, M., P. Castiñeiras, J. M. Casas, M. Liesa, J. Fernández Suárez, A. Barnolas, J. Carreras, and I. Gil-Peña, 2010, Geochemical characterization and isotopic age of Caradocian magmatism in the northeastern Iberian Peninsula: Insights into the Late Ordovician evolution of the northern Gondwana margin: Gondwana Research, v. 17, no. 2, p. 325-337, doi:10.1016/j.gr.2009.11.013.

Odlum, M. L., and D. F. Stockli, 2019, Thermotectonic Evolution of the North Pyrenean Agly Massif During Early Cretaceous Hyperextension Using Multi-mineral U/Pb Thermochronometry: Tectonics, v. 0, no. 0, doi:10.1029/2018TC005298.

Odlum, M., and D. F. Stockli, 2017, Thermotectonic evolution of the North Pyrenean Agly Massif from hyperextension through inversion using multi-mineral thermochronometry: p. 11277.

Oggiano, G., L. Gaggero, A. Funedda, L. Buzzi, and M. Tiepolo, 2010, Multiple early Paleozoic volcanic events at the northern Gondwana margin: U-Pb age evidence from the Southern Variscan branch (Sardinia, Italy): Gondwana Research, v. 17, no. 1, p. 44-58, doi:10.1016/j.gr.2009.06.001.

Olivier, P., G. Gleizes, and J. L. Paquette, 2004, Gneiss domes and granite emplacement in an obliquely convergent regime: New interpretation of the Variscan Agly Massif (Eastern Pyrenees, France), in D. L. Whitney, C. Teyssier, and C. S. Siddoway, eds., Gneiss Domes in Orogeny: Boulder, Geological Soc Amer Inc, p. 229-242.

Olivier, P., G. Gleizes, J.-L. Paquette, and C. Munoz Saez, 2008, Structure and U Pb dating of the Saint-Arnac pluton and the Ansignan charnockite (Agly Massif): a cross-section from the upper to the middle crust of the Variscan Eastern Pyrenees: Journal of the Geological Society, v. 165, no. 1, p. 141-152, doi:10.1144/0016-76492006-185.

Oms, O., J. Dinarès-Turell, E. Vicens, R. Estrada, B. Vila, à. Galobart, and A. M. Bravo, 2007, Integrated stratigraphy from the Vallcebre Basin (southeastern Pyrenees, Spain): New insights on the continental Cretaceous–Tertiary transition in southwest Europe: Palaeogeography, Palaeoclimatology, Palaeoecology, v. 255, no. 1-2, p. 35-47, doi:10.1016/j.palaeo.2007.02.039.

Padel, M., J. J. Álvaro, S. Clausen, F. Guillot, M. Poujol, M. Chichorro, É. Monceret, M. F. Pereira, and D. Vizcaïno, 2017, U-Pb laser ablation ICP-MS zircon dating across the Ediacaran-Cambrian transition of the Montagne Noire, southern France: Comptes Rendus Geoscience, doi:10.1016/j.crte.2016.11.002.

Paquette, J.-L., R.-P. Ménot, C. Pin, and J.-B. Orsini, 2003, Episodic and short-lived granitic pulses in a post-collisional setting: evidence from precise U-Pb zircon dating through a crustal cross-section in Corsica: Chemical Geology, v. 198, no. 1-2, p. 1-20, doi:10.1016/S0009-2541(02)00401-1.

Pavanetto, P., 2011, Zircon U/Pb and Lu-Hf isotopic data from some Perigondwana Variscan terranes (Sardinia-Corsica block and Calabropeloritan arc): New insight on the Cenozoic geodynamic evolution of the central Mediterranean basin: Università degli Studi di Cagliari.

Pavanetto, P., A. Funedda, C. J. Northrup, M. Schmitz, J. Crowley, and A. Loi, 2012, Structure and U/Pb zircon geochronology in the Variscan foreland of SW Sardinia, Italy: STRUCTURE AND U/PB GEOCHRONOLOGY IN THE SARDINIAN VARISCAN FORELAND: Geological Journal, v. 47, no. 4, p. 426-445, doi:10.1002/gj.1350.

Plaziat, J.-C., 1981, Late cretaceous to late eocene palaeogeographic evolution of southwest Europe: Palaeogeography, Palaeoclimatology, Palaeoecology, v. 36, no. 3, p. 263-320, doi:10.1016/0031-0182(81)90110-3.

Poilvet, J.-C., M. Poujol, P. Pitra, J. Van Den Driessche, and J.-L. Paquette, 2011, The Montalet granite, Montagne Noire, France: An Early Permian syn-extensional pluton as evidenced by new U-Th-Pb data on zircon and monazite: Comptes Rendus Geoscience, v. 343, no. 7, p. 454-461, doi:10.1016/j.crte.2011.06.002.

Poujol, M., P. Pitra, J. Van Den Driessche, R. Tartèse, G. Ruffet, J.-L. Paquette, and J.-C. Poilvet, 2017, Two-stage partial melting during the Variscan extensional tectonics (Montagne Noire, France): International Journal of Earth Sciences, v. 106, no. 2, p. 477-500, doi:10.1007/s00531-016-1369-1.

Rahl, J. M., S. H. Haines, and B. A. van der Pluijm, 2011, Links between orogenic wedge deformation and erosional exhumation: Evidence from illite age analysis of fault rock and detrital thermochronology of syn-tectonic conglomerates in the Spanish Pyrenees: Earth and Planetary Science Letters, v. 307, no. 1, p. 180-190, doi:10.1016/j.epsl.2011.04.036.

Rahl, J. M., P. W. Reiners, I. H. Campbell, S. Nicolescu, and C. M. Allen, 2003, Combined single-grain (U-Th)/He and U/Pb dating of detrital zircons from the Navajo Sandstone, Utah: Geology, v. 31, no. 9, p. 761, doi:10.1130/G19653.1.

Reiners, P. W., and M. T. Brandon, 2006, Using Thermochronology to Understand Orogenic Erosion: Annual Review of Earth and Planetary Sciences, v. 34, no. 1, p. 419-466, doi:10.1146/annurev.earth.34.031405.125202.

Reiners, P. W., I. H. Campbell, S. Nicolescu, C. M. Allen, J. K. Hourigan, J. I. Garver, J. M. Mattinson, and D. S. Cowan, 2005, (U-Th)/(He-Pb) double dating of detrital zircons: American Journal of Science, v. 305, no. 4, p. 259-311.

Reiners, P. W., K. A. Farley, and H. J. Hickes, 2002, He diffusion and (U-Th)/He thermochronometry of zircon: initial results from Fish Canyon Tuff and Gold Butte: Tectonophysics, v. 349, no. 1, p. 297-308.

Reiners, P. W., T. L. Spell, S. Nicolescu, and K. A. Zanetti, 2004, Zircon (U-Th)/He thermochronometry: He diffusion and comparisons with (40)Ar/(39)Ar dating: Geochimica Et Cosmochimica Acta, v. 68, no. 8, p. 1857-1887, doi:10.1016/J.GCA.2003.10.021.

Roger, F., C. Teyssier, J.-P. Respaut, P. F. Rey, M. Jolivet, D. L. Whitney, J.-L. Paquette, and M. Brunel, 2015, Timing of formation and exhumation of the Montagne Noire double dome, French Massif Central: Tectonophysics, v. 640-641, p. 53-69, doi:10.1016/j.tecto.2014.12.002.

Rossi, P., A. Cocherie, C. M. Fanning, and É. Deloule, 2006, Variscan to eo-Alpine events recorded in European lower-crust zircons sampled from the French Massif Central and Corsica, France: Lithos, v. 87, no. 3, p. 235-260, doi:10.1016/j.lithos.2005.06.009.

Rossi, P., G. Oggiano, and A. Cocherie, 2009, A restored section of the “southern Variscan realm” across the Corsica-Sardinia microcontinent: Comptes Rendus Geoscience, v. 341, no. 2, p. 224-238, doi:10.1016/j.crte.2008.12.005.

Rougier, G., M. Ford, F. Christophoul, and A.-G. Bader, 2016, Stratigraphic and tectonic studies in the central Aquitaine Basin, northern Pyrenees: Constraints on the subsidence and deformation history of a retro-foreland basin: Comptes Rendus Geoscience, v. 348, no. 3-4, p. 224-235, doi:10.1016/j.crte.2015.12.005.

Shuster, D. L., R. M. Flowers, and K. A. Farley, 2006, The influence of natural radiation damage on helium diffusion kinetics in apatite: Earth and Planetary Science Letters, v. 249, no. 3-4, p. 148-161, doi:10.1016/j.epsl.2006.07.028.

Sinclair, H. D., M. Gibson, M. Naylor, and R. G. Morris, 2005, Asymmetric growth of the Pyrenees revealed through measurement and modeling of orogenic fluxes: American Journal of Science, v. 305, no. 5, p. 369-406, doi:10.2475/ajs.305.5.369.

Souquet, P., B. Peybernès, M. Bilotte, and E.-J. Debroas, 1977, La chaîne alpine des Pyrénées: Géologie Alp, v. 53, p. 193-216.

Ternois, S., M. Odlum, M. Ford, R. Pik, D. Stockli, B. Tibari, A. Vacherat, and V. Bernard, 2019, Thermochronological evidence of early orogenesis, eastern Pyrenees, France: Tectonics, doi:10.1029/2018TC005254.

Thomson, K. D., D. F. Stockli, J. D. Clark, C. Puigdefàbregas, and A. Fildani, 2017, Detrital zircon (U-Th)/(He-Pb) double-dating constraints on provenance and foreland basin evolution of the Ainsa Basin, south-central Pyrenees, Spain: Tectonics, v. 36, no. 7, p. 2017TC004504, doi:10.1002/2017TC004504.

Tournaire Guille, B., Ph. Olivier, J.-L. Paquette, V. Bosse, and D. Guillaume, 2018, Evolution of the middle crust of the Pyrenees during the Paleozoic: new data on the plutonic rocks from the North Pyrenean Agly Massif: International Journal of Earth Sciences, doi:10.1007/s00531-018-1652-4.

Tugend, J., G. Manatschal, N. J. Kusznir, E. Masini, G. Mohn, and I. Thinon, 2014, Formation and deformation of hyperextended rift systems: Insights from rift domain mapping in the Bay of Biscay-Pyrenees: Tectonics, v. 33, no. 7, p. 1239-1276, doi:10.1002/2014TC003529.

Vacherat, A. et al., 2016, Rift-to-collision transition recorded by tectonothermal evolution of the northern Pyrenees: COOLING HISTORY OF THE NORTHERN PYRENEES: Tectonics, v. 35, no. 4, p. 907-933, doi:10.1002/2015TC004016.

Vacherat, A., F. Mouthereau, R. Pik, M. Bernet, C. Gautheron, E. Masini, L. Le Pourhiet, B. Tibari, and A. Lahfid, 2014, Thermal imprint of rift-related processes in orogens as recorded in the Pyrenees: Earth and Planetary Science Letters, v. 408, p. 296-306, doi:10.1016/j.epsl.2014.10.014.

Vacherat, A., F. Mouthereau, R. Pik, D. Huyghe, J.-L. Paquette, F. Christophoul, N. Loget, and B. Tibari, 2017, Rift-to-collision sediment routing in the Pyrenees: A synthesis from sedimentological, geochronological and kinematic constraints: Earth-Science Reviews, v. 172, p. 43-74, doi:10.1016/j.earscirev.2017.07.004.

Van Lichtervelde, M., A. Grand'Homme, M. de Saint-Blanquat, P. Olivier, A. Gerdes, J.-L. Paquette, J. C. Melgarejo, E. Druguet, and P. Alfonso, 2017, U/Pb geochronology on zircon and columbite-group minerals of the Cap de Creus pegmatites, NE Spain: Mineralogy and Petrology, v. 111, no. 1, p. 1-21, doi:10.1007/s00710-016-0455-1.

Vermeesch, P., 2012, On the visualisation of detrital age distributions: Chemical Geology, v. 312-313, p. 190-194, doi:10.1016/j.chemgeo.2012.04.021.

Vila, B., À. Galobart, J. I. Canudo, J. Le Loeuff, J. Dinarès-Turell, V. Riera, O. Oms, T. Tortosa, and R. Gaete, 2012, The diversity of sauropod dinosaurs and their first taxonomic succession from the latest Cretaceous of southwestern Europe: Clues to demise and extinction: Palaeogeography, Palaeoclimatology, Palaeoecology, v. 350-352, p. 19-38, doi:10.1016/j.palaeo.2012.06.008.

Whitchurch, A. L., A. Carter, H. D. Sinclair, R. A. Duller, A. C. Whittaker, and P. A. Allen, 2011, Sediment routing system evolution within a diachronously uplifting orogen: Insights from detrital zircon thermochronological analyses from the South-Central Pyrenees: American Journal of Science, v. 311, no. 5, p. 442-482.

Fourth Part

Conclusion

Chapter 7
VII. Conclusions and Perspectives

A better understanding of a system, whatever it may be, requires a study of the temporal and spatial interactions that it has with others. In the case of a collisional orogenic system, the interval considered in this thesis is the rifting-collision transition. In particular, this thesis aims to study the processes governing the establishment of an orogen from extension to collision, in order to provide answers to the following questions: (1) Does early orogenesis have a thermal signature distinguishable from other thermal events such as those associated with preceding rifting or later collision? (2) How is a (hyper-) thinned distal margin incorporated into the continental accretionary prism at the beginning of convergence? (3) Does the thermal and structural inheritance play a role in early orogenesis? (4) What is the sediment response and the contribution of dynamic topography to sedimentary passways?

In order to address these issues, particular attention was paid to the North Pyrenean foreland retro-system. Such a system developed on the European plate from the late Santonian (84 Ma) to the middle Miocene. The orogenic retro-prism (North Pyrenean Zone) was formed in place of an old Aptian-Cenomanian rift system (114-97 Ma) where the continental crust was strongly thinned and the sub-continental mantle exhumed. Only 10 Ma separate the end of rifting and the onset of convergence, so that the lithosphere involved in the convergence has not reached thermal equilibrium. First, it is therefore necessary to characterize the thermal evolution of a hyper-thinned distal margin from its formation during rifting to its inversion during early convergence (Chapter 5). Second, it is important to study the tectonic-erosion coupling existing between the orogenic prism and the early foreland basins (Chapter 6).

The first study of this thesis (Chapter 5, questions 1, 2 and 3) focused on the reconstruction of the thermal and structural history of the north-Pyrenean Agly-Salvezines massif, using inverse and forward modeling of zircon and apatite (U-Th)/He data. The thermal sensitivity range of these two thermochronometers makes it possible to investigate the thermal history of the crustal block in a larger and less discretized temperature range (45-250 °C), and therefore over a longer period of time, than previously attempted. The Agly-Salvezines massif belongs to the North Pyrenean Zone and lies between two sedimentary domains affected by the high temperature-low pressure metamorphism (250-600 °C) that developed during the aptian-cenomanian rifting phase. Thus, this massif is classically represented as the inverted European distal continental margin of the Aptian-Cenomanian rift system. Conventional (U-Th)/He data obtained for 17 basement samples, and inverse and forward modeling of these data, reveal two periods of rapid cooling for the massif, each recorded by one of the two thermochronometers used. The first phase of cooling (zircon) is Late Campanian-Maastrichtian and is related to early inversion of the distal rifted margin. The second phase of cooling (apatite) is Ypresian-Bartonian and is related to main collision. No cooling is evidenced during the Paleocene during which tectonic quiescence is recorded in the adjacent Aquitaine retroforeland basin. An earlier, late Aptian-Turonian cooling history is detected, possibly related to rifting and/or postrift, as recently evidenced by Odlum and Stockli (2019). On the basis of these data, observations and field geological

data, as well as the literature, a crustal-scale sequentially restored model for the tectonic and thermal transition from extension to peak orogenesis in the eastern Pyrenees has been proposed. This suggests that both thrusting and underplating processes contributed to early inversion of the Aptian-Cenomanian rift system. It shows the northward inversion of the distal margin in the early stages of convergence (Campanian-Maastrichtian). In the absence of erosion at this time, thermal relaxation can only occur by underplating of the Iberian distal margin beneath the Agly-Salvezines crustal block and coeval northward thrusting of this block onto the colder, northern European crust. Shortening decreases sharply during the Paleocene and the sampled rocks remained at a depth of *ca.* 2 km. At the beginning of the Eocene, convergence resumed and the distal margin is shortened again before the deformation propagated further north in the foreland. This thermo-tectonic reconstruction of the European distal margin thus shows a two-stage inversion of the margin and the absence of deep basement rocks to erosion at the end of early orogenesis in the present-day Eastern Pyrenees. The reliefs formed in this region were not important at the onset of convergence.

The second study of this thesis (Chapter 6, questions 1, 3 and 4) focused on reconstructing the thermal and structural history of an even earlier orogenic edifice than the one previously identified. In order to study an edifice that has since been destroyed by the Oligocene-Miocene opening of the Gulf of Lion, a detrital low temperature thermochronology approach on zircon was used and sampling of pre- and syn-orogenic deposits was conducted in the retroforeland basin (Rennes-les-Bains/Couiza area). In order to precisely identify the signature of early orogenesis (thermal and spatial), the detrital low temperature thermochronology approach was combined with a detrital U/Pb geochronology approach on zircon, on the same grains (concept of double dating). Given the inadequacy between the methods commonly used in thermochronology (U-Th)/He on zircon and the objectives of this study, a geo-thermochronological double-dating method by *in situ* laser ablation was implement and developed at the CRPG, in collaboration with two other laboratories, Georessources and the Jean Lamour Institute. The instruments, the analytical protocol and the analysis conditions were tested, calibrated and optimized for routine use in this study. The double dating data obtained by the newly installed method at the CRPG on 5 pre-syn-orogenic detrital samples (Turonian-basal Campanian) reveal the existence of pre-existing topography at the onset of convergence, inherited from a phase prior to the convergence. The geo-thermochronological signature of this eroding topography is similar to that of Sardinia at present, and seems to point this region as a probable source for sediments deposited between the Turonian and the lower Campanian on the European proximal margin. The double dating data obtained on 5 other syn-orogenic detrital samples (middle Maastrichtian to lower Ypresian) highlight the thermochronological duality existing between the cooling signals related to the Aptian-Cenomanian rifting and the Campanian-Maastrichtian early orogenesis: from the early Maastrichtian onwards, the two signals are transferred into the basin and largely carried by grains typical of Pyrenean Variscan granites. On the one hand, this reflects exhumation of deep crustal rocks (known between 5 and 10 km depth) having recorded

both a major thermal event during Aptian-Cenomanian rifting and a major thermal event related to early orogenesis (low and high eU, 140-160 °C). On the other hand, this indicates a very rapid transfer of eroded material from the source to the sink (10 Ma) during early orogenesis, suggesting average exhumation rates close to 500 m/Ma at the onset of orogenesis. Several fluctuations in the geochronological signal are recorded, and favor a scenario of migrating exhumation towards the west during early orogenesis and at the onset of collision. This migration is consistent with the results obtained by other teams on the southern side of the Pyrenees. Numerous detrital double dating studies have been conducted extensively, before and during this doctoral work (e.g. Odlum et al., 2019; Thomson et al., 2019). However, they have always used conventional dating, thus limiting the number of grains dated to around 20. These studies reveal a major source change at the onset of collision (Ypresian), with sediment supply changing from the Ebro Massif-Sardinia-Corsica to the south and east towards the Pyrenees to the north. Record of early orogenesis from Maastrichtian-Paleocene sediments in the pro-foreland basin is present but strongly diluted by the signature of the areas already present in the landscape at that time. Change from orogen-parallel to orogen-transverse sediment routing systems in the northern and southern Pyrenees seem relatively synchronous on the basis of our data.

By highlighting the thermochronological duality between the cooling signals associated with rifting and early orogenesis and by proposing a progressive migration of exhumation towards the west during early orogenesis and early collision, this thesis shows the fundamental role of thermal and structural inheritance of the lithosphere in orogenic wedge growth at the onset of convergence. In the Pyrenees, inheritance, perhaps even pre-rifting (Variscan for example) influenced the following episode by conditioning and localizing preferentially the compressive deformation in zones of rheological weakness. In particular, our data suggest that the early Pyrenean edifice and the Early Cretaceous rift extended further east, in an area which has since been destroyed by the Oligocene-Miocene opening of the Gulf of Lion. Thanks to detrital and *in situ* geo-thermochronology, this thesis brings temporal, thermal, structural and spatial constraints on the timing of inversion, the distribution of shortening and the localization of erosion zones at the onset of the Pyrenean convergence.

To go further in the future and confirm/clarify the conclusions of this thesis:

- Applying additional source tracing tools to the already performed (U-Th)/He - U/Pb double dating: heavy minerals and U/ Pb on rutile to better constrain the source of sediments;
- Documenting regions such as Corsica, Sardinia, the Massif of Mouthoumet and the Massif Central, for which no zircon (U-Th)/He data exists, preventing better identification of the source of sediments;
- Densifying sampling in Paleocene sediments to clarify the timing of tectonic quiescence further east in the early Lion-Pyrenees orogen: is there an EW diachronism relating to the resumption of convergence and the initiation of continental collision in the Pyrenees?

- Comparing the Pyrenean system with a non-inverted (hyper-) extended system to better characterize thermal, structural and compositional inheritance of a distal (hyper-) thinned margin.

From a methodological point of view, this thesis shows the potential of zircon (U-Th)/He thermochronometry, alone or in combination with other dating approaches. The multi-thermochronometric character of this thermochronometer allows a complex but continuous recording of the cooling history of a rock through various isotherms. Although the diffusion-radiation damage models available for zircon do not currently make it possible to use this thermochronometer for accurately estimating exhumation rate or cooling rate, it is clear that this thermochronometer is able to differentiate major thermal events on timescales to which other methods such as fission traces do not have access. Thanks to the *in situ* laser ablation dating technique, this effect is even reinforced and benefits from a relative ease of sampling and analysis.

Following these promising results, two main tracks are envisaged:

- Continuing the development of multi-dating on zircon by performing first fission-track dating then (U-Th)/He - U/Pb double dating (this was actually tested during the thesis but abandoned due to the lack of analytical precision mentioned in Chapter 4);
- Designing a statistical approach adapted to the zircon (U-Th)/He system for the interpretation of detrital data.

REFERENCES

Odlum, M. L., Stockli, D. F., Capaldi, T. N., Thomson, K. D., Clark, J., Puigdefàbregas, C., & Fildani, A. (2019). Tectonic and sediment provenance evolution of the South Eastern Pyrenean foreland basins during rift margin inversion and orogenic uplift. Tectonophysics, S0040195119301921. https://doi.org/10.1016/j.tecto.2019.05.008

Thomson, K. D., Stockli, D. F., Odlum, M. L., Tolentino, P., Puigdefàbregas, C., Clark, J., & Fildani, A. (2019). Sediment provenance and routing evolution in the Late Cretaceous–Eocene Ager Basin, south-central Pyrenees, Spain. Basin Research, 0(0). https://doi.org/10.1111/bre.12376

Fifth Part

Appendices

Appendices
All chapters

LIST OF APPENDICES

ADDITIONAL SUPPORTING INFORMATION (CHAPTER 4)

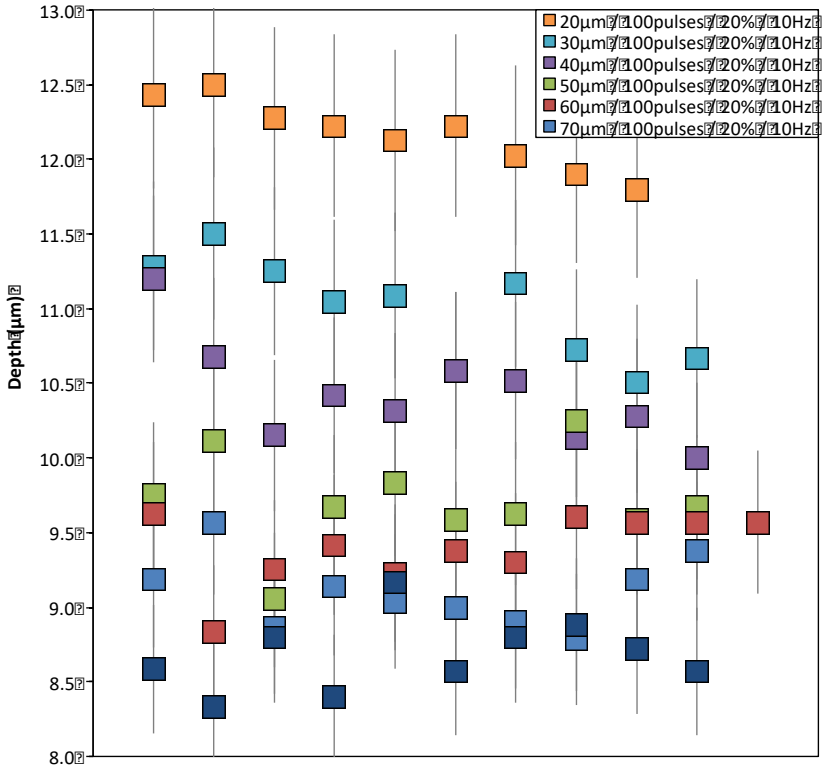

Appendix 1: Depth results for repeatability tests with varying spot size (homogeneous zircon crystal).

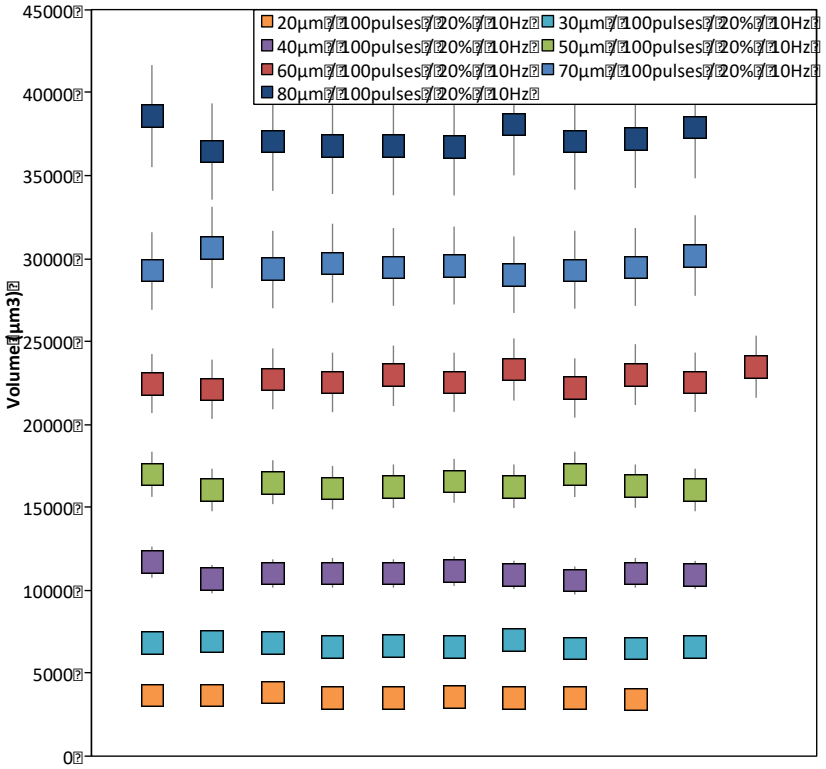

Appendix 2: Volume results for repeatability tests with varying spot size (homogeneous zircon crystal).

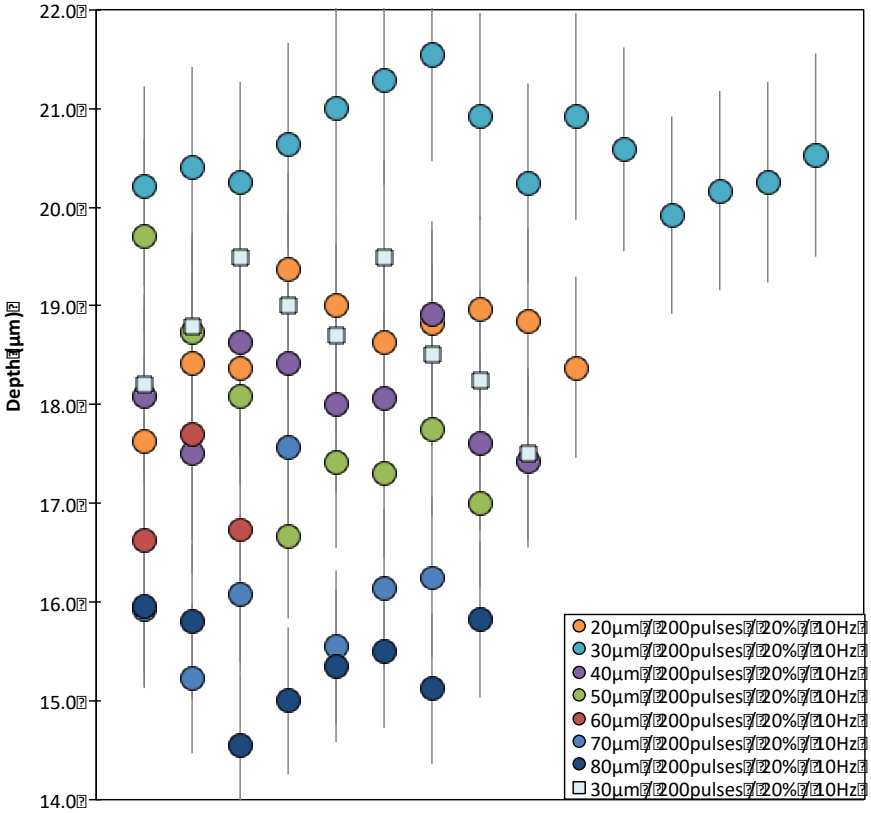

Appendix 3: Depth results for repeatability tests with varying spot size (different zircon crystals).

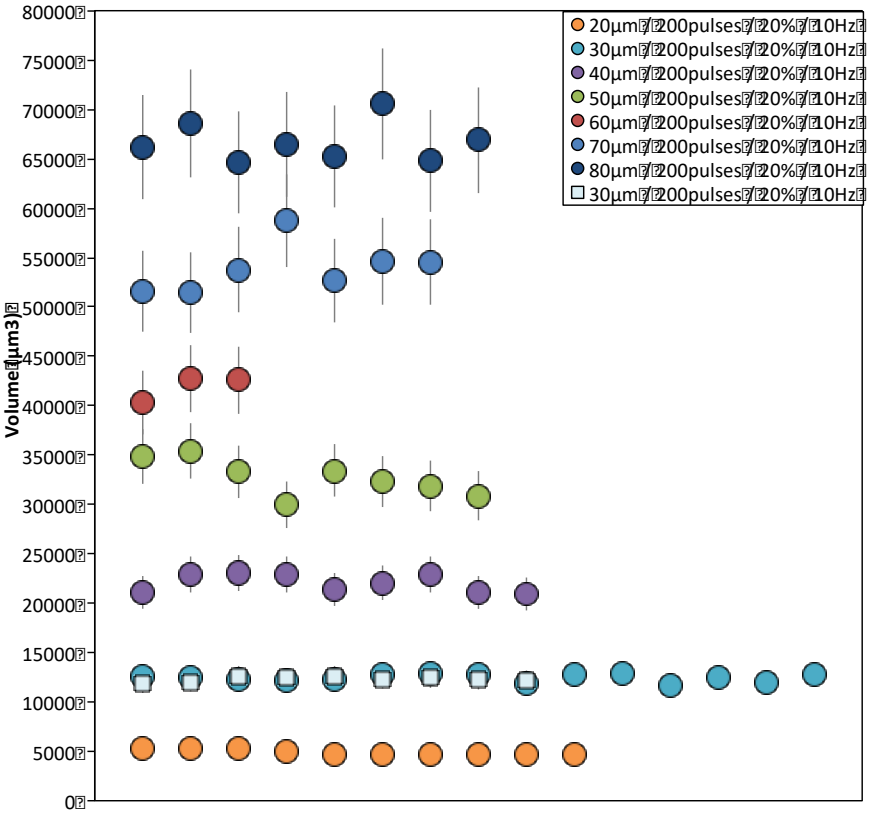

Appendix 4: Volume results for repeatability tests with varying spot size (different zircon crystals).

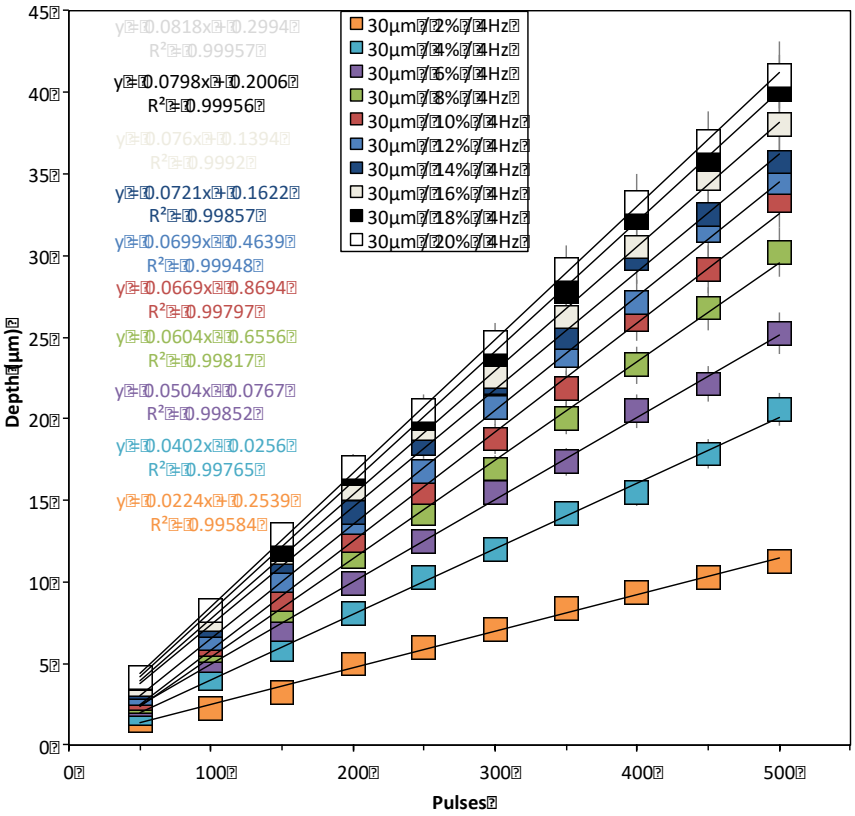

Appendix 5: Depth results showing linear dependency of depth with pulses (homogeneous zircon).

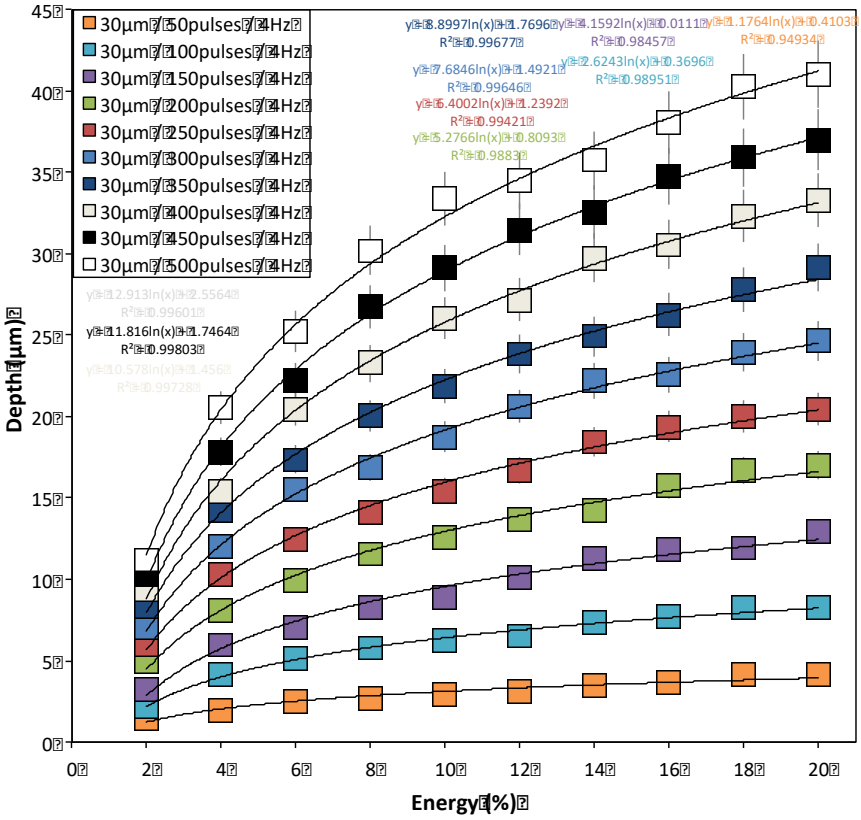

Appendix 6: Depth results showing log dependency of depth with energy (homogeneous zircon).

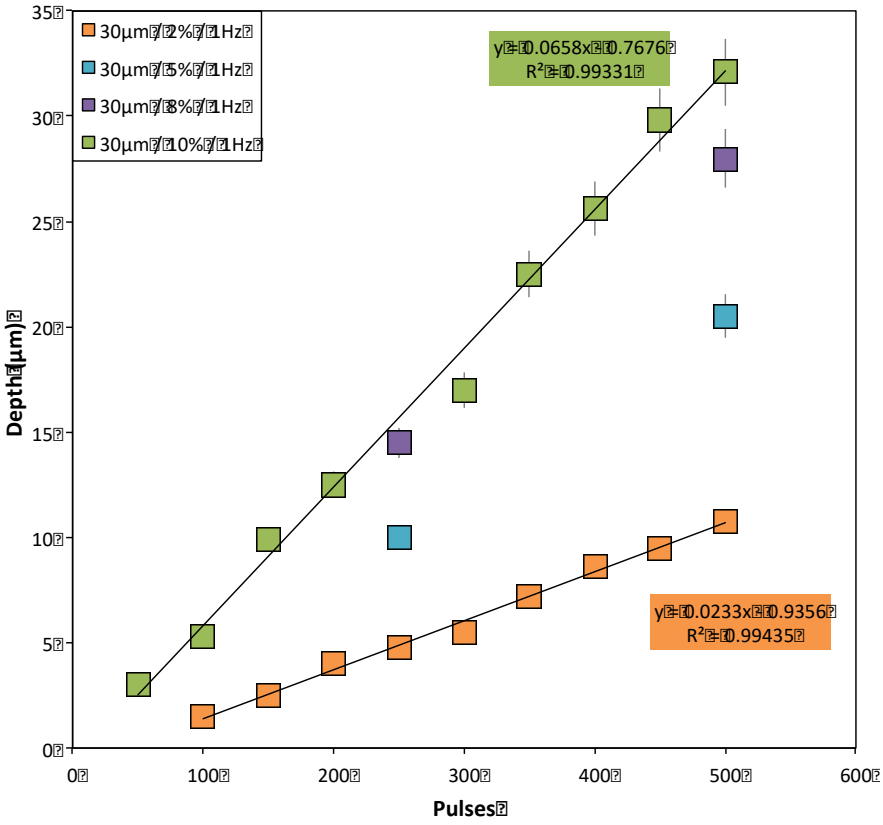

Appendix 7: Linear increase in depth as a function of pulses for varying energy (1 Hz, homogenous).

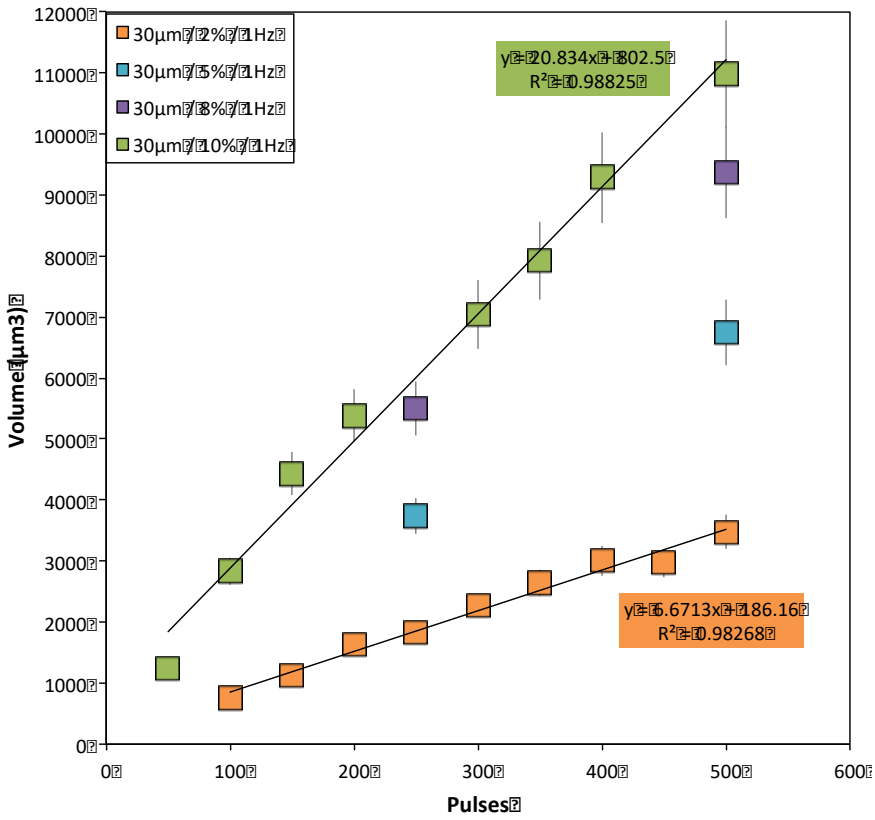

Appendix 8: Linear increase in volume as a function of pulses for varying energy (1 Hz, homogenous).

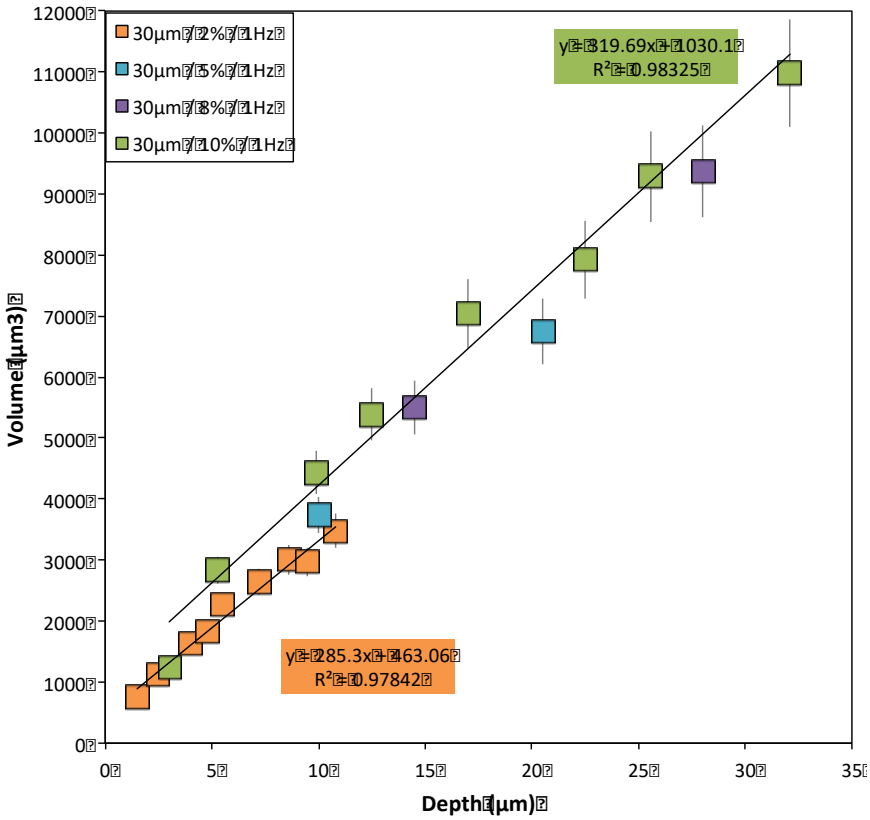

Appendix 9: Linear increase in volume as a function of depth for varying energy (1 Hz, homogenous).

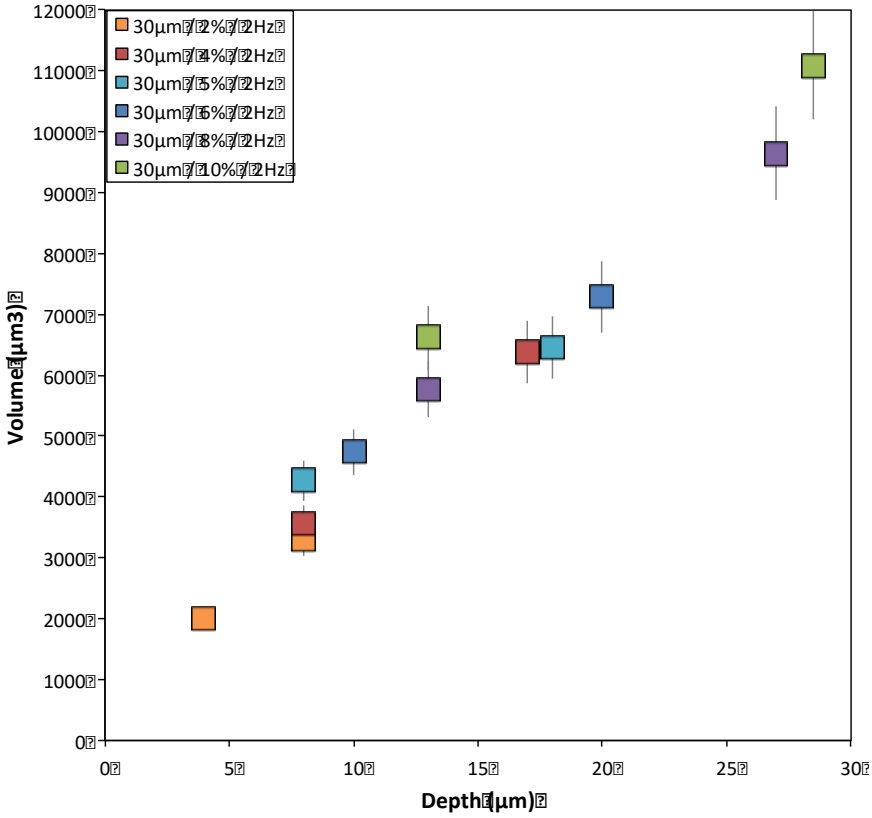

Appendix 10: Linear increase in volume as a function of depth for varying energy (2 Hz, homogenous).

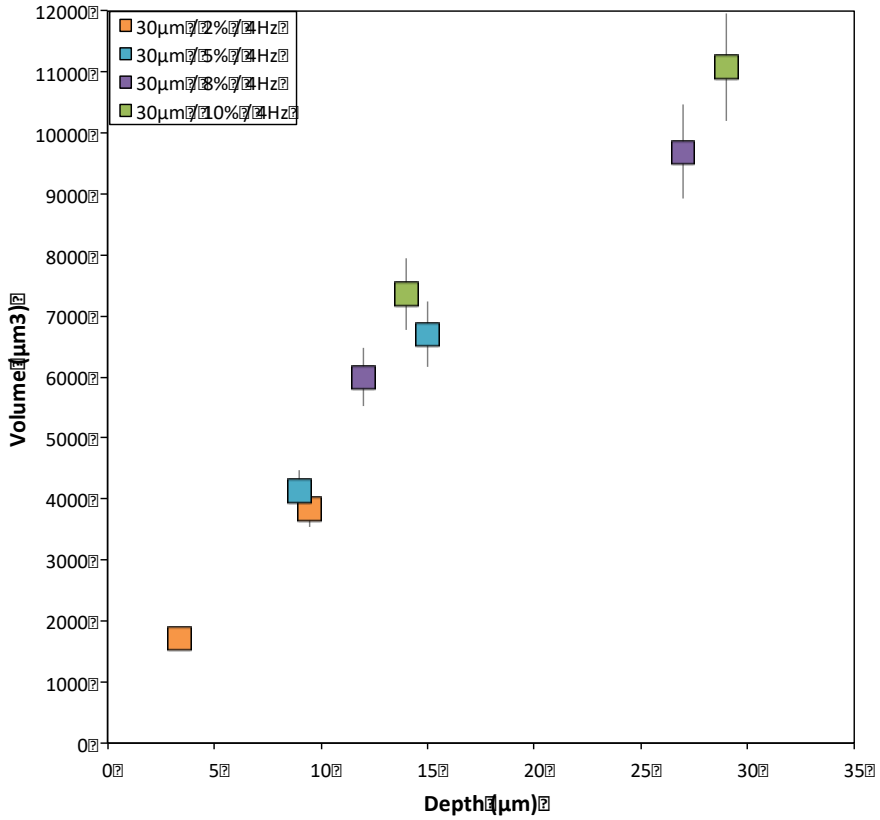

Appendix 11: Linear increase in volume as a function of depth for varying energy (4 Hz, homogenous).

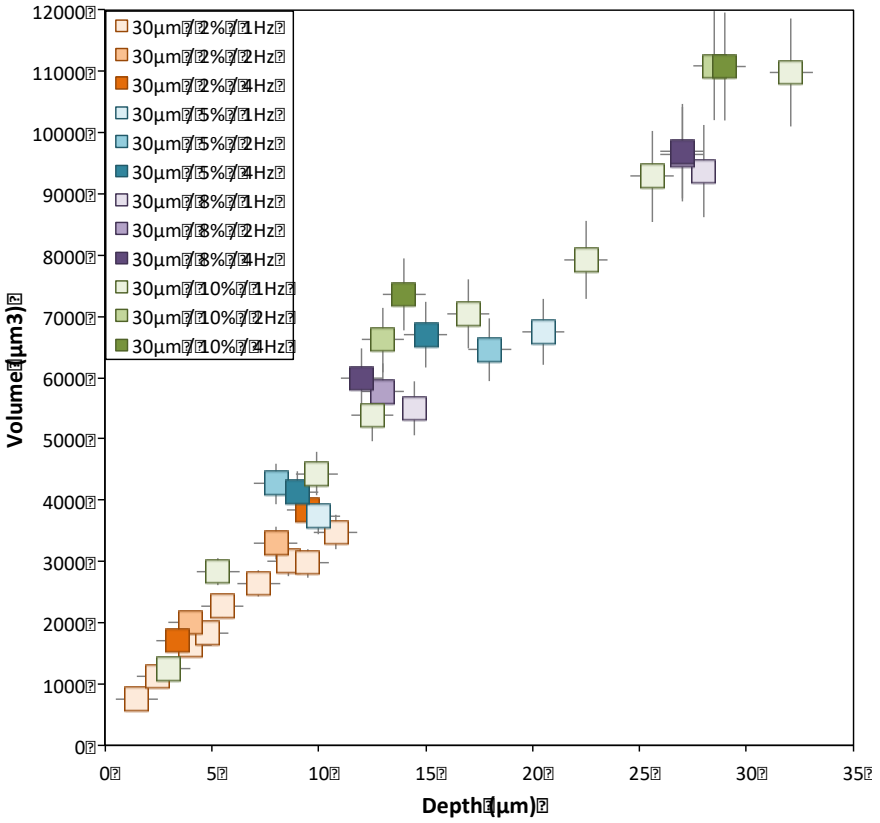

Appendix 12: Combination of Appendices 9, 10 and 11.

Zoning pattern	Core width	Rim width	Total integrated volume	Total integrated He concentration	Total integrated U concentration	Total integrated Th concentration	Total integrated Sm concentration	Volume of the core as a sphere with 15 µm radius	Theoretical volume of the core as a sphere with 15 µm radius	Volume of the outer, spherical 15 µm large envelope	Theoretical volume of the outer, spherical 15 µm large envelope	Weighetd mean He concentration for the core	Weighetd mean U concentration for the outer, spherical envelope	Weighetd mean Th concentration for the outer, spherical envelope	Weighetd mean Sm concentration for the outer, spherical envelope	**Ablation age (Horne et al. procedure)**	volume of 0-50 microns	weighted mean He concentration	weighted mean U concentration	weighted mean Th concentration	**Ablation age (Evans et al. procedure)**	HeFty uncorrected age	HeFty corrected age	FT	Profile mean age corrected from alpha ejection/conventional age (Ma)
Enriched core	40	5	381510	1.48E-07	952	952	5	8201	8177	135940	135543	2.38E-07	1250	1250	5	**28.5**	65954	2.36E-07	1250	1250	**28.4**	23.0	28.5	0.81	29.0
Enriched core	35	10	381510	1.19E-07	724	724	5	8201	8177	135940	135543	2.38E-07	1250	1250	5	**28.5**	65954	2.20E-07	1250	1250	**26.4**	24.6	28.5	0.86	28.7
Enriched core	30	15	381510	9.31E-08	548	548	5	8201	8177	135940	135543	2.38E-07	1027	1027	5	**34.7**	65954	1.90E-07	1250	1250	**22.8**	25.0	28.5	0.88	29.0
Enriched core	25	20	381510	6.89E-08	423	423	5	8201	8177	135940	135543	2.22E-07	675	675	5	**49.4**	65954	1.52E-07	1250	1250	**18.2**	24.1	28.5	0.85	28.9
Enriched core	20	25	381510	5.10E-08	339	339	5	8201	8177	135940	135543	1.60E-07	438	438	5	**54.9**	65954	1.10E-07	763	763	**21.7**	22.9	28.5	0.80	28.1
Enriched core	15	30	381510	4.14E-08	287	287	5	8201	8177	135940	135543	1.01E-07	295	295	5	**51.5**	65954	8.00E-08	467	467	**25.7**	21.9	28.5	0.77	28.1
Enriched core	10	35	381510	3.64E-08	261	261	5	8201	8177	135940	135543	6.20E-08	250	250	5	**37.2**	65954	5.87E-08	315	315	**28.0**	21.2	28.5	0.74	28.1
Enriched core	5	40	381510	3.47E-08	251	251	5	8201	8177	135940	135543	4.79E-08	250	250	5	**28.7**	65954	4.86E-08	258	258	**28.3**	20.9	28.5	0.73	21.0
Depleted core	40	5	381510	6.00E-08	548	548	5	8201	8177	135940	135543	4.78E-08	250	250	5	**28.7**	65954	4.88E-08	250	250	**29.3**	17.1	28.4	0.60	27.3
Depleted core	35	10	381510	8.81E-08	776	776	5	8201	8177	135940	135543	4.79E-08	250	250	5	**28.7**	65954	6.48E-08	250	250	**38.9**	17.4	28.4	0.61	27.8
Depleted core	30	15	381510	1.16E-07	952	952	5	8201	8177	135940	135543	4.79E-08	473	473	5	**15.2**	65954	9.62E-08	250	250	**57.8**	18.4	28.5	0.65	28.2
Depleted core	25	20	381510	1.39E-07	1077	1077	5	8201	8177	135940	135543	6.29E-08	825	825	5	**11.4**	65954	1.33E-07	250	250	**80.0**	19.6	28.5	0.69	28.2
Depleted core	20	25	381510	1.58E-07	1161	1161	5	8201	8177	135940	135543	1.26E-07	1062	1062	5	**17.8**	65954	1.76E-07	737	737	**35.7**	20.4	28.5	0.72	28.4
Depleted core	15	30	381510	1.67E-07	1213	1213	5	8201	8177	135940	135543	1.86E-07	1205	1205	5	**23.1**	65954	2.06E-07	1033	1033	**30.0**	20.7	28.5	0.73	28.5
Depleted core	10	35	381510	1.72E-07	1239	1239	5	8201	8177	135940	135543	2.23E-07	1250	1250	5	**26.8**	65954	2.26E-07	1185	1185	**28.7**	20.9	28.5	0.73	28.3
Depleted core	5	40	381510	1.74E-07	1249	1249	5	8201	8177	135940	135543	2.37E-07	1250	1250	5	**28.5**	65954	2.37E-07	1242	1242	**28.6**	20.9	28.5	0.73	28.4
Oscillatory, enriched core	5	-	381510	1.08E-07	835	835	5	8201	8177	135940	135543	1.46E-07	754	754	5	**29.0**	65954	1.41E-07	898	898	**23.6**	22.0	28.5	0.77	25.1
Oscillatory, enriched core	10	-	381510	9.65E-08	666	666	5	8201	8177	135940	135543	1.36E-07	746	746	5	**27.4**	65954	1.42E-07	610	610	**34.9**	22.0	28.5	0.77	28.2
Oscillatory, enriched core	15	-	381510	1.12E-07	845	845	5	8201	8177	135940	135543	1.61E-07	754	754	5	**32.1**	65954	1.52E-07	954	954	**23.9**	20.0	28.5	0.70	28.2
Oscillatory, enriched core	20	-	381510	1.02E-07	693	693	5	8201	8177	135940	135543	1.75E-07	791	791	5	**33.1**	65954	1.62E-07	763	763	**31.9**	20.0	28.5	0.70	21.6
Oscillatory, depleted core	5	-	381510	9.74E-08	665	665	5	8201	8177	135940	135543	1.35E-07	746	746	5	**27.1**	65954	1.40E-07	602	602	**34.8**	21.6	28.5	0.76	29.0
Oscillatory, depleted core	10	-	381510	1.07E-07	834	834	5	8201	8177	135940	135543	1.46E-07	754	754	5	**29.1**	65954	1.40E-07	890	890	**23.6**	21.6	28.5	0.76	25.5
Oscillatory, depleted core	15	-	381510	9.56E-08	655	655	5	8201	8177	135940	135543	1.21E-07	746	746	5	**24.3**	65954	1.30E-07	546	546	**35.7**	21.6	28.5	0.76	28.9
Oscillatory, depleted core	20	-	381510	1.03E-07	807	807	5	8201	8177	135940	135543	1.06E-07	709	709	5	**22.4**	65954	1.19E-07	737	737	**24.2**	19.6	28.5	0.69	27.8
Extreme, oscillatory, enriched core	5	-	381510	9.55E-08	657	657	5	8201	8177	135940	135543	1.24E-07	746	746	5	**24.8**	65954	1.33E-07	554	554	**36.1**	22.0	28.5	0.77	28.3
Extreme, oscillatory, enriched core	15	-	381510	6.34E-08	455	455	5	8201	8177	135940	135543	1.54E-07	443	443	5	**52.0**	65954	1.21E-07	751	751	**24.1**	20.0	28.5	0.70	29.8

Appendix 13: Modelling results - procedure of Horne et al. (2016) versus procedure of Evans et al. (2015).

Zoning pattern	Core width	Rim width	Total integrated volume	Total integrated He concentration	Total integrated U concentration	Total integrated Th concentration	Total integrated Sm concentration	Volume of the core as a sphere with 15 µm radius	Theoretical volume of the core as a sphere with 15 µm radius	Volume of the outer, spherical 15 µm large envelope	Theoretical volume of the outer, spherical 15 µm large envelope	Weighetd mean He concentration for the core	Weighetd mean U concentration for the outer, spherical envelope	Weighetd mean Th concentration for the outer, spherical envelope	Weighetd mean Sm concentration for the outer, spherical envelope	**Ablation age (procedure in this PhD thesis)**	Volume of the core as a sphere with 15 µm radius	Theoretical volume of the core as a sphere with 15 µm radius	Volume of the outer, spherical 15 µm large envelope	Theoretical volume of the outer, spherical 15 µm large envelope	Weighetd mean He concentration for the core	Weighetd mean U concentration for the outer, spherical envelope	Weighetd mean Th concentration for the outer, spherical envelope	Weighetd mean Sm concentration for the outer, spherical envelope	**Ablation age (Horne et al. procedure)**
Enriched core	40	5	381510	1.48E-07	952	952	5	14296	14130	99573	98910	2.38E-07	1250	1250	5	**28.5**	8201	8177	135940	135543	2.38E-07	1250	1250	5	**28.5**
Enriched core	35	10	381510	1.19E-07	724	724	5	14296	14130	99573	98910	2.38E-07	1250	1250	5	**28.5**	8201	8177	135940	135543	2.38E-07	1250	1250	5	**28.5**
Enriched core	30	15	381510	9.31E-08	548	548	5	14296	14130	99573	98910	2.36E-07	1250	1250	5	**28.3**	8201	8177	135940	135543	2.38E-07	1027	1027	5	**34.7**
Enriched core	25	20	381510	6.89E-08	423	423	5	14296	14130	99573	98910	2.06E-07	769	769	5	**40.1**	8201	8177	135940	135543	2.22E-07	675	675	5	**49.4**
Enriched core	20	25	381510	5.10E-08	339	339	5	14296	14130	99573	98910	1.48E-07	446	446	5	**49.6**	8201	8177	135940	135543	1.60E-07	438	438	5	**54.9**
Enriched core	15	30	381510	4.14E-08	287	287	5	14296	14130	99573	98910	9.77E-08	250	250	5	**58.6**	8201	8177	135940	135543	1.01E-07	295	295	5	**51.5**
Enriched core	10	35	381510	3.64E-08	261	261	5	14296	14130	99573	98910	6.40E-08	250	250	5	**38.4**	8201	8177	135940	135543	6.20E-08	250	250	5	**37.2**
Enriched core	5	40	381510	3.47E-08	251	251	5	14296	14130	99573	98910	4.92E-08	250	250	5	**29.5**	8201	8177	135940	135543	4.79E-08	250	250	5	**28.7**
Depleted core	40	5	381510	6.00E-08	548	548	5	14296	14130	99573	98910	4.78E-08	250	250	5	**28.7**	8201	8177	135940	135543	4.78E-08	250	250	5	**28.7**
Depleted core	35	10	381510	8.81E-08	776	776	5	14296	14130	99573	98910	4.79E-08	250	250	5	**28.7**	8201	8177	135940	135543	4.79E-08	250	250	5	**28.7**
Depleted core	30	15	381510	1.16E-07	952	952	5	14296	14130	99573	98910	5.00E-08	250	250	5	**30.0**	8201	8177	135940	135543	4.79E-08	473	473	5	**15.2**
Depleted core	25	20	381510	1.39E-07	1077	1077	5	14296	14130	99573	98910	7.89E-08	731	731	5	**16.2**	8201	8177	135940	135543	6.29E-08	825	825	5	**11.4**
Depleted core	20	25	381510	1.58E-07	1161	1161	5	14296	14130	99573	98910	1.39E-07	1054	1054	5	**19.7**	8201	8177	135940	135543	1.26E-07	1062	1062	5	**17.8**
Depleted core	15	30	381510	1.67E-07	1213	1213	5	14296	14130	99573	98910	1.89E-07	1250	1250	5	**22.7**	8201	8177	135940	135543	1.86E-07	1205	1205	5	**23.1**
Depleted core	10	35	381510	1.72E-07	1239	1239	5	14296	14130	99573	98910	2.21E-07	1250	1250	5	**26.5**	8201	8177	135940	135543	2.23E-07	1250	1250	5	**26.8**
Depleted core	5	40	381510	1.74E-07	1249	1249	5	14296	14130	99573	98910	2.36E-07	1250	1250	5	**28.3**	8201	8177	135940	135543	2.37E-07	1250	1250	5	**28.5**
Oscillatory, enriched core	5	-	381510	1.08E-07	835	835	5	14296	14130	99573	98910	1.41E-07	573	573	5	**36.8**	8201	8177	135940	135543	1.46E-07	754	754	5	**29.0**
Oscillatory, enriched core	10	-	381510	9.65E-08	666	666	5	14296	14130	99573	98910	1.43E-07	927	927	5	**23.2**	8201	8177	135940	135543	1.36E-07	746	746	5	**27.4**
Oscillatory, enriched core	15	-	381510	1.12E-07	845	845	5	14296	14130	99573	98910	1.56E-07	573	573	5	**41.0**	8201	8177	135940	135543	1.61E-07	754	754	5	**32.1**
Oscillatory, enriched core	20	-	381510	1.02E-07	693	693	5	14296	14130	99573	98910	1.76E-07	927	927	5	**28.4**	8201	8177	135940	135543	1.75E-07	791	791	5	**33.1**
Oscillatory, depleted core	5	-	381510	9.74E-08	665	665	5	14296	14130	99573	98910	1.40E-07	927	927	5	**22.7**	8201	8177	135940	135543	1.35E-07	746	746	5	**27.1**
Oscillatory, depleted core	10	-	381510	1.07E-07	834	834	5	14296	14130	99573	98910	1.40E-07	573	573	5	**36.5**	8201	8177	135940	135543	1.46E-07	754	754	5	**29.1**
Oscillatory, depleted core	15	-	381510	9.56E-08	655	655	5	14296	14130	99573	98910	1.26E-07	927	927	5	**20.3**	8201	8177	135940	135543	1.21E-07	746	746	5	**24.3**
Oscillatory, depleted core	20	-	381510	1.03E-07	807	807	5	14296	14130	99573	98910	1.05E-07	573	573	5	**27.5**	8201	8177	135940	135543	1.06E-07	709	709	5	**22.4**
Extreme, oscillatory, enriched core	5	-	381510	9.55E-08	657	657	5	14296	14130	99573	98910	1.30E-07	927	927	5	**21.0**	8201	8177	135940	135543	1.24E-07	746	746	5	**24.8**
Extreme, oscillatory, enriched core	15	-	381510	6.34E-08	455	455	5	14296	14130	99573	98910	1.48E-07	331	331	5	**66.9**	8201	8177	135940	135543	1.54E-07	443	443	5	**52.0**

Appendix 14: Modelling results - our procedure versus procedure of Horne et al. (2016).

ADDITIONAL SUPPORTING INFORMATION (CHAPTER 5)

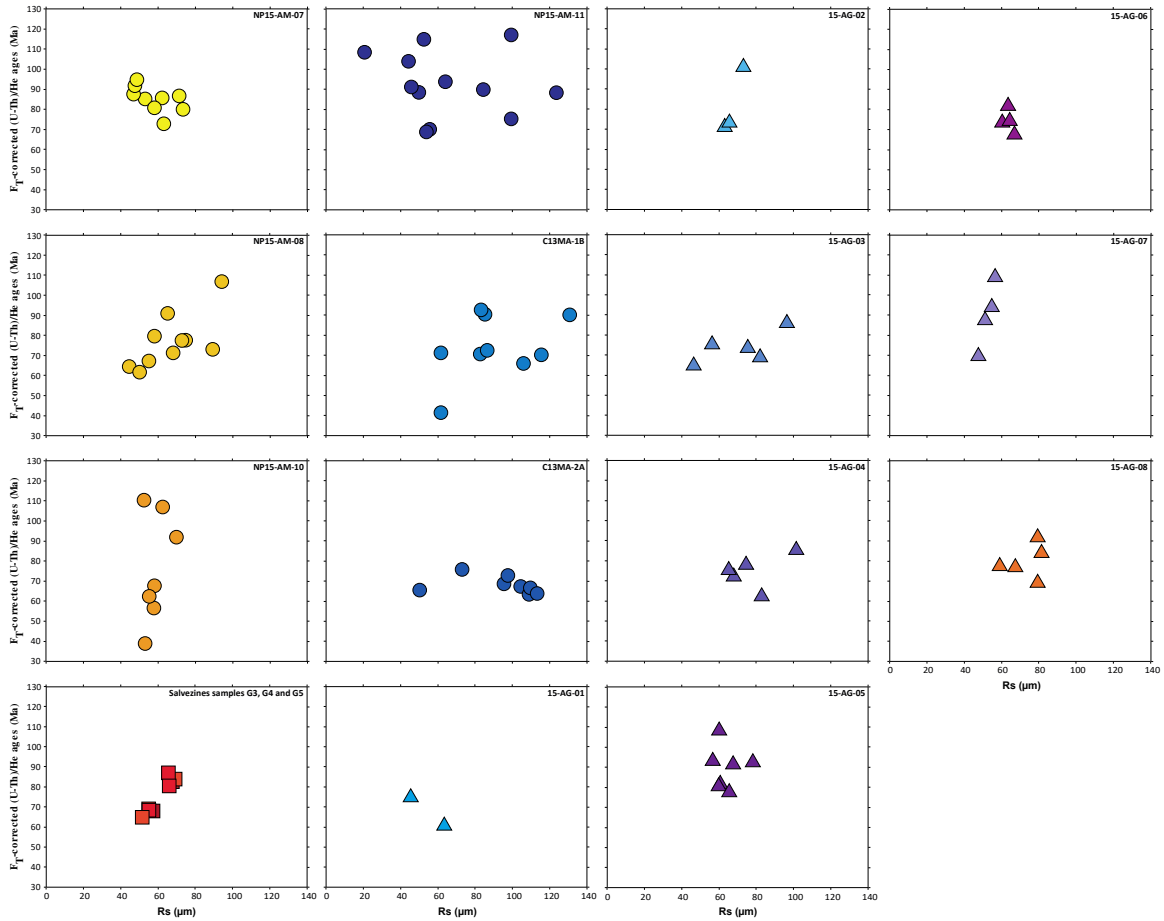

Appendix 15: Individual sample single-grain zircon (U-Th)/He age data (Ma) plotted against the equivalent spherical radius, Rs (µm). Only data for Salvezines samples are plotted together. As an estimate of the radius of a sphere with an equivalent surface-to-volume ratio, Rs is an approximation of grain size. No clear, systematically increasing trends between age and grain size are observed, suggesting grain size alone cannot explain the age variability in the Agly-Salvezines dataset. For better comparison, note that the scale of both axes is kept constant.

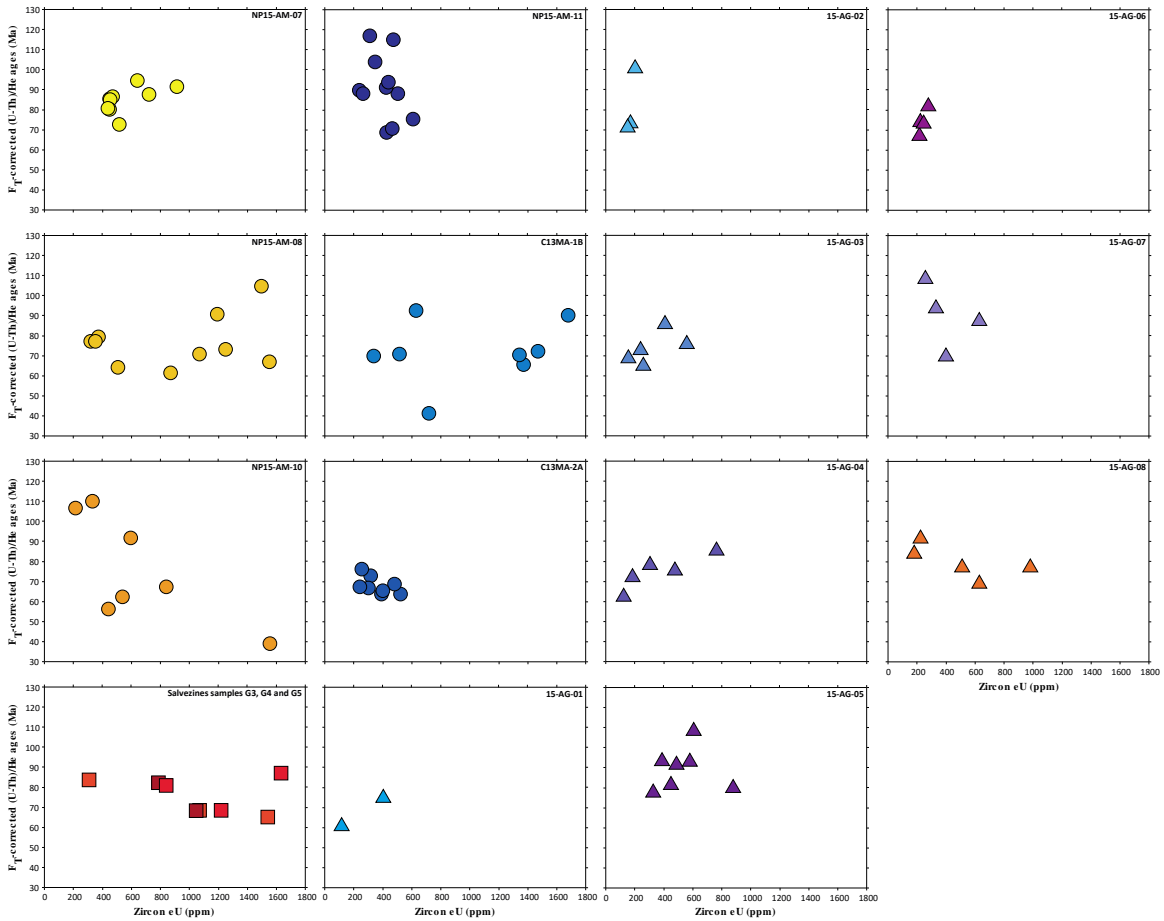

Appendix 16: Individual sample single-grain zircon (U-Th)/He age data (Ma) plotted against the bulk effective uranium concentration, eU (ppm). Only data for Salvezines samples are plotted together. Bulk eU is calculated for each grain as the concentration of the two main contributors to alpha particle production, U and Th. As a proxy for the production rate of alpha particles, eU is a measurement proportional to radiation damage. Age-eU correlations (positive or negative), albeit not straight, are observed for most samples. Grain size and zoning (not measured) are likely sources for second order age variation. For better comparison, note that the scale of both axes is kept constant.

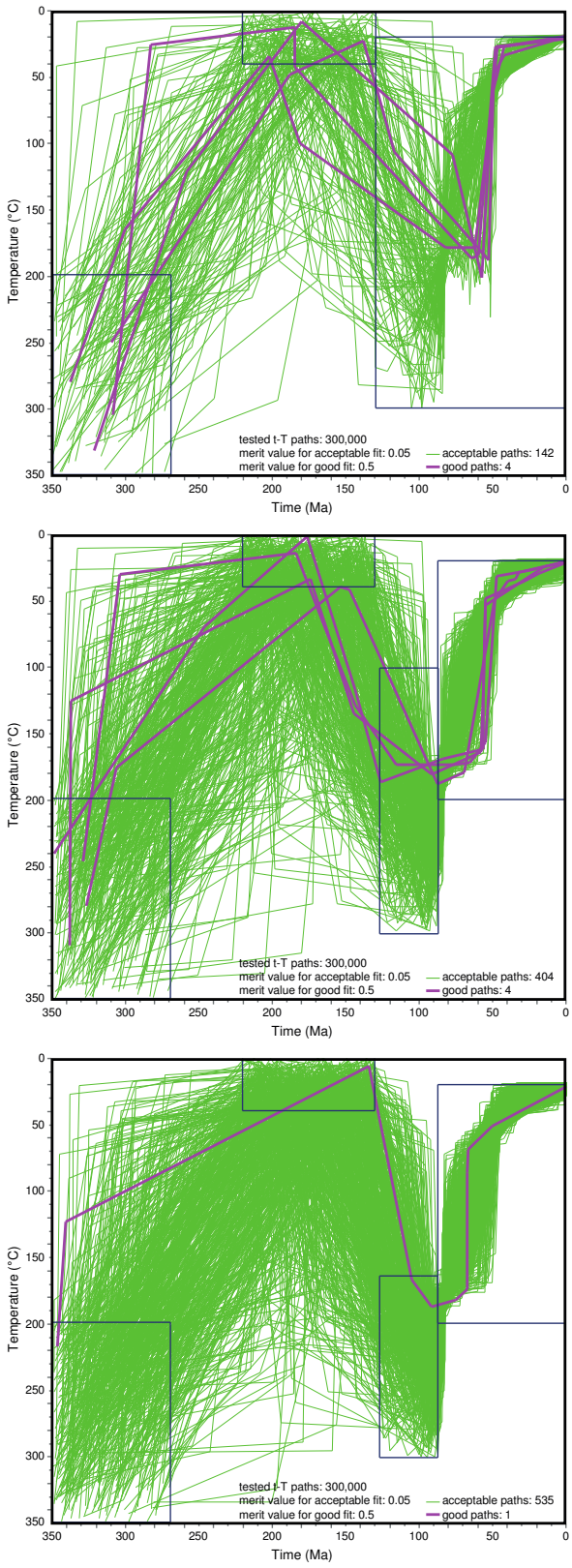

Appendix 17: Inverse modelling results for Agly-Salvezines ZHe and AHe data depicted as individual t-T paths. Purple paths indicate good fit to the data (GOF values >0.5) while green paths represents acceptable paths (GOF values >0.05). Inverse modelling inputs and constraints are reported in Appendix 21. From top to bottom (simulations #1 to #3), we constrained the software to search t-T paths incorporating an increasing number of thermal constraints during the Cretaceous. This aimed to test the hypothesis that background temperatures in Agly-Salvezines were as high as 350 °C during the HT/albitization event.

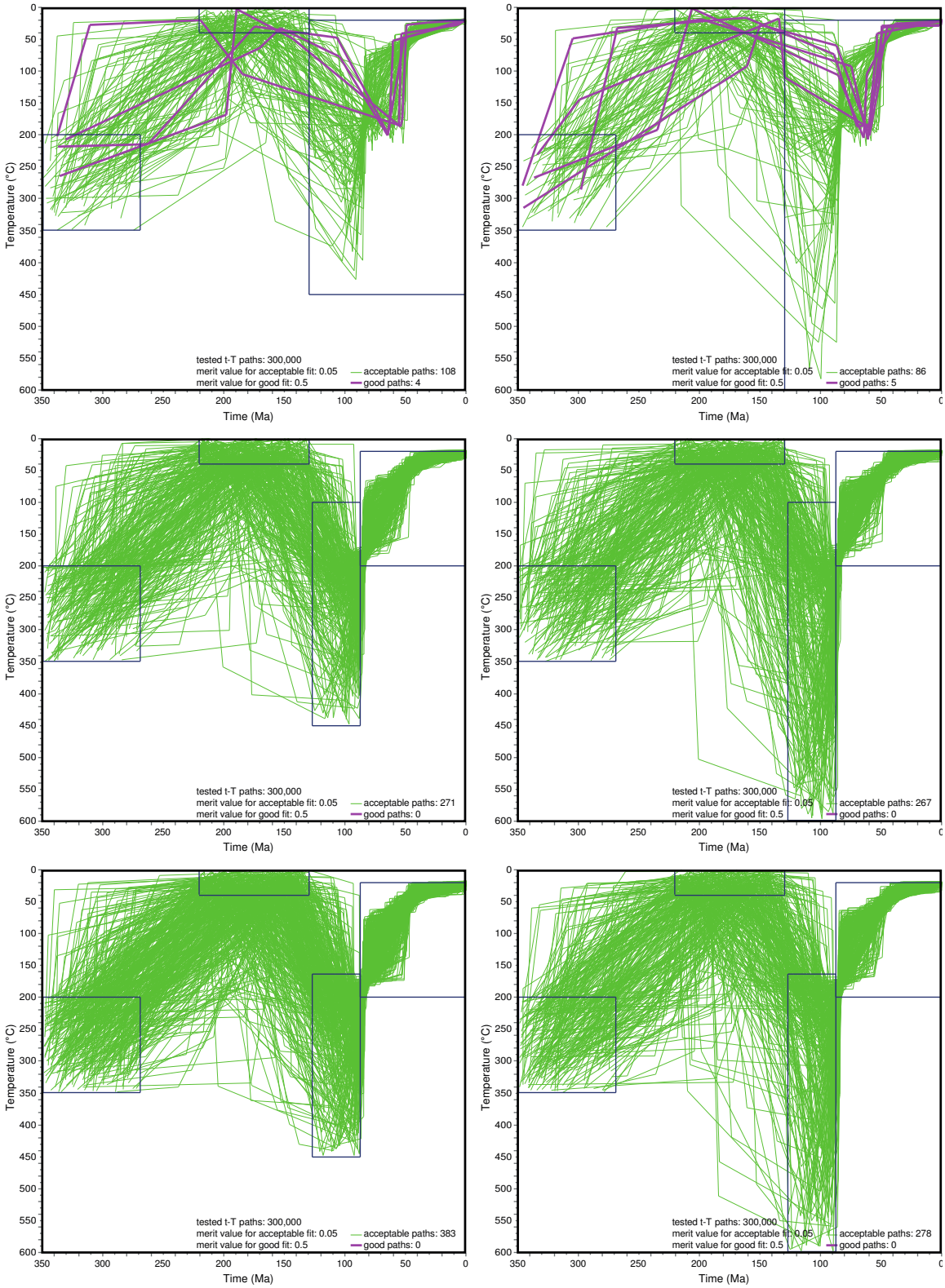

Appendix 18: Inverse modelling results for Agly-Salvezines ZHe and AHe data depicted as individual t-T paths. Purple paths indicate good fit to the data (GOF values >0.5) while green paths represents acceptable paths (GOF values >0.05). Inverse modelling inputs and constraints are reported in Appendix 21. The top two panels show the simulations #4 and #7 results while testing the hypothesis that background temperatures in Agly-Salvezines reached 450 °C (left side) or 600 °C (right side) during the HT/albitization event. From top to bottom (simulations #4-6, left side, and #7-9, right side), we constrained the software to search t-T paths incorporating an increasing number of thermal constraints during the Cretaceous.

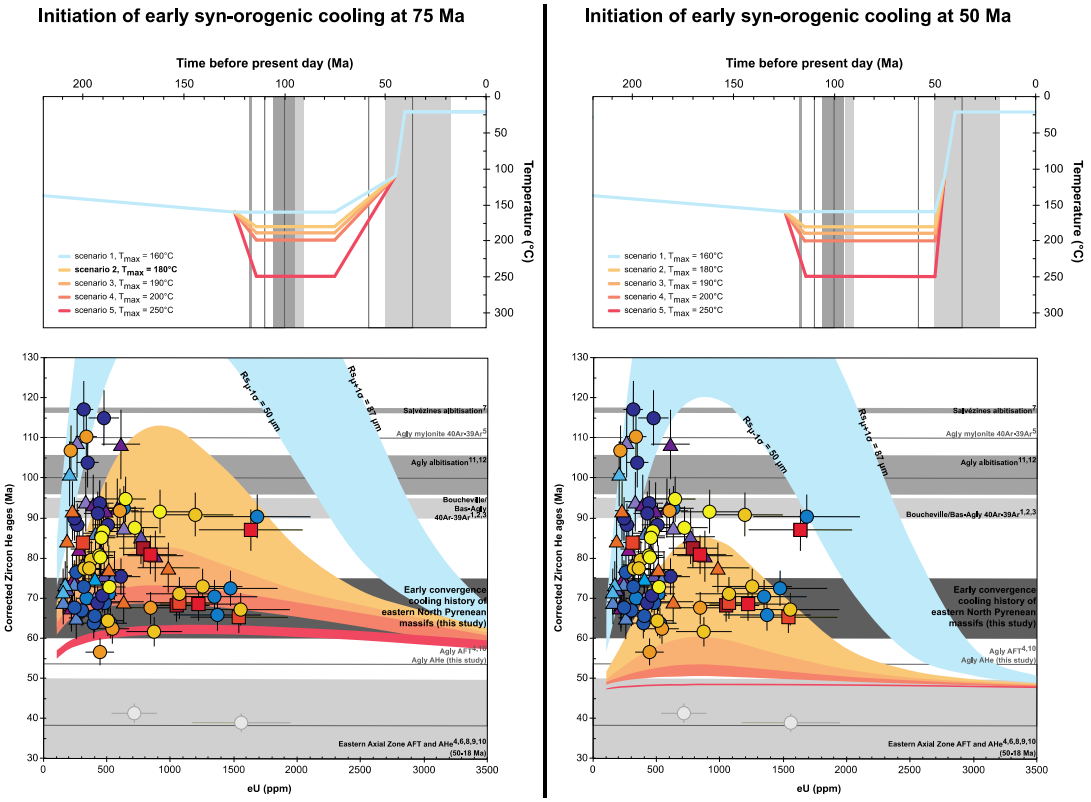

Appendix 19: Type 1 forward model results for the Agly-Salvezines dataset, assuming (i) a depth of 4 to 5 km for our samples from end Permian to early Aptian, and (ii) rapid heating during Early Cretaceous extension. See Figure V.3 for references 1-12 and Figure V.4 for description.

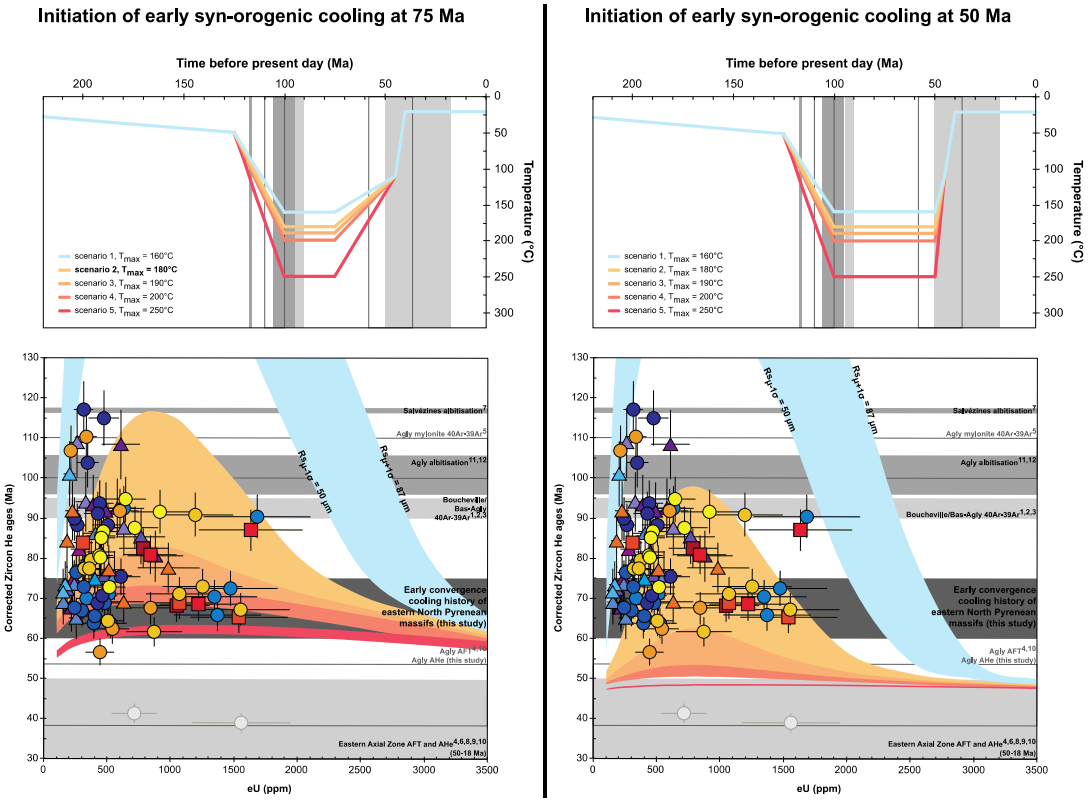

Appendix 20: Type 1 forward model results for the Agly-Salvezines dataset, assuming (i) shallow depths of our samples from end Permian to early Aptian, and (ii) slower heating than in Figure V.4 during Early Cretaceous extension. See Figure V.3 for references 1-12 and Figure V.4 for description.

1. Thermochronological data

Samples and data used in simulations

	Simulation #					All data needed for modelling published?
	Sim #0	Sim #1 to #3	Sim #4 to #6	Sim #7 to #9	Data source	
AHe data						
15-AG-03	x	x	x	x	This study, Data Set S1	yes
15-AG-06	x	x	x	x	This study, Data Set S1	yes
15-AG-08	x	x	x	x	This study, Data Set S1	yes
ZHe data						
NP15-AM-A07	x	x	x	x	This study, Data Set S1	yes
NP15-AM-A08	x	x	x	x	This study, Data Set S1	yes
NP15-AM-A10	x	x	x	x	This study, Data Set S1	yes
NP15-AM-A11	x	x	x	x	This study, Data Set S1	yes
C13MA-1B	x	x	x	x	This study, Data Set S1	yes
C13MA-2A	x	x	x	x	This study, Data Set S1	yes
15-AG-01	x	x	x	x	This study, Data Set S1	yes
15-AG-02	x	x	x	x	This study, Data Set S1	yes
15-AG-03	x	x	x	x	This study, Data Set S1	yes
15-AG-04	x	x	x	x	This study, Data Set S1	yes
15-AG-05	x	x	x	x	This study, Data Set S1	yes
15-AG-06	x	x	x	x	This study, Data Set S1	yes
15-AG-07	x	x	x	x	This study, Data Set S1	yes
15-AG-08	x	x	x	x	This study, Data Set S1	yes
AFT data						
AGLY1	x				Gunnell et al. (2009)	yes (but see section 6.1.2)
AGLY5	x				Gunnell et al. (2009)	yes (but see section 6.1.2)

Data treatment, uncertainties, and other relevant constraints

ZHe data

Treatment: After each of the individual sample datasets was attributed to either the Gp1 or Gp2 datasets (depending on sample location and rock type), they were combined as a unique ZHe dataset for Agly-Salvezines based on all their low-temperature thermochronology similarities. A 2D (FT-corrected age and eU) kernel density estimation of the data via the Parzen-Rosenblatt window method was generated (Figure 3b).

He ages (Ma): Three FT-corrected age clusters were identified. The central age of these clusters was selected.

Error (Ma) applied in modelling: The error for each cluster central age was chosen to represent the age cluster standard deviation (~2 times the 1σ analytical uncertainty for zircon ages).

r (μm): Mean equivalent spherical radius of the each age cluster.

eU (ppm): Mean eU of each age cluster.

eU zonation: None, the level of zonation for each grain was not measured and zonation is too variable to select a representative profile. A sense of zoning style is given in section 4.

AHe data

Treatment: Same reasoning to ZHe data was applied.

He ages (Ma): Two age clusters were identified. The central age of these clusters was selected.

Error (Ma) applied in modelling: The error for each cluster central age was chosen to represent the age cluster standard deviation (~2 times the 1σ analytical uncertainty for apatite ages).

r (μm): Mean equivalent spherical radius of the each age cluster.

eU (ppm): Mean eU of each age cluster.

eU zonation: None.

AFT data

ζ (CN2): 339±5

Total Ns (tr): 6266

ρd (CN5) (tr/cm2): 1.131E+06

Mean Cl (wt%): 0.204% for AGLY1 (min-max = 0.13-0.303%); 0.052% for AGLY5 (min-max = 0.035-0.061%)

Default initial mean track length: from Cl (wt%)

Track length reduction standard: 0.893

2. Additional geological information

Assumption	Explanation and data source
At surface temperature of 20°C by 0 Ma	Typical of modelling in the Pyrenees (e.g., Bosch et al., 2016; Vacherat et al., 2016; Hart et al., 2017).
Peak temperature occurred at 115-85 Ma	Assumes peak temperature was attained near the timing of HT-LP metamorphism and/or albitization.
At near-surface temperature at 220-130 Ma	Post-Variscan, major denudation of the Agly Massif by Liassic times is generally argued, most likely linked with post-orogenic thermal re-equilibration of the crust during the Permian (Delay, 1989; Berger et al., 1993, and references therein). Field data indicate that the Agly granite and gneisses were at or near the surface by the time of deposition of Triassic sediments began (Berger et al., 1993), and thus had cooled to near-surface temperatures.
Simulations begin at 350-270 Ma	The latest large-volume granitic bodies (Saint-Arnac and Salvezines in the Variscan upper crust, Ansignan at the base of the middle crust) were emplaced around 305 Ma (Olivier et al., 2004, 2008; Tournaire et al., 2018; Odlum et al., in revision).
Simulations begin at peak temperatures of 350-200°C	Is not the main focus of this study and assumes any initial temperature constraint above the partial annealing zone of 310-223°C as defined in the ZRDAAM (Guenthner et al., 2013) will not significantly affect the prediction results. Igneous zircons probably crystallized around 300±50°C (U/Pb closure temperature in zircon; Lee et al., 1997; Cherniak and Watson, 2001). Zircons with metamorphic overgrowth likely experienced T > 500°C (Carboniferous HT-LP metamorphism; e.g., Andrieux, 1982).

3. System- and model-specific parameters

He kinetic model: RDAAM for AHe (Flowers et al., 2009); ZRDAAM for ZHe (Guenthner et al., 2013)

FT annealing model: multicompositional (Ketcham et al., 2007)

FT c-axis projection: 5.0M (Ketcham et al., 2007)

FT GOF method: Kuiper's statistic

FT calibration mode: IKCH 2015

FT Uncertainty mode: 1.5E

FT kinetic parameter: Cl (wt%)

Statistical fitting criteria: Default HeFTy values. GOF values > 0.5 are good fits. GOF values > 0.05 are acceptable fits.

Modelling Code: HeFTy v1.9.2

Number of t-T paths attempted: 300,000 for all simulations.

t-T path characteristics: Episodic history with 3 to 4 defined linear segments (monotonic consistent path between constraints, episodic randomizer style, maximum dT/dt non imposed). The first segments (old geological time periods) can be halved once, the last one (up to present day) twice. Heating only allowed from 220 Ma to 85 Ma.

Appendix 21: Thermal history model input table for inverse modelling simulations of the Agly-Salvezines ZHe and AHe data, following the communication recommendations of Flowers et al. (2015). Simulation #0 is the simulation for which the HeFTy software failed to return any solutions using all the thermochronological contraints at disposal (ZHe, AHe and already published AFT data). Simulations #1-3 results are presented in Appendix 17. SImulations #4-9 results are presented in Appendix 18.

Sample	Latitude (decimal degrees)	Longitude (decimal degrees)	Mineral (-)	Aliquot LabID	Mass (µg)	ESR (µm)	U (ppm)	Th (ppm)	Sm (ppm)	4He (nmol/g)	eU (ppm)	FT (-)	Corrected age (Ma)	Error (1σ)	Owner (-)	Notes (-)
NP15-AM-A07	42.797596	2.520622	zircon	2	4.22	48.6	629	63	10	246.6	644	0.75	94.7	5.7	Sébastien Ternois	1σ (6%)
NP15-AM-A07	42.797596	2.520622	zircon	3	9.29	62.3	441	50	2	167.2	452	0.80	85.5	5.1	Sébastien Ternois	1σ (6%)
NP15-AM-A07	42.797596	2.520622	zircon	4	4.02	47.0	708	56	1	252.5	721	0.74	87.6	5.3	Sébastien Ternois	1σ (6%)
NP15-AM-A07	42.797596	2.520622	zircon	5	3.93	47.6	875	182	11	337.7	918	0.75	91.6	5.5	Sébastien Ternois	1σ (6%)
NP15-AM-A07	42.797596	2.520622	zircon	6	11.24	71.4	461	48	2	182.9	472	0.83	86.6	5.2	Sébastien Ternois	1σ (6%)
NP15-AM-A07	42.797596	2.520622	zircon	7	8.81	63.3	495	97	0	163.6	517	0.81	72.8	4.4	Sébastien Ternois	1σ (6%)
NP15-AM-A07	42.797596	2.520622	zircon	8	6.84	58.2	427	43	0	150.3	438	0.79	80.7	4.8	Sébastien Ternois	1σ (6%)
NP15-AM-A07	42.797596	2.520622	zircon	10	4.29	53.2	437	69	8	162.4	453	0.78	85.1	5.1	Sébastien Ternois	1σ (6%)
NP15-AM-A07	42.797596	2.520622	zircon	11	17.71	73.4	437	53	3	160.9	449	0.83	80.2	4.8	Sébastien Ternois	1σ (6%)
NP15-AM-A08	42.794266	2.542533	zircon	1	9.13	65.4	1148	201	0	475.8	1195	0.81	90.8	5.5	Sébastien Ternois	1σ (6%)
NP15-AM-A08	42.794266	2.542533	zircon	2	6.51	58.2	350	103	0	126.9	375	0.79	79.5	4.8	Sébastien Ternois	1σ (6%)
NP15-AM-A08	42.794266	2.542533	zircon	3	17.09	73.0	294	112	0	110.5	320	0.83	77.4	4.6	Sébastien Ternois	1σ (6%)
NP15-AM-A08	42.794266	2.542533	zircon	4	20.20	74.7	327	121	1	123.4	356	0.83	77.4	4.6	Sébastien Ternois	1σ (6%)
NP15-AM-A08	42.794266	2.542533	zircon	5	6.46	55.3	1406	628	8	437.1	1554	0.78	67.2	4.0	Sébastien Ternois	1σ (6%)
NP15-AM-A08	42.794266	2.542533	zircon	7	4.18	50.1	644	977	14	219.1	873	0.75	61.7	3.7	Sébastien Ternois	1σ (6%)
NP15-AM-A08	42.794266	2.542533	zircon	8	3.06	44.6	479	116	0	128.3	507	0.73	64.4	3.9	Sébastien Ternois	1σ (6%)
NP15-AM-A08	42.794266	2.542533	zircon	9	12.84	68.2	1005	282	1	335.2	1071	0.82	71.1	4.3	Sébastien Ternois	1σ (6%)
NP15-AM-A08	42.794266	2.542533	zircon	10	33.08	89.4	1049	867	15	422.0	1253	0.86	72.9	4.4	Sébastien Ternois	1σ (6%)
NP15-AM-A10	42.767838	2.561394	zircon	3	5.75	53.2	1399	679	46	251.6	1559	0.77	39.0	2.3	Sébastien Ternois	1σ (6%) Outlier
NP15-AM-A10	42.767838	2.561394	zircon	4	8.03	57.9	412	136	4	106.4	444	0.79	56.6	3.4	Sébastien Ternois	1σ (6%)
NP15-AM-A10	42.767838	2.561394	zircon	5	5.68	55.2	510	133	11	141.9	542	0.78	62.4	3.7	Sébastien Ternois	1σ (6%)
NP15-AM-A10	42.767838	2.561394	zircon	6	10.46	58.3	810	147	1	242.0	845	0.79	67.6	4.1	Sébastien Ternois	1σ (6%)
NP15-AM-A10	42.767838	2.561394	zircon	7	5.17	52.8	311	96	0	152.5	334	0.77	110.2	6.6	Sébastien Ternois	1σ (6%)
NP15-AM-A10	42.767838	2.561394	zircon	9	12.04	69.9	567	142	15	244.2	600	0.82	91.8	5.5	Sébastien Ternois	1σ (6%)
NP15-AM-A10	42.767838	2.561394	zircon	10	8.05	62.5	193	85	1	98.7	213	0.80	106.8	6.4	Sébastien Ternois	1σ (6%)
NP15-AM-A11	42.752033	2.578824	zircon	10	3.33	44.3	316	128	2	140.5	346	0.72	103.9	6.2	Sébastien Ternois	1σ (6%)
NP15-AM-A11	42.752033	2.578824	zircon	12	64.68	123.6	242	93	5	112.5	264	0.90	88.3	5.3	Sébastien Ternois	1σ (6%)
NP15-AM-A11	42.752033	2.578824	zircon	13	36.84	99.4	265	206	16	172.5	313	0.87	117.1	7.0	Sébastien Ternois	1σ (6%)
NP15-AM-A11	42.752033	2.578824	zircon	14	5.19	49.8	497	34	0	181.3	505	0.75	88.3	5.3	Sébastien Ternois	1σ (6%)
NP15-AM-A11	42.752033	2.578824	zircon	15	9.34	64.0	423	72	6	179.6	440	0.81	93.7	5.6	Sébastien Ternois	1σ (6%)
NP15-AM-A11	42.752033	2.578824	zircon	16	4.00	45.7	416	37	3	153.1	425	0.73	91.2	5.5	Sébastien Ternois	1σ (6%)
NP15-AM-A11	42.752033	2.578824	zircon	17	4.87	52.2	443	128	3	224.7	473	0.77	115.0	6.9	Sébastien Ternois	1σ (6%)
NP15-AM-A11	42.752033	2.578824	zircon	18	21.02	84.3	229	49	3	99.3	241	0.85	89.8	5.4	Sébastien Ternois	1σ (6%)
NP15-AM-A11	42.752033	2.578824	zircon	19	4.96	53.8	416	48	0	122.9	427	0.78	68.8	4.1	Sébastien Ternois	1σ (6%)
NP15-AM-A11	42.752033	2.578824	zircon	20	31.61	99.5	605	24	2	217.1	610	0.88	75.4	4.5	Sébastien Ternois	1σ (6%)
NP15-AM-A11	42.752033	2.578824	zircon	21	5.37	55.5	456	40	3	138.8	465	0.78	70.7	4.2	Sébastien Ternois	1σ (6%)
C13MA-1B	42.743465	2.638568	zircon	A	26.49	85.2	1614	293	25	698.4	1683	0.85	90.4	5.4	Vincent Bernard/Sébastien Ternois	1σ (6%)
C13MA-1B	42.743465	2.638568	zircon	C	36.92	105.9	1352	87	8	430.3	1372	0.88	65.9	4.0	Vincent Bernard/Sébastien Ternois	1σ (6%)
C13MA-1B	42.743465	2.638568	zircon	1	28.17	86.5	1431	188	8	492.1	1475	0.85	72.5	4.3	Sébastien Ternois	1σ (6%)
C13MA-1B	42.743465	2.638568	zircon	3	7.30	61.7	500	65	3	158.8	515	0.80	71.1	4.3	Sébastien Ternois	1σ (6%)
C13MA-1B	42.743465	2.638568	zircon	4	22.02	83.1	594	166	11	267.3	633	0.85	92.4	5.5	Sébastien Ternois	1σ (6%)
C13MA-1B	42.743465	2.638568	zircon	5	7.41	61.7	691	101	14	127.9	715	0.80	41.3	2.5	Sébastien Ternois	1σ (6%) Outlier
C13MA-1B	42.743465	2.638568	zircon	9	48.60	115.4	332	27	2	113.9	338	0.89	70.0	4.2	Sébastien Ternois	1σ (6%)
C13MA-1B	42.743465	2.638568	zircon	10	26.92	82.6	1313	145	7	432.7	1347	0.85	70.4	4.2	Sébastien Ternois	1σ (6%)
C13MA-2A	42.728971	2.599332	zircon	A	34.54	95.4	466	61	11	154.7	481	0.87	68.8	4.1	Vincent Bernard/Sébastien Ternois	1σ (6%)
C13MA-2A	42.728971	2.599332	zircon	B	44.42	108.8	370	102	14	119.9	394	0.88	63.8	3.8	Vincent Bernard/Sébastien Ternois	1σ (6%)
C13MA-2A	42.728971	2.599332	zircon	C	46.24	113.2	512	56	4	160.7	525	0.89	63.8	3.8	Vincent Bernard/Sébastien Ternois	1σ (6%)
C13MA-2A	42.728971	2.599332	zircon	1	42.11	109.7	297	24	0	96.9	303	0.89	67.0	4.0	Sébastien Ternois	1σ (6%)
C13MA-2A	42.728971	2.599332	zircon	2	15.63	73.0	243	56	0	87.4	256	0.83	76.4	4.6	Sébastien Ternois	1σ (6%)
C13MA-2A	42.728971	2.599332	zircon	3	34.79	97.6	309	30	3	108.0	316	0.87	72.9	4.4	Sébastien Ternois	1σ (6%)
C13MA-2A	42.728971	2.599332	zircon	4	37.92	104.4	238	19	2	77.7	242	0.88	67.5	4.1	Sébastien Ternois	1σ (6%)
C13MA-2A	42.728971	2.599332	zircon	8	4.06	50.3	393	38	6	108.1	402	0.76	65.5	3.9	Sébastien Ternois	1σ (6%)
G3	42.781383	2.296808	zircon	4	10.44	69.0	304	21	6	114.7	309	0.82	83.8	5.0	Arnaud Vacherat/Sébastien Ternois	1σ (6%)
G3	42.781383	2.296808	zircon	5	12.00	51.5	1439	430	31	427.9	1541	0.79	65.2	3.9	Arnaud Vacherat/Sébastien Ternois	1σ (6%)
G3	42.781383	2.296808	zircon	6	9.30	55.0	1060	43	10	317.3	1070	0.80	68.9	4.1	Arnaud Vacherat/Sébastien Ternois	1σ (6%)
G4	42.783850	2.299086	zircon	4	9.05	66.4	765	325	21	300.9	841	0.82	80.9	4.9	Arnaud Vacherat/Sébastien Ternois	1σ (6%)
G4	42.783850	2.299086	zircon	5	9.49	54.9	1091	549	54	361.3	1220	0.80	68.5	4.1	Arnaud Vacherat/Sébastien Ternois	1σ (6%)
G4	42.783850	2.299086	zircon	6	4.57	65.5	1312	1367	130	577.1	1633	0.75	87.1	5.2	Arnaud Vacherat/Sébastien Ternois	1σ (6%)
G5	42.780272	2.305992	zircon	5	9.52	67.5	764	99	14	286.3	787	0.82	82.5	4.9	Arnaud Vacherat/Sébastien Ternois	1σ (6%)
G5	42.780272	2.305992	zircon	6	24.26	57.5	1012	149	8	324.1	1047	0.84	68.2	4.1	Arnaud Vacherat/Sébastien Ternois	1σ (6%)
15-AG-01	42.721985	2.647460	zircon	2	12.05	63.5	107	44	1	31.3	117	0.81	60.7	2.4	Margaret Odlum	1σ (4%)
15-AG-01	42.721985	2.647460	zircon	4	4.72	45.3	398	30	8	123.1	405	0.75	74.8	3.0	Margaret Odlum	1σ (4%)
15-AG-02	42.717569	2.623752	zircon	1	11.43	65.6	169	15	1	56.3	172	0.82	73.4	2.9	Margaret Odlum	1σ (4%)
15-AG-02	42.717569	2.623752	zircon	4	17.79	73.1	184	78	11	92.7	202	0.84	101.0	4.0	Margaret Odlum	1σ (4%)
15-AG-02	42.717569	2.623752	zircon	7	12.19	63.9	147	24	2	48.2	152	0.82	71.6	2.9	Margaret Odlum	1σ (4%)
15-AG-03	42.725274	2.598257	zircon	1	4.56	46.4	235	107	3	68.5	260	0.75	65.0	2.6	Margaret Odlum	1σ (4%)
15-AG-03	42.725274	2.598257	zircon	13	43.23	96.4	381	113	2	166.7	407	0.87	86.2	3.4	Margaret Odlum	1σ (4%)
15-AG-03	42.725274	2.598257	zircon	14	19.90	75.5	218	94	3	80.5	240	0.84	73.5	2.9	Margaret Odlum	1σ (4%)
15-AG-03	42.725274	2.598257	zircon	16	8.04	56.3	507	218	3	180.6	558	0.79	75.6	3.0	Margaret Odlum	1σ (4%)
15-AG-03	42.725274	2.598257	zircon	28	23.36	81.9	146	46	2	50.0	157	0.85	69.0	2.8	Margaret Odlum	1σ (4%)
15-AG-04	42.731801	2.576429	zircon	1	45.96	101.3	758	37	1	313.3	766	0.88	85.4	3.4	Margaret Odlum	1σ (4%)
15-AG-04	42.731801	2.576429	zircon	18	14.25	67.8	180	29	2	60.4	187	0.83	72.3	2.9	Margaret Odlum	1σ (4%)
15-AG-04	42.731801	2.576429	zircon	19	11.96	65.1	472	31	1	161.4	479	0.82	75.7	3.0	Margaret Odlum	1σ (4%)
15-AG-04	42.731801	2.576429	zircon	20	24.86	82.9	122	20	1	36.6	126	0.86	62.4	2.5	Margaret Odlum	1σ (4%)
15-AG-04	42.731801	2.576429	zircon	35	20.25	74.5	299	35	4	109.7	307	0.84	78.3	3.1	Margaret Odlum	1σ (4%)
15-AG-05A	42.752549	2.510177	zircon	1	14.37	67.7	454	149	28	200.8	489	0.82	91.7	3.7	Margaret Odlum	1σ (4%)
15-AG-05A	42.752549	2.510177	zircon	2	9.94	60.3	427	101	3	160.5	451	0.81	81.5	3.3	Margaret Odlum	1σ (4%)
15-AG-05A	42.752549	2.510177	zircon	3	8.56	56.6	377	56	2	157.2	390	0.80	93.4	3.7	Margaret Odlum	1σ (4%)
15-AG-05A	42.752549	2.510177	zircon	4	9.85	60.2	595	50	2	288.4	607	0.81	108.4	4.3	Margaret Odlum	1σ (4%)
15-AG-05A	42.752549	2.510177	zircon	5	11.76	65.5	318	38	1	113.0	326	0.82	77.8	3.1	Margaret Odlum	1σ (4%)
15-AG-05B	42.754946	2.509743	zircon	1	10.17	59.9	860	82	2	309.5	879	0.81	80.5	3.2	Margaret Odlum	1σ (4%)
15-AG-05B	42.754946	2.509743	zircon	2	22.52	78.0	568	57	7	247.9	582	0.85	92.5	3.7	Margaret Odlum	1σ (4%)
15-AG-06	42.770559	2.513623	zircon	15	11.26	64.4	221	22	1	74.6	226	0.82	74.4	3.0	Margaret Odlum	1σ (4%)
15-AG-06	42.770559	2.513623	zircon	16	10.81	63.4	268	53	2	101.8	280	0.82	82.2	3.3	Margaret Odlum	1σ (4%)
15-AG-06	42.770559	2.513623	zircon	17	12.73	66.2	214	16	1	65.8	218	0.82	67.6	2.7	Margaret Odlum	1σ (4%)
15-AG-06	42.770559	2.513623	zircon	18	9.11	60.4	242	17	0	79.5	246	0.81	73.8	3.0	Margaret Odlum	1σ (4%)
15-AG-06	42.770559	2.513623	zircon	2	7.41	53.9	212	23	1	63.3	217	0.79	68.4	2.7	Margaret Odlum	1σ (4%)
15-AG-07	42.775400	2.521001	zircon	1	5.85	51.1	577	225	4	230.7	630	0.77	87.6	3.5	Margaret Odlum	1σ (4%)
15-AG-07	42.775400	2.521001	zircon	2	7.33	56.4	244	72	4	122.2	261	0.79	108.8	4.4	Margaret Odlum	1σ (4%)
15-AG-07	42.775400	2.521001	zircon	3	4.65	47.4	381	81	3	115.0	400	0.76	70.0	2.8	Margaret Odlum	1σ (4%)
15-AG-07	42.775400	2.521001	zircon	5	7.27	54.8	314	75	6	133.3	332	0.79	94.1	3.8	Margaret Odlum	1σ (4%)
15-AG-08	42.796609	2.501499	zircon	1	27.15	81.3	172	44	1	71.2	183	0.85	84.2	3.4	Margaret Odlum	1σ (4%)
15-AG-08	42.796609	2.501499	zircon	2	21.25	79.2	592	168	4	200.7	631	0.85	69.1	2.8	Margaret Odlum	1σ (4%)
15-AG-08	42.796609	2.501499	zircon	3	23.15	79.1	209	70	2	95.2	225	0.85	91.8	3.7	Margaret Odlum	1σ (4%)
15-AG-08	42.796609	2.501499	zircon	4	11.21	59.0	944	171	4	332.0	984	0.80	77.6	3.1	Margaret Odlum	1σ (4%)
15-AG-08	42.796609	2.501499	zircon	5	14.23	67.3	478	143	3	176.3	512	0.82	77.1	3.1	Margaret Odlum	1σ (4%)
15-AG-03	42.725274	2.598257	apatite	2	4.74	56.9	49	0	314	11.5	51	0.75	55.0	1.6	Margaret Odlum	1σ (3%)
15-AG-03	42.725274	2.598257	apatite	3	8.31	67.2	59	0	289	12.1	61	0.78	46.1	1.4	Margaret Odlum	1σ (3%)
15-AG-06	42.796609	2.501499	apatite	1	14.22	84.3	7	0	18	1.2	7	0.83	40.1	1.2	Margaret Odlum	1σ (3%)
15-AG-06	42.796609	2.501499	apatite	2	24.15	96.3	7	0	18	1.5	8	0.85	43.0	1.3	Margaret Odlum	1σ (3%)
15-AG-08	42.796609	2.501499	apatite	2	3.36	50.0	13	11	226	3.0	17	0.70	44.1	1.3	Margaret Odlum	1σ (3%)
15-AG-08	42.796609	2.501499	apatite	3	4.25	56.9	11	5	223	2.5	13	0.74	45.5	1.4	Margaret Odlum	1σ (3%)

Appendix 22: Dataset that contains the reduced (U-Th)/He data for all analyses performed for the Agly-Salvezines area. Data is formatted in an Excel .xls file format and plotted in Figure V.3.

ADDITIONAL SUPPORTING INFORMATION (CHAPTER 6)

Appendix 23: Detrital zircon (U-Th)/He data for sample B1.

Grain #	V (µm3)	+/- 2σ	4He (mol)	Corrected 4He (mol)	+/- 2σ	4He (mol/g)	Corrected4He (mol/g)	+/- 2σ	232Th (ppm)	+/- 2σ	238U (ppm)	+/- 2σ	147Sm (ppm)	+/- 2σ	eU	Th/U	ZHe age (Ma)	+/- 2σ
B1b1-1	10413	521	8.04E-15	5.36E-15	1.96E-16	1.66E-07	1.11E-07	9.23E-09	33	1	111	2	0	0	118	0.30	260.2	15.1
B1b1-2	10422	521	2.34E-14	1.56E-14	5.88E-16	4.84E-07	3.23E-07	2.71E-08	122	2	294	5	0	0	323	0.41	277.8	16.0
B1b1-4	10440	522	1.03E-14	6.85E-15	3.50E-16	2.12E-07	1.41E-07	1.28E-08	119	1	206	2	15	0	234	0.58	167.7	10.3
B1b1-5	10449	522	1.01E-14	6.76E-15	3.83E-16	2.09E-07	1.39E-07	1.31E-08	87	3	107	3	4	0	128	0.81	303.3	20.0
B1b1-6	10457	523	1.60E-14	1.07E-14	4.06E-16	3.30E-07	2.20E-07	1.85E-08	72	2	214	4	0	0	231	0.34	264.9	15.4
B1b1-7	10511	526	2.04E-14	1.36E-14	3.45E-16	4.18E-07	2.79E-07	2.21E-08	609	10	262	4	5	0	406	2.32	190.6	10.3
B1b1-8	10599	530	2.37E-14	1.58E-14	4.18E-16	4.81E-07	3.21E-07	2.55E-08	< LOD	4	442	9	6	0	-	-	-	-
B1b1-9	10617	531	3.74E-14	2.49E-14	6.92E-16	7.58E-07	5.05E-07	4.04E-08	335	25	1451	64	11	1	1530	0.23	92.0	6.2
B1b1-10	10626	531	8.69E-15	5.80E-15	2.75E-16	1.76E-07	1.17E-07	1.04E-08	< LOD	5	507	10	< LOD	0	-	-	-	-
B1b1-11	10635	532	5.62E-15	3.75E-15	2.47E-16	1.14E-07	7.58E-08	7.57E-09	47	1	< LOD	2	< LOD	0	-	-	-	-
B1b1-12	10644	532	2.03E-14	1.35E-14	3.66E-16	4.10E-07	2.73E-07	2.18E-08	124	6	735	31	5	0	764	0.17	99.6	6.7
B1b1-13	10662	533	8.87E-15	5.91E-15	1.63E-16	1.79E-07	1.19E-07	9.53E-09	< LOD	1	< LOD	2	< LOD	0	-	-	-	-
B1b1-14	10670	534	3.50E-14	2.33E-14	5.76E-16	7.05E-07	4.70E-07	3.71E-08	338	5	590	9	5	0	670	0.57	195.3	10.6
B1b1-15	10679	534	2.25E-14	1.50E-14	4.28E-16	4.52E-07	3.02E-07	2.42E-08	85	2	227	4	6	0	247	0.37	340.1	19.2
B1b1-17	10733	537	4.34E-14	2.89E-14	7.10E-16	8.69E-07	5.79E-07	4.57E-08	271	17	1032	61	51	5	1096	0.26	147.2	11.3
B1b1-18	10741	537	3.39E-14	2.26E-14	4.72E-16	6.78E-07	4.52E-07	3.52E-08	214	4	352	6	7	0	402	0.61	312.5	16.8
B1b1-19	10946	547	2.52E-15	1.68E-15	1.85E-16	4.95E-08	3.30E-08	4.40E-09	16	0	26	1	0	0	30	0.61	-	
B1b1-20	10954	548	6.97E-15	4.65E-15	2.16E-16	1.37E-07	9.13E-08	8.05E-09	202	23	363	25	26	5	410	0.56	61.8	5.3
B1b1-21	10466	523	1.82E-14	1.22E-14	3.73E-16	3.74E-07	2.50E-07	2.02E-08	150	10	207	6	0	0	242	0.72	286.7	17.0
B1b1-23	10484	524	4.69E-14	3.13E-14	5.39E-16	9.62E-07	6.42E-07	4.94E-08	307	5	512	8	7	0	584	0.60	305.3	16.2
B1b1-24	10493	525	6.56E-15	4.37E-15	3.28E-16	1.34E-07	8.96E-08	9.51E-09	71	2	75	2	6	0	92	0.95	271.6	19.8
B1b1-25	10502	525	5.96E-14	3.97E-14	7.34E-16	1.22E-06	8.13E-07	6.28E-08	358	11	732	17	14	1	816	0.49	277.3	15.4
B1b1-26	10520	526	1.77E-14	1.18E-14	3.76E-16	3.62E-07	2.41E-07	1.97E-08	89	2	675	10	3	0	696	0.13	96.5	5.4
B1b1-27	10528	526	1.14E-14	7.57E-15	3.21E-16	2.32E-07	1.55E-07	1.33E-08	63	2	100	2	4	0	115	0.63	375.6	23.0
B1b1-28	10537	527	2.24E-14	1.49E-14	4.39E-16	4.57E-07	3.05E-07	2.45E-08	2450	270	972	18	428	53	1548	2.52	54.6	3.8
B1b1-29	10546	527	5.64E-15	3.76E-15	3.35E-16	1.15E-07	7.67E-08	8.92E-09	70	2	< LOD	2	9	0	-	-	-	-
B1b1-30	10555	528	1.63E-14	1.09E-14	2.70E-16	3.33E-07	2.22E-07	1.75E-08	157	3	894	15	4	0	931	0.18	66.4	3.7

B1b1-31	10564	528	3.34E-14	2.23E-14	5.70E-16	6.80E-07	4.54E-07	3.59E-08	276	12	360	10	9	1	425	0.77	296.9	17.3
B1b1-32	10573	529	3.12E-14	2.08E-14	4.40E-16	6.34E-07	4.22E-07	3.29E-08	324	5	305	5	5	0	381	1.06	308.4	16.5
B1b1-33	10582	529	1.11E-14	7.37E-15	2.20E-16	2.25E-07	1.50E-07	1.21E-08	61	4	118	6	51	5	133	0.51	314.2	22.5
B1b1-34	10591	530	3.34E-14	2.23E-14	6.17E-16	6.78E-07	4.52E-07	3.61E-08	533	16	738	13	27	2	863	0.72	145.6	8.1
B1b1-35	10608	530	1.22E-14	8.14E-15	2.49E-16	2.48E-07	1.65E-07	1.34E-08	168	3	120	2	20	1	159	1.40	287.6	16.1
B1b1-37	10688	534	8.57E-15	5.71E-15	2.60E-16	1.72E-07	1.15E-07	1.01E-08	179	3	66	1	6	0	108	2.70	-	
B1b1-38	10706	535	1.14E-14	7.58E-15	2.90E-16	2.28E-07	1.52E-07	1.28E-08	75	1	161	3	0	0	178	0.47	237.8	13.9
B1b1-39	10715	536	4.05E-14	2.70E-14	5.58E-16	8.13E-07	5.42E-07	4.22E-08	231	4	722	15	5	0	776	0.32	194.3	10.8
B1b1-40	10724	536	1.99E-14	1.32E-14	3.62E-16	3.98E-07	2.66E-07	2.12E-08	68	1	1029	17	3	0	1045	0.07	70.8	3.9
B1b1-41	10750	538	1.78E-14	1.19E-14	3.78E-16	3.57E-07	2.38E-07	1.94E-08	123	3	< LOD	4	3	0	-	-	-	-
B1b1-42	10759	538	1.86E-13	1.24E-13	2.02E-15	3.71E-06	2.47E-06	1.90E-07	NA	NA	NA	NA	NA	NA	-	-	-	-
B1b1-43	10768	538	5.14E-14	3.42E-14	6.36E-16	1.03E-06	6.84E-07	5.28E-08	284	6	< LOD	6	< LOD	0	-	-	-	-
B1b1-44	10777	539	3.42E-14	2.28E-14	5.12E-16	6.82E-07	4.55E-07	3.56E-08	132	2	394	7	2	0	425	0.33	297.6	16.3
B1b1-45	10786	539	8.30E-15	5.53E-15	2.30E-16	1.65E-07	1.10E-07	9.46E-09	102	2	75	2	4	0	99	1.37	310.5	18.5
B1b1-46	10795	540	1.35E-14	9.03E-15	4.27E-16	2.70E-07	1.80E-07	1.60E-08	70	2	548	14	3	0	564	0.13	88.8	5.7
B1b1-47	10804	540	1.95E-14	1.30E-14	3.37E-16	3.88E-07	2.59E-07	2.05E-08	138	3	286	6	110	5	319	0.48	225.9	12.7
B1b1-48	10812	541	8.25E-15	5.50E-15	2.35E-16	1.64E-07	1.09E-07	9.44E-09	169	3	188	3	4	0	228	0.90	133.2	7.9
B1b1-49	10821	541	3.02E-14	2.02E-14	6.34E-16	6.01E-07	4.01E-07	3.26E-08	207	14	321	10	7	1	369	0.65	301.7	18.3
B1b1-50	10830	542	1.48E-14	9.85E-15	4.26E-16	2.94E-07	1.96E-07	1.69E-08	132	5	280	7	7	0	311	0.47	175.3	10.8
B1b1-51	10839	542	9.23E-15	6.16E-15	2.08E-16	1.83E-07	1.22E-07	1.00E-08	55	2	145	4	19	4	158	0.38	215.2	12.9
B1b1-52	10848	542	1.69E-14	1.13E-14	3.10E-16	3.35E-07	2.23E-07	1.79E-08	214	4	314	6	9	0	364	0.68	170.6	9.5
B1b1-53	10857	543	1.89E-14	1.26E-14	3.75E-16	3.74E-07	2.49E-07	2.01E-08	48	1	176	4	5	0	187	0.27	371.2	21.6
B1b1-54	10866	543	5.01E-14	3.34E-14	6.69E-16	9.91E-07	6.61E-07	5.13E-08	129	2	430	8	20	2	460	0.30	399.4	21.7
B1b1-55	10875	544	2.66E-14	1.77E-14	5.14E-16	5.26E-07	3.50E-07	2.82E-08	42	2	289	6	0	0	299	0.15	326.3	18.8

Appendix 24: Reduced detrital zircon U-Pb data for sample B1.

Grain #	Age 206/238	+/- 2σ	Age 207/235	+/- 2σ	Age 207/206	+/- 2σ	% Discordance	Selected U/Pb age (Ma)	+/- 2σ	Ratio 206/238	+/- 2σ	Ratio 207/235	+/- 2σ	Ratio 207/206	+/- 2σ
B1b1-1	501.3	8.7	515.0	22.0	520.0	120.0	3%	501.3	8.7	0.0808	0.0014	0.664	0.036	0.0575	0.0033
B1b1-2	2213.0	17.0	2236.0	13.0	2212.0	22.0	1%	2236.0	13.0	0.4093	0.0038	8.06	0.11	0.1389	0.0018
B1b1-4	1632.0	13.0	1633.0	13.0	1597.0	35.0	0%	1633.0	13.0	0.2881	0.0026	3.988	0.066	0.0988	0.0018
B1b1-5	576.0	10.0	543.0	30.0	310.0	140.0	6%	576.0	10.0	0.0936	0.0018	0.726	0.051	0.0543	0.0038
B1b1-6	522.8	7.0	527.0	16.0	498.0	93.0	1%	522.8	7.0	0.0845	0.0012	0.675	0.027	0.0576	0.0025
B1b1-7	706.0	8.5	682.0	17.0	595.0	75.0	4%	706.0	8.5	0.1158	0.0015	0.963	0.034	0.0604	0.0021
B1b1-8	2231.0	18.0	2471.0	13.0	2649.0	16.0	10%	2471.0	13.0	0.4129	0.004	10.4	0.15	0.1796	0.0017
B1b1-9	377.7	5.7	401.5	8.3	554.0	48.0	6%	377.7	5.7	0.06036	0.00094	0.485	0.012	0.059	0.0013
B1b1-10	481.0	7.4	497.0	14.0	519.0	75.0	3%	481.0	7.4	0.0774	0.0012	0.634	0.023	0.0588	0.002
B1b1-11	558.0	10.0	549.0	26.0	490.0	140.0	2%	558.0	10.0	0.0904	0.0017	0.732	0.046	0.0576	0.0037
B1b1-12	407.1	5.6	407.0	10.0	480.0	57.0	0%	407.1	5.6	0.0652	0.00092	0.491	0.016	0.0564	0.0015
B1b1-13	2125.0	25.0	2158.0	21.0	2182.0	40.0	2%	2158.0	21.0	0.3902	0.0054	7.41	0.18	0.1357	0.0032
B1b1-14	1663.0	11.0	1710.0	12.0	1744.0	22.0	3%	1710.0	12.0	0.2943	0.0023	4.394	0.064	0.1069	0.0013
B1b1-15	347.9	5.7	333.0	16.0	190.0	120.0	4%	347.9	5.7	0.05537	0.00092	0.39	0.023	0.05	0.003
B1b1-17	621.0	22.0	798.0	19.0	1332.0	38.0	22%	621.0	22.0	0.1014	0.0037	1.199	0.042	0.0862	0.0016
B1b1-18	586.5	6.3	573.0	14.0	495.0	67.0	2%	586.5	6.3	0.0953	0.0011	0.759	0.025	0.0575	0.0017
B1b1-19	1959.0	34.0	1985.0	38.0	1959.0	80.0	1%	1985.0	38.0	0.3557	0.0072	6.13	0.25	0.1223	0.0055
B1b1-20	329.0	5.7	618.0	40.0	1770.0	140.0	47%	329.0	5.7	0.05238	0.00093	0.876	0.075	0.1169	0.0087
B1b1-21	617.0	8.3	627.0	17.0	575.0	85.0	2%	617.0	8.3	0.1005	0.0014	0.853	0.032	0.0601	0.0024
B1b1-23	364.1	4.7	472.0	24.0	920.0	130.0	23%	364.1	4.7	0.05811	0.00077	0.587	0.038	0.0719	0.0045
B1b1-24	2744.0	27.0	2863.0	21.0	2938.0	31.0	4%	2863.0	21.0	0.5311	0.0066	15.78	0.33	0.2153	0.0042
B1b1-25	282.6	4.9	296.1	9.0	408.0	71.0	5%	282.6	4.9	0.04483	0.00079	0.339	0.012	0.0551	0.0018
B1b1-26	331.1	3.4	320.7	7.2	253.0	62.0	3%	331.1	3.4	0.0527	0.00056	0.3725	0.0097	0.0513	0.0015
B1b1-27	1881.0	23.0	1857.0	25.0	1846.0	41.0	1%	1857.0	25.0	0.339	0.0048	5.21	0.15	0.1136	0.0026
B1b1-28	304.7	3.3	292.9	7.0	182.0	58.0	4%	304.7	3.3	0.04841	0.00054	0.3354	0.0092	0.0498	0.0013
B1b1-29	1066.0	16.0	1081.0	24.0	1120.0	71.0	1%	1066.0	16.0	0.18	0.0029	1.925	0.068	0.0765	0.0027
B1b1-30	300.9	3.5	306.4	8.2	324.0	66.0	2%	300.9	3.5	0.04779	0.00058	0.354	0.011	0.0531	0.0016
B1b1-31	542.9	6.2	555.0	13.0	577.0	72.0	2%	542.9	6.2	0.0879	0.001	0.73	0.023	0.06	0.002
B1b1-32	2005.0	16.0	1982.0	13.0	1955.0	23.0	1%	1982.0	13.0	0.3649	0.0034	6.054	0.089	0.1202	0.0015

B1b1-33	744.0	11.0	827.0	31.0	1020.0	110.0	10%	744.0	11.0	0.1223	0.002	1.253	0.067	0.0753	0.004
B1b1-34	395.6	4.7	470.0	10.0	867.0	57.0	16%	395.6	4.7	0.0633	0.00078	0.589	0.016	0.0678	0.0019
B1b1-35	556.5	7.9	541.0	24.0	440.0	120.0	3%	556.5	7.9	0.0902	0.0013	0.697	0.041	0.0571	0.0033
B1b1-37	636.0	9.9	593.0	31.0	410.0	140.0	7%	636.0	9.9	0.1035	0.0017	0.802	0.056	0.0556	0.0039
B1b1-38	236.7	4.8	201.0	19.0	-90.0	190.0	18%	236.7	4.8	0.0374	0.00078	0.226	0.023	0.0438	0.0046
B1b1-39	239.7	3.1	239.2	7.9	242.0	80.0	0%	239.7	3.1	0.03789	0.0005	0.266	0.01	0.0511	0.0019
B1b1-40	441.7	4.1	432.1	8.5	377.0	54.0	2%	441.7	4.1	0.07086	0.00067	0.531	0.013	0.0545	0.0013
B1b1-41	782.3	9.9	788.0	19.0	765.0	72.0	1%	782.3	9.9	0.1291	0.0017	1.179	0.041	0.0654	0.0022
B1b1-42	280.7	2.8	279.4	3.2	247.0	22.0	0%	280.7	2.8	0.04451	0.00045	0.317	0.0042	0.05121	0.00048
B1b1-43	2029.0	15.0	2023.0	13.0	2022.0	19.0	0%	2023.0	13.0	0.37	0.0031	6.342	0.089	0.1245	0.0014
B1b1-44	481.4	5.8	461.0	13.0	359.0	79.0	4%	481.4	5.8	0.07755	0.00097	0.576	0.021	0.0544	0.002
B1b1-45	951.0	16.0	942.0	29.0	900.0	100.0	1%	951.0	16.0	0.1591	0.003	1.548	0.071	0.0707	0.0033
B1b1-46	358.9	4.2	355.0	11.0	331.0	77.0	1%	358.9	4.2	0.05726	0.00069	0.419	0.015	0.0537	0.0019
B1b1-47	412.1	6.0	392.0	15.0	361.0	95.0	5%	412.1	6.0	0.06603	0.00099	0.476	0.021	0.0542	0.0024
B1b1-48	672.3	8.1	647.0	21.0	558.0	98.0	4%	672.3	8.1	0.1098	0.0014	0.897	0.038	0.0585	0.0025
B1b1-49	661.6	7.4	637.0	14.0	584.0	59.0	4%	661.6	7.4	0.1081	0.0013	0.875	0.026	0.0598	0.0016
B1b1-50	248.8	4.0	253.0	13.0	300.0	120.0	2%	248.8	4.0	0.03935	0.00064	0.287	0.017	0.0535	0.0031
B1b1-51	2061.0	22.0	2096.0	20.0	2137.0	36.0	2%	2096.0	20.0	0.3771	0.0046	6.89	0.15	0.133	0.0027
B1b1-52	244.7	4.1	255.0	16.0	300.0	150.0	4%	244.7	4.1	0.0387	0.00066	0.288	0.021	0.0541	0.004
B1b1-53	506.4	8.3	526.0	25.0	630.0	120.0	4%	506.4	8.3	0.0818	0.0014	0.691	0.04	0.0625	0.0035
B1b1-54	641.8	7.5	667.0	16.0	772.0	66.0	4%	641.8	7.5	0.1047	0.0013	0.932	0.031	0.0657	0.0021
B1b1-55	591.2	8.8	572.0	16.0	528.0	74.0	3%	591.2	8.8	0.0961	0.0015	0.758	0.027	0.0586	0.002

Appendix 25: Detrital zircon (U-Th)/He data for sample B2.

Grain #	V (µm3)	+/- 2σ	4He (mol)	Corrected 4He (mol)	+/- 2σ	4He (mol/g)	Corrected 4He (mol/g)	+/- 2σ	232Th (ppm)	+/- 2σ	238U (ppm)	+/- 2σ	147Sm (ppm)	+/- 2σ	eU	Th/U	ZHe age (Ma)	+/- 2σ
B2b1-1	11096	555	5.69E-14	3.79E-14	8.95E-16	1.10E-06	7.35E-07	5.78E-08	513	70	2200	130	175	22	2321	0.23	88.2	6.8
B2b1-2	11094	555	5.46E-14	3.64E-14	8.09E-16	1.06E-06	7.06E-07	5.52E-08	644	25	970	30	63	3	1121	0.66	175.0	10.3
B2b1-4	11091	555	2.97E-14	1.98E-14	5.35E-16	5.76E-07	3.84E-07	3.06E-08	115	2	450	10	6	0	477	0.26	224.0	12.8
B2b1-5	11090	554	1.66E-14	1.11E-14	3.30E-16	3.22E-07	2.15E-07	1.73E-08	76	2	177	3	6	0	194	0.43	307.5	17.3
B2b1-7	11087	554	1.36E-14	9.05E-15	3.11E-16	2.63E-07	1.76E-07	1.45E-08	50	3	323	9	4	0	335	0.15	146.0	8.9
B2b1-8	11085	554	1.61E-14	1.07E-14	3.39E-16	3.11E-07	2.08E-07	1.69E-08	300	8	186	4	11	0	256	1.61	224.9	12.7
B2b1-10	11082	554	2.17E-14	1.44E-14	4.38E-16	4.20E-07	2.80E-07	2.27E-08	393	9	303	5	24	1	395	1.30	197.1	11.0
B2b1-11	11081	554	6.14E-14	4.10E-14	7.02E-16	1.19E-06	7.95E-07	6.11E-08	157	9	844	22	21	1	881	0.19	251.1	14.3
B2b1-15	11074	554	2.71E-14	1.81E-14	5.14E-16	5.26E-07	3.51E-07	2.81E-08	164	3	342	7	9	0	381	0.48	256.3	14.5
B2b1-16	11073	554	9.95E-15	6.64E-15	3.16E-16	1.93E-07	1.29E-07	1.14E-08	62	2	161	4	1	0	176	0.39	204.3	12.9
B2b1-19	11068	553	1.95E-14	1.30E-14	4.76E-16	3.78E-07	2.52E-07	2.10E-08	173	5	274	6	9	0	314	0.63	222.9	13.2
B2b1-20	11067	553	1.48E-14	9.90E-15	3.04E-16	2.88E-07	1.92E-07	1.56E-08	74	21	119	25	3	1	136	0.62	392.1	76.2
B2b1-24	11061	553	2.83E-14	1.89E-14	3.98E-16	5.50E-07	3.67E-07	2.86E-08	121	6	476	22	4	0	504	0.25	202.3	13.7
B2b1-25	11059	553	1.76E-14	1.18E-14	5.01E-16	3.43E-07	2.29E-07	1.97E-08	104	8	263	7	12	1	287	0.39	221.6	14.0
B2b1-26	11058	553	2.57E-14	1.71E-14	4.52E-16	5.00E-07	3.33E-07	2.65E-08	85	5	398	13	5	0	418	0.21	221.9	13.6
B2b1-27	11056	553	7.06E-15	4.70E-15	2.08E-16	1.37E-07	9.15E-08	7.96E-09	28	0	111	2	2	0	117	0.26	217.4	12.9
B2b1-28	11054	553	2.85E-14	1.90E-14	4.72E-16	5.54E-07	3.69E-07	2.92E-08	44	2	478	19	4	0	488	0.09	210.6	13.8
B2b1-29	11053	553	2.28E-14	1.52E-14	3.12E-16	4.43E-07	2.95E-07	2.30E-08	93	1	300	5	7	0	322	0.31	255.0	13.8
B2b1-30	11051	553	2.07E-14	1.38E-14	5.09E-16	4.03E-07	2.69E-07	2.24E-08	200	7	193	6	11	0	240	1.04	311.4	19.1
B2b1-31	11050	552	2.76E-14	1.84E-14	5.75E-16	5.37E-07	3.58E-07	2.91E-08	171	6	444	23	9	0	484	0.39	205.8	14.8
B2b1-34	11045	552	3.35E-14	2.24E-14	4.89E-16	6.53E-07	4.35E-07	3.40E-08	328	30	542	20	17	2	619	0.61	195.6	12.2
B2b1-35	11044	552	1.88E-14	1.25E-14	3.98E-16	3.66E-07	2.44E-07	1.99E-08	48	2	208	3	4	0	219	0.23	309.8	17.5
B2b1-36	11042	552	6.85E-14	4.57E-14	6.80E-16	1.33E-06	8.89E-07	6.80E-08	140	10	869	21	3	0	902	0.16	274.6	15.4
B2b1-37	11041	552	6.12E-14	4.08E-14	7.68E-16	1.19E-06	7.95E-07	6.15E-08	172	5	1218	40	17	1	1258	0.14	175.9	10.7
B2b1-39	11038	552	3.54E-14	2.36E-14	4.86E-16	6.89E-07	4.59E-07	3.57E-08	161	6	457	12	7	0	495	0.35	258.3	14.8
B2b1-40	11036	552	1.48E-14	9.86E-15	3.07E-16	2.88E-07	1.92E-07	1.56E-08	126	8	217	22	9	0	247	0.58	216.6	22.6
B2b1-41	11034	552	2.27E-14	1.51E-14	4.76E-16	4.42E-07	2.95E-07	2.40E-08	44	2	313	6	9	2	323	0.14	253.9	14.4
B2b1-42	11033	552	9.51E-15	6.34E-15	2.70E-16	1.85E-07	1.24E-07	1.07E-08	91	2	147	3	7	0	169	0.62	203.7	12.1
B2b1-43	11031	552	2.09E-14	1.40E-14	2.78E-16	4.08E-07	2.72E-07	2.11E-08	129	3	279	5	9	0	309	0.46	244.8	13.3

B2b1-44	11030	551	1.34E-14	8.95E-15	3.80E-16	2.62E-07	1.75E-07	1.50E-08	48	1	165	3	5	0	176	0.29	276.3	16.8
B2b1-45	11028	551	4.55E-14	3.03E-14	5.81E-16	8.87E-07	5.91E-07	4.58E-08	275	4	635	9	13	1	700	0.43	235.1	12.5
B2b1-46	11027	551	3.87E-14	2.58E-14	6.05E-16	7.54E-07	5.03E-07	3.95E-08	111	9	613	83	37	12	639	0.18	219.0	30.7
B2b1-47	11025	551	2.81E-14	1.87E-14	5.46E-16	5.47E-07	3.65E-07	2.94E-08	173	6	447	11	14	1	488	0.39	208.1	12.1
B2b1-48	11024	551	4.94E-15	3.29E-15	2.09E-16	9.63E-08	6.42E-08	6.31E-09	31	1	37	1	4	0	45	0.83	-	
B2b1-50	11021	551	6.72E-15	4.48E-15	2.34E-16	1.31E-07	8.74E-08	7.99E-09	40	1	98	2	4	0	107	0.41	227.3	14.2
B2b1-51	11019	551	4.66E-14	3.11E-14	5.92E-16	9.09E-07	6.06E-07	4.69E-08	113	2	572	11	7	0	599	0.20	281.8	15.4
B2b1-52	11018	551	1.77E-14	1.18E-14	3.48E-16	3.46E-07	2.30E-07	1.86E-08	38	1	918	28	1	0	927	0.04	69.2	4.3
B2b1-53	11016	551	1.37E-14	9.12E-15	3.38E-16	2.67E-07	1.78E-07	1.49E-08	119	3	162	5	4	0	190	0.73	260.1	15.9
B2b1-54	11014	551	5.44E-15	3.63E-15	1.45E-16	1.06E-07	7.09E-08	6.02E-09	101	3	63	2	4	0	87	1.62	-	
B2b1-55	11013	551	3.70E-14	2.46E-14	3.93E-16	7.22E-07	4.81E-07	3.69E-08	252	5	492	9	12	0	551	0.51	242.6	13.0
B2b1-56	11011	551	4.64E-14	3.09E-14	7.85E-16	9.06E-07	6.04E-07	4.78E-08	316	6	596	11	7	1	670	0.53	250.8	13.9
B2b1-58	11008	550	2.15E-14	1.43E-14	4.22E-16	4.19E-07	2.80E-07	2.25E-08	95	7	279	13	12	1	301	0.34	258.1	17.8
B2b1-59	11007	550	2.72E-14	1.81E-14	4.10E-16	5.31E-07	3.54E-07	2.77E-08	135	6	346	9	6	0	377	0.39	261.1	14.9
B2b1-60	11005	550	7.38E-15	4.92E-15	2.65E-16	1.44E-07	9.62E-08	8.88E-09	80	2	92	2	6	0	110	0.88	242.3	15.5
B2b1-61	11004	550	3.28E-14	2.19E-14	5.81E-16	6.41E-07	4.27E-07	3.40E-08	50	2	397	10	4	0	409	0.13	290.9	17.0
B2b1-62	11002	550	7.40E-15	4.94E-15	2.83E-16	1.45E-07	9.65E-08	9.11E-09	141	3	128	3	11	0	162	1.10	166.0	10.9
B2b1-64	10999	550	2.46E-14	1.64E-14	4.80E-16	4.81E-07	3.21E-07	2.58E-08	94	2	416	9	5	0	438	0.23	203.6	11.7
B2b1-65	10998	550	1.20E-14	7.98E-15	2.48E-16	2.34E-07	1.56E-07	1.27E-08	52	1	153	3	4	0	165	0.34	263.9	15.1
B2b1-66	10996	550	1.66E-14	1.11E-14	3.73E-16	3.25E-07	2.16E-07	1.78E-08	56	1	251	5	8	0	265	0.22	227.6	13.2
B2b1-67	10995	550	2.79E-14	1.86E-14	4.69E-16	5.45E-07	3.63E-07	2.88E-08	288	8	351	8	15	1	418	0.82	241.3	13.6
B2b1-68	10993	550	2.37E-14	1.58E-14	5.07E-16	4.65E-07	3.10E-07	2.53E-08	191	10	333	9	10	0	378	0.57	227.8	13.7
B2b1-69	10991	550	9.96E-15	6.64E-15	3.62E-16	1.95E-07	1.30E-07	1.20E-08	34	1	138	3	2	0	146	0.24	247.8	16.1
B2b1-71	10988	549	3.07E-14	2.05E-14	4.57E-16	6.01E-07	4.01E-07	3.14E-08	84	4	269	10	8	0	289	0.31	386.0	24.0
B2b1-73	10985	549	1.78E-14	1.19E-14	4.54E-16	3.49E-07	2.33E-07	1.96E-08	67	2	234	5	5	0	250	0.29	259.5	15.5
B2b1-74	10984	549	2.19E-14	1.46E-14	4.62E-16	4.28E-07	2.86E-07	2.32E-08	71	1	230	7	2	0	247	0.31	321.7	19.9
B2b1-75	10982	549	2.49E-14	1.66E-14	4.27E-16	4.88E-07	3.25E-07	2.58E-08	111	4	312	9	9	0	338	0.36	267.9	15.9
B2b1-76	10981	549	1.69E-14	1.13E-14	4.03E-16	3.32E-07	2.21E-07	1.84E-08	448	14	660	18	18	1	765	0.68	80.4	4.8
B2b1-77	10979	549	4.78E-14	3.19E-14	6.78E-16	9.36E-07	6.24E-07	4.86E-08	165	9	536	21	2	0	575	0.31	302.1	19.2
B2b1-78	10978	549	1.03E-14	6.86E-15	2.70E-16	2.02E-07	1.34E-07	1.14E-08	250	8	514	12	23	1	573	0.49	65.3	3.9
B2b1-81	10973	549	8.71E-15	5.81E-15	3.03E-16	1.71E-07	1.14E-07	1.04E-08	100	4	182	6	5	0	205	0.55	154.3	10.6
B2b1-82	10971	549	2.34E-15	1.56E-15	2.40E-16	4.59E-08	3.06E-08	5.23E-09	7	0	45	1	1	0	47	0.16	-	

B2b1-83	10970	548	1.41E-14	9.42E-15	2.81E-16	2.77E-07	1.85E-07	1.49E-08	87	4	217	6	5	0	237	0.40	216.5	12.9
B2b1-84	10968	548	5.68E-14	3.79E-14	6.05E-16	1.11E-06	7.42E-07	5.69E-08	461	19	966	25	61	3	1074	0.48	192.2	10.8
B2b1-85	10967	548	3.60E-14	2.40E-14	4.33E-16	7.07E-07	4.71E-07	3.63E-08	341	8	507	12	11	0	587	0.67	223.1	12.4
B2b1-86	10965	548	1.86E-15	1.24E-15	1.39E-16	3.65E-08	2.44E-08	3.28E-09	<1.7	/	<2.9	/	<0.29	/	-	-	-	-
B2b1-87	10964	548	1.08E-14	7.22E-15	2.71E-16	2.12E-07	1.42E-07	1.19E-08	68	1	145	3	7	0	161	0.47	244.3	14.3
B2b1-88	10962	548	9.64E-15	6.42E-15	2.73E-16	1.89E-07	1.26E-07	1.09E-08	109	3	114	3	8	0	139	0.96	251.5	15.3
B2b1-89	10961	548	1.38E-14	9.18E-15	2.31E-16	2.70E-07	1.80E-07	1.43E-08	124	7	156	7	16	1	185	0.79	270.0	17.7
B2b1-91	10958	548	6.01E-14	4.00E-14	5.75E-16	1.18E-06	7.86E-07	6.00E-08	499	12	726	18	19	1	843	0.69	259.1	14.3
B2b1-92	10956	548	2.65E-14	1.77E-14	5.78E-16	5.20E-07	3.47E-07	2.84E-08	206	5	420	11	13	1	468	0.49	206.0	12.2
B2b1-93	10955	548	2.12E-14	1.42E-14	5.30E-16	4.17E-07	2.78E-07	2.33E-08	138	6	295	7	8	0	327	0.47	236.2	14.2
B2b1-94	10953	548	1.82E-14	1.21E-14	4.04E-16	3.58E-07	2.38E-07	1.96E-08	123	3	266	6	8	0	294	0.46	225.3	13.1
B2b1-95	10951	548	6.14E-15	4.09E-15	3.29E-16	1.21E-07	8.04E-08	8.83E-09	13	0	61	2	3	0	64	0.22	-	
B2b1-96	10950	547	4.47E-14	2.98E-14	5.86E-16	8.79E-07	5.86E-07	4.54E-08	217	14	680	15	15	2	731	0.32	223.0	12.4
B2b1-98	10947	547	2.88E-14	1.92E-14	5.72E-16	5.67E-07	3.78E-07	3.05E-08	116	4	397	16	6	0	424	0.29	247.9	16.3
B2b1-99	10945	547	4.08E-14	2.72E-14	5.58E-16	8.02E-07	5.35E-07	4.16E-08	478	18	578	20	22	1	690	0.83	215.4	12.9
B2b1-100	10944	547	2.74E-14	1.83E-14	4.84E-16	5.39E-07	3.59E-07	2.86E-08	112	11	465	80	20	3	491	0.24	203.6	34.9
B2b1-101	10942	547	1.14E-14	7.61E-15	2.23E-16	2.24E-07	1.50E-07	1.20E-08	79	2	172	3	8	0	190	0.46	218.4	12.3
B2b1-102	10941	547	5.74E-15	3.83E-15	2.28E-16	1.13E-07	7.52E-08	7.21E-09	51	1	57	2	3	0	69	0.90	-	
B2b1-103	10939	547	1.71E-14	1.14E-14	4.32E-16	3.35E-07	2.24E-07	1.88E-08	79	2	215	5	6	0	233	0.37	266.9	15.9
B2b1-104	10938	547	7.43E-15	4.96E-15	2.72E-16	1.46E-07	9.75E-08	9.06E-09	35	1	116	2	3	0	124	0.30	218.4	14.1

Appendix 26: Reduced detrital zircon U-Pb data for sample B2.

Grain #	Age 206/238	+/- 2σ	Age 207/235	+/- 2σ	Age 207/206	+/- 2σ	% Discordance	Selected U/Pb age (Ma)	+/- 2σ	Ratio 206/238	+/- 2σ	Ratio 207/235	+/- 2σ	Ratio 207/206	+/- 2σ
B2b1-1	309.0	12.0	409.0	11.0	1094.0	48.0	24%	309.0	12.0	0.0491	0.002	0.5	0.016	0.0758	0.0017
B2b1-2	423.7	5.5	514.4	9.2	948.0	44.0	18%	423.7	5.5	0.06794	0.00092	0.66	0.015	0.0709	0.0015
B2b1-4	312.8	4.2	312.0	11.0	320.0	80.0	0%	312.8	4.2	0.04973	0.00068	0.358	0.015	0.0532	0.002
B2b1-5	318.7	4.8	304.0	17.0	190.0	130.0	5%	318.7	4.8	0.05068	0.00078	0.356	0.023	0.0508	0.0033
B2b1-7	456.8	5.7	512.0	12.0	736.0	69.0	11%	456.8	5.7	0.07344	0.00095	0.657	0.02	0.0651	0.0021
B2b1-8	616.3	7.9	624.0	17.0	667.0	79.0	1%	616.3	7.9	0.1004	0.0013	0.845	0.033	0.0618	0.0024
B2b1-10	630.3	6.4	616.0	13.0	580.0	65.0	2%	630.3	6.4	0.1026	0.0011	0.832	0.024	0.0594	0.0018
B2b1-11	424.8	5.0	459.5	8.6	655.0	49.0	8%	424.8	5.0	0.06812	0.00083	0.574	0.013	0.0617	0.0014
B2b1-15	459.4	5.4	449.0	13.0	370.0	79.0	2%	459.4	5.4	0.07387	0.0009	0.561	0.02	0.0554	0.0021
B2b1-16	689.2	8.3	711.0	20.0	810.0	74.0	3%	689.2	8.3	0.1129	0.0014	1.024	0.038	0.066	0.0022
B2b1-19	464.1	5.8	454.0	13.0	424.0	79.0	2%	464.1	5.8	0.07466	0.00097	0.566	0.02	0.0559	0.002
B2b1-20	542.0	10.0	557.0	25.0	600.0	130.0	3%	542.0	10.0	0.0876	0.0018	0.719	0.044	0.0618	0.0037
B2b1-24	321.5	3.4	326.4	8.9	387.0	67.0	2%	321.5	3.4	0.05114	0.00055	0.379	0.012	0.0546	0.0017
B2b1-25	463.7	5.2	468.0	16.0	450.0	89.0	1%	463.7	5.2	0.07459	0.00086	0.585	0.025	0.0562	0.0023
B2b1-26	461.1	4.4	460.0	11.0	441.0	65.0	0%	461.1	4.4	0.07416	0.00074	0.57	0.017	0.0561	0.0017
B2b1-27	303.0	5.5	319.0	21.0	350.0	150.0	5%	303.0	5.5	0.04814	0.00089	0.377	0.029	0.0573	0.0044
B2b1-28	472.9	4.6	509.0	10.0	661.0	60.0	7%	472.9	4.6	0.07613	0.00077	0.653	0.017	0.0621	0.0017
B2b1-29	592.1	6.1	659.0	15.0	867.0	62.0	10%	592.1	6.1	0.0962	0.001	0.912	0.029	0.069	0.0022
B2b1-30	621.6	7.6	602.0	16.0	529.0	76.0	3%	621.6	7.6	0.1013	0.0013	0.811	0.029	0.0582	0.0021
B2b1-31	453.4	4.8	458.9	9.6	495.0	55.0	1%	453.4	4.8	0.07288	0.00079	0.572	0.015	0.0575	0.0014
B2b1-34	424.0	5.8	442.7	9.9	609.0	66.0	4%	424.0	5.8	0.068	0.00096	0.549	0.015	0.0602	0.0018
B2b1-35	307.2	4.3	317.0	14.0	320.0	110.0	3%	307.2	4.3	0.04881	0.0007	0.366	0.019	0.0547	0.0029
B2b1-36	307.9	2.7	303.3	7.0	250.0	62.0	2%	307.9	2.7	0.04893	0.00045	0.3465	0.0094	0.0509	0.0014
B2b1-37	524.2	5.5	542.2	8.6	602.0	37.0	3%	524.2	5.5	0.08472	0.00092	0.708	0.014	0.0602	0.001
B2b1-39	623.9	7.1	625.0	11.0	630.0	52.0	0%	623.9	7.1	0.1016	0.0012	0.855	0.021	0.0609	0.0015
B2b1-40	571.0	21.0	602.0	22.0	697.0	82.0	5%	571.0	21.0	0.0928	0.0035	0.833	0.042	0.0651	0.0028
B2b1-41	523.1	5.7	525.0	11.0	546.0	65.0	0%	523.1	5.7	0.08455	0.00095	0.678	0.019	0.059	0.0017
B2b1-42	865.0	10.0	875.0	19.0	893.0	64.0	1%	865.0	10.0	0.1437	0.0018	1.377	0.043	0.0689	0.0021
B2b1-43	455.1	5.6	451.0	12.0	443.0	73.0	1%	455.1	5.6	0.07316	0.00094	0.557	0.019	0.0563	0.0019

B2b1-44	303.9	5.1	322.0	16.0	430.0	120.0	6%	303.9	5.1	0.04829	0.00083	0.37	0.022	0.0565	0.0033
B2b1-45	632.9	5.6	630.0	10.0	601.0	49.0	0%	632.9	5.6	0.10317	0.00096	0.863	0.021	0.0607	0.0014
B2b1-46	491.0	22.0	502.0	18.0	735.0	80.0	2%	491.0	22.0	0.0793	0.0036	0.644	0.03	0.0648	0.0025
B2b1-47	451.0	5.2	493.0	13.0	695.0	71.0	9%	451.0	5.2	0.0724	0.00085	0.629	0.021	0.0627	0.0021
B2b1-48	690.0	15.0	716.0	40.0	720.0	160.0	4%	690.0	15.0	0.1129	0.0026	1.053	0.079	0.0682	0.0052
B2b1-50	577.5	8.4	590.0	21.0	590.0	100.0	2%	577.5	8.4	0.0938	0.0014	0.789	0.039	0.0611	0.003
B2b1-51	376.2	6.2	390.8	9.9	484.0	57.0	4%	376.2	6.2	0.0601	0.001	0.471	0.015	0.0575	0.0015
B2b1-52	315.8	3.8	311.7	6.8	286.0	49.0	1%	315.8	3.8	0.05022	0.00063	0.3604	0.0091	0.0523	0.0012
B2b1-53	1898.0	33.0	2109.0	24.0	2345.0	24.0	10%	2109.0	24.0	0.3429	0.0069	6.97	0.18	0.1495	0.0021
B2b1-54	1726.0	23.0	1739.0	21.0	1735.0	49.0	1%	1739.0	21.0	0.3073	0.0046	4.49	0.12	0.1076	0.0027
B2b1-55	462.0	4.5	452.0	11.0	386.0	60.0	2%	462.0	4.5	0.0743	0.00076	0.56	0.016	0.0543	0.0015
B2b1-56	583.2	5.1	600.0	10.0	675.0	47.0	3%	583.2	5.1	0.0947	0.00087	0.805	0.018	0.0621	0.0014
B2b1-58	506.6	6.7	556.0	14.0	769.0	75.0	9%	506.6	6.7	0.0818	0.0011	0.73	0.024	0.0655	0.0022
B2b1-59	437.4	5.0	442.0	13.0	444.0	75.0	1%	437.4	5.0	0.07022	0.00082	0.547	0.02	0.0562	0.002
B2b1-60	657.0	10.0	655.0	22.0	648.0	95.0	0%	657.0	10.0	0.1073	0.0018	0.904	0.043	0.062	0.0028
B2b1-61	552.2	6.2	549.0	11.0	573.0	55.0	1%	552.2	6.2	0.0894	0.001	0.717	0.019	0.059	0.0015
B2b1-62	1608.0	22.0	1766.0	21.0	1997.0	34.0	9%	1766.0	21.0	0.2835	0.0044	4.69	0.12	0.1226	0.0024
B2b1-64	492.8	5.9	519.0	12.0	632.0	63.0	5%	492.8	5.9	0.07946	0.00098	0.669	0.02	0.061	0.0018
B2b1-65	317.3	5.5	339.0	16.0	480.0	120.0	6%	317.3	5.5	0.05047	0.0009	0.4	0.022	0.0575	0.0032
B2b1-66	614.1	6.1	638.0	15.0	687.0	69.0	4%	614.1	6.1	0.1	0.001	0.87	0.027	0.0627	0.0019
B2b1-67	545.8	6.9	628.0	14.0	963.0	64.0	13%	545.8	6.9	0.0884	0.0012	0.859	0.026	0.0715	0.0023
B2b1-68	523.3	6.0	559.0	14.0	693.0	65.0	6%	523.3	6.0	0.0846	0.001	0.732	0.025	0.0625	0.002
B2b1-69	308.5	4.9	326.0	15.0	450.0	120.0	5%	308.5	4.9	0.04904	0.00079	0.38	0.021	0.0559	0.0033
B2b1-71	2379.0	19.0	2379.0	14.0	2385.0	20.0	0%	2379.0	14.0	0.4458	0.0042	9.42	0.14	0.1536	0.0018
B2b1-73	308.6	4.1	302.0	12.0	273.0	95.0	2%	308.6	4.1	0.04904	0.00067	0.343	0.016	0.0517	0.0023
B2b1-74	2074.0	26.0	2224.0	20.0	2364.0	20.0	7%	2224.0	20.0	0.38	0.0055	7.92	0.17	0.1515	0.0018
B2b1-75	401.0	6.7	409.0	13.0	440.0	78.0	2%	401.0	6.7	0.0641	0.0011	0.498	0.019	0.0562	0.0021
B2b1-76	544.5	6.9	581.6	9.6	755.0	40.0	6%	544.5	6.9	0.088	0.0012	0.771	0.017	0.0648	0.0012
B2b1-77	666.2	7.4	684.0	11.0	756.0	44.0	3%	666.2	7.4	0.1089	0.0013	0.965	0.021	0.0647	0.0013
B2b1-78	1452.0	21.0	1673.0	23.0	1954.0	35.0	13%	1673.0	23.0	0.2525	0.004	4.22	0.12	0.1209	0.0026
B2b1-81	1966.0	19.0	2008.0	15.0	2057.0	24.0	2%	2008.0	15.0	0.3567	0.004	6.24	0.1	0.1268	0.0017
B2b1-82	625.0	13.0	630.0	34.0	620.0	150.0	1%	625.0	13.0	0.1019	0.0023	0.86	0.062	0.0624	0.0049

B2b1-83	446.6	5.4	528.0	17.0	910.0	85.0	15%	446.6	5.4	0.07176	0.00089	0.679	0.029	0.0692	0.0028
B2b1-84	278.3	2.4	488.2	9.4	1658.0	48.0	43%	278.3	2.4	0.04412	0.00039	0.618	0.015	0.1013	0.0026
B2b1-85	456.9	4.4	462.0	10.0	462.0	60.0	1%	456.9	4.4	0.07346	0.00073	0.578	0.016	0.0567	0.0015
B2b1-86	3690.0	100.0	4512.0	38.0	4936.0	52.0	18%	4512.0	38.0	0.775	0.028	84.4	3.2	0.789	0.023
B2b1-87	301.8	5.2	303.0	17.0	310.0	140.0	0%	301.8	5.2	0.04793	0.00085	0.35	0.023	0.0535	0.0036
B2b1-88	1889.0	16.0	1895.0	15.0	1895.0	29.0	0%	1895.0	15.0	0.3406	0.0033	5.488	0.094	0.1161	0.0018
B2b1-89	1357.0	26.0	1597.0	21.0	1929.0	41.0	15%	1597.0	21.0	0.2346	0.005	3.83	0.1	0.118	0.0026
B2b1-91	450.1	3.5	459.4	8.2	497.0	48.0	2%	450.1	3.5	0.07232	0.00059	0.574	0.013	0.0575	0.0012
B2b1-92	445.4	5.3	465.0	12.0	553.0	69.0	4%	445.4	5.3	0.07155	0.00088	0.58	0.019	0.0589	0.0019
B2b1-93	447.8	4.1	460.0	13.0	489.0	83.0	3%	447.8	4.1	0.07195	0.00068	0.571	0.021	0.0572	0.0022
B2b1-94	598.1	7.6	632.0	14.0	757.0	63.0	5%	598.1	7.6	0.0973	0.0013	0.87	0.025	0.0649	0.002
B2b1-95	506.4	8.7	537.0	28.0	630.0	140.0	6%	506.4	8.7	0.0818	0.0015	0.693	0.048	0.0608	0.0041
B2b1-96	448.9	6.1	525.5	9.4	887.0	59.0	15%	448.9	6.1	0.072	0.001	0.68	0.016	0.0687	0.002
B2b1-98	1425.0	21.0	1586.0	17.0	1796.0	24.0	10%	1586.0	17.0	0.2477	0.0041	3.783	0.077	0.1101	0.0014
B2b1-99	444.5	5.0	450.7	9.4	484.0	61.0	1%	444.5	5.0	0.07139	0.00083	0.56	0.015	0.0569	0.0016
B2b1-100	260.2	4.6	324.0	14.0	800.0	110.0	20%	260.2	4.6	0.04119	0.00074	0.379	0.019	0.0655	0.0036
B2b1-101	810.3	7.4	811.0	19.0	827.0	69.0	0%	810.3	7.4	0.134	0.0013	1.228	0.041	0.0667	0.0022
B2b1-102	617.0	11.0	601.0	31.0	480.0	150.0	3%	617.0	11.0	0.1005	0.0018	0.822	0.055	0.0596	0.0042
B2b1-103	306.0	4.2	300.0	13.0	250.0	110.0	2%	306.0	4.2	0.04863	0.00069	0.348	0.017	0.0519	0.0026
B2b1-104	452.0	25.0	628.0	55.0	1270.0	140.0	28%	452.0	25.0	0.073	0.0042	0.94	0.11	0.0877	0.0062

Appendix 27: Detrital zircon (U-Th)/He data for sample B3.

Grain #	V (µm3)	+/- 2σ	4He (mol)	Corrected 4He (mol)	+/- 2σ	4He (mol/g)	Corrected 4He (mol/g)	+/- 2σ	232Th (ppm)	+/- 2σ	238U (ppm)	+/- 2σ	147Sm (ppm)	+/- 2σ	eU	Th/U	ZHe age (Ma)	+/- 2σ
B3b1-1	12022	601	1.10E-14	7.31E-15	2.50E-16	1.96E-07	1.31E-07	1.08E-08	170	3	110	2	11	0	150	1.54	242.1	13.7
B3b1-5	12038	602	5.01E-15	3.34E-15	2.12E-16	8.95E-08	5.97E-08	5.87E-09	64	2	63	2	6	0	78	1.01	-	
B3b1-6	12042	602	5.63E-14	3.75E-14	7.88E-16	1.00E-06	6.70E-07	5.22E-08	195	5	517	12	10	0	563	0.38	331.1	18.6
B3b1-7	12046	602	9.42E-16	6.28E-16	1.24E-16	1.68E-08	1.12E-08	2.38E-09	<3	/	<8.6	/	<0.6	/	-	-	-	-
B3b1-8	12050	602	3.34E-14	2.23E-14	4.99E-16	5.97E-07	3.98E-07	3.11E-08	265	8	453	7	3	0	515	0.59	214.9	11.6
B3b1-10	12058	603	8.58E-14	5.72E-14	9.65E-16	1.53E-06	1.02E-06	7.85E-08	448	8	772	11	8	0	877	0.58	323.6	17.1
B3b1-12	12066	603	1.33E-14	8.89E-15	4.13E-16	2.38E-07	1.59E-07	1.40E-08	135	4	491	16	6	0	523	0.28	84.4	5.6
B3b1-16	12082	604	2.22E-14	1.48E-14	3.85E-16	3.95E-07	2.63E-07	2.09E-08	150	3	276	7	7	0	312	0.54	234.9	13.5
B3b1-18	12090	604	4.16E-15	2.78E-15	2.54E-16	7.41E-08	4.94E-08	5.85E-09	33	1	129	2	3	0	136	0.25	100.8	8.1
B3b1-19	12094	605	2.38E-14	1.59E-14	4.35E-16	4.23E-07	2.82E-07	2.25E-08	151	4	440	15	5	0	476	0.34	165.2	10.2
B3b1-22	12106	605	5.52E-14	3.68E-14	6.44E-16	9.81E-07	6.54E-07	5.04E-08	107	3	299	5	9	0	324	0.36	560.7	30.2
B3b1-24	12114	606	2.74E-14	1.83E-14	5.89E-16	4.87E-07	3.25E-07	2.65E-08	44	1	1092	17	1	0	1102	0.04	82.0	4.6
B3b1-25	12118	606	1.78E-14	1.19E-14	3.98E-16	3.16E-07	2.11E-07	1.73E-08	37	1	125	2	3	0	134	0.30	438.6	25.3
B3b1-26	12122	606	1.86E-14	1.24E-14	3.53E-16	3.30E-07	2.20E-07	1.77E-08	150	13	324	6	10	1	359	0.46	170.7	9.6
B3b1-27	12126	606	1.32E-14	8.78E-15	2.56E-16	2.33E-07	1.56E-07	1.25E-08	71	2	100	9	2	0	116	0.71	372.9	34.1
B3b1-28	12130	606	4.46E-14	2.98E-14	6.69E-16	7.92E-07	5.28E-07	4.13E-08	129	5	404	8	5	0	434	0.32	338.3	18.7
B3b1-30	12138	607	3.29E-14	2.19E-14	6.59E-16	5.83E-07	3.88E-07	3.14E-08	353	13	457	17	8	0	540	0.77	200.0	12.5
B3b1-31	12142	607	2.23E-14	1.48E-14	4.52E-16	3.94E-07	2.63E-07	2.13E-08	63	1	208	8	6	0	223	0.30	328.4	21.5
B3b1-32	12146	607	3.85E-14	2.56E-14	4.26E-16	6.81E-07	4.54E-07	3.49E-08	196	17	441	18	8	1	487	0.44	259.4	16.5
B3b1-34	12153	608	4.54E-14	3.03E-14	7.69E-16	8.03E-07	5.35E-07	4.24E-08	457	18	1248	46	78	4	1355	0.37	109.9	6.9
B3b1-35	12157	608	3.19E-14	2.13E-14	5.97E-16	5.64E-07	3.76E-07	3.01E-08	118	5	426	16	8	1	454	0.28	230.9	14.8
B3b1-36	12161	608	7.37E-14	4.91E-14	1.13E-15	1.30E-06	8.69E-07	6.81E-08	45	1	811	11	0	0	821	0.05	294.5	15.9
B3b1-37	12165	608	1.98E-14	1.32E-14	3.50E-16	3.49E-07	2.33E-07	1.85E-08	113	4	299	22	15	1	326	0.38	199.1	17.1
B3b1-39	12173	609	1.11E-13	7.37E-14	1.29E-15	1.95E-06	1.30E-06	1.00E-07	2025	92	2325	38	130	4	2801	0.87	129.2	6.9
B3b1-40	12177	609	3.34E-15	2.23E-15	1.54E-16	5.90E-08	3.93E-08	4.02E-09	77	1	66	1	1	0	84	1.17	-	
B3b1-41	12181	609	4.03E-14	2.68E-14	5.77E-16	7.11E-07	4.74E-07	3.70E-08	202	7	419	6	5	0	466	0.48	282.8	15.2
B3b1-42	12185	609	3.40E-14	2.27E-14	3.98E-16	6.01E-07	4.00E-07	3.08E-08	132	7	622	10	6	0	653	0.21	170.7	9.1

Appendix 28: Reduced detrital zircon U-Pb data for sample B3.

Grain #	Age 206/238	+/- 2σ	Age 207/235	+/- 2σ	Age 207/206	+/- 2σ	% Discordance	Selected U/Pb age (Ma)	+/- 2σ	Ratio 206/238	+/- 2σ	Ratio 207/235	+/- 2σ	Ratio 207/206	+/- 2σ
B3b1-1	2460.0	27.0	2547.0	17.0	2594.0	25.0	3%	2547.0	17.0	0.4645	0.006	11.27	0.21	0.1743	0.0027
B3b1-5	621.0	12.0	821.0	47.0	1400.0	150.0	24%	621.0	12.0	0.1012	0.0021	1.29	0.11	0.0926	0.0073
B3b1-6	431.6	3.5	467.0	12.0	645.0	64.0	8%	431.6	3.5	0.06925	0.00058	0.586	0.019	0.0618	0.0018
B3b1-7	3950.0	64.0	4571.0	27.0	4878.0	19.0	14%	4571.0	27.0	0.849	0.018	90.3	2.3	0.7626	0.0083
B3b1-8	626.6	5.2	696.0	14.0	904.0	67.0	10%	626.6	5.2	0.10209	0.00088	0.987	0.028	0.0699	0.0022
B3b1-10	303.6	2.9	309.0	8.3	323.0	67.0	2%	303.6	2.9	0.04823	0.00046	0.354	0.011	0.0537	0.0016
B3b1-12	700.0	12.0	721.0	18.0	789.0	52.0	3%	700.0	12.0	0.1146	0.0021	1.043	0.036	0.0658	0.0016
B3b1-16	553.9	5.7	575.0	16.0	631.0	74.0	4%	553.9	5.7	0.08974	0.00096	0.766	0.028	0.0609	0.0021
B3b1-18	304.0	5.8	286.0	19.0	150.0	150.0	6%	304.0	5.8	0.04831	0.00095	0.329	0.026	0.051	0.0041
B3b1-19	301.7	4.9	303.0	11.0	299.0	81.0	0%	301.7	4.9	0.04785	0.00081	0.349	0.014	0.0523	0.002
B3b1-22	467.8	5.2	510.0	16.0	717.0	75.0	8%	467.8	5.2	0.07528	0.00087	0.654	0.026	0.0644	0.0023
B3b1-24	301.1	3.6	299.8	6.5	294.0	54.0	0%	301.1	3.6	0.04782	0.00059	0.3419	0.0087	0.052	0.0012
B3b1-25	308.1	5.7	343.0	22.0	510.0	150.0	10%	308.1	5.7	0.04896	0.00092	0.41	0.03	0.0611	0.0045
B3b1-26	420.0	5.1	455.0	14.0	630.0	76.0	8%	420.0	5.1	0.06733	0.00084	0.564	0.021	0.0611	0.0021
B3b1-27	529.0	21.0	560.0	33.0	740.0	120.0	6%	529.0	21.0	0.0858	0.0036	0.747	0.057	0.0657	0.0037
B3b1-28	538.1	6.7	558.0	13.0	674.0	71.0	4%	538.1	6.7	0.0871	0.0011	0.733	0.021	0.062	0.0021
B3b1-30	845.0	12.0	861.0	13.0	906.0	37.0	2%	845.0	12.0	0.14	0.0021	1.341	0.029	0.0695	0.0012
B3b1-31	667.7	8.3	667.0	19.0	642.0	76.0	0%	667.7	8.3	0.1092	0.0014	0.923	0.036	0.0619	0.0021
B3b1-32	439.3	4.3	484.0	13.0	721.0	69.0	9%	439.3	4.3	0.07053	0.00071	0.604	0.02	0.0634	0.0022
B3b1-34	243.1	5.9	428.0	8.6	1658.0	62.0	43%	243.1	5.9	0.03844	0.00096	0.526	0.013	0.1033	0.0034
B3b1-35	454.9	5.3	591.0	32.0	1180.0	190.0	23%	454.9	5.3	0.07313	0.00089	0.95	0.26	0.111	0.035
B3b1-36	2390.0	13.0	2390.0	17.0	2411.0	13.0	0%	2390.0	17.0	0.449	0.003	9.4	0.24	0.1561	0.0012
B3b1-37	453.0	16.0	473.0	24.0	579.0	91.0	4%	453.0	16.0	0.0729	0.0027	0.61	0.039	0.0616	0.0026
B3b1-39	165.7	3.0	278.0	12.0	1365.0	96.0	40%	165.7	3.0	0.02605	0.00048	0.317	0.016	0.088	0.0045
B3b1-40	2538.0	24.0	2553.0	23.0	2601.0	34.0	1%	2553.0	23.0	0.4827	0.0056	11.37	0.26	0.1747	0.0036
B3b1-41	977.8	7.0	975.0	14.0	956.0	39.0	0%	977.8	7.0	0.1637	0.0012	1.61	0.036	0.0711	0.0013
B3b1-42	450.5	4.2	485.0	13.0	693.0	64.0	7%	450.5	4.2	0.07239	0.0007	0.617	0.02	0.0632	0.0019

Appendix 29: Detrital zircon (U-Th)/He data for sample B6.

Grain #	V (µm3)	+/- 2σ	4He (mol)	Corrected 4He (mol)	+/- 2σ	4He (mol/g)	Corrected 4He (mol/g)	+/- 2σ	232Th (ppm)	+/- 2σ	238U (ppm)	+/- 2σ	147Sm (ppm)	+/- 2σ	eU	Th/U	ZHe age (Ma)	+/- 2σ
B6b2-2	11332	567	7.67E-15	5.12E-15	4.38E-16	1.46E-07	9.71E-08	1.11E-08	34	1	39	1	4	0	47		573.4	44.5
B6b2-4	11314	566	3.81E-14	2.54E-14	1.39E-15	7.24E-07	4.83E-07	4.48E-08	209	11	719	17	15	1	768		174.9	11.5
B6b2-5	11304	565	1.10E-14	7.35E-15	6.71E-16	2.10E-07	1.40E-07	1.65E-08	80	6	135	5	38	6	153		253.8	21.5
B6b2-6	11295	565	2.45E-14	1.64E-14	1.00E-15	4.67E-07	3.12E-07	3.02E-08	160	5	390	24	10	1	428		202.7	17.4
B6b2-7	11286	564	1.78E-14	1.18E-14	6.14E-16	3.39E-07	2.26E-07	2.06E-08	102	1	313	4	3	0	337		186.4	11.5
B6b2-9	11267	563	4.48E-14	2.98E-14	1.27E-15	8.54E-07	5.70E-07	4.91E-08	220	17	386	15	11	1	438		361.9	24.4
B6b2-10	11258	563	1.06E-14	7.07E-15	1.01E-15	2.03E-07	1.35E-07	2.18E-08	113	6	184	7	3	0	210		178.9	20.2
B6b2-11	11248	562	1.31E-14	8.71E-15	4.75E-16	2.50E-07	1.67E-07	1.54E-08	70	2	143	3	2	0	159		291.4	18.9
B6b2-12	11239	562	2.57E-14	1.71E-14	1.01E-15	4.92E-07	3.28E-07	3.12E-08	< LOD	1	< LOD	1	< LOD	0	-		-	-
B6b2-13	11230	561	2.69E-14	1.80E-14	1.14E-15	5.16E-07	3.44E-07	3.38E-08	< LOD	0	< LOD	1	< LOD	0	-		-	-
B6b2-14	11220	561	1.14E-14	7.58E-15	7.23E-16	2.18E-07	1.45E-07	1.76E-08	< LOD	0	< LOD	1	< LOD	0	-		-	-
B6b2-15	11211	561	3.61E-14	2.41E-14	1.06E-15	6.92E-07	4.61E-07	4.01E-08	< LOD	0	< LOD	1	< LOD	0	-		-	-
B6b2-16	11202	560	1.96E-14	1.31E-14	6.07E-16	3.76E-07	2.51E-07	2.21E-08	< LOD	0	< LOD	1	< LOD	0	-		-	-
B6b2-17	11193	560	1.26E-14	8.40E-15	6.95E-16	2.42E-07	1.61E-07	1.80E-08	< LOD	0	< LOD	1	< LOD	0	-		-	-
B6b2-18	11183	559	7.47E-15	4.98E-15	4.58E-16	1.44E-07	9.57E-08	1.14E-08	< LOD	1	< LOD	1	< LOD	0	-		-	-
B6b2-19	11174	559	3.98E-14	2.65E-14	1.58E-15	7.66E-07	5.11E-07	4.89E-08	< LOD	0	< LOD	1	< LOD	0	-		-	-
B6b2-21	11155	558	5.36E-16	3.58E-16	4.24E-16	1.03E-08	6.89E-09	8.18E-09	< LOD	1	< LOD	2	< LOD	1	-		-	-
B6b2-22	11146	557	2.46E-14	1.64E-14	9.89E-16	4.75E-07	3.17E-07	3.05E-08	< LOD	0	< LOD	1	< LOD	0	-		-	-
B6b2-23	11137	557	2.71E-14	1.80E-14	1.01E-15	5.23E-07	3.48E-07	3.26E-08	< LOD	3	< LOD	1	< LOD	0	-		-	-
B6b2-24	11127	556	7.71E-14	5.14E-14	1.98E-15	1.49E-06	9.94E-07	8.37E-08	< LOD	0	< LOD	1	< LOD	0	-		-	-
B6b2-25	11118	556	3.55E-15	2.36E-15	5.37E-16	6.86E-08	4.57E-08	1.09E-08	< LOD	7	< LOD	1	< LOD	0	-		-	-
B6b2-26	11109	555	2.63E-14	1.76E-14	1.20E-15	5.10E-07	3.40E-07	3.45E-08	< LOD	0	< LOD	1	< LOD	0	-		-	-
B6b2-27	11099	555	3.80E-14	2.53E-14	1.36E-15	7.35E-07	4.90E-07	4.53E-08	< LOD	3	< LOD	1	< LOD	0	-		-	-
B6b2-28	11090	555	3.03E-14	2.02E-14	1.41E-15	5.87E-07	3.92E-07	4.02E-08	< LOD	2	< LOD	1	< LOD	0	-		-	-
B6b2-29	11081	554	1.35E-14	9.02E-15	5.88E-16	2.63E-07	1.75E-07	1.74E-08	< LOD	1	< LOD	1	< LOD	0	-		-	-
B6b2-30	11071	554	1.54E-14	1.03E-14	8.19E-16	2.99E-07	2.00E-07	2.18E-08	< LOD	3	< LOD	1	< LOD	0	-		-	-
B6b2-31	11062	553	3.98E-14	2.65E-14	8.10E-16	7.74E-07	5.16E-07	4.18E-08	< LOD	5	< LOD	1	< LOD	0	-		-	-
B6b2-32	11053	553	3.07E-14	2.05E-14	1.37E-15	5.98E-07	3.99E-07	4.01E-08	< LOD	1	< LOD	1	< LOD	0	-		-	-
B6b2-34	11034	552	7.68E-15	5.12E-15	1.86E-16	1.50E-07	9.97E-08	8.31E-09	< LOD	0	< LOD	1	< LOD	0	-		-	-

B6b2-35	11025	551	9.11E-15	6.07E-15	1.96E-16	1.78E-07	1.18E-07	9.67E-09	< LOD	5	< LOD	1	< LOD	0	-	-	-
B6b2-37	11006	550	2.20E-14	1.46E-14	2.81E-16	4.29E-07	2.86E-07	2.21E-08	111	3	224	3	4	0	250	317.8	16.9
B6b2-38	10997	550	1.92E-14	1.28E-14	2.70E-16	3.76E-07	2.51E-07	1.95E-08	89	2	320	8	10	0	340	205.0	11.6
B6b2-40	10978	549	2.70E-14	1.80E-14	2.68E-16	5.29E-07	3.52E-07	2.70E-08	54	1	163	2	4	0	175	559.7	29.5
B6b2-41	10969	548	2.57E-14	1.71E-14	3.20E-16	5.04E-07	3.36E-07	2.60E-08	73	2	193	5	4	0	211	443.6	25.3
B6b2-42	10960	548	2.68E-14	1.79E-14	3.68E-16	5.26E-07	3.50E-07	2.73E-08	346	4	279	5	8	0	360	270.2	14.4
B6b2-43	10950	548	6.99E-15	4.66E-15	1.47E-16	1.37E-07	9.16E-08	7.45E-09	76	1	73	1	5	0	91	280.3	15.4
B6b2-44	10941	547	3.10E-14	2.07E-14	3.66E-16	6.09E-07	4.06E-07	3.13E-08	236	6	307	8	8	0	362	311.6	17.6
B6b2-45	10932	547	2.98E-14	1.99E-14	3.31E-16	5.87E-07	3.91E-07	3.01E-08	69	1	354	13	13	1	370	294.3	18.3
B6b2-47	10913	546	1.87E-14	1.24E-14	3.15E-16	3.68E-07	2.45E-07	1.94E-08	76	1	317	4	4	0	335	204.1	11.1
B6b2-48	10904	545	3.61E-14	2.41E-14	4.06E-16	7.12E-07	4.74E-07	3.65E-08	145	6	300	10	6	0	335	394.5	23.3
B6b2-49	10894	545	1.18E-14	7.86E-15	1.85E-16	2.33E-07	1.55E-07	1.22E-08	187	15	256	13	7	1	300	143.7	9.9
B6b2-50	10885	544	3.55E-14	2.37E-14	3.20E-16	7.01E-07	4.67E-07	3.56E-08	257	5	461	5	12	0	521	249.3	12.9
B6b2-51	10876	544	2.17E-14	1.44E-14	3.19E-16	4.28E-07	2.85E-07	2.23E-08	68	2	303	3	7	0	319	248.8	13.2
B6b2-52	10866	543	8.23E-15	5.49E-15	1.60E-16	1.63E-07	1.09E-07	8.73E-09	91	4	99	6	5	0	120	251.2	18.8
B6b2-53	10857	543	4.32E-15	2.88E-15	1.32E-16	8.56E-08	5.70E-08	5.02E-09	64	1	140	5	7	0	155	102.2	6.7
B6b2-54	10848	542	1.43E-14	9.53E-15	2.12E-16	2.83E-07	1.89E-07	1.48E-08	117	2	210	3	13	0	237	221.3	11.8
B6b2-55	10838	542	2.30E-14	1.53E-14	3.10E-16	4.56E-07	3.04E-07	2.36E-08	172	4	263	5	3	0	304	278.7	15.1
B6b2-56	10829	541	3.57E-14	2.38E-14	3.34E-16	7.09E-07	4.72E-07	3.61E-08	166	2	760	12	25	1	799	164.6	8.7
B6b2-57	10820	541	5.10E-14	3.40E-14	4.49E-16	1.01E-06	6.76E-07	5.15E-08	136	6	453	13	7	0	485	388.1	22.3
B6b2-58	10811	541	1.04E-14	6.95E-15	1.77E-16	2.07E-07	1.38E-07	1.09E-08	42	1	204	6	7	0	214	179.9	10.9
B6b2-59	10801	540	1.83E-14	1.22E-14	1.99E-16	3.65E-07	2.43E-07	1.87E-08	59	1	185	4	4	0	198	341.4	19.0
B6b2-60	10792	540	4.74E-15	3.16E-15	1.39E-16	9.44E-08	6.29E-08	5.47E-09	18	0	39	0	5	0	44	400.6	23.6
B6b2-61	10783	539	9.98E-15	6.65E-15	1.80E-16	1.99E-07	1.33E-07	1.06E-08	74	2	111	3	7	0	129	286.2	16.6
B6b2-62	10773	539	4.21E-14	2.80E-14	3.42E-16	8.39E-07	5.60E-07	4.25E-08	153	13	463	17	6	0	499	312.1	19.1
B6b2-63	10764	538	2.05E-14	1.37E-14	2.73E-16	4.09E-07	2.73E-07	2.12E-08	112	2	198	4	6	0	224	338.6	18.8
B6b2-64	10755	538	7.98E-15	5.32E-15	1.63E-16	1.60E-07	1.06E-07	8.61E-09	95	2	199	5	4	0	221	134.0	7.9
B6b2-65	10745	537	2.65E-14	1.77E-14	2.72E-16	5.30E-07	3.54E-07	2.71E-08	96	4	268	7	4	0	291	338.1	18.9
B6b2-66	10736	537	2.08E-14	1.38E-14	3.14E-16	4.16E-07	2.77E-07	2.17E-08	117	3	243	7	8	0	271	285.1	16.7
B6b2-68	10717	536	3.56E-15	2.37E-15	9.49E-17	7.15E-08	4.76E-08	4.05E-09	21	0	53	1	8	0	58	229.8	13.9
B6b2-69	10708	535	8.94E-15	5.96E-15	2.10E-16	1.80E-07	1.20E-07	9.92E-09	100	2	193	4	2	0	216	153.9	9.0
B6b2-70	10699	535	1.36E-14	9.05E-15	1.95E-16	2.73E-07	1.82E-07	1.42E-08	40	1	103	3	2	0	112	452.2	26.1

B6b2-71	10689	534	3.22E-14	2.15E-14	3.28E-16	6.48E-07	4.32E-07	3.31E-08	161	9	930	26	47	1	968		124.2	7.2
B6b2-72	10680	534	3.66E-14	2.44E-14	3.41E-16	7.36E-07	4.91E-07	3.75E-08	78	3	545	14	17	2	563		242.6	13.7
B6b2-73	10671	534	2.85E-14	1.90E-14	3.44E-16	5.74E-07	3.83E-07	2.95E-08	60	1	250	5	2	0	264		404.1	22.4
B6b2-74	10661	533	4.28E-14	2.85E-14	4.14E-16	8.64E-07	5.76E-07	4.40E-08	141	4	487	11	7	0	520		308.0	17.0
B6b2-75	10652	533	2.81E-14	1.88E-14	3.53E-16	5.68E-07	3.79E-07	2.93E-08	37	2	266	8	2	0	275		383.9	22.7
B6b2-76	10643	532	6.64E-14	4.43E-14	5.79E-16	1.34E-06	8.95E-07	6.81E-08	1044	26	2023	48	169	6	2268		109.7	6.0
B6b2-77	10634	532	1.44E-14	9.60E-15	1.72E-16	2.91E-07	1.94E-07	1.50E-08	85	2	137	3	5	0	156		345.1	18.7
B6b2-78	10624	531	1.13E-14	7.52E-15	1.78E-16	2.28E-07	1.52E-07	1.20E-08	163	3	138	3	38	1	177		239.4	13.2
B6b2-79	10615	531	2.57E-14	1.71E-14	2.52E-16	5.21E-07	3.47E-07	2.65E-08	93	5	371	11	7	0	393		246.0	14.3
B6b2-80	10606	530	3.25E-14	2.16E-14	3.21E-16	6.58E-07	4.39E-07	3.36E-08	162	4	154	4	14	1	192		635.4	35.3
B6b2-81	10596	530	2.98E-14	1.98E-14	3.26E-16	6.04E-07	4.03E-07	3.09E-08	257	6	355	8	6	0	415		269.7	14.7
B6b2-82	10587	529	8.43E-14	5.62E-14	6.65E-16	1.71E-06	1.14E-06	8.67E-08	51	4	854	18	31	3	866		367.2	20.1
B6b2-83	10578	529	4.79E-14	3.19E-14	4.47E-16	9.74E-07	6.49E-07	4.95E-08	618	18	2636	72	196	8	2781		65.0	3.7
B6b2-84	10568	528	1.34E-14	8.94E-15	2.20E-16	2.73E-07	1.82E-07	1.44E-08	55	1	194	4	2	0	207		244.6	13.6
B6b2-85	10559	528	2.82E-14	1.88E-14	3.12E-16	5.74E-07	3.82E-07	2.94E-08	130	17	331	15	5	0	362		294.4	19.7
B6b2-86	10550	527	3.65E-14	2.43E-14	4.34E-16	7.43E-07	4.95E-07	3.82E-08	275	9	371	9	8	0	436		316.0	17.5
B6b2-87	10540	527	1.44E-14	9.58E-15	2.29E-16	2.93E-07	1.95E-07	1.54E-08	48	1	408	11	4	0	419		129.8	7.6
B6b2-88	10531	527	4.55E-14	3.03E-14	4.16E-16	9.29E-07	6.19E-07	4.72E-08	162	7	554	16	20	1	592		291.1	16.8
B6b2-89	10522	526	1.70E-14	1.13E-14	2.22E-16	3.47E-07	2.31E-07	1.79E-08	92	3	144	3	3	0	166		387.4	21.5
B6b2-90	10512	526	4.31E-14	2.87E-14	4.08E-16	8.81E-07	5.87E-07	4.48E-08	262	13	571	21	9	1	633		258.4	15.7
B6b1-1	10722	536	9.45E-15	6.30E-15	2.85E-16	1.90E-07	1.26E-07	1.11E-08	97	3	82	1	2	0	105	1.18	334.9	19.9
B6b1-2	10735	537	4.38E-14	2.92E-14	6.24E-16	8.77E-07	5.85E-07	4.56E-08	160	4	382	9	12	0	419	0.42	388.2	21.7
B6b1-3	10747	537	1.88E-14	1.25E-14	3.94E-16	3.77E-07	2.51E-07	2.04E-08	181	2	171	3	5	0	213	1.06	327.6	18.2
B6b1-4	10759	538	1.65E-14	1.10E-14	3.30E-16	3.30E-07	2.20E-07	1.77E-08	65	1	219	6	3	0	235	0.30	260.7	15.4
B6b1-5	10772	539	3.18E-14	2.12E-14	4.96E-16	6.36E-07	4.24E-07	3.33E-08	77	1	397	6	6	0	415	0.19	284.0	15.3
B6b1-6	10784	539	1.53E-14	1.02E-14	3.61E-16	3.05E-07	2.04E-07	1.69E-08	71	1	126	2	2	0	143	0.56	396.3	22.5
B6b1-8	10808	540	1.06E-14	7.06E-15	2.67E-16	2.11E-07	1.41E-07	1.18E-08	78	1	72	2	3	0	90	1.09	431.9	25.2
B6b1-12	10858	543	2.16E-14	1.44E-14	5.50E-16	4.28E-07	2.86E-07	2.40E-08	45	1	232	3	3	0	243	0.19	327.9	18.9
B6b1-13	10870	544	6.18E-14	4.12E-14	6.07E-16	1.22E-06	8.15E-07	6.23E-08	129	3	708	32	28	3	738	0.18	307.1	20.5
B6b1-14	10882	544	2.98E-14	1.99E-14	5.85E-16	5.89E-07	3.93E-07	3.16E-08	44	1	133	2	4	0	143	0.33	761.9	42.2
B6b1-16	10907	545	4.20E-14	2.80E-14	6.48E-16	8.28E-07	5.52E-07	4.33E-08	240	5	404	6	8	0	460	0.59	333.3	18.0
B6b1-17	10919	546	2.02E-14	1.35E-14	5.16E-16	3.98E-07	2.65E-07	2.24E-08	74	3	192	5	4	0	209	0.39	352.6	21.4

B6b1-18	10932	547	3.52E-15	2.34E-15	2.28E-16	6.92E-08	4.61E-08	5.66E-09	26	0	29	1	2	0	35	0.92	-	
B6b1-19	10944	547	1.31E-14	8.76E-15	3.72E-16	2.58E-07	1.72E-07	1.48E-08	44	1	135	2	4	0	145	0.33	330.4	19.6
B6b1-20	10956	548	1.45E-14	9.64E-15	3.06E-16	2.84E-07	1.89E-07	1.54E-08	78	2	182	4	2	0	200	0.43	263.3	15.2

Appendix 30: Reduced detrital zircon U-Pb data for sample B6.

Grain #	Age 206/238	+/- 2σ	Age 207/235	+/- 2σ	Age 207/206	+/- 2σ	% Discordance	Selected U/Pb age (Ma)	+/- 2σ	Ratio 206/238	+/- 2σ	Ratio 207/235	+/- 2σ	Ratio 207/206	+/- 2σ
B6b2-2	1934.0	16.0	1944.0	15.0	1952.0	25.0	1%	1944.0	15.0	0.3501	0.0034	5.788	0.095	0.12	0.0017
B6b2-4	394.9	4.2	505.6	9.3	1080.0	47.0	22%	394.9	4.2	0.06312	0.00068	0.646	0.015	0.0759	0.0018
B6b2-5	1399.0	29.0	1460.0	19.0	1567.0	19.0	4%	1399.0	29.0	0.2429	0.0056	3.222	0.077	0.097	0.001
B6b2-6	279.0	11.0	412.0	11.0	1270.0	120.0	32%	279.0	11.0	0.0442	0.0017	0.504	0.016	0.0892	0.005
B6b2-7	608.0	4.7	599.1	6.0	578.0	29.0	1%	608.0	4.7	0.09893	0.00081	0.805	0.011	0.05931	0.00078
B6b2-9	534.1	5.2	558.2	7.0	648.0	37.0	4%	534.1	5.2	0.0864	0.00087	0.732	0.012	0.0615	0.001
B6b2-10	333.8	4.9	313.0	12.0	263.0	86.0	7%	333.8	4.9	0.05315	0.0008	0.363	0.016	0.051	0.002
B6b2-11	1660.0	14.0	1748.0	12.0	1831.0	15.0	5%	1748.0	12.0	0.2938	0.0028	4.606	0.065	0.11201	0.00094
B6b2-12	531.0	10.0	538.0	15.0	672.0	33.0	1%	531.0	10.0	0.0859	0.0017	0.704	0.025	0.06168	0.00092
B6b2-13	545.5	4.5	525.0	6.7	542.0	28.0	4%	545.5	4.5	0.08817	0.00075	0.679	0.011	0.05837	0.00076
B6b2-14	835.3	7.7	800.1	9.6	789.0	34.0	4%	835.3	7.7	0.1384	0.0014	1.202	0.021	0.0657	0.0011
B6b2-15	2007.0	11.0	2047.8	7.2	2124.0	10.0	2%	2047.8	7.2	0.3651	0.0022	6.506	0.053	0.13191	0.00076
B6b2-16	1005.1	7.3	973.5	8.6	976.0	28.0	3%	1005.1	7.3	0.1685	0.0013	1.612	0.022	0.07173	0.00098
B6b2-17	2529.0	30.0	2579.0	24.0	2660.0	14.0	2%	2579.0	24.0	0.481	0.0067	11.87	0.25	0.1806	0.0015
B6b2-18	1978.0	15.0	1959.0	12.0	1974.0	17.0	1%	1959.0	12.0	0.3592	0.0031	5.875	0.085	0.1213	0.0012
B6b2-19	1024.9	6.8	995.1	7.8	956.0	17.0	3%	1024.9	6.8	0.1724	0.0012	1.666	0.02	0.07095	0.00059
B6b2-21	1004.0	13.0	1048.0	20.0	1032.0	70.0	4%	1004.0	13.0	0.1686	0.0024	1.808	0.057	0.074	0.0025
B6b2-22	1649.0	13.0	1790.0	13.0	1832.0	14.0	8%	1790.0	13.0	0.2917	0.0026	4.834	0.072	0.11214	0.00085
B6b2-23	1295.0	15.0	1631.0	33.0	1971.0	69.0	21%	1631.0	33.0	0.2227	0.0029	4.08	0.16	0.1243	0.0046
B6b2-24	330.0	4.6	350.2	6.7	296.0	27.0	6%	330.0	4.6	0.05253	0.00075	0.4113	0.0093	0.05245	0.00061
B6b2-25	1139.0	22.0	1675.0	97.0	2200.0	160.0	32%	1675.0	97.0	0.1935	0.0041	5.11	0.64	0.165	0.017
B6b2-26	449.3	3.2	474.8	6.4	484.0	35.0	5%	449.3	3.2	0.07219	0.00053	0.597	0.01	0.05681	0.00089
B6b2-27	542.3	5.0	643.0	22.0	954.0	86.0	16%	542.3	5.0	0.08777	0.00084	0.903	0.046	0.0738	0.0036
B6b2-28	757.8	7.4	874.0	12.0	1248.0	33.0	13%	757.8	7.4	0.1246	0.0013	1.367	0.028	0.0819	0.0014
B6b2-29	1092.4	9.8	1099.0	9.5	1201.0	30.0	1%	1092.4	9.8	0.1847	0.0018	1.946	0.027	0.0805	0.0012
B6b2-30	539.1	6.2	601.0	12.0	976.0	45.0	10%	539.1	6.2	0.0872	0.0011	0.805	0.022	0.0718	0.0015
B6b2-31	429.0	4.5	553.2	9.4	1132.0	52.0	22%	429.0	4.5	0.06882	0.00075	0.726	0.016	0.0782	0.0021
B6b2-32	365.7	5.0	404.5	6.4	721.0	37.0	10%	365.7	5.0	0.05838	0.00083	0.4904	0.0093	0.0633	0.0011
B6b2-34	303.3	2.9	315.9	6.6	467.0	54.0	4%	303.3	2.9	0.04817	0.00047	0.366	0.0088	0.0569	0.0014

B6b2-35	448.0	13.0	795.0	28.0	1930.0	73.0	44%	448.0	13.0	0.072	0.0022	1.198	0.059	0.1215	0.0048
B6b2-37	531.5	5.6	559.0	10.0	584.0	50.0	5%	531.5	5.6	0.08595	0.00095	0.737	0.018	0.0598	0.0014
B6b2-38	429.1	4.1	444.2	7.5	567.0	46.0	3%	429.1	4.1	0.06884	0.00068	0.55	0.012	0.0592	0.0012
B6b2-40	296.4	3.1	304.4	7.7	242.0	68.0	3%	296.4	3.1	0.04705	0.00051	0.351	0.01	0.0513	0.0017
B6b2-41	294.2	3.7	311.0	8.6	297.0	69.0	5%	294.2	3.7	0.0467	0.0006	0.356	0.011	0.0527	0.0017
B6b2-42	259.2	2.8	276.9	6.1	264.0	56.0	6%	259.2	2.8	0.04102	0.00045	0.3116	0.0077	0.0517	0.0013
B6b2-43	255.5	4.3	278.0	12.0	320.0	110.0	8%	255.5	4.3	0.04043	0.00069	0.316	0.016	0.0541	0.0029
B6b2-44	571.0	11.0	928.0	43.0	1830.0	110.0	38%	571.0	11.0	0.0926	0.0018	1.56	0.12	0.1139	0.0067
B6b2-45	435.9	7.5	545.0	11.0	1024.0	62.0	20%	435.9	7.5	0.07	0.0012	0.711	0.018	0.0741	0.0023
B6b2-47	405.6	4.2	471.3	7.7	677.0	42.0	14%	405.6	4.2	0.06494	0.0007	0.59	0.012	0.0621	0.0012
B6b2-48	498.1	5.5	531.0	8.4	561.0	42.0	6%	498.1	5.5	0.08035	0.00093	0.689	0.014	0.0592	0.0011
B6b2-49	511.8	6.5	535.8	8.3	530.0	45.0	4%	511.8	6.5	0.0825	0.0011	0.697	0.014	0.0581	0.0012
B6b2-50	409.3	4.5	439.3	5.9	492.0	34.0	7%	409.3	4.5	0.06555	0.00074	0.5422	0.009	0.05701	0.00085
B6b2-51	415.9	4.2	450.8	7.8	520.0	45.0	8%	415.9	4.2	0.06664	0.0007	0.559	0.012	0.058	0.0012
B6b2-52	558.0	8.4	632.0	18.0	882.0	64.0	12%	558.0	8.4	0.0905	0.0014	0.866	0.033	0.0689	0.0021
B6b2-53	537.4	8.9	641.0	17.0	958.0	56.0	16%	537.4	8.9	0.087	0.0015	0.882	0.03	0.0713	0.0019
B6b2-54	399.7	7.5	541.8	9.9	1207.0	47.0	26%	399.7	7.5	0.0639	0.0012	0.704	0.016	0.0801	0.0018
B6b2-55	308.1	4.0	321.5	7.4	319.0	57.0	4%	308.1	4.0	0.04897	0.00065	0.3716	0.0097	0.0531	0.0014
B6b2-56	261.1	4.0	452.5	5.5	1539.0	29.0	42%	261.1	4.0	0.04133	0.00064	0.5622	0.0084	0.0954	0.0015
B6b2-57	319.7	3.0	408.0	10.0	924.0	44.0	22%	319.7	3.0	0.05085	0.0005	0.498	0.015	0.0698	0.0015
B6b2-58	411.0	12.0	547.0	12.0	1189.0	66.0	25%	411.0	12.0	0.0658	0.002	0.718	0.02	0.0801	0.0026
B6b2-59	525.4	6.4	547.0	10.0	545.0	51.0	4%	525.4	6.4	0.0849	0.0011	0.717	0.017	0.0588	0.0014
B6b2-60	995.0	14.0	1399.0	28.0	2035.0	63.0	29%	995.0	14.0	0.167	0.0026	2.97	0.11	0.1248	0.0046
B6b2-61	659.0	13.0	653.0	23.0	655.0	98.0	1%	659.0	13.0	0.1075	0.0021	0.915	0.044	0.0613	0.0028
B6b2-62	461.7	7.0	504.0	13.0	694.0	67.0	8%	461.7	7.0	0.0743	0.0012	0.643	0.022	0.063	0.002
B6b2-63	741.0	11.0	752.0	19.0	779.0	70.0	1%	741.0	11.0	0.1219	0.0019	1.094	0.04	0.0653	0.0022
B6b2-64	373.2	7.8	459.0	21.0	920.0	110.0	19%	373.2	7.8	0.0596	0.0013	0.577	0.032	0.0698	0.0037
B6b2-65	675.2	9.2	658.0	17.0	615.0	71.0	3%	675.2	9.2	0.1103	0.0016	0.919	0.032	0.0609	0.002
B6b2-66	439.1	7.9	427.0	18.0	364.0	93.0	3%	439.1	7.9	0.0705	0.0013	0.521	0.028	0.0548	0.0026
B6b2-68	775.0	17.0	767.0	34.0	740.0	120.0	1%	775.0	17.0	0.1279	0.0029	1.147	0.071	0.0651	0.0039
B6b2-69	329.0	6.1	334.0	16.0	370.0	110.0	1%	329.0	6.1	0.05238	0.00099	0.394	0.021	0.055	0.0029
B6b2-70	1642.0	24.0	1674.0	23.0	1741.0	41.0	2%	1674.0	23.0	0.2904	0.0047	4.23	0.11	0.1071	0.0025

B6b2-71	417.0	15.0	836.0	23.0	2153.0	34.0	50%	417.0	15.0	0.067	0.0025	1.277	0.05	0.1342	0.0027
B6b2-72	514.7	7.3	498.0	13.0	467.0	62.0	3%	514.7	7.3	0.0831	0.0012	0.638	0.021	0.0568	0.0016
B6b2-73	1730.0	23.0	1726.0	17.0	1745.0	30.0	0%	1726.0	17.0	0.3081	0.0047	4.469	0.094	0.1065	0.0017
B6b2-74	407.3	6.3	455.0	16.0	728.0	75.0	10%	407.3	6.3	0.0652	0.001	0.567	0.024	0.0636	0.0022
B6b2-75	505.2	9.1	481.0	19.0	399.0	79.0	5%	505.2	9.1	0.0814	0.0015	0.608	0.031	0.0549	0.0021
B6b2-76	181.0	2.7	749.0	11.0	3378.0	25.0	76%	181.0	2.7	0.02848	0.00042	1.094	0.022	0.2837	0.0045
B6b2-77	505.2	8.4	651.0	24.0	1220.0	89.0	22%	505.2	8.4	0.0816	0.0014	0.909	0.046	0.0804	0.0036
B6b2-78	445.1	9.1	546.0	22.0	980.0	110.0	18%	445.1	9.1	0.0715	0.0015	0.723	0.038	0.0723	0.0037
B6b2-79	433.3	7.5	420.0	14.0	322.0	81.0	3%	433.3	7.5	0.0696	0.0012	0.51	0.022	0.0527	0.002
B6b2-80	1833.0	36.0	2344.0	22.0	2821.0	26.0	22%	2344.0	22.0	0.3297	0.0075	9.09	0.22	0.1998	0.0033
B6b2-81	607.1	7.1	601.0	15.0	580.0	59.0	1%	607.1	7.1	0.0988	0.0012	0.814	0.027	0.0602	0.0016
B6b2-82	1062.0	14.0	1203.0	14.0	1413.0	38.0	12%	1062.0	14.0	0.1791	0.0026	2.264	0.044	0.0898	0.0018
B6b2-83	242.1	4.9	631.7	8.3	2490.0	29.0	62%	242.1	4.9	0.03828	0.00079	0.861	0.015	0.1637	0.0028
B6b2-84	1339.0	16.0	1341.0	19.0	1344.0	45.0	0%	1339.0	16.0	0.2307	0.0029	2.74	0.066	0.0854	0.002
B6b2-85	447.6	9.2	452.0	16.0	479.0	84.0	1%	447.6	9.2	0.0719	0.0015	0.563	0.025	0.0575	0.0022
B6b2-86	602.3	8.0	590.0	14.0	576.0	59.0	2%	602.3	8.0	0.098	0.0014	0.792	0.025	0.0591	0.0017
B6b2-87	520.1	7.5	518.0	14.0	522.0	75.0	0%	520.1	7.5	0.084	0.0013	0.669	0.023	0.0585	0.002
B6b2-88	466.9	6.9	865.0	15.0	2129.0	39.0	46%	466.9	6.9	0.0751	0.0011	1.35	0.033	0.1329	0.0029
B6b2-89	563.0	11.0	534.0	19.0	407.0	94.0	5%	563.0	11.0	0.0914	0.0018	0.694	0.033	0.055	0.0024
B6b2-90	541.0	13.0	572.0	25.0	732.0	73.0	5%	541.0	13.0	0.0876	0.0023	0.749	0.045	0.0637	0.0022
B6b1-1	622.7	6.4	642.0	17.0	683.0	77.0	3%	622.7	6.4	0.1014	0.0011	0.888	0.031	0.0631	0.0023
B6b1-2	386.0	3.5	543.4	8.0	1289.0	34.0	29%	386.0	3.5	0.06171	0.00058	0.708	0.014	0.0842	0.0015
B6b1-3	619.5	5.9	615.0	12.0	626.0	51.0	1%	619.5	5.9	0.1009	0.001	0.834	0.021	0.0612	0.0015
B6b1-4	502.2	5.5	508.0	14.0	557.0	70.0	1%	502.2	5.5	0.08103	0.00092	0.654	0.023	0.0599	0.002
B6b1-5	593.7	5.2	613.8	7.8	704.0	28.0	3%	593.7	5.2	0.09649	0.00088	0.832	0.014	0.06279	0.00081
B6b1-6	2795.0	19.0	2801.6	9.9	2813.0	13.0	0%	2801.6	9.9	0.5431	0.0046	14.76	0.15	0.1985	0.0016
B6b1-8	628.0	6.9	627.0	15.0	611.0	71.0	0%	628.0	6.9	0.1022	0.0012	0.856	0.027	0.0615	0.002
B6b1-12	539.5	6.0	546.2	8.9	578.0	40.0	1%	539.5	6.0	0.0873	0.001	0.712	0.015	0.0595	0.0011
B6b1-13	570.0	24.0	1036.0	23.0	2240.0	31.0	45%	570.0	24.0	0.0926	0.0041	1.787	0.061	0.1418	0.0026
B6b1-14	331.5	5.7	616.0	26.0	1853.0	94.0	46%	331.5	5.7	0.05278	0.00094	0.843	0.046	0.1158	0.0058
B6b1-16	601.4	6.7	889.0	25.0	1674.0	62.0	32%	601.4	6.7	0.0978	0.0011	1.421	0.06	0.1054	0.0036
B6b1-17	456.6	5.6	463.0	11.0	478.0	64.0	1%	456.6	5.6	0.07341	0.00093	0.578	0.016	0.0574	0.0017

B6b1-18	971.0	16.0	965.0	29.0	940.0	96.0	1%	971.0	16.0	0.1627	0.0028	1.591	0.072	0.0714	0.0032
B6b1-19	313.8	4.2	428.0	15.0	1082.0	88.0	27%	313.8	4.2	0.04989	0.00069	0.521	0.023	0.0769	0.0033
B6b1-20	306.3	3.8	307.0	10.0	320.0	79.0	0%	306.3	3.8	0.04867	0.00063	0.352	0.013	0.0528	0.002

Appendix 31: Detrital zircon (U-Th)/He data for sample B4.

Grain #	V (µm3)	+/- 2σ	4He (mol)	Corrected 4He (mol)	+/- 2σ	4He (mol/g)	Corrected 4He (mol/g)	+/- 2σ	232Th (ppm)	+/- 2σ	238U (ppm)	+/- 2σ	147Sm (ppm)	+/- 2σ	eU	Th/U	ZHe age (Ma)	+/- 2σ
B4b1-2	10346	517	2.03E-14	1.36E-14	5.61E-16	4.23E-07	2.82E-07	2.41E-08	64	1	167	3	2	0	182	0.38	431.2	25.8
B4b1-3	10350	517	2.57E-14	1.71E-14	4.29E-16	5.34E-07	3.56E-07	2.81E-08	62	4	286	4	3	0	301	0.22	329.2	18.0
B4b1-4	10354	518	8.36E-15	5.58E-15	3.12E-16	1.74E-07	1.16E-07	1.08E-08	175	4	127	4	5	0	168	1.38	191.6	12.6
B4b1-5	10357	518	6.05E-14	4.03E-14	6.18E-16	1.26E-06	8.37E-07	6.41E-08	292	3	649	7	3	0	717	0.45	324.6	16.9
B4b1-6	10361	518	1.60E-14	1.07E-14	3.63E-16	3.32E-07	2.21E-07	1.82E-08	82	6	195	11	9	1	214	0.42	287.4	21.7
B4b1-7	10365	518	7.69E-15	5.13E-15	3.51E-16	1.60E-07	1.06E-07	1.08E-08	25	1	81	2	2	0	87	0.31	341.4	24.2
B4b1-9	10373	519	3.37E-15	2.25E-15	1.99E-16	6.99E-08	4.66E-08	5.41E-09	45	0	96	1	3	0	106	0.47	121.9	9.5
B4b1-10	10377	519	5.74E-15	3.82E-15	3.07E-16	1.19E-07	7.92E-08	8.70E-09	32	0	106	1	3	0	114	0.30	193.7	14.3
B4b1-11	10380	519	7.39E-14	4.92E-14	9.39E-16	1.53E-06	1.02E-06	7.89E-08	324	3	728	8	6	0	804	0.45	352.8	18.5
B4b1-12	10384	519	5.18E-14	3.45E-14	6.38E-16	1.07E-06	7.15E-07	5.53E-08	2000	100	893	29	6	0	1363	2.24	145.6	8.5
B4b1-13	10388	519	7.26E-15	4.84E-15	2.01E-16	1.50E-07	1.00E-07	8.60E-09	46	1	63	2	4	0	73	0.74	-	
B4b1-14	10392	520	5.47E-15	3.64E-15	2.19E-16	1.13E-07	7.54E-08	7.25E-09	70	2	129	3	11	0	145	0.54	144.5	9.9
B4b1-15	10396	520	1.12E-14	7.43E-15	3.32E-16	2.31E-07	1.54E-07	1.34E-08	51	1	123	2	4	0	135	0.42	317.5	18.9
B4b1-16	10400	520	1.42E-15	9.50E-16	1.40E-16	2.95E-08	1.96E-08	3.25E-09	36	1	37	1	5	0	45	0.98	-	
B4b1-17	10403	520	1.97E-14	1.32E-14	5.49E-16	4.08E-07	2.72E-07	2.34E-08	281	4	193	4	12	0	259	1.46	292.0	17.2
B4b1-18	10407	520	2.40E-14	1.60E-14	4.70E-16	4.95E-07	3.30E-07	2.66E-08	128	3	241	4	5	0	271	0.53	339.3	18.9
B4b1-19	10411	521	4.78E-15	3.19E-15	2.22E-16	9.87E-08	6.58E-08	6.74E-09	27	0	58	1	4	0	64	0.46	-	
B4b1-20	10415	521	3.00E-14	2.00E-14	5.13E-16	6.20E-07	4.14E-07	3.28E-08	188	10	345	10	28	2	389	0.54	295.6	17.5
B4b1-21	10419	521	5.86E-15	3.91E-15	2.36E-16	1.21E-07	8.06E-08	7.76E-09	18	0	42	1	2	0	46	0.44	-	
B4b1-22	10422	521	1.84E-14	1.22E-14	5.03E-16	3.79E-07	2.53E-07	2.16E-08	65	1	298	4	2	0	313	0.22	224.8	13.1
B4b1-23	10426	521	1.82E-14	1.21E-14	4.65E-16	3.75E-07	2.50E-07	2.11E-08	82	2	208	4	4	0	227	0.39	306.1	18.2
B4b1-24	10430	522	7.09E-15	4.72E-15	3.09E-16	1.46E-07	9.74E-08	9.70E-09	74	1	112	1	7	0	130	0.66	208.7	14.0
B4b1-25	10434	522	2.81E-14	1.87E-14	4.82E-16	5.79E-07	3.86E-07	3.06E-08	145	5	474	12	4	0	508	0.31	211.4	12.2
B4b1-26	10438	522	1.03E-14	6.87E-15	3.60E-16	2.12E-07	1.42E-07	1.30E-08	47	1	117	2	2	0	128	0.41	307.4	19.1
B4b1-27	10442	522	1.69E-14	1.13E-14	2.99E-16	3.48E-07	2.32E-07	1.84E-08	123	2	157	2	7	0	186	0.78	345.9	18.9
B4b1-28	10445	522	1.34E-14	8.96E-15	2.29E-16	2.77E-07	1.85E-07	1.46E-08	77	1	157	2	9	0	175	0.49	293.9	16.0
B4b1-29	10449	522	2.76E-14	1.84E-14	5.11E-16	5.68E-07	3.78E-07	3.03E-08	8	0	359	5	1	0	361	0.02	291.7	16.0
B4b1-30	10453	523	1.73E-14	1.15E-14	4.29E-16	3.56E-07	2.38E-07	1.99E-08	110	2	163	2	1	0	188	0.67	350.9	20.0
B4b1-31	10457	523	9.40E-15	6.27E-15	1.88E-16	1.93E-07	1.29E-07	1.04E-08	50	1	114	2	8	0	126	0.44	285.5	15.8

B4b1-32	10461	523	1.14E-14	7.57E-15	3.14E-16	2.34E-07	1.56E-07	1.33E-08	64	3	178	4	3	0	194	0.36	223.9	13.7
B4b1-34	10468	523	5.55E-14	3.70E-14	5.97E-16	1.14E-06	7.60E-07	5.83E-08	179	6	578	17	11	0	620	0.31	341.2	19.8
B4b1-35	10472	524	4.16E-15	2.77E-15	2.21E-16	8.53E-08	5.69E-08	6.22E-09	22	0	62	1	2	0	67	0.35	-	
B4b1-36	10476	524	1.86E-14	1.24E-14	4.81E-16	3.81E-07	2.54E-07	2.15E-08	130	2	224	3	10	0	254	0.58	277.9	16.0
B4b1-37	10480	524	2.52E-14	1.68E-14	3.30E-16	5.16E-07	3.44E-07	2.67E-08	92	6	188	9	5	0	209	0.49	457.9	30.4
B4b1-38	10484	524	6.45E-14	4.30E-14	8.77E-16	1.32E-06	8.82E-07	6.86E-08	404	7	543	9	13	0	638	0.74	384.3	20.7
B4b1-39	10487	524	1.67E-14	1.11E-14	3.62E-16	3.42E-07	2.28E-07	1.86E-08	159	4	168	4	8	0	206	0.94	308.2	17.7
B4b1-40	10491	525	4.42E-14	2.94E-14	6.41E-16	9.05E-07	6.03E-07	4.71E-08	520	7	679	9	8	0	801	0.77	209.6	11.1
B4b1-41	10495	525	2.86E-14	1.91E-14	6.22E-16	5.87E-07	3.91E-07	3.20E-08	114	7	383	11	10	1	410	0.30	265.8	16.2
B4b2-1	12453	623	1.42E-14	9.45E-15	1.59E-16	2.45E-07	1.63E-07	1.25E-08	103	2	182	3	0	0	206	0.57	220.5	11.8
B4b2-2	12450	622	1.08E-14	7.19E-15	1.24E-16	1.86E-07	1.24E-07	9.56E-09	41	1	130	4	3	0	139	0.32	247.9	14.3
B4b2-3	12447	622	3.97E-14	2.65E-14	7.17E-16	6.86E-07	4.57E-07	3.65E-08	79	2	321	8	4	0	339	0.25	375.2	21.9
B4b2-4	12444	622							98	3	390	8	4	0	414	0.25	-	
B4b2-5	12442	622	6.58E-14	4.38E-14	8.52E-16	1.14E-06	7.58E-07	5.87E-08	152	5	1213	25	29	3	1249	0.12	169.0	9.4
B4b2-6	12439	622	3.20E-14	2.14E-14	5.37E-16	5.54E-07	3.69E-07	2.92E-08	119	1	317	4	5	0	345	0.38	298.3	16.1
B4b2-7	12436	622	8.16E-14	5.44E-14	1.16E-15	1.41E-06	9.40E-07	7.33E-08	948	16	881	16	27	1	1104	1.08	236.7	12.8
B4b2-8	12433	622	7.48E-15	4.98E-15	2.85E-16	1.29E-07	8.62E-08	8.13E-09	63	1	82	1	0	0	97	0.77	247.5	16.0
B4b2-9	12431	622	2.12E-14	1.42E-14	3.40E-16	3.67E-07	2.45E-07	1.93E-08	297	4	302	4	15	0	371	0.98	183.3	9.9
B4b2-10	12428	621	2.30E-14	1.53E-14	6.05E-16	3.98E-07	2.65E-07	2.25E-08	96	3	199	6	9	0	222	0.48	332.7	20.7
B4b2-11	12425	621	1.81E-14	1.21E-14	3.92E-16	3.14E-07	2.09E-07	1.71E-08	55	2	211	4	0	0	223	0.26	260.7	15.0
B4b2-12	12422	621	7.83E-15	5.22E-15	2.63E-16	1.36E-07	9.04E-08	8.17E-09	38	1	138	2	3	0	147	0.28	170.7	10.6
B4b2-13	12420	621	5.38E-14	3.59E-14	7.69E-16	9.31E-07	6.21E-07	4.84E-08	179	3	257	4	4	0	300	0.70	576.3	31.0
B4b2-14	12417	621	3.28E-14	2.18E-14	8.01E-16	5.67E-07	3.78E-07	3.16E-08	27	1	402	7	0	0	408	0.07	258.2	15.1
B4b2-16	12411	621	6.73E-15	4.48E-15	2.06E-16	1.17E-07	7.77E-08	6.83E-09	55	1	77	1	4	0	90	0.71	240.5	14.5
B4b2-17	12409	620	4.66E-15	3.11E-15	2.42E-16	8.08E-08	5.39E-08	5.83E-09	31	1	66	1	0	0	73	0.47	-	
B4b2-18	12406	620	2.27E-14	1.51E-14	4.82E-16	3.93E-07	2.62E-07	2.14E-08	158	3	215	3	11	0	252	0.74	289.4	16.2
B4b2-19	12403	620	1.27E-14	8.48E-15	3.05E-16	2.21E-07	1.47E-07	1.22E-08	67	2	120	4	7	0	136	0.56	301.4	18.9
B4b2-20	12400	620	1.45E-14	9.68E-15	3.62E-16	2.52E-07	1.68E-07	1.41E-08	38	1	157	2	2	0	166	0.24	281.0	16.2
B4b2-21	12398	620	1.60E-14	1.07E-14	4.04E-16	2.78E-07	1.85E-07	1.56E-08	90	2	160	2	9	0	181	0.56	284.1	16.4
B4b2-22	12395	620	7.07E-14	4.71E-14	6.45E-16	1.23E-06	8.18E-07	6.24E-08	314	11	750	18	15	1	824	0.42	276.2	15.3
B4b2-23	12392	620	6.18E-15	4.12E-15	2.00E-16	1.07E-07	7.15E-08	6.38E-09	46	1	87	1	0	0	97	0.53	204.2	12.5
B4b2-24	12389	619	6.05E-14	4.03E-14	6.81E-16	1.05E-06	7.00E-07	5.38E-08	195	3	646	13	10	0	692	0.30	281.6	15.4

B4b2-25	12387	619	3.29E-14	2.20E-14	6.39E-16	5.72E-07	3.81E-07	3.07E-08	78	2	289	5	0	0	307	0.27	345.7	19.3
B4b2-26	12384	619	1.75E-14	1.17E-14	4.09E-16	3.04E-07	2.02E-07	1.68E-08	75	2	248	6	0	0	266	0.30	212.0	12.7
B4b2-27	12381	619	1.17E-13	7.81E-14	1.19E-15	2.04E-06	1.36E-06	1.04E-07	359	18	1423	19	30	2	1507	0.25	250.5	13.2
B4b2-28	12378	619	1.91E-14	1.27E-14	4.22E-16	3.32E-07	2.21E-07	1.81E-08	51	3	215	4	7	1	227	0.24	271.4	15.5
B4b2-29	12376	619	2.10E-14	1.40E-14	3.78E-16	3.65E-07	2.43E-07	1.94E-08	42	1	168	5	0	0	178	0.25	379.4	23.1
B4b2-30	12373	619	6.08E-14	4.05E-14	7.33E-16	1.06E-06	7.04E-07	5.44E-08	106	2	665	11	0	0	690	0.16	284.3	15.3
B4b2-31	12370	619	1.69E-14	1.12E-14	4.31E-16	2.93E-07	1.95E-07	1.65E-08	136	2	233	3	0	0	265	0.58	205.1	11.8
B4b2-32	12367	618	6.85E-15	4.57E-15	1.60E-16	1.19E-07	7.94E-08	6.58E-09	98	2	179	3	0	0	202	0.55	109.2	6.2
B4b2-34	12362	618	3.67E-14	2.45E-14	5.65E-16	6.39E-07	4.26E-07	3.34E-08	283	6	316	5	5	0	382	0.90	309.9	16.7
B4b2-35	12359	618	1.18E-14	7.85E-15	3.83E-16	2.05E-07	1.37E-07	1.22E-08	< LOD	1	140	3	< LOD	0	-	-	-	-
B4b2-36	12356	618	1.61E-14	1.07E-14	3.33E-16	2.81E-07	1.87E-07	1.52E-08	38	1	123	6	4	0	131	0.31	395.8	27.6
B4b2-37	12354	618	1.88E-14	1.25E-14	3.78E-16	3.27E-07	2.18E-07	1.76E-08	87	3	198	3	3	0	218	0.44	278.3	15.5
B4b2-38	12351	618	9.29E-15	6.19E-15	3.01E-16	1.62E-07	1.08E-07	9.64E-09	70	1	103	2	3	0	120	0.67	250.3	15.3
B4b2-39	12348	617	1.72E-14	1.14E-14	4.38E-16	2.99E-07	1.99E-07	1.68E-08	58	1	142	2	3	0	155	0.41	357.2	20.3
B4b2-40	12345	617	4.95E-14	3.30E-14	7.62E-16	8.62E-07	5.74E-07	4.51E-08	372	8	441	8	11	0	528	0.84	302.4	16.5
B4b2-41	12343	617	3.47E-14	2.31E-14	4.24E-16	6.04E-07	4.03E-07	3.11E-08	131	2	350	5	0	0	381	0.37	294.0	15.6
B4b2-42	12340	617	2.31E-14	1.54E-14	4.56E-16	4.03E-07	2.69E-07	2.17E-08	156	3	256	4	10	0	293	0.61	255.3	14.3
B4b2-43	12337	617	2.42E-14	1.61E-14	5.69E-16	4.22E-07	2.82E-07	2.33E-08	15	0	228	7	0	0	232	0.07	338.4	21.5
B4b2-44	12334	617	6.18E-14	4.12E-14	6.70E-16	1.08E-06	7.19E-07	5.52E-08	217	6	736	12	8	0	787	0.29	254.2	13.6
B4b2-45	12332	617	3.49E-14	2.33E-14	4.90E-16	6.09E-07	4.06E-07	3.16E-08	110	2	362	6	9	1	388	0.30	291.3	15.8
B4b2-46	12329	616	4.63E-14	3.09E-14	6.39E-16	8.08E-07	5.39E-07	4.19E-08	83	2	502	19	0	0	522	0.17	287.5	18.2
B4b2-47	12326	616	1.84E-14	1.23E-14	2.64E-16	3.21E-07	2.14E-07	1.67E-08	50	1	181	4	3	0	193	0.27	308.9	17.4
B4b2-48	12323	616	1.29E-14	8.63E-15	2.32E-16	2.26E-07	1.51E-07	1.20E-08	53	2	187	7	4	0	199	0.29	210.2	13.3
B4b2-49	12321	616	1.77E-14	1.18E-14	4.00E-16	3.08E-07	2.06E-07	1.69E-08	65	1	179	3	0	0	194	0.36	295.1	17.0
B4b2-50	12318	616	1.18E-14	7.86E-15	2.65E-16	2.06E-07	1.37E-07	1.13E-08	100	4	85	3	5	0	108	1.18	352.1	21.5
B4b2-51	12315	616	3.74E-14	2.49E-14	4.34E-16	6.53E-07	4.35E-07	3.35E-08	177	3	505	8	6	0	547	0.35	221.6	11.8
B4b2-52	12312	616	3.60E-14	2.40E-14	6.89E-16	6.29E-07	4.19E-07	3.37E-08	307	8	369	9	10	0	441	0.83	264.1	15.1
B4b2-53	12310	615	1.16E-14	7.72E-15	3.04E-16	2.02E-07	1.35E-07	1.14E-08	< LOD	1	149	3	< LOD	0	-	-	-	-
B4b2-54	12307	615	1.70E-14	1.13E-14	3.84E-16	2.97E-07	1.98E-07	1.63E-08	116	2	281	4	4	0	308	0.41	178.9	10.1
B4b2-55	12304	615	2.18E-14	1.45E-14	4.44E-16	3.81E-07	2.54E-07	2.06E-08	256	8	210	5	17	1	270	1.22	260.6	15.1
B4b2-56	12301	615	1.68E-14	1.12E-14	3.71E-16	2.94E-07	1.96E-07	1.61E-08	< LOD	3	232	7	< LOD	0	-	-	-	-
B4b2-57	12299	615	2.65E-14	1.77E-14	4.21E-16	4.64E-07	3.09E-07	2.43E-08	59	3	331	13	4	0	345	0.18	249.5	16.1

B4b2-58	12296	615	4.62E-14	3.08E-14	6.98E-16	8.08E-07	5.39E-07	4.22E-08	166	5	528	13	11	0	567	0.31	264.3	15.1
B4b2-59	12293	615	3.17E-14	2.11E-14	4.45E-16	5.54E-07	3.70E-07	2.88E-08	77	2	356	7	9	1	374	0.22	275.3	15.1
B4b2-60	12290	615	2.73E-14	1.82E-14	4.33E-16	4.77E-07	3.18E-07	2.50E-08	54	3	271	9	0	0	283	0.20	312.8	19.0
B4b2-62	12285	614	1.78E-14	1.19E-14	3.69E-16	3.12E-07	2.08E-07	1.69E-08	94	3	208	4	6	0	230	0.45	251.4	14.3
B4b2-63	12282	614	1.16E-14	7.71E-15	3.08E-16	2.03E-07	1.35E-07	1.15E-08	84	2	154	5	11	0	174	0.54	216.0	13.5
B4b2-64	12279	614	1.49E-14	9.93E-15	2.59E-16	2.61E-07	1.74E-07	1.38E-08	135	3	143	3	3	0	174	0.95	277.0	15.4
B4b2-65	12277	614	3.75E-15	2.50E-15	2.24E-16	6.57E-08	4.38E-08	5.11E-09	< LOD	1	< LOD	1	< LOD	0	-	-	-	-
B4b2-66	12274	614	3.97E-14	2.65E-14	6.78E-16	6.96E-07	4.64E-07	3.68E-08	74	4	431	18	7	0	448	0.17	288.3	19.1
B4b2-67	12271	614	4.50E-14	3.00E-14	6.34E-16	7.88E-07	5.25E-07	4.09E-08	59	2	456	13	0	0	470	0.13	311.2	18.3
B4b2-68	12268	613	1.39E-14	9.27E-15	3.19E-16	2.44E-07	1.62E-07	1.34E-08	70	3	122	4	7	1	138	0.58	327.3	19.9
B4b2-69	12266	613	8.02E-14	5.35E-14	1.09E-15	1.41E-06	9.38E-07	7.29E-08	169	3	766	12	3	0	806	0.22	324.1	17.5
B4b2-70	12263	613	3.79E-14	2.53E-14	5.69E-16	6.66E-07	4.44E-07	3.47E-08	218	6	504	14	17	2	555	0.43	222.3	12.9
B4b2-71	12260	613	3.06E-14	2.04E-14	5.13E-16	5.37E-07	3.58E-07	2.83E-08	178	8	309	15	10	1	351	0.58	283.7	19.3
B4b2-72	12257	613	1.98E-14	1.32E-14	4.65E-16	3.48E-07	2.32E-07	1.92E-08	202	8	< LOD	10	< LOD	0	-	-	-	-
B4b2-73	12255	613	4.60E-14	3.07E-14	6.43E-16	8.07E-07	5.38E-07	4.19E-08	103	22	790	110	32	7	814	0.13	184.1	26.7
B4b2-74	12252	613	2.01E-14	1.34E-14	6.64E-16	3.53E-07	2.35E-07	2.11E-08	154	14	460	29	5	1	496	0.33	132.0	11.1
B4b2-75	12249	612	1.53E-14	1.02E-14	3.87E-16	2.69E-07	1.79E-07	1.51E-08	79	6	207	18	8	1	226	0.38	221.1	21.6
B4b2-76	12246	612	4.91E-14	3.27E-14	6.63E-16	8.62E-07	5.75E-07	4.46E-08	214	5	736	17	5	0	786	0.29	203.4	11.4
B4b2-77	12244	612	2.75E-14	1.83E-14	6.30E-16	4.82E-07	3.22E-07	2.65E-08	58	58	200	200	6	6	214	0.29	418.9	393.5
B4b2-78	12241	612	8.78E-15	5.85E-15	2.71E-16	1.54E-07	1.03E-07	9.06E-09	93	5	116	6	7	1	137	0.81	208.0	15.5
B4b2-79	12238	612	5.09E-14	3.39E-14	7.34E-16	8.94E-07	5.96E-07	4.65E-08	558	22	641	23	9	1	772	0.87	214.5	12.9
B4b2-80	12235	612	1.47E-14	9.80E-15	2.66E-16	2.58E-07	1.72E-07	1.37E-08	< LOD	4	< LOD	12	4	0	-	-	-	-
B4b2-81	12233	612	3.82E-14	2.54E-14	6.04E-16	6.71E-07	4.47E-07	3.52E-08	237	22	500	36	3	0	556	0.47	224.0	18.8
B4b2-82	12230	611	2.89E-14	1.93E-14	5.03E-16	5.08E-07	3.39E-07	2.69E-08	300	51	284	38	5	0	355	1.06	265.6	33.0
B4b2-83	12227	611	1.56E-14	1.04E-14	4.98E-16	2.75E-07	1.83E-07	1.63E-08	129	11	143	15	6	1	173	0.90	293.5	31.1
B4b2-84	12224	611	3.13E-14	2.09E-14	5.28E-16	5.50E-07	3.67E-07	2.90E-08	336	16	263	10	15	1	342	1.28	298.1	18.3
B4b2-85	12222	611	9.70E-15	6.47E-15	2.99E-16	1.71E-07	1.14E-07	1.00E-08	60	4	311	19	4	1	325	0.19	97.4	8.1
B4b2-86	12219	611	4.46E-14	2.97E-14	4.74E-16	7.85E-07	5.23E-07	4.01E-08	150	170	500	120	9	9	535	0.30	272.0	65.8
B4b2-87	12216	611	1.31E-14	8.71E-15	2.16E-16	2.30E-07	1.53E-07	1.21E-08	80	7	193	18	7	1	212	0.42	201.4	20.2
B4b2-88	12213	611	7.31E-14	4.87E-14	6.31E-16	1.29E-06	8.58E-07	6.53E-08	NA	NA	NA	NA	NA	NA	-	-	-	-
B4b2-89	12211	611	2.82E-14	1.88E-14	5.19E-16	4.96E-07	3.31E-07	2.64E-08	NA	NA	NA	NA	NA	NA	-	-	-	-
B4b2-90	12208	610	1.49E-14	9.92E-15	3.64E-16	2.62E-07	1.75E-07	1.46E-08	79	15	213	53	2	1	232	0.37	209.9	49.5

B4b2-91	12205	610	8.37E-15	5.58E-15	3.15E-16	1.47E-07	9.83E-08	9.23E-09	29	29	100	100	3	3	107	0.29	256.1	240.7
B4b2-92	12202	610	4.71E-14	3.14E-14	7.07E-16	8.31E-07	5.54E-07	4.34E-08	112	8	459	47	0	0	485	0.24	317.7	35.0
B4b2-93	12200	610	7.39E-15	4.93E-15	2.46E-16	1.30E-07	8.69E-08	7.82E-09	NA	NA	NA	NA	NA	NA	-	-	-	-
B4b2-94	12197	610	2.49E-14	1.66E-14	6.39E-16	4.38E-07	2.92E-07	2.46E-08	228	26	219	24	3	0	273	1.04	298.0	31.8
B4b2-95	12194	610	7.47E-15	4.98E-15	1.91E-16	1.32E-07	8.79E-08	7.40E-09	83	2	92	8	5	1	112	0.90	218.2	19.8
B4b2-96	12191	610	4.46E-14	2.97E-14	8.03E-16	7.86E-07	5.24E-07	4.18E-08	272	28	564	62	6	1	628	0.48	232.2	26.1
B4b2-97	12189	609	6.05E-15	4.04E-15	1.93E-16	1.07E-07	7.12E-08	6.33E-09	93	93	260	260	6	6	282	0.36	70.3	65.2
B4b2-98	12186	609	3.57E-15	2.38E-15	1.88E-16	6.30E-08	4.20E-08	4.57E-09	NA	NA	NA	NA	NA	NA	-	-	-	-
B4b2-99	12183	609	1.04E-14	6.94E-15	3.37E-16	1.84E-07	1.22E-07	1.09E-08	84	6	91	4	8	3	111	0.92	307.8	21.1
B4b2-100	12180	609	3.50E-14	2.33E-14	5.64E-16	6.18E-07	4.12E-07	3.25E-08	175	85	400	220	0	0	441	0.44	259.8	130.7

Appendix 32: Reduced detrital zircon U-Pb data for sample B4.

Grain #	Age 206/238	+/- 2σ	Age 207/235	+/- 2σ	Age 207/206	+/- 2σ	% Discordance	Selected U/Pb age (Ma)	+/- 2σ	Ratio 206/238	+/- 2σ	Ratio 207/235	+/- 2σ	Ratio 207/206	+/- 2σ
B4b1-2	864.0	7.8	854.0	14.0	831.0	45.0	1%	864.0	7.8	0.1433	0.0014	1.33	0.031	0.0671	0.0015
B4b1-3	436.9	4.0	449.0	11.0	500.0	62.0	3%	436.9	4.0	0.07013	0.00066	0.563	0.017	0.0575	0.0016
B4b1-4	1610.0	12.0	1684.0	14.0	1776.0	29.0	4%	1684.0	14.0	0.2837	0.0023	4.321	0.087	0.1092	0.0018
B4b1-5	2248.0	28.0	2371.0	20.0	2464.0	12.0	5%	2371.0	20.0	0.418	0.0062	9.35	0.2	0.1609	0.0012
B4b1-6	489.0	21.0	1190.0	100.0	2680.0	200.0	59%	489.0	21.0	0.0791	0.0036	2.87	0.47	0.252	0.027
B4b1-7	316.8	4.7	321.0	18.0	340.0	120.0	1%	316.8	4.7	0.05038	0.00077	0.373	0.025	0.0541	0.0032
B4b1-9	620.1	6.4	605.0	18.0	511.0	88.0	2%	620.1	6.4	0.101	0.0011	0.826	0.033	0.0586	0.0024
B4b1-10	316.0	5.1	306.0	15.0	240.0	100.0	3%	316.0	5.1	0.05025	0.00084	0.359	0.02	0.0527	0.0027
B4b1-11	1008.9	7.1	1015.2	8.4	1023.0	20.0	1%	1008.9	7.1	0.1694	0.0013	1.722	0.023	0.07339	0.00072
B4b1-12	100.7	1.1	100.0	3.6	69.0	67.0	1%	100.7	1.1	0.01574	0.00017	0.1035	0.0039	0.047	0.0015
B4b1-13	688.6	8.4	670.0	22.0	610.0	89.0	3%	688.6	8.4	0.1127	0.0015	0.959	0.045	0.0619	0.0027
B4b1-14	562.1	6.0	547.0	15.0	458.0	70.0	3%	562.1	6.0	0.0911	0.001	0.723	0.026	0.0571	0.0019
B4b1-15	308.9	3.7	303.0	14.0	210.0	100.0	2%	308.9	3.7	0.04909	0.00061	0.346	0.017	0.0514	0.0025
B4b1-16	606.0	11.0	627.0	28.0	670.0	130.0	3%	606.0	11.0	0.0986	0.0018	0.869	0.054	0.0627	0.0038
B4b1-17	633.5	6.0	646.0	12.0	659.0	54.0	2%	633.5	6.0	0.1033	0.001	0.894	0.022	0.0622	0.0016
B4b1-18	323.5	3.1	321.5	8.4	288.0	67.0	1%	323.5	3.1	0.05147	0.0005	0.375	0.011	0.0525	0.0016
B4b1-19	465.7	6.9	476.0	21.0	480.0	110.0	2%	465.7	6.9	0.0748	0.0011	0.612	0.034	0.0579	0.0031
B4b1-20	427.5	6.5	538.0	18.0	996.0	81.0	21%	427.5	6.5	0.0686	0.0011	0.718	0.033	0.0748	0.0032
B4b1-21	856.0	11.0	835.0	28.0	797.0	95.0	3%	856.0	11.0	0.1421	0.002	1.294	0.063	0.0672	0.003
B4b1-22	475.3	4.2	471.1	9.9	419.0	54.0	1%	475.3	4.2	0.07652	0.00071	0.589	0.015	0.0555	0.0014
B4b1-23	316.2	3.7	319.0	10.0	309.0	81.0	1%	316.2	3.7	0.05028	0.0006	0.368	0.014	0.0527	0.002
B4b1-24	2527.0	18.0	2492.0	11.0	2461.0	18.0	1%	2492.0	11.0	0.4803	0.0041	10.64	0.13	0.1608	0.0017
B4b1-25	238.3	3.2	234.4	6.9	245.0	58.0	2%	238.3	3.2	0.03766	0.00051	0.2611	0.0085	0.0512	0.0014
B4b1-26	471.3	5.7	469.0	13.0	441.0	79.0	0%	471.3	5.7	0.0758	0.00094	0.586	0.02	0.0564	0.0021
B4b1-27	375.2	4.2	377.0	13.0	345.0	89.0	0%	375.2	4.2	0.05993	0.00068	0.448	0.019	0.0537	0.0022
B4b1-28	481.6	5.2	468.0	14.0	361.0	81.0	3%	481.6	5.2	0.07758	0.00087	0.585	0.022	0.0549	0.0021
B4b1-29	617.4	4.9	618.1	8.6	598.0	36.0	0%	617.4	4.9	0.10052	0.00084	0.841	0.016	0.0598	0.001
B4b1-30	472.3	4.6	461.0	13.0	399.0	74.0	2%	472.3	4.6	0.07603	0.00077	0.589	0.022	0.0557	0.0019
B4b1-31	460.3	5.2	461.0	15.0	448.0	88.0	0%	460.3	5.2	0.07404	0.00087	0.575	0.024	0.0561	0.0023

B4b1-32	314.0	3.2	301.0	11.0	194.0	87.0	4%	314.0	3.2	0.04992	0.00052	0.351	0.015	0.0498	0.0021
B4b1-34	313.2	3.2	314.1	6.6	334.0	49.0	0%	313.2	3.2	0.04979	0.00052	0.368	0.01	0.0532	0.0012
B4b1-35	318.2	5.6	361.0	26.0	640.0	150.0	12%	318.2	5.6	0.05055	0.00091	0.444	0.038	0.0648	0.0049
B4b1-36	467.5	4.6	461.0	11.0	410.0	53.0	1%	467.5	4.6	0.07523	0.00077	0.577	0.017	0.0553	0.0013
B4b1-37	471.8	5.5	466.0	12.0	428.0	70.0	1%	471.8	5.5	0.07596	0.00092	0.584	0.021	0.0555	0.0018
B4b1-38	780.3	7.0	762.9	8.9	727.0	28.0	2%	780.3	7.0	0.1287	0.0012	1.124	0.019	0.06358	0.00083
B4b1-39	317.9	3.8	312.0	13.0	268.0	91.0	2%	317.9	3.8	0.05051	0.00062	0.356	0.019	0.0524	0.0024
B4b1-40	300.3	2.1	292.6	9.5	266.0	44.0	3%	300.3	2.1	0.04769	0.00035	0.3436	0.0079	0.052	0.001
B4b1-41	441.0	4.6	439.0	8.9	434.0	52.0	0%	441.0	4.6	0.07082	0.00076	0.542	0.014	0.056	0.0013
B4b2-1	294.5	4.3	335.0	19.0	640.0	130.0	12%	294.5	4.3	0.04675	0.0007	0.397	0.026	0.0621	0.004
B4b2-2	317.9	5.7	306.0	20.0	230.0	150.0	4%	317.9	5.7	0.05057	0.00094	0.356	0.026	0.0516	0.0038
B4b2-3	570.2	5.6	574.0	13.0	631.0	61.0	1%	570.2	5.6	0.09249	0.00094	0.762	0.023	0.0609	0.0017
B4b2-4	429.3	6.0	435.0	12.0	454.0	78.0	1%	429.3	6.0	0.06888	0.00099	0.538	0.019	0.0563	0.002
B4b2-5	595.0	11.0	662.0	11.0	901.0	32.0	10%	595.0	11.0	0.0967	0.0019	0.917	0.021	0.0693	0.0011
B4b2-6	490.0	11.0	539.0	19.0	772.0	69.0	9%	490.0	11.0	0.0791	0.0018	0.706	0.033	0.0654	0.0023
B4b2-7	545.0	5.4	548.4	8.5	548.0	42.0	1%	545.0	5.4	0.08823	0.00091	0.714	0.015	0.0586	0.0011
B4b2-8	477.2	9.1	472.0	27.0	380.0	140.0	1%	477.2	9.1	0.0769	0.0015	0.603	0.044	0.0559	0.004
B4b2-9	290.1	3.8	294.0	11.0	293.0	95.0	1%	290.1	3.8	0.04603	0.00061	0.335	0.014	0.0529	0.0023
B4b2-10	446.7	7.1	437.0	15.0	387.0	96.0	2%	446.7	7.1	0.0718	0.0012	0.539	0.023	0.0546	0.0025
B4b2-11	306.3	5.0	308.0	15.0	280.0	120.0	1%	306.3	5.0	0.04868	0.00082	0.359	0.02	0.0536	0.0031
B4b2-12	309.4	5.5	318.0	18.0	350.0	130.0	3%	309.4	5.5	0.04918	0.0009	0.373	0.025	0.0554	0.0037
B4b2-13	2722.0	21.0	2712.0	11.0	2699.0	16.0	0%	2712.0	11.0	0.5256	0.0049	13.48	0.16	0.1854	0.0018
B4b2-14	453.1	4.2	478.0	14.0	584.0	73.0	5%	453.1	4.2	0.07282	0.00069	0.601	0.022	0.0602	0.002
B4b2-16	534.7	9.8	539.0	28.0	520.0	150.0	1%	534.7	9.8	0.0865	0.0016	0.71	0.048	0.0601	0.0042
B4b2-17	680.0	11.0	664.0	34.0	570.0	140.0	2%	680.0	11.0	0.1112	0.0019	0.937	0.063	0.0609	0.0041
B4b2-18	304.2	4.7	305.0	13.0	345.0	99.0	0%	304.2	4.7	0.04819	0.00077	0.35	0.018	0.0538	0.0025
B4b2-19	607.9	9.5	606.0	23.0	600.0	100.0	0%	607.9	9.5	0.0989	0.0016	0.81	0.041	0.061	0.0031
B4b2-20	302.5	4.6	292.0	17.0	170.0	130.0	4%	302.5	4.6	0.04806	0.00074	0.33	0.023	0.049	0.0033
B4b2-21	443.9	7.2	485.0	17.0	645.0	98.0	8%	443.9	7.2	0.0713	0.0012	0.618	0.027	0.0625	0.0028
B4b2-22	395.7	3.6	402.8	8.2	435.0	56.0	2%	395.7	3.6	0.06331	0.00059	0.489	0.012	0.0559	0.0014
B4b2-23	342.3	8.0	335.0	24.0	260.0	170.0	2%	342.3	8.0	0.0546	0.0013	0.387	0.035	0.0517	0.0049
B4b2-24	440.5	4.9	458.0	10.0	558.0	64.0	4%	440.5	4.9	0.07074	0.00082	0.572	0.016	0.0581	0.0017

B4b2-25	448.8	5.2	447.0	15.0	413.0	92.0	0%	448.8	5.2	0.07211	0.00086	0.555	0.023	0.0559	0.0024
B4b2-26	1706.0	15.0	2043.0	14.0	2402.0	22.0	16%	2043.0	14.0	0.303	0.003	6.488	0.099	0.1545	0.002
B4b2-27	1040.0	27.0	1496.0	20.0	2223.0	15.0	30%	1040.0	27.0	0.1755	0.005	3.366	0.085	0.1396	0.0012
B4b2-28	456.1	6.1	448.0	16.0	401.0	97.0	2%	456.1	6.1	0.0733	0.001	0.552	0.025	0.0553	0.0025
B4b2-29	586.8	9.6	558.0	20.0	485.0	86.0	5%	586.8	9.6	0.0953	0.0016	0.734	0.034	0.0579	0.0024
B4b2-30	1333.0	39.0	1749.0	45.0	2310.0	30.0	24%	1749.0	45.0	0.2305	0.0074	4.8	0.26	0.1477	0.0026
B4b2-31	300.7	4.8	410.0	20.0	1100.0	120.0	27%	300.7	4.8	0.04776	0.00078	0.499	0.032	0.0776	0.0045
B4b2-32	288.9	4.7	299.0	15.0	350.0	120.0	3%	288.9	4.7	0.04577	0.00075	0.346	0.02	0.0553	0.0032
B4b2-34	308.2	3.7	314.0	12.0	350.0	95.0	2%	308.2	3.7	0.04898	0.0006	0.366	0.017	0.0543	0.0025
B4b2-35	606.6	8.7	620.0	22.0	650.0	100.0	2%	606.6	8.7	0.0987	0.0015	0.852	0.04	0.0626	0.0029
B4b2-36	562.8	7.4	588.0	25.0	580.0	120.0	4%	562.8	7.4	0.0912	0.0013	0.787	0.046	0.0611	0.0034
B4b2-37	1768.0	14.0	1978.0	17.0	2211.0	27.0	11%	1978.0	17.0	0.3156	0.0029	6.03	0.11	0.1392	0.0022
B4b2-38	454.8	7.7	432.0	23.0	320.0	130.0	5%	454.8	7.7	0.0731	0.0013	0.537	0.034	0.0539	0.0035
B4b2-39	655.8	7.8	658.0	20.0	694.0	89.0	0%	655.8	7.8	0.1071	0.0013	0.913	0.037	0.0629	0.0026
B4b2-40	289.2	3.8	290.0	10.0	282.0	85.0	0%	289.2	3.8	0.04589	0.00062	0.331	0.014	0.0521	0.002
B4b2-41	2050.0	17.0	2121.0	11.0	2186.0	21.0	3%	2121.0	11.0	0.3742	0.0036	7.081	0.085	0.1369	0.0016
B4b2-42	454.3	6.0	444.0	17.0	358.0	98.0	2%	454.3	6.0	0.07303	0.00099	0.547	0.026	0.0544	0.0025
B4b2-43	311.6	4.9	303.0	14.0	230.0	120.0	3%	311.6	4.9	0.04954	0.00079	0.345	0.02	0.0509	0.003
B4b2-44	308.9	3.9	315.6	8.4	398.0	70.0	2%	308.9	3.9	0.0491	0.00064	0.365	0.011	0.0546	0.0018
B4b2-45	1826.0	16.0	1862.0	16.0	1873.0	30.0	2%	1862.0	16.0	0.3276	0.0034	5.258	0.096	0.115	0.0019
B4b2-46	537.9	6.0	528.0	12.0	499.0	61.0	2%	537.9	6.0	0.087	0.001	0.687	0.019	0.0577	0.0015
B4b2-47	461.3	8.0	453.0	17.0	410.0	100.0	2%	461.3	8.0	0.0742	0.0013	0.568	0.026	0.0555	0.0026
B4b2-48	306.5	6.2	305.0	15.0	360.0	120.0	0%	306.5	6.2	0.0486	0.001	0.348	0.02	0.0531	0.0033
B4b2-49	578.5	7.6	623.0	21.0	741.0	98.0	7%	578.5	7.6	0.0939	0.0013	0.86	0.038	0.0659	0.0031
B4b2-50	637.0	10.0	603.0	27.0	490.0	130.0	6%	637.0	10.0	0.1038	0.0018	0.826	0.05	0.0584	0.0036
B4b2-51	301.4	4.2	307.8	9.4	371.0	79.0	2%	301.4	4.2	0.04787	0.00069	0.356	0.012	0.0548	0.002
B4b2-52	449.6	5.4	443.0	12.0	367.0	70.0	1%	449.6	5.4	0.07225	0.00089	0.547	0.019	0.0544	0.0017
B4b2-53	306.0	5.6	360.0	22.0	680.0	150.0	15%	306.0	5.6	0.04862	0.00091	0.425	0.03	0.0646	0.0045
B4b2-54	1478.0	24.0	1662.0	23.0	1922.0	32.0	11%	1662.0	23.0	0.2576	0.0048	4.13	0.12	0.1172	0.0021
B4b2-55	450.3	7.6	450.0	16.0	416.0	98.0	0%	450.3	7.6	0.0724	0.0013	0.564	0.024	0.0567	0.0027
B4b2-56	460.9	5.8	450.0	15.0	435.0	90.0	2%	460.9	5.8	0.07412	0.00097	0.559	0.023	0.056	0.0024
B4b2-57	456.6	6.3	460.0	14.0	445.0	77.0	1%	456.6	6.3	0.0734	0.0011	0.579	0.022	0.0569	0.0021

B4b2-58	440.2	5.0	506.0	13.0	780.0	61.0	13%	440.2	5.0	0.07068	0.00084	0.639	0.021	0.066	0.0019
B4b2-59	706.3	7.9	701.0	14.0	691.0	52.0	1%	706.3	7.9	0.1158	0.0014	0.997	0.027	0.0626	0.0015
B4b2-60	809.0	16.0	832.0	24.0	883.0	60.0	3%	809.0	16.0	0.1339	0.0027	1.275	0.054	0.0689	0.002
B4b2-62	441.6	6.7	450.0	17.0	490.0	100.0	2%	441.6	6.7	0.0709	0.0011	0.565	0.027	0.0582	0.0028
B4b2-63	473.2	7.7	498.0	21.0	590.0	110.0	5%	473.2	7.7	0.0762	0.0013	0.632	0.033	0.0602	0.0031
B4b2-64	605.0	11.0	621.0	24.0	600.0	110.0	3%	605.0	11.0	0.0984	0.0019	0.841	0.046	0.0619	0.0033
B4b2-65	674.0	13.0	690.0	38.0	710.0	150.0	2%	674.0	13.0	0.1098	0.0023	1.022	0.073	0.0677	0.0049
B4b2-66	452.2	5.7	456.0	13.0	471.0	69.0	1%	452.2	5.7	0.07268	0.00094	0.57	0.019	0.0571	0.0018
B4b2-67	453.6	6.2	450.0	12.0	454.0	69.0	1%	453.6	6.2	0.0729	0.001	0.558	0.018	0.0565	0.0018
B4b2-68	2287.0	25.0	2429.0	17.0	2535.0	23.0	6%	2429.0	17.0	0.4262	0.0056	9.96	0.18	0.1675	0.0023
B4b2-69	1952.0	13.0	1957.0	10.0	1964.0	17.0	0%	1957.0	10.0	0.3537	0.0027	5.878	0.068	0.1206	0.0012
B4b2-70	328.7	5.4	345.0	10.0	434.0	77.0	5%	328.7	5.4	0.05232	0.00089	0.404	0.015	0.0556	0.002
B4b2-71	448.9	6.0	449.0	13.0	427.0	82.0	0%	448.9	6.0	0.0721	0.001	0.559	0.02	0.0562	0.0021
B4b2-72	2009.0	18.0	2008.0	13.0	1995.0	24.0	0%	2008.0	13.0	0.3659	0.0039	6.24	0.096	0.1232	0.0017
B4b2-73	314.0	16.0	342.0	18.0	625.0	74.0	8%	314.0	16.0	0.0501	0.0026	0.408	0.025	0.061	0.002
B4b2-74	446.4	5.0	518.0	13.0	822.0	69.0	14%	446.4	5.0	0.07171	0.00082	0.665	0.022	0.0671	0.0022
B4b2-75	465.4	6.1	520.0	21.0	730.0	110.0	11%	465.4	6.1	0.0749	0.001	0.669	0.033	0.0654	0.0033
B4b2-76	562.1	6.1	567.4	9.4	568.0	42.0	1%	562.1	6.1	0.0911	0.001	0.749	0.016	0.0592	0.0011
B4b2-77	309.8	5.0	306.0	13.0	272.0	94.0	1%	309.8	5.0	0.04924	0.00081	0.354	0.017	0.0527	0.0024
B4b2-78	825.0	12.0	839.0	23.0	859.0	92.0	2%	825.0	12.0	0.1365	0.0021	1.295	0.052	0.0688	0.0029
B4b2-79	307.3	4.3	302.7	9.1	264.0	76.0	2%	307.3	4.3	0.04883	0.0007	0.346	0.013	0.0523	0.0018
B4b2-80	458.3	7.0	430.0	20.0	280.0	110.0	7%	458.3	7.0	0.0736	0.0012	0.535	0.031	0.0534	0.003
B4b2-81	295.0	4.3	307.8	8.8	416.0	71.0	4%	295.0	4.3	0.04684	0.00069	0.353	0.012	0.0555	0.0018
B4b2-82	644.9	8.9	634.0	18.0	581.0	74.0	2%	644.9	8.9	0.1053	0.0015	0.866	0.033	0.0593	0.002
B4b2-83	352.1	6.5	364.0	22.0	370.0	140.0	3%	352.1	6.5	0.0562	0.0011	0.431	0.031	0.0559	0.0039
B4b2-84	2341.0	22.0	2453.0	14.0	2536.0	20.0	5%	2453.0	14.0	0.4381	0.0049	10.22	0.15	0.1682	0.002
B4b2-85	2414.0	23.0	2514.0	15.0	2597.0	17.0	4%	2514.0	15.0	0.4546	0.0052	10.9	0.17	0.1741	0.0018
B4b2-86	507.0	11.0	781.0	69.0	1560.0	190.0	35%	507.0	11.0	0.0819	0.0019	1.24	0.17	0.106	0.012
B4b2-87	523.2	9.5	526.0	19.0	520.0	100.0	1%	523.2	9.5	0.0846	0.0016	0.678	0.032	0.059	0.0028
B4b2-88	313.5	4.4	312.3	8.4	276.0	65.0	0%	313.5	4.4	0.04984	0.00071	0.36	0.011	0.0518	0.0015
B4b2-89	488.4	7.0	489.0	12.0	487.0	64.0	0%	488.4	7.0	0.0787	0.0012	0.619	0.019	0.0573	0.0016
B4b2-90	2770.0	26.0	2980.0	12.0	3112.0	16.0	7%	2980.0	12.0	0.5373	0.0063	17.84	0.22	0.2392	0.0025

B4b2-91	295.1	6.2	297.0	21.0	270.0	160.0	1%	295.1	6.2	0.0469	0.001	0.34	0.028	0.0542	0.0043
B4b2-92	2749.0	26.0	3042.0	11.0	3216.0	12.0	10%	3042.0	11.0	0.5322	0.0062	19.01	0.22	0.2553	0.002
B4b2-93	283.4	5.7	284.0	20.0	270.0	170.0	0%	283.4	5.7	0.04496	0.00093	0.314	0.029	0.0509	0.0048
B4b2-94	604.2	7.3	629.0	15.0	683.0	71.0	4%	604.2	7.3	0.0983	0.0012	0.855	0.027	0.0627	0.0021
B4b2-95	992.0	16.0	1006.0	32.0	991.0	99.0	1%	992.0	16.0	0.1664	0.0029	1.73	0.086	0.0753	0.0041
B4b2-96	460.7	6.4	575.0	29.0	1000.0	120.0	20%	460.7	6.4	0.0741	0.0011	0.777	0.052	0.0761	0.0045
B4b2-97	528.4	8.1	664.0	28.0	1110.0	110.0	20%	528.4	8.1	0.0855	0.0014	0.929	0.054	0.0786	0.0042
B4b2-98	1165.0	24.0	1228.0	54.0	1330.0	140.0	5%	1165.0	24.0	0.1979	0.0045	2.42	0.17	0.0896	0.0065
B4b2-99	533.0	8.8	562.0	24.0	650.0	120.0	5%	533.0	8.8	0.0862	0.0015	0.74	0.043	0.0626	0.0037
B4b2-100	355.5	5.8	342.0	13.0	226.0	92.0	4%	355.5	5.8	0.0566	0.00096	0.403	0.017	0.0518	0.0023

Appendix 33: Detrital zircon (U-Th)/He data for sample D15.

Grain #	V (µm3)	+/- 2σ	4He (mol)	Corrected 4He (mol)	+/- 2σ	4He (mol/g)	Corrected 4He (mol/g)	+/- 2σ	232Th (ppm)	+/- 2σ	238U (ppm)	+/- 2σ	147Sm (ppm)	+/- 2σ	eU	Th/U	ZHe age (Ma)	+/- 2σ
D15b1_2	7450	372	5.72E-15	3.81E-15	1.28E-16	1.65E-07	1.10E-07	9.04E-09	58	0	107	1	5	0	120	0.54	254.3	14.1
D15b1_3	7456	373	5.29E-15	3.52E-15	1.98E-16	1.52E-07	1.02E-07	9.52E-09	48	0	147	5	1	0	159	0.33	178.3	12.6
D15b1_5	7467	373	9.70E-15	6.46E-15	2.62E-16	2.79E-07	1.86E-07	1.59E-08	43	1	160	2	3	0	170	0.27	305.4	17.9
D15b1_7	7507	375	1.54E-14	1.03E-14	2.96E-16	4.42E-07	2.95E-07	2.37E-08	96	4	236	7	10	1	259	0.41	317.5	18.8
D15b1_8	7565	378	6.79E-15	4.52E-15	3.02E-16	1.93E-07	1.29E-07	1.29E-08	53	1	116	1	8	0	129	0.46	278.3	18.9
D15b1_9	7576	379	2.19E-14	1.46E-14	4.42E-16	6.23E-07	4.15E-07	3.36E-08	45	1	246	3	2	0	257	0.18	449.7	24.8
D15b1_10	7582	379	1.13E-14	7.56E-15	2.66E-16	3.22E-07	2.14E-07	1.78E-08	216	9	273	6	5	0	324	0.79	184.2	10.8
D15b1_11	7587	379	1.46E-14	9.71E-15	3.53E-16	4.13E-07	2.75E-07	2.29E-08	93	3	194	3	5	0	216	0.48	354.8	20.5
D15b1_13	7605	380	1.07E-14	7.14E-15	2.30E-16	3.03E-07	2.02E-07	1.65E-08	205	2	323	3	2	0	371	0.64	151.2	8.3
D15b1_16	7628	381	3.32E-14	2.22E-14	5.59E-16	9.37E-07	6.25E-07	4.94E-08	212	6	453	11	7	0	503	0.47	345.7	19.8
D15b1_17	7651	383	3.34E-15	2.23E-15	1.57E-16	9.40E-08	6.26E-08	6.44E-09	20	1	38	2	8	1	43	0.54	-	
D15b1_18	7656	383	8.10E-16	5.40E-16	1.33E-16	2.28E-08	1.52E-08	3.90E-09	31	1	25	1	7	0	32	1.22	-	
D15b1_19	7788	389	2.54E-14	1.69E-14	3.97E-16	7.01E-07	4.67E-07	3.67E-08	117	2	249	2	7	0	276	0.47	470.4	24.9
D15b1_20	7794	390	8.44E-15	5.63E-15	3.19E-16	2.33E-07	1.55E-07	1.46E-08	71	2	206	3	3	0	223	0.35	194.0	12.4
D15b1_21	7478	374	1.58E-14	1.05E-14	2.32E-16	4.55E-07	3.03E-07	2.37E-08	209	1	249	3	10	0	298	0.84	282.8	15.1
D15b1_22	7484	374	3.66E-14	2.44E-14	4.28E-16	1.05E-06	7.02E-07	5.40E-08	370	79	379	37	97	24	466	0.98	418.4	42.9
D15b1_23	7490	374	3.19E-14	2.13E-14	3.73E-16	9.16E-07	6.11E-07	4.70E-08	103	1	442	4	2	0	466	0.23	364.4	18.9
D15b1_24	7496	375	4.91E-15	3.28E-15	1.80E-16	1.41E-07	9.40E-08	8.74E-09	211	11	195	5	12	0	244	1.08	106.8	7.1
D15b1_25	7501	375	3.81E-14	2.54E-14	4.77E-16	1.09E-06	7.28E-07	5.63E-08	106	1	416	6	3	0	440	0.25	460.0	24.4
D15b1_26	7513	376	2.76E-14	1.84E-14	2.97E-16	7.89E-07	5.26E-07	4.03E-08	164	5	460	15	10	1	499	0.36	293.5	17.4
D15b1_27	7519	376	3.53E-15	2.36E-15	2.13E-16	1.01E-07	6.74E-08	7.92E-09	122	1	122	1	3	0	151	1.00	124.2	9.8
D15b1_28	7524	376	3.50E-14	2.34E-14	5.62E-16	1.00E-06	6.67E-07	5.26E-08	627	11	910	14	51	1	1057	0.69	175.5	9.5
D15b1_29	7530	377	1.11E-14	7.43E-15	3.39E-16	3.18E-07	2.12E-07	1.86E-08	135	2	159	2	3	0	190	0.85	310.0	18.5
D15b1_30	7536	377	1.16E-14	7.74E-15	3.57E-16	3.31E-07	2.21E-07	1.95E-08	72	1	181	2	3	0	198	0.40	310.4	18.5
D15b1_31	7542	377	1.37E-14	9.16E-15	3.76E-16	3.92E-07	2.61E-07	2.23E-08	104	2	242	3	4	0	267	0.43	272.7	15.9
D15b1_32	7547	377	6.67E-15	4.45E-15	1.55E-16	1.90E-07	1.27E-07	1.05E-08	55	1	80	1	4	0	93	0.69	379.7	21.3
D15b1_33	7553	378	8.00E-15	5.33E-15	1.71E-16	2.28E-07	1.52E-07	1.24E-08	58	1	128	2	1	0	142	0.45	298.3	16.7
D15b1_34	7559	378	1.27E-14	8.49E-15	2.57E-16	3.62E-07	2.41E-07	1.95E-08	131	4	191	5	10	0	221	0.69	303.2	17.7
D15b1_35	7570	379	3.25E-15	2.17E-15	1.11E-16	9.24E-08	6.16E-08	5.60E-09	60	3	123	5	2	0	137	0.48	125.1	9.0

D15b1_36	7599	380	8.72E-15	5.81E-15	2.83E-16	2.47E-07	1.64E-07	1.47E-08	97	1	217	2	5	0	240	0.45	191.0	11.5
D15b1_37	7622	381	1.37E-14	9.10E-15	4.13E-16	3.85E-07	2.57E-07	2.25E-08	44	3	49	4	3	0	60	0.89	-	
D15b1_38	7633	382	6.37E-14	4.25E-14	7.57E-16	1.80E-06	1.20E-06	9.23E-08	178	1	1236	6	1	0	1278	0.14	260.9	13.5
D15b1_39	7639	382	2.19E-14	1.46E-14	4.55E-16	6.15E-07	4.10E-07	3.33E-08	69	2	203	10	6	0	219	0.34	521.3	36.3
D15b1_40	7645	382	4.55E-14	3.03E-14	5.79E-16	1.28E-06	8.53E-07	6.60E-08	337	4	582	7	25	1	661	0.58	359.1	18.9
D15b1_41	7662	383	2.37E-14	1.58E-14	3.98E-16	6.66E-07	4.44E-07	3.51E-08	120	4	301	5	4	0	329	0.40	375.3	20.7
D15b1_42	7668	383	1.38E-14	9.20E-15	3.46E-16	3.87E-07	2.58E-07	2.17E-08	126	2	244	3	9	0	274	0.52	262.4	15.0
D15b1_43	7674	384	1.79E-14	1.19E-14	3.45E-16	5.01E-07	3.34E-07	2.69E-08	317	7	482	9	8	0	557	0.66	166.8	9.4
D15b1_44	7679	384	1.96E-14	1.31E-14	3.06E-16	5.49E-07	3.66E-07	2.88E-08	124	1	205	2	5	0	235	0.60	433.9	23.0
D15b1_46	7691	385	1.13E-14	7.52E-15	3.21E-16	3.15E-07	2.10E-07	1.81E-08	162	1	278	2	3	0	316	0.58	185.0	10.7
D15b1_47	7696	385	9.25E-14	6.17E-14	9.85E-16	2.59E-06	1.72E-06	1.32E-07	40	2	665	10	3	0	675	0.06	711.6	37.8
D15b1_54	7737	387	1.62E-14	1.08E-14	2.87E-16	4.52E-07	3.01E-07	2.39E-08	64	3	292	5	6	0	308	0.22	272.5	15.0
D15b1_55	7742	387	3.16E-14	2.11E-14	7.32E-16	8.79E-07	5.86E-07	4.84E-08	110	2	413	6	8	2	439	0.27	371.2	21.2
D15b1_56	7748	387	1.90E-14	1.27E-14	4.34E-16	5.28E-07	3.52E-07	2.90E-08	31	2	349	6	2	0	356	0.09	274.9	15.8
D15b1_57	7754	388	2.46E-15	1.64E-15	1.55E-16	6.82E-08	4.55E-08	5.49E-09	55	0	106	1	1	0	118	0.52	106.8	8.6
D15b1_58	7760	388	1.76E-14	1.17E-14	4.75E-16	4.87E-07	3.25E-07	2.77E-08	98	1	257	3	5	0	280	0.38	322.7	18.6
D15b1_59	7765	388	1.21E-14	8.10E-15	3.10E-16	3.36E-07	2.24E-07	1.89E-08	81	1	140	1	3	0	160	0.58	390.8	22.1
D15b1_60	7771	389	9.74E-15	6.49E-15	2.71E-16	2.70E-07	1.80E-07	1.54E-08	40	0	128	1	13	0	138	0.31	363.3	20.9
D15b1_61	7777	389	4.27E-14	2.85E-14	4.96E-16	1.18E-06	7.88E-07	6.07E-08	139	2	960	8	20	1	992	0.15	221.0	11.5
D15b1_62	7783	389	6.86E-15	4.57E-15	1.43E-16	1.89E-07	1.26E-07	1.03E-08	52	1	152	2	3	0	164	0.34	214.9	11.8
D15b1_65	7811	391	1.16E-14	7.76E-15	1.89E-16	3.21E-07	2.14E-07	1.69E-08	157	2	154	2	5	0	191	1.02	310.8	16.6
D15b1_66	7817	391	1.47E-14	9.78E-15	4.85E-16	4.04E-07	2.69E-07	2.42E-08	55	2	320	26	9	1	333	0.17	225.0	22.2
D15b1_67	7823	391	1.14E-14	7.63E-15	3.51E-16	3.15E-07	2.10E-07	1.85E-08	302	12	442	15	10	0	513	0.68	113.7	7.5
D15b1_68	7828	391	6.26E-15	4.18E-15	2.33E-16	1.72E-07	1.15E-07	1.07E-08	115	1	110	2	11	0	137	1.05	232.4	14.8
D15b1_69	7834	392	1.95E-14	1.30E-14	3.82E-16	5.34E-07	3.56E-07	2.87E-08	116	11	371	10	5	0	398	0.31	248.7	14.8
D15b1_70	7840	392	1.01E-14	6.72E-15	2.62E-16	2.76E-07	1.84E-07	1.56E-08	109	4	201	7	5	0	227	0.54	226.2	14.6
D15b1_71	7846	392	2.26E-14	1.51E-14	3.85E-16	6.20E-07	4.13E-07	3.27E-08	161	3	341	8	6	0	379	0.47	303.2	17.2
D15b1_72	7851	393	2.65E-14	1.77E-14	5.41E-16	7.26E-07	4.84E-07	3.92E-08	281	9	471	8	15	0	537	0.60	250.7	14.1
D15b1_73	7857	393	1.61E-14	1.07E-14	3.34E-16	4.41E-07	2.94E-07	2.39E-08	47	1	420	6	5	1	431	0.11	190.0	10.6
D15b1_74	7863	393	5.67E-15	3.78E-15	1.93E-16	1.55E-07	1.03E-07	9.37E-09	54	2	89	3	3	0	101	0.60	283.5	18.6
D15b1_75	7869	393	3.99E-14	2.66E-14	5.73E-16	1.09E-06	7.27E-07	5.68E-08	286	24	945	95	179	24	1012	0.30	200.0	21.5
D15b1_76	7874	394	3.92E-14	2.61E-14	5.77E-16	1.07E-06	7.14E-07	5.58E-08	120	1	703	9	3	0	731	0.17	271.6	14.5

D15b1_77	7880	394	2.37E-15	1.58E-15	7.47E-17	6.48E-08	4.32E-08	3.83E-09	23	1	56	2	8	0	62	0.41	-	
D15b1_78	7886	394	1.48E-14	9.89E-15	3.54E-16	4.05E-07	2.70E-07	2.24E-08	83	3	166	5	3	0	186	0.50	404.1	25.3
D15b1_79	7892	395	4.88E-15	3.25E-15	1.55E-16	1.33E-07	8.87E-08	7.87E-09	50	3	153	10	4	0	165	0.33	149.9	12.5
D15b1_80	7897	395	3.43E-14	2.29E-14	5.78E-16	9.34E-07	6.22E-07	4.93E-08	210	10	380	13	8	0	429	0.55	403.2	24.6
D15b1_81	7903	395	1.26E-15	8.42E-16	1.37E-16	3.44E-08	2.29E-08	4.12E-09	22	0	40	1	1	0	45	0.55	-	
D15b1_82	7909	395	4.77E-14	3.18E-14	6.96E-16	1.30E-06	8.64E-07	6.75E-08	192	5	235	5	3	0	280	0.82	858.8	47.2
D15b1_83	7914	396	2.29E-14	1.53E-14	4.34E-16	6.23E-07	4.15E-07	3.33E-08	24	2	371	9	2	0	377	0.06	307.1	18.0
D15b1_84	7920	396	2.23E-14	1.49E-14	3.76E-16	6.05E-07	4.03E-07	3.19E-08	129	1	272	2	3	0	303	0.47	370.9	19.7
D15b1_85	7926	396	1.03E-14	6.90E-15	2.04E-16	2.81E-07	1.87E-07	1.51E-08	126	4	150	2	11	0	179	0.84	290.1	15.9
D15b1_86	7932	397	1.41E-14	9.42E-15	2.92E-16	3.83E-07	2.55E-07	2.07E-08	76	6	206	12	5	0	224	0.37	317.4	24.2
D15b1_87	7937	397	1.75E-14	1.16E-14	3.98E-16	4.73E-07	3.15E-07	2.60E-08	224	10	669	18	57	5	722	0.33	121.6	7.3
D15b1_88	7943	397	2.07E-14	1.38E-14	2.77E-16	5.61E-07	3.74E-07	2.90E-08	174	5	375	11	16	2	416	0.46	250.1	14.6
D15b1_89	7949	397	1.76E-14	1.17E-14	2.72E-16	4.76E-07	3.17E-07	2.49E-08	246	5	227	3	14	1	285	1.08	309.3	16.6
D15b1_90	7955	398	1.50E-14	9.99E-15	2.81E-16	4.05E-07	2.70E-07	2.16E-08	119	2	261	3	10	0	289	0.46	260.3	14.1
D15b1_91	7960	398	1.41E-14	9.39E-15	2.98E-16	3.80E-07	2.54E-07	2.07E-08	36	1	274	10	9	0	283	0.13	249.7	16.1
D15b1_92	7966	398	1.89E-14	1.26E-14	3.53E-16	5.09E-07	3.40E-07	2.72E-08	64	2	63	2	4	0	78	1.02	-	
D15b1_93	7972	399	3.39E-14	2.26E-14	3.56E-16	9.15E-07	6.10E-07	4.67E-08	244	16	1024	83	13	1	1081	0.24	157.0	14.5
D15b1_94	7978	399	8.79E-15	5.86E-15	2.51E-16	2.37E-07	1.58E-07	1.36E-08	41	1	135	2	3	0	144	0.31	304.7	17.9
D15b1_95	7983	399	1.10E-14	7.36E-15	2.32E-16	2.97E-07	1.98E-07	1.61E-08	113	2	197	3	6	0	224	0.57	246.3	13.8
D15b1_96	7989	399	1.85E-14	1.24E-14	3.38E-16	4.99E-07	3.33E-07	2.66E-08	53	0	189	2	1	0	202	0.28	459.1	24.9
D15b1_97	7995	400	4.54E-15	3.03E-15	2.37E-16	1.22E-07	8.15E-08	8.83E-09	89	2	191	5	3	0	212	0.47	107.0	8.1
D15b1_98	8001	400	2.85E-15	1.90E-15	1.61E-16	7.67E-08	5.11E-08	5.78E-09	39	1	58	1	2	0	67	0.68	-	
D15b1_99	8006	400	1.03E-14	6.86E-15	2.55E-16	2.76E-07	1.84E-07	1.54E-08	181	2	249	3	4	0	292	0.73	175.5	9.9
D15b1_100	8012	401	1.42E-14	9.43E-15	2.46E-16	3.80E-07	2.53E-07	2.01E-08	55	0	266	2	11	0	279	0.21	253.0	13.6
D15b1_102	8024	401	2.65E-15	1.77E-15	1.70E-16	7.12E-08	4.74E-08	5.78E-09	31	1	52	1	2	0	59	0.59	-	
D15b1_103	8029	401	2.20E-15	1.47E-15	1.39E-16	5.90E-08	3.94E-08	4.75E-09	63	1	103	1	3	0	118	0.61	93.0	7.5
D15b1_104	8035	402	7.74E-15	5.16E-15	2.76E-16	2.07E-07	1.38E-07	1.27E-08	101	2	118	2	9	1	142	0.86	270.2	16.9
D15b1_106	8046	402	1.89E-14	1.26E-14	3.18E-16	5.04E-07	3.36E-07	2.66E-08	232	3	362	2	4	0	416	0.64	224.6	11.9
D15b1_109	8064	403	1.77E-14	1.18E-14	3.32E-16	4.72E-07	3.15E-07	2.52E-08	51	0	83	1	2	0	95	0.62	922.1	49.7
D15b1_110	8069	403	1.82E-14	1.21E-14	2.67E-16	4.84E-07	3.23E-07	2.52E-08	130	3	287	4	4	0	318	0.45	282.8	15.1
D15b1_111	8075	404	1.29E-14	8.62E-15	2.29E-16	3.44E-07	2.30E-07	1.83E-08	12	0	294	2	0	0	297	0.04	215.1	11.5
D15b1_113	8087	404	1.38E-14	9.20E-15	2.71E-16	3.67E-07	2.45E-07	1.97E-08	25	1	50	1	4	0	56	0.50	-	

D15b1_114	8092	405	2.84E-14	1.89E-14	4.00E-16	7.55E-07	5.03E-07	3.92E-08	113	2	317	4	9	0	344	0.36	407.4	21.6
D15b1_115	8098	405	1.10E-14	7.32E-15	2.80E-16	2.92E-07	1.94E-07	1.64E-08	157	1	153	1	8	0	189	1.03	285.2	16.2
D15b1_116	8104	405	1.12E-14	7.45E-15	2.30E-16	2.96E-07	1.98E-07	1.60E-08	112	1	237	2	3	0	263	0.48	209.0	11.4
D15b1_118	8115	406	3.49E-15	2.33E-15	1.32E-16	9.25E-08	6.17E-08	5.80E-09	17	1	34	1	3	0	38	0.51	-	
D15b1_119	8121	406	6.31E-15	4.21E-15	1.94E-16	1.67E-07	1.11E-07	9.81E-09	81	1	119	1	7	0	138	0.68	224.2	13.3
D15b1_120	8127	406	1.72E-15	1.14E-15	9.50E-17	4.54E-08	3.03E-08	3.39E-09	63	2	46	1	6	0	60	1.37	-	
D15b1_123	8144	407	1.56E-14	1.04E-14	2.70E-16	4.11E-07	2.74E-07	2.17E-08	178	9	254	7	14	1	296	0.70	257.0	15.1
D15b1_124	8150	407	2.54E-14	1.69E-14	3.95E-16	6.70E-07	4.46E-07	3.51E-08	62	1	381	3	3	0	395	0.16	314.6	16.7
D15b1_125	8155	408	1.55E-14	1.03E-14	2.10E-16	4.08E-07	2.72E-07	2.11E-08	109	1	218	2	21	2	244	0.50	310.4	16.2
D15b1_126	8161	408	4.00E-15	2.67E-15	1.99E-16	1.05E-07	7.03E-08	7.43E-09	109	1	146	2	2	0	171	0.75	114.2	8.1
D15b1_127	8167	408	6.47E-15	4.31E-15	2.15E-16	1.70E-07	1.14E-07	1.02E-08	72	1	100	2	3	0	117	0.72	269.5	16.9
D15b1_129	8178	409	2.09E-14	1.39E-14	2.91E-16	5.49E-07	3.66E-07	2.85E-08	271	9	532	7	10	0	596	0.51	170.8	9.1
D15b1_131	8190	409	2.91E-14	1.94E-14	3.82E-16	7.64E-07	5.09E-07	3.95E-08	783	24	867	15	35	2	1051	0.90	134.7	7.3
D15b1_132	8196	410	2.34E-15	1.56E-15	1.47E-16	6.14E-08	4.09E-08	4.93E-09	54	1	31	1	4	0	44	1.75	-	
D15b1_134	8207	410	6.18E-15	4.12E-15	2.07E-16	1.62E-07	1.08E-07	9.75E-09	57	2	119	3	3	0	132	0.48	227.5	14.7
D15b1_135	8213	411	1.28E-14	8.51E-15	2.68E-16	3.34E-07	2.23E-07	1.81E-08	154	6	278	9	10	0	314	0.55	197.4	12.2
D15b1_136	8219	411	5.36E-14	3.58E-14	6.72E-16	1.40E-06	9.36E-07	7.24E-08	196	5	951	8	10	1	997	0.21	261.3	13.6
D15b1_137	8224	411	8.39E-15	5.60E-15	2.10E-16	2.19E-07	1.46E-07	1.23E-08	50	2	161	4	3	0	173	0.31	235.2	14.1
D15b1_138	8230	412	2.38E-14	1.59E-14	4.65E-16	6.22E-07	4.14E-07	3.34E-08	309	2	402	5	9	1	474	0.77	242.9	13.3
D15b1_140	8242	412	1.54E-16	1.03E-16	8.24E-17	4.02E-09	2.68E-09	2.16E-09	136	2	386	5	2	0	418	0.35	1.8	1.0
D15b1_142	8253	413	7.94E-15	5.29E-15	1.91E-16	2.07E-07	1.38E-07	1.15E-08	52	2	62	1	7	0	75	0.83	-	
D15b1_143	8259	413	1.92E-14	1.28E-14	3.27E-16	5.01E-07	3.34E-07	2.64E-08	224	5	371	9	12	0	423	0.60	219.4	12.4
D15b1_144	8264	413	1.24E-14	8.28E-15	2.53E-16	3.23E-07	2.16E-07	1.75E-08	67	2	155	3	2	0	171	0.43	350.5	19.8
D15b1_146	8276	414	5.04E-15	3.36E-15	2.06E-16	1.31E-07	8.73E-08	8.46E-09	82	1	96	1	6	0	115	0.86	211.3	13.7
D15b1_147	8282	414	4.92E-14	3.28E-14	7.78E-16	1.28E-06	8.52E-07	6.70E-08	239	5	609	14	30	4	665	0.39	356.2	20.1
D15b1_150	8299	415	2.43E-14	1.62E-14	4.13E-16	6.29E-07	4.19E-07	3.32E-08	94	2	281	6	4	0	303	0.34	385.4	21.7
D15b1_154	8322	416	1.19E-14	7.94E-15	3.20E-16	3.08E-07	2.05E-07	1.75E-08	98	1	179	1	3	0	202	0.55	283.1	16.2
D15b1_155	8328	416	9.30E-15	6.20E-15	3.64E-16	2.40E-07	1.60E-07	1.52E-08	65	2	288	7	8	0	303	0.23	146.9	9.9
D15b1_156	8333	417	6.20E-15	4.13E-15	1.90E-16	1.60E-07	1.07E-07	9.38E-09	246	9	418	11	11	1	476	0.59	62.3	3.9

Appendix 34: Reduced detrital zircon U-Pb data for sample D15.

Grain #	Age 206/238	+/- 2σ	Age 207/235	+/- 2σ	Age 207/206	+/- 2σ	% Discordance	Selected U/Pb age (Ma)	+/- 2σ	Ratio 206/238	+/- 2σ	Ratio 207/235	+/- 2σ	Ratio 207/206	+/- 2σ
D15b1_2	542.2	4.8	570.0	16.0	647.0	80.0	5%	542.2	4.8	0.08776	0.0008	0.755	0.028	0.0618	0.0024
D15b1_3	453.9	4.3	492.0	16.0	634.0	85.0	8%	453.9	4.3	0.07296	0.00072	0.651	0.034	0.0645	0.0032
D15b1_5	545.5	5.0	538.0	12.0	508.0	62.0	1%	545.5	5.0	0.08824	0.00083	0.701	0.02	0.0575	0.0017
D15b1_7	461.8	3.6	456.2	9.1	414.0	53.0	1%	461.8	3.6	0.07427	0.0006	0.569	0.014	0.0554	0.0014
D15b1_8	655.4	5.4	649.0	14.0	635.0	60.0	1%	655.4	5.4	0.10695	0.00092	0.893	0.025	0.0612	0.0017
D15b1_9	2641.0	12.0	2660.5	7.3	2674.0	10.0	1%	2660.5	7.3	0.5065	0.0028	12.746	0.099	0.1826	0.0011
D15b1_10	660.1	4.9	673.7	9.0	722.0	39.0	2%	660.1	4.9	0.10784	0.00084	0.943	0.017	0.0636	0.0012
D15b1_11	554.9	4.1	583.0	11.0	676.0	55.0	5%	554.9	4.1	0.0899	0.00069	0.773	0.02	0.0618	0.0017
D15b1_13	364.4	4.8	533.0	34.0	1240.0	130.0	32%	364.4	4.8	0.05816	0.00079	0.715	0.062	0.0889	0.0063
D15b1_16	471.3	2.9	483.4	7.3	534.0	41.0	3%	471.3	2.9	0.07585	0.00048	0.611	0.011	0.0583	0.0011
D15b1_17	916.0	19.0	943.0	29.0	1065.0	99.0	3%	916.0	19.0	0.1526	0.0034	1.562	0.077	0.0783	0.0041
D15b1_18	1755.0	17.0	1766.0	26.0	1817.0	54.0	1%	1766.0	26.0	0.3131	0.0035	4.67	0.14	0.1119	0.0032
D15b1_19	1840.0	13.0	1891.8	9.8	1938.0	16.0	3%	1891.8	9.8	0.3303	0.0028	5.448	0.062	0.119	0.0011
D15b1_20	1688.6	9.8	1714.6	8.3	1734.0	17.0	2%	1714.6	8.3	0.2995	0.002	4.413	0.044	0.1061	0.001
D15b1_21	584.6	4.5	579.5	8.3	568.0	42.0	1%	584.6	4.5	0.09493	0.00077	0.771	0.015	0.0591	0.0011
D15b1_22	1654.0	33.0	1735.0	17.0	1865.0	22.0	5%	1735.0	17.0	0.2932	0.0064	4.542	0.09	0.1142	0.0015
D15b1_23	1015.5	5.1	1020.5	7.3	1021.0	23.0	0%	1015.5	5.1	0.17063	0.00093	1.73	0.02	0.07336	0.00085
D15b1_24	317.9	3.1	316.7	9.2	311.0	77.0	0%	317.9	3.1	0.05055	0.00051	0.364	0.013	0.0524	0.0018
D15b1_25	1034.4	5.3	1031.1	8.2	1032.0	23.0	0%	1034.4	5.3	0.17407	0.00096	1.759	0.022	0.07366	0.00082
D15b1_26	325.9	2.4	364.0	13.0	551.0	79.0	10%	325.9	2.4	0.05186	0.0004	0.437	0.019	0.0612	0.0025
D15b1_27	652.6	5.5	654.0	12.0	652.0	53.0	0%	652.6	5.5	0.10656	0.00095	0.909	0.022	0.0616	0.0015
D15b1_28	386.1	4.0	583.1	5.5	1459.0	22.0	34%	386.1	4.0	0.06174	0.00065	0.7746	0.0097	0.0918	0.0011
D15b1_29	542.7	5.1	556.0	10.0	613.0	56.0	2%	542.7	5.1	0.08785	0.00087	0.732	0.018	0.0606	0.0015
D15b1_30	561.0	4.8	568.0	11.0	589.0	54.0	1%	561.0	4.8	0.09086	0.0008	0.748	0.018	0.06	0.0014
D15b1_31	549.5	3.8	563.0	10.0	595.0	52.0	2%	549.5	3.8	0.08898	0.00064	0.74	0.018	0.0602	0.0014
D15b1_32	609.5	6.8	620.0	18.0	640.0	87.0	2%	609.5	6.8	0.0991	0.0011	0.843	0.032	0.0617	0.0025
D15b1_33	784.3	6.0	768.0	14.0	725.0	54.0	2%	784.3	6.0	0.1294	0.0011	1.14	0.029	0.0641	0.0016
D15b1_34	636.2	4.5	633.0	11.0	611.0	53.0	1%	636.2	4.5	0.10368	0.00076	0.863	0.02	0.0605	0.0015
D15b1_35	2633.0	27.0	2836.0	13.0	2982.0	15.0	7%	2836.0	13.0	0.5047	0.0063	15.35	0.21	0.2205	0.002

D15b1_36	732.1	5.4	813.0	13.0	1039.0	43.0	10%	732.1	5.4	0.12029	0.00093	1.233	0.029	0.0736	0.0016
D15b1_37	2604.0	20.0	2687.0	15.0	2757.0	21.0	3%	2687.0	15.0	0.4977	0.0045	13.08	0.2	0.1914	0.0024
D15b1_38	396.6	1.9	391.5	4.2	330.0	29.0	1%	396.6	1.9	0.06345	0.00032	0.47	0.006	0.0532	0.00069
D15b1_39	456.5	3.9	494.0	10.0	666.0	55.0	8%	456.5	3.9	0.0734	0.00065	0.628	0.016	0.0623	0.0015
D15b1_40	1296.0	13.0	1337.7	9.0	1408.0	19.0	3%	1337.7	13.0	0.2225	0.0024	2.738	0.033	0.08913	0.00084
D15b1_41	572.2	3.8	574.6	8.3	593.0	43.0	0%	572.2	3.8	0.09282	0.00065	0.762	0.014	0.0598	0.0012
D15b1_42	450.8	3.7	467.2	9.5	532.0	53.0	4%	450.8	3.7	0.07245	0.00062	0.586	0.015	0.0582	0.0014
D15b1_43	527.5	3.5	551.8	6.8	644.0	33.0	4%	527.5	3.5	0.08527	0.00058	0.723	0.012	0.06132	0.00093
D15b1_44	1143.6	6.8	1138.0	11.0	1121.0	28.0	0%	1143.6	6.8	0.1941	0.0013	2.068	0.032	0.0772	0.0011
D15b1_46	288.2	2.4	295.3	7.2	326.0	63.0	2%	288.2	2.4	0.04573	0.00039	0.3368	0.0094	0.0532	0.0015
D15b1_47	735.4	5.5	761.2	6.6	840.0	25.0	3%	735.4	5.5	0.12085	0.00096	1.117	0.014	0.06693	0.00083
D15b1_54	442.3	4.4	443.6	8.7	450.0	51.0	0%	442.3	4.4	0.07103	0.00072	0.549	0.013	0.0564	0.0013
D15b1_55	685.3	6.3	705.8	8.0	789.0	31.0	3%	685.3	6.3	0.1121	0.0011	1.004	0.016	0.06551	0.00097
D15b1_56	451.9	3.7	448.4	8.0	438.0	48.0	1%	451.9	3.7	0.07257	0.00061	0.554	0.012	0.0559	0.0012
D15b1_57	336.7	3.9	330.0	14.0	270.0	100.0	2%	336.7	3.9	0.05363	0.00064	0.391	0.02	0.0534	0.0027
D15b1_58	662.0	5.5	656.0	10.0	639.0	45.0	1%	662.0	5.5	0.10818	0.00094	0.908	0.019	0.0612	0.0013
D15b1_59	971.8	7.2	972.0	12.0	966.0	40.0	0%	971.8	7.2	0.1626	0.0013	1.603	0.031	0.0715	0.0014
D15b1_60	1707.0	9.2	1716.0	11.0	1731.0	24.0	1%	1716.0	11.0	0.3032	0.0019	4.435	0.058	0.1058	0.0014
D15b1_61	415.9	6.7	446.1	6.8	587.0	30.0	7%	415.9	6.7	0.0667	0.0011	0.552	0.01	0.05949	0.00083
D15b1_62	593.2	4.4	590.0	12.0	573.0	61.0	1%	593.2	4.4	0.09633	0.00076	0.791	0.022	0.0594	0.0017
D15b1_65	460.2	4.8	462.0	12.0	441.0	68.0	0%	460.2	4.8	0.07401	0.00081	0.579	0.018	0.0566	0.0017
D15b1_66	480.0	13.0	522.0	27.0	820.0	120.0	8%	480.0	13.0	0.0773	0.0022	0.669	0.048	0.0667	0.0042
D15b1_67	440.7	3.4	458.8	6.9	539.0	38.0	4%	440.7	3.4	0.07076	0.00057	0.573	0.011	0.0585	0.001
D15b1_68	542.7	6.7	550.0	16.0	550.0	73.0	1%	542.7	6.7	0.0879	0.0011	0.736	0.031	0.0604	0.0023
D15b1_69	441.1	5.1	481.0	13.0	699.0	70.0	8%	441.1	5.1	0.07083	0.00085	0.604	0.021	0.0627	0.002
D15b1_70	749.3	5.1	747.0	11.0	735.0	46.0	0%	749.3	5.1	0.12328	0.00089	1.09	0.023	0.0644	0.0014
D15b1_71	2582.0	18.0	2613.0	11.0	2638.0	11.0	1%	2613.0	11.0	0.4929	0.0042	12.14	0.14	0.1783	0.0012
D15b1_72	536.4	3.4	556.8	7.3	631.0	38.0	4%	536.4	3.4	0.08678	0.00057	0.731	0.012	0.061	0.001
D15b1_73	393.0	3.8	437.8	6.6	663.0	46.0	10%	393.0	3.8	0.06286	0.00062	0.539	0.01	0.062	0.0013
D15b1_74	2570.0	22.0	2627.0	15.0	2680.0	16.0	2%	2627.0	15.0	0.4903	0.0051	12.31	0.19	0.1826	0.0018
D15b1_75	368.1	9.3	610.0	15.0	1636.0	30.0	40%	368.1	9.3	0.0588	0.0015	0.83	0.028	0.1009	0.0016
D15b1_76	379.6	2.4	388.4	6.0	436.0	40.0	2%	379.6	2.4	0.06065	0.0004	0.465	0.0086	0.05577	0.00098

D15b1_77	472.0	13.0	513.0	23.0	710.0	120.0	8%	472.0	13.0	0.076	0.0021	0.658	0.037	0.0655	0.0036
D15b1_78	2659.0	25.0	2820.0	20.0	2931.0	22.0	6%	2820.0	20.0	0.5107	0.006	15.09	0.32	0.2131	0.0028
D15b1_79	668.7	6.0	697.0	14.0	784.0	57.0	4%	668.7	6.0	0.1092	0.001	0.988	0.028	0.0656	0.0017
D15b1_80	560.0	4.0	562.8	9.3	579.0	43.0	0%	560.0	4.0	0.09077	0.00067	0.744	0.016	0.0592	0.0012
D15b1_81	581.0	9.3	590.0	26.0	630.0	120.0	2%	581.0	9.3	0.0944	0.0016	0.794	0.046	0.062	0.0036
D15b1_82	735.3	6.2	735.0	10.0	745.0	36.0	0%	735.3	6.2	0.1208	0.0011	1.063	0.02	0.0644	0.0011
D15b1_83	449.0	3.3	456.8	8.1	483.0	48.0	2%	449.0	3.3	0.07215	0.00055	0.568	0.013	0.0572	0.0012
D15b1_84	1050.6	6.2	1050.0	10.0	1051.0	29.0	0%	1050.6	6.2	0.177	0.0011	1.809	0.028	0.0746	0.0011
D15b1_85	627.9	5.8	635.0	12.0	643.0	59.0	1%	627.9	5.8	0.1022	0.001	0.864	0.023	0.0612	0.0017
D15b1_86	417.4	5.5	436.0	13.0	515.0	79.0	4%	417.4	5.5	0.0669	0.00091	0.531	0.019	0.0578	0.0021
D15b1_87	1619.0	23.0	1743.0	15.0	1928.0	11.0	7%	1743.0	15.0	0.2858	0.0045	4.582	0.076	0.11824	0.00074
D15b1_88	573.7	9.6	622.0	11.0	859.0	49.0	8%	573.7	9.6	0.0931	0.0016	0.843	0.02	0.0677	0.0017
D15b1_89	613.5	5.4	677.0	18.0	893.0	68.0	9%	613.5	5.4	0.09986	0.00093	0.958	0.035	0.0699	0.0023
D15b1_90	1163.6	7.5	1168.1	9.7	1176.0	26.0	0%	1163.6	7.5	0.1977	0.0014	2.164	0.03	0.0792	0.0011
D15b1_91	466.4	5.6	498.0	13.0	605.0	65.0	6%	466.4	5.6	0.07505	0.00094	0.636	0.021	0.0605	0.0018
D15b1_92	2252.0	22.0	2509.0	15.0	2712.0	22.0	10%	2509.0	15.0	0.418	0.0048	10.8	0.18	0.187	0.0025
D15b1_93	324.3	2.9	381.8	9.1	751.0	55.0	15%	324.3	2.9	0.0516	0.00047	0.458	0.013	0.0651	0.0017
D15b1_94	526.5	4.7	548.0	16.0	624.0	72.0	4%	526.5	4.7	0.08511	0.00079	0.717	0.027	0.0615	0.0021
D15b1_95	290.7	3.8	332.0	14.0	670.0	110.0	12%	290.7	3.8	0.04613	0.00062	0.386	0.02	0.062	0.0033
D15b1_96	1538.6	8.9	1561.0	10.0	1594.0	22.0	1%	1561.0	10.0	0.2696	0.0018	3.65	0.046	0.0985	0.0012
D15b1_97	465.9	4.0	477.0	11.0	510.0	58.0	2%	465.9	4.0	0.07495	0.00066	0.604	0.017	0.0579	0.0015
D15b1_98	2046.0	25.0	2055.0	22.0	2095.0	33.0	0%	2055.0	22.0	0.3738	0.0053	6.54	0.16	0.1301	0.0025
D15b1_99	585.0	4.6	705.0	22.0	1079.0	79.0	17%	585.0	4.6	0.095	0.00079	1.026	0.047	0.0788	0.0033
D15b1_100	554.5	4.0	663.0	18.0	1063.0	73.0	16%	554.5	4.0	0.08984	0.00068	0.933	0.035	0.0753	0.0026
D15b1_102	1087.0	12.0	1100.0	18.0	1144.0	57.0	1%	1087.0	12.0	0.1837	0.0022	1.968	0.052	0.0779	0.0022
D15b1_103	648.8	5.9	649.0	15.0	630.0	74.0	0%	648.8	5.9	0.1059	0.001	0.893	0.028	0.0618	0.0021
D15b1_104	1857.0	13.0	1871.0	12.0	1879.0	25.0	1%	1871.0	12.0	0.3334	0.0026	5.303	0.077	0.1149	0.0016
D15b1_106	426.0	2.9	440.4	8.1	498.0	51.0	3%	426.0	2.9	0.06827	0.00048	0.544	0.012	0.0572	0.0013
D15b1_109	2409.0	16.0	2468.0	11.0	2511.0	19.0	2%	2468.0	11.0	0.4532	0.0035	10.4	0.12	0.1657	0.0019
D15b1_110	340.7	2.8	364.9	9.1	483.0	67.0	7%	340.7	2.8	0.05428	0.00045	0.432	0.013	0.0574	0.0017
D15b1_111	434.3	7.2	472.0	14.0	631.0	59.0	8%	434.3	7.2	0.0697	0.0012	0.597	0.022	0.0615	0.0017
D15b1_113	1906.0	24.0	2019.0	21.0	2153.0	33.0	6%	2019.0	21.0	0.344	0.005	6.3	0.15	0.1344	0.0025

D15b1_114	1748.6	9.0	1759.1	8.2	1771.0	14.0	1%	1759.1	8.2	0.3117	0.0018	4.652	0.045	0.10824	0.00081
D15b1_115	2084.0	13.0	2082.0	9.5	2086.0	16.0	0%	2082.0	9.5	0.3816	0.0027	6.781	0.071	0.1293	0.0012
D15b1_116	1579.7	9.8	1621.8	8.7	1676.0	19.0	3%	1621.8	8.7	0.2778	0.002	3.945	0.043	0.1028	0.001
D15b1_118	596.0	12.0	657.0	34.0	770.0	140.0	9%	596.0	12.0	0.0969	0.002	0.9	0.062	0.0673	0.0047
D15b1_119	702.5	5.8	700.0	13.0	672.0	61.0	0%	702.5	5.8	0.1151	0.001	0.992	0.026	0.0623	0.0018
D15b1_120	1774.0	14.0	1842.0	26.0	1925.0	52.0	4%	1842.0	26.0	0.3169	0.0029	5.16	0.16	0.1186	0.0034
D15b1_123	1721.0	17.0	2145.0	17.0	2588.0	18.0	20%	2145.0	17.0	0.3058	0.0034	7.27	0.14	0.1732	0.0018
D15b1_124	2419.0	13.0	2510.1	7.7	2580.0	10.0	4%	2510.1	7.7	0.4554	0.0029	10.846	0.088	0.1725	0.0011
D15b1_125	465.6	4.1	509.0	12.0	707.0	62.0	9%	465.6	4.1	0.0749	0.00069	0.656	0.02	0.0636	0.0019
D15b1_126	360.9	5.1	404.0	17.0	570.0	100.0	11%	360.9	5.1	0.05759	0.00084	0.495	0.025	0.0619	0.0031
D15b1_127	1598.0	11.0	1621.0	14.0	1649.0	29.0	1%	1621.0	14.0	0.2815	0.0022	3.931	0.068	0.1014	0.0015
D15b1_129	482.2	4.4	696.0	33.0	1400.0	110.0	31%	482.2	4.4	0.07768	0.00073	1.021	0.069	0.0944	0.0058
D15b1_131	501.0	4.3	684.0	8.4	1324.0	32.0	27%	501.0	4.3	0.08083	0.00072	0.963	0.016	0.086	0.0015
D15b1_132	1698.0	26.0	1799.0	24.0	1958.0	44.0	6%	1799.0	24.0	0.3014	0.0052	4.91	0.14	0.1208	0.003
D15b1_134	670.7	5.4	706.0	17.0	829.0	66.0	5%	670.7	5.4	0.10966	0.00093	1.008	0.034	0.0659	0.0021
D15b1_135	452.9	3.3	456.5	9.6	468.0	58.0	1%	452.9	3.3	0.07279	0.00055	0.568	0.015	0.0567	0.0015
D15b1_136	1432.0	18.0	1802.0	15.0	2249.0	11.0	21%	1802.0	15.0	0.2485	0.0035	4.893	0.087	0.14196	0.00091
D15b1_137	348.9	4.6	369.0	12.0	482.0	83.0	5%	348.9	4.6	0.05563	0.00076	0.439	0.017	0.0578	0.0024
D15b1_138	828.9	4.8	826.4	7.6	816.0	25.0	0%	828.9	4.8	0.13724	0.00085	1.257	0.017	0.06632	0.0008
D15b1_140	1128.4	8.7	1123.0	10.0	1129.0	29.0	0%	1128.4	8.7	0.1913	0.0016	2.022	0.03	0.0773	0.0011
D15b1_142	1259.0	11.0	1281.0	17.0	1314.0	45.0	2%	1281.0	11.0	0.2158	0.0021	2.529	0.06	0.0844	0.0019
D15b1_143	476.7	4.7	835.0	23.0	1960.0	66.0	43%	476.7	4.7	0.07676	0.00078	1.287	0.051	0.1216	0.0042
D15b1_144	367.2	3.2	366.0	11.0	320.0	75.0	0%	367.2	3.2	0.05863	0.00053	0.432	0.015	0.0535	0.0019
D15b1_146	979.4	8.3	1073.0	24.0	1264.0	67.0	9%	979.4	8.3	0.1641	0.0015	1.919	0.072	0.0855	0.0031
D15b1_147	370.0	4.5	642.0	42.0	1530.0	140.0	42%	370.0	4.5	0.0591	0.00075	0.95	0.088	0.1102	0.0088
D15b1_150	621.5	4.7	622.0	11.0	649.0	49.0	0%	621.5	4.7	0.10123	0.0008	0.846	0.021	0.0612	0.0014
D15b1_154	586.2	4.3	618.0	12.0	716.0	59.0	5%	586.2	4.3	0.09515	0.00073	0.839	0.022	0.0635	0.0017
D15b1_155	501.3	5.1	510.0	11.0	549.0	60.0	2%	501.3	5.1	0.08089	0.00086	0.655	0.019	0.0591	0.0016
D15b1_156	308.9	2.6	320.2	7.8	380.0	63.0	4%	308.9	2.6	0.04908	0.00042	0.371	0.011	0.0547	0.0016

Appendix 35: Detrital zircon (U-Th)/He data for sample D21.

Grain #	V (µm3)	+/- 2σ	4He (mol)	Corrected 4He (mol)	+/- 2σ	4He (mol/g)	Corrected 4He (mol/g)	+/- 2σ	232Th (ppm)	+/- 2σ	238U (ppm)	+/- 2σ	147Sm (ppm)	+/- 2σ	eU	Th/U	ZHe age (Ma)	+/- 2σ
D21b1_2	9055	453	2.24E-15	1.49E-15	1.35E-16	5.31E-08	3.54E-08	4.16E-09	22	0	92	1	2	0	97	0.24	101.9	8.0
D21b1_3	9050	452	6.86E-15	4.57E-15	2.20E-16	1.63E-07	1.09E-07	9.69E-09	131	2	286	4	7	0	317	0.46	95.5	5.8
D21b1_4	9045	452	1.02E-14	6.82E-15	2.25E-16	2.43E-07	1.62E-07	1.33E-08	99	2	82	1	7	0	105	1.20	427.8	23.7
D21b1_5	9040	452	3.57E-14	2.38E-14	4.99E-16	8.50E-07	5.67E-07	4.41E-08	30	1	430	6	3	0	437	0.07	360.7	19.3
D21b1_6	9035	452	1.42E-14	9.44E-15	3.31E-16	3.37E-07	2.25E-07	1.86E-08	176	2	558	9	6	0	600	0.32	104.3	6.0
D21b1_7	9004	450	8.96E-15	5.97E-15	2.45E-16	2.14E-07	1.43E-07	1.22E-08	148	2	492	29	4	0	527	0.30	75.4	6.0
D21b1_8	8954	448	1.08E-14	7.20E-15	2.39E-16	2.60E-07	1.73E-07	1.42E-08	68	1	144	2	1	0	160	0.47	300.4	16.9
D21b1_9	8944	447	1.02E-14	6.82E-15	2.91E-16	2.46E-07	1.64E-07	1.42E-08	265	13	672	15	8	0	734	0.39	62.1	3.8
D21b1_10	8938	447	2.32E-14	1.54E-14	4.12E-16	5.57E-07	3.71E-07	2.96E-08	218	3	357	5	2	0	408	0.61	253.3	13.8
D21b1_11	8933	447	6.02E-15	4.01E-15	1.55E-16	1.45E-07	9.66E-08	8.14E-09	209	6	518	10	6	0	567	0.40	47.4	2.8
D21b1_12	8928	446	2.25E-14	1.50E-14	3.73E-16	5.42E-07	3.61E-07	2.86E-08	186	11	484	16	9	0	528	0.38	190.6	11.6
D21b1_14	8913	446	2.71E-14	1.81E-14	5.07E-16	6.55E-07	4.36E-07	3.49E-08	337	5	387	5	2	0	466	0.87	260.3	14.2
D21b1_15	8908	445	1.12E-14	7.45E-15	2.66E-16	2.70E-07	1.80E-07	1.49E-08	282	17	852	13	8	1	918	0.33	54.5	3.1
D21b1_16	8898	445	9.19E-15	6.13E-15	3.49E-16	2.22E-07	1.48E-07	1.39E-08	74	2	152	3	2	0	169	0.49	244.0	15.9
D21b1_17	8878	444	4.91E-14	3.28E-14	8.11E-16	1.19E-06	7.94E-07	6.27E-08	348	8	791	9	15	0	872	0.44	253.1	13.6
D21b1_18	8873	444	1.10E-15	7.33E-16	8.00E-17	2.67E-08	1.78E-08	2.35E-09	30	0	27	0	1	0	34	1.11	-	
D21b1_19	8757	438	1.66E-14	1.11E-14	2.73E-16	4.09E-07	2.72E-07	2.15E-08	221	4	927	47	8	0	979	0.24	77.5	5.5
D21b1_20	8752	438	1.00E-14	6.70E-15	2.66E-16	2.47E-07	1.65E-07	1.40E-08	171	4	517	15	7	0	557	0.33	82.2	5.1
D21b1_21	9029	451	3.16E-15	2.11E-15	1.40E-16	7.53E-08	5.02E-08	5.03E-09	55	1	127	2	1	0	140	0.44	99.9	6.9
D21b1_22	9024	451	6.41E-15	4.27E-15	2.40E-16	1.53E-07	1.02E-07	9.55E-09	22	0	135	4	2	0	140	0.16	203.1	13.7
D21b1_23	9019	451	2.09E-14	1.39E-14	2.50E-16	4.97E-07	3.32E-07	2.56E-08	407	15	925	16	11	1	1021	0.44	90.4	4.9
D21b1_24	9014	451	2.69E-14	1.80E-14	6.21E-16	6.43E-07	4.29E-07	3.54E-08	45	0	354	3	1	0	364	0.13	327.4	18.2
D21b1_25	9009	450	8.59E-15	5.73E-15	3.04E-16	2.05E-07	1.37E-07	1.26E-08	48	1	89	1	2	0	100	0.54	379.4	23.5
D21b1_26	8999	450	7.42E-15	4.95E-15	2.09E-16	1.77E-07	1.18E-07	1.02E-08	45	1	29	0	1	0	40	1.53	-	
D21b1_27	8994	450	1.72E-15	1.15E-15	1.16E-16	4.11E-08	2.74E-08	3.45E-09	14	0	27	0	5	0	30	0.51	-	
D21b1_28	8989	449	5.35E-15	3.57E-15	2.10E-16	1.28E-07	8.53E-08	8.13E-09	149	7	325	10	7	0	360	0.46	66.0	4.6
D21b1_29	8984	449	4.96E-15	3.30E-15	1.99E-16	1.19E-07	7.91E-08	7.60E-09	178	15	74	4	7	1	116	2.42	189.9	15.2
D21b1_31	8974	449	3.15E-15	2.10E-15	1.75E-16	7.55E-08	5.03E-08	5.64E-09	48	1	81	1	2	0	92	0.60	151.6	11.4
D21b1_32	8969	448	7.88E-15	5.25E-15	2.35E-16	1.89E-07	1.26E-07	1.10E-08	93	1	151	2	2	0	173	0.62	202.3	11.9

D21b1_33	8964	448	1.79E-14	1.19E-14	2.61E-16	4.29E-07	2.86E-07	2.24E-08	414	12	729	14	12	0	826	0.57	96.4	5.3
D21b1_34	8959	448	8.27E-15	5.51E-15	2.99E-16	1.98E-07	1.32E-07	1.22E-08	36	3	137	2	1	0	146	0.26	252.8	16.1
D21b1_35	8949	447	9.09E-15	6.06E-15	2.57E-16	2.19E-07	1.46E-07	1.25E-08	216	7	420	12	10	0	471	0.51	86.1	5.4
D21b1_36	8923	446	9.59E-15	6.39E-15	2.79E-16	2.31E-07	1.54E-07	1.34E-08	138	4	291	4	11	0	323	0.48	132.7	7.9
D21b1_37	8903	445	4.63E-15	3.09E-15	1.41E-16	1.12E-07	7.45E-08	6.55E-09	100	3	216	5	4	0	239	0.46	86.6	5.4
D21b1_38	8893	445	9.00E-15	6.00E-15	1.91E-16	2.18E-07	1.45E-07	1.18E-08	219	2	457	4	5	0	508	0.48	79.5	4.4
D21b1_39	8888	444	6.18E-15	4.12E-15	1.23E-16	1.50E-07	9.97E-08	8.05E-09	65	2	164	4	20	1	180	0.40	154.4	9.1
D21b1_40	8883	444	1.12E-14	7.49E-15	2.85E-16	2.72E-07	1.81E-07	1.52E-08	222	9	650	17	2	0	702	0.34	71.8	4.4
D21b1_41	8868	443	1.23E-14	8.20E-15	2.56E-16	2.98E-07	1.99E-07	1.62E-08	32	0	99	2	39	8	107	0.32	519.0	30.1
D21b1_42	8863	443	2.14E-14	1.43E-14	3.32E-16	5.20E-07	3.46E-07	2.72E-08	18	0	339	3	3	0	343	0.05	281.2	14.9
D21b1_43	8858	443	1.62E-14	1.08E-14	2.94E-16	3.94E-07	2.62E-07	2.09E-08	73	5	232	3	5	0	249	0.31	293.0	16.0
D21b1_44	8853	443	3.67E-15	2.45E-15	1.81E-16	8.92E-08	5.95E-08	6.26E-09	102	1	130	1	7	0	154	0.79	107.4	7.6
D21b1_45	8848	442	8.28E-15	5.52E-15	1.62E-16	2.01E-07	1.34E-07	1.08E-08	167	2	340	6	9	0	379	0.49	98.5	5.5
D21b1_47	8837	442	8.86E-15	5.91E-15	1.79E-16	2.16E-07	1.44E-07	1.16E-08	62	1	93	2	16	1	108	0.67	371.0	21.0
D21b1_48	8832	442	1.00E-14	6.68E-15	2.17E-16	2.44E-07	1.63E-07	1.33E-08	71	2	182	2	7	0	199	0.39	227.8	12.7
D21b1_49	8827	441	4.47E-15	2.98E-15	2.08E-16	1.09E-07	7.26E-08	7.43E-09	102	1	233	6	11	2	257	0.44	78.6	5.7
D21b1_50	8822	441	2.92E-14	1.95E-14	5.06E-16	7.11E-07	4.74E-07	3.76E-08	129	1	247	2	3	0	277	0.52	475.5	25.4
D21b1_51	8817	441	7.64E-15	5.09E-15	2.32E-16	1.86E-07	1.24E-07	1.09E-08	253	10	396	7	9	0	456	0.64	75.8	4.6
D21b1_52	8812	441	7.88E-15	5.25E-15	2.69E-16	1.92E-07	1.28E-07	1.16E-08	22	0	27	0	6	0	33	0.82	-	
D21b1_53	8807	440	1.94E-14	1.30E-14	3.27E-16	4.75E-07	3.16E-07	2.50E-08	74	1	269	2	2	0	286	0.28	308.0	16.5
D21b1_54	8802	440	1.44E-14	9.57E-15	2.93E-16	3.51E-07	2.34E-07	1.89E-08	71	2	194	4	7	0	210	0.37	309.1	17.8
D21b1_55	8797	440	2.11E-14	1.41E-14	3.24E-16	5.16E-07	3.44E-07	2.70E-08	259	11	756	25	32	2	817	0.34	117.2	7.1
D21b1_56	8792	440	1.48E-14	9.89E-15	3.56E-16	3.63E-07	2.42E-07	2.01E-08	44	1	40	1	8	0	50	1.10	-	
D21b1_57	8787	439	7.90E-15	5.27E-15	2.93E-16	1.93E-07	1.29E-07	1.20E-08	36	1	73	2	3	0	81	0.49	442.0	30.3
D21b1_58	8782	439	1.30E-14	8.68E-15	3.21E-16	3.19E-07	2.13E-07	1.78E-08	88	1	246	5	4	0	266	0.36	222.2	13.0
D21b1_59	8777	439	2.36E-14	1.57E-14	4.86E-16	5.78E-07	3.86E-07	3.13E-08	86	4	856	30	1	0	876	0.10	122.5	7.8
D21b1_60	8772	439	6.28E-15	4.19E-15	2.01E-16	1.54E-07	1.03E-07	9.14E-09	34	1	59	1	1	0	67	0.57	-	
D21b1_61	8767	438	2.03E-14	1.35E-14	3.70E-16	4.97E-07	3.31E-07	2.65E-08	43	1	287	6	4	0	297	0.15	310.4	17.6
D21b1_62	8762	438	6.14E-15	4.10E-15	2.17E-16	1.51E-07	1.01E-07	9.23E-09	140	2	181	1	5	0	214	0.77	130.6	8.0
D21b1_64	8741	437	1.28E-14	8.51E-15	3.36E-16	3.14E-07	2.09E-07	1.77E-08	255	11	623	9	4	0	683	0.41	85.3	5.0
D21b1_65	8736	437	9.83E-15	6.55E-15	2.32E-16	2.42E-07	1.61E-07	1.34E-08	41	1	398	14	4	0	408	0.10	110.2	7.2
D21b1_66	8731	437	2.32E-15	1.55E-15	1.76E-16	5.71E-08	3.81E-08	5.19E-09	42	1	136	2	5	0	146	0.31	72.6	6.6

D21b1_67	8726	436	6.08E-15	4.05E-15	2.52E-16	1.50E-07	9.99E-08	9.73E-09	28	1	81	2	2	0	88	0.34	316.6	21.7
D21b1_68	8721	436	2.15E-14	1.43E-14	3.02E-16	5.30E-07	3.54E-07	2.75E-08	150	5	430	9	5	0	466	0.35	211.4	11.6
D21b1_69	8716	436	1.77E-14	1.18E-14	3.36E-16	4.36E-07	2.91E-07	2.33E-08	156	5	306	7	15	1	343	0.51	235.9	13.6
D21b1_70	8711	436	7.76E-15	5.18E-15	2.53E-16	1.92E-07	1.28E-07	1.14E-08	155	5	409	12	6	0	445	0.38	79.8	5.2
D21b1_71	8706	435	4.42E-15	2.95E-15	1.33E-16	1.09E-07	7.28E-08	6.37E-09	31	1	57	1	2	0	64	0.55	-	
D21b1_72	8701	435	1.78E-14	1.19E-14	3.85E-16	4.41E-07	2.94E-07	2.40E-08	175	2	463	4	4	0	504	0.38	162.3	9.0
D21b1_73	8696	435	2.14E-14	1.43E-14	3.05E-16	5.30E-07	3.54E-07	2.76E-08	164	2	305	4	3	0	343	0.54	286.6	15.2
D21b1_74	8691	435	6.87E-15	4.58E-15	1.70E-16	1.70E-07	1.13E-07	9.49E-09	69	2	252	4	5	0	268	0.27	117.7	6.8
D21b1_75	8686	434	1.17E-14	7.78E-15	2.06E-16	2.89E-07	1.93E-07	1.53E-08	251	3	373	5	3	0	432	0.67	123.8	6.8
D21b1_76	8681	434	5.34E-15	3.56E-15	2.04E-16	1.32E-07	8.82E-08	8.33E-09	64	3	138	3	2	0	153	0.46	160.2	10.5
D21b1_77	8676	434	1.14E-14	7.60E-15	2.95E-16	2.82E-07	1.88E-07	1.59E-08	88	2	139	2	4	0	160	0.63	327.3	19.0
D21b1_79	8666	433	1.78E-14	1.19E-14	2.52E-16	4.43E-07	2.95E-07	2.30E-08	55	1	423	21	8	0	436	0.13	188.5	13.4
D21b1_80	8661	433	5.22E-15	3.48E-15	1.92E-16	1.30E-07	8.64E-08	8.05E-09	28	1	339	9	3	0	346	0.08	69.6	4.7
D21b1_81	8655	433	3.26E-15	2.17E-15	1.40E-16	8.10E-08	5.40E-08	5.33E-09	168	2	126	4	1	0	165	1.33	90.8	6.3
D21b1_82	8650	433	6.68E-16	4.45E-16	1.03E-16	1.66E-08	1.11E-08	2.69E-09	13	0	15	0	2	0	18	0.89	-	
D21b1_83	8645	432	2.24E-14	1.49E-14	3.91E-16	5.57E-07	3.71E-07	2.95E-08	312	6	287	5	6	0	360	1.09	286.4	15.8
D21b1_84	8640	432	6.08E-15	4.05E-15	2.37E-16	1.51E-07	1.01E-07	9.60E-09	47	1	158	3	7	1	169	0.30	166.4	11.0
D21b1_85	8635	432	7.28E-15	4.86E-15	2.30E-16	1.81E-07	1.21E-07	1.07E-08	59	1	91	1	5	0	104	0.65	322.4	19.3
D21b1_86	8630	432	1.47E-14	9.83E-15	2.53E-16	3.67E-07	2.45E-07	1.94E-08	126	3	235	4	3	0	264	0.53	257.9	14.1
D21b1_87	8625	431	2.70E-15	1.80E-15	1.44E-16	6.72E-08	4.48E-08	4.92E-09	16	1	69	1	3	0	73	0.24	-	
D21b1_88	8620	431	3.21E-14	2.14E-14	4.39E-16	8.00E-07	5.33E-07	4.15E-08	137	7	347	10	9	1	380	0.40	390.8	22.7
D21b1_89	8615	431	3.27E-15	2.18E-15	1.36E-16	8.17E-08	5.45E-08	5.30E-09	72	3	153	3	16	2	169	0.47	89.4	6.0
D21b1_90	8610	431	8.72E-15	5.81E-15	1.69E-16	2.18E-07	1.45E-07	1.17E-08	41	1	127	1	4	0	137	0.32	295.6	16.1
D21b1_91	8605	430	1.59E-14	1.06E-14	3.69E-16	3.98E-07	2.65E-07	2.19E-08	80	2	227	3	5	0	246	0.35	300.5	17.0
D21b1_92	8600	430	2.67E-14	1.78E-14	3.90E-16	6.67E-07	4.45E-07	3.48E-08	241	2	337	4	9	1	393	0.71	314.4	16.7
D21b1_93	8595	430	6.95E-15	4.63E-15	2.02E-16	1.74E-07	1.16E-07	1.00E-08	234	6	375	3	5	0	430	0.62	75.0	4.4
D21b1_94	8590	429	9.98E-15	6.66E-15	2.54E-16	2.50E-07	1.67E-07	1.40E-08	70	1	160	2	2	0	177	0.44	262.5	14.9
D21b1_96	8580	429	5.56E-15	3.71E-15	1.91E-16	1.39E-07	9.29E-08	8.45E-09	59	1	111	3	3	0	124	0.53	207.8	13.3
D21b1_97	8575	429	3.96E-14	2.64E-14	4.72E-16	9.94E-07	6.63E-07	5.11E-08	209	5	589	10	10	0	638	0.36	289.0	15.5
D21b1_98	8570	428	4.46E-15	2.97E-15	2.45E-16	1.12E-07	7.46E-08	8.31E-09	91	2	244	2	5	0	265	0.37	78.2	5.8
D21b1_99	8565	428	1.09E-14	7.24E-15	2.39E-16	2.73E-07	1.82E-07	1.49E-08	155	7	578	8	3	0	614	0.27	82.5	4.6
D21b1_100	8559	428	3.75E-15	2.50E-15	1.29E-16	9.43E-08	6.29E-08	5.71E-09	36	1	70	2	6	0	79	0.51	222.6	14.2

D21b1_101	8554	428	2.09E-15	1.39E-15	1.23E-16	5.26E-08	3.51E-08	4.07E-09	34	1	47	1	7	0	55	0.73	-	
D21b1_102	8549	427	1.02E-14	6.80E-15	3.39E-16	2.57E-07	1.71E-07	1.54E-08	330	17	476	9	10	0	554	0.69	85.9	5.4
D21b1_103	8544	427	2.80E-14	1.87E-14	4.72E-16	7.06E-07	4.70E-07	3.72E-08	356	3	766	6	26	1	850	0.46	154.0	8.2
D21b1_104	8539	427	1.42E-14	9.44E-15	2.65E-16	3.57E-07	2.38E-07	1.90E-08	543	16	320	8	6	0	447	1.70	147.6	8.4
D21b1_105	8534	427	2.91E-14	1.94E-14	5.91E-16	7.33E-07	4.89E-07	3.96E-08	161	3	272	3	4	0	310	0.59	439.4	24.1
D21b1_106	8529	426	2.39E-15	1.60E-15	1.11E-16	6.04E-08	4.02E-08	4.12E-09	36	0	140	2	2	0	149	0.26	75.4	5.2
D21b1_107	8524	426	1.41E-14	9.37E-15	3.73E-16	3.54E-07	2.36E-07	2.01E-08	3	0	5	0	1	0	5	0.62	-	
D21b1_108	8519	426	6.48E-16	4.32E-16	1.30E-16	1.64E-08	1.09E-08	3.37E-09	80	1	92	1	9	0	111	0.87	27.4	5.6
D21b1_109	8514	426	3.71E-14	2.48E-14	7.29E-16	9.38E-07	6.25E-07	5.04E-08	57	1	78	1	2	0	92	0.72	1894.3	102.6
D21b1_110	8509	425	5.52E-15	3.68E-15	2.06E-16	1.39E-07	9.29E-08	8.70E-09	124	1	206	2	3	0	235	0.60	109.9	6.9
D21b1_111	8504	425	6.55E-15	4.37E-15	2.39E-16	1.66E-07	1.10E-07	1.03E-08	314	3	347	3	5	0	421	0.90	73.0	4.5
D21b1_112	8499	425	3.79E-15	2.52E-15	2.17E-16	9.58E-08	6.39E-08	7.29E-09	104	1	88	1	9	0	113	1.18	157.5	12.1
D21b1_113	8494	425	2.11E-15	1.41E-15	1.57E-16	5.34E-08	3.56E-08	4.78E-09	85	2	44	1	21	2	64	1.94	-	
D21b1_114	8489	424	2.71E-14	1.80E-14	4.58E-16	6.85E-07	4.57E-07	3.62E-08	217	5	1360	37	5	0	1411	0.16	90.1	5.3
D21b1_115	8484	424	8.84E-15	5.90E-15	2.82E-16	2.24E-07	1.49E-07	1.33E-08	297	13	560	8	5	0	630	0.53	66.0	4.0
D21b1_116	8479	424	3.62E-14	2.42E-14	5.13E-16	9.19E-07	6.13E-07	4.78E-08	65	1	88	1	2	0	103	0.74	1655.5	87.3
D21b1_117	8474	424	1.45E-14	9.66E-15	3.09E-16	3.68E-07	2.45E-07	2.00E-08	107	1	212	2	5	0	238	0.51	287.1	15.8
D21b1_118	8468	423	3.24E-13	2.16E-13	2.33E-15	8.23E-06	5.49E-06	4.16E-07	1008000	53000	116300	6700	600000	32000	353180	8.67	4.3	0.3
D21b1_119	8463	423	3.15E-15	2.10E-15	1.22E-16	8.01E-08	5.34E-08	5.06E-09	<540	/	242	15	<360	/	-	-	-	-
D21b1_122	8448	422	8.16E-15	5.44E-15	3.31E-16	2.08E-07	1.39E-07	1.34E-08	61	1	157	2	4	0	171	0.39	225.2	14.8
D21b1_123	8443	422	1.19E-14	7.92E-15	3.41E-16	3.03E-07	2.02E-07	1.74E-08	118	2	224	2	2	0	252	0.53	223.0	13.0
D21b1_124	8438	422	1.46E-14	9.70E-15	1.97E-16	3.71E-07	2.47E-07	1.92E-08	73	1	256	3	2	0	273	0.28	251.9	13.4
D21b1_125	8433	422	4.29E-15	2.86E-15	1.66E-16	1.09E-07	7.30E-08	6.92E-09	38	0	128	1	3	0	137	0.30	148.1	9.5
D21b1_126	8428	421	9.90E-15	6.60E-15	2.35E-16	2.53E-07	1.68E-07	1.40E-08	138	6	463	8	5	0	495	0.30	94.7	5.4
D21b1_127	8423	421	5.28E-15	3.52E-15	1.54E-16	1.35E-07	8.99E-08	7.81E-09	113	6	324	9	4	0	351	0.35	71.3	4.6
D21b1_128	8418	421	1.12E-14	7.45E-15	2.90E-16	2.85E-07	1.90E-07	1.61E-08	97	2	241	4	2	0	264	0.40	200.9	11.7
D21b1_129	8413	421	4.10E-15	2.73E-15	1.93E-16	1.05E-07	6.99E-08	7.19E-09	136	2	163	1	5	0	195	0.84	99.7	6.9
D21b1_130	8408	420	8.96E-15	5.97E-15	2.86E-16	2.29E-07	1.53E-07	1.36E-08	118	1	119	1	3	0	146	0.99	290.0	17.4
D21b1_131	8403	420	2.70E-15	1.80E-15	1.04E-16	6.92E-08	4.61E-08	4.37E-09	69	1	103	3	7	0	119	0.67	107.5	7.2
D21b1_132	8398	420	1.88E-14	1.25E-14	3.25E-16	4.81E-07	3.20E-07	2.54E-08	221	10	1092	16	6	0	1144	0.20	78.0	4.3
D21b1_133	8393	420	7.69E-15	5.13E-15	2.04E-16	1.97E-07	1.31E-07	1.12E-08	83	3	204	5	5	0	224	0.41	163.4	10.1
D21b1_134	8388	419	4.26E-15	2.84E-15	1.52E-16	1.09E-07	7.28E-08	6.71E-09	133	1	210	2	3	0	241	0.63	83.8	5.2

D21b1_135	8383	419	1.65E-14	1.10E-14	2.99E-16	4.23E-07	2.82E-07	2.25E-08	150	3	207	4	3	0	242	0.72	323.2	18.1
D21b1_136	8378	419	8.69E-15	5.80E-15	2.62E-16	2.23E-07	1.49E-07	1.30E-08	94	2	206	4	4	0	228	0.46	181.4	11.1
D21b1_137	8372	419	8.65E-15	5.77E-15	3.31E-16	2.22E-07	1.48E-07	1.40E-08	56	1	60	1	3	0	73	0.93	-	
D21b1_138	8367	418	2.75E-15	1.84E-15	1.67E-16	7.08E-08	4.72E-08	5.56E-09	30	0	108	1	1	0	115	0.27	113.8	9.0
D21b1_139	8362	418	2.02E-14	1.35E-14	3.69E-16	5.19E-07	3.46E-07	2.76E-08	173	6	165	4	8	0	205	1.05	468.2	26.7
D21b1_140	8357	418	1.15E-14	7.66E-15	2.31E-16	2.96E-07	1.97E-07	1.59E-08	209	2	595	4	7	0	644	0.35	85.2	4.6
D21b1_141	8352	418	2.12E-14	1.41E-14	3.64E-16	5.46E-07	3.64E-07	2.89E-08	171	7	232	6	10	0	273	0.74	371.1	21.3
D21b1_142	8347	417	3.69E-15	2.46E-15	1.27E-16	9.52E-08	6.35E-08	5.77E-09	33	1	62	1	2	0	70	0.54	-	
D21b1_143	8342	417	8.36E-15	5.58E-15	3.67E-16	2.16E-07	1.44E-07	1.43E-08	85	1	223	3	9	0	243	0.38	164.8	11.1
D21b1_144	8337	417	1.30E-15	8.70E-16	1.18E-16	3.36E-08	2.24E-08	3.49E-09	22	0	36	1	3	0	41	0.61	-	
D21b1_145	8332	417	6.84E-15	4.56E-15	2.72E-16	1.77E-07	1.18E-07	1.13E-08	112	4	494	5	7	1	520	0.23	63.0	4.1
D21b1_148	8317	416	3.62E-15	2.42E-15	1.71E-16	9.37E-08	6.25E-08	6.43E-09	14	0	36	1	1	0	39	0.40	-	
D21b1_149	8312	416	9.55E-15	6.37E-15	2.28E-16	2.47E-07	1.65E-07	1.37E-08	44	2	278	41	3	0	288	0.16	159.1	24.3
D21b1_150	8307	415	1.33E-14	8.90E-15	2.83E-16	3.46E-07	2.30E-07	1.88E-08	76	2	142	2	1	0	160	0.54	400.5	22.5
D21b1_151	8302	415	9.15E-15	6.10E-15	2.69E-16	2.37E-07	1.58E-07	1.38E-08	197	4	489	7	3	0	535	0.40	82.1	4.9
D21b1_152	8297	415	5.67E-15	3.78E-15	1.80E-16	1.47E-07	9.80E-08	8.70E-09	77	2	219	10	4	0	237	0.35	115.1	8.4
D21b1_155	8282	414	7.89E-15	5.26E-15	2.29E-16	2.05E-07	1.37E-07	1.18E-08	41	2	346	16	3	0	356	0.12	106.9	7.8
D21b1_156	8276	414	9.05E-15	6.03E-15	2.63E-16	2.35E-07	1.57E-07	1.36E-08	500	9	560	9	18	0	677	0.89	64.3	3.8
D21b1_157	8271	414	3.21E-14	2.14E-14	5.38E-16	8.34E-07	5.56E-07	4.40E-08	879	32	1716	43	27	1	1923	0.51	80.4	4.6
D21b1_158	8266	413	1.04E-14	6.92E-15	2.49E-16	2.70E-07	1.80E-07	1.50E-08	261	12	555	9	4	0	616	0.47	81.3	4.7
D21b1_159	8261	413	1.78E-15	1.19E-15	1.52E-16	4.65E-08	3.10E-08	4.59E-09	11	0	25	0	1	0	28	0.46	-	
D21b1_160	8256	413	9.12E-15	6.08E-15	2.05E-16	2.37E-07	1.58E-07	1.30E-08	135	2	293	3	8	0	325	0.46	135.6	7.6
D21b1_161	8251	413	2.18E-14	1.45E-14	3.09E-16	5.68E-07	3.78E-07	2.95E-08	119	2	418	4	4	0	446	0.28	236.1	12.4
D21b1_163	8241	412	2.11E-14	1.40E-14	3.88E-16	5.50E-07	3.66E-07	2.93E-08	70	1	135	3	2	0	151	0.51	673.6	37.7
D21b1_164	8236	412	9.19E-15	6.13E-15	2.32E-16	2.40E-07	1.60E-07	1.34E-08	30	0	172	2	2	0	179	0.17	249.5	14.1
D21b1_165	8231	412	2.15E-14	1.43E-14	3.93E-16	5.61E-07	3.74E-07	2.99E-08	12	0	1184	12	2	0	1187	0.01	87.8	4.8
D21b1_166	8226	411	1.14E-15	7.61E-16	9.46E-17	2.98E-08	1.99E-08	2.89E-09	20	1	36	1	3	0	41	0.56	-	
D21b1_167	8221	411	4.85E-15	3.23E-15	1.86E-16	1.27E-07	8.46E-08	8.00E-09	64	1	105	1	4	0	120	0.61	196.7	12.6
D21b1_168	8216	411	0.00E+00	0.00E+00	#DIV/0!	0.00E+00	0.00E+00	#DIV/0!	84	2	59	1	18	1	79	1.41	-	
D21b1_169	8211	411	8.58E-15	5.72E-15	1.94E-16	2.25E-07	1.50E-07	1.23E-08	110	3	130	2	3	0	156	0.85	267.5	15.2
D21b1_170	8206	410	5.21E-14	3.47E-14	6.43E-16	1.37E-06	9.10E-07	7.03E-08	330	4	1005	20	3	0	1083	0.33	234.0	12.8
D21b1_171	8201	410	6.64E-15	4.43E-15	2.67E-16	1.74E-07	1.16E-07	1.12E-08	303	4	363	4	10	0	434	0.84	74.4	4.8

D21b1_173	8191	410	1.78E-14	1.19E-14	2.75E-16	4.68E-07	3.12E-07	2.45E-08	68	1	1279	11	7	0	1295	0.05	67.1	3.6
D21b1_174	8185	409	1.88E-14	1.25E-14	3.18E-16	4.94E-07	3.29E-07	2.61E-08	46	1	196	2	4	0	207	0.23	443.6	23.7
D21b1_175	8180	409	3.23E-14	2.15E-14	5.60E-16	8.50E-07	5.66E-07	4.50E-08	1566	50	2138	22	29	2	2506	0.73	62.8	3.4
D21b1_176	8175	409	1.57E-14	1.05E-14	3.33E-16	4.13E-07	2.75E-07	2.24E-08	120	2	216	3	11	0	245	0.55	313.0	17.5
D21b1_181	8150	408	1.28E-14	8.50E-15	2.78E-16	3.37E-07	2.24E-07	1.84E-08	281	9	713	11	3	0	779	0.39	80.1	4.5
D21b1_184	8135	407	1.16E-14	7.71E-15	3.85E-16	3.06E-07	2.04E-07	1.84E-08	311	8	567	10	5	0	640	0.55	88.5	5.5
D21b1_186	8125	406	2.28E-14	1.52E-14	4.29E-16	6.04E-07	4.03E-07	3.23E-08	140	3	1388	12	6	0	1421	0.10	78.9	4.3

Appendix 36: Reduced detrital zircon U-Pb data for sample D21.

Grain #	Age 206/238	+/- 2σ	Age 207/235	+/- 2σ	Age 207/206	+/- 2σ	% Discordance	Selected U/Pb age (Ma)	+/- 2σ	Ratio 206/238	+/- 2σ	Ratio 207/235	+/- 2σ	Ratio 207/206	+/- 2σ
D21b1_2	936.4	9.3	1090.0	20.0	1388.0	55.0	14%	936.4	9.3	1.925	0.056	0.1564	0.0017	0.089	0.0025
D21b1_3	501.2	3.9	505.0	11.0	529.0	55.0	1%	501.2	3.9	0.645	0.017	0.08087	0.00066	0.0588	0.0015
D21b1_4	2706.0	15.0	2694.0	11.0	2701.0	19.0	0%	2694.0	11.0	13.21	0.15	0.5216	0.0036	0.1853	0.0021
D21b1_5	2228.0	12.0	2395.4	7.6	2539.0	11.0	7%	2395.4	7.6	9.582	0.081	0.4127	0.0026	0.1682	0.0011
D21b1_6	322.8	2.4	339.3	6.6	426.0	50.0	5%	322.8	2.4	0.3979	0.0092	0.05136	0.0004	0.056	0.0013
D21b1_7	633.6	5.6	622.1	9.2	599.0	39.0	2%	633.6	5.6	0.845	0.016	0.1033	0.00096	0.0603	0.0011
D21b1_8	570.8	5.7	562.0	14.0	526.0	70.0	2%	570.8	5.7	0.742	0.025	0.09261	0.00096	0.0585	0.002
D21b1_9	330.4	3.2	331.4	7.4	326.0	52.0	0%	330.4	3.2	0.387	0.01	0.05259	0.00052	0.0534	0.0013
D21b1_10	344.5	3.6	336.9	8.8	255.0	67.0	2%	344.5	3.6	0.392	0.012	0.0549	0.00058	0.0517	0.0016
D21b1_11	306.8	2.6	357.2	7.1	712.0	48.0	14%	306.8	2.6	0.422	0.01	0.04875	0.00043	0.0638	0.0014
D21b1_12	448.6	4.7	465.1	8.4	553.0	51.0	4%	448.6	4.7	0.58	0.013	0.07208	0.00078	0.0592	0.0014
D21b1_14	295.1	2.7	290.0	8.5	245.0	70.0	2%	295.1	2.7	0.332	0.011	0.04685	0.00044	0.0515	0.0017
D21b1_15	314.0	2.7	319.2	5.4	368.0	43.0	2%	314.0	2.7	0.3694	0.0072	0.04993	0.00044	0.0544	0.001
D21b1_16	660.9	6.6	661.0	15.0	675.0	71.0	0%	660.9	6.6	0.925	0.029	0.108	0.0011	0.0629	0.0021
D21b1_17	608.7	3.4	624.2	8.4	677.0	37.0	2%	608.7	3.4	0.852	0.015	0.099	0.00059	0.0625	0.0011
D21b1_18	2397.0	30.0	2388.0	24.0	2370.0	42.0	0%	2388.0	24.0	9.54	0.24	0.4504	0.0068	0.1539	0.0038
D21b1_19	403.9	4.4	418.4	6.9	498.0	38.0	3%	403.9	4.4	0.511	0.01	0.06468	0.00073	0.05745	0.00098
D21b1_20	642.0	30.0	1280.0	120.0	2120.0	210.0	50%	642.0	30.0	4.25	0.6	0.1047	0.0051	0.221	0.024
D21b1_21	2520.0	16.0	2450.0	11.0	2400.0	19.0	3%	2450.0	11.0	10.19	0.12	0.4786	0.0037	0.1554	0.0017
D21b1_22	2701.0	19.0	2680.0	13.0	2672.0	20.0	1%	2680.0	13.0	13.02	0.18	0.5206	0.0043	0.1822	0.0022
D21b1_23	319.3	2.3	316.9	6.6	283.0	52.0	1%	319.3	2.3	0.3674	0.0089	0.05079	0.00037	0.0524	0.0012
D21b1_24	1440.0	10.0	1627.0	11.0	1868.0	19.0	11%	1627.0	11.0	3.962	0.052	0.2502	0.0019	0.1144	0.0012
D21b1_25	1740.0	15.0	1798.0	14.0	1855.0	30.0	3%	1798.0	14.0	4.854	0.084	0.31	0.0031	0.1135	0.0018
D21b1_26	2894.0	27.0	2791.0	18.0	2727.0	30.0	4%	2791.0	18.0	14.66	0.29	0.5659	0.0065	0.189	0.0035
D21b1_27	994.0	14.0	956.0	38.0	840.0	120.0	4%	994.0	14.0	1.568	0.094	0.1669	0.0025	0.0708	0.0041
D21b1_28	321.6	3.1	319.9	8.6	288.0	69.0	1%	321.6	3.1	0.37	0.012	0.05116	0.00051	0.0524	0.0017
D21b1_29	668.6	8.4	660.0	23.0	590.0	100.0	1%	668.6	8.4	0.93	0.043	0.1091	0.0014	0.0608	0.0029
D21b1_31	1887.0	15.0	1879.0	15.0	1863.0	31.0	0%	1879.0	15.0	5.36	0.096	0.3404	0.0032	0.114	0.0019
D21b1_32	755.4	6.3	782.0	15.0	815.0	59.0	3%	755.4	6.3	1.161	0.031	0.1244	0.0011	0.0669	0.0018

D21b1_33	488.3	3.0	494.1	7.4	517.0	38.0	1%	488.3	3.0	0.627	0.012	0.0787	0.00049	0.058	0.001
D21b1_34	318.9	3.8	321.0	15.0	280.0	110.0	1%	318.9	3.8	0.372	0.02	0.05073	0.00062	0.0532	0.0029
D21b1_35	513.3	5.4	499.9	9.6	459.0	49.0	3%	513.3	5.4	0.638	0.015	0.08291	0.00091	0.0564	0.0012
D21b1_36	476.7	4.0	474.9	9.9	435.0	56.0	0%	476.7	4.0	0.599	0.016	0.07676	0.00066	0.0561	0.0015
D21b1_37	325.2	3.6	335.0	10.0	363.0	77.0	3%	325.2	3.6	0.39	0.014	0.05175	0.00058	0.0549	0.002
D21b1_38	590.5	4.5	588.6	7.8	582.0	36.0	0%	590.5	4.5	0.785	0.014	0.09595	0.00076	0.05942	0.00099
D21b1_39	685.0	16.0	884.0	16.0	1471.0	53.0	23%	685.0	16.0	1.397	0.037	0.1117	0.0028	0.0926	0.0026
D21b1_40	319.6	2.6	316.4	6.5	289.0	53.0	1%	319.6	2.6	0.3673	0.0087	0.05083	0.00042	0.0522	0.0013
D21b1_41	1023.0	13.0	1015.0	19.0	958.0	59.0	1%	1023.0	13.0	1.71	0.052	0.172	0.0024	0.0723	0.0021
D21b1_42	1694.5	9.8	1671.3	8.5	1642.0	18.0	1%	1671.3	8.5	4.182	0.043	0.3007	0.002	0.10106	0.00095
D21b1_43	558.5	4.7	575.0	13.0	606.0	62.0	3%	558.5	4.7	0.761	0.022	0.09052	0.00079	0.0608	0.0018
D21b1_44	2045.0	13.0	2020.0	12.0	1994.0	23.0	1%	2020.0	12.0	6.305	0.085	0.3733	0.0027	0.1226	0.0016
D21b1_45	463.3	4.2	462.0	10.0	437.0	57.0	0%	463.3	4.2	0.575	0.016	0.07453	0.0007	0.0561	0.0015
D21b1_47	1820.0	33.0	2979.0	42.0	3891.0	38.0	39%	2979.0	42.0	18.07	0.73	0.3263	0.0068	0.3968	0.0098
D21b1_48	705.3	6.5	713.0	13.0	716.0	55.0	1%	705.3	6.5	1.021	0.026	0.1156	0.0011	0.0642	0.0016
D21b1_49	643.7	7.1	644.0	11.0	672.0	47.0	0%	643.7	7.1	0.885	0.021	0.1049	0.0012	0.0621	0.0014
D21b1_50	1410.3	8.2	1402.0	11.0	1394.0	26.0	1%	1410.3	8.2	2.982	0.044	0.2446	0.0016	0.0885	0.0012
D21b1_51	716.9	6.3	902.0	24.0	1395.0	79.0	21%	716.9	6.3	1.469	0.06	0.1177	0.0011	0.0913	0.0038
D21b1_52	2158.0	23.0	2149.0	23.0	2141.0	47.0	0%	2149.0	23.0	7.3	0.19	0.3978	0.005	0.1354	0.0035
D21b1_53	618.0	4.6	608.0	11.0	577.0	51.0	2%	618.0	4.6	0.823	0.02	0.10063	0.00079	0.0596	0.0013
D21b1_54	469.2	4.3	520.0	15.0	737.0	75.0	10%	469.2	4.3	0.672	0.024	0.07552	0.00072	0.0646	0.0024
D21b1_55	397.2	3.4	506.4	6.9	1049.0	37.0	22%	397.2	3.4	0.647	0.011	0.06356	0.00056	0.0741	0.0014
D21b1_56	2479.0	22.0	2486.0	17.0	2488.0	30.0	0%	2486.0	17.0	10.64	0.2	0.4688	0.005	0.1636	0.003
D21b1_57	1645.0	20.0	1791.0	21.0	1977.0	35.0	8%	1791.0	21.0	4.88	0.12	0.2904	0.004	0.1208	0.0023
D21b1_58	619.4	5.0	629.0	11.0	645.0	52.0	2%	619.4	5.0	0.857	0.021	0.10086	0.00086	0.0618	0.0015
D21b1_59	312.6	2.8	328.1	9.6	410.0	58.0	5%	312.6	2.8	0.385	0.014	0.04969	0.00045	0.0555	0.0016
D21b1_60	693.8	7.6	692.0	22.0	640.0	92.0	0%	693.8	7.6	0.979	0.043	0.1136	0.0013	0.0615	0.0028
D21b1_61	484.6	4.2	482.0	12.0	430.0	64.0	1%	484.6	4.2	0.609	0.018	0.07808	0.00071	0.056	0.0016
D21b1_62	302.3	3.6	296.0	12.0	212.0	96.0	2%	302.3	3.6	0.341	0.016	0.04802	0.00058	0.0517	0.0025
D21b1_64	431.0	3.5	554.3	8.6	1077.0	41.0	22%	431.0	3.5	0.726	0.015	0.06915	0.00059	0.0753	0.0015
D21b1_65	514.9	9.4	525.0	12.0	628.0	52.0	2%	514.9	9.4	0.677	0.02	0.0832	0.0016	0.0612	0.0014
D21b1_66	542.5	5.5	538.0	15.0	501.0	76.0	1%	542.5	5.5	0.709	0.026	0.08782	0.00093	0.0588	0.0023

D21b1_67	610.2	7.8	619.0	21.0	606.0	96.0	1%	610.2	7.8	0.848	0.038	0.0991	0.0013	0.0622	0.0028
D21b1_68	317.4	2.7	319.5	7.8	317.0	62.0	1%	317.4	2.7	0.37	0.011	0.05047	0.00043	0.0531	0.0015
D21b1_69	486.4	3.7	484.0	10.0	447.0	60.0	0%	486.4	3.7	0.613	0.016	0.07833	0.00062	0.0563	0.0015
D21b1_70	611.0	47.0	1520.0	150.0	2600.0	240.0	60%	1520.0	150.0	6.13	0.95	0.1014	0.0083	0.318	0.032
D21b1_71	749.9	8.8	745.0	27.0	670.0	100.0	1%	749.9	8.8	1.08	0.057	0.1234	0.0015	0.0624	0.0032
D21b1_72	365.4	3.3	529.0	20.0	1251.0	89.0	31%	365.4	3.3	0.696	0.032	0.05832	0.00055	0.0856	0.0036
D21b1_73	1708.4	9.9	1723.4	9.2	1730.0	17.0	1%	1723.4	9.2	4.458	0.049	0.3034	0.002	0.1062	0.001
D21b1_74	529.7	4.8	533.0	11.0	523.0	56.0	1%	529.7	4.8	0.689	0.018	0.0856	0.00081	0.0584	0.0015
D21b1_75	2343.0	20.0	2560.7	9.5	2735.0	12.0	9%	2560.7	9.5	11.44	0.12	0.4388	0.0044	0.1892	0.0014
D21b1_76	350.9	4.0	338.0	15.0	220.0	100.0	4%	350.9	4.0	0.397	0.02	0.05596	0.00066	0.0508	0.0026
D21b1_77	303.7	3.5	359.0	17.0	650.0	120.0	15%	303.7	3.5	0.427	0.024	0.04825	0.00058	0.0637	0.0036
D21b1_79	487.0	3.7	478.9	9.6	410.0	54.0	2%	487.0	3.7	0.603	0.015	0.07848	0.00062	0.0557	0.0014
D21b1_80	632.7	6.8	648.0	11.0	687.0	44.0	2%	632.7	6.8	0.896	0.02	0.1032	0.0012	0.0625	0.0013
D21b1_81	550.1	5.4	550.0	15.0	520.0	78.0	0%	550.1	5.4	0.718	0.026	0.08905	0.0009	0.0589	0.0022
D21b1_82	1321.0	23.0	1364.0	44.0	1380.0	120.0	3%	1321.0	23.0	2.93	0.17	0.228	0.0044	0.0918	0.0054
D21b1_83	491.1	4.4	481.0	11.0	424.0	62.0	2%	491.1	4.4	0.607	0.018	0.07917	0.00074	0.0558	0.0016
D21b1_84	1039.5	9.0	1069.0	17.0	1123.0	50.0	3%	1039.5	9.0	1.878	0.049	0.1749	0.0016	0.0772	0.0019
D21b1_85	634.9	7.9	648.0	20.0	616.0	92.0	2%	634.9	7.9	0.893	0.04	0.1036	0.0014	0.0621	0.0028
D21b1_86	432.4	3.5	457.0	13.0	521.0	80.0	5%	432.4	3.5	0.572	0.02	0.06939	0.00059	0.0589	0.0022
D21b1_87	1972.0	16.0	1977.0	15.0	1971.0	34.0	0%	1977.0	15.0	5.99	0.1	0.3576	0.0034	0.1223	0.0023
D21b1_88	569.7	5.3	660.0	12.0	965.0	60.0	14%	569.7	5.3	0.917	0.023	0.09242	0.00089	0.0721	0.0021
D21b1_89	569.8	5.6	589.0	16.0	607.0	76.0	3%	569.8	5.6	0.786	0.029	0.09237	0.00095	0.0618	0.0022
D21b1_90	820.8	7.8	799.0	17.0	719.0	67.0	3%	820.8	7.8	1.206	0.036	0.1358	0.0014	0.0645	0.002
D21b1_91	581.8	4.3	579.0	11.0	540.0	57.0	0%	581.8	4.3	0.772	0.02	0.09441	0.00073	0.0591	0.0015
D21b1_92	1085.4	7.2	1107.0	11.0	1132.0	32.0	2%	1085.4	7.2	1.973	0.033	0.1834	0.0013	0.0778	0.0012
D21b1_93	1599.0	11.0	1611.0	10.0	1615.0	21.0	1%	1611.0	10.0	3.881	0.049	0.2815	0.0022	0.0999	0.0011
D21b1_94	2014.0	12.0	1945.0	11.0	1887.0	23.0	4%	1945.0	11.0	5.804	0.076	0.3668	0.0025	0.1156	0.0014
D21b1_96	476.9	5.4	487.0	17.0	553.0	94.0	2%	476.9	5.4	0.618	0.027	0.0768	0.00091	0.0582	0.0026
D21b1_97	457.7	4.0	643.0	11.0	1362.0	44.0	29%	457.7	4.0	0.887	0.021	0.0736	0.00066	0.0883	0.002
D21b1_98	589.3	4.9	578.0	13.0	499.0	63.0	2%	589.3	4.9	0.768	0.022	0.09563	0.00083	0.058	0.0017
D21b1_99	316.5	2.7	311.5	7.0	263.0	59.0	2%	316.5	2.7	0.3604	0.0094	0.05033	0.00043	0.0515	0.0014
D21b1_100	925.6	9.9	910.0	24.0	813.0	88.0	2%	925.6	9.9	1.475	0.059	0.1543	0.0018	0.0683	0.0028

D21b1_101	746.4	9.4	747.0	30.0	650.0	120.0	0%	746.4	9.4	1.075	0.06	0.1226	0.0016	0.0633	0.0036
D21b1_102	538.9	4.6	651.0	11.0	1070.0	42.0	17%	538.9	4.6	0.898	0.021	0.08721	0.00078	0.0751	0.0016
D21b1_103	347.0	2.7	521.2	8.5	1386.0	41.0	33%	347.0	2.7	0.673	0.014	0.05531	0.00044	0.0882	0.0018
D21b1_104	830.9	7.0	856.0	11.0	908.0	39.0	3%	830.9	7.0	1.32	0.025	0.1376	0.0012	0.0693	0.0013
D21b1_105	348.0	3.4	350.3	9.8	327.0	73.0	1%	348.0	3.4	0.411	0.014	0.05547	0.00055	0.054	0.0018
D21b1_106	320.3	3.9	307.0	12.0	180.0	100.0	4%	320.3	3.9	0.355	0.017	0.05096	0.00064	0.05	0.0025
D21b1_107	1138.3	9.1	1134.0	18.0	1106.0	56.0	0%	1138.3	9.1	2.065	0.053	0.1932	0.0017	0.0776	0.0021
D21b1_108	2164.0	59.0	2076.0	69.0	1920.0	150.0	4%	2076.0	69.0	7.09	0.52	0.402	0.013	0.133	0.01
D21b1_109	1944.0	14.0	1901.0	16.0	1854.0	35.0	2%	1901.0	16.0	5.52	0.1	0.352	0.003	0.1132	0.0022
D21b1_110	296.5	3.4	295.0	11.0	260.0	89.0	1%	296.5	3.4	0.338	0.015	0.04707	0.00056	0.0522	0.0023
D21b1_111	2030.0	11.0	2006.0	8.7	1987.0	16.0	1%	2006.0	8.7	6.222	0.062	0.3695	0.0023	0.1222	0.0011
D21b1_112	667.8	7.4	658.0	21.0	571.0	91.0	1%	667.8	7.4	0.904	0.039	0.1092	0.0013	0.0598	0.0026
D21b1_113	875.0	16.0	1915.0	40.0	3359.0	57.0	54%	1915.0	40.0	5.65	0.25	0.1454	0.0028	0.2796	0.0097
D21b1_114	326.0	2.4	321.8	4.6	284.0	35.0	1%	326.0	2.4	0.3723	0.0064	0.05188	0.00039	0.05211	0.0008
D21b1_115	316.0	2.4	318.8	7.1	320.0	56.0	1%	316.0	2.4	0.368	0.0096	0.05024	0.00039	0.0532	0.0013
D21b1_116	3163.0	17.0	3073.0	11.0	3015.0	16.0	3%	3073.0	11.0	19.63	0.23	0.6333	0.0043	0.2248	0.0023
D21b1_117	439.3	3.9	469.0	12.0	600.0	67.0	6%	439.3	3.9	0.585	0.018	0.07054	0.00065	0.0603	0.0019
D21b1_118	248.9	1.6	264.0	2.2	380.0	19.0	6%	248.9	1.6	0.2967	0.0028	0.03937	0.00025	0.0543	0.00046
D21b1_119	433.3	9.3	442.0	16.0	478.0	75.0	2%	433.3	9.3	0.552	0.024	0.0696	0.0016	0.0571	0.002
D21b1_122	491.9	5.8	482.0	17.0	407.0	92.0	2%	491.9	5.8	0.604	0.026	0.07931	0.00097	0.0561	0.0025
D21b1_123	350.9	3.5	346.0	12.0	290.0	84.0	1%	350.9	3.5	0.408	0.017	0.05595	0.00058	0.0527	0.0021
D21b1_124	639.7	5.0	634.0	12.0	613.0	57.0	1%	639.7	5.0	0.867	0.023	0.10435	0.00086	0.0606	0.0017
D21b1_125	867.1	7.9	855.0	16.0	814.0	58.0	1%	867.1	7.9	1.326	0.036	0.1439	0.0014	0.0664	0.0018
D21b1_126	375.8	4.1	392.8	8.3	482.0	57.0	4%	375.8	4.1	0.474	0.012	0.06004	0.00068	0.0575	0.0015
D21b1_127	307.6	2.8	307.3	9.0	293.0	68.0	0%	307.6	2.8	0.35	0.012	0.04888	0.00045	0.0522	0.0017
D21b1_128	570.9	4.5	565.0	13.0	491.0	66.0	1%	570.9	4.5	0.746	0.023	0.09251	0.00078	0.0574	0.0017
D21b1_129	2557.0	17.0	2536.0	12.0	2520.0	15.0	1%	2536.0	12.0	11.17	0.14	0.487	0.0038	0.1662	0.0015
D21b1_130	1082.5	8.4	1077.0	15.0	1057.0	48.0	1%	1082.5	8.4	1.876	0.043	0.1828	0.0015	0.075	0.0018
D21b1_131	475.5	6.1	466.0	18.0	400.0	100.0	2%	475.5	6.1	0.587	0.028	0.0765	0.001	0.0569	0.0028
D21b1_132	315.3	2.0	310.6	5.1	271.0	42.0	2%	315.3	2.0	0.3579	0.0068	0.05013	0.00032	0.05187	0.00096
D21b1_133	355.1	6.6	358.0	15.0	316.0	92.0	1%	355.1	6.6	0.425	0.02	0.0567	0.0011	0.0529	0.0023
D21b1_134	458.4	4.1	455.0	13.0	405.0	72.0	1%	458.4	4.1	0.567	0.019	0.07371	0.00069	0.0556	0.0019

D21b1_135	654.2	7.5	636.0	14.0	562.0	61.0	3%	654.2	7.5	0.874	0.025	0.1069	0.0013	0.0592	0.0017
D21b1_136	572.6	5.1	571.0	14.0	546.0	67.0	0%	572.6	5.1	0.75	0.022	0.09284	0.00087	0.0596	0.0018
D21b1_137	1943.0	16.0	1893.0	18.0	1836.0	38.0	3%	1893.0	18.0	5.47	0.11	0.3518	0.0033	0.1128	0.0024
D21b1_138	504.6	5.8	476.0	17.0	324.0	94.0	6%	504.6	5.8	0.604	0.027	0.08146	0.00097	0.0539	0.0025
D21b1_139	492.9	5.0	487.0	14.0	458.0	77.0	1%	492.9	5.0	0.613	0.023	0.07941	0.00084	0.0573	0.0021
D21b1_140	585.7	4.3	579.2	8.2	552.0	40.0	1%	585.7	4.3	0.769	0.015	0.09512	0.00074	0.0589	0.0011
D21b1_141	564.7	5.2	548.0	13.0	475.0	66.0	3%	564.7	5.2	0.716	0.022	0.09157	0.00088	0.0579	0.0018
D21b1_142	667.4	9.3	771.0	31.0	1070.0	110.0	13%	667.4	9.3	1.171	0.065	0.109	0.0016	0.0791	0.0045
D21b1_143	656.4	5.1	649.0	13.0	628.0	57.0	1%	656.4	5.1	0.902	0.024	0.10721	0.00088	0.0607	0.0016
D21b1_144	610.0	14.0	791.0	35.0	1300.0	130.0	23%	610.0	14.0	1.177	0.074	0.0992	0.0024	0.0881	0.0054
D21b1_145	368.9	3.3	399.6	8.3	565.0	57.0	8%	368.9	3.3	0.483	0.012	0.0589	0.00054	0.0596	0.0016
D21b1_148	1617.0	19.0	1698.0	26.0	1800.0	59.0	5%	1698.0	26.0	4.33	0.14	0.2849	0.0038	0.1101	0.0034
D21b1_149	566.0	16.0	626.0	26.0	833.0	73.0	10%	566.0	16.0	0.889	0.049	0.0919	0.0028	0.0691	0.0024
D21b1_150	2214.0	15.0	2146.0	12.0	2085.0	19.0	3%	2146.0	12.0	7.272	0.098	0.4097	0.0033	0.1293	0.0014
D21b1_151	323.0	2.7	317.7	7.3	275.0	59.0	2%	323.0	2.7	0.3674	0.0098	0.05136	0.00044	0.0524	0.0014
D21b1_152	350.2	5.2	592.0	34.0	1510.0	130.0	41%	350.2	5.2	0.833	0.062	0.05585	0.00085	0.1056	0.0069
D21b1_155	551.0	20.0	549.0	22.0	570.0	55.0	0%	551.0	20.0	0.734	0.038	0.0896	0.0034	0.0597	0.0016
D21b1_156	319.3	2.6	334.4	8.8	432.0	64.0	5%	319.3	2.6	0.388	0.012	0.05079	0.00042	0.056	0.0016
D21b1_157	330.7	3.1	372.0	12.0	562.0	59.0	11%	330.7	3.1	0.449	0.018	0.05265	0.00051	0.0605	0.0018
D21b1_158	321.3	2.6	312.7	7.1	243.0	57.0	3%	321.3	2.6	0.3607	0.0097	0.05111	0.00042	0.0514	0.0014
D21b1_159	2285.0	26.0	2238.0	25.0	2179.0	49.0	2%	2238.0	25.0	8.1	0.22	0.4263	0.0059	0.1378	0.0038
D21b1_160	536.7	4.8	586.0	12.0	778.0	55.0	8%	536.7	4.8	0.785	0.02	0.08683	0.00081	0.0658	0.0017
D21b1_161	322.1	2.8	329.2	7.6	373.0	60.0	2%	322.1	2.8	0.382	0.01	0.05124	0.00045	0.0543	0.0015
D21b1_163	1873.0	12.0	1868.0	13.0	1863.0	26.0	0%	1868.0	13.0	5.298	0.079	0.3371	0.0025	0.1142	0.0016
D21b1_164	727.7	6.2	702.0	14.0	624.0	63.0	4%	727.7	6.2	1	0.028	0.1195	0.0011	0.0608	0.0018
D21b1_165	318.7	2.1	316.9	4.8	313.0	37.0	1%	318.7	2.1	0.3667	0.0065	0.05069	0.00034	0.05269	0.00087
D21b1_166	1105.0	14.0	1098.0	28.0	1102.0	84.0	1%	1105.0	14.0	1.947	0.082	0.1872	0.0025	0.0755	0.0032
D21b1_167	605.5	6.9	600.0	18.0	549.0	85.0	1%	605.5	6.9	0.812	0.032	0.0984	0.0012	0.0599	0.0024
D21b1_168	1901.0	14.0	1893.0	19.0	1891.0	40.0	0%	1893.0	19.0	5.44	0.12	0.3426	0.0028	0.1154	0.0026
D21b1_169	1015.1	7.6	1019.0	15.0	1044.0	48.0	0%	1015.1	7.6	1.734	0.04	0.1706	0.0014	0.0741	0.0018
D21b1_170	330.4	2.4	341.3	6.5	418.0	43.0	3%	330.4	2.4	0.3999	0.009	0.05259	0.00039	0.0554	0.0011
D21b1_171	321.2	3.0	317.5	8.4	285.0	67.0	1%	321.2	3.0	0.368	0.011	0.0511	0.00048	0.0529	0.0017

D21b1_173	318.0	2.1	310.5	4.3	267.0	35.0	2%	318.0	2.1	0.358	0.0057	0.05057	0.00034	0.05188	0.00081
D21b1_174	2130.0	10.0	2113.0	10.0	2099.0	19.0	1%	2113.0	10.0	7.007	0.083	0.3914	0.0022	0.1304	0.0014
D21b1_175	489.3	3.4	526.9	5.0	690.0	24.0	7%	489.3	3.4	0.6802	0.0083	0.07886	0.00056	0.06246	0.0007
D21b1_176	486.4	4.6	474.0	11.0	428.0	64.0	3%	486.4	4.6	0.598	0.018	0.07838	0.00077	0.0556	0.0017
D21b1_181	328.0	2.6	346.4	7.9	481.0	65.0	5%	328.0	2.6	0.404	0.011	0.0522	0.00042	0.0563	0.0017
D21b1_184	312.6	2.5	306.7	7.1	255.0	58.0	2%	312.6	2.5	0.3533	0.0095	0.04969	0.00041	0.0518	0.0014
D21b1_186	334.7	1.9	335.7	4.3	334.0	34.0	0%	334.7	1.9	0.3922	0.0059	0.0533	0.00031	0.05336	0.00082

Appendix 37: Detrital zircon (U-Th)/He data for sample D17.

Grain #	V (µm3)	+/- 2σ	4He (mol)	Corrected 4He (mol)	+/- 2σ	4He (mol/g)	Corrected 4He (mol/g)	+/- 2σ	232Th (ppm)	+/- 2σ	238U (ppm)	+/- 2σ	147Sm (ppm)	+/- 2σ	eU	Th/U	ZHe age (Ma)	+/- 2σ
D17b1-1	9900	495	2.37E-14	1.58E-14	5.70E-16	5.14E-07	3.42E-07	2.85E-08	197	7	1044	20	0	0	1090	0.19	87.5	5.1
D17b1-2	9894	495	7.41E-15	4.94E-15	3.47E-16	1.61E-07	1.07E-07	1.10E-08	123	10	342	17	4	0	371	0.36	80.6	6.7
D17b1-3	9889	494	2.36E-14	1.57E-14	4.23E-16	5.14E-07	3.42E-07	2.73E-08	49	1	337	6	7	0	348	0.14	273.7	15.3
D17b1-4	9883	494	3.83E-15	2.56E-15	1.92E-16	8.34E-08	5.56E-08	5.91E-09	< LOD	0	< LOD	1	< LOD	0	-	-	-	-
D17b1-5	9877	494	3.70E-14	2.47E-14	4.17E-16	8.06E-07	5.37E-07	4.13E-08	1399	28	1531	29	8	0	1860	0.91	80.3	4.3
D17b1-6	9871	494	7.29E-15	4.86E-15	2.41E-16	1.59E-07	1.06E-07	9.51E-09	145	2	293	5	0	0	327	0.50	90.0	5.6
D17b1-7	9866	493	2.72E-14	1.82E-14	6.88E-16	5.93E-07	3.96E-07	3.32E-08	168	9	323	10	6	0	362	0.52	303.9	18.9
D17b1-8	9860	493	1.32E-14	8.83E-15	2.71E-16	2.89E-07	1.93E-07	1.56E-08	10	1	96	6	0	0	98	0.11	544.9	42.8
D17b1-9	9854	493	7.37E-15	4.91E-15	1.89E-16	1.61E-07	1.07E-07	9.04E-09	144	3	262	5	0	0	296	0.55	100.7	5.9
D17b1-10	9848	492	2.31E-14	1.54E-14	4.05E-16	5.05E-07	3.36E-07	2.67E-08	37	2	228	4	0	0	236	0.16	396.4	22.1
D17b1-11	9843	492	1.02E-14	6.82E-15	3.23E-16	2.23E-07	1.49E-07	1.32E-08	11	0	107	3	3	0	110	0.11	377.9	25.1
D17b1-12	9837	492	9.88E-15	6.59E-15	3.65E-16	2.16E-07	1.44E-07	1.34E-08	11	0	140	4	2	0	143	0.08	280.5	18.8
D17b1-13	9831	492	4.38E-14	2.92E-14	6.63E-16	9.59E-07	6.39E-07	5.01E-08	117	6	517	8	4	0	545	0.23	326.9	17.8
D17b1-14	9826	491	5.65E-15	3.76E-15	2.09E-16	1.24E-07	8.24E-08	7.69E-09	< LOD	0	94	4	< LOD	0	-	-	-	-
D17b1-15	9820	491	2.46E-15	1.64E-15	1.08E-16	5.38E-08	3.58E-08	3.58E-09	67	1	107	2	4	0	123	0.63	81.2	5.6
D17b1-16	9814	491	4.87E-15	3.24E-15	2.28E-16	1.07E-07	7.11E-08	7.31E-09	98	3	156	3	3	0	179	0.63	110.7	7.8
D17b1-17	9808	490	3.87E-15	2.58E-15	1.37E-16	8.48E-08	5.65E-08	5.20E-09	122	6	141	6	7	0	169	0.86	92.8	6.6
D17b1-18	9803	490	1.02E-14	6.77E-15	2.00E-16	2.23E-07	1.49E-07	1.20E-08	198	4	391	7	18	0	438	0.51	94.4	5.3
D17b1-19	9797	490	3.08E-14	2.05E-14	5.84E-16	6.76E-07	4.51E-07	3.61E-08	159	11	371	9	5	0	409	0.43	306.8	17.9
D17b1-20	9791	490	5.37E-15	3.58E-15	1.94E-16	1.18E-07	7.86E-08	7.27E-09	217	4	178	3	19	0	229	1.22	95.4	6.0
D17b1-21	9785	489	7.07E-14	4.71E-14	1.01E-15	1.55E-06	1.04E-06	8.08E-08	187	6	710	11	6	0	754	0.26	382.5	20.7
D17b1-22	9780	489	1.93E-14	1.29E-14	4.26E-16	4.25E-07	2.83E-07	2.32E-08	21	1	245	10	3	0	250	0.09	315.5	21.1
D17b1-23	9774	489	5.64E-15	3.76E-15	2.33E-16	1.24E-07	8.28E-08	8.05E-09	89	1	141	2	7	0	161	0.63	142.7	9.5
D17b1-24	9768	488	3.00E-15	2.00E-15	1.26E-16	6.60E-08	4.40E-08	4.31E-09	3	0	39	2	< LOD	0	40	0.08	-	
D17b1-25	9762	488	3.51E-14	2.34E-14	8.38E-16	7.72E-07	5.15E-07	4.28E-08	85	8	486	12	19	1	506	0.18	283.3	17.1
D17b1-26	9757	488	5.83E-15	3.89E-15	2.28E-16	1.29E-07	8.57E-08	8.16E-09	13	1	78	2	0	0	81	0.16	295.7	20.2
D17b1-27	9751	488	1.67E-15	1.11E-15	1.39E-16	3.68E-08	2.45E-08	3.57E-09	17	1	68	2	4	0	72	0.26	-	
D17b1-28	9745	487	1.71E-14	1.14E-14	3.66E-16	3.78E-07	2.52E-07	2.06E-08	296	12	686	26	68	2	756	0.43	92.9	6.0
D17b1-29	9740	487	1.98E-14	1.32E-14	5.27E-16	4.36E-07	2.91E-07	2.47E-08	31	1	194	9	0	0	201	0.16	402.2	28.8

D17b1-30	9734	487	1.02E-14	6.77E-15	2.26E-16	2.25E-07	1.50E-07	1.23E-08	172	5	470	11	23	1	510	0.37	81.6	4.8
D17b1-31	9728	486	1.50E-14	9.97E-15	3.79E-16	3.31E-07	2.20E-07	1.85E-08	74	3	179	3	0	0	196	0.41	312.7	18.4
D17b1-32	9722	486	6.95E-15	4.64E-15	2.82E-16	1.54E-07	1.03E-07	9.90E-09	75	2	340	17	7	0	358	0.22	79.8	6.4
D17b1-33	9717	486	6.89E-15	4.60E-15	1.83E-16	1.53E-07	1.02E-07	8.64E-09	56	1	219	4	3	0	233	0.26	121.7	7.2
D17b1-34	9711	486	1.06E-15	7.06E-16	1.31E-16	2.35E-08	1.56E-08	3.13E-09	45	1	36	1	1	0	46	1.25	-	
D17b1-35	9705	485	3.33E-14	2.22E-14	6.89E-16	7.39E-07	4.93E-07	4.00E-08	291	8	553	10	10	0	621	0.53	220.5	12.4
D17b1-36	9699	485	3.00E-14	2.00E-14	4.08E-16	6.66E-07	4.44E-07	3.45E-08	214	7	468	11	13	1	518	0.46	238.4	13.4
D17b1-37	9694	485	2.55E-15	1.70E-15	2.23E-16	5.66E-08	3.77E-08	5.70E-09	37	1	114	2	2	0	122	0.32	85.8	8.8
D17b1-38	9688	484	4.79E-15	3.19E-15	1.51E-16	1.06E-07	7.09E-08	6.29E-09	85	2	32	1	5	0	52	2.66	-	
D17b1-39	9682	484	1.24E-14	8.24E-15	2.69E-16	2.75E-07	1.83E-07	1.50E-08	72	2	140	8	3	0	157	0.52	324.0	23.6
D17b1-40	9677	484	8.63E-14	5.75E-14	1.41E-15	1.92E-06	1.28E-06	1.01E-07	158	4	1350	27	22	1	1387	0.12	256.5	14.4
D17b1-41	9671	484	3.11E-14	2.07E-14	4.89E-16	6.92E-07	4.61E-07	3.63E-08	24	1	299	10	9	1	305	0.08	421.5	26.1
D17b1-42	9665	483	4.15E-14	2.76E-14	5.95E-16	9.23E-07	6.15E-07	4.80E-08	375	25	404	12	12	1	492	0.93	347.5	20.4
D17b1-43	9659	483	9.57E-15	6.38E-15	3.65E-16	2.13E-07	1.42E-07	1.34E-08	15	1	110	6	0	0	114	0.13	348.5	28.4
D17b1-44	9654	483	1.85E-14	1.24E-14	4.48E-16	4.13E-07	2.75E-07	2.29E-08	222	15	554	25	4	0	606	0.40	126.3	8.8
D17b1-45	9648	482	1.54E-14	1.02E-14	4.16E-16	3.43E-07	2.28E-07	1.95E-08	135	5	204	6	27	2	236	0.66	269.5	16.7
D17b1-46	9642	482	1.70E-14	1.13E-14	2.97E-16	3.80E-07	2.53E-07	2.01E-08	21	1	245	7	3	0	250	0.09	282.1	16.8
D17b1-47	9636	482	2.39E-14	1.59E-14	5.32E-16	5.33E-07	3.55E-07	2.92E-08	33	1	339	6	3	0	346	0.10	285.4	16.5
D17b1-48	9631	482	7.29E-15	4.86E-15	2.15E-16	1.63E-07	1.09E-07	9.44E-09	192	3	206	4	10	0	251	0.93	120.4	7.2
D17b1-49	9625	481	1.12E-14	7.46E-15	3.40E-16	2.50E-07	1.67E-07	1.46E-08	44	1	220	4	5	0	231	0.20	201.0	12.3
D17b1-50	9619	481	5.46E-15	3.64E-15	1.96E-16	1.22E-07	8.13E-08	7.51E-09	112	3	199	4	2	0	226	0.56	100.2	6.5
D17b1-51	9613	481	2.03E-15	1.35E-15	2.21E-16	4.54E-08	3.03E-08	5.44E-09	7	0	38	1	0	0	39	0.18	-	
D17b1-52	9608	480	1.02E-14	6.82E-15	2.87E-16	2.29E-07	1.53E-07	1.31E-08	587	37	114	4	19	1	252	5.13	167.5	11.5
D17b1-53	9602	480	1.27E-14	8.46E-15	3.21E-16	2.84E-07	1.89E-07	1.59E-08	233	6	442	10	26	1	497	0.53	106.1	6.3
D17b1-55	9591	480	1.75E-14	1.16E-14	4.66E-16	3.92E-07	2.61E-07	2.22E-08	85	2	189	4	25	1	208	0.45	348.4	20.6
D17b1-56	9585	479	2.88E-14	1.92E-14	5.89E-16	6.45E-07	4.30E-07	3.49E-08	216	23	371	13	7	1	422	0.58	283.7	18.0
D17b1-57	9579	479	3.53E-14	2.36E-14	5.25E-16	7.93E-07	5.29E-07	4.14E-08	430	21	1246	28	24	2	1347	0.35	109.2	6.1
D17b1-58	9573	479	5.88E-15	3.92E-15	2.89E-16	1.32E-07	8.81E-08	9.26E-09	97	2	156	3	7	0	178	0.62	137.5	9.9
D17b1-59	9568	478	3.13E-15	2.09E-15	1.46E-16	7.04E-08	4.69E-08	4.81E-09	59	1	56	2	6	0	69	1.05	-	
D17b1-60	9562	478	2.01E-14	1.34E-14	3.46E-16	4.53E-07	3.02E-07	2.39E-08	144	5	838	20	14	1	872	0.17	96.3	5.6
D17b1-61	9556	478	3.48E-14	2.32E-14	5.94E-16	7.84E-07	5.22E-07	4.14E-08	46	1	494	10	4	0	504	0.09	288.5	16.3
D17b1-62	9550	478	3.13E-14	2.09E-14	6.19E-16	7.05E-07	4.70E-07	3.79E-08	416	20	433	16	30	6	531	0.96	246.2	15.3

D17b1-63	9545	477	7.74E-15	5.16E-15	2.73E-16	1.74E-07	1.16E-07	1.07E-08	< LOD	0	54	2	< LOD	0	-	-	-	
D17b1-64	9539	477	5.22E-14	3.48E-14	8.48E-16	1.18E-06	7.84E-07	6.18E-08	72	2	658	18	11	1	675	0.11	323.5	19.1
D17b1-65	9533	477	3.28E-14	2.18E-14	5.42E-16	7.39E-07	4.93E-07	3.89E-08	58	2	377	7	0	0	391	0.15	351.0	19.5
D17b1-67	9522	476	2.14E-14	1.42E-14	5.10E-16	4.83E-07	3.22E-07	2.67E-08	140	7	311	6	6	0	344	0.45	260.1	15.2
D17b1-69	9510	476	3.19E-14	2.13E-14	5.43E-16	7.22E-07	4.82E-07	3.81E-08	46	2	385	12	4	0	396	0.12	338.8	20.6
D17b1-70	9505	475	2.61E-14	1.74E-14	4.83E-16	5.92E-07	3.94E-07	3.15E-08	78	5	330	6	5	0	349	0.24	315.0	17.8
D17b1-71	9499	475	4.26E-15	2.84E-15	2.77E-16	9.65E-08	6.44E-08	7.92E-09	< LOD	0	36	2	1	0	-	-	-	
D17b1-72	9493	475	2.83E-14	1.89E-14	3.25E-16	6.41E-07	4.28E-07	3.29E-08	51	1	358	8	5	0	370	0.14	321.8	17.9
D17b1-73	9487	474	2.28E-15	1.52E-15	1.88E-16	5.16E-08	3.44E-08	4.98E-09	61	1	110	2	7	0	124	0.55	77.1	7.6
D17b1-74	9482	474	9.01E-15	6.01E-15	2.42E-16	2.04E-07	1.36E-07	1.16E-08	147	4	141	3	10	0	175	1.05	216.3	13.0
D17b1-75	9476	474	8.78E-15	5.85E-15	2.64E-16	1.99E-07	1.33E-07	1.16E-08	150	10	267	29	8	0	302	0.56	122.2	13.7
D17b1-76	9470	474	8.93E-15	5.95E-15	3.76E-16	2.03E-07	1.35E-07	1.33E-08	112	3	382	9	5	0	409	0.29	92.1	6.3
D17b1-77	9464	473	1.56E-14	1.04E-14	4.33E-16	3.53E-07	2.36E-07	2.02E-08	118	12	109	5	29	5	137	1.08	477.3	34.6
D17b1-78	9459	473	5.40E-15	3.60E-15	2.61E-16	1.23E-07	8.19E-08	8.53E-09	14	1	159	10	2	0	162	0.09	140.8	13.0
D17b1-79	9453	473	5.22E-15	3.48E-15	2.55E-16	1.19E-07	7.92E-08	8.30E-09	85	4	204	4	11	0	224	0.42	98.4	7.1
D17b1-81	9441	472	3.63E-15	2.42E-15	2.41E-16	8.27E-08	5.51E-08	6.87E-09	< LOD	0	33	1	1	0	-	-	-	
D17b1-82	9436	472	2.55E-14	1.70E-14	3.38E-16	5.82E-07	3.88E-07	3.01E-08	109	6	362	7	5	0	387	0.30	278.6	15.3
D17b1-83	9430	472	2.13E-14	1.42E-14	4.08E-16	4.86E-07	3.24E-07	2.60E-08	141	7	383	11	9	0	416	0.37	216.6	13.0
D17b1-84	9424	471	3.20E-15	2.13E-15	1.97E-16	7.30E-08	4.86E-08	5.79E-09	96	3	110	3	8	0	133	0.87	102.0	8.4
D17b1-85	9419	471	1.16E-14	7.76E-15	3.10E-16	2.66E-07	1.77E-07	1.51E-08	6	1	87	7	0	0	89	0.06	556.8	54.6
D17b1-86	9413	471	3.58E-14	2.39E-14	6.07E-16	8.19E-07	5.46E-07	4.32E-08	51	3	458	13	4	1	470	0.11	323.4	19.3
D17b1-87	9407	470	3.83E-14	2.55E-14	6.65E-16	8.75E-07	5.83E-07	4.63E-08	532	19	1096	28	5	0	1221	0.49	132.9	7.7
D17b1-88	9401	470	1.86E-14	1.24E-14	5.32E-16	4.26E-07	2.84E-07	2.45E-08	41	2	250	15	3	0	260	0.16	304.5	24.8
D17b1-89	9396	470	5.53E-15	3.69E-15	2.62E-16	1.27E-07	8.44E-08	8.72E-09	< LOD	0	55	4	< LOD	0	-	-	-	
D17b1-90	9390	469	5.20E-15	3.47E-15	1.72E-16	1.19E-07	7.94E-08	7.14E-09	7	0	59	2	0	0	61	0.12	-	
D17b1-93	9373	469	4.13E-15	2.75E-15	2.59E-16	9.48E-08	6.32E-08	7.61E-09	56	1	73	2	2	0	86	0.77	203.9	16.8
D17b1-94	9367	468	4.05E-15	2.70E-15	1.60E-16	9.30E-08	6.20E-08	5.93E-09	100	3	167	4	5	0	190	0.60	90.6	6.0
D17b1-95	9361	468	2.37E-14	1.58E-14	5.34E-16	5.43E-07	3.62E-07	2.98E-08	206	7	183	6	23	1	232	1.12	434.3	26.7
D17b1-96	9355	468	1.30E-14	8.65E-15	2.79E-16	2.98E-07	1.99E-07	1.62E-08	146	3	132	3	11	0	166	1.10	332.1	19.1
D17b1-97	9350	467	7.64E-15	5.09E-15	1.96E-16	1.76E-07	1.17E-07	9.87E-09	61	2	119	3	3	0	133	0.51	244.9	14.8
D17b1-98	9344	467	8.07E-15	5.38E-15	2.25E-16	1.86E-07	1.24E-07	1.06E-08	283	6	340	7	5	0	406	0.83	84.7	5.1
D17b1-99	9338	467	1.91E-14	1.27E-14	4.51E-16	4.39E-07	2.93E-07	2.43E-08	39	2	426	14	4	0	435	0.09	187.4	12.0

D17b1-101	9327	466	4.07E-14	2.71E-14	4.77E-16	9.39E-07	6.26E-07	4.82E-08	52	2	539	14	24	4	551	0.10	316.2	18.1
D17b1-104	9310	465	1.15E-14	7.64E-15	3.88E-16	2.65E-07	1.76E-07	1.60E-08	27	3	62	3	0	0	69	0.43	-	
D17b1-105	9304	465	2.45E-15	1.63E-15	1.35E-16	5.66E-08	3.77E-08	4.21E-09	40	1	78	2	3	0	88	0.52	119.7	9.2
D17b1-106	9298	465	5.66E-15	3.77E-15	2.75E-16	1.31E-07	8.72E-08	9.13E-09	155	7	244	9	15	1	280	0.63	86.6	6.6
D17b1-107	9292	465	2.62E-14	1.74E-14	5.12E-16	6.06E-07	4.04E-07	3.25E-08	43	1	270	13	3	0	280	0.16	401.2	28.5
D17b1-108	9287	464	6.34E-14	4.23E-14	8.43E-16	1.47E-06	9.80E-07	7.60E-08	249	11	867	41	39	1	926	0.29	294.5	20.1
D17b1-109	9281	464	2.55E-14	1.70E-14	5.45E-16	5.90E-07	3.93E-07	3.21E-08	35	2	349	12	4	0	357	0.10	306.4	19.6
D17b1-110	9275	464	3.80E-14	2.53E-14	6.92E-16	8.81E-07	5.88E-07	4.69E-08	42	2	687	28	6	0	697	0.06	234.8	15.7
D17b1-111	9270	463	1.66E-14	1.11E-14	3.38E-16	3.86E-07	2.57E-07	2.08E-08	22	1	87	6	2	0	92	0.25	781.0	63.1
D17b1-112	9264	463	2.76E-15	1.84E-15	1.53E-16	6.40E-08	4.27E-08	4.78E-09	55	1	106	2	5	0	119	0.52	100.0	7.7
D17b1-113	9258	463	1.24E-14	8.23E-15	3.59E-16	2.87E-07	1.91E-07	1.66E-08	264	9	340	6	0	0	402	0.78	132.2	7.9
D17b1-114	9252	463	1.55E-14	1.04E-14	4.66E-16	3.61E-07	2.41E-07	2.11E-08	< LOD	0	804	16	2	0	-	-	-	-

Appendix 38: Reduced detrital zircon U-Pb data for sample D17.

Grain #	Age 206/238	+/- 2σ	Age 207/235	+/- 2σ	Age 207/206	+/- 2σ	% Discordance	Selected U/Pb age (Ma)	+/- 2σ	Ratio 206/238	+/- 2σ	Ratio 207/235	+/- 2σ	Ratio 207/206	+/- 2σ
D17b1-1	2102.0	25.0	2283.0	12.0	2457.0	13.0	8%	2283.0	12.0	0.3853	0.0054	8.48	0.11	0.1603	0.0012
D17b1-2	562.8	7.1	571.0	15.0	612.0	76.0	1%	562.8	7.1	0.0913	0.0012	0.757	0.027	0.0603	0.0021
D17b1-3	539.4	6.8	541.0	13.0	525.0	66.0	0%	539.4	6.8	0.0873	0.0011	0.704	0.022	0.0584	0.0018
D17b1-4	339.0	14.0	350.0	58.0	210.0	350.0	3%	339.0	14.0	0.054	0.0023	0.455	0.079	0.063	0.011
D17b1-5	306.4	3.4	308.5	6.2	301.0	53.0	1%	306.4	3.4	0.04868	0.00056	0.3551	0.0082	0.0524	0.0012
D17b1-6	287.1	4.1	281.0	13.0	240.0	110.0	2%	287.1	4.1	0.04555	0.00066	0.319	0.017	0.0503	0.0027
D17b1-7	358.6	5.4	370.0	14.0	415.0	91.0	3%	358.6	5.4	0.05721	0.00089	0.441	0.02	0.0561	0.0023
D17b1-8	365.1	8.4	354.0	25.0	290.0	160.0	3%	365.1	8.4	0.0583	0.0014	0.421	0.034	0.0539	0.0041
D17b1-9	2396.0	20.0	2400.0	13.0	2412.0	16.0	0%	2400.0	13.0	0.4505	0.0044	9.66	0.14	0.1558	0.0015
D17b1-10	403.0	5.9	415.0	15.0	460.0	100.0	3%	403.0	5.9	0.06443	0.00097	0.506	0.023	0.0573	0.0028
D17b1-11	337.4	7.3	372.0	26.0	600.0	170.0	9%	337.4	7.3	0.0536	0.0012	0.443	0.036	0.062	0.0052
D17b1-12	403.9	6.5	426.0	21.0	540.0	120.0	5%	403.9	6.5	0.0647	0.0011	0.524	0.032	0.0595	0.0034
D17b1-13	398.2	4.0	394.0	13.0	414.0	74.0	1%	398.2	4.0	0.06373	0.00066	0.476	0.018	0.0556	0.002
D17b1-14	405.6	8.2	381.0	26.0	200.0	160.0	6%	405.6	8.2	0.065	0.0014	0.467	0.037	0.0525	0.0042
D17b1-15	610.0	11.0	590.0	24.0	570.0	120.0	3%	610.0	11.0	0.0993	0.0018	0.789	0.043	0.0606	0.0033
D17b1-16	653.9	8.8	652.0	19.0	660.0	81.0	0%	653.9	8.8	0.1066	0.0015	0.902	0.036	0.0626	0.0024
D17b1-17	622.9	9.2	608.0	21.0	543.0	99.0	2%	622.9	9.2	0.1013	0.0016	0.814	0.038	0.0586	0.0027
D17b1-18	290.6	3.7	382.0	20.0	950.0	110.0	24%	290.6	3.7	0.04611	0.00061	0.465	0.029	0.0737	0.004
D17b1-19	378.9	4.9	382.0	11.0	380.0	72.0	1%	378.9	4.9	0.06056	0.0008	0.457	0.017	0.055	0.0018
D17b1-20	574.8	7.5	568.0	19.0	567.0	90.0	1%	574.8	7.5	0.0933	0.0013	0.756	0.032	0.0604	0.0025
D17b1-21	401.5	3.5	395.1	8.9	370.0	56.0	2%	401.5	3.5	0.06427	0.00059	0.476	0.013	0.0543	0.0013
D17b1-22	430.3	6.6	435.0	19.0	500.0	100.0	1%	430.3	6.6	0.0688	0.0011	0.539	0.029	0.0583	0.0029
D17b1-23	994.3	9.8	998.0	20.0	1006.0	59.0	0%	994.3	9.8	0.1666	0.0017	1.657	0.051	0.0733	0.0021
D17b1-24	333.1	9.2	334.0	41.0	250.0	270.0	0%	333.1	9.2	0.0529	0.0015	0.416	0.057	0.0582	0.0082
D17b1-25	366.7	6.3	420.0	13.0	790.0	79.0	13%	366.7	6.3	0.0586	0.001	0.512	0.019	0.0654	0.0026
D17b1-26	354.3	8.1	358.0	28.0	350.0	190.0	1%	354.3	8.1	0.0565	0.0013	0.415	0.04	0.0531	0.0051
D17b1-27	628.0	10.0	650.0	30.0	710.0	130.0	3%	628.0	10.0	0.1023	0.0018	0.886	0.057	0.0632	0.004
D17b1-28	580.6	5.8	586.0	13.0	665.0	43.0	1%	580.6	5.8	0.09426	0.00099	0.786	0.023	0.062	0.0013
D17b1-29	446.5	7.0	458.0	19.0	550.0	110.0	3%	446.5	7.0	0.0716	0.0012	0.574	0.031	0.0591	0.003

D17b1-30	885.6	7.7	879.0	13.0	886.0	37.0	1%	885.6	7.7	0.1473	0.0014	1.384	0.031	0.0684	0.0012
D17b1-31	370.4	5.8	359.0	18.0	360.0	110.0	3%	370.4	5.8	0.05904	0.00093	0.429	0.025	0.055	0.0031
D17b1-32	312.8	4.1	354.0	12.0	606.0	83.0	12%	312.8	4.1	0.04973	0.00066	0.421	0.017	0.0607	0.0023
D17b1-33	2575.0	22.0	2604.0	16.0	2644.0	18.0	1%	2604.0	16.0	0.4903	0.0049	12.09	0.2	0.179	0.0019
D17b1-34	2417.0	29.0	2448.0	25.0	2507.0	39.0	1%	2448.0	25.0	0.4548	0.0066	10.22	0.26	0.1649	0.0038
D17b1-35	441.1	4.6	446.0	12.0	480.0	66.0	1%	441.1	4.6	0.07083	0.00076	0.543	0.018	0.0576	0.0018
D17b1-36	366.8	4.5	410.0	12.0	704.0	70.0	11%	366.8	4.5	0.05856	0.00074	0.499	0.017	0.0637	0.0021
D17b1-37	818.5	9.9	819.0	22.0	828.0	85.0	0%	818.5	9.9	0.1354	0.0017	1.244	0.049	0.0679	0.0027
D17b1-38	1336.0	24.0	1602.0	32.0	2023.0	73.0	17%	1602.0	32.0	0.2306	0.0046	3.84	0.16	0.1259	0.0053
D17b1-39	427.2	7.9	428.0	20.0	410.0	120.0	0%	427.2	7.9	0.0685	0.0013	0.532	0.031	0.0553	0.0031
D17b1-40	379.6	3.5	389.0	7.6	459.0	40.0	2%	379.6	3.5	0.06066	0.00057	0.468	0.011	0.0563	0.001
D17b1-41	371.7	6.0	403.0	13.0	631.0	84.0	8%	371.7	6.0	0.05937	0.00099	0.488	0.019	0.0615	0.0024
D17b1-42	404.8	4.4	402.0	13.0	355.0	82.0	1%	404.8	4.4	0.06482	0.00072	0.485	0.019	0.0546	0.0021
D17b1-43	351.7	7.8	341.0	23.0	280.0	160.0	3%	351.7	7.8	0.0561	0.0013	0.405	0.031	0.0541	0.0043
D17b1-44	391.7	5.7	399.0	12.0	453.0	76.0	2%	391.7	5.7	0.06265	0.00093	0.483	0.017	0.0563	0.002
D17b1-45	478.3	6.0	564.0	23.0	970.0	100.0	15%	478.3	6.0	0.07692	0.00098	0.755	0.04	0.0716	0.0035
D17b1-46	421.3	5.7	424.0	15.0	416.0	94.0	1%	421.3	5.7	0.06755	0.00095	0.522	0.023	0.0562	0.0025
D17b1-47	403.6	5.3	403.0	13.0	412.0	83.0	0%	403.6	5.3	0.06461	0.00087	0.488	0.019	0.0557	0.0021
D17b1-48	659.4	7.6	885.0	27.0	1478.0	83.0	25%	659.4	7.6	0.1077	0.0013	1.394	0.063	0.0938	0.004
D17b1-49	377.0	4.7	450.0	17.0	897.0	98.0	16%	377.0	4.7	0.06024	0.00078	0.548	0.024	0.0691	0.0032
D17b1-50	1666.0	20.0	1737.0	21.0	1838.0	30.0	4%	1737.0	21.0	0.2951	0.004	4.54	0.11	0.1124	0.0018
D17b1-51	342.6	8.6	329.0	39.0	130.0	250.0	4%	342.6	8.6	0.0545	0.0014	0.399	0.052	0.0565	0.0078
D17b1-52	981.0	12.0	966.0	22.0	1008.0	66.0	2%	981.0	12.0	0.1645	0.0021	1.593	0.055	0.0729	0.0025
D17b1-53	403.3	4.6	400.0	12.0	362.0	73.0	1%	403.3	4.6	0.06458	0.00077	0.482	0.017	0.0545	0.0019
D17b1-55	409.6	5.8	422.0	18.0	470.0	110.0	3%	409.6	5.8	0.06562	0.00096	0.518	0.026	0.0567	0.0029
D17b1-56	562.4	9.3	557.0	14.0	490.0	62.0	1%	562.4	9.3	0.0912	0.0016	0.723	0.024	0.0574	0.0016
D17b1-57	319.3	3.1	366.1	8.1	711.0	43.0	13%	319.3	3.1	0.05078	0.00051	0.434	0.011	0.0629	0.0013
D17b1-58	576.9	7.6	595.0	21.0	678.0	95.0	3%	576.9	7.6	0.0937	0.0013	0.789	0.037	0.0626	0.0029
D17b1-59	1941.0	27.0	1891.0	27.0	1862.0	49.0	3%	1891.0	27.0	0.3517	0.0056	5.48	0.16	0.1141	0.0032
D17b1-60	668.9	6.1	683.0	11.0	759.0	40.0	2%	668.9	6.1	0.1094	0.001	0.962	0.021	0.0644	0.0012
D17b1-61	428.5	4.0	424.0	11.0	402.0	65.0	1%	428.5	4.0	0.06873	0.00067	0.519	0.016	0.0552	0.0016
D17b1-62	410.1	4.4	417.0	11.0	458.0	67.0	2%	410.1	4.4	0.06569	0.00072	0.512	0.017	0.0563	0.0017

D17b1-63	345.4	8.5	308.0	31.0	200.0	220.0	12%	345.4	8.5	0.0549	0.0014	0.372	0.042	0.052	0.0059
D17b1-64	444.8	4.2	456.0	10.0	525.0	53.0	2%	444.8	4.2	0.07144	0.0007	0.568	0.015	0.0581	0.0013
D17b1-65	387.4	4.2	398.0	13.0	466.0	80.0	3%	387.4	4.2	0.06194	0.0007	0.481	0.019	0.0572	0.002
D17b1-67	447.4	5.8	455.0	14.0	459.0	82.0	2%	447.4	5.8	0.07189	0.00096	0.568	0.022	0.057	0.0021
D17b1-69	448.4	4.9	453.0	13.0	492.0	71.0	1%	448.4	4.9	0.07205	0.00082	0.566	0.019	0.0577	0.0019
D17b1-70	420.5	5.0	409.0	14.0	382.0	81.0	3%	420.5	5.0	0.06742	0.00083	0.498	0.02	0.0548	0.002
D17b1-71	377.0	12.0	331.0	40.0	60.0	250.0	14%	377.0	12.0	0.0603	0.002	0.413	0.054	0.0502	0.0069
D17b1-72	457.9	5.4	457.0	15.0	446.0	82.0	0%	457.9	5.4	0.07362	0.0009	0.567	0.024	0.0568	0.0022
D17b1-73	629.1	9.7	654.0	27.0	760.0	120.0	4%	629.1	9.7	0.1028	0.0017	0.919	0.053	0.0663	0.0037
D17b1-74	547.4	8.6	762.0	35.0	1400.0	120.0	28%	547.4	8.6	0.0885	0.0014	1.143	0.076	0.0934	0.0057
D17b1-75	501.0	17.0	489.0	26.0	463.0	89.0	2%	501.0	17.0	0.0809	0.0028	0.632	0.041	0.0568	0.0024
D17b1-76	298.1	4.2	290.0	11.0	211.0	90.0	3%	298.1	4.2	0.04733	0.00068	0.329	0.014	0.051	0.0022
D17b1-77	2043.0	18.0	2050.0	21.0	2073.0	34.0	0%	2050.0	21.0	0.373	0.0037	6.55	0.15	0.1292	0.0024
D17b1-78	439.8	6.6	413.0	20.0	270.0	120.0	6%	439.8	6.6	0.0706	0.0011	0.493	0.031	0.0519	0.0032
D17b1-79	758.6	8.4	798.0	16.0	934.0	65.0	5%	758.6	8.4	0.1249	0.0015	1.198	0.036	0.071	0.0022
D17b1-81	344.0	11.0	332.0	44.0	160.0	280.0	4%	344.0	11.0	0.0547	0.0018	0.419	0.06	0.0541	0.0082
D17b1-82	1231.0	53.0	1415.0	53.0	1697.0	40.0	13%	1231.0	53.0	0.2119	0.0098	3.14	0.2	0.1048	0.0022
D17b1-83	747.0	7.9	754.0	14.0	792.0	43.0	1%	747.0	7.9	0.1229	0.0014	1.105	0.029	0.0655	0.0014
D17b1-84	882.9	9.9	881.0	24.0	900.0	82.0	0%	882.9	9.9	0.1465	0.0018	1.383	0.058	0.0691	0.0027
D17b1-85	335.1	7.4	315.0	30.0	220.0	200.0	6%	335.1	7.4	0.0534	0.0012	0.374	0.038	0.054	0.0057
D17b1-86	411.5	5.7	420.0	12.0	449.0	71.0	2%	411.5	5.7	0.06593	0.00094	0.516	0.017	0.0563	0.0018
D17b1-87	346.3	4.1	378.0	18.0	560.0	100.0	8%	346.3	4.1	0.05519	0.00067	0.46	0.028	0.0614	0.0034
D17b1-88	353.4	5.0	386.0	17.0	520.0	110.0	8%	353.4	5.0	0.05636	0.00082	0.467	0.024	0.0598	0.0029
D17b1-89	392.0	10.0	347.0	37.0	90.0	230.0	13%	392.0	10.0	0.0628	0.0016	0.42	0.05	0.0502	0.006
D17b1-90	367.4	7.2	350.0	28.0	260.0	180.0	5%	367.4	7.2	0.0587	0.0012	0.421	0.041	0.0509	0.0051
D17b1-93	1457.0	20.0	1610.0	43.0	1833.0	76.0	10%	1610.0	43.0	0.2537	0.0039	3.89	0.2	0.1121	0.0049
D17b1-94	624.4	7.6	609.0	19.0	552.0	87.0	3%	624.4	7.6	0.1017	0.0013	0.83	0.034	0.0595	0.0024
D17b1-95	661.6	8.6	648.0	17.0	639.0	75.0	2%	661.6	8.6	0.1081	0.0015	0.902	0.031	0.0618	0.0022
D17b1-96	629.9	8.5	668.0	23.0	792.0	93.0	6%	629.9	8.5	0.1025	0.0015	0.923	0.044	0.0644	0.0029
D17b1-97	822.0	33.0	887.0	59.0	1090.0	130.0	7%	822.0	33.0	0.1365	0.0058	1.53	0.15	0.0773	0.0047
D17b1-98	974.6	9.1	975.0	14.0	997.0	43.0	0%	974.6	9.1	0.1633	0.0017	1.618	0.036	0.0725	0.0015
D17b1-99	382.8	4.7	406.0	11.0	492.0	70.0	6%	382.8	4.7	0.06118	0.00077	0.495	0.016	0.0577	0.0018

D17b1-101	330.9	4.1	334.0	10.0	356.0	68.0	1%	330.9	4.1	0.05267	0.00067	0.389	0.014	0.0541	0.0017
D17b1-104	337.5	8.2	339.0	25.0	320.0	170.0	0%	337.5	8.2	0.0538	0.0013	0.384	0.037	0.0531	0.0051
D17b1-105	477.9	9.5	449.0	27.0	360.0	140.0	6%	477.9	9.5	0.077	0.0016	0.567	0.041	0.0544	0.0039
D17b1-106	631.7	6.7	632.0	17.0	639.0	75.0	0%	631.7	6.7	0.103	0.0012	0.86	0.03	0.0615	0.0021
D17b1-107	393.6	5.4	406.0	17.0	468.0	88.0	3%	393.6	5.4	0.06297	0.0009	0.491	0.024	0.057	0.0024
D17b1-108	437.2	5.4	450.0	11.0	539.0	50.0	3%	437.2	5.4	0.07019	0.0009	0.559	0.016	0.0584	0.0014
D17b1-109	400.4	4.6	423.0	13.0	550.0	83.0	5%	400.4	4.6	0.06409	0.00077	0.514	0.02	0.0594	0.0022
D17b1-110	432.4	3.3	457.0	10.0	567.0	54.0	5%	432.4	3.3	0.06937	0.00055	0.566	0.015	0.0593	0.0015
D17b1-111	395.5	8.9	373.0	26.0	240.0	170.0	6%	395.5	8.9	0.0633	0.0015	0.45	0.039	0.0526	0.0046
D17b1-112	612.8	8.3	581.0	24.0	520.0	100.0	5%	612.8	8.3	0.0998	0.0014	0.778	0.041	0.0587	0.0028
D17b1-113	580.5	4.6	584.0	15.0	599.0	65.0	1%	580.5	4.6	0.09423	0.00079	0.784	0.026	0.0603	0.0018
D17b1-114	301.3	3.0	291.7	8.3	242.0	62.0	3%	301.3	3.0	0.04781	0.00048	0.333	0.011	0.0517	0.0015

Appendix 39: Detrital zircon (U-Th)/He data for sample D22.

Grain #	V (µm3)	+/- 2σ	4He (mol)	Corrected 4He (mol)	+/- 2σ	4He (mol/g)	Corrected 4He (mol/g)	+/- 2σ	232Th (ppm)	+/- 2σ	238U (ppm)	+/- 2σ	147Sm (ppm)	+/- 2σ	eU	Th/U	ZHe age (Ma)	+/- 2σ
D22b1_1	9578	479	4.27E-15	2.85E-15	1.64E-16	9.58E-08	6.39E-08	6.05E-09	64	2	219	5	3	0	234	0.29	76.0	5.0
D22b1_2	9571	479	6.92E-15	4.61E-15	1.13E-16	1.55E-07	1.04E-07	8.17E-09	85	1	213	2	2	0	233	0.40	123.9	6.6
D22b1_3	9565	478	1.33E-15	8.84E-16	1.51E-16	2.98E-08	1.99E-08	3.71E-09	56	1	75	1	2	0	88	0.75	63.0	7.9
D22b1_4	9558	478	7.88E-15	5.25E-15	1.41E-16	1.77E-07	1.18E-07	9.42E-09	253	9	356	9	8	0	416	0.71	79.1	4.5
D22b1_5	9552	478	2.51E-14	1.67E-14	3.70E-16	5.65E-07	3.77E-07	2.95E-08	232	10	862	41	1	0	917	0.27	114.5	7.9
D22b1_6	9546	477	7.00E-15	4.67E-15	2.01E-16	1.58E-07	1.05E-07	9.09E-09	96	2	322	4	4	0	345	0.30	84.8	5.0
D22b1_7	9539	477	1.78E-14	1.19E-14	3.69E-16	4.02E-07	2.68E-07	2.17E-08	118	8	345	23	4	0	373	0.34	199.9	16.4
D22b1_8	9533	477	3.70E-14	2.47E-14	4.79E-16	8.34E-07	5.56E-07	4.31E-08	179	3	426	12	8	0	468	0.42	330.6	19.1
D22b1_9	9526	476	2.37E-14	1.58E-14	4.53E-16	5.36E-07	3.57E-07	2.87E-08	72	1	803	34	0	0	820	0.09	121.3	8.2
D22b1_10	9520	476	1.89E-14	1.26E-14	3.73E-16	4.26E-07	2.84E-07	2.29E-08	256	18	763	51	1	0	823	0.34	96.1	7.9
D22b1_11	9513	476	1.81E-14	1.21E-14	3.03E-16	4.09E-07	2.73E-07	2.16E-08	309	11	750	25	4	0	823	0.41	92.2	5.6
D22b1_12	9507	475	1.11E-14	7.39E-15	2.88E-16	2.51E-07	1.67E-07	1.41E-08	80	3	109	3	7	0	127	0.73	364.6	22.2
D22b1_13	9500	475	8.94E-15	5.96E-15	2.79E-16	2.02E-07	1.35E-07	1.19E-08	314	10	463	7	7	0	536	0.68	70.0	4.2
D22b1_14	9494	475	1.68E-14	1.12E-14	3.71E-16	3.80E-07	2.54E-07	2.08E-08	80	1	797	10	9	0	815	0.10	86.6	4.8
D22b1_15	9487	474	4.12E-14	2.75E-14	6.49E-16	9.34E-07	6.23E-07	4.90E-08	225	1	699	4	6	0	752	0.32	230.5	12.1
D22b1_16	9481	474	9.28E-15	6.19E-15	2.03E-16	2.11E-07	1.40E-07	1.15E-08	62	3	184	8	15	2	198	0.34	196.8	13.3
D22b1_17	9475	474	1.02E-14	6.81E-15	2.25E-16	2.32E-07	1.55E-07	1.27E-08	213	3	235	4	4	0	285	0.91	150.7	8.5
D22b1_18	9468	473	3.91E-15	2.61E-15	9.44E-17	8.89E-08	5.92E-08	4.93E-09	367	8	168	3	44	1	254	2.18	64.6	3.7
D22b1_19	9462	473	1.01E-15	6.76E-16	1.09E-16	2.30E-08	1.54E-08	2.74E-09	70	1	22	0	6	0	39	3.14	-	
D22b1_20	9455	473	1.19E-14	7.91E-15	2.01E-16	2.70E-07	1.80E-07	1.42E-08	205	4	556	8	8	0	604	0.37	82.9	4.5
D22b1_21	9449	472	4.09E-15	2.72E-15	1.32E-16	9.30E-08	6.20E-08	5.54E-09	68	2	165	3	5	0	181	0.42	95.5	5.9
D22b1_22	9442	472	9.43E-15	6.28E-15	2.14E-16	2.15E-07	1.43E-07	1.18E-08	113	3	413	5	1	0	439	0.27	90.6	5.1
D22b1_23	9436	472	6.56E-15	4.37E-15	1.44E-16	1.49E-07	9.96E-08	8.16E-09	90	3	385	11	5	0	406	0.23	68.3	4.2
D22b1_24	9429	471	3.42E-14	2.28E-14	6.28E-16	7.79E-07	5.19E-07	4.15E-08	101	2	501	5	7	0	525	0.20	275.4	14.9
D22b1_25	9423	471	8.73E-15	5.82E-15	3.27E-16	1.99E-07	1.33E-07	1.24E-08	199	13	433	16	8	1	480	0.46	77.0	5.5
D22b1_26	9417	471	3.69E-15	2.46E-15	1.29E-16	8.42E-08	5.61E-08	5.14E-09	167	5	145	2	9	0	184	1.15	84.6	5.3
D22b1_27	9410	471	4.75E-15	3.17E-15	2.61E-16	1.09E-07	7.24E-08	8.07E-09	66	0	338	4	5	0	354	0.20	57.0	4.3
D22b1_28	9404	470	8.32E-15	5.55E-15	3.24E-16	1.90E-07	1.27E-07	1.21E-08	136	2	213	3	3	0	245	0.64	143.7	9.3
D22b1_29	9397	470	1.36E-14	9.10E-15	2.73E-16	3.12E-07	2.08E-07	1.68E-08	55	1	161	1	2	0	174	0.34	333.4	18.1

D22b1_30	9391	470	1.58E-15	1.05E-15	1.20E-16	3.61E-08	2.41E-08	3.28E-09	13	0	40	1	0	/	43	0.33	-	
D22b1_31	9384	469	5.29E-15	3.53E-15	1.97E-16	1.21E-07	8.08E-08	7.56E-09	69	1	241	3	2	0	257	0.29	87.5	5.6
D22b1_32	9378	469	4.29E-14	2.86E-14	4.13E-16	9.83E-07	6.55E-07	5.00E-08	281	4	683	5	4	0	749	0.41	243.5	12.5
D22b1_33	9371	469	2.50E-14	1.67E-14	5.25E-16	5.74E-07	3.83E-07	3.11E-08	266	18	1303	12	23	4	1366	0.20	78.0	4.3
D22b1_34	9365	468	2.08E-14	1.39E-14	4.49E-16	4.77E-07	3.18E-07	2.60E-08	241	3	969	9	4	0	1026	0.25	86.3	4.8
D22b1_35	9358	468	2.33E-14	1.56E-14	4.85E-16	5.36E-07	3.58E-07	2.90E-08	239	2	1242	32	5	0	1298	0.19	76.7	4.6
D22b1_36	9352	468	2.00E-14	1.33E-14	2.73E-16	4.59E-07	3.06E-07	2.38E-08	140	6	738	43	3	0	771	0.19	110.5	8.4
D22b1_37	9346	467	3.45E-15	2.30E-15	1.43E-16	7.95E-08	5.30E-08	5.16E-09	55	1	142	10	3	0	155	0.38	95.0	8.5
D22b1_38	9339	467	1.15E-14	7.68E-15	2.54E-16	2.65E-07	1.77E-07	1.45E-08	350	17	429	14	9	0	511	0.82	96.1	5.9
D22b1_39	9333	467	1.13E-14	7.51E-15	2.16E-16	2.59E-07	1.73E-07	1.39E-08	21	0	74	1	4	0	79	0.29	610.8	33.5
D22b1_40	9326	466	5.92E-15	3.95E-15	1.57E-16	1.36E-07	9.10E-08	7.72E-09	134	2	246	8	9	0	277	0.54	91.3	5.8
D22b1_41	9320	466	2.77E-14	1.84E-14	5.56E-16	6.38E-07	4.25E-07	3.44E-08	569	12	1170	21	4	0	1304	0.49	90.8	5.1
D22b1_42	9313	466	5.78E-15	3.85E-15	2.42E-16	1.33E-07	8.89E-08	8.71E-09	70	1	111	7	3	0	128	0.63	193.7	16.9
D22b1_43	9307	465	4.52E-15	3.01E-15	1.36E-16	1.04E-07	6.96E-08	6.09E-09	107	1	296	4	3	0	321	0.36	60.3	3.6
D22b1_44	9300	465	1.09E-14	7.24E-15	3.03E-16	2.51E-07	1.67E-07	1.44E-08	91	3	400	20	3	0	421	0.23	110.6	8.2
D22b1_45	9294	465	3.03E-14	2.02E-14	3.86E-16	7.02E-07	4.68E-07	3.62E-08	263	13	1780	35	6	0	1842	0.15	70.7	3.9
D22b1_46	9288	464	3.60E-14	2.40E-14	4.37E-16	8.34E-07	5.56E-07	4.29E-08	392	17	1898	14	59	8	1990	0.21	77.8	4.0
D22b1_47	9281	464	3.04E-15	2.03E-15	1.25E-16	7.06E-08	4.70E-08	4.57E-09	55	1	160	4	4	0	173	0.35	75.8	5.2
D22b1_48	9275	464	6.17E-15	4.11E-15	1.74E-16	1.43E-07	9.54E-08	8.21E-09	133	3	520	31	24	2	551	0.26	48.2	3.9
D22b1_49	9268	463	2.29E-14	1.52E-14	3.05E-16	5.31E-07	3.54E-07	2.75E-08	47	0	1167	8	2	0	1177	0.04	83.7	4.4
D22b1_50	9262	463	8.12E-15	5.41E-15	2.73E-16	1.88E-07	1.26E-07	1.14E-08	132	7	306	7	6	0	337	0.43	103.7	6.6
D22b1_51	9255	463	1.12E-14	7.47E-15	2.02E-16	2.60E-07	1.74E-07	1.38E-08	319	14	630	16	5	0	705	0.51	68.5	4.0
D22b1_52	9249	462	4.81E-15	3.20E-15	1.45E-16	1.12E-07	7.45E-08	6.52E-09	257	2	226	3	16	1	286	1.14	72.3	4.3
D22b1_53	9242	462	2.20E-14	1.47E-14	3.42E-16	5.13E-07	3.42E-07	2.69E-08	76	1	184	3	5	0	202	0.41	471.7	25.6
D22b1_54	9236	462	2.04E-14	1.36E-14	3.30E-16	4.75E-07	3.17E-07	2.50E-08	175	6	819	28	5	0	860	0.21	102.5	6.3
D22b1_55	9230	461	1.33E-14	8.88E-15	2.42E-16	3.10E-07	2.07E-07	1.65E-08	176	6	555	21	9	1	596	0.32	96.6	6.2
D22b1_56	9223	461	1.50E-14	1.00E-14	3.28E-16	3.50E-07	2.34E-07	1.91E-08	24	1	847	10	2	0	852	0.03	76.4	4.3
D22b1_57	9217	461	9.21E-15	6.14E-15	2.41E-16	2.15E-07	1.43E-07	1.21E-08	40	1	159	1	1	0	168	0.25	237.2	13.5
D22b1_58	9210	461	7.48E-15	4.99E-15	1.64E-16	1.75E-07	1.16E-07	9.54E-09	118	1	133	2	17	1	160	0.89	201.9	11.2
D22b1_59	9204	460	3.79E-15	2.53E-15	1.53E-16	8.86E-08	5.91E-08	5.69E-09	107	1	172	1	3	0	197	0.62	83.4	5.4
D22b1_60	9197	460	1.92E-14	1.28E-14	2.41E-16	4.49E-07	2.99E-07	2.32E-08	820	55	697	22	20	1	890	1.18	93.5	5.5
D22b1_61	9191	460	5.17E-15	3.44E-15	1.79E-16	1.21E-07	8.06E-08	7.35E-09	83	1	230	2	2	0	249	0.36	90.1	5.5

D22b1_62	9184	459	1.96E-14	1.31E-14	3.39E-16	4.59E-07	3.06E-07	2.43E-08	135	2	264	3	2	0	296	0.51	287.4	15.5
D22b1_63	9178	459	5.15E-15	3.43E-15	2.37E-16	1.21E-07	8.04E-08	8.20E-09	83	2	159	6	6	0	178	0.52	125.4	9.6
D22b1_64	9171	459	6.52E-15	4.35E-15	1.77E-16	1.53E-07	1.02E-07	8.70E-09	159	2	263	3	3	0	300	0.60	94.5	5.5
D22b1_65	9165	458	3.52E-15	2.34E-15	1.45E-16	8.25E-08	5.50E-08	5.35E-09	199	2	136	2	18	0	183	1.47	83.5	5.5
D22b1_66	9159	458	1.52E-14	1.01E-14	3.51E-16	3.57E-07	2.38E-07	1.97E-08	301	21	606	24	2	0	677	0.50	97.9	6.5
D22b1_67	9152	458	1.74E-15	1.16E-15	1.13E-16	4.10E-08	2.73E-08	3.35E-09	29	1	58	1	3	0	65	0.51	-	
D22b1_68	9146	457	1.03E-14	6.86E-15	2.18E-16	2.42E-07	1.61E-07	1.31E-08	28	1	483	4	2	0	490	0.06	91.6	5.0
D22b1_69	9139	457	2.55E-15	1.70E-15	1.24E-16	5.99E-08	3.99E-08	4.19E-09	71	2	106	2	26	2	123	0.67	90.5	6.5
D22b1_70	9133	457	5.74E-15	3.83E-15	1.52E-16	1.35E-07	9.01E-08	7.65E-09	80	2	252	7	8	0	271	0.32	92.7	5.7
D22b1_71	9126	456	1.28E-14	8.52E-15	2.83E-16	3.01E-07	2.01E-07	1.65E-08	109	1	188	1	3	0	213	0.58	262.1	14.4
D22b1_72	9120	456	5.35E-15	3.57E-15	2.51E-16	1.26E-07	8.41E-08	8.64E-09	101	3	333	5	2	0	357	0.30	65.5	4.6
D22b1_73	9113	456	5.88E-15	3.92E-15	2.89E-16	1.39E-07	9.25E-08	9.73E-09	101	4	256	9	6	0	279	0.39	92.1	7.0
D22b1_74	9107	455	2.08E-14	1.39E-14	4.10E-16	4.91E-07	3.27E-07	2.64E-08	128	7	717	50	4	0	747	0.18	121.9	10.5
D22b1_75	9101	455	5.81E-15	3.87E-15	1.60E-16	1.37E-07	9.16E-08	7.84E-09	37	0	43	1	4	0	52	0.86	-	
D22b1_76	9094	455	7.41E-15	4.94E-15	1.70E-16	1.75E-07	1.17E-07	9.64E-09	172	9	381	6	2	0	421	0.45	77.1	4.4
D22b1_77	9088	454	8.26E-17	5.51E-17	1.52E-16	1.96E-09	1.30E-09	3.60E-09	63	2	66	1	3	0	80	0.96	-	
D22b1_78	9081	454	4.86E-15	3.24E-15	2.35E-16	1.15E-07	7.67E-08	8.00E-09	38	2	127	8	2	0	136	0.30	157.3	14.1
D22b1_79	9075	454	1.62E-14	1.08E-14	3.80E-16	3.84E-07	2.56E-07	2.12E-08	91	1	339	4	11	1	361	0.27	197.8	11.2
D22b1_80	9068	453	1.66E-14	1.11E-14	3.61E-16	3.94E-07	2.63E-07	2.15E-08	41	2	174	2	4	0	184	0.23	398.0	22.2
D22b1_81	9062	453	5.12E-15	3.41E-15	1.71E-16	1.21E-07	8.10E-08	7.30E-09	98	4	202	12	6	0	225	0.48	100.1	8.1
D22b1_82	9055	453	1.09E-14	7.25E-15	3.04E-16	2.58E-07	1.72E-07	1.48E-08	75	2	606	4	5	0	624	0.12	76.8	4.4
D22b1_83	9049	452	2.42E-14	1.62E-14	4.72E-16	5.76E-07	3.84E-07	3.09E-08	207	3	378	7	4	0	427	0.55	250.3	14.1
D22b1_84	9042	452	3.64E-15	2.43E-15	1.46E-16	8.65E-08	5.77E-08	5.55E-09	158	3	42	2	6	0	79	3.79	-	
D22b1_85	9036	452	5.49E-14	3.66E-14	6.43E-16	1.31E-06	8.70E-07	6.70E-08	24	0	26	0	10	2	32	0.93	-	
D22b1_86	9030	451	1.81E-14	1.21E-14	2.54E-16	4.31E-07	2.88E-07	2.24E-08	190	2	984	8	4	0	1029	0.19	77.8	4.1
D22b1_87	9023	451	1.91E-14	1.27E-14	2.88E-16	4.56E-07	3.04E-07	2.38E-08	349	11	1111	19	5	0	1193	0.31	70.9	3.9
D22b1_88	9017	451	1.41E-15	9.41E-16	1.27E-16	3.37E-08	2.24E-08	3.46E-09	23	1	39	1	3	0	45	0.59	-	
D22b1_89	9010	451	3.76E-15	2.50E-15	1.50E-16	8.97E-08	5.98E-08	5.74E-09	58	3	227	2	3	0	241	0.25	69.1	4.5
D22b1_90	9004	450	1.94E-14	1.29E-14	2.47E-16	4.63E-07	3.09E-07	2.39E-08	194	2	305	3	2	0	351	0.64	245.0	12.8
D22b1_91	8997	450	2.60E-15	1.74E-15	1.37E-16	6.22E-08	4.15E-08	4.52E-09	124	2	134	1	5	0	164	0.92	70.5	5.2
D22b1_92	8991	450	1.17E-14	7.82E-15	2.92E-16	2.81E-07	1.87E-07	1.57E-08	200	7	285	10	11	1	332	0.70	156.7	10.0
D22b1_93	8984	449	3.40E-15	2.26E-15	1.64E-16	8.13E-08	5.42E-08	5.65E-09	78	1	143	1	3	0	161	0.55	93.6	6.6

D22b1_94	8978	449	2.26E-15	1.51E-15	1.42E-16	5.41E-08	3.61E-08	4.35E-09	81	5	79	3	11	1	97	1.03	102.8	8.8
D22b1_95	8972	449	1.35E-14	9.03E-15	3.55E-16	3.25E-07	2.16E-07	1.83E-08	70	1	179	2	2	0	195	0.39	308.1	17.8
D22b1_96	8965	448	9.63E-15	6.42E-15	2.87E-16	2.31E-07	1.54E-07	1.35E-08	28	0	88	1	1	0	94	0.32	454.0	27.0
D22b1_97	8959	448	1.41E-14	9.40E-15	3.59E-16	3.38E-07	2.26E-07	1.90E-08	326	14	542	12	11	0	619	0.60	101.4	6.0
D22b1_98	8952	448	2.80E-14	1.86E-14	4.55E-16	6.72E-07	4.48E-07	3.53E-08	158	2	512	4	3	0	550	0.31	226.8	12.0
D22b1_99	8946	447	1.52E-14	1.02E-14	2.84E-16	3.67E-07	2.44E-07	1.96E-08	40	0	54	0	2	0	63	0.74	-	
D22b1_100	8939	447	2.99E-14	2.00E-14	3.16E-16	7.20E-07	4.80E-07	3.68E-08	502	14	1499	45	15	0	1617	0.33	82.7	4.8
D22b1_101	8933	447	3.52E-15	2.35E-15	1.43E-16	8.48E-08	5.66E-08	5.46E-09	87	1	189	2	3	0	210	0.46	75.0	4.9
D22b1_102	8926	446	8.57E-15	5.71E-15	1.96E-16	2.06E-07	1.38E-07	1.13E-08	135	5	277	5	5	0	308	0.49	124.2	7.1
D22b1_103	8920	446	4.82E-15	3.22E-15	2.07E-16	1.16E-07	7.75E-08	7.67E-09	46	2	258	3	29	5	269	0.18	80.2	5.4
D22b1_104	8913	446	4.09E-15	2.73E-15	2.01E-16	9.87E-08	6.58E-08	6.91E-09	102	2	185	4	12	1	209	0.55	87.4	6.4
D22b1_105	8907	445	6.90E-15	4.60E-15	2.48E-16	1.67E-07	1.11E-07	1.03E-08	225	3	306	3	8	0	359	0.73	86.0	5.3
D22b1_106	8901	445	1.66E-14	1.11E-14	3.52E-16	4.02E-07	2.68E-07	2.18E-08	50	1	688	34	9	1	700	0.07	106.7	7.8
D22b1_107	8894	445	1.17E-14	7.81E-15	2.61E-16	2.83E-07	1.89E-07	1.55E-08	211	6	375	8	8	0	425	0.56	123.6	7.2
D22b1_108	8888	444	2.54E-14	1.69E-14	3.05E-16	6.14E-07	4.09E-07	3.16E-08	150	4	1286	23	3	0	1321	0.12	86.2	4.7
D22b1_109	8881	444	2.15E-15	1.44E-15	1.09E-16	5.22E-08	3.48E-08	3.72E-09	80	1	98	1	3	0	117	0.81	82.6	6.0
D22b1_110	8875	444	1.12E-14	7.43E-15	1.93E-16	2.70E-07	1.80E-07	1.43E-08	36	0	568	7	3	0	576	0.06	87.1	4.7
D22b1_111	8868	443	1.61E-14	1.07E-14	3.31E-16	3.91E-07	2.61E-07	2.11E-08	60	2	57	1	6	0	71	1.05	-	
D22b1_112	8862	443	1.75E-14	1.17E-14	3.05E-16	4.25E-07	2.83E-07	2.25E-08	59	0	122	1	3	0	136	0.48	578.5	30.8
D22b1_113	8855	443	4.63E-15	3.09E-15	2.11E-16	1.12E-07	7.50E-08	7.60E-09	156	2	291	5	3	0	327	0.54	63.7	4.4
D22b1_114	8849	442	9.62E-15	6.42E-15	2.20E-16	2.34E-07	1.56E-07	1.29E-08	58	1	138	1	3	0	152	0.42	285.9	15.9
D22b1_115	8843	442	9.62E-15	6.41E-15	2.11E-16	2.34E-07	1.56E-07	1.28E-08	46	1	26	0	3	0	36	1.80	-	
D22b1_116	8836	442	5.41E-15	3.61E-15	2.27E-16	1.32E-07	8.78E-08	8.59E-09	168	3	400	4	4	0	439	0.42	55.6	3.7
D22b1_117	8830	441	6.77E-15	4.51E-15	2.24E-16	1.65E-07	1.10E-07	9.88E-09	96	1	324	6	10	0	347	0.29	88.2	5.5
D22b1_118	8823	441	2.75E-14	1.84E-14	3.35E-16	6.71E-07	4.47E-07	3.45E-08	228	3	485	4	6	0	539	0.47	230.9	12.0
D22b1_119	8817	441	4.29E-15	2.86E-15	1.03E-16	1.05E-07	6.97E-08	5.81E-09	157	2	183	1	9	0	220	0.85	88.1	4.9
D22b1_120	8810	441	4.54E-15	3.03E-15	2.16E-16	1.11E-07	7.39E-08	7.65E-09	58	3	127	11	5	1	141	0.46	146.3	15.3
D22b1_121	8804	440	8.82E-15	5.88E-15	3.24E-16	2.15E-07	1.44E-07	1.34E-08	129	3	595	25	1	0	625	0.22	63.9	4.7
D22b1_122	8797	440	1.48E-14	9.85E-15	2.75E-16	3.61E-07	2.41E-07	1.93E-08	222	5	619	8	14	1	671	0.36	99.9	5.5
D22b1_123	8791	440	5.33E-15	3.55E-15	2.27E-16	1.30E-07	8.69E-08	8.55E-09	121	5	224	8	9	0	252	0.54	95.7	6.9
D22b1_124	8784	439	1.05E-14	7.02E-15	2.29E-16	2.58E-07	1.72E-07	1.40E-08	74	1	137	1	4	0	154	0.54	309.8	17.1
D22b1_125	8778	439	9.07E-15	6.05E-15	2.76E-16	2.22E-07	1.48E-07	1.30E-08	125	5	613	10	3	0	642	0.20	64.2	3.9

D22b1_126	8772	439	2.68E-15	1.79E-15	2.09E-16	6.58E-08	4.39E-08	6.08E-09	23	0	101	1	1	0	106	0.23	115.0	10.7
D22b1_127	8765	438	4.22E-15	2.81E-15	2.13E-16	1.03E-07	6.90E-08	7.35E-09	46	1	207	4	4	0	217	0.22	88.3	6.5
D22b1_128	8759	438	6.88E-15	4.59E-15	2.18E-16	1.69E-07	1.13E-07	1.00E-08	198	1	272	2	4	0	319	0.73	98.3	5.8
D22b1_129	8752	438	1.45E-14	9.68E-15	3.47E-16	3.57E-07	2.38E-07	1.98E-08	347	10	882	17	12	1	964	0.39	68.7	4.0
D22b1_130	8746	437	1.47E-14	9.79E-15	2.68E-16	3.61E-07	2.41E-07	1.92E-08	183	3	745	14	4	0	788	0.25	85.0	4.8
D22b1_131	8739	437	1.64E-14	1.09E-14	3.70E-16	4.03E-07	2.69E-07	2.21E-08	107	2	572	38	1	0	597	0.19	125.3	10.5
D22b1_132	8733	437	8.56E-15	5.70E-15	2.77E-16	2.11E-07	1.40E-07	1.25E-08	112	9	515	12	4	0	541	0.22	72.2	4.6
D22b1_133	8726	436	3.85E-15	2.56E-15	1.63E-16	9.48E-08	6.32E-08	6.22E-09	50	1	76	1	2	0	87	0.66	201.1	13.3
D22b1_134	8720	436	2.37E-14	1.58E-14	4.25E-16	5.85E-07	3.90E-07	3.11E-08	158	8	1124	15	2	0	1161	0.14	93.6	5.1
D22b1_135	8714	436	2.02E-14	1.35E-14	3.56E-16	4.98E-07	3.32E-07	2.64E-08	603	8	1028	29	9	0	1170	0.59	79.0	4.6
D22b1_136	8707	435	1.06E-14	7.04E-15	2.22E-16	2.61E-07	1.74E-07	1.41E-08	239	6	422	14	10	0	478	0.57	101.1	6.2
D22b1_137	8701	435	7.55E-15	5.04E-15	2.24E-16	1.87E-07	1.24E-07	1.09E-08	130	6	490	3	5	0	521	0.26	66.5	3.9
D22b1_138	8694	435	3.25E-15	2.16E-15	1.77E-16	8.03E-08	5.36E-08	5.94E-09	86	2	181	11	3	0	201	0.47	74.0	6.8
D22b1_139	8688	434	8.44E-15	5.63E-15	2.38E-16	2.09E-07	1.39E-07	1.20E-08	342	9	333	4	10	0	413	1.03	93.7	5.5
D22b1_140	8681	434	1.02E-14	6.81E-15	3.08E-16	2.53E-07	1.69E-07	1.48E-08	29	0	582	6	7	0	589	0.05	79.8	4.7
D22b1_141	8688	434	3.58E-15	2.39E-15	1.51E-16	8.86E-08	5.90E-08	5.79E-09	79	4	206	6	48	7	225	0.39	73.1	5.1
D22b1_142	8681	434	5.87E-15	3.92E-15	1.95E-16	1.46E-07	9.70E-08	8.73E-09	178	2	366	7	13	1	408	0.49	66.2	4.1
D22b1_143	8675	434	5.57E-15	3.71E-15	2.33E-16	1.38E-07	9.20E-08	9.01E-09	142	4	262	11	18	1	295	0.54	86.7	6.5
D22b1_144	8668	433	9.38E-15	6.25E-15	2.22E-16	2.33E-07	1.55E-07	1.29E-08	163	2	438	6	8	0	476	0.37	90.6	5.1
D22b1_145	8662	433	4.66E-14	3.11E-14	6.86E-16	1.16E-06	7.71E-07	6.03E-08	217	1	2360	26	4	0	2411	0.09	89.1	4.7
D22b1_146	8655	433	6.95E-15	4.63E-15	2.15E-16	1.73E-07	1.15E-07	1.01E-08	107	2	322	4	10	1	347	0.33	92.2	5.5
D22b1_147	8649	432	1.85E-14	1.23E-14	2.71E-16	4.60E-07	3.06E-07	2.39E-08	166	6	355	7	13	2	394	0.47	216.5	11.9
D22b1_148	8643	432	1.24E-14	8.26E-15	2.90E-16	3.08E-07	2.05E-07	1.70E-08	168	2	525	12	4	0	564	0.32	101.3	6.0
D22b1_149	8636	432	3.98E-15	2.65E-15	1.28E-16	9.91E-08	6.60E-08	5.89E-09	52	1	149	3	4	0	161	0.35	113.9	7.1
D22b1_150	8630	431	2.19E-14	1.46E-14	3.76E-16	5.45E-07	3.64E-07	2.88E-08	169	5	795	41	4	0	835	0.21	121.2	8.7
D22b1_151	8623	431	4.38E-15	2.92E-15	1.40E-16	1.09E-07	7.29E-08	6.49E-09	186	2	262	3	5	0	306	0.71	66.3	4.0
D22b1_152	8617	431	4.28E-14	2.86E-14	3.67E-16	1.07E-06	7.13E-07	5.42E-08	459	5	1650	47	2	0	1758	0.28	112.9	6.5
D22b1_153	8610	431	8.86E-15	5.91E-15	2.12E-16	2.21E-07	1.48E-07	1.23E-08	322	9	312	10	4	0	387	1.03	105.9	6.4
D22b1_154	8604	430	1.37E-14	9.14E-15	2.33E-16	3.43E-07	2.28E-07	1.81E-08	273	3	935	12	3	0	999	0.29	63.6	3.4
D22b1_155	8597	430	7.20E-15	4.80E-15	1.90E-16	1.80E-07	1.20E-07	1.02E-08	38	1	346	19	4	0	355	0.11	94.1	7.3
D22b1_156	8591	430	3.37E-15	2.24E-15	1.33E-16	8.42E-08	5.62E-08	5.37E-09	65	2	165	2	4	0	181	0.39	86.5	5.6
D22b1_157	8585	429	4.90E-14	3.27E-14	6.69E-16	1.23E-06	8.18E-07	6.36E-08	650	6	2594	18	5	0	2747	0.25	82.9	4.3

D22b1_158	8578	429	1.17E-14	7.77E-15	2.13E-16	2.92E-07	1.95E-07	1.56E-08	793	23	398	8	15	1	585	1.99	92.4	5.2
D22b1_159	8572	429	1.15E-14	7.67E-15	2.13E-16	2.89E-07	1.92E-07	1.54E-08	243	17	302	18	5	0	359	0.80	149.0	11.0
D22b1_160	8565	428	6.69E-15	4.46E-15	1.65E-16	1.68E-07	1.12E-07	9.37E-09	62	2	355	9	3	0	370	0.18	84.4	5.1
D22b1_161	8559	428	1.80E-14	1.20E-14	2.65E-16	4.52E-07	3.01E-07	2.36E-08	116	2	242	2	3	0	270	0.48	311.0	16.3
D22b1_162	8552	428	1.63E-15	1.09E-15	1.08E-16	4.09E-08	2.73E-08	3.41E-09	30	2	107	2	0	0	114	0.28	66.8	5.7
D22b1_163	8546	427	8.97E-15	5.98E-15	1.87E-16	2.26E-07	1.50E-07	1.22E-08	123	9	285	21	5	0	314	0.43	133.4	11.5
D22b1_164	8539	427	1.06E-14	7.10E-15	1.84E-16	2.68E-07	1.79E-07	1.42E-08	61	4	93	6	6	0	108	0.65	461.7	35.6
D22b1_165	8533	427	1.34E-14	8.92E-15	2.67E-16	3.37E-07	2.25E-07	1.82E-08	74	1	183	2	7	0	201	0.40	311.4	17.0
D22b1_166	8527	426	2.43E-15	1.62E-15	1.00E-16	6.13E-08	4.09E-08	3.98E-09	56	1	132	2	3	0	145	0.43	78.2	5.2
D22b1_167	8520	426	4.98E-15	3.32E-15	2.12E-16	1.26E-07	8.39E-08	8.26E-09	57	1	127	1	2	0	140	0.45	166.7	11.0
D22b1_168	8514	426	2.54E-15	1.69E-15	1.14E-16	6.42E-08	4.28E-08	4.31E-09	54	1	136	3	2	0	149	0.40	80.2	5.6
D22b1_169	8507	425	3.06E-15	2.04E-15	1.27E-16	7.73E-08	5.15E-08	5.02E-09	105	2	171	1	6	0	196	0.61	73.2	4.8
D22b1_170	8501	425	5.40E-15	3.60E-15	1.87E-16	1.37E-07	9.10E-08	8.31E-09	83	4	301	4	4	0	320	0.28	79.1	4.9
D22b1_171	8494	425	9.17E-15	6.12E-15	2.72E-16	2.32E-07	1.55E-07	1.35E-08	36	0	119	1	2	0	127	0.30	339.6	19.9
D22b1_172	8488	424	1.09E-14	7.24E-15	1.97E-16	2.75E-07	1.83E-07	1.46E-08	62	1	536	38	7	1	550	0.11	92.8	8.1
D22b1_173	8481	424	5.92E-15	3.95E-15	1.40E-16	1.50E-07	1.00E-07	8.31E-09	60	4	189	14	2	0	203	0.31	137.3	12.1
D22b1_174	8475	424	4.58E-15	3.05E-15	1.37E-16	1.16E-07	7.74E-08	6.77E-09	66	1	233	12	6	0	248	0.28	86.7	6.6
D22b1_175	8468	423	4.93E-15	3.29E-15	1.73E-16	1.25E-07	8.35E-08	7.65E-09	64	5	148	13	2	0	163	0.43	142.5	14.3
D22b1_176	8462	423	1.66E-14	1.11E-14	2.46E-16	4.22E-07	2.81E-07	2.20E-08	129	5	864	26	4	0	894	0.15	87.5	5.2
D22b1_177	8456	423	1.66E-14	1.11E-14	3.52E-16	4.23E-07	2.82E-07	2.30E-08	47	2	850	31	3	0	861	0.05	91.2	5.9

Appendix 40: Reduced detrital zircon U-Pb data for sample D22.

Grain #	Age 206/238	+/- 2σ	Age 207/235	+/- 2σ	Age 207/206	+/- 2σ	% Discordance	Selected U/Pb age (Ma)	+/- 2σ	Ratio 206/238	+/- 2σ	Ratio 207/235	+/- 2σ	Ratio 207/206	+/- 2σ
D22b1_1	304.0	3.1	309.0	12.0	371.0	94.0	2%	304.0	3.1	0.04826	0.0005	0.36	0.016	0.0544	0.0024
D22b1_2	499.8	4.6	485.0	13.0	428.0	75.0	3%	499.8	4.6	0.08063	0.00078	0.614	0.022	0.0555	0.002
D22b1_3	306.9	5.1	293.0	21.0	120.0	150.0	5%	306.9	5.1	0.04878	0.00084	0.343	0.026	0.0509	0.004
D22b1_4	302.1	2.8	303.6	9.1	277.0	73.0	0%	302.1	2.8	0.04799	0.00045	0.347	0.012	0.0528	0.0019
D22b1_5	302.7	1.9	302.6	5.8	295.0	48.0	0%	302.7	1.9	0.04808	0.0003	0.3468	0.0077	0.0526	0.0012
D22b1_6	303.6	2.8	296.9	8.1	244.0	68.0	2%	303.6	2.8	0.04824	0.00045	0.336	0.011	0.0514	0.0017
D22b1_7	303.4	3.5	339.0	11.0	559.0	85.0	11%	303.4	3.5	0.0482	0.00056	0.399	0.015	0.0604	0.0024
D22b1_8	299.2	2.4	330.1	9.5	511.0	73.0	9%	299.2	2.4	0.04751	0.00039	0.385	0.013	0.0576	0.0019
D22b1_9	307.9	2.1	305.0	5.9	272.0	50.0	1%	307.9	2.1	0.04892	0.00034	0.3512	0.008	0.052	0.0012
D22b1_10	622.6	3.2	626.1	8.5	622.0	38.0	1%	622.6	3.2	0.10141	0.00054	0.852	0.016	0.0604	0.0011
D22b1_11	543.2	5.8	543.2	8.7	551.0	38.0	0%	543.2	5.8	0.08795	0.00097	0.711	0.015	0.059	0.0011
D22b1_12	549.3	6.6	547.0	19.0	502.0	95.0	0%	549.3	6.6	0.089	0.0011	0.723	0.032	0.0597	0.0028
D22b1_13	610.6	4.3	606.0	8.4	589.0	41.0	1%	610.6	4.3	0.09937	0.00074	0.814	0.015	0.0598	0.0011
D22b1_14	301.7	2.1	305.2	5.8	298.0	49.0	1%	301.7	2.1	0.04792	0.00033	0.3514	0.0078	0.0525	0.0012
D22b1_15	296.9	2.1	318.7	7.3	464.0	55.0	7%	296.9	2.1	0.04713	0.00035	0.3692	0.0097	0.0565	0.0014
D22b1_16	463.0	8.9	445.0	16.0	362.0	80.0	4%	463.0	8.9	0.0745	0.0015	0.558	0.025	0.0547	0.0021
D22b1_17	420.3	3.5	414.0	11.0	377.0	71.0	2%	420.3	3.5	0.06738	0.00058	0.503	0.016	0.0545	0.0018
D22b1_18	571.5	5.2	576.0	15.0	571.0	77.0	1%	571.5	5.2	0.09273	0.00088	0.768	0.026	0.0605	0.0022
D22b1_19	1901.0	24.0	1941.0	33.0	1976.0	70.0	2%	1941.0	33.0	0.3431	0.005	5.77	0.22	0.1217	0.0047
D22b1_20	318.3	2.4	341.0	7.8	479.0	58.0	7%	318.3	2.4	0.05063	0.00039	0.399	0.011	0.0572	0.0015
D22b1_21	562.9	5.4	610.0	15.0	760.0	74.0	8%	562.9	5.4	0.09127	0.00092	0.83	0.028	0.0661	0.0023
D22b1_22	592.2	4.4	597.3	9.2	604.0	49.0	1%	592.2	4.4	0.09618	0.00074	0.803	0.016	0.0605	0.0014
D22b1_23	301.2	2.6	302.1	8.2	269.0	67.0	0%	301.2	2.6	0.04784	0.00042	0.346	0.011	0.0521	0.0016
D22b1_24	443.0	16.0	608.0	29.0	1228.0	59.0	27%	443.0	16.0	0.0712	0.0027	0.839	0.052	0.082	0.0024
D22b1_25	289.7	2.4	306.5	8.4	405.0	68.0	5%	289.7	2.4	0.04596	0.0004	0.353	0.011	0.0556	0.0018
D22b1_26	539.1	5.6	537.0	14.0	523.0	74.0	0%	539.1	5.6	0.08724	0.00094	0.7	0.023	0.0589	0.0021
D22b1_27	398.1	3.9	493.0	11.0	949.0	59.0	19%	398.1	3.9	0.06372	0.00064	0.624	0.018	0.0714	0.002
D22b1_28	288.5	3.2	278.0	11.0	170.0	99.0	4%	288.5	3.2	0.04578	0.00051	0.319	0.015	0.0498	0.0025
D22b1_29	1743.0	10.0	1736.0	13.0	1724.0	27.0	0%	1736.0	13.0	0.3104	0.0021	4.537	0.068	0.1056	0.0016

D22b1_30	654.0	11.0	633.0	30.0	520.0	130.0	3%	654.0	11.0	0.1069	0.0019	0.837	0.056	0.059	0.004
D22b1_31	618.1	4.2	619.0	13.0	602.0	60.0	0%	618.1	4.2	0.10064	0.00072	0.846	0.023	0.0608	0.0017
D22b1_32	573.6	3.0	575.8	6.8	580.0	36.0	0%	573.6	3.0	0.09307	0.0005	0.763	0.012	0.05923	0.00098
D22b1_33	314.0	1.7	312.5	4.6	292.0	41.0	0%	314.0	1.7	0.04991	0.00028	0.3602	0.0061	0.05225	0.00093
D22b1_34	310.8	1.9	311.0	5.7	305.0	47.0	0%	310.8	1.9	0.04938	0.0003	0.3574	0.0076	0.0528	0.0011
D22b1_35	309.5	1.8	312.3	4.8	331.0	41.0	1%	309.5	1.8	0.04918	0.00029	0.36	0.0064	0.05344	0.00099
D22b1_36	319.6	2.7	350.2	8.3	541.0	63.0	9%	319.6	2.7	0.05084	0.00044	0.412	0.012	0.0591	0.0018
D22b1_37	514.0	14.0	532.0	21.0	614.0	87.0	3%	514.0	14.0	0.0831	0.0024	0.703	0.035	0.0612	0.0025
D22b1_38	305.3	2.4	305.3	8.0	263.0	63.0	0%	305.3	2.4	0.0485	0.00039	0.349	0.011	0.0522	0.0016
D22b1_39	1778.0	13.0	1794.0	18.0	1794.0	43.0	1%	1794.0	18.0	0.3173	0.0027	4.86	0.11	0.1099	0.0026
D22b1_40	532.0	6.1	530.0	14.0	523.0	67.0	0%	532.0	6.1	0.0861	0.001	0.693	0.022	0.0583	0.0018
D22b1_41	306.6	1.9	307.0	4.6	287.0	40.0	0%	306.6	1.9	0.04871	0.00031	0.3538	0.0061	0.05221	0.00093
D22b1_42	931.0	25.0	894.0	29.0	903.0	66.0	4%	931.0	25.0	0.156	0.0044	1.439	0.069	0.07	0.0021
D22b1_43	682.4	6.5	710.0	12.0	768.0	51.0	4%	682.4	6.5	0.1117	0.0011	1.016	0.024	0.0654	0.0016
D22b1_44	315.8	2.6	310.2	8.2	243.0	68.0	2%	315.8	2.6	0.05022	0.00043	0.358	0.011	0.0512	0.0016
D22b1_45	303.2	2.0	336.8	4.8	550.0	38.0	10%	303.2	2.0	0.04816	0.00033	0.3938	0.0065	0.0586	0.001
D22b1_46	421.3	2.7	500.9	6.2	870.0	30.0	16%	421.3	2.7	0.06754	0.00045	0.639	0.01	0.06825	0.00099
D22b1_47	473.9	8.0	551.0	19.0	802.0	98.0	14%	473.9	8.0	0.0763	0.0013	0.733	0.033	0.0682	0.0032
D22b1_48	472.0	3.7	483.0	10.0	513.0	57.0	2%	472.0	3.7	0.07598	0.00062	0.612	0.016	0.0582	0.0015
D22b1_49	303.5	1.7	306.0	5.4	311.0	45.0	1%	303.5	1.7	0.04821	0.00028	0.3517	0.0073	0.0528	0.0011
D22b1_50	623.7	6.7	615.0	12.0	598.0	53.0	1%	623.7	6.7	0.1016	0.0011	0.837	0.022	0.0602	0.0015
D22b1_51	614.4	3.5	613.9	8.3	587.0	40.0	0%	614.4	3.5	0.10001	0.00059	0.83	0.015	0.0597	0.0011
D22b1_52	624.5	7.1	757.0	32.0	1100.0	100.0	18%	624.5	7.1	0.1017	0.0012	1.155	0.072	0.0802	0.0042
D22b1_53	340.8	3.7	342.0	13.0	325.0	89.0	0%	340.8	3.7	0.05429	0.0006	0.403	0.018	0.0534	0.0024
D22b1_54	335.6	3.3	392.0	12.0	691.0	67.0	14%	335.6	3.3	0.05345	0.00053	0.478	0.017	0.0644	0.002
D22b1_55	720.6	8.0	708.0	10.0	659.0	39.0	2%	720.6	8.0	0.1181	0.0014	1.008	0.02	0.0619	0.0011
D22b1_56	303.5	2.1	300.6	5.3	267.0	44.0	1%	303.5	2.1	0.04822	0.00034	0.3452	0.0069	0.052	0.001
D22b1_57	494.2	5.0	477.0	15.0	356.0	82.0	4%	494.2	5.0	0.07969	0.00084	0.605	0.023	0.0548	0.0021
D22b1_58	312.5	4.4	375.0	17.0	740.0	110.0	17%	312.5	4.4	0.04969	0.00071	0.449	0.025	0.0668	0.0037
D22b1_59	291.3	3.7	286.0	12.0	180.0	100.0	2%	291.3	3.7	0.04623	0.0006	0.323	0.016	0.0506	0.0026
D22b1_60	311.1	2.2	318.8	7.0	347.0	58.0	2%	311.1	2.2	0.04945	0.00036	0.3688	0.0095	0.0541	0.0014
D22b1_61	300.1	2.8	294.1	9.4	253.0	83.0	2%	300.1	2.8	0.04765	0.00045	0.336	0.013	0.0511	0.002

D22b1_62	340.5	3.8	325.0	11.0	212.0	80.0	5%	340.5	3.8	0.05424	0.00062	0.379	0.014	0.051	0.002
D22b1_63	523.7	6.5	502.0	18.0	420.0	89.0	4%	523.7	6.5	0.0847	0.0011	0.645	0.028	0.0564	0.0024
D22b1_64	882.9	6.1	897.0	11.0	916.0	42.0	2%	882.9	6.1	0.1467	0.0011	1.416	0.027	0.0702	0.0014
D22b1_65	1712.0	15.0	1823.0	15.0	1945.0	29.0	6%	1823.0	15.0	0.3043	0.003	5.036	0.086	0.1196	0.0019
D22b1_66	312.4	4.0	330.8	8.6	434.0	54.0	6%	312.4	4.0	0.04967	0.00066	0.392	0.013	0.0565	0.0015
D22b1_67	950.0	11.0	951.0	24.0	956.0	81.0	0%	950.0	11.0	0.1589	0.002	1.571	0.062	0.0721	0.0028
D22b1_68	320.5	2.4	323.9	8.2	316.0	64.0	1%	320.5	2.4	0.05097	0.00039	0.376	0.011	0.0535	0.0016
D22b1_69	528.3	6.4	558.0	18.0	665.0	91.0	5%	528.3	6.4	0.0854	0.0011	0.74	0.032	0.0634	0.0027
D22b1_70	440.9	4.0	445.0	11.0	424.0	65.0	1%	440.9	4.0	0.0708	0.00067	0.549	0.016	0.056	0.0017
D22b1_71	2022.0	12.0	2023.0	11.0	2015.0	24.0	0%	2023.0	11.0	0.3686	0.0025	6.35	0.084	0.1246	0.0017
D22b1_72	645.4	4.7	645.0	10.0	616.0	46.0	0%	645.4	4.7	0.10527	0.00081	0.887	0.018	0.061	0.0013
D22b1_73	307.0	3.1	311.0	11.0	340.0	89.0	1%	307.0	3.1	0.04879	0.00051	0.359	0.015	0.054	0.0023
D22b1_74	329.4	3.0	325.1	6.7	299.0	51.0	1%	329.4	3.0	0.05237	0.0005	0.3771	0.0092	0.053	0.0012
D22b1_75	1675.0	16.0	1674.0	22.0	1650.0	54.0	0%	1674.0	22.0	0.297	0.0033	4.21	0.11	0.1023	0.0029
D22b1_76	305.1	2.5	303.6	8.1	258.0	69.0	0%	305.1	2.5	0.04847	0.0004	0.346	0.011	0.0517	0.0018
D22b1_77	592.9	8.5	579.0	22.0	490.0	110.0	2%	592.9	8.5	0.0963	0.0014	0.774	0.039	0.0587	0.0031
D22b1_78	706.0	6.9	722.0	20.0	735.0	84.0	2%	706.0	6.9	0.1158	0.0012	1.032	0.041	0.0643	0.0026
D22b1_79	311.7	2.8	315.6	9.5	313.0	74.0	1%	311.7	2.8	0.04955	0.00046	0.366	0.013	0.0531	0.0019
D22b1_80	1064.1	6.9	1072.0	13.0	1087.0	41.0	1%	1064.1	6.9	0.1794	0.0013	1.867	0.039	0.0751	0.0016
D22b1_81	313.5	3.4	314.0	12.0	298.0	95.0	0%	313.5	3.4	0.04985	0.00055	0.362	0.016	0.0521	0.0024
D22b1_82	603.2	3.8	608.8	8.2	621.0	40.0	1%	603.2	3.8	0.0981	0.00064	0.82	0.014	0.0608	0.0011
D22b1_83	296.0	2.8	290.3	8.4	243.0	73.0	2%	296.0	2.8	0.047	0.00045	0.331	0.011	0.0514	0.0018
D22b1_84	1790.0	27.0	1830.0	24.0	1867.0	50.0	2%	1830.0	24.0	0.3208	0.0055	5.04	0.14	0.1138	0.0031
D22b1_85	1329.0	16.0	1356.0	35.0	1370.0	94.0	2%	1329.0	16.0	0.229	0.0031	2.83	0.13	0.0898	0.0043
D22b1_86	318.9	1.9	317.3	5.8	287.0	47.0	1%	318.9	1.9	0.05072	0.00031	0.3653	0.0078	0.0524	0.0011
D22b1_87	307.2	2.1	305.9	5.0	274.0	43.0	0%	307.2	2.1	0.04882	0.00035	0.3507	0.0066	0.0521	0.001
D22b1_88	908.0	20.0	1156.0	32.0	1619.0	86.0	21%	908.0	20.0	0.1515	0.0035	2.185	0.094	0.1031	0.0045
D22b1_89	429.1	7.9	448.0	15.0	462.0	81.0	4%	429.1	7.9	0.0689	0.0013	0.557	0.022	0.0575	0.0022
D22b1_90	295.9	2.7	288.0	11.0	215.0	84.0	3%	295.9	2.7	0.04698	0.00044	0.33	0.014	0.0503	0.0021
D22b1_91	859.0	6.1	875.0	15.0	895.0	57.0	2%	859.0	6.1	0.1426	0.0011	1.357	0.035	0.0687	0.0019
D22b1_92	452.0	3.7	511.0	16.0	760.0	80.0	12%	452.0	3.7	0.07264	0.00061	0.652	0.025	0.0652	0.0025
D22b1_93	690.4	5.6	688.0	16.0	661.0	70.0	0%	690.4	5.6	0.11291	0.00095	0.98	0.031	0.0626	0.002

D22b1_94	575.1	9.6	597.0	25.0	640.0	110.0	4%	575.1	9.6	0.0934	0.0016	0.814	0.044	0.0634	0.0034
D22b1_95	308.4	3.6	310.0	13.0	300.0	100.0	1%	308.4	3.6	0.04901	0.00059	0.361	0.017	0.0534	0.0026
D22b1_96	569.6	6.9	616.0	22.0	720.0	110.0	8%	569.6	6.9	0.0924	0.0012	0.844	0.04	0.0671	0.0035
D22b1_97	309.4	4.1	342.0	22.0	377.0	89.0	10%	309.4	4.1	0.04918	0.00067	0.446	0.054	0.0607	0.0047
D22b1_98	317.9	2.8	388.0	18.0	730.0	100.0	18%	317.9	2.8	0.05056	0.00046	0.469	0.026	0.0672	0.0034
D22b1_99	1914.0	15.0	1892.0	20.0	1874.0	41.0	1%	1892.0	20.0	0.3454	0.0032	5.43	0.12	0.1141	0.0026
D22b1_100	313.4	1.9	318.9	5.1	338.0	41.0	2%	313.4	1.9	0.04982	0.00031	0.3692	0.0069	0.05341	0.00097
D22b1_101	956.7	7.0	967.0	14.0	967.0	47.0	1%	956.7	7.0	0.16	0.0013	1.598	0.036	0.0718	0.0016
D22b1_102	537.3	4.9	537.0	11.0	531.0	58.0	0%	537.3	4.9	0.08694	0.00083	0.699	0.019	0.0588	0.0016
D22b1_103	552.6	5.7	788.0	38.0	1500.0	130.0	30%	552.6	5.7	0.08952	0.00097	1.28	0.1	0.1023	0.0078
D22b1_104	531.2	5.9	575.0	14.0	714.0	72.0	8%	531.2	5.9	0.0859	0.001	0.763	0.024	0.0641	0.0021
D22b1_105	534.3	4.1	539.0	11.0	544.0	55.0	1%	534.3	4.1	0.08638	0.0007	0.698	0.018	0.0584	0.0015
D22b1_106	512.1	4.5	518.2	8.9	566.0	40.0	1%	512.1	4.5	0.08263	0.00076	0.666	0.014	0.0591	0.0011
D22b1_107	301.7	2.7	334.0	10.0	534.0	77.0	10%	301.7	2.7	0.04792	0.00044	0.392	0.014	0.0591	0.0022
D22b1_108	316.9	2.1	331.6	4.5	432.0	33.0	4%	316.9	2.1	0.05038	0.00035	0.387	0.0061	0.05574	0.00083
D22b1_109	315.5	4.5	323.0	18.0	280.0	130.0	2%	315.5	4.5	0.05017	0.00073	0.362	0.025	0.0513	0.0036
D22b1_110	302.8	2.2	303.9	6.1	296.0	53.0	0%	302.8	2.2	0.04809	0.00035	0.3492	0.0082	0.0527	0.0013
D22b1_111	2784.0	20.0	2801.0	13.0	2803.0	26.0	1%	2801.0	13.0	0.5405	0.0048	14.8	0.2	0.1975	0.003
D22b1_112	1024.9	7.0	1035.0	16.0	1036.0	52.0	1%	1024.9	7.0	0.1724	0.0013	1.78	0.044	0.0748	0.0019
D22b1_113	311.9	3.0	310.0	11.0	267.0	86.0	1%	311.9	3.0	0.04958	0.00049	0.359	0.015	0.0524	0.0022
D22b1_114	580.0	5.1	563.0	15.0	472.0	77.0	3%	580.0	5.1	0.09416	0.00086	0.738	0.027	0.057	0.0021
D22b1_115	2740.0	24.0	2723.0	20.0	2693.0	37.0	1%	2723.0	20.0	0.5304	0.0058	13.53	0.28	0.1854	0.0042
D22b1_116	544.3	4.6	537.6	9.4	495.0	50.0	1%	544.3	4.6	0.08811	0.00077	0.701	0.016	0.0575	0.0013
D22b1_117	414.8	4.1	432.0	11.0	512.0	66.0	4%	414.8	4.1	0.06647	0.00068	0.532	0.016	0.0579	0.0017
D22b1_118	241.1	1.9	248.6	7.3	300.0	71.0	3%	241.1	1.9	0.03811	0.00031	0.2794	0.0092	0.0531	0.0018
D22b1_119	542.2	5.6	561.0	15.0	603.0	72.0	3%	542.2	5.6	0.08777	0.00094	0.73	0.025	0.06	0.002
D22b1_120	603.0	21.0	592.0	27.0	579.0	78.0	2%	603.0	21.0	0.0982	0.0036	0.825	0.049	0.0594	0.0022
D22b1_121	313.9	2.5	313.3	6.9	294.0	59.0	0%	313.9	2.5	0.04987	0.0004	0.3633	0.0092	0.0524	0.0014
D22b1_122	489.4	5.6	493.5	8.9	500.0	47.0	1%	489.4	5.6	0.07891	0.00094	0.627	0.014	0.0576	0.0012
D22b1_123	657.5	5.5	664.0	13.0	664.0	61.0	1%	657.5	5.5	0.10734	0.00094	0.925	0.025	0.0626	0.0017
D22b1_124	311.5	4.2	302.0	15.0	190.0	120.0	3%	311.5	4.2	0.04952	0.00068	0.353	0.02	0.0522	0.003
D22b1_125	427.3	4.5	550.0	28.0	1070.0	120.0	22%	427.3	4.5	0.06854	0.00074	0.758	0.058	0.081	0.0055

D22b1_126	310.8	4.7	315.0	17.0	300.0	130.0	1%	310.8	4.7	0.04941	0.00076	0.352	0.024	0.0517	0.0036
D22b1_127	663.8	6.1	657.0	13.0	636.0	59.0	1%	663.8	6.1	0.1085	0.001	0.913	0.025	0.0616	0.0016
D22b1_128	699.9	5.4	706.0	12.0	706.0	50.0	1%	699.9	5.4	0.11471	0.00093	1.007	0.023	0.0634	0.0015
D22b1_129	418.3	2.6	434.4	6.3	514.0	40.0	4%	418.3	2.6	0.06704	0.00044	0.5349	0.0097	0.0578	0.0011
D22b1_130	337.9	3.2	365.4	7.9	513.0	53.0	8%	337.9	3.2	0.05382	0.00052	0.434	0.011	0.0584	0.0014
D22b1_131	601.5	4.3	598.0	10.0	569.0	46.0	1%	601.5	4.3	0.09782	0.00074	0.8	0.017	0.0594	0.0013
D22b1_132	421.7	3.9	416.7	7.6	399.0	46.0	1%	421.7	3.9	0.06762	0.00065	0.507	0.011	0.055	0.0011
D22b1_133	2000.0	14.0	1989.0	15.0	1956.0	34.0	1%	1989.0	15.0	0.3638	0.0031	6.06	0.11	0.1201	0.0023
D22b1_134	386.3	2.4	443.9	8.0	733.0	53.0	13%	386.3	2.4	0.06172	0.0004	0.548	0.012	0.0637	0.0016
D22b1_135	318.1	2.3	316.1	6.0	299.0	50.0	1%	318.1	2.3	0.05054	0.00037	0.3648	0.0081	0.053	0.0012
D22b1_136	307.1	2.3	299.4	8.5	218.0	71.0	3%	307.1	2.3	0.0488	0.00038	0.345	0.011	0.0512	0.0017
D22b1_137	318.7	2.8	349.2	8.2	540.0	60.0	9%	318.7	2.8	0.05069	0.00046	0.41	0.012	0.0588	0.0017
D22b1_138	2304.0	20.0	2454.0	18.0	2586.0	22.0	6%	2454.0	18.0	0.4297	0.0044	10.29	0.19	0.1735	0.0022
D22b1_139	599.7	4.4	599.0	10.0	586.0	52.0	0%	599.7	4.4	0.09751	0.00075	0.805	0.019	0.0602	0.0015
D22b1_140	304.6	2.2	300.0	6.4	252.0	55.0	2%	304.6	2.2	0.04839	0.00036	0.3452	0.0084	0.0514	0.0013
D22b1_141	503.9	5.8	518.0	16.0	552.0	81.0	3%	503.9	5.8	0.08133	0.00097	0.664	0.026	0.0602	0.0023
D22b1_142	541.6	6.2	556.0	12.0	638.0	53.0	3%	541.6	6.2	0.0877	0.001	0.734	0.02	0.0611	0.0015
D22b1_143	526.7	7.4	648.0	23.0	1078.0	83.0	19%	526.7	7.4	0.0852	0.0012	0.907	0.042	0.0767	0.003
D22b1_144	535.3	3.6	529.9	9.2	494.0	47.0	1%	535.3	3.6	0.0866	0.0006	0.686	0.015	0.0573	0.0013
D22b1_145	321.6	1.7	317.5	3.5	289.0	29.0	1%	321.6	1.7	0.05115	0.00028	0.3676	0.0048	0.05232	0.00068
D22b1_146	2164.0	15.0	2655.0	11.0	3048.0	12.0	18%	2655.0	11.0	0.399	0.0032	12.66	0.15	0.2294	0.0016
D22b1_147	404.0	22.0	515.0	36.0	925.0	84.0	22%	404.0	22.0	0.065	0.0037	0.718	0.072	0.0733	0.003
D22b1_148	308.5	2.1	316.1	7.2	339.0	59.0	2%	308.5	2.1	0.04903	0.00035	0.3653	0.0097	0.0538	0.0015
D22b1_149	314.0	4.1	308.0	13.0	240.0	110.0	2%	314.0	4.1	0.04992	0.00066	0.355	0.018	0.052	0.0028
D22b1_150	317.8	2.6	316.6	6.9	284.0	54.0	0%	317.8	2.6	0.05055	0.00042	0.3628	0.0089	0.0524	0.0013
D22b1_151	621.1	5.6	631.0	13.0	651.0	55.0	2%	621.1	5.6	0.10117	0.00095	0.865	0.024	0.0619	0.0016
D22b1_152	610.1	3.8	608.5	5.2	606.0	23.0	0%	610.1	3.8	0.09928	0.00064	0.8201	0.0093	0.06008	0.00064
D22b1_153	304.8	2.7	306.5	9.7	287.0	77.0	1%	304.8	2.7	0.04842	0.00044	0.355	0.013	0.0526	0.0019
D22b1_154	651.4	3.4	655.1	6.7	656.0	29.0	1%	651.4	3.4	0.10634	0.00059	0.905	0.012	0.06168	0.00083
D22b1_155	561.7	4.9	554.0	12.0	509.0	59.0	1%	561.7	4.9	0.09106	0.00083	0.727	0.02	0.0581	0.0016
D22b1_156	383.2	3.9	382.0	13.0	317.0	86.0	0%	383.2	3.9	0.06126	0.00064	0.461	0.018	0.0535	0.0022
D22b1_157	312.5	1.5	313.7	3.4	314.0	29.0	0%	312.5	1.5	0.04967	0.00024	0.3624	0.0045	0.05272	0.00068

D22b1_158	584.8	5.3	589.0	10.0	569.0	50.0	1%	584.8	5.3	0.09498	0.0009	0.786	0.018	0.0598	0.0014
D22b1_159	319.0	3.4	309.0	11.0	213.0	85.0	3%	319.0	3.4	0.05074	0.00056	0.359	0.015	0.0508	0.0021
D22b1_160	308.1	2.4	302.7	9.0	224.0	69.0	2%	308.1	2.4	0.04896	0.00039	0.347	0.012	0.0515	0.0017
D22b1_161	617.6	5.6	646.0	14.0	687.0	62.0	4%	617.6	5.6	0.10057	0.00095	0.892	0.026	0.0631	0.0018
D22b1_162	1544.0	17.0	1531.0	18.0	1513.0	38.0	1%	1531.0	18.0	0.2705	0.0034	3.525	0.078	0.095	0.0019
D22b1_163	323.8	4.0	318.0	11.0	281.0	85.0	2%	323.8	4.0	0.05153	0.00066	0.371	0.016	0.0525	0.0022
D22b1_164	299.7	5.1	319.0	16.0	380.0	120.0	6%	299.7	5.1	0.0476	0.00083	0.352	0.024	0.0543	0.0038
D22b1_165	458.8	4.2	451.0	15.0	375.0	87.0	2%	458.8	4.2	0.07377	0.0007	0.566	0.023	0.0545	0.0023
D22b1_166	305.6	4.0	294.0	14.0	180.0	110.0	4%	305.6	4.0	0.04856	0.00065	0.343	0.018	0.0503	0.0029
D22b1_167	310.8	4.7	310.0	16.0	270.0	120.0	0%	310.8	4.7	0.04941	0.00077	0.36	0.022	0.0535	0.0033
D22b1_168	2076.0	19.0	2349.0	12.0	2594.0	20.0	12%	2349.0	12.0	0.3803	0.0041	9.13	0.12	0.1737	0.002
D22b1_169	647.7	5.7	672.0	16.0	746.0	66.0	4%	647.7	5.7	0.10573	0.00097	0.944	0.029	0.0649	0.0019
D22b1_170	730.1	9.9	737.0	13.0	747.0	51.0	1%	730.1	9.9	0.1197	0.0017	1.069	0.027	0.0648	0.0015
D22b1_171	973.5	9.1	977.0	17.0	973.0	54.0	0%	973.5	9.1	0.163	0.0016	1.627	0.043	0.0718	0.0019
D22b1_172	546.5	4.5	565.0	12.0	629.0	53.0	3%	546.5	4.5	0.08849	0.00076	0.747	0.021	0.061	0.0016
D22b1_173	466.2	6.3	465.0	14.0	398.0	77.0	0%	466.2	6.3	0.075	0.0011	0.588	0.023	0.0552	0.002
D22b1_174	504.5	8.4	504.0	14.0	481.0	62.0	0%	504.5	8.4	0.0814	0.0014	0.643	0.022	0.0577	0.0016
D22b1_175	630.5	6.8	634.0	18.0	597.0	81.0	1%	630.5	6.8	0.1028	0.0012	0.869	0.033	0.0614	0.0024
D22b1_176	371.3	6.1	370.5	8.2	367.0	45.0	0%	371.3	6.1	0.0593	0.001	0.441	0.012	0.054	0.0011
D22b1_177	342.5	6.3	345.4	7.9	368.0	45.0	1%	342.5	6.3	0.0546	0.001	0.405	0.011	0.0541	0.0011

Appendix 41: Detrital zircon (U-Th)/He data for sample D20.

Grain #	V (µm3)	+/- 2σ	4He (mol)	Corrected 4He (mol)	+/- 2σ	4He (mol/g)	Corrected 4He (mol/g)	+/- 2σ	232Th (ppm)	+/- 2σ	238U (ppm)	+/- 2σ	147Sm (ppm)	+/- 2σ	eU	Th/U	ZHe age (Ma)	+/- 2σ
D20b1_3	9892	495	9.66E-15	6.44E-15	2.49E-16	2.10E-07	1.40E-07	1.18E-08	210	4	557	6	2	0	607	0.38	64.2	3.7
D20b1_4	9885	494	6.73E-15	4.48E-15	2.25E-16	1.46E-07	9.75E-08	8.81E-09	49	2	301	9	5	0	312	0.16	86.9	5.8
D20b1_5	9877	494	2.07E-14	1.38E-14	3.25E-16	4.52E-07	3.01E-07	2.37E-08	45	4	480	11	3	0	491	0.09	170.9	9.7
D20b1_6	9870	494	9.65E-15	6.44E-15	2.24E-16	2.10E-07	1.40E-07	1.16E-08	99	2	199	3	11	0	223	0.50	175.2	10.0
D20b1_7	9863	493	1.08E-14	7.17E-15	2.59E-16	2.35E-07	1.56E-07	1.30E-08	263	4	539	10	9	0	601	0.49	72.4	4.2
D20b1_8	9856	493	4.51E-15	3.01E-15	2.25E-16	9.84E-08	6.56E-08	6.95E-09	55	1	164	3	2	0	177	0.34	103.0	7.5
D20b1_9	9848	492	2.88E-15	1.92E-15	9.92E-17	6.29E-08	4.20E-08	3.82E-09	73	3	65	1	10	1	83	1.12	-	
D20b1_10	9841	492	1.51E-14	1.01E-14	2.50E-16	3.29E-07	2.20E-07	1.74E-08	44	1	211	4	6	0	221	0.21	276.4	15.5
D20b1_11	9834	492	1.30E-14	8.67E-15	2.53E-16	2.85E-07	1.90E-07	1.53E-08	184	5	604	7	4	0	647	0.31	81.6	4.5
D20b1_12	9827	491	4.97E-15	3.32E-15	2.02E-16	1.09E-07	7.26E-08	7.01E-09	39	1	64	2	7	0	73	0.61	-	
D20b1_13	9819	491	4.57E-15	3.05E-15	2.29E-16	1.00E-07	6.68E-08	7.09E-09	60	2	238	8	5	0	252	0.25	73.8	5.7
D20b1_14	9812	491	7.53E-15	5.02E-15	2.78E-16	1.65E-07	1.10E-07	1.03E-08	131	2	382	4	4	0	413	0.34	74.2	4.7
D20b1_15	9805	490	8.11E-15	5.41E-15	2.22E-16	1.78E-07	1.19E-07	1.01E-08	64	2	361	15	5	0	376	0.18	87.8	6.1
D20b1_16	9797	490	2.74E-14	1.83E-14	3.68E-16	6.01E-07	4.01E-07	3.11E-08	41	2	597	35	12	2	607	0.07	184.0	14.3
D20b1_17	9790	490	7.85E-15	5.23E-15	2.14E-16	1.72E-07	1.15E-07	9.83E-09	63	4	471	10	4	0	486	0.13	65.9	4.0
D20b1_18	9783	489	1.79E-15	1.20E-15	1.55E-16	3.95E-08	2.63E-08	3.95E-09	27	1	74	2	2	0	80	0.37	91.6	9.4
D20b1_19	9776	489	1.90E-14	1.26E-14	4.07E-16	4.17E-07	2.78E-07	2.27E-08	128	9	247	5	4	0	277	0.52	279.6	16.1
D20b1_20	9768	488	3.86E-14	2.57E-14	5.03E-16	8.49E-07	5.66E-07	4.39E-08	183	10	322	28	12	1	365	0.57	431.3	40.0
D20b1_21	9761	488	6.07E-14	4.05E-14	1.01E-15	1.34E-06	8.92E-07	7.05E-08	208	11	478	29	26	2	527	0.44	470.9	35.9
D20b1_22	9754	488	2.79E-14	1.86E-14	4.45E-16	6.16E-07	4.11E-07	3.23E-08	132	3	499	15	10	0	530	0.26	215.7	12.9
D20b1_23	9746	487	1.26E-14	8.41E-15	2.98E-16	2.78E-07	1.86E-07	1.54E-08	74	1	194	3	7	0	211	0.38	244.3	13.9
D20b1_24	9739	487	6.51E-15	4.34E-15	2.26E-16	1.44E-07	9.58E-08	8.75E-09	107	1	287	5	5	0	312	0.37	85.4	5.4
D20b1_25	9732	487	6.92E-15	4.61E-15	1.92E-16	1.53E-07	1.02E-07	8.74E-09	20	0	48	1	2	0	53	0.42	-	
D20b1_26	9725	486	3.49E-14	2.32E-14	4.82E-16	7.71E-07	5.14E-07	4.00E-08	312	10	637	18	20	1	710	0.49	201.3	11.6
D20b1_27	9717	486	2.71E-14	1.81E-14	3.57E-16	6.00E-07	4.00E-07	3.10E-08	164	3	449	3	9	1	487	0.37	228.4	11.9
D20b1_28	9710	485	1.79E-14	1.19E-14	2.87E-16	3.97E-07	2.64E-07	2.08E-08	86	1	226	2	9	0	246	0.38	299.2	16.0
D20b1_29	9703	485	2.15E-14	1.43E-14	4.54E-16	4.77E-07	3.18E-07	2.59E-08	342	7	777	15	12	1	857	0.44	103.1	5.9
D20b1_30	9695	485	1.48E-14	9.86E-15	2.98E-16	3.28E-07	2.19E-07	1.77E-08	78	1	243	3	5	1	261	0.32	232.8	12.8
D20b1_31	9688	484	3.86E-15	2.57E-15	1.46E-16	8.57E-08	5.71E-08	5.37E-09	15	0	55	1	0	0	59	0.26	-	

D20b1_32	9681	484	1.05E-14	7.03E-15	2.43E-16	2.34E-07	1.56E-07	1.29E-08	269	12	343	10	15	1	406	0.78	106.8	6.5
D20b1_33	9674	484	3.86E-15	2.57E-15	1.27E-16	8.57E-08	5.71E-08	5.14E-09	59	0	144	2	8	0	158	0.41	100.8	6.2
D20b1_34	9666	483	1.93E-14	1.29E-14	3.77E-16	4.29E-07	2.86E-07	2.30E-08	117	1	129	3	1	0	156	0.91	508.3	29.2
D20b1_35	9659	483	1.12E-14	7.49E-15	2.48E-16	2.50E-07	1.67E-07	1.37E-08	51	2	238	10	2	0	250	0.21	185.6	12.5
D20b1_36	9652	483	6.96E-15	4.64E-15	2.28E-16	1.55E-07	1.03E-07	9.28E-09	34	0	58	1	3	0	66	0.59	-	
D20b1_37	9644	482	4.93E-16	3.29E-16	7.57E-17	1.10E-08	7.33E-09	1.77E-09	22	0	32	0	13	1	37	0.70	-	
D20b1_38	9637	482	8.77E-15	5.85E-15	2.12E-16	1.96E-07	1.30E-07	1.09E-08	100	5	171	4	4	0	195	0.58	186.4	11.0
D20b1_39	9630	481	1.66E-14	1.10E-14	2.59E-16	3.70E-07	2.46E-07	1.94E-08	75	1	214	4	6	0	232	0.35	296.1	16.1
D20b1_40	9623	481	5.24E-15	3.50E-15	2.16E-16	1.17E-07	7.81E-08	7.59E-09	40	1	252	3	3	0	262	0.16	83.1	5.5
D20b1_41	9615	481	2.46E-14	1.64E-14	4.18E-16	5.51E-07	3.67E-07	2.91E-08	114	1	245	2	2	0	272	0.47	375.2	20.0
D20b1_42	9608	480	1.82E-15	1.21E-15	1.64E-16	4.07E-08	2.71E-08	4.19E-09	138	5	87	3	10	1	120	1.57	62.9	6.6
D20b1_43	9601	480	7.84E-15	5.23E-15	1.56E-16	1.76E-07	1.17E-07	9.45E-09	194	8	266	7	3	0	312	0.73	104.4	6.2
D20b1_44	9593	480	6.45E-14	4.30E-14	6.91E-16	1.45E-06	9.64E-07	7.39E-08	285	10	616	18	10	1	683	0.46	392.5	22.6
D20b1_45	9586	479	8.16E-15	5.44E-15	2.32E-16	1.83E-07	1.22E-07	1.05E-08	59	2	108	1	4	0	122	0.54	278.1	16.4
D20b1_46	9579	479	4.51E-14	3.01E-14	4.79E-16	1.01E-06	6.75E-07	5.17E-08	105	1	648	7	9	0	672	0.16	279.4	14.6
D20b1_47	9572	479	3.38E-15	2.25E-15	1.70E-16	7.59E-08	5.06E-08	5.39E-09	33	2	302	13	2	0	310	0.11	45.5	3.8
D20b1_48	9564	478	2.38E-15	1.59E-15	1.33E-16	5.35E-08	3.57E-08	4.01E-09	46	1	131	2	5	0	142	0.35	69.9	5.3
D20b1_49	9557	478	1.96E-14	1.31E-14	2.59E-16	4.41E-07	2.94E-07	2.28E-08	36	3	258	5	3	0	266	0.14	307.6	16.8
D20b1_50	9550	477	1.28E-14	8.51E-15	3.01E-16	2.87E-07	1.92E-07	1.59E-08	28	0	121	1	1	0	127	0.23	418.6	23.4
D20b1_51	9542	477	1.71E-14	1.14E-14	3.52E-16	3.85E-07	2.56E-07	2.08E-08	319	9	867	12	3	0	942	0.37	75.8	4.2
D20b1_52	9535	477	8.13E-15	5.42E-15	2.47E-16	1.83E-07	1.22E-07	1.07E-08	231	18	240	14	10	1	294	0.96	115.4	8.9
D20b1_53	9528	476	5.12E-15	3.41E-15	1.47E-16	1.16E-07	7.70E-08	6.66E-09	56	1	171	2	5	0	184	0.33	116.3	6.8
D20b1_54	9521	476	7.90E-15	5.26E-15	1.83E-16	1.78E-07	1.19E-07	9.83E-09	201	8	264	6	4	0	312	0.76	106.1	6.2
D20b1_55	9513	476	2.41E-14	1.61E-14	4.14E-16	5.45E-07	3.64E-07	2.88E-08	135	1	342	4	3	0	373	0.40	270.9	14.5
D20b1_56	9506	475	1.02E-14	6.78E-15	2.15E-16	2.30E-07	1.53E-07	1.25E-08	82	2	136	2	3	0	155	0.60	274.7	15.3
D20b1_57	9499	475	1.39E-14	9.28E-15	2.83E-16	3.15E-07	2.10E-07	1.70E-08	21	1	828	8	2	0	833	0.03	70.3	3.8
D20b1_58	9491	475	9.76E-15	6.51E-15	2.69E-16	2.21E-07	1.47E-07	1.26E-08	170	3	311	7	32	5	351	0.55	116.9	7.1
D20b1_59	9484	474	7.92E-15	5.28E-15	1.61E-16	1.79E-07	1.20E-07	9.69E-09	50	2	348	4	4	0	360	0.14	92.6	5.1
D20b1_60	9477	474	1.10E-14	7.34E-15	2.10E-16	2.50E-07	1.67E-07	1.34E-08	141	5	532	7	5	0	565	0.26	82.2	4.5
D20b1_61	9470	473	4.37E-14	2.91E-14	5.37E-16	9.92E-07	6.61E-07	5.11E-08	187	5	534	11	4	0	578	0.35	318.3	17.5
D20b1_62	9462	473	3.94E-15	2.63E-15	1.42E-16	8.96E-08	5.98E-08	5.52E-09	84	2	212	2	3	0	232	0.40	71.8	4.5
D20b1_63	9455	473	1.39E-14	9.25E-15	3.22E-16	3.16E-07	2.10E-07	1.74E-08	94	3	271	6	29	4	293	0.35	199.6	11.8

D20b1_64	9448	472	7.88E-15	5.26E-15	1.90E-16	1.79E-07	1.20E-07	9.96E-09	160	6	293	8	18	1	331	0.54	100.7	6.1
D20b1_65	9440	472	1.53E-14	1.02E-14	2.85E-16	3.50E-07	2.33E-07	1.86E-08	40	0	29	0	4	0	38	1.39	-	
D20b1_66	9433	472	6.44E-15	4.29E-15	2.29E-16	1.47E-07	9.79E-08	9.01E-09	94	2	141	2	3	0	164	0.67	166.4	10.5
D20b1_67	9426	471	1.42E-14	9.46E-15	4.12E-16	3.24E-07	2.16E-07	1.87E-08	129	2	216	8	7	0	247	0.60	243.4	16.2
D20b1_68	9419	471	1.36E-14	9.08E-15	3.77E-16	3.11E-07	2.07E-07	1.78E-08	68	2	195	5	7	0	211	0.35	273.7	16.8
D20b1_69	9411	471	4.76E-15	3.17E-15	1.97E-16	1.09E-07	7.25E-08	7.06E-09	16	0	46	1	2	0	50	0.35	-	
D20b1_70	9404	470	5.98E-15	3.99E-15	2.27E-16	1.37E-07	9.12E-08	8.59E-09	47	1	83	1	7	0	93	0.56	271.4	17.3
D20b1_71	9397	470	1.16E-14	7.71E-15	2.54E-16	2.65E-07	1.77E-07	1.45E-08	69	1	166	2	6	0	183	0.42	269.0	15.0
D20b1_72	9389	469	1.42E-14	9.49E-15	2.17E-16	3.26E-07	2.17E-07	1.70E-08	112	1	243	2	2	0	269	0.46	224.9	11.9
D20b1_73	9382	469	1.02E-14	6.82E-15	2.45E-16	2.34E-07	1.56E-07	1.30E-08	121	8	536	8	2	0	564	0.23	77.1	4.4
D20b1_74	9375	469	6.48E-15	4.32E-15	1.93E-16	1.49E-07	9.92E-08	8.65E-09	99	4	233	4	6	0	256	0.42	107.8	6.5
D20b1_75	9368	468	1.07E-14	7.11E-15	3.39E-16	2.45E-07	1.63E-07	1.45E-08	124	4	228	2	4	0	257	0.55	176.7	10.6
D20b1_76	9360	468	8.44E-15	5.63E-15	2.36E-16	1.94E-07	1.29E-07	1.11E-08	168	10	258	10	8	0	297	0.65	121.1	8.0
D20b1_77	9353	468	2.84E-14	1.89E-14	4.40E-16	6.52E-07	4.35E-07	3.41E-08	117	7	305	17	7	1	332	0.38	364.1	26.7
D20b1_78	9346	467	7.17E-15	4.78E-15	1.89E-16	1.65E-07	1.10E-07	9.33E-09	101	3	268	9	13	1	292	0.38	104.9	6.7
D20b1_79	9338	467	9.33E-15	6.22E-15	2.70E-16	2.15E-07	1.43E-07	1.24E-08	92	2	258	6	9	0	279	0.36	142.8	8.8
D20b1_80	9331	467	5.19E-15	3.46E-15	1.49E-16	1.20E-07	7.97E-08	6.89E-09	113	1	362	4	14	1	389	0.31	57.0	3.3
D20b1_81	9324	466	2.27E-14	1.51E-14	3.22E-16	5.23E-07	3.48E-07	2.72E-08	180	3	409	6	11	0	451	0.44	214.8	11.5
D20b1_82	9317	466	1.19E-14	7.91E-15	2.26E-16	2.74E-07	1.83E-07	1.47E-08	179	5	471	8	6	0	514	0.38	98.9	5.5
D20b1_83	9309	465	6.54E-15	4.36E-15	1.67E-16	1.51E-07	1.01E-07	8.48E-09	133	3	315	15	8	0	346	0.42	80.9	5.7
D20b1_84	9302	465	1.57E-14	1.04E-14	2.48E-16	3.62E-07	2.41E-07	1.90E-08	138	1	219	2	7	1	251	0.63	267.3	14.1
D20b1_85	9295	465	6.20E-15	4.14E-15	1.27E-16	1.44E-07	9.57E-08	7.75E-09	277	5	333	3	6	0	398	0.83	66.8	3.6
D20b1_86	9288	464	6.09E-15	4.06E-15	1.51E-16	1.41E-07	9.41E-08	7.87E-09	85	2	322	5	5	0	342	0.26	76.5	4.4
D20b1_87	9280	464	1.37E-14	9.12E-15	2.72E-16	3.17E-07	2.11E-07	1.70E-08	51	1	267	3	3	0	279	0.19	211.1	11.6
D20b1_88	9273	464	3.19E-14	2.13E-14	2.79E-16	7.41E-07	4.94E-07	3.76E-08	39	1	1529	14	9	0	1538	0.03	89.4	4.6
D20b1_89	9266	463	6.75E-15	4.50E-15	2.11E-16	1.57E-07	1.04E-07	9.23E-09	47	2	290	17	5	1	301	0.16	96.5	7.9
D20b1_90	9258	463	1.87E-14	1.24E-14	3.61E-16	4.33E-07	2.89E-07	2.32E-08	240	8	498	11	8	0	554	0.48	145.0	8.3
D20b1_91	9251	463	1.59E-15	1.06E-15	1.27E-16	3.70E-08	2.47E-08	3.48E-09	47	1	62	1	4	0	73	0.76	-	
D20b1_92	9244	462	2.02E-14	1.35E-14	3.64E-16	4.70E-07	3.13E-07	2.50E-08	53	4	388	9	6	0	400	0.14	217.8	12.6
D20b1_93	9237	462	1.05E-14	6.97E-15	2.90E-16	2.44E-07	1.62E-07	1.39E-08	61	0	96	1	4	0	110	0.64	410.8	23.6
D20b1_94	9229	461	9.87E-16	6.58E-16	1.32E-16	2.30E-08	1.53E-08	3.28E-09	29	0	76	1	1	0	83	0.37	51.4	7.3
D20b1_95	9222	461	1.79E-14	1.19E-14	2.76E-16	4.17E-07	2.78E-07	2.18E-08	42	1	753	31	3	0	763	0.06	101.5	6.7

D20b1_96	9215	461	5.71E-14	3.81E-14	5.23E-16	1.33E-06	8.89E-07	6.78E-08	451	7	637	8	2	0	743	0.71	332.8	17.3
D20b1_97	9207	460	2.13E-15	1.42E-15	1.48E-16	4.99E-08	3.32E-08	4.26E-09	33	1	60	1	5	0	68	0.55	-	
D20b1_98	9200	460	1.97E-14	1.31E-14	4.64E-16	4.60E-07	3.06E-07	2.54E-08	16	1	868	10	4	0	872	0.02	97.9	5.5
D20b1_99	9193	460	1.81E-14	1.21E-14	2.95E-16	4.24E-07	2.83E-07	2.23E-08	75	3	910	17	12	2	928	0.08	84.9	4.7
D20b1_100	9186	459	2.50E-14	1.67E-14	4.36E-16	5.85E-07	3.90E-07	3.10E-08	89	3	406	4	5	0	426	0.22	254.6	13.7
D20b1_101	9178	459	1.77E-14	1.18E-14	4.21E-16	4.14E-07	2.76E-07	2.29E-08	58	1	234	2	3	0	247	0.25	310.7	17.4
D20b1_102	9171	459	1.53E-14	1.02E-14	3.15E-16	3.59E-07	2.39E-07	1.94E-08	86	2	226	4	3	0	246	0.38	270.4	15.2
D20b1_103	9164	458	3.52E-14	2.35E-14	4.19E-16	8.26E-07	5.51E-07	4.25E-08	119	10	243	13	12	1	271	0.49	565.3	40.0
D20b1_104	9156	458	2.25E-14	1.50E-14	3.60E-16	5.28E-07	3.52E-07	2.77E-08	158	4	348	4	13	2	385	0.45	254.3	13.6
D20b1_105	9149	457	2.81E-14	1.88E-14	4.46E-16	6.61E-07	4.41E-07	3.47E-08	164	3	350	6	6	0	388	0.47	315.9	17.2
D20b1_106	9142	457	4.30E-14	2.86E-14	6.12E-16	1.01E-06	6.74E-07	5.26E-08	400	6	657	8	9	0	751	0.61	249.5	13.2
D20b1_107	9135	457	1.95E-14	1.30E-14	3.59E-16	4.59E-07	3.06E-07	2.44E-08	81	2	267	3	9	0	286	0.30	297.6	16.3
D20b1_108	9127	456	1.66E-14	1.11E-14	3.69E-16	3.91E-07	2.61E-07	2.14E-08	91	1	321	15	8	0	342	0.28	211.8	14.8
D20b1_109	9120	456	3.56E-15	2.38E-15	1.22E-16	8.40E-08	5.60E-08	5.10E-09	69	5	89	6	7	0	105	0.77	148.1	12.4
D20b1_110	9113	456	1.99E-14	1.33E-14	3.48E-16	4.69E-07	3.13E-07	2.49E-08	86	2	106	2	4	0	126	0.82	691.1	37.7
D20b1_111	9105	455	9.77E-15	6.51E-15	2.08E-16	2.31E-07	1.54E-07	1.25E-08	62	1	373	22	8	0	388	0.17	110.5	8.7
D20b1_112	9098	455	1.70E-14	1.14E-14	3.97E-16	4.03E-07	2.68E-07	2.22E-08	80	3	194	5	8	0	212	0.42	351.4	21.0
D20b1_113	9091	455	7.57E-15	5.05E-15	2.20E-16	1.79E-07	1.19E-07	1.04E-08	39	0	129	2	3	0	138	0.30	241.5	14.4
D20b1_114	9084	454	3.03E-14	2.02E-14	4.22E-16	7.18E-07	4.79E-07	3.73E-08	383	14	427	6	8	0	517	0.90	257.5	13.8
D20b1_115	9076	454	1.70E-14	1.14E-14	3.56E-16	4.04E-07	2.69E-07	2.19E-08	71	1	198	2	2	0	215	0.36	348.7	19.1
D20b1_116	9069	453	5.31E-15	3.54E-15	2.31E-16	1.26E-07	8.39E-08	8.35E-09	112	1	110	2	7	0	136	1.02	171.5	11.6
D20b1_117	9062	453	3.73E-15	2.48E-15	1.53E-16	8.85E-08	5.90E-08	5.72E-09	48	0	109	1	4	0	120	0.44	136.5	8.9
D20b1_118	9054	453	1.26E-14	8.38E-15	3.07E-16	2.99E-07	1.99E-07	1.66E-08	123	2	194	2	13	1	223	0.63	248.2	14.0
D20b1_119	9047	452	5.50E-15	3.67E-15	2.55E-16	1.31E-07	8.71E-08	8.91E-09	32	1	278	11	4	0	286	0.12	84.9	6.6
D20b1_120	9040	452	1.44E-14	9.61E-15	4.04E-16	3.43E-07	2.29E-07	1.97E-08	113	1	262	4	7	0	289	0.43	220.3	12.9
D20b1_121	9033	452	3.02E-14	2.02E-14	2.50E-16	7.20E-07	4.80E-07	3.65E-08	190	5	362	8	8	0	407	0.52	328.2	17.7
D20b1_122	9025	451	8.99E-15	5.99E-15	2.52E-16	2.14E-07	1.43E-07	1.23E-08	72	3	92	4	5	0	109	0.78	365.0	24.2
D20b1_123	9018	451	8.45E-15	5.63E-15	2.21E-16	2.02E-07	1.34E-07	1.14E-08	142	6	394	6	6	0	428	0.36	87.4	5.1
D20b1_124	9011	451	1.21E-14	8.09E-15	2.30E-16	2.90E-07	1.93E-07	1.55E-08	78	1	581	20	6	0	599	0.13	89.7	5.7
D20b1_125	9003	450	3.14E-14	2.09E-14	4.74E-16	7.49E-07	4.99E-07	3.91E-08	111	1	177	2	1	0	203	0.63	685.1	36.1
D20b1_126	8996	450	2.04E-14	1.36E-14	3.22E-16	4.87E-07	3.24E-07	2.55E-08	42	1	1219	28	1	0	1229	0.03	73.5	4.2
D20b1_127	8989	449	1.11E-14	7.38E-15	2.30E-16	2.65E-07	1.76E-07	1.43E-08	94	1	136	2	3	0	158	0.69	310.2	17.2

D20b1_128	8982	449	1.30E-14	8.69E-15	2.82E-16	3.12E-07	2.08E-07	1.70E-08	101	1	198	2	3	0	222	0.51	261.2	14.4
D20b1_129	8974	449	1.29E-14	8.58E-15	2.36E-16	3.08E-07	2.06E-07	1.64E-08	92	2	156	3	2	0	177	0.59	322.6	17.9
D20b1_130	8967	448	1.55E-14	1.03E-14	2.62E-16	3.71E-07	2.47E-07	1.96E-08	128	5	354	3	4	0	384	0.36	179.4	9.6
D20b1_131	8960	448	3.20E-14	2.13E-14	5.37E-16	7.68E-07	5.12E-07	4.05E-08	367	11	385	11	14	1	471	0.95	302.1	17.5
D20b1_132	8952	448	1.21E-14	8.07E-15	3.30E-16	2.91E-07	1.94E-07	1.66E-08	202	5	534	11	6	0	581	0.38	92.7	5.6
D20b1_133	8945	447	2.39E-14	1.59E-14	3.99E-16	5.75E-07	3.83E-07	3.03E-08	171	5	344	7	7	0	384	0.50	277.9	15.4
D20b1_134	8938	447	3.21E-14	2.14E-14	3.57E-16	7.72E-07	5.15E-07	3.96E-08	72	3	548	12	5	0	565	0.13	253.8	14.1
D20b1_135	8931	447	8.38E-15	5.58E-15	1.82E-16	2.02E-07	1.34E-07	1.10E-08	236	11	508	18	15	2	563	0.46	66.4	4.2
D20b1_136	8923	446	9.89E-15	6.59E-15	2.20E-16	2.38E-07	1.59E-07	1.30E-08	95	1	104	1	21	3	126	0.92	350.8	19.4
D20b1_137	8916	446	7.68E-15	5.12E-15	2.04E-16	1.85E-07	1.24E-07	1.05E-08	84	1	125	1	4	0	145	0.68	237.5	13.6
D20b1_138	8909	445	1.80E-14	1.20E-14	2.58E-16	4.36E-07	2.90E-07	2.27E-08	27	1	270	3	4	0	277	0.10	292.4	15.6
D20b1_139	8901	445	1.09E-14	7.24E-15	2.74E-16	2.63E-07	1.75E-07	1.47E-08	58	1	164	4	5	0	177	0.35	274.9	16.8
D20b1_140	8894	445	4.81E-15	3.21E-15	1.81E-16	1.16E-07	7.76E-08	7.28E-09	35	0	56	1	4	1	64	0.62	-	
D20b1_141	8887	444	3.81E-14	2.54E-14	4.98E-16	9.23E-07	6.15E-07	4.77E-08	417	9	824	16	16	1	922	0.51	185.6	10.1
D20b1_142	8880	444	1.24E-14	8.23E-15	2.33E-16	2.99E-07	1.99E-07	1.60E-08	49	1	150	3	4	0	161	0.33	343.8	19.3
D20b1_143	8872	444	2.19E-14	1.46E-14	3.20E-16	5.31E-07	3.54E-07	2.77E-08	122	1	351	3	4	0	379	0.35	259.8	13.6
D20b1_144	8865	443	1.91E-14	1.27E-14	4.04E-16	4.64E-07	3.09E-07	2.52E-08	88	3	374	4	4	0	395	0.24	218.1	12.1
D20b1_145	8858	443	7.99E-15	5.33E-15	1.62E-16	1.94E-07	1.29E-07	1.05E-08	89	4	212	7	2	0	233	0.42	154.5	9.6
D20b1_146	8850	443	4.05E-15	2.70E-15	1.44E-16	9.83E-08	6.55E-08	6.03E-09	65	2	330	13	7	0	345	0.20	52.8	3.8
D20b1_147	8843	442	1.55E-14	1.03E-14	3.26E-16	3.76E-07	2.51E-07	2.04E-08	188	4	255	6	5	0	299	0.74	232.9	13.5
D20b1_148	8836	442	1.80E-14	1.20E-14	2.91E-16	4.38E-07	2.92E-07	2.30E-08	38	1	291	3	4	0	300	0.13	271.0	14.6
D20b1_149	8829	441	2.93E-14	1.95E-14	4.17E-16	7.13E-07	4.75E-07	3.71E-08	499	14	477	11	18	1	594	1.05	222.2	12.3
D20b1_150	8821	441	2.79E-14	1.86E-14	4.02E-16	6.80E-07	4.53E-07	3.54E-08	104	2	525	7	4	0	549	0.20	229.8	12.3
D20b1_151	8814	441	2.26E-14	1.51E-14	3.68E-16	5.52E-07	3.68E-07	2.90E-08	195	5	343	4	7	0	389	0.57	263.2	14.1
D20b1_152	8807	440	4.73E-14	3.15E-14	4.84E-16	1.16E-06	7.70E-07	5.90E-08	380	5	800	12	19	0	889	0.48	241.0	12.7
D20b1_153	8799	440	1.55E-14	1.03E-14	3.44E-16	3.79E-07	2.53E-07	2.08E-08	471	10	827	13	10	0	938	0.57	75.0	4.2
D20b1_154	8792	440	2.74E-14	1.83E-14	4.08E-16	6.70E-07	4.47E-07	3.50E-08	216	5	464	9	27	2	515	0.47	241.5	13.3
D20b1_155	8785	439	1.49E-15	9.95E-16	1.14E-16	3.66E-08	2.44E-08	3.33E-09	15	0	64	2	2	0	68	0.24	-	
D20b1_156	8778	439	6.45E-15	4.30E-15	2.05E-16	1.58E-07	1.05E-07	9.36E-09	99	1	283	3	3	0	306	0.35	95.8	5.8
D20b1_157	8770	439	5.74E-15	3.83E-15	1.78E-16	1.41E-07	9.39E-08	8.28E-09	60	1	113	1	9	1	127	0.53	204.9	12.3
D20b1_158	8763	438	4.95E-15	3.30E-15	1.99E-16	1.21E-07	8.09E-08	7.79E-09	48	1	36	1	7	0	48	1.31	-	
D20b1_159	8756	438	4.45E-14	2.97E-14	5.29E-16	1.09E-06	7.29E-07	5.62E-08	151	2	728	9	3	0	763	0.21	265.7	14.0

D20b1_160	8749	437	1.00E-14	6.68E-15	2.24E-16	2.46E-07	1.64E-07	1.35E-08	554	44	396	5	14	1	526	1.40	86.8	5.1
D20b1_161	8741	437	9.29E-15	6.20E-15	2.45E-16	2.29E-07	1.52E-07	1.29E-08	152	12	382	19	5	0	418	0.40	101.5	7.4
D20b1_162	8734	437	1.14E-14	7.62E-15	2.77E-16	2.82E-07	1.88E-07	1.56E-08	106	3	205	8	5	0	230	0.52	227.3	15.0
D20b1_163	8727	436	2.68E-15	1.79E-15	1.37E-16	6.62E-08	4.41E-08	4.73E-09	32	0	125	5	5	0	132	0.25	92.8	7.4
D20b1_164	8719	436	1.02E-14	6.79E-15	2.30E-16	2.51E-07	1.67E-07	1.38E-08	116	2	143	2	6	0	170	0.81	274.2	15.3
D20b1_165	8712	436	3.33E-15	2.22E-15	1.67E-16	8.22E-08	5.48E-08	5.83E-09	91	3	132	4	2	0	153	0.69	99.4	7.4
D20b1_166	8705	435	4.23E-14	2.82E-14	4.62E-16	1.05E-06	6.97E-07	5.35E-08	165	3	670	10	8	0	709	0.25	274.0	14.5
D20b1_167	8698	435	1.86E-14	1.24E-14	4.37E-16	4.61E-07	3.07E-07	2.55E-08	157	2	216	3	2	0	252	0.73	338.4	19.1
D20b1_168	8690	435	7.76E-15	5.17E-15	2.35E-16	1.92E-07	1.28E-07	1.12E-08	51	1	79	2	2	0	91	0.64	391.0	24.9
D20b1_169	8683	434	1.37E-14	9.15E-15	2.58E-16	3.40E-07	2.27E-07	1.82E-08	147	11	182	4	298	37	216	0.81	290.8	16.9
D20b1_170	8676	434	5.64E-14	3.76E-14	5.98E-16	1.40E-06	9.32E-07	7.14E-08	116	1	873	8	7	0	900	0.13	288.2	15.0
D20b1_171	8668	433	2.39E-14	1.59E-14	3.33E-16	5.92E-07	3.95E-07	3.07E-08	478	26	1061	30	5	0	1173	0.45	93.6	5.4
D20b1_172	8661	433	5.47E-15	3.65E-15	1.70E-16	1.36E-07	9.05E-08	8.00E-09	72	2	303	8	10	0	320	0.24	78.8	5.0
D20b1_173	8654	433	9.38E-15	6.25E-15	2.51E-16	2.33E-07	1.55E-07	1.32E-08	228	7	412	8	10	1	465	0.55	92.9	5.5
D20b1_174	8647	432	8.46E-15	5.64E-15	1.76E-16	2.10E-07	1.40E-07	1.14E-08	107	2	247	11	6	0	272	0.43	143.3	9.7
D20b1_175	8639	432	1.67E-14	1.11E-14	2.18E-16	4.16E-07	2.77E-07	2.15E-08	87	4	338	11	3	0	358	0.26	215.3	12.9

Appendix 42: Reduced detrital zircon U-Pb data for sample D20.

Grain #	Age 206/238	+/- 2σ	Age 207/235	+/- 2σ	Age 207/206	+/- 2σ	% Discordance	Selected U/Pb age (Ma)	+/- 2σ	Ratio 206/238	+/- 2σ	Ratio 207/235	+/- 2σ	Ratio 207/206	+/- 2σ
D20b1_3	583.7	4.2	581.8	9.1	546.0	39.0	0%	583.7	4.2	0.09473	0.00072	0.772	0.016	0.0588	0.001
D20b1_4	552.4	7.7	554.0	12.0	542.0	53.0	0%	552.4	7.7	0.0895	0.0013	0.722	0.021	0.059	0.0014
D20b1_5	450.4	3.3	446.2	8.8	391.0	53.0	1%	450.4	3.3	0.07238	0.00054	0.552	0.013	0.055	0.0013
D20b1_6	484.5	4.1	489.0	12.0	468.0	66.0	1%	484.5	4.1	0.07806	0.00069	0.619	0.019	0.0573	0.0018
D20b1_7	486.1	4.1	502.3	9.1	588.0	44.0	3%	486.1	4.1	0.07834	0.00069	0.639	0.014	0.0596	0.0012
D20b1_8	521.3	4.8	539.0	13.0	573.0	67.0	3%	521.3	4.8	0.08424	0.0008	0.703	0.021	0.0609	0.0019
D20b1_9	2764.0	19.0	2718.0	14.0	2679.0	21.0	2%	2718.0	14.0	0.5355	0.0046	13.52	0.19	0.1832	0.0024
D20b1_10	1117.8	7.5	1119.0	13.0	1106.0	36.0	0%	1117.8	7.5	0.1893	0.0014	2.013	0.038	0.0768	0.0014
D20b1_11	478.8	4.5	499.4	8.4	582.0	39.0	4%	478.8	4.5	0.07711	0.00075	0.637	0.014	0.0595	0.001
D20b1_12	1013.0	10.0	1057.0	20.0	1112.0	67.0	4%	1013.0	10.0	0.1701	0.0018	1.835	0.058	0.0776	0.0026
D20b1_13	504.3	9.7	501.0	15.0	472.0	64.0	1%	504.3	9.7	0.0815	0.0016	0.643	0.024	0.0574	0.0017
D20b1_14	321.8	3.0	428.0	17.0	1021.0	92.0	25%	321.8	3.0	0.0512	0.00049	0.535	0.026	0.0768	0.0036
D20b1_15	474.0	11.0	467.0	13.0	470.0	53.0	1%	474.0	11.0	0.0762	0.0018	0.589	0.021	0.0571	0.0014
D20b1_16	521.0	13.0	549.0	12.0	711.0	48.0	5%	521.0	13.0	0.0843	0.0022	0.722	0.021	0.0641	0.0014
D20b1_17	524.3	4.0	533.8	8.2	586.0	41.0	2%	524.3	4.0	0.08474	0.00068	0.69	0.014	0.0595	0.0012
D20b1_18	1189.0	11.0	1307.0	20.0	1487.0	49.0	9%	1189.0	11.0	0.2027	0.002	2.62	0.071	0.0933	0.0024
D20b1_19	328.4	3.1	308.0	10.0	157.0	79.0	7%	328.4	3.1	0.05226	0.00051	0.354	0.013	0.0496	0.0019
D20b1_20	525.0	11.0	530.0	13.0	660.0	50.0	1%	525.0	11.0	0.085	0.0019	0.69	0.021	0.0614	0.0014
D20b1_21	1250.0	97.0	1802.0	66.0	2709.0	16.0	31%	1802.0	66.0	0.22	0.019	5.47	0.46	0.1866	0.0018
D20b1_22	508.6	4.5	523.2	9.2	586.0	45.0	3%	508.6	4.5	0.08211	0.00075	0.676	0.015	0.0597	0.0013
D20b1_23	1518.0	17.0	1499.0	16.0	1471.0	27.0	1%	1499.0	16.0	0.2657	0.0032	3.372	0.07	0.0922	0.0014
D20b1_24	529.3	7.4	525.0	13.0	513.0	59.0	1%	529.3	7.4	0.0856	0.0012	0.682	0.021	0.058	0.0016
D20b1_25	1663.0	13.0	1645.0	22.0	1604.0	52.0	1%	1645.0	22.0	0.2944	0.0026	4.04	0.11	0.0997	0.0027
D20b1_26	713.8	8.7	977.0	32.0	1580.0	73.0	27%	713.8	8.7	0.1172	0.0015	1.656	0.085	0.1017	0.0041
D20b1_27	602.4	6.6	598.3	9.9	622.0	41.0	1%	602.4	6.6	0.098	0.0011	0.801	0.017	0.0607	0.0012
D20b1_28	594.9	4.8	573.0	11.0	512.0	59.0	4%	594.9	4.8	0.09669	0.00082	0.759	0.02	0.0572	0.0016
D20b1_29	274.2	3.0	293.7	6.2	455.0	51.0	7%	274.2	3.0	0.04347	0.00049	0.3364	0.0082	0.0563	0.0012
D20b1_30	613.7	7.8	720.0	36.0	1000.0	110.0	15%	613.7	7.8	0.0999	0.0013	1.15	0.11	0.0816	0.0067
D20b1_31	500.1	7.5	473.0	23.0	340.0	130.0	6%	500.1	7.5	0.0807	0.0013	0.609	0.035	0.0538	0.0034

D20b1_32	456.4	3.8	448.1	8.7	384.0	53.0	2%	456.4	3.8	0.07337	0.00064	0.555	0.013	0.0553	0.0014
D20b1_33	1082.4	7.2	1107.0	15.0	1158.0	43.0	2%	1082.4	7.2	0.1828	0.0013	1.98	0.045	0.0786	0.0017
D20b1_34	2102.0	18.0	2339.0	16.0	2562.0	20.0	10%	2339.0	16.0	0.3856	0.0039	9.03	0.15	0.1709	0.002
D20b1_35	664.5	4.9	651.0	12.0	603.0	56.0	2%	664.5	4.9	0.10859	0.00084	0.903	0.023	0.0602	0.0016
D20b1_36	1101.0	11.0	1098.0	21.0	1060.0	66.0	0%	1101.0	11.0	0.1862	0.002	1.97	0.06	0.0762	0.0025
D20b1_37	1019.0	15.0	1002.0	31.0	970.0	100.0	2%	1019.0	15.0	0.1715	0.0027	1.711	0.079	0.0738	0.0037
D20b1_38	2785.0	14.0	2825.6	8.4	2861.0	13.0	1%	2825.6	8.4	0.5406	0.0033	15.18	0.13	0.2038	0.0017
D20b1_39	836.8	5.5	832.0	12.0	813.0	45.0	1%	836.8	5.5	0.13864	0.00098	1.265	0.026	0.0666	0.0014
D20b1_40	554.0	3.8	567.0	11.0	581.0	55.0	2%	554.0	3.8	0.08976	0.00064	0.75	0.018	0.0604	0.0015
D20b1_41	1104.0	6.0	1107.0	11.0	1106.0	34.0	0%	1104.0	6.0	0.1868	0.0011	1.98	0.031	0.0764	0.0013
D20b1_42	650.0	6.8	663.0	20.0	669.0	91.0	2%	650.0	6.8	0.1061	0.0012	0.919	0.038	0.0627	0.0027
D20b1_43	657.5	5.3	756.0	18.0	1042.0	63.0	13%	657.5	5.3	0.10739	0.00091	1.106	0.036	0.0749	0.0023
D20b1_44	1194.0	7.8	1179.2	8.6	1160.0	21.0	1%	1194.0	7.8	0.2035	0.0015	2.195	0.027	0.07872	0.00083
D20b1_45	694.9	6.7	701.0	19.0	675.0	82.0	1%	694.9	6.7	0.1139	0.0012	0.985	0.037	0.0635	0.0024
D20b1_46	490.6	3.4	517.7	7.6	619.0	39.0	5%	490.6	3.4	0.07908	0.00056	0.665	0.013	0.061	0.0011
D20b1_47	407.7	8.8	407.0	12.0	393.0	64.0	0%	407.7	8.8	0.0653	0.0015	0.49	0.017	0.0554	0.0016
D20b1_48	557.5	5.4	571.0	16.0	584.0	80.0	2%	557.5	5.4	0.09035	0.00091	0.759	0.027	0.0601	0.0022
D20b1_49	471.8	3.3	470.0	10.0	434.0	59.0	0%	471.8	3.3	0.07595	0.00056	0.592	0.016	0.0563	0.0015
D20b1_50	1665.0	10.0	1648.0	13.0	1633.0	30.0	1%	1648.0	13.0	0.2946	0.0021	4.085	0.066	0.1009	0.0016
D20b1_51	682.7	3.3	699.4	7.2	750.0	28.0	2%	682.7	3.3	0.11172	0.00057	0.993	0.014	0.06454	0.00086
D20b1_52	473.1	4.1	468.0	12.0	420.0	71.0	1%	473.1	4.1	0.07616	0.00068	0.588	0.019	0.0565	0.0018
D20b1_53	554.4	4.5	540.0	13.0	474.0	68.0	3%	554.4	4.5	0.08983	0.00076	0.699	0.022	0.057	0.0018
D20b1_54	317.4	3.9	338.0	11.0	415.0	75.0	6%	317.4	3.9	0.05048	0.00063	0.391	0.015	0.0565	0.002
D20b1_55	322.0	2.8	314.5	8.5	254.0	70.0	2%	322.0	2.8	0.05119	0.00045	0.363	0.011	0.0518	0.0017
D20b1_56	557.6	5.1	538.0	15.0	426.0	79.0	4%	557.6	5.1	0.09037	0.00086	0.7	0.026	0.0562	0.0021
D20b1_57	333.4	3.1	331.1	6.7	287.0	50.0	1%	333.4	3.1	0.05308	0.0005	0.3847	0.0091	0.0525	0.0012
D20b1_58	523.4	4.9	523.0	11.0	528.0	51.0	0%	523.4	4.9	0.08459	0.00082	0.671	0.017	0.0584	0.0014
D20b1_59	550.8	4.0	549.1	9.9	530.0	49.0	0%	550.8	4.0	0.08921	0.00067	0.719	0.017	0.0585	0.0013
D20b1_60	504.2	4.2	505.4	8.1	487.0	42.0	0%	504.2	4.2	0.08138	0.0007	0.646	0.013	0.057	0.0011
D20b1_61	319.6	2.1	323.0	7.0	354.0	54.0	1%	319.6	2.1	0.05083	0.00035	0.3744	0.0096	0.0537	0.0013
D20b1_62	538.3	5.7	544.0	14.0	557.0	67.0	1%	538.3	5.7	0.08704	0.00095	0.709	0.023	0.0596	0.0018
D20b1_63	2395.0	23.0	2525.0	14.0	2643.0	13.0	5%	2525.0	14.0	0.4496	0.0052	11.03	0.16	0.1791	0.0014

D20b1_64	607.4	4.2	605.0	11.0	583.0	51.0	0%	607.4	4.2	0.09882	0.00072	0.811	0.019	0.0594	0.0014
D20b1_65	2023.0	20.0	1965.0	24.0	1912.0	50.0	3%	1965.0	24.0	0.3691	0.0042	5.97	0.16	0.1181	0.0032
D20b1_66	604.8	5.4	588.0	15.0	478.0	76.0	3%	604.8	5.4	0.09832	0.00093	0.784	0.027	0.0578	0.002
D20b1_67	861.0	33.0	1056.0	40.0	1512.0	51.0	18%	861.0	33.0	0.144	0.006	1.9	0.12	0.0943	0.0026
D20b1_68	478.6	4.4	477.0	12.0	459.0	67.0	0%	478.6	4.4	0.07708	0.00073	0.604	0.019	0.0575	0.0018
D20b1_69	2917.0	24.0	2857.0	16.0	2823.0	25.0	2%	2857.0	16.0	0.5715	0.0058	15.72	0.26	0.1998	0.003
D20b1_70	1611.0	14.0	1679.0	15.0	1734.0	37.0	4%	1679.0	15.0	0.2839	0.0028	4.21	0.082	0.1074	0.0022
D20b1_71	582.0	5.7	608.0	15.0	693.0	68.0	4%	582.0	5.7	0.09451	0.00096	0.828	0.027	0.0637	0.002
D20b1_72	669.9	5.0	662.0	13.0	612.0	55.0	1%	669.9	5.0	0.10953	0.00087	0.924	0.025	0.0603	0.0015
D20b1_73	514.8	4.1	513.3	8.8	501.0	45.0	0%	514.8	4.1	0.08315	0.00069	0.658	0.015	0.0574	0.0012
D20b1_74	479.1	7.0	491.0	13.0	524.0	61.0	2%	479.1	7.0	0.0772	0.0012	0.625	0.02	0.0588	0.0016
D20b1_75	342.4	3.3	336.0	10.0	284.0	76.0	2%	342.4	3.3	0.05456	0.00054	0.393	0.014	0.0522	0.0019
D20b1_76	344.1	3.3	372.0	12.0	529.0	80.0	8%	344.1	3.3	0.05483	0.00054	0.441	0.017	0.0578	0.0022
D20b1_77	312.2	4.1	335.0	10.0	495.0	75.0	7%	312.2	4.1	0.04963	0.00068	0.391	0.014	0.0574	0.002
D20b1_78	601.0	13.0	617.0	17.0	687.0	55.0	3%	601.0	13.0	0.0976	0.0022	0.839	0.03	0.0626	0.0016
D20b1_79	310.0	3.0	377.0	12.0	777.0	86.0	18%	310.0	3.0	0.04926	0.00049	0.452	0.018	0.0663	0.0026
D20b1_80	579.6	4.2	579.0	9.1	584.0	46.0	0%	579.6	4.2	0.09403	0.00072	0.771	0.016	0.0595	0.0013
D20b1_81	654.0	18.0	1368.0	88.0	2500.0	150.0	52%	654.0	18.0	0.1071	0.0032	3.35	0.38	0.212	0.018
D20b1_82	313.8	2.3	318.7	7.0	333.0	58.0	2%	313.8	2.3	0.04989	0.00037	0.3706	0.0094	0.0536	0.0014
D20b1_83	585.6	8.1	581.0	13.0	557.0	55.0	1%	585.6	8.1	0.0951	0.0014	0.779	0.023	0.0598	0.0015
D20b1_84	604.2	4.7	599.0	12.0	549.0	59.0	1%	604.2	4.7	0.09828	0.0008	0.807	0.021	0.0592	0.0016
D20b1_85	564.5	4.3	566.1	9.5	535.0	49.0	0%	564.5	4.3	0.09148	0.00072	0.746	0.016	0.0589	0.0013
D20b1_86	366.9	4.9	369.0	11.0	357.0	73.0	1%	366.9	4.9	0.05858	0.0008	0.44	0.016	0.0544	0.0019
D20b1_87	578.4	4.6	581.0	11.0	602.0	54.0	0%	578.4	4.6	0.09383	0.00078	0.773	0.019	0.0604	0.0016
D20b1_88	321.1	2.1	313.3	4.4	241.0	38.0	2%	321.1	2.1	0.05108	0.00034	0.3613	0.0057	0.05118	0.00086
D20b1_89	729.0	17.0	737.0	18.0	809.0	48.0	1%	729.0	17.0	0.1199	0.003	1.077	0.037	0.0668	0.0015
D20b1_90	306.6	2.4	320.9	7.2	404.0	60.0	4%	306.6	2.4	0.04871	0.00039	0.3715	0.0099	0.0554	0.0015
D20b1_91	592.6	8.0	584.0	24.0	500.0	110.0	1%	592.6	8.0	0.0963	0.0014	0.776	0.042	0.0581	0.0032
D20b1_92	440.3	4.3	442.0	10.0	423.0	63.0	0%	440.3	4.3	0.0707	0.00071	0.545	0.015	0.0559	0.0016
D20b1_93	1596.0	11.0	1567.0	16.0	1531.0	39.0	2%	1567.0	16.0	0.2809	0.0022	3.703	0.075	0.0954	0.0021
D20b1_94	326.0	5.3	294.0	20.0	30.0	140.0	11%	326.0	5.3	0.05183	0.00087	0.358	0.028	0.0507	0.004
D20b1_95	366.3	3.0	374.2	7.3	406.0	47.0	2%	366.3	3.0	0.05847	0.0005	0.447	0.01	0.0553	0.0012

D20b1_96	2152.0	14.0	2307.4	8.8	2452.1	9.9	7%	2307.4	8.8	0.3965	0.003	8.707	0.083	0.15942	0.00093
D20b1_97	665.1	8.3	644.0	25.0	540.0	110.0	3%	665.1	8.3	0.1086	0.0014	0.891	0.047	0.0601	0.0033
D20b1_98	359.5	4.9	373.7	7.7	436.0	38.0	4%	359.5	4.9	0.05731	0.0008	0.444	0.011	0.05595	0.00099
D20b1_99	361.4	4.6	365.8	7.2	383.0	44.0	1%	361.4	4.6	0.05768	0.00076	0.435	0.01	0.0546	0.0011
D20b1_100	550.2	3.7	542.5	8.0	505.0	42.0	1%	550.2	3.7	0.08911	0.00062	0.706	0.014	0.0577	0.0011
D20b1_101	325.4	3.0	327.0	11.0	319.0	83.0	0%	325.4	3.0	0.05177	0.00048	0.379	0.015	0.0531	0.0021
D20b1_102	334.5	3.5	398.0	17.0	760.0	100.0	16%	334.5	3.5	0.05326	0.00057	0.482	0.024	0.066	0.0032
D20b1_103	230.7	7.5	267.0	12.0	645.0	85.0	14%	230.7	7.5	0.0365	0.0012	0.303	0.015	0.0623	0.0026
D20b1_104	502.9	8.8	578.0	11.0	864.0	56.0	13%	502.9	8.8	0.0811	0.0015	0.77	0.019	0.0682	0.0018
D20b1_105	318.4	3.2	310.4	8.8	278.0	71.0	3%	318.4	3.2	0.05064	0.00052	0.36	0.012	0.0522	0.0017
D20b1_106	663.0	4.8	657.2	7.8	635.0	35.0	1%	663.0	4.8	0.10834	0.00082	0.911	0.014	0.06102	0.00099
D20b1_107	445.1	5.6	473.0	11.0	599.0	63.0	6%	445.1	5.6	0.07151	0.00092	0.594	0.016	0.0607	0.0018
D20b1_108	334.8	7.0	382.0	12.0	785.0	70.0	12%	334.8	7.0	0.0533	0.0012	0.459	0.018	0.0655	0.0022
D20b1_109	123.9	3.6	199.0	23.0	810.0	260.0	38%	123.9	3.6	0.01941	0.00057	0.233	0.03	0.091	0.012
D20b1_110	1976.0	14.0	1940.0	14.0	1900.0	28.0	2%	1940.0	14.0	0.3579	0.003	5.761	0.092	0.1163	0.0018
D20b1_111	420.8	4.0	419.6	9.1	415.0	57.0	0%	420.8	4.0	0.06747	0.00066	0.513	0.013	0.0559	0.0015
D20b1_112	797.6	6.9	794.0	13.0	775.0	48.0	0%	797.6	6.9	0.1317	0.0012	1.179	0.027	0.0652	0.0015
D20b1_113	369.9	6.1	872.0	30.0	2482.0	78.0	58%	369.9	6.1	0.0591	0.001	1.399	0.07	0.1684	0.0075
D20b1_114	972.4	8.4	968.0	11.0	946.0	27.0	0%	972.4	8.4	0.1628	0.0015	1.59	0.027	0.07049	0.00092
D20b1_115	590.1	5.1	574.0	13.0	501.0	63.0	3%	590.1	5.1	0.09581	0.00088	0.756	0.022	0.0579	0.0017
D20b1_116	1661.0	12.0	1662.0	15.0	1642.0	33.0	0%	1662.0	15.0	0.294	0.0024	4.112	0.076	0.1011	0.0018
D20b1_117	1393.0	12.0	1356.0	17.0	1290.0	42.0	3%	1393.0	12.0	0.2411	0.0022	2.798	0.063	0.0842	0.0018
D20b1_118	792.4	7.8	876.0	22.0	1092.0	67.0	10%	792.4	7.8	0.1308	0.0014	1.399	0.055	0.077	0.0026
D20b1_119	514.5	6.7	500.0	12.0	445.0	59.0	3%	514.5	6.7	0.083	0.0011	0.637	0.019	0.0565	0.0015
D20b1_120	584.9	9.0	639.0	12.0	809.0	54.0	8%	584.9	9.0	0.0949	0.0015	0.873	0.022	0.0663	0.0017
D20b1_121	637.8	4.6	630.1	9.9	606.0	44.0	1%	637.8	4.6	0.10401	0.00079	0.858	0.018	0.0604	0.0012
D20b1_122	661.1	7.3	822.0	30.0	1255.0	93.0	20%	661.1	7.3	0.108	0.0013	1.293	0.07	0.085	0.0042
D20b1_123	630.1	8.3	616.0	12.0	544.0	51.0	2%	630.1	8.3	0.1027	0.0014	0.836	0.021	0.059	0.0013
D20b1_124	966.1	5.5	959.0	7.7	955.0	24.0	1%	966.1	5.5	0.1617	0.00099	1.572	0.02	0.07093	0.00082
D20b1_125	1743.9	9.7	1717.0	11.0	1678.0	25.0	2%	1717.0	11.0	0.3107	0.002	4.419	0.06	0.1031	0.0013
D20b1_126	315.6	2.0	316.4	5.2	300.0	43.0	0%	315.6	2.0	0.05018	0.00032	0.3661	0.0071	0.05238	0.00098
D20b1_127	2587.0	19.0	2561.0	12.0	2540.0	16.0	1%	2561.0	12.0	0.4936	0.0044	11.47	0.15	0.168	0.0016

D20b1_128	2622.0	12.0	2603.4	8.9	2594.0	16.0	1%	2603.4	8.9	0.5017	0.0028	11.99	0.11	0.1739	0.0016
D20b1_129	1969.6	9.5	1957.0	11.0	1948.0	21.0	1%	1957.0	11.0	0.3574	0.002	5.878	0.071	0.1196	0.0014
D20b1_130	587.2	5.2	594.0	11.0	598.0	52.0	1%	587.2	5.2	0.09539	0.00088	0.795	0.019	0.0607	0.0014
D20b1_131	510.6	5.5	529.0	11.0	587.0	54.0	3%	510.6	5.5	0.08246	0.00092	0.68	0.019	0.0602	0.0015
D20b1_132	318.7	2.3	313.9	7.5	272.0	60.0	2%	318.7	2.3	0.05069	0.00037	0.3622	0.0099	0.0522	0.0014
D20b1_133	463.1	3.7	468.0	11.0	455.0	64.0	1%	463.1	3.7	0.0745	0.00062	0.588	0.017	0.0568	0.0017
D20b1_134	489.2	3.6	489.8	8.7	492.0	51.0	0%	489.2	3.6	0.07885	0.00061	0.622	0.014	0.0577	0.0014
D20b1_135	520.5	3.8	529.9	9.4	585.0	47.0	2%	520.5	3.8	0.0841	0.00063	0.684	0.016	0.0597	0.0014
D20b1_136	643.6	6.3	683.0	19.0	818.0	80.0	6%	643.6	6.3	0.105	0.0011	0.972	0.038	0.0671	0.0026
D20b1_137	1473.0	15.0	1514.0	17.0	1578.0	34.0	3%	1514.0	17.0	0.2566	0.0029	3.451	0.074	0.0979	0.0018
D20b1_138	469.5	3.7	466.0	11.0	417.0	66.0	1%	469.5	3.7	0.07556	0.00063	0.58	0.018	0.0561	0.0017
D20b1_139	464.5	5.6	493.0	14.0	615.0	77.0	6%	464.5	5.6	0.0746	0.00093	0.634	0.023	0.061	0.0021
D20b1_140	1415.0	22.0	1465.0	23.0	1548.0	55.0	3%	1415.0	22.0	0.2459	0.0042	3.206	0.092	0.0971	0.0028
D20b1_141	493.2	7.9	523.5	7.6	674.0	34.0	6%	493.2	7.9	0.0796	0.0013	0.673	0.013	0.0623	0.001
D20b1_142	559.3	5.8	540.0	15.0	433.0	73.0	4%	559.3	5.8	0.09066	0.00098	0.702	0.025	0.0559	0.002
D20b1_143	946.2	5.5	927.0	10.0	894.0	31.0	2%	946.2	5.5	0.15812	0.00098	1.496	0.024	0.0691	0.0011
D20b1_144	463.8	4.0	534.0	11.0	823.0	51.0	13%	463.8	4.0	0.07461	0.00067	0.69	0.018	0.0666	0.0016
D20b1_145	368.2	3.8	350.0	12.0	236.0	83.0	5%	368.2	3.8	0.05879	0.00063	0.416	0.016	0.0512	0.002
D20b1_146	455.3	4.6	455.0	11.0	447.0	64.0	0%	455.3	4.6	0.07321	0.00076	0.566	0.018	0.0564	0.0016
D20b1_147	726.2	7.3	733.0	12.0	744.0	47.0	1%	726.2	7.3	0.1192	0.0013	1.061	0.025	0.0647	0.0014
D20b1_148	467.7	3.7	464.0	10.0	460.0	59.0	1%	467.7	3.7	0.07526	0.00061	0.578	0.016	0.0566	0.0015
D20b1_149	561.3	9.4	589.0	12.0	730.0	39.0	5%	561.3	9.4	0.091	0.0016	0.786	0.02	0.0638	0.0012
D20b1_150	2430.0	12.0	2539.0	6.9	2617.0	10.0	4%	2539.0	6.9	0.458	0.0027	11.187	0.084	0.1763	0.0011
D20b1_151	553.9	4.3	557.0	10.0	559.0	52.0	1%	553.9	4.3	0.08974	0.00073	0.732	0.017	0.0591	0.0014
D20b1_152	300.2	2.9	321.4	6.1	483.0	48.0	7%	300.2	2.9	0.04767	0.00047	0.3727	0.0083	0.057	0.0013
D20b1_153	589.3	5.1	589.9	7.6	616.0	35.0	0%	589.3	5.1	0.09574	0.00086	0.79	0.014	0.06051	0.00098
D20b1_154	1757.0	17.0	1960.0	12.0	2208.0	16.0	10%	1960.0	12.0	0.3133	0.0034	5.887	0.077	0.1382	0.0012
D20b1_155	538.0	19.0	659.0	34.0	1100.0	110.0	18%	538.0	19.0	0.087	0.0031	0.937	0.064	0.0775	0.0041
D20b1_156	679.8	5.8	677.0	11.0	676.0	47.0	0%	679.8	5.8	0.1112	0.001	0.947	0.021	0.0622	0.0013
D20b1_157	437.7	5.6	450.0	18.0	480.0	100.0	3%	437.7	5.6	0.07029	0.00093	0.568	0.028	0.0585	0.0029
D20b1_158	2817.0	23.0	2760.0	17.0	2714.0	29.0	2%	2760.0	17.0	0.5483	0.0056	14.15	0.25	0.1881	0.0033
D20b1_159	1315.0	23.0	1562.0	20.0	1902.0	16.0	16%	1562.0	20.0	0.2265	0.0043	3.683	0.091	0.1167	0.001

D20b1_160	321.2	3.7	447.0	18.0	1113.0	81.0	28%	321.2	3.7	0.0511	0.00061	0.567	0.029	0.0794	0.0033
D20b1_161	449.2	3.5	482.9	8.8	639.0	52.0	7%	449.2	3.5	0.07217	0.00059	0.61	0.014	0.0618	0.0015
D20b1_162	926.6	8.5	985.0	15.0	1125.0	44.0	6%	926.6	8.5	0.1545	0.0015	1.633	0.038	0.0772	0.0017
D20b1_163	555.5	9.8	540.0	17.0	495.0	75.0	3%	555.5	9.8	0.0901	0.0017	0.703	0.029	0.0583	0.002
D20b1_164	586.3	5.3	580.0	14.0	530.0	69.0	1%	586.3	5.3	0.09524	0.0009	0.774	0.025	0.0592	0.0019
D20b1_165	910.0	18.0	876.0	23.0	816.0	59.0	4%	910.0	18.0	0.1518	0.0032	1.388	0.053	0.0674	0.0019
D20b1_166	554.9	4.8	576.8	7.7	663.0	41.0	4%	554.9	4.8	0.08979	0.00081	0.763	0.014	0.0615	0.0011
D20b1_167	1614.0	18.0	1657.0	17.0	1711.0	25.0	3%	1657.0	17.0	0.2846	0.0036	4.121	0.086	0.105	0.0014
D20b1_168	893.1	9.3	897.0	19.0	921.0	69.0	0%	893.1	9.3	0.1485	0.0017	1.398	0.045	0.069	0.0023
D20b1_169	1520.0	12.0	1559.0	12.0	1616.0	27.0	3%	1559.0	12.0	0.2659	0.0024	3.65	0.053	0.0995	0.0014
D20b1_170	666.0	14.0	956.0	20.0	1714.0	30.0	30%	666.0	14.0	0.109	0.0024	1.586	0.052	0.1052	0.0017
D20b1_171	307.9	2.7	311.1	5.6	307.0	44.0	1%	307.9	2.7	0.0489	0.00044	0.3579	0.0074	0.0526	0.0011
D20b1_172	293.0	4.1	332.9	9.8	620.0	74.0	12%	293.0	4.1	0.04651	0.00067	0.389	0.013	0.0615	0.0021
D20b1_173	1273.0	39.0	1664.0	40.0	2157.0	35.0	23%	1664.0	40.0	0.2171	0.0074	4.1	0.2	0.1355	0.0025
D20b1_174	510.6	9.8	497.0	14.0	544.0	64.0	3%	510.6	9.8	0.0825	0.0016	0.629	0.023	0.0591	0.0018
D20b1_175	453.0	3.8	456.4	9.0	476.0	55.0	1%	453.0	3.8	0.07282	0.00064	0.565	0.014	0.0573	0.0015

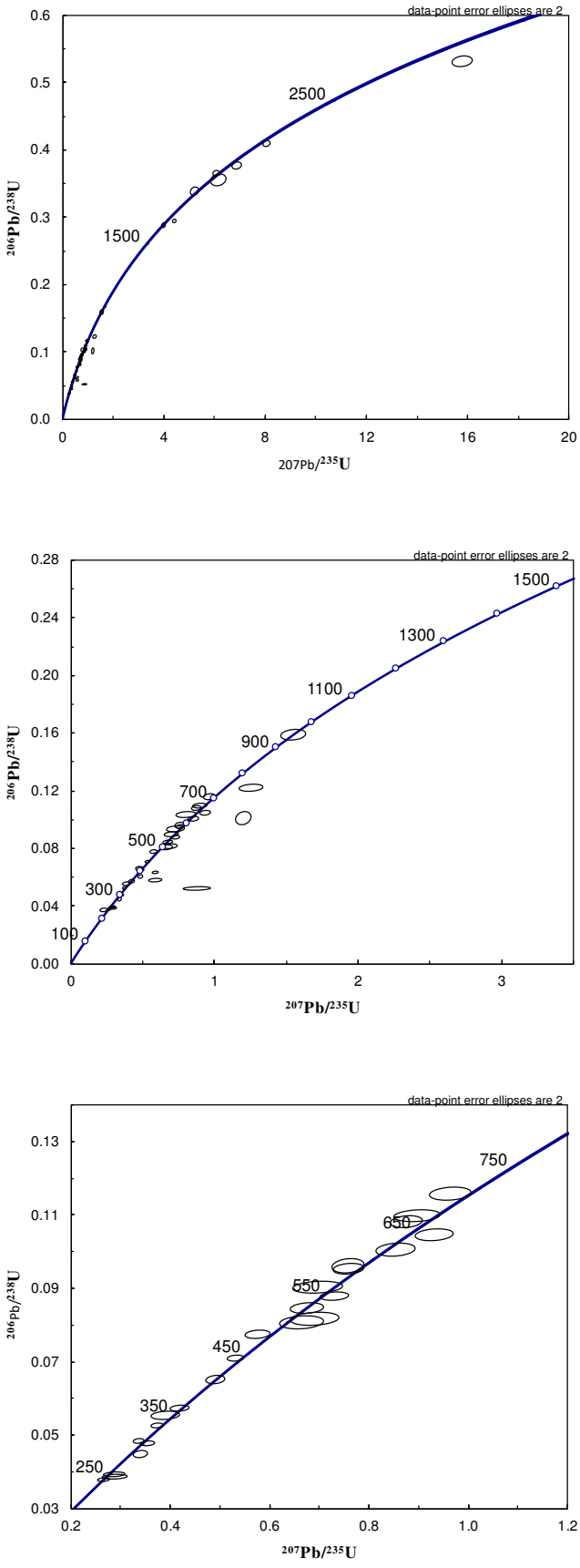

Appendix 43: Concordia plots for sample B1. Bottom: concordant ages only between 250 and 800 Ma. Middle: all ages between 0 and 1500 Ma. Top: all ages between 0 and 3000 Ma.

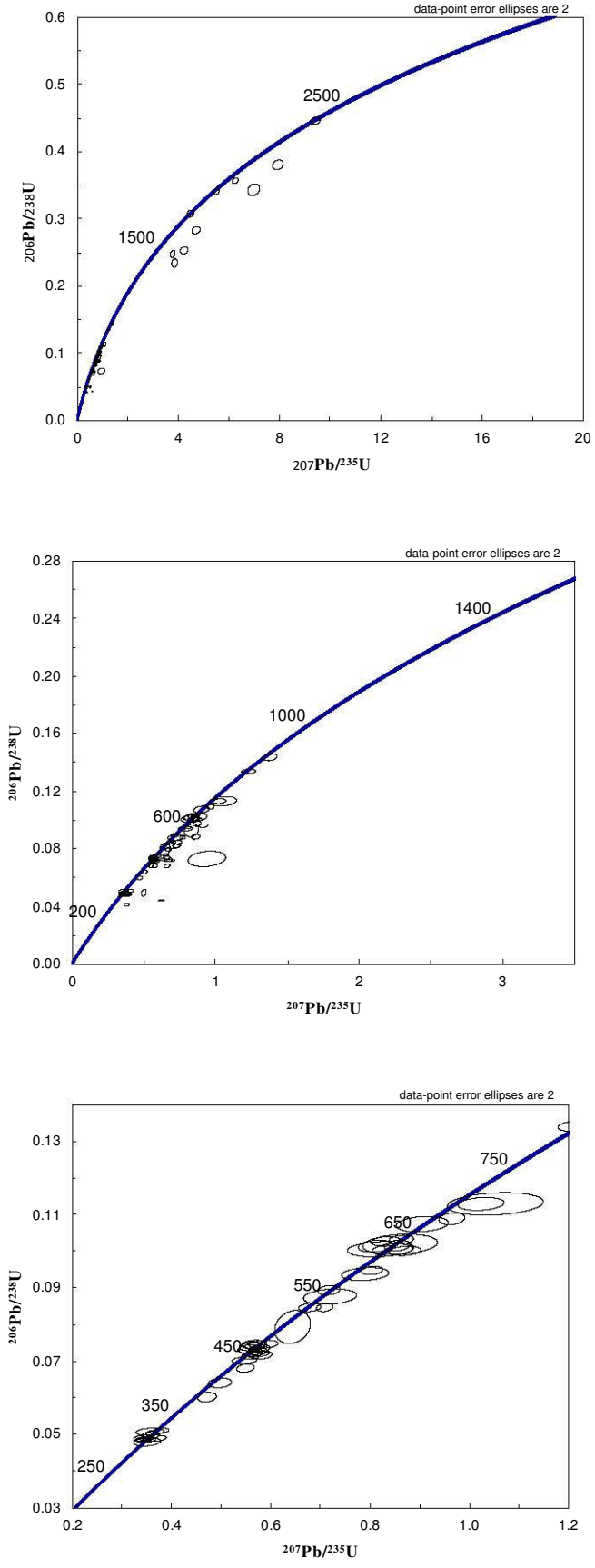

Appendix 44: Concordia plots for sample B2. Bottom: concordant ages only between 250 and 800 Ma. Middle: all ages between 0 and 1500 Ma. Top: all ages between 0 and 3000 Ma.

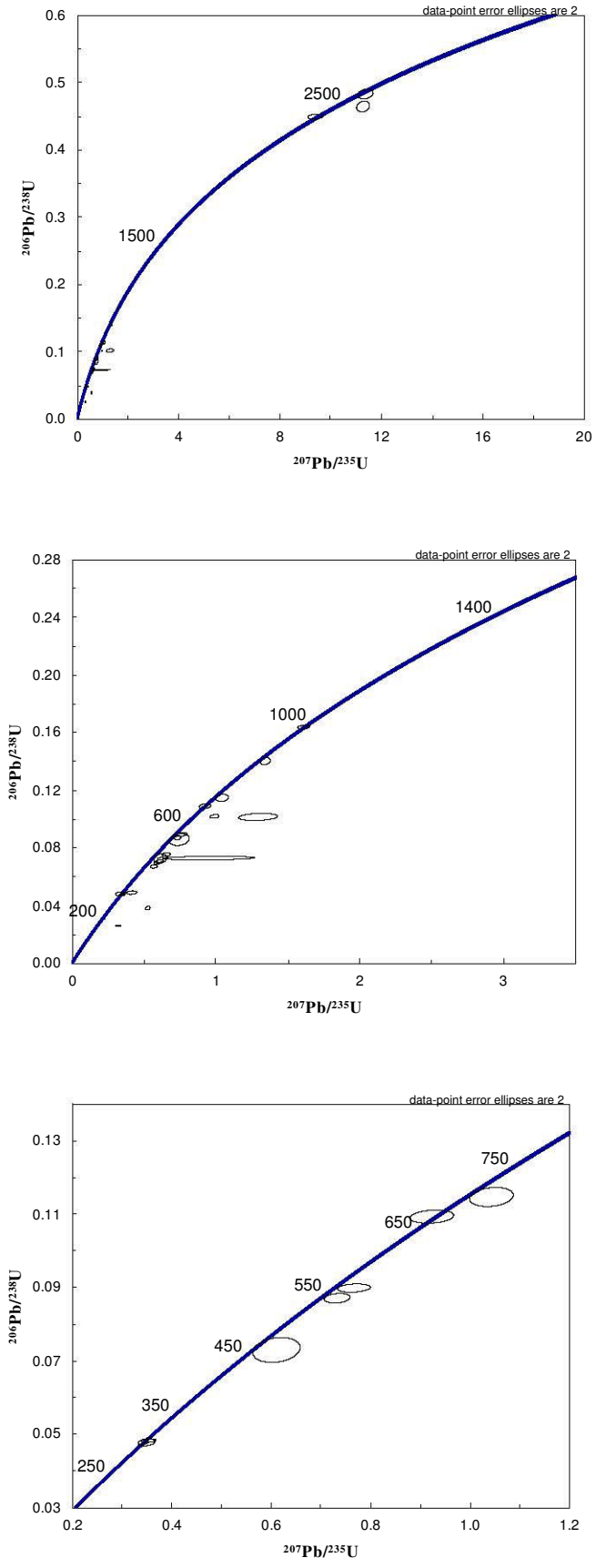

Appendix 45: Concordia plots for sample B3. Bottom: concordant ages only between 250 and 800 Ma. Middle: all ages between 0 and 1500 Ma. Top: all ages between 0 and 3000 Ma.

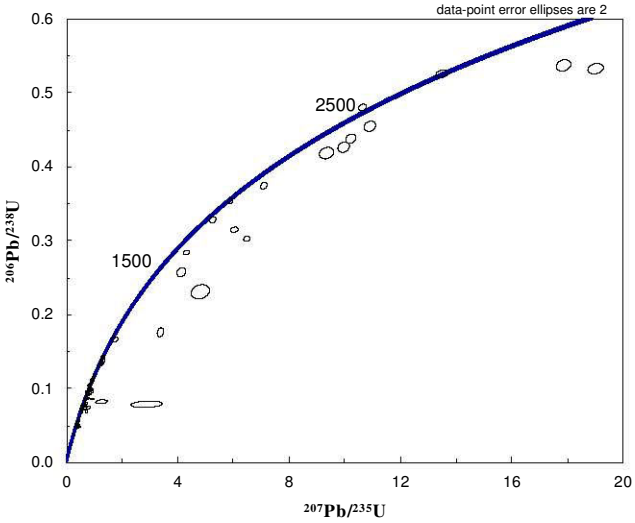

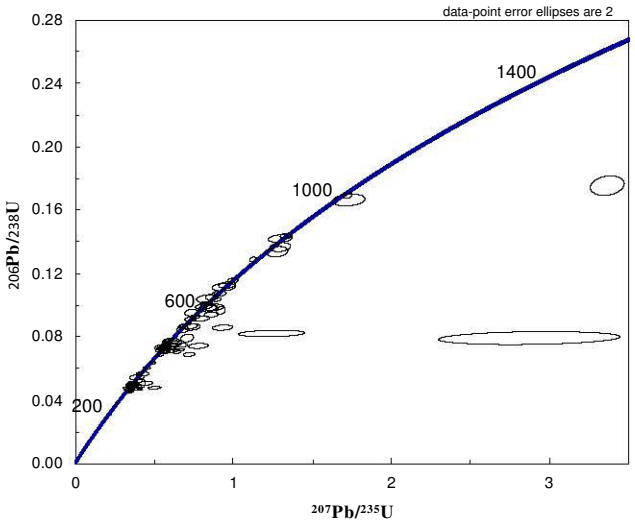

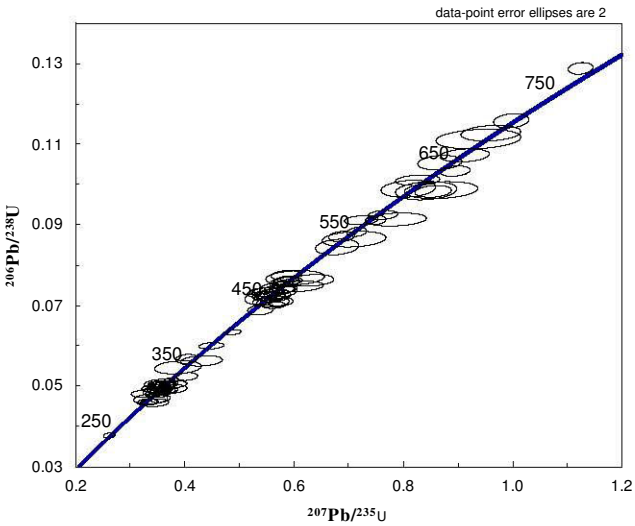

Appendix 46: Concordia plots for sample B4. Bottom: concordant ages only between 250 and 800 Ma. Middle: all ages between 0 and 1500 Ma. Top: all ages between 0 and 3000 Ma.

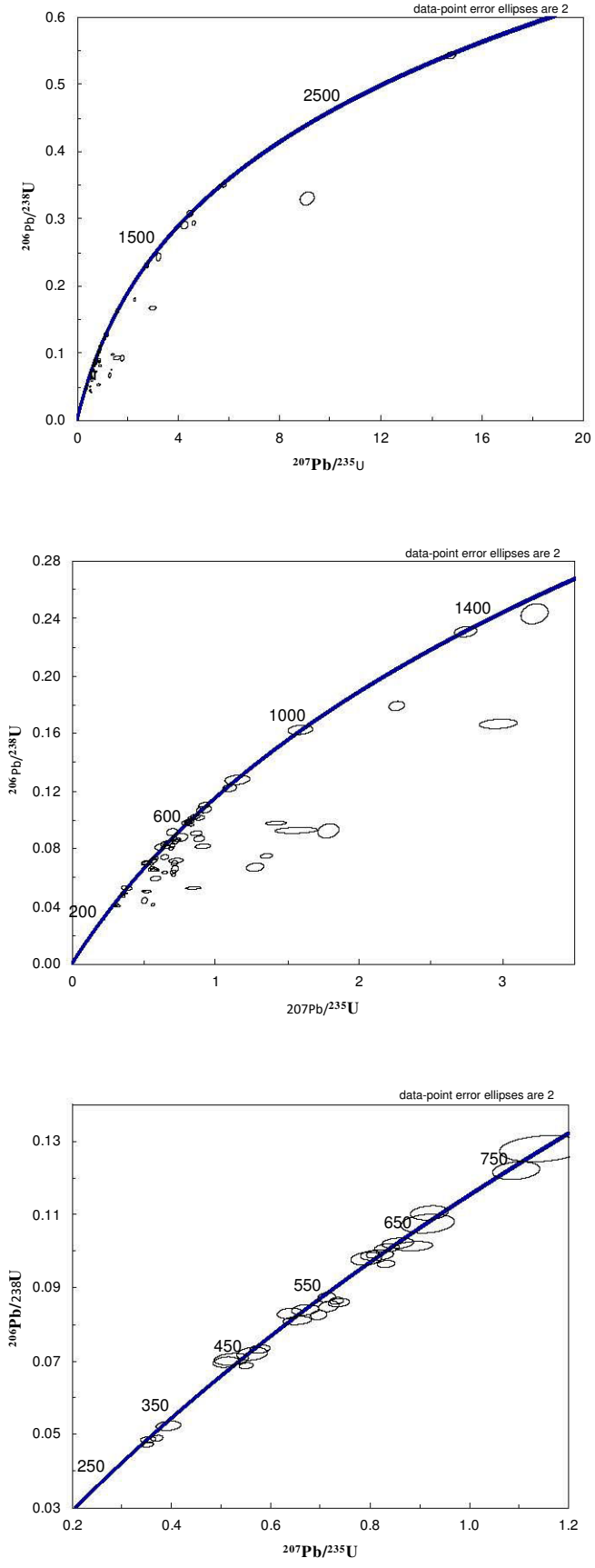

Appendix 47: Concordia plots for sample B6. Bottom: concordant ages only between 250 and 800 Ma. Middle: all ages between 0 and 1500 Ma. Top: all ages between 0 and 3000 Ma.

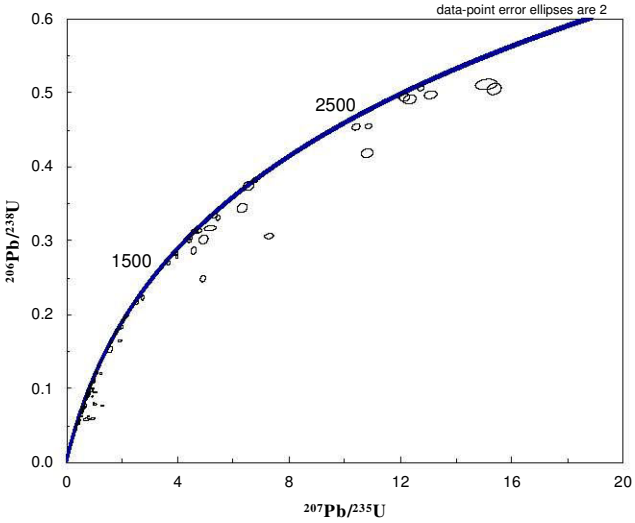

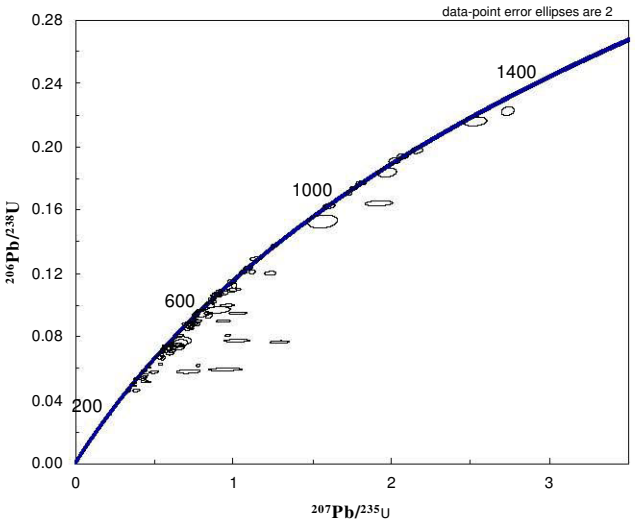

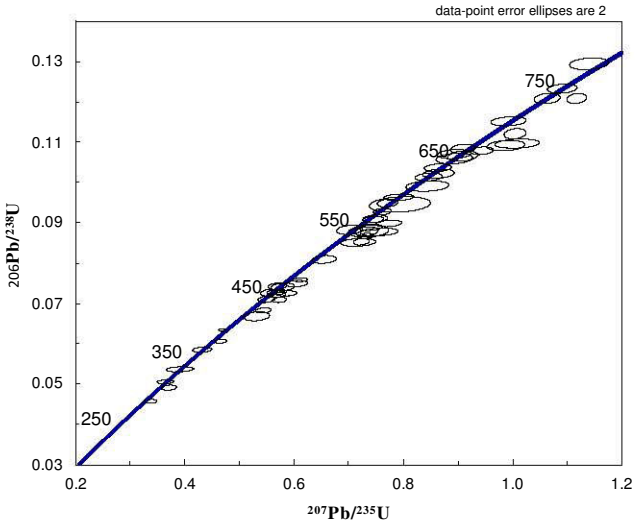

Appendix 48: Concordia plots for sample D15. Bottom: concordant ages only between 250 and 800 Ma. Middle: all ages between 0 and 1500 Ma. Top: all ages between 0 and 3000 Ma.

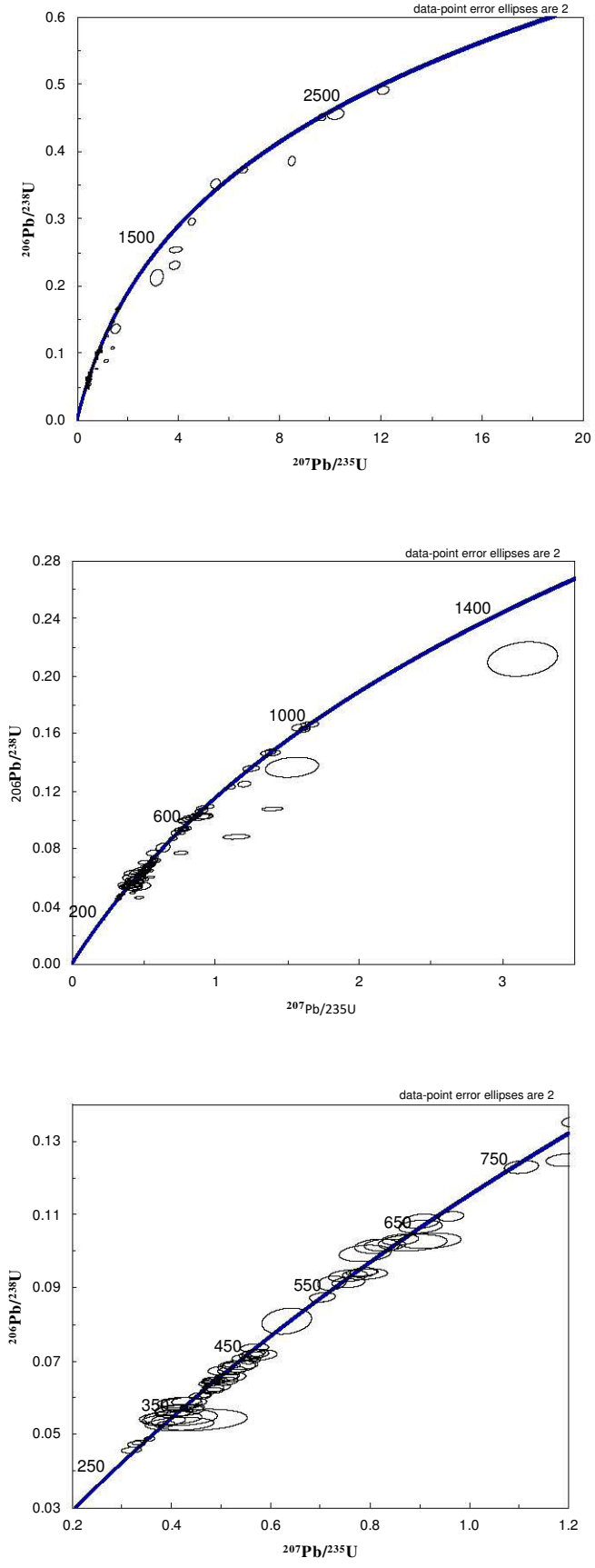

Appendix 49: Concordia plots for sample D17. Bottom: concordant ages only between 250 and 800 Ma. Middle: all ages between 0 and 1500 Ma. Top: all ages between 0 and 3000 Ma.

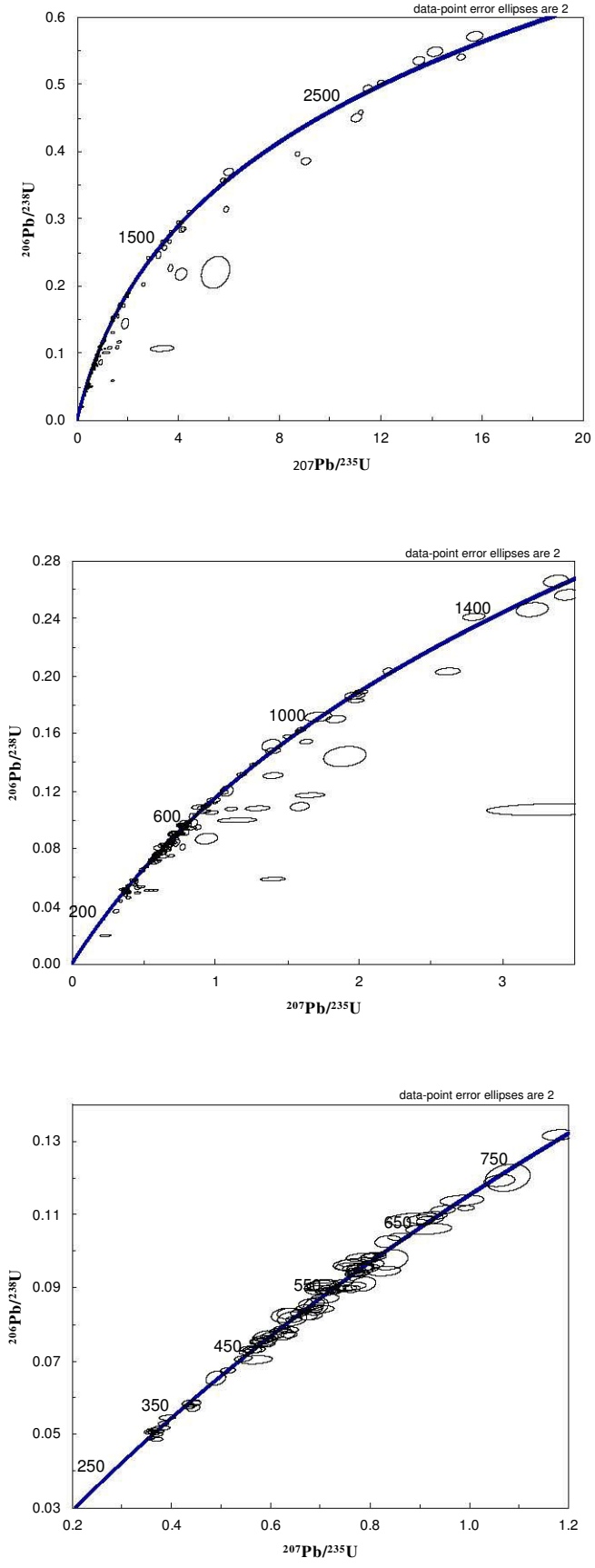

Appendix 50: Concordia plots for sample D20. Bottom: concordant ages only between 250 and 800 Ma. Middle: all ages between 0 and 1500 Ma. Top: all ages between 0 and 3000 Ma.

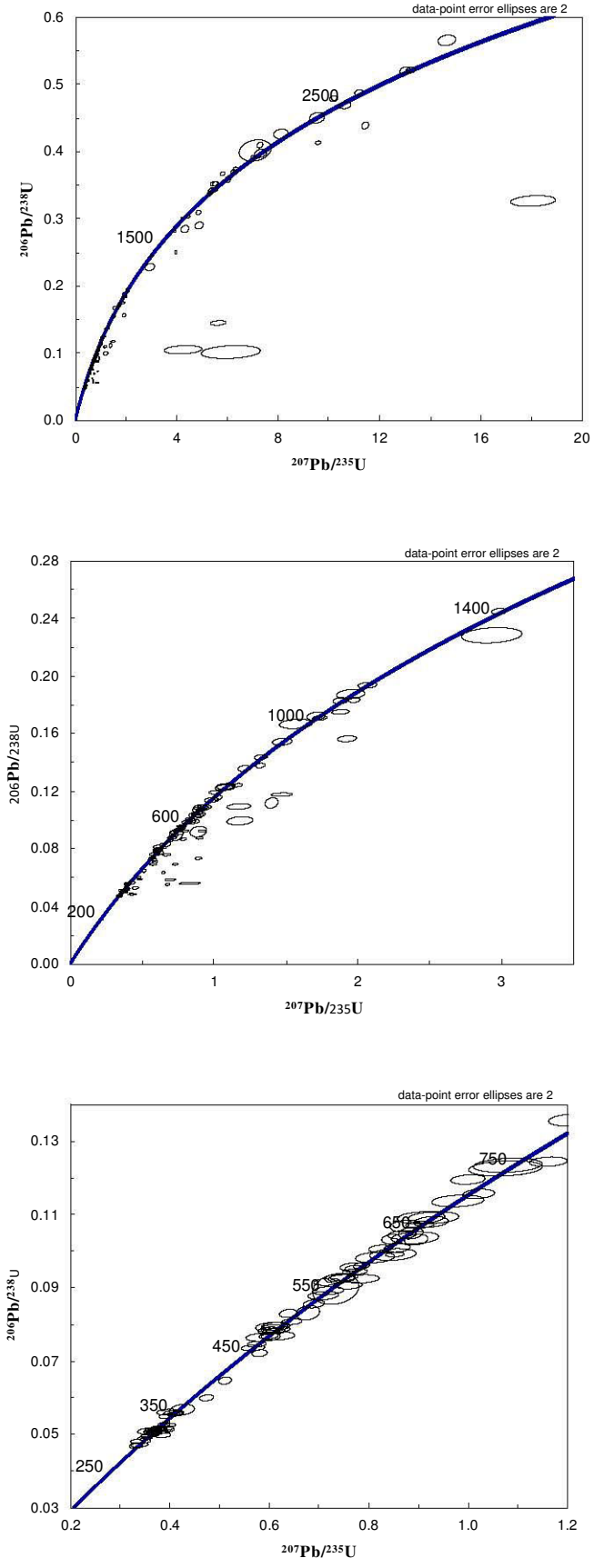

Appendix 51: Concordia plots for sample D21. Bottom: concordant ages only between 250 and 800 Ma. Middle: all ages between 0 and 1500 Ma. Top: all ages between 0 and 3000 Ma.

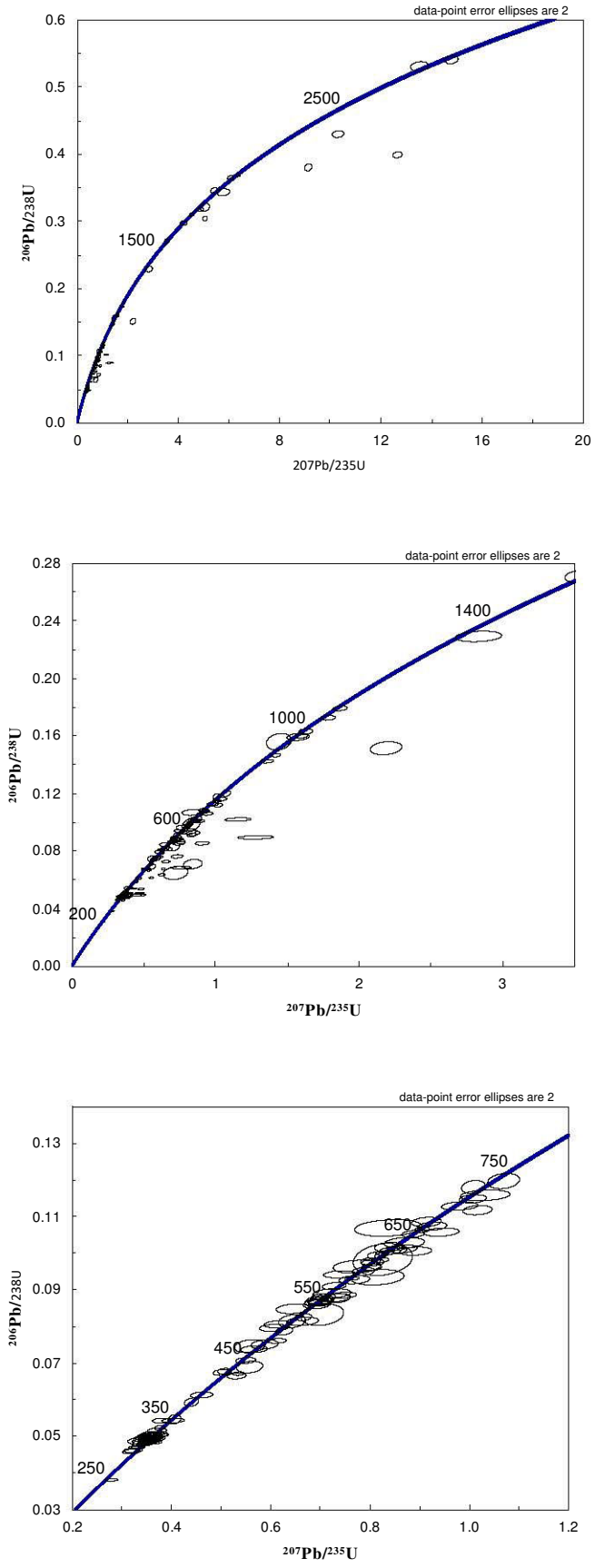

Appendix 52: Concordia plots for sample D22. Bottom: concordant ages only between 250 and 800 Ma. Middle: all ages between 0 and 1500 Ma. Top: all ages between 0 and 3000 Ma.

RECONSTRUCTION DE LA DYNAMIQUE PRÉCOCE D'UN OROGÈNE
MISE EN ÉVIDENCE DE LA TRANSITION RIFTING-COLLISION DANS LE SYSTÈME EST-PYRÉNÉEN (FRANCE) PAR LA GÉO-THERMOCHRONOLOGIE

Les orogènes collisionnels sont classiquement décrits comme le résultat de l'accrétion continentale de marges proximales. Cette accrétion conduit à la surrection des reliefs et à l'export important de produits d'érosion dans les bassins d'avant-pays qui les jalonnent. Dans ce schéma géodynamique sont alors uniquement considérés les domaines pré-orogéniques les moins déformés. Pourtant, un nombre croissant d'évidences géologiques de terrain indiquent la conservation voire la réutilisation de structures héritées de la phase extensive précédant la convergence et la collision au coeur des orogènes. À partir de l'étude géo-thermochronométrique de la bordure orientale du domaine hyper-étiré nord-pyrénéen (massif de l'Agly, Zone Nord Pyrénéenne) et de son avant-pays précoce (synclinal de Rennes-les-Bains, Bassin Aquitain), cette thèse a pour objectifs de décrire l'évolution d'une marge distale au cours des premiers stades de convergence, de quantifier les processus source-réceptacle associés et d'apporter des contraintes temporelles et paléogéographiques quant à la création des tout premiers reliefs pyrénéens issus de son inversion. Grâce à l'utilisation du multi-thermochronomètre (U-Th)/He sur zircon et apatite, deux épisodes de refroidissement sont mis en évidence dans le prisme nord-pyrénéen (Campano-Maastrichtien et Eocène), chacun d'eux synchrone d'une phase de subsidence dans le bassin d'avant-pays. J'ai ainsi pu proposer un modèle équilibré d'évolution d'une marge distale hyper-amincie par inversion de structures héritées, chevauchements de socle et sous-placage continental se matérialisant par une signature thermochronologique claire de refroidissement sans érosion au début de la convergence. L'absence d'enregistrement de refroidissement au Paléocène par l'arrêt prématuré de l'inversion précoce dans le prisme nord-pyrénéen indique l'absence significative d'érosion et la position bordière de ce prisme par rapport à un édifice déjà construit plus à l'est à cette époque. Pour caractériser cet édifice aujourd'hui disparu du fait de l'ouverture du Golfe du Lion, j'ai utilisé une approche détritique de double datation in situ (U-Th)/He - U/Pb sur zircon et mis en évidence une histoire de dénudation rapide pendant le Campano-Maastrichtien, caractéristique de la création d'une topographie précoce. Ce travail montre pour la première fois clairement la migration progressive de la déformation d'est en ouest par l'inversion de structures héritées au début de la convergence pyrénéenne, ce qui suggère l'existence d'un domaine ouvert à l'est à la fin de l'épisode extensif précédant la convergence. Cette étude met en avant le rôle de l'architecture des systèmes hyper-amincis dans la formation des orogènes collisionnels et confirme les liens étroits existant entre un orogène et ses bassins d'avant-pays.

Mots-clés : Pyrénées, orogène collisionnel, rétro-prisme précoce, rétro-bassin d'avant-pays précoce, transition rifting-collision, héritage, provenance sédimentaire, géo-thermochronologie, (U-Th)/He, U/Pb, zircon, ablation laser, datation *in situ*

RECONSTRUCTION OF EARLY OROGEN DYNAMICS
GEO-THERMOCHRONOLOGICAL EVIDENCE OF THE RIFT-TO-COLLISION TRANSITION IN THE EASTERN PYRENEES (FRANCE)

Collisional orogens are classically described as the result of continental accretion of proximal margins. This accretion leads to the creation of relief and to the important export of erosion products in the directly adjacent foreland basins. In this geodynamic scheme, only the least deformed pre-orogenic domains are considered. However, a growing number of geological field evidences indicate the preservation or even the reuse of structures inherited from the rifting phase preceding convergence and collision within orogens. By conducting a geo-thermochronometric study of the easternmost, inverted hyperextended Aptian-Cenomanian rift system (Agly massif, North Pyrenean Zone) and the adjacent early retroforeland (Rennes-les-Bains syncline, Aquitaine Basin), this thesis aims to describe the evolution of a distal rifted margin during the first stages of convergence, to quantify the associated source-to-sink processes and to provide temporal and paleogeographic constraints regarding the creation of the very first Pyrenean reliefs resulting from inversion of the margin. Using the zircon and apatite (U-Th)/He multi-thermochronometers, I show that the Pyrenean retro-wedge records two clear phases of orogenic cooling, Late Campanian-Maastrichtian and Ypresian-Bartonian, which I relate to early inversion of the distal rifted margin and main collision, respectively. I have thus been able to propose a crustal-scale sequentially restored model for the tectonic and thermal transition from extension to peak orogenesis in the eastern Pyrenees, which suggests that both thrusting and underplating processes contributed to early inversion of the Aptian-Cenomanian rift system. The absence of Paleocene cooling record indicates little to no erosion of the Pyrenean retro-wedge, suggesting the existence of a more easterly source area supplying early retroforeland sediments at this time. To characterize this eastern edifice, which has since been destroyed by the Oligocene-Miocene opening of the Gulf of Lion, I used in situ (U-Th)/He - U/Pb double dating on detrital zircons and show rapid denudation rates during early convergence, characteristic of early topographic growth. This work shows for the first time clearly the progressive migration of deformation from east to west by inversion of inherited structures at the beginning of Pyrenean convergence. This suggests the existence of an open domain in the east at the end of the rifting phase preceding convergence. This study highlights the role of the architecture of hyper-thinned systems in the formation of collisional orogens and confirms the close links between an orogen and its foreland basins.

Keywords: Pyrenees, collisional orogen, early retro-wedge, early retro-foreland basin, rift-to-collision transition, inheritance, sedimentary provenance, geo-thermochronology, (U-Th)/He, U/Pb, zircon, laser ablation, *in situ* dating